Table of Contents for 17 Volumes of C. Connor Scientific Notebook No. 115E: Igneous Activity	
1 of 17	Finite Difference Model Used to Model Heat Transfer in a Cooling Cinder Cone Must be Evaluated by Comparison to an Analytic Solution for a Simple Geometry
2 of 17	Investigation of the Dependence of Alkalinity Index on Spatio-Temporal Recurrence Rate in the Springerville Volcanic Field
3 of 17	Self-Potential Data Collected at Cerro Negro Cinder Cone During the 1995 Eruption
4 of 17	Ground Magnetic Data collected in Crater Flat and the Amargosa Desert
5 of 17	Procedure for Measuring Radon Gas Concentration in Soils in the Field
6 of 17	Structure and Volcanism: Results of Looking at the Ratio of High Dilation Tendency Faults to all Faults on Volcanism Probability
7 of 17	Development of Radiation Boundary Condition
8 of 17	Aero Magnetic Anomalies and Volcanism
9 of 17	Summary of CNWRA Workshop on the Consequences of Volcanic Activity
10 of 17	Codes and Procedures Used by CNWRA to Perform a Probabilistic Volcanic Hazard Assessment for Proposed Yucca Mountain, Nevada, Repository
11 of 17	Probabilistic Volcanic Hazard Assessment Identifying Specific Hazards and Estimating the Probability of their Occurrence
12 of 17	Assessment of Volcanic Hazards Programs
13 of 17	Calculation of Expected Magnetic Field Anomalies Produced by Buried Geologic Structures
14 of 17	Ash Plume, Cluster, Seismic Hazard, and Cluster Codes Development; Physical Analog Models
15 of 17	This Volume Is Not Included because it Contains Non-U.S. Nuclear Regulatory Commission-Yucca Mountain Material
16 of 17	Ash Plume Code Development, Testing, and Summary; Ash Dispersion Modeling
17 of 17	Development of Steady-State Code for Magma Flow

1817

Heat Transfer Problem (Finite Cylinder)

Chuck Connor

Chuck Connor

Scientific Notebook No. 115

6/26/98

The finite difference model used to model heat transfer in a cooling cinder cone must be evaluated by comparison to an analytic solution for a simple geometry. A vertical cylinder is used for this purpose.

The finite difference solution to the heat conduction equation in radial coordinates must be evaluated using simple boundary conditions. The method formulated to do this is to simplify the geometry to the extent that an analytical solution can be determined. In this case radial coordinates are used - which introduces a problem - as the solution to heat conduction equations in radial coordinates are approximated using Fourier series. The methods used here are described in detail in White (White, F.M. 1988. Heat and Mass Transfer, Addison-Wesley Publishing Co.: Reading, Ma: pages 205-225). Also see Ozisik (Ozisik, M.N., 1980. Heat Conduction. John Wiley and Sons, New York, NY).

1.0 Transient Conduction Solution for Cylinder

1.1 Heisler Approximation (Infinite Cylinder)

The heat conduction equation for an infinite cylinder that is suddenly immersed in a solution (air - water, etc.) is:

$$\frac{\partial T}{\partial t} = \frac{\alpha}{r}\frac{\partial}{\partial r}\left(r\frac{\partial T}{\partial r}\right) \qquad \text{(EQ 1)}$$

Carslaw (Carslaw, H.S., 1921. Introduction to the Mathematical Theory of the Conduction of Heat in Solids, MacMillian and Co., London) discussed the solution to this equation using Fourier series. Heisler (Heisler, M.P. 1947. Temperature charts for induction and constant temperature heating, ASME Transactions, 69: 227-236.) found that the temperature at the center point of the cylinder can be described by a single term in the Fourier series as long as the calculation is made a comparatively long time after immer-

sion. This time can be written dimensionlessly is terms of the thermal diffusivity of the cylinder (α), time elapsed (t), and the radius of the cylinder (r_o):

$$t^\circ = \frac{\alpha t}{r_0} \qquad \text{(EQ 2)}$$

The temperature at the center point (defined as $r = 0, k = 0$) is given by:

$$T = T_i C_1 e^{-\beta^2 t^\circ} \qquad \text{(EQ 3)}$$

where T_i is the initial temperature of the cylinder and it is assumed that the temperature of the fluid into which the cylinder is immersed is 0°C. The constants C_1 and β_1 are determined by the Biot number

$$Bi = \frac{h_o r_o}{k} \qquad \text{(EQ 4)}$$

where h_o is the heat transfer coefficient and k is the thermal conductivity.Heisler provides look-up table for C_1 and β_1 given Bi (the values used here were taken from White (1988, page 210) and were checked against values from Ozisik.

1.2 Example Calculation for Infinite Cylinder

This is a sample calculation using the above equations for heat conduction in an infinite cylinder:

k = 93.75 W/mK, α = 2e-5 m^2/s, r = 15m, ho = 25 W/mK^2,

To = 0, Ti = 1200°C, t = 5e6 s

In this case Bi = 4 and t° = 0.444. From the Heisler tables : C_1 = 1.4698 and β_1 = 1.9081. The dimensionless temperature = 0.291 and given To = 0, Ti = 1200°C, the temperature at the center point has cooled to 349.7°C after t = 5e6 s.

The True Basic code written for these calculations is:

- let k = 93.75
- let t = 5e6
- let alpha = 2e-5
- let h0 = 25
- let r0 = 15
-
-
- let t0 = 0

```
• let ti = 1200
•
• let bi = h0*r0/k
• print "bi = ";bi
•
• let b1 = 1.9081  ! this must be looked up in the Tables
• let c1 = 1.4698
• let tstar = alpha*t/r0^2
• print "t* = ";tstar
• let thetc = c1*exp(-(b1^2)*tstar)
•
• print "thetc = ";thetc
•
• print "temperature at centerline (infinite) = ";thetc*ti
•
• end
```

According to White (1988), the use of only a single term in the Fourier series gives better than 1% accuracy at $t^o > 0.2$.

1.3 Modification for Finite Vertical Cylinder

It is possible to modify the above solution for a finite vertical cylinder, although in practise it is clear that nearly all of the heat is lost from the side walls for cylinders that are longer than their radii.

White (1988) truncates the infinite cylinder uses an infinite slab. If 2*L is the total length of the cylinder, then the dimensionless temperature at time = t is:

$$\theta(0,0,t) = P(0,t)\,C(0,t) = \theta(slab)\,\theta(cylinder) \qquad \text{(EQ 5)}$$

$$Bi(slab) = \frac{h_o L}{k} \qquad \text{(EQ 6)}$$

$$t^o = \frac{\alpha t}{L^2} \qquad \text{(EQ 7)}$$

Substituting in values from equations 6 and 7 into 3 gives θ(slab). Using the same parameters as used above, to < 0.2 and the contribution due to heat transfer at the ends of the cylinder is negligible and the Heisler model is a poor approximation of this truncation.

The True basic code for the finite cylinder is :

```
let k = 93.75
let t = 5e6
let alpha = 2e-5
let h0 = 25
let r0 = 15


let t0 = 0
let ti = 1200

let bi = h0*r0/k
print "bi = ";bi

let b1 = 1.9081
let c1 = 1.4698
let tstar = alpha*t/r0^2
print "t* = ";tstar
let thetc = c1*exp(-(b1^2)*tstar)

print "thetc = ";thetc

print "temperature at centerline (infinite) = ";thetc*ti

let L = 50
let bis = h0*L/k
print "bis = ";bis

let b1s = 1.32
let c1s = 1.242
let tstars = alpha*t/L^2
let thetcs = c1s*exp(-(b1s^2)*tstars)
print "t* slab = ";tstars

print "temperature at centerline (finite) = ";thetc*ti*thetc
end
```

2.0 Finite Difference Approximation

The finite difference solution is advantageous because the geometry can be generalized beyond what can be solved analytically, even using approximation methods, such as those of Heisler. Here the finite difference code is developed for a vertical cylinder so the results can be checked against the Heisler solution. This code is then used to investigate heat transfer in cones - a much more complex geometry, but one which can still be assumed to be axially symmetric. The finite difference approximation geometry is as follows:

FIGURE 1. Finite difference geometry

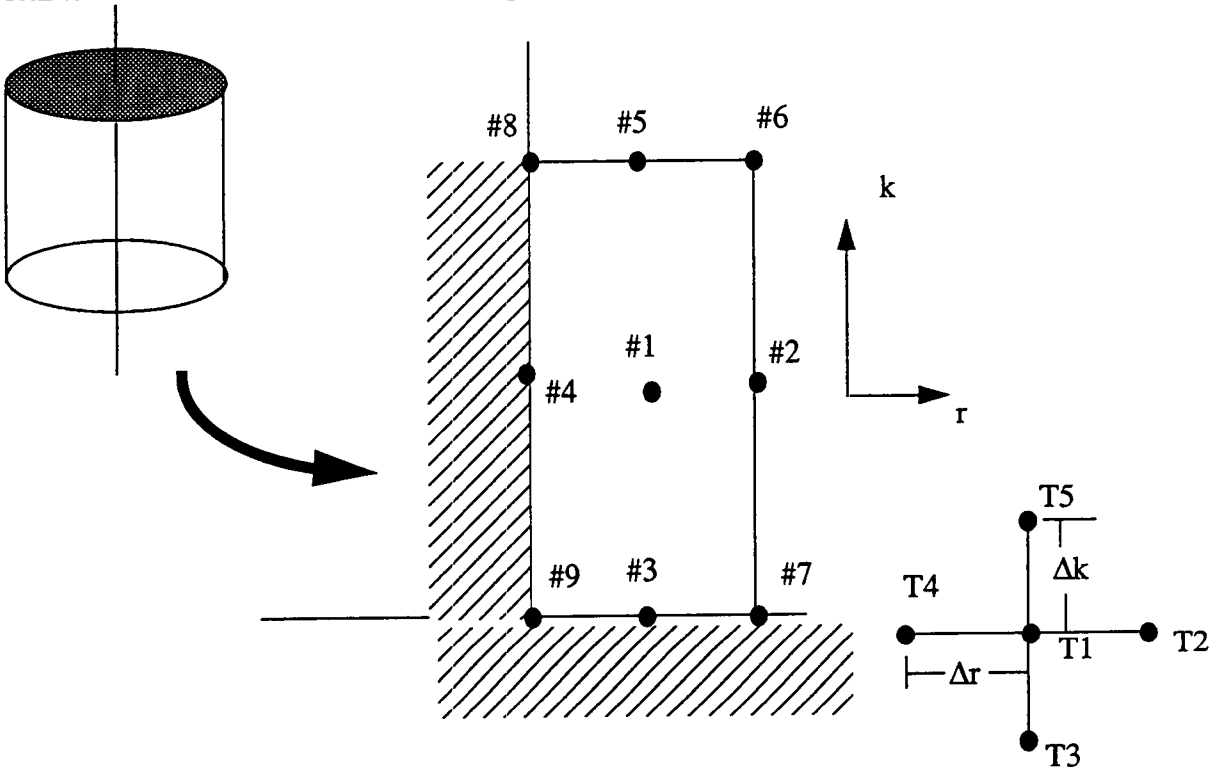

The shape, in this case a vertical cylinder is assumed to be axially symmetric, so a cylindrical coordinate system (r,k) is used. As usual, temperatures are estimated at a point (T1) at time t+1 from the temperature distribution at five points at time t. These points are T1-T5, shown in Figure 1. Insulated boundary conditions exist on two boundaries (#3 and #4) and convective conditions exist on two boundaries (#2 and #5). Because of the geometry imposed by these boundaries, temperatures must be estimated at T1 using

a total of nine different equations. The first (corresponding to point #1, on Figure 1) is simply the temperature in interior nodes. The others are convective boundaries (#2, 5, and #6), insulated boundaries (#3,#4, and #9), or intersections of insulated and convective boundaries (#7 and #8).

2.1 Boundary Conditions

2.1.1 Temperature at Point #1

For point #1: interior point, use the finite difference approximation of

$$\frac{1}{r}\frac{\partial T}{\partial r} + \frac{\partial^2 T}{\partial r^2} + \frac{\partial^2 T}{\partial k^2} = \frac{1}{\alpha}\frac{\partial^2 T}{\partial t^2} \qquad \text{(EQ 8)}$$

is given by Ozisik(1980, page 506-507), this was rederived as:

$$\frac{1}{\Delta r^2}\left\{\left(1-\frac{1}{2i}\right)T5 - 2T1 + \left(1+\frac{1}{2i}\right)T3\right\} + \qquad \text{(EQ 9)}$$
$$\frac{1}{\Delta k^2}\{T4 - 2T1 + T2\} = \frac{1}{\alpha\Delta t}(T1^{t+\Delta t} - T1)$$

where T1-T5, Δr and Δk are geometric variables defined in Figure 1, T is temperature, t is time, Δt is the time step, α is thermal diffusivity, and i is the node number in the r direction such that $r = i\Delta r$.

2.1.2 Temperature at Point #7

Eq.9 must be modified for different boundary conditions. For points #7 and #8 (Figure 1) the value of temperature at T1 at time t + Dt must be calculated using Eq. 9 modified to take into account the insulated condition at T4 and the convective boundary condition at T3. The boundary condition at point #7 (Figure 1) is shown in Figure 2. Points T2 and T1 are located outside the body of the cylinder. Values for temperature at these points

FIGURE 2.

Boundary Condition at Point #7

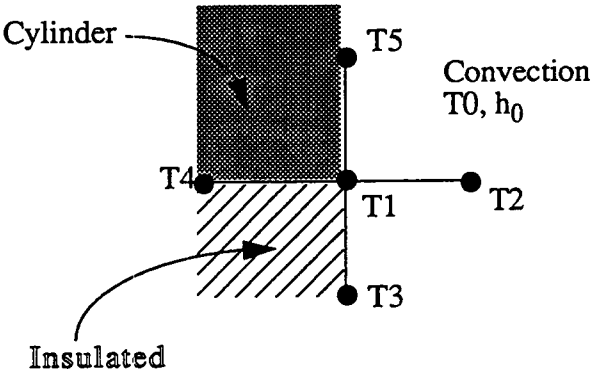

must be taken recast in terms of T4 and T5. The node T2 represents a convective boundary. In this case, temperature can be represented as:

$$k_1 \frac{\partial T}{\partial r} + h_0 T = h_0 T_0 \qquad \text{(EQ 10)}$$

The finite difference approximation for Eq. 10 and the node distribution shown in Figure 2 is:

$$T2 = T4 - \frac{2h_0 \Delta r}{k_1} T1 + \frac{2h_0 \Delta r}{k_1} T_0 \qquad \text{(EQ 11)}$$

where k_1 is the thermal conductivity of the cylinder, h_o is the heat transfer coefficient at the convective boundary and T_o is the temperature of the fluid surrounding the cylinder. At the insulated boundary shown in Figure 2, T3 = T5. So Eq. 9 is modified

$$\frac{1}{\Delta r^2}\left\{\left(1 - \frac{1}{2i}\right)T4 - 2T1 + \left(1 + \frac{1}{2i}\right)\left(T4 - \frac{2h_0 \Delta r}{k_1} T1 - \frac{2h_0 \Delta r}{k_1} T_0\right)\right\} \qquad \text{(EQ 12)}$$
$$+ \frac{1}{\Delta k^2}\{2T5 - 2T1\} = \frac{1}{\alpha \Delta t}(T^{t+\Delta t} - T1)$$

$$\frac{1}{\Delta r^2}(2T4 - 2T1) + \frac{2h_0 \Delta r}{k_1}\left(1 + \frac{1}{2i}\right)(T_0 - T1) \qquad \text{(EQ 13)}$$
$$+ \frac{1}{\Delta k^2}(2T5 - 2T1) = \frac{1}{\alpha \Delta t}(T1^{t+\Delta t} - T1)$$

2.1.3 Temperature at point #4

The temperature of the cylinder along the interior part of the centerline (point(s) #4) is estimated by realizing that Eq.8 is modified at the limit of r = 0:

$$\lim_{r\to 0}\left(\frac{1}{r}\frac{\partial T}{\partial r}\right) = \frac{\partial^2 T}{\partial r^2} \qquad \text{(EQ 14)}$$

As a result the finite difference approximation is modified

$$\frac{4(T2-T1)}{\Delta r^2} + \frac{T3-2T1+T5}{\Delta k^2} = \frac{1}{\alpha\Delta t}(T1^{t+\Delta t}-T1) \qquad \text{(EQ 15)}$$

2.1.4 Temperature at point #9

The temperature at the very center of the cylinder (r=0, k=0) is at an insulated boundary (in the k direction) and at $r \to 0$. The only modification to Eq. 15 is that $\partial T/\partial k = 0$:

$$\frac{4(T2-T1)}{\Delta r^2} + \frac{2(T5-T1)}{\Delta k^2} = \frac{1}{\alpha\Delta t}(T1^{t+\Delta t}-T1) \qquad \text{(EQ 16)}$$

2.1.5 Temperature at point #8

The temperature at the top - center of the cylinder is like that given in Eq. 15, except that a convective boundary exists in the k-direction, together with $r \to 0$.

$$k_1\frac{\partial T}{\partial k} + h_0 T = h_0 T_0 \qquad \text{(EQ 17)}$$

$$T5 = T3 - \frac{2h_0\Delta k}{k_1}T1 + \frac{2h_0\Delta k}{k_1}T_0 \qquad \text{(EQ 18)}$$

The equation at this boundary becomes:

$$\frac{4(T2-T1)}{\Delta r^2} + \frac{2(T3-T1)}{\Delta k^2} + \frac{2h_0\Delta k}{k_1}(T_0-T1) = \frac{1}{\alpha\Delta t}(T1^{t+\Delta t}-T1) \qquad \text{(EQ 19)}$$

2.1.6 Temperature at point #6

Convective conditions in both r and k directions exist at the outside top corner of the cylinder (point #6). To estimate heat transfer at this boundary, Eq.18 and Eq. 11 are substituted into Eq. 9:

$$\frac{1}{\Delta r^2}(2T4-2T1)+\frac{2h_0\Delta r}{k_1}\left(1+\frac{1}{2i}\right)(T_0-T1) \quad \text{(EQ 20)}$$
$$+\frac{2(T3-T1)}{\Delta k^2}$$
$$+\frac{2h_0\Delta k}{k_1}(T_0-T1) = \frac{1}{\alpha\Delta t}(T1^{t+\Delta t}-T1)$$

2.1.7 Temperature at point #2

Temperature at the convective boundary of the cylinder side is given by

$$\frac{1}{\Delta r^2}(2T4-2T1)+\frac{2h_0\Delta r}{k_1}\left(1+\frac{1}{2i}\right)(T_0-T1) \quad \text{(EQ 21)}$$
$$+\frac{1}{\Delta k^2}(T5-2T1+T3) = \frac{1}{\alpha\Delta t}(T1^{t+\Delta t}-T1)$$

There is a convective boundary in the r direction and a normal interior geometry in the k-direction.

2.1.8 Temperature at Point #3

Temperature on the bottom (insulated) side of the cylinder is given by:

$$\frac{1}{\Delta r^2}\left\{\left(1-\frac{1}{2i}\right)T5-2T1+\left(1+\frac{1}{2i}\right)T3\right\}+\frac{2}{\Delta k^2}(T5-T1) \quad \text{(EQ 22)}$$
$$= \frac{1}{\alpha\Delta t}(T1^{t+\Delta t}-T1)$$

2.1.9 Temperature at Point #5

Temperature at the top side of the cylinder is given by:

$$\frac{1}{\Delta r^2}\left\{\left(1-\frac{1}{2i}\right)T5-2T1+\left(1+\frac{1}{2i}\right)T3\right\}+\frac{2(T3-T1)}{\Delta k^2} \quad \text{(EQ 23)}$$
$$+\frac{2h_0\Delta k}{k_1}(T_0-T1) = \frac{1}{\alpha\Delta t}(T1^{t+\Delta t}-T1)$$

2.2 Program

The solution, using the above equations for boundary conditions, was coded as follows:

- ! Program "Cylinder Finite Diff Model
- ! Language: TrueBasic
- !Author: Chuck Connor
- !Date: August, 1994
-
- Purpose
- !This program calculates the transient temperature within a

```
! cylinder using explicit finite difference methods the output
! includes a Heissler approximation for comparison

!Files: the File "test" is created and/or erased by this program
!Matrices: matrix t(r,k) contains the temperature values
!       for the cylinder, were r is the radius of the cylinder
!       and k is one-half the length of the cylinder
!       matrix temp(r,k) contains temperature values at
!       intermediate steps
!Constants: rn = radius of cylinder (m)
!        kn = half-length of cylinder (m)
!        delz = step in k -direction (m)
!        delr = step in r direction (m)
!        alpha = thermal diffusivity of cylinder (m2/s)
!        kond = thermal conductivity of cylinder (W/mC)
!        h0 = heat transfer coeff. (W/m2C)
!        delt = time step (s)
!        t0 = fluid temperature (C)
!        r0 = radius of cylinder (m)
!        b1 = constant for Heissler Approx (only if Bi = 4)
!        c1 = constant for Heissler Approx (only if Bi = 4)

dim t(0:15,0:50), temp(0:15,0:50)

open #1: name "test" , create newold
erase #1

let rn = 15
let kn = 50

LET delz = 1
LET delr = 1
LET alpha = 2e-5
LET kond = 93.75
LET h0 = 25
LET delt = 10000
LET t0 = 0
```

```
•
• let r0 = 15
• let b1 = 1.9081
• let c1 = 1.4698
•
• LET sigr = alpha*delt/delr^2
• LET sigz = alpha*delt/delz^2
• LET bir = h0*delr/kond
• LET biz = h0*delz/kond
• print "sigr = ";sigr
• let error = 1/(2*(2+bir))
• print "error = "; error
• if error < sigr then print "sigma is too big!!!!"
•
• FOR k = 0 to kn
•   FOR i = 0 to rn
•     LET t(i,k) = 1200
•   NEXT i
• NEXT k
•
• FOR tim = delt to 1000*delt step delt
•
•   ! 1 interior node
•   FOR k = 1 to kn-1
•     FOR i = 1 to rn-1
•       LET r1 = 1+1/(2*i)
•       LET r2 = 1-1/(2*i)
•       LET t1 = t(i,k)
•       LET t2 = t(i+1,k)
•       LET t3 = t(i,k-1)
•       LET t4 = t(i-1,k)
•       LET t5 = t(i,k+1)
•
•       ! interior node
•       LET temp(i,k) = sigr*(r2*t4 - 2*t1 + r1*t2) + sigz*(t3 - 2*t1 + t5) + t1
•     NEXT i
•   NEXT k
```

```
•
•    ! 2 top of cylinder (convective)
•
•    LET k = kn
•    FOR i = 1 to rm-1
•       LET r1 = 1+1/(2*i)
•       LET r2 = 1-1/(2*i)
•       LET t1 = t(i,k)
•       LET t2 = t(i+1,k)
•       LET t3 = t(i,k-1)
•       LET t4 = t(i-1,k)
•       !let t5 = t(i,k+1)
•       LET temp(i,k) = sigr*(r2*t4 - 2*t1 + r1*t2) + 2*sigz*(t3-t1) + 2*biz*sigz*(t0 -
t1) + t1
•    NEXT i
•
•    ! 3 side of cylinder (convective)
•
•    LET i = rm
•    FOR k = 1 to kn-1
•       LET r1 = 1+1/(2*i)
•       LET r2 = 1-1/(2*i)
•       LET t1 = t(i,k)
•       !let t2 = t(i+1,k)
•       LET t3 = t(i,k-1)
•       LET t4 = t(i-1,k)
•       LET t5 = t(i,k+1)
•
•       LET temp(i,k) = 2*sigr*(t4-t1) + 2*bir*sigr*r1*(t0-t1) + sigz*(t3 - 2*t1 + t5) +
t1
•    NEXT k
•
•
•    ! 4 r=0 side of cylinder
•    LET i = 0
•    FOR k = 1 to kn-1
•       !let r1 = 1+1/(2*i)
•       !let r2 = 1-1/(2*i)
```

```
    LET t1 = t(i,k)
    LET t2 = t(i+1,k)
    LET t3 = t(i,k-1)
    !let t4 = t(i-1,k)
    LET t5 = t(i,k+1)

    LET temp(i,k) = 4*sigr*(t2-t1) + sigz*(t3 - 2*t1 + t5) + t1
  NEXT k

  ! 5 insulated condition at bottom of cylinder

  LET k = 0
  FOR i = 1 to rn-1
    LET r1 = 1+1/(2*i)
    LET r2 = 1-1/(2*i)
    LET t1 = t(i,k)
    LET t2 = t(i+1,k)
    !let t3 = t(i,k-1)
    LET t4 = t(i-1,k)
    LET t5 = t(i,k+1)

    LET temp(i,k) = sigr*(r2*t4 - 2*t1 + r1*t2) + 2*sigz*(t5 - t1) + t1
  NEXT i

  ! 6 r = 0 top of cylinder with convective boundary

  LET k = kn
  LET i = 0
  LET t1 = t(i,k)
  LET t2 = t(i+1,k)
  LET t3 = t(i,k-1)
  !let t4 = t(i-1,k)
  !let t5 = t(i,k+1)
  LET temp(i,k) = 4*sigr*(t2-t1) + 2*sigz*(t3-t1) + 2*biz*sigz*(t0 - t1) + t1

  ! 7 outside top corner of cylinder (convective boundary)
```

- LET k = kn
- LET i = rn
- LET r1 = 1+1/(2*i)
- LET r2 = 1-1/(2*i)
- LET t1 = t(i,k)
- !let t2 = t(i+1,k)
- LET t3 = t(i,k-1)
- LET t4 = t(i-1,k)
- !let t5 = t(i,k+1)
-
- LET temp(i,k) = 2*sigr*(t4-t1) + 2*bir*sigr*r1*(t0-t1) + 2*sigz*(t3-t1) + 2*biz*sigz*(t0-t1) + t1
-
- ! 8 outside lower corner (convective and insulate boundary)
-
- LET k = 0
- LET i = rn
- LET r1 = 1+1/(2*i)
- LET r2 = 1-1/(2*i)
- LET t1 = t(i,k)
- !let t2 = t(i+1,k)
- !let t3 = t(i,k-1)
- LET t4 = t(i-1,k)
- LET t5 = t(i,k+1)
-
- LET temp(i,k) = 2*sigr*(t4-t1) + 2*bir*sigr*r1*(t0-t1) + 2*sigz*(t5-t1) + t1
-
- ! 9 0,0 of cylinder
- LET i = 0
- LET k = 0
- !let r1 = 1+1/(2*i)
- !let r2 = 1-1/(2*i)
- LET t1 = t(i,k)
- LET t2 = t(i+1,k)
- !let t3 = t(i,k-1)
- !let t4 = t(i-1,k)
- LET t5 = t(i,k+1)

```
•
•     LET temp(i,k) = 4*sigr*(t2-t1) + 2*sigz*(t5-t1) + t1
•
•     mat t = temp
•
• let tstar = alpha*tim/225
•
• if tstar > .3 then
• let tc = 1200*c1*exp(-(b1^2)*tstar)
•
•     print #1: tim,t(0,0),tc
• end if
•
• NEXT tim
•
• END
```

Temperatures were solved for using the above program. Input parameters used were:

- rn = radius of cylinder = 15m
- kn = half-length of cylinder = 50 m
- delz = step in k -direction= 1 m
- delr = step in r direction= 1 m
- alpha = thermal diffusivity of cylinder = 2e-5 m2/s
- kond = thermal conductivity of cylinder = 93.75 W/mC
- h0 = heat transfer coeff. =25 W/m2C
- delt = time step = 10,000 s
- t0 = fluid temperature = 0 °C

The stability was checked at the outside top corner of the cylinder. This point is most effected by instability if the time-step is too large for the heat transfer conditions. Experimentation, comparing the Bi number and dimensionless time, indicate that a time step of 10,000 s is sufficiently small. The program was run for 300 iterations (3e7 s) and the final temperatures were output to a file. These data were then contoured in Spyglass transform. The resulting image is shown in Figure 3. It is clear from inspection of Figure 3 that the model is behaving well:

- Steepest gradients exist at the edges of the cylinder
- Temperatures are highest at the center
- More heat is being lost from the side than the ends of the cylinder

These observations indicate that the model describes heat transfer correctly - in a qualitative sense. A quantitative comparison with the analytical solution is next.

FIGURE 3. Temperatures inside the test cylinder

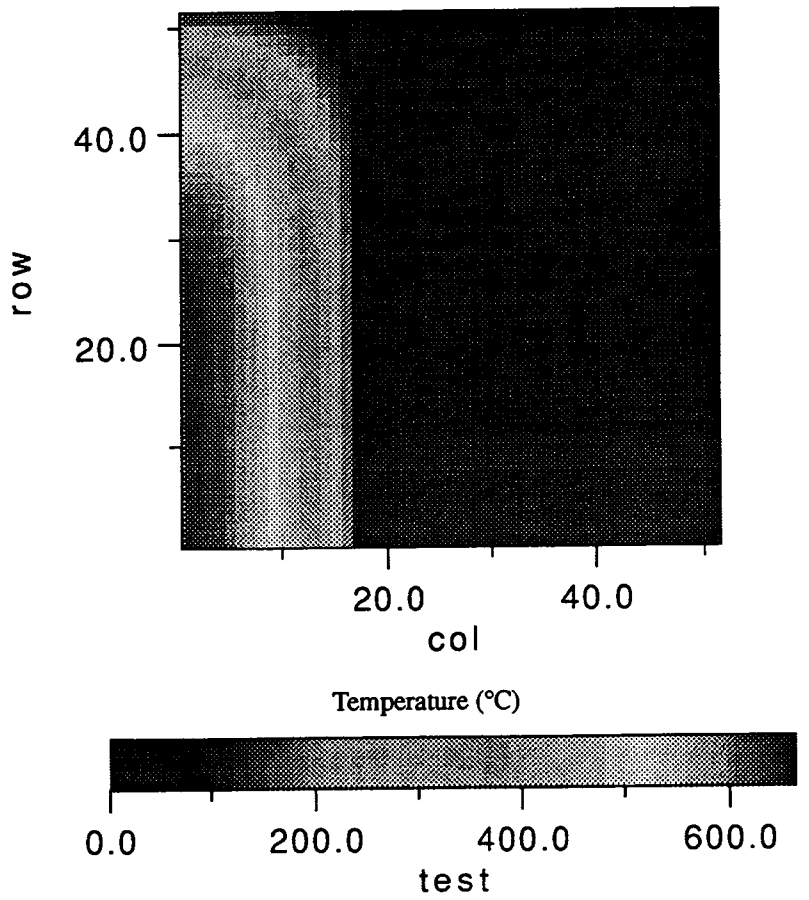

3.0 Comparison of Heissler Approximation and Finite Difference Model

The Heissler Approximation and the finite difference models were compared to test the boundary conditions, using the above program. The infinite cylinder model was used for the Heissler approximation because a relatively long cylinder was used. Parameters used for the comparison were the same as those used above. Namely:

- rn = radius of cylinder = 15m
- kn = half-length of cylinder = 50 m
- delz = step in k -direction= 1 m
- delr = step in r direction= 1 m

- alpha = thermal diffusivity of cylinder = 2e-5 m2/s
- kond = thermal conductivity of cylinder = 93.75 W/mC
- h0 = heat transfer coeff. =25 W/m2C
- delt = time step = 10,000 s
- t0 = fluid temperature = 0 °C

Additional parameters for Heisler Calculation

- r0 = radius of cylinder = 15 m
- b1 = constant for Heissler Approx (only if Bi = 4) = 1.9081
- c1 = constant for Heissler Approx (only if Bi = 4) = 1.4698

The starting temperature of the cylinder is taken to be 1200°C. Thus, the boundary conditions are similar is scale to those that will be used to model cooling cinder cones. Table 1 shows the temperatures calculated at the center point (r=0, k=0) for several times (where dimensionless time is greater than 0.3 (see Eq.2)).

TABLE 1. Comparison of Temperatures for Selected Times

Time (years)	Finite Difference model (°C)	Heisler Approximation (°C)
0.10711	**588.29**	**590.71**
0.15052	378.20	379.16
0.24970	136.50	137.69
0.30009	80.967	82.304

The maximum difference in temperatures calculated using the two methods is about 2.5°C at a time just slightly greater then $t^0 = 0.3$. The difference between the two calculations decreases with increasing time, so that at 0.3 years the difference is less than 0.5°C. The data are plotted for comparison in Figure 4. Note that there is a trivial difference between the two curves over a broad range in times. What difference there is can be attributed to:

1. The finite length of the cylinder - the Heissler approximation does not take this into account
2. The Heissler approximation truncates the Fourier series.

FIGURE 4. Comparison of the two models

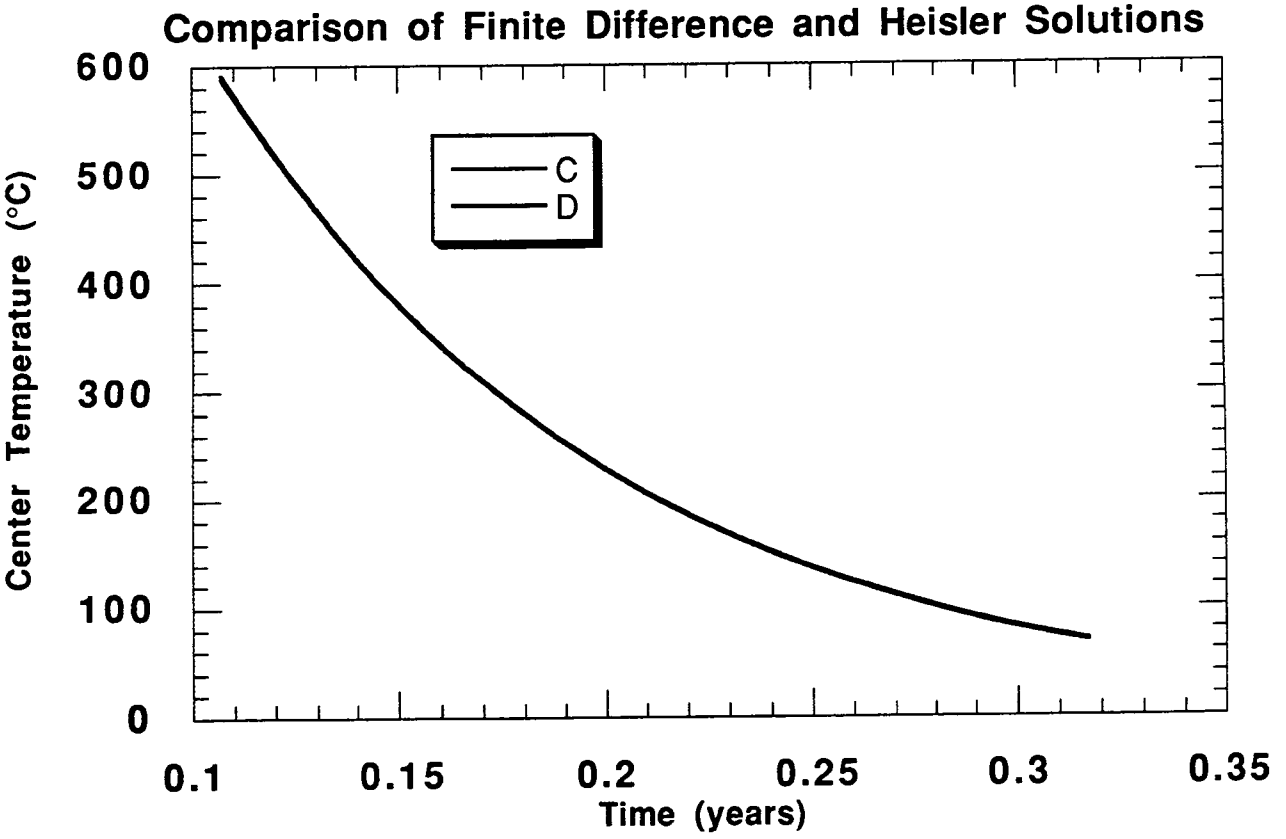

4.0 Conclusion

It is concluded that the finite difference model works well for approximating the temperature distribution in a vertical cylinder. Therefore the model should work well for approximating the temperature distribution in more complex shapes, for which an analytical solution is not available.

November 2, 1994

Temperature Experiments at Tolbachik Cinder Cone, Russia

Chuck Connor

Chuck Connor

Temperature data were collected at several cinder cones formed during the Tolbachik eruption, Kamchatka, Russia. These temperature data include continuous temperature measurements made in high-temperature fractures, on the cones, shallow temperature gradients measured in volcanic ash and cinders on the cones, and shallow temperature gradients measured on the lava flows and across shallow dikes which did not erupt at the surface.

Field work was conducted at Tolbachik volcano, Kamchatka, Russia between June 29 and August 5, 1994. The goals of this field work are described in the Project Plan for Field Volcanism and Connor (1993, Technical and Regulatory Basis for the Study of Recently Active Cinder Cones, IM, 5704-141-001).

The study of temperature distributions at the surface of cinder cones at Tolbachik fall under Task 3 of the Field Volcanism project: study of the cooling and degassing of recently active cinder cones.

Primary goals of this work were to:

- Determine the temperatures of fractures at Tolbachik
- Determine the area effected by increased heat flow
- Collect data to help constrain cooling rates at cinder cones
- Determine if heat continues to be transprted from depth at these cinde cones

The field work is divided into three separate experiments.

- Monitoring temperatures along individual fractures for several days
- mapping shallow temperature gradients on the cones
- mapping shallow temperature gradients across a dike

These experiments took place at the same time and involved the same personnel. Connor was responsible for all of the measurements made as part of this field work. Temperature measurements were made with the assistance of Yuri Taran, Russian Academy of Sciences, Phil Doubik, a Ph.D. candidate at SUNY - Buffalo, and Mike Conway, a postdoc at Florida International University, Miami.

1.0 Continuous Temperature Measurements

1.1 Purpose

High-temperature fractures were monitored over periods of several days. These fractures are located along the rim of Cone I and Cone II at Tolbachik. The purpose of monitoring these fumaroles is to determine the degree of variation in temperature over time, determine if this variation can be related to atmospheric forcing (barometric pressure, air temperature), and to determine if the flow in these fractures can be characterized as steady-state on time scales of several days or less.

1.2 Instrumentation

A programmable Campbell Scientific Instruments datalogger (model CR-10) was used to measure temperatures in the fumaroles. This instrument is designed for precise temperature measurements and as an atmospheric monitoring station. The instrument was selected because

1. The instrument is known for its resilience in adverse field conditions
2. The instrument is designed for the types of measurements we were making
3. Connor has used this instrument to collect fumarole temperature before, and followed the field procedure he developed - published in Connor et al. 1993. Continueous monitoring of high-temperature fumaroles, Journal of Geophysical Research 98:19,713-19,722.

The datalogger was tested for calibration both by Campbell Scientific and SwRI Calibration lab prior field measurements. The SwRI calibration was done on datalogger CR10, SN 19545 (the only one we have). Calibration was performed at the calibration lab at air temperature = 68°F and Humiduty = 40%. Votage was applied to input channel three of the datalogger and read with the following results

TABLE 1. Calibration of DataLogger

Standard	Reading
2.5000V	2.5005V
2.0000V	2.0002V

TABLE 1. Calibration of DataLogger

Standard	Reading
1.0000V	1.0000V
100.00mV	99.833mV

The datalogger is calibrated to the degree necessary to perfom the required temperature measurements.

The datalogger samples according to programmable instructions. The instructions used in this field work were:

- Program: measures baro press + 4 TC
- Flag Usage:
- instruction 86 is used to send data to final storage
- instruction 92 is used to send data to CSM1
- Input Channel Usage:
- 1H = 10TCRT red wire
- 1L = barometer (orange wire)
- 2H - 5L = TCs
- Excitation Channel Usage:
- 1E = barometer (yellow)
- 3E = 10TCRT (black)
- Control Port Usage: none
- Pulse Input Channel Usage: none
- Output Array Definitions:
- col 1 = channel header
- col 2 = julian day
- col 3 = hours and minutes
- col 4 = baro pres (add 600 to get mbar)
- col 5 = 10TCRT temperature
- col 6 = channel 2 TC
- col 7 = chanel 3 TC
- col 8 = channel 4 TC
- col 9 = channel 5 TC
-

```
*  1     Table 1 Programs
 01: 60     Sec. Execution Interval
instruction p4 is used for the visala mountain
barometer. This works with the CR10 wired as
orange = 1L (single ended input port number 2
yellow = E1 (excit port 1)
purple = G (ground)
clear = G (ground)
red = 12V (12 volt power from panel)
white = AG (analog ground)

 instruction P11 is used to make
a reference temp measurement using
the 10TCRT. In this case the reference
location used to store the reference temp
is loc 2. The reading is in deg C
The wiring for the 10TCRT is
red = 1H (single ended input channel 1)
black = E3 (excit channel 3)
clear = AG (analog ground)

Instruction P14 is used to measure
thermocouples. In this case, 4 K-type
TCs are used, starting in channel 2 and
referenced to the 10TCRT reading stored in
location 2.  Wiring:
TC 1: red = 2H, yellow = 2L
TC 2: red = 3H, yellow = 3L
TC 3: red = 4H, yellow = 4L
TC 4: red = 5H, yellow = 5L
the chromel wire (+) is yellow

Page 2  Table 1

the alumel wire (-) is red
```

- 01: P4 Excite,Delay,Volt(SE)
- 01: 1 Rep
- 02: 5 2500 mV slow Range
- 03: 2 IN Chan
- 04: 1 Excite all reps w/EXchan 1
- 05: 300 Delay (units .01sec)
- 06: 2500 mV Excitation
- 07: 1 Loc :
- 08: 0.184 Mult
- 09: 0 Offset
-
- 02: P11 Temp 107 Probe
- 01: 1 Rep
- 02: 1 IN Chan
- 03: 3 Excite all reps w/EXchan 3
- 04: 2 Loc :
- 05: 1 Mult
- 06: 0.0000 Offset
-
- 03: P14 Thermocouple Temp (DIFF)
- 01: 4 Reps
- 02: 3 25 mV slow Range
- 03: 2 IN Chan
- 04: 3 Type K (Chromel-Alumel)
- 05: 2 Ref Temp Loc
- 06: 3 Loc :
- 07: 1 Mult
- 08: 0.0000 Offset
-
- 04: P86 Do
- 01: 10 Set high Flag 0 (output)
-
- 05: P77 Real Time
- 01: 110 Day,Hour-Minute
-
- 06: P70 Sample
- 01: 6 Reps

- 02: 1 Loc
-
- 07: P96 Serial Output
- 01: 71 SM192/SM716/CSM1
-
- 08: P End Table 1

1.3 Data Collected at Cone II

Temperature data were collected on the crater rim of Cone II between July 6 and July July 15. A preliminary survey of the crater rim was made to locate areas of highest temperature fractures. The zone of highest temperatures on the upper East rim was selected and this area was mapped using tape and compass techniques. Figure 1, "Location of thermocpouples on Cone II," on page 6 shows the locations of thermocouples used in the monitoring period. T1 was located at the intersection of several fractures. A Ti tube was driven into the fracture to a depth of apprximately 0.85 m and the thermocouple was inserted into this tube. T2, T3, and T4 were located along the same fracture, located about 10 m from T1. Both fractures extend to the crater rim. The fracture containing T2-T4 was more open. T2, the coolest thermocouple, was located closest to the crater rim, then T3 and finally T4. T2 and T3 were inserted directly into the fracture to a depth of approximately 15 cm. The fracture was narrow (less than 1 cm wide) below this depth. T4 was inserted into a Ti rod, driven into the fracture to a depth of 0.75 m. Air temperature and barometric pressure were recorded simultaneous with thermocouple measurements. Air temperature is the air temperature in the data logger case. In this area the air temperature is slightly elevated (5-10°C) due to proximity to the hot fractures (Figure 2, "Air temperature at Cone II," on page 6).

FIGURE 1. Location of thermocpouples on Cone II

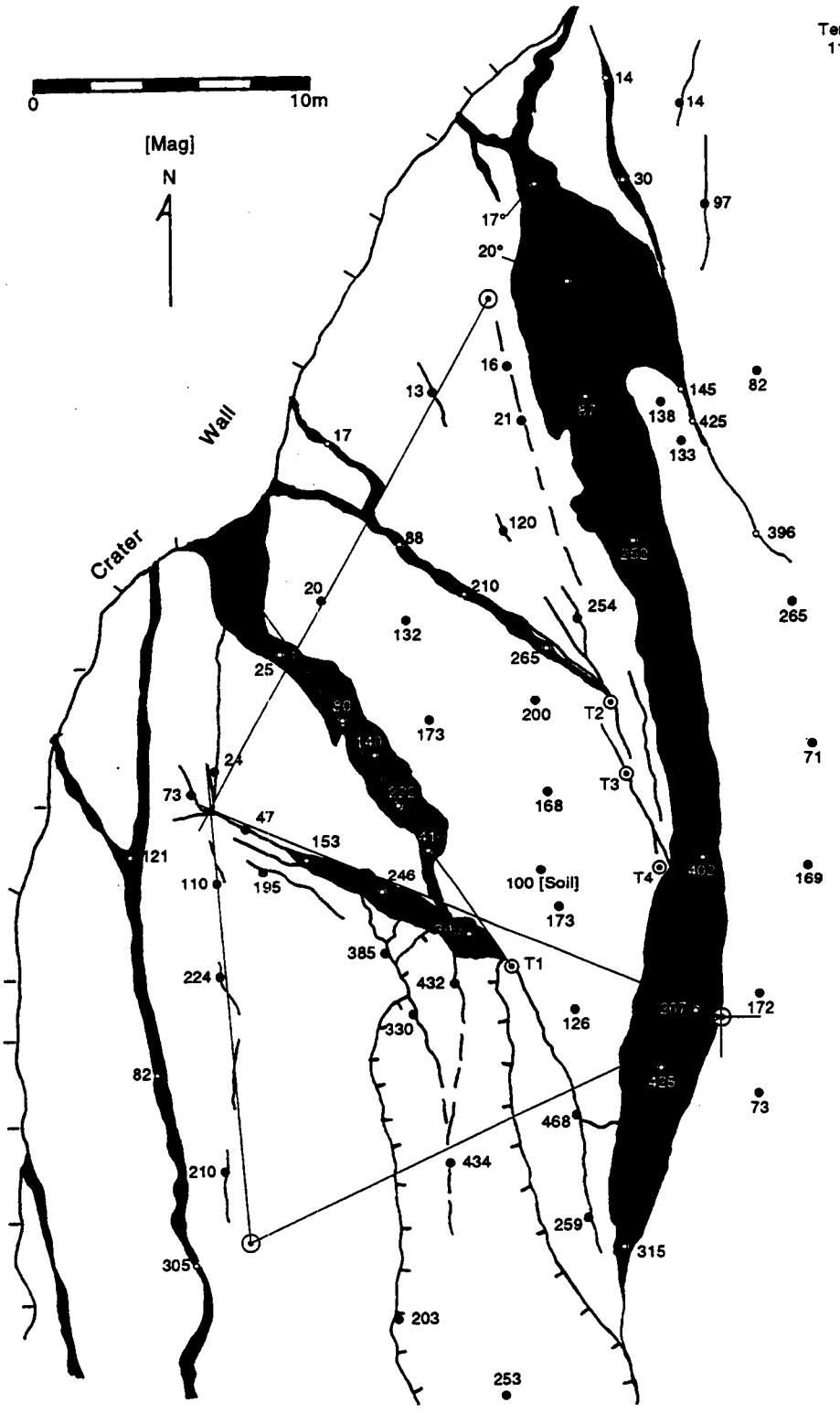

FIGURE 2. Air temperature at Cone II

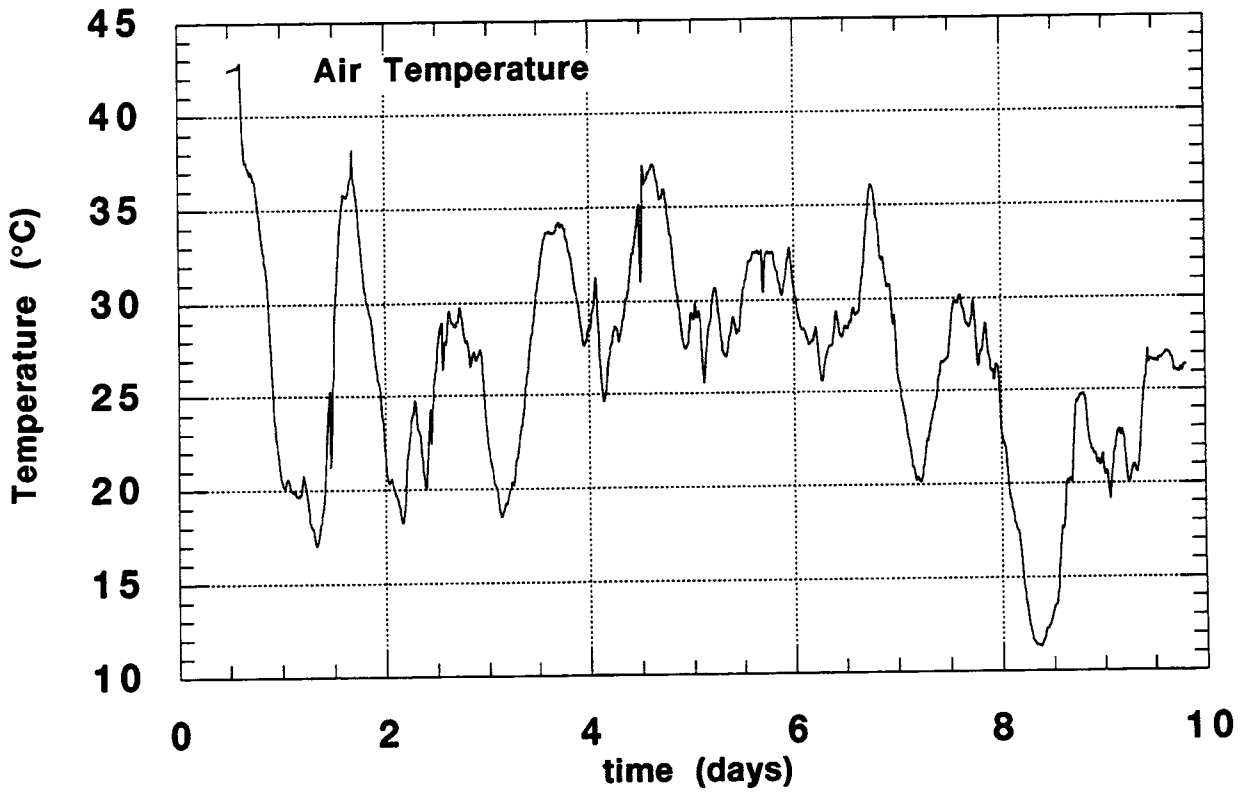

FIGURE 3. Atmospheric pressure at Cone II

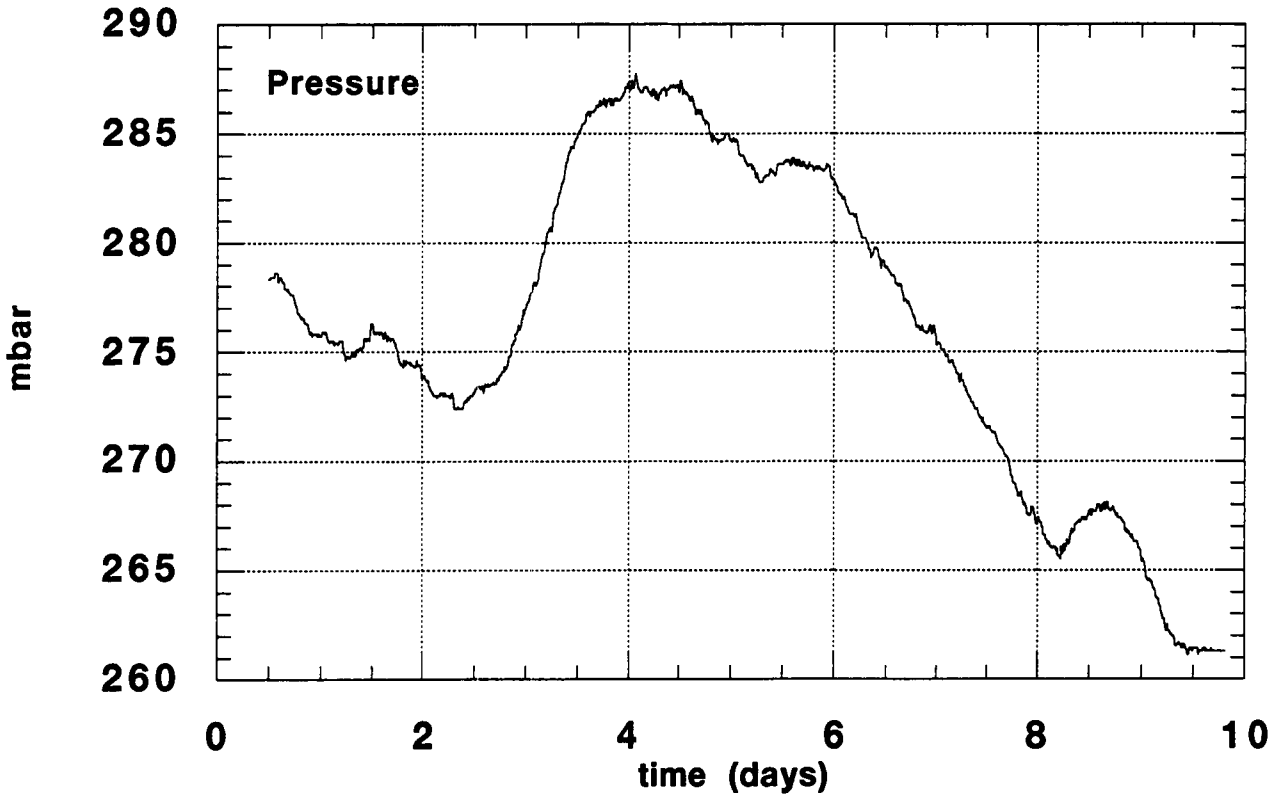

Barometric pressure varied by about 30 mbar during the sampling period. Values in Figure 3, "Atmospheric pressure at Cone II," on page 7 should be corrected by adding 700 mbar and then correcting to sea level (elevation of barometric pressure measurement was about 1000 m above sea level.

Temperaturers in T1 varied between about 435 °C and 495°C during the sampling period (Figure 4, "Temperature in Fracture T1, Cone II," on page 9). Daily variations of 40-50°C occur in T1, and are especially clear during the central portion of the recording period, days 3 - 7. During this period the temperatures in T1 appear to be roughly inversely correlated with air temperature. No correlation with atmospheric pressure is apparent.

FIGURE 4. Temperature in Fracture T1, Cone II

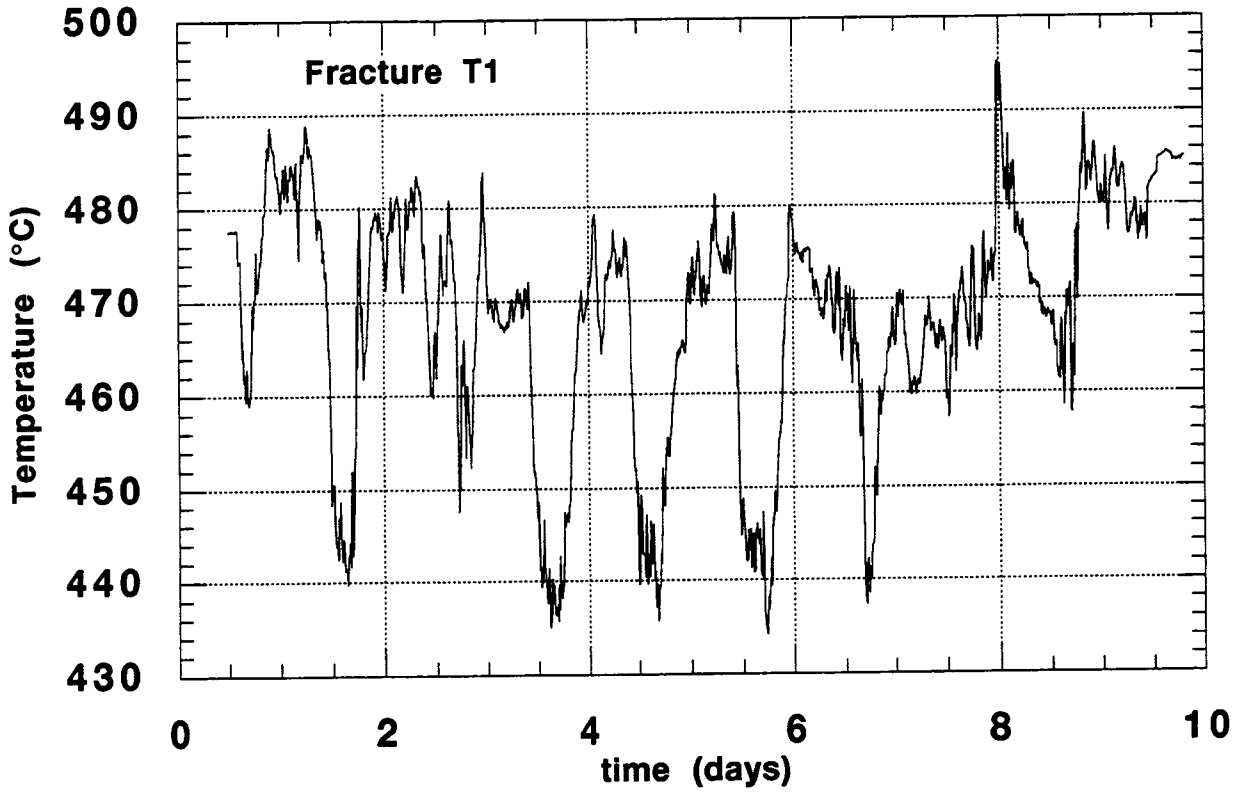

Temperature variation in T2 is much larger and less systematic than is observed in T1. Temperatures varied from 100 °C to 235°C during the sampling period. Temperature variations of more than 100°C were common in this fracture during a single day and frequently occur during a single hour (Figure 5, "Temperatures in Fracture T2, Cone II," on page 10). Overall, there is a great deal of apparently random temperature variation in this protion of the fracture.

FIGURE 5. Temperatures in Fracture T2, Cone II

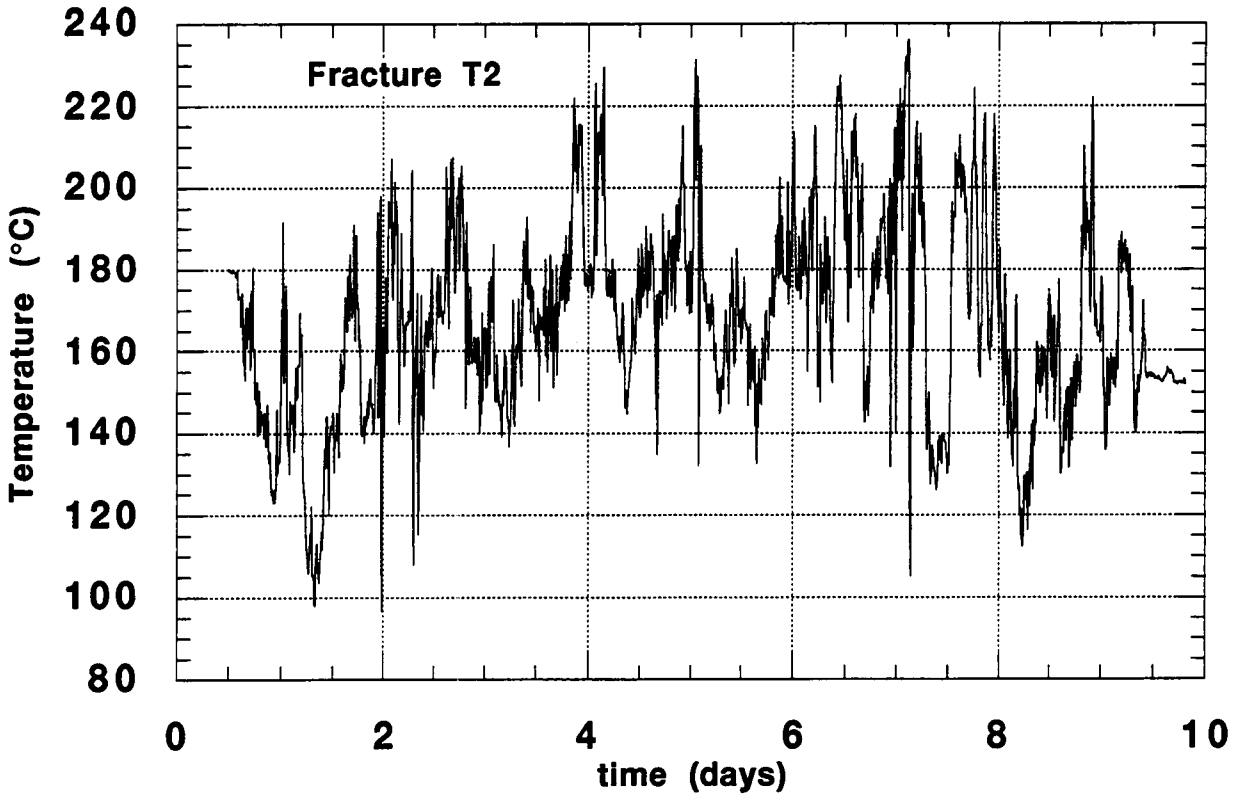

Data collected in T3 (Figure 1, "Location of thermocpouples on Cone II," on page 6) show more systematic variation than temperatures in T2. Temperatures varied by about 100°C in this part of the fracture during the sampling period (Figure 6, "Temperatures in fracture T3, Cone II," on page 11). There is good correlation between variation in T1 and variation in T3 during the time period day 3 - day 6. At other times the correlation appears to break-down, or at least be less clear.

FIGURE 6. Temperatures in fracture T3, Cone II

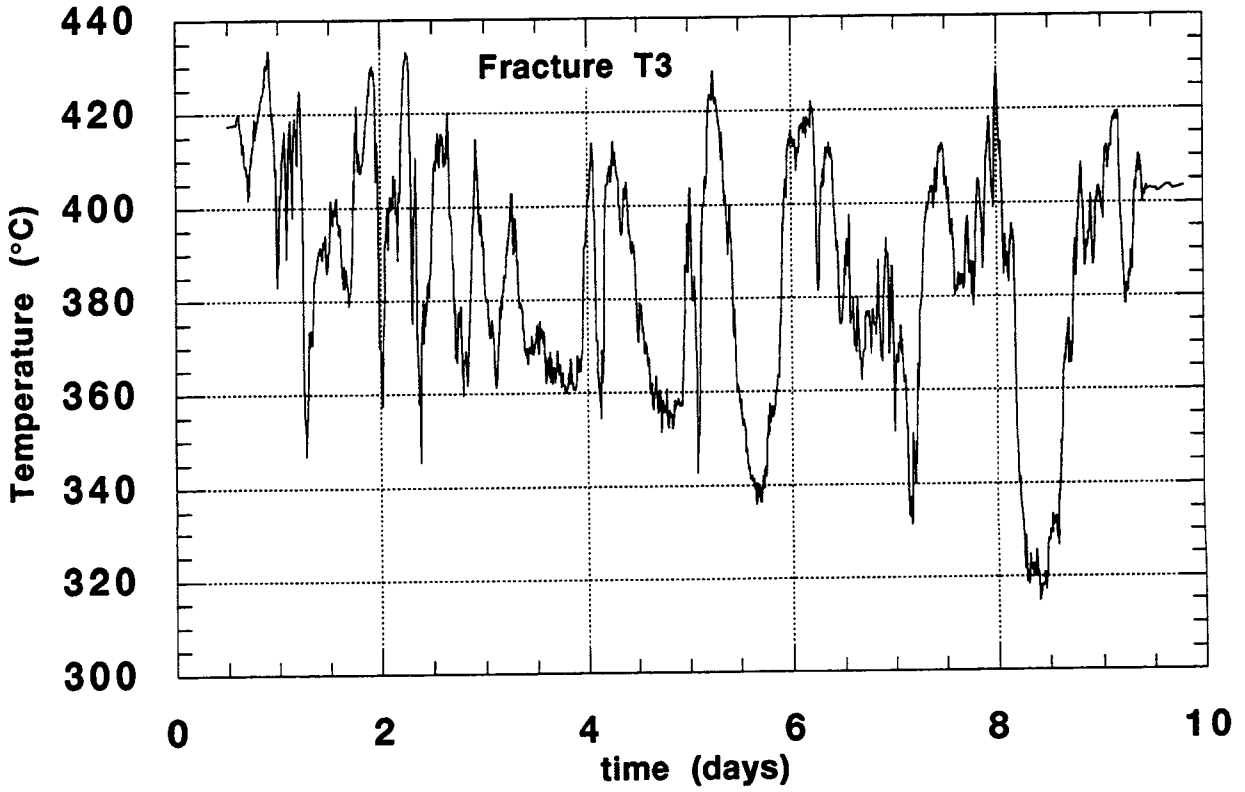

Temperatures at T4 vary from about 490°C to about 535°C, making this the hottest fumarole monitored on Cone II on average (Figure 7, "Tempratures in fracture T4, Cone II," on page 12). Overall, variation is less in this fumarole than in the others, and is more systematic. There is good correlation between T1, T3 and T4. The largest + increase in temperature occurs at about 0:00 on day 8 in both T4 and T1. This is a clear indication that whatever is forcing changes in temperature (or flow) in the two fractures, it is acting in the same way. Indicating that it is likely atmospheric forcing changing temperatures. Data gaps in T4 data occur during times gas samples were being collected from this fumarole.

FIGURE 7. Temperatures in fracture T4, Cone II

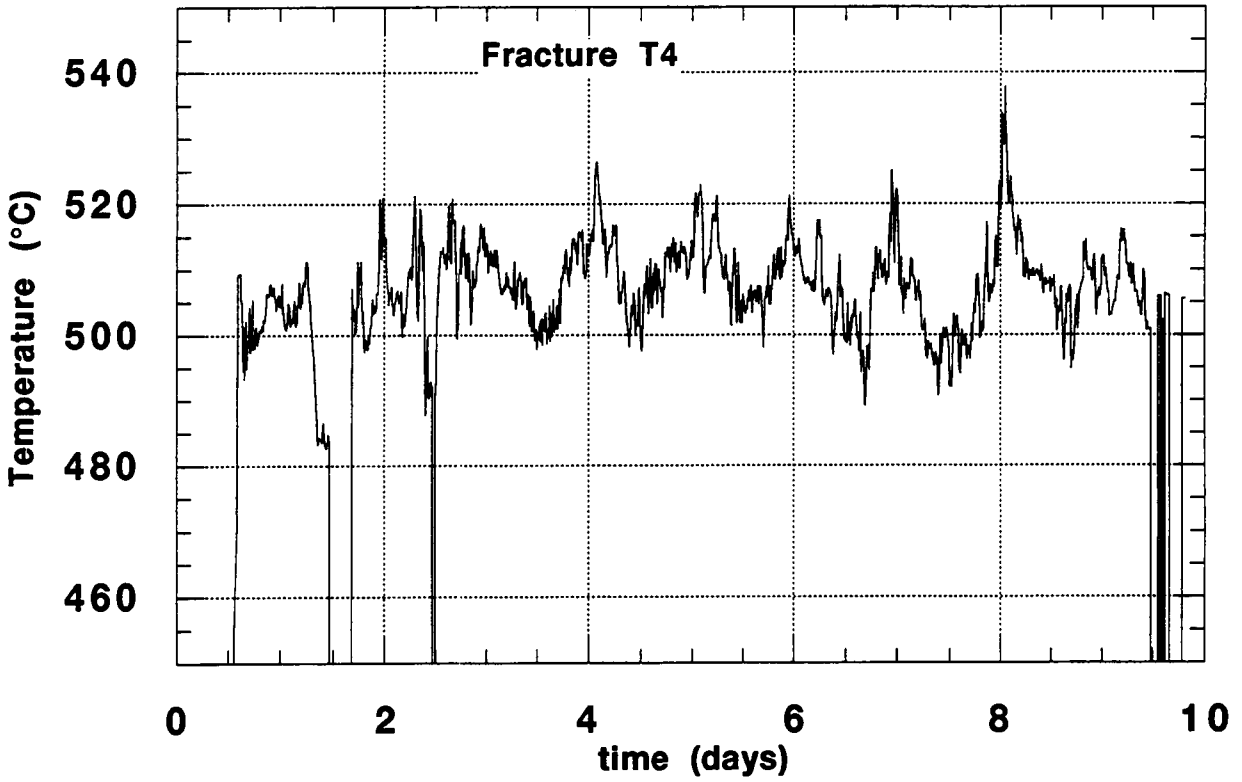

In summary of observations made about continuous temperature measurements at Cone II:

- it is clear that temperatures are steady-state in the sense that trends are absent in the data on the time scale of the survey (days)
- temperatures vary systematically by position, temperatures are cooler and variations more erratic closer to the crater wall, indicating mixing is important
- daily variations occur and are more distinctive in T1 and T4 the higher temperature fumaroles, than in T2 and T3; on average, the higher the mean temperature of the fumarole, the smaller the magnitude of the daily variation
- cross-correlation is good between T1 and t3 and T4, which are located in a separte fracture. The simialr variation in T1 and T4 is especially clear around 0:00 on day 8
- there is no obvious correlation between atmospheric P and variations in fracture temperature.

Additional analysis of these data appears to be warranted. Probably a good approach is to calculate the FFT for each time series and compare them systemtatically. Calculation of simple statistics will also help.

1.4 Data Collected at Cone I

Temperature data were collected continuously along fractures on the crater rim of Cone I during July 17 - July, 21 - approximately 4 full days of monitoring. The data were collected at 10 minute intervals and atmospheric temperature and pressure were collected simultaneously.

The locations of thermocouples deployed in fractures on the crater rim are shown in Figure 8, "Location of thermocouples on Cone I," on page 13. Several aspects of this scene are important to note:

- The fractures on the rim of Cone I are much narrower and less open than those on Cone II
- there is abundant alteration of rocks around these fumaroels - much deuteric oxidation of the Fe - bearing minerals, etc. Sublimate minerals are also present inthis area.
- although the fractures are very close to the crater rim - they do not intersect the rim in as direct a manner here as on Cone II. There is much less opportunity for the re-circulation of air in these fractures.
- These fumaroles are in and on the edge of a moist green zone - looks like a lot of sealing is occurring in this system.

FIGURE 8. Location of thermocouples on Cone I

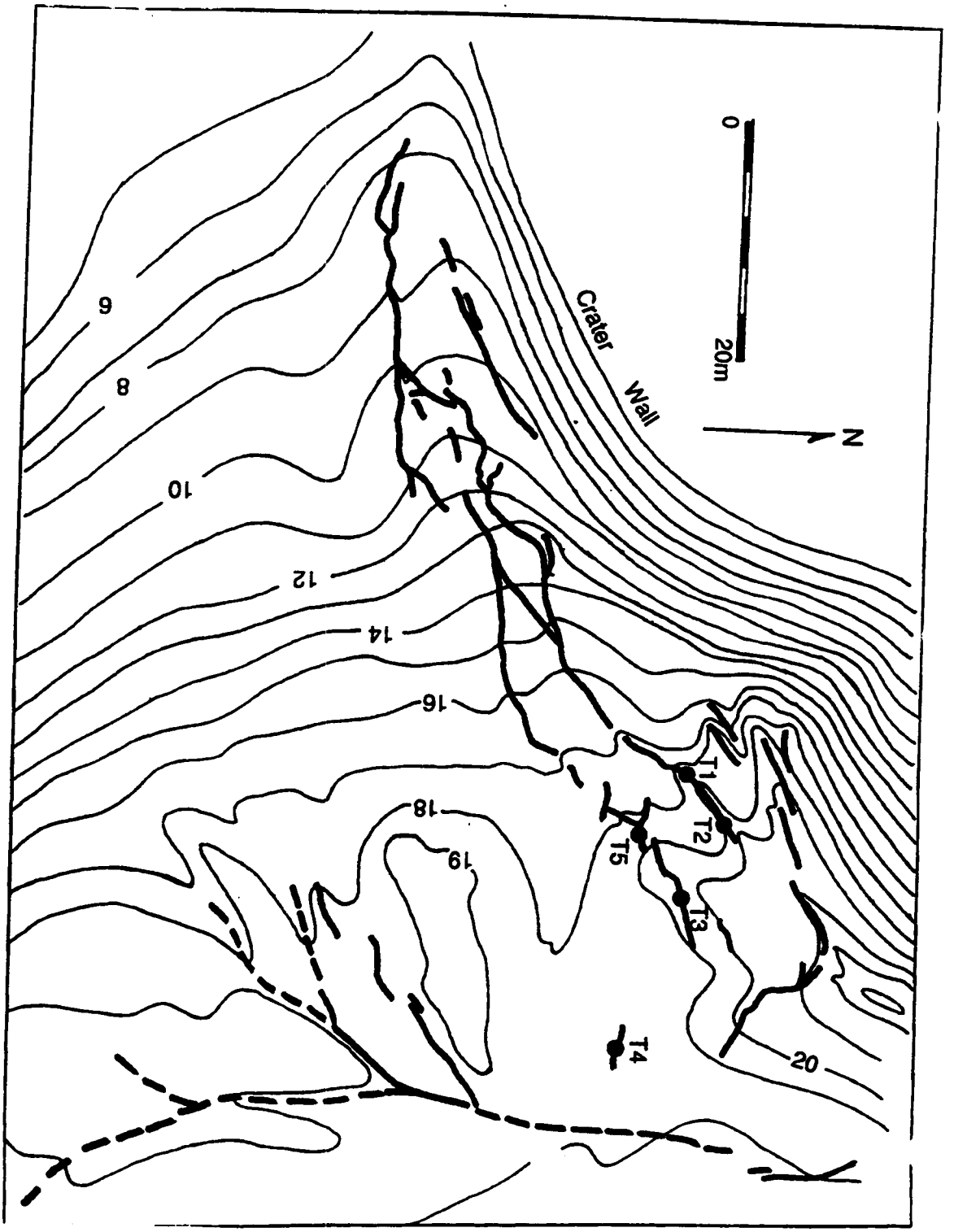

Air temperature and pressure data are plotted in Figure 9, "Air Temperatures at Cone I," on page 14 and Figure 10, "Atmospheric Pressure at Cone I," on page 15. The normal diurnal temperature change is noted. Pressure variations were very small and regular during the sampling interval - about 2 mbar total variation during days 11 - 14. This corresponds to a period of intermittent rain and drying on days 11 - 12, clear weather through day 15, and then the onset of rain on day 16, at which point the pressure is falling. The diurnal cycle suggests tidal forcing - which is commonly observed when large scale atmospheric effects don not overwhelm it.

FIGURE 9. Air Temperatures at Cone I

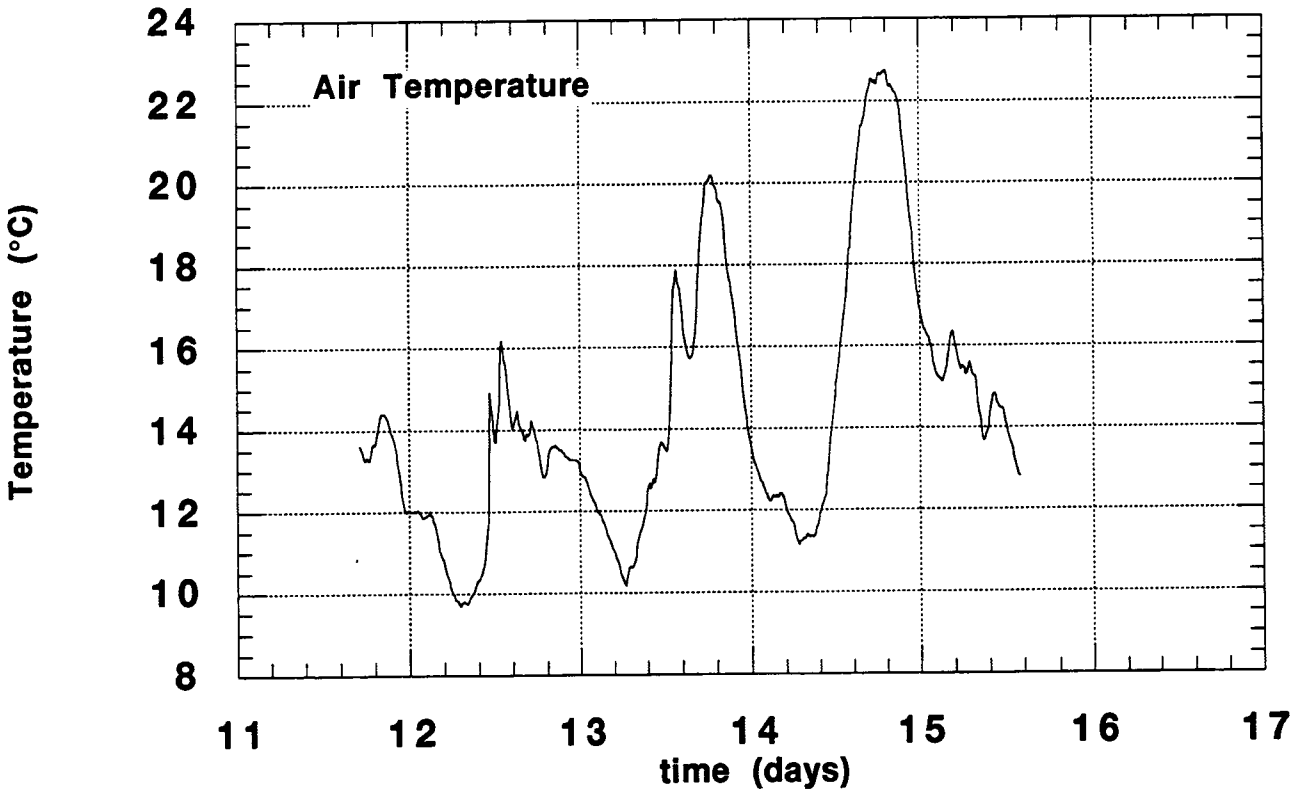

Thermocouple T1 was inserted into a fracture to a depth of approximately 0.5 m. This fracture is the hottest identified at Cone I. Temperatures at a depth of 1.85 m in this fracture were about 618°C 1.5 m from the location of T1. Data collected in T1 are plotted together with pressure data in Figure 11, "Comparison of Atmospheric Pressure and temperatures in fracture T1 at Cone I," on page 16. Temperature variation in this fumarole is from about 573 to 578°C - only about 5°C total during the observation period.

FIGURE 10. Atmospheric Pressure at Cone I

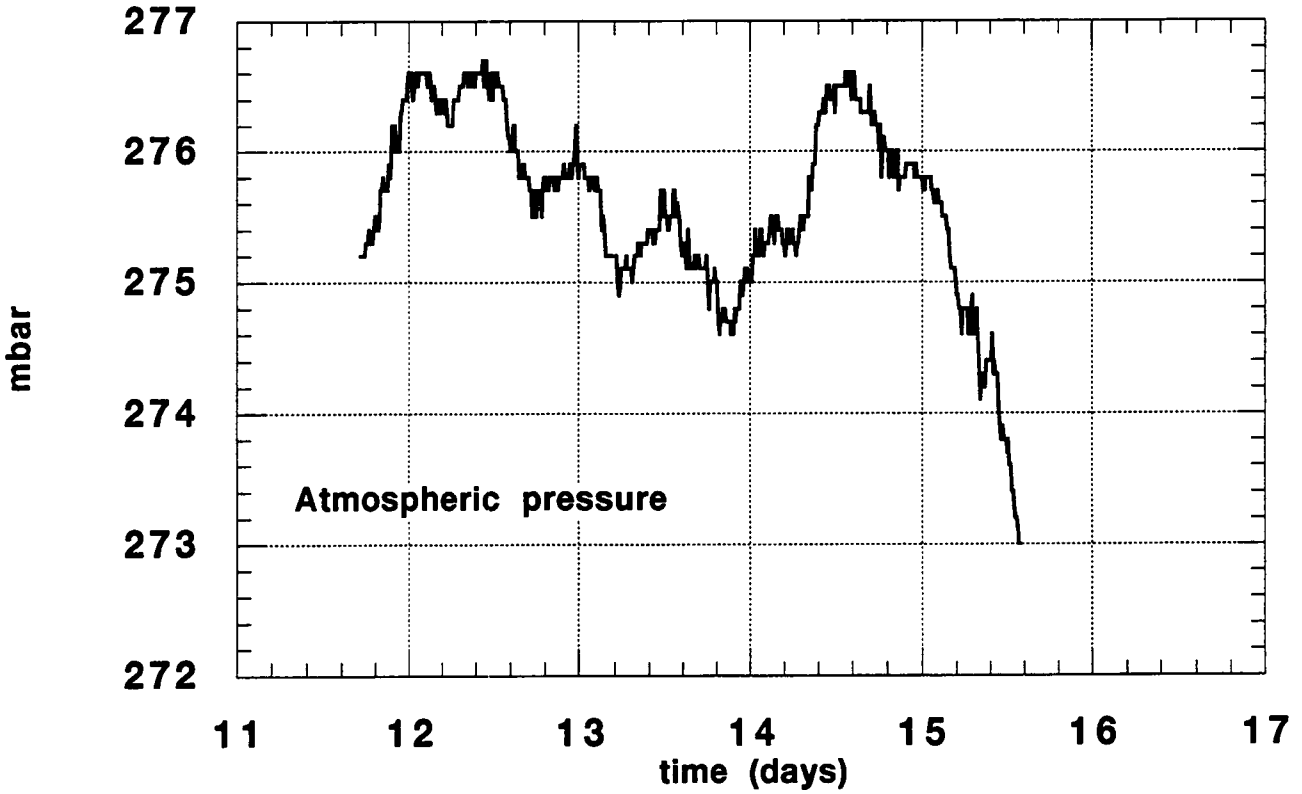

Like at Cone II, the higher temperature fumaroles are showing the least daily variation. In detail, the temperature variation that is observed in T1 correlates (negatively) very well with atmospheric pressure on days 12 through 15. At the very beginning of the series in appears that there is a direct dependence. During this period the cone was drying out (day 11), from several days of rain. The fumarole may have been heating slightly in response to evaporation of water in the area at this point.

FIGURE 11. Comparison of Atmospheric Pressure and temperatures in fracture T1 at Cone I

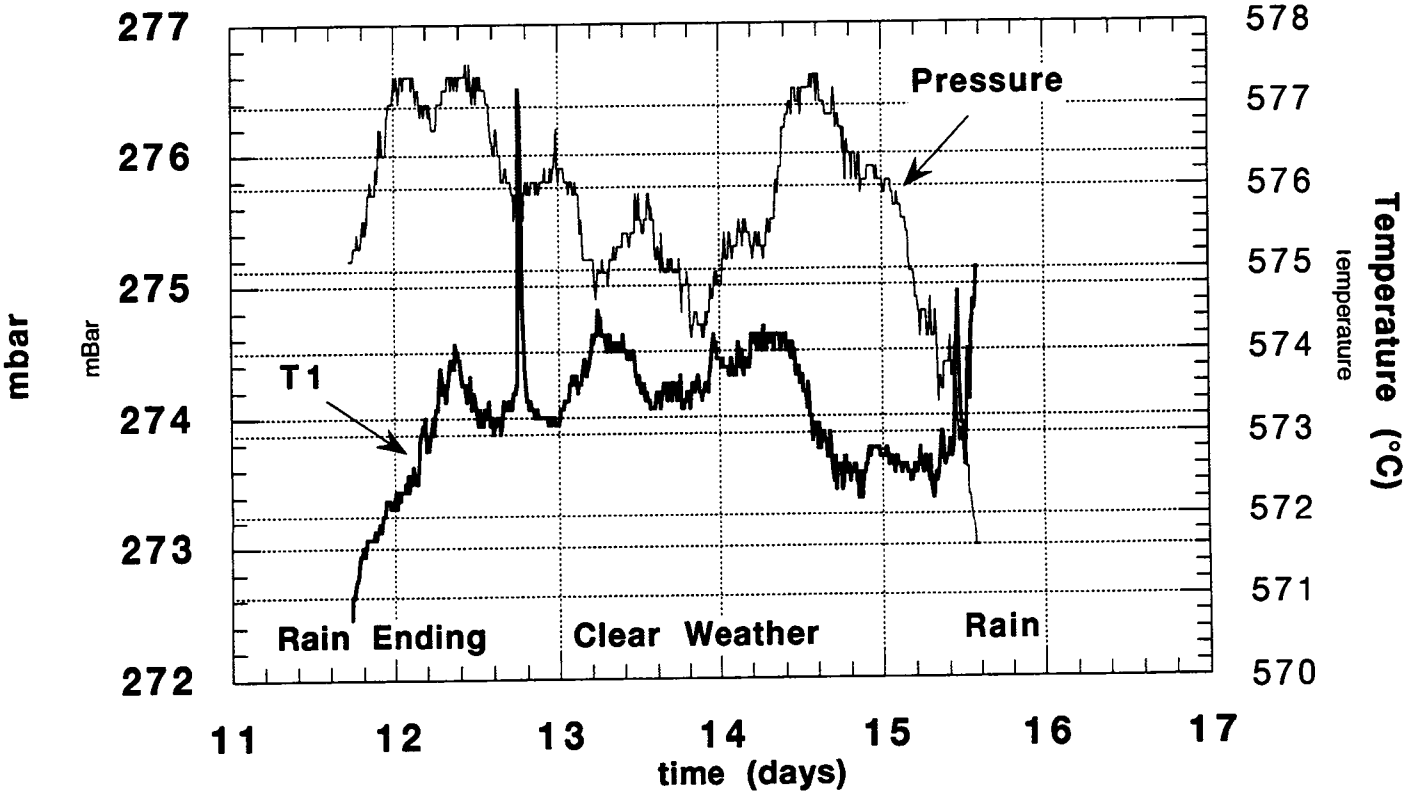

T2 was located in the same fracture as T1. This fumaroles was cooler and located along a narrower portion of the fracture. The thermocouple could be inserted to a depth of 25 cm. Total temperature variation in T2 is on the order of 8 °C between day 11 and day 15 (Figure 12, "Fracture T2, Cone I," on page 17). Some correlation exists between T! and T2. For example, the spikes in temperature on days 12 and 15 are clear in both time series. Other, broader variations do no correlate as well.

FIGURE 12. Fracture T2, Cone I

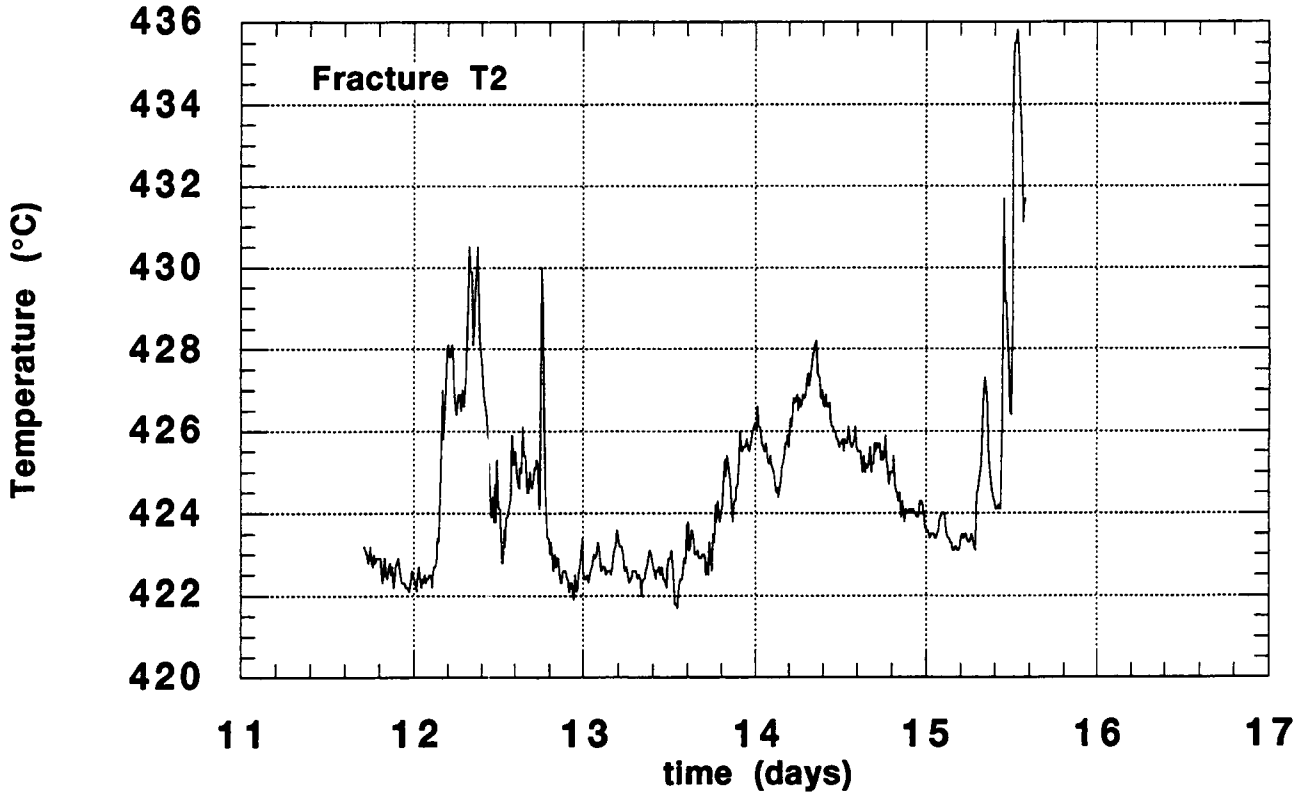

Temperatures in collected by thermocouple T3 are plotted in Figure 13, "Fractue T3, Cone 1," on page 18. This thermocouple was inserted in a crack located about 10 m from the crack containing T1 and T2. Initially, T3 was inserted in a 2 m long Ti tube to a depth of 1.75 m. This tube was removed for other sampling on day 12 and the thermocouple was re-inserted at the same location but could only be inserted (without the tube) to a depth of 70 cm. This results in a step on the temperature plot. Data collected after the tube was removed are plotted on an expanded scale in Figure 14, "Expanded view of Fracture T3 temperatures, Cone I," on page 19).

FIGURE 13. Fractue T3, Cone 1

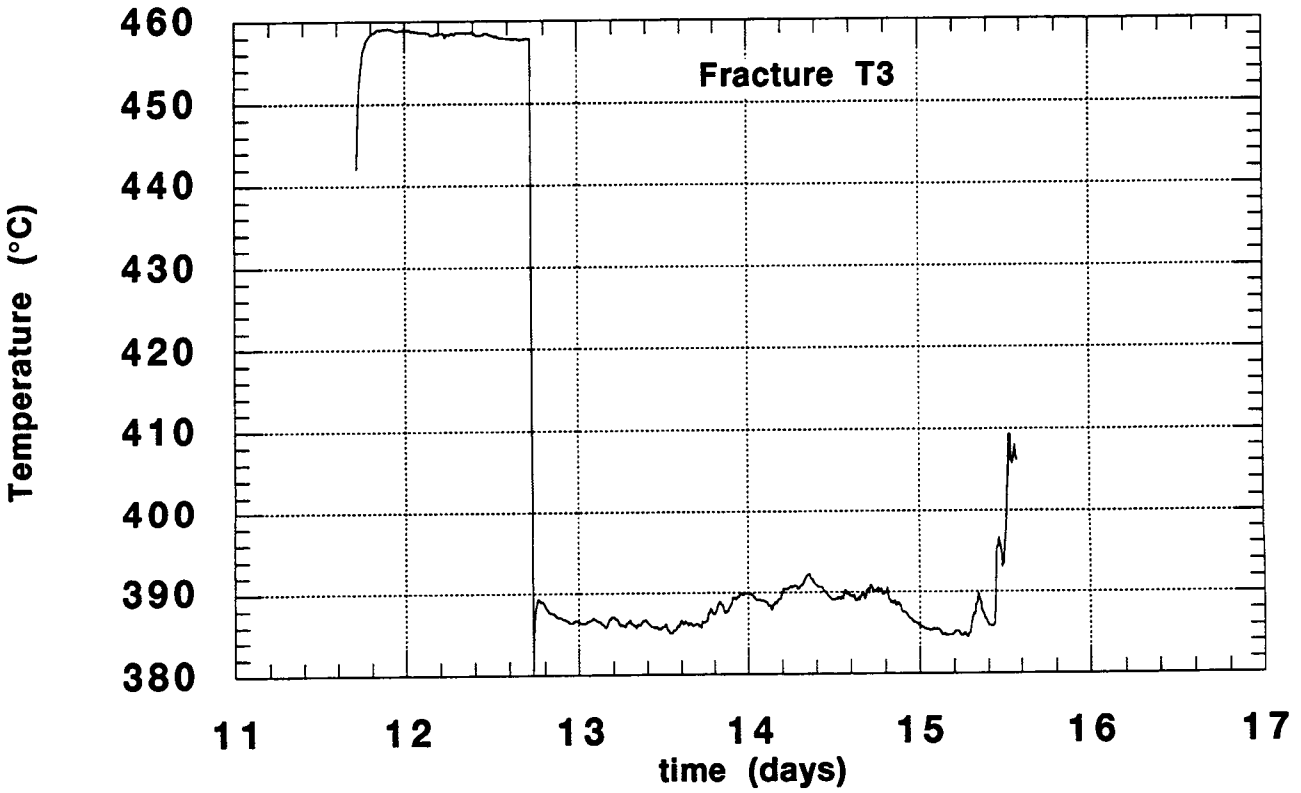

FIGURE 14. Expanded view of Fracture T3 temperatures, Cone I

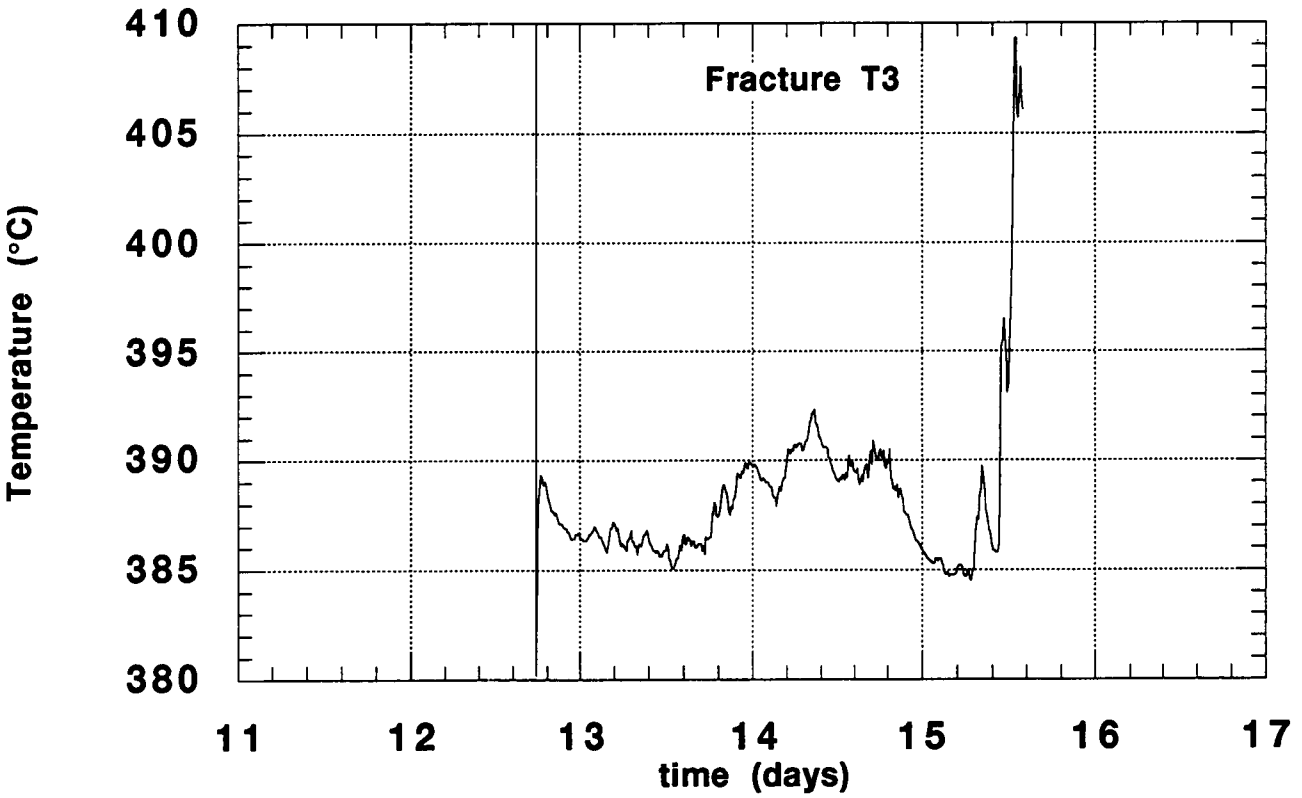

There is remarkable correlation between variations in temperature in T2 and variations in T3 between day 12 and day 15. This indicates that the process controlling temperatures is the same in the two different fractures.

T4 data were collected along the same fracture as data collected in T3. The fracture was narrower at this location and the thermocouple could be inserted to about 25 cm depth. There is excellent correlation between temperatures collected in T4 (Figure 15, "Fracture T4, Cone," on page 20) and T3 and T2. However, temperature changes in T4 that correlate well with T2 and T3 are super-imposed on a "long - term" positive trend, that changes average temperatures in the fumarole by about 15 °C between 0:00 on day 12 and 12:00 on day 14.

FIGURE 15. Fracture T4, Cone I

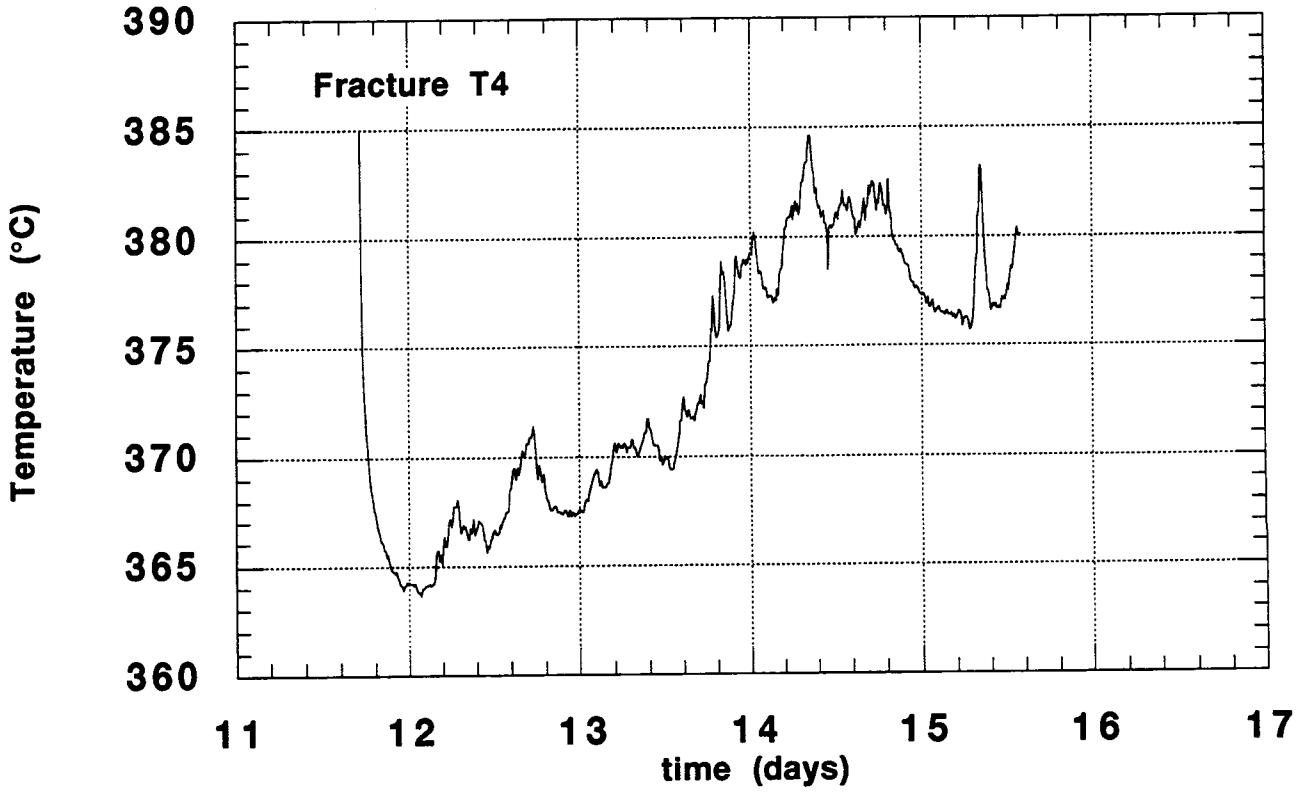

Summary of continuous temperature observations at Cone I:

- As at Cone II, temperatures are basically steady-state on the time scale of the survey. An exception is T4, which shows a definite increasing trend over several days.
- Short - term variation is present in all of the fumaroles
- changes in T1 correlate extremely well with changes in barometric pressure. Variation in T2-T4 does not appear to correlate with barometric pressure as well
- Excellent correlation exists between T3,T4, and T2.

Further analysis of these data should include FFT analysis.

1.5 Gradient Measurements

The datalogger was also used at Cone I to measure temperatures at depths of 30 cm, 60 cm, 90 cm, and 185 cm. This was done by driving stainless steel (inside diameter = 3/8 inches) and Ti tubes into the cone to the various depths. The location was chosen to be off any fractures. The sampling station is located on the crater rim of Cone I.

Temperature data were collected in these tubes on days 9 through 11. The data are shown in Figure 16, "Temperature at a Depth of 30 cm (Cone I)," on page 21,Figure 17, "Temperature at 60cm (Cone I)," on page 22,Figure 18, "Temperature at 90 cm (Cone I)," on page 23, and Figure 19, "Temperature at 185 cm (Cone I)," on page 24. In addition, atmospheric temperature and barometric pressure data were collected. These series are shown in Figure 20, "Atmospheric temperature measured at Cone I," on page 25 and Figure 21, "Atmospheric pressure measured at Cone I," on page 26. The weather was bad during this sampling interval. On day 9 it began to rain intermittently. It rained alll day on day 10 and intermittently to clearing on day 11.

FIGURE 16. Temperature at a Depth of 30 cm (Cone I)

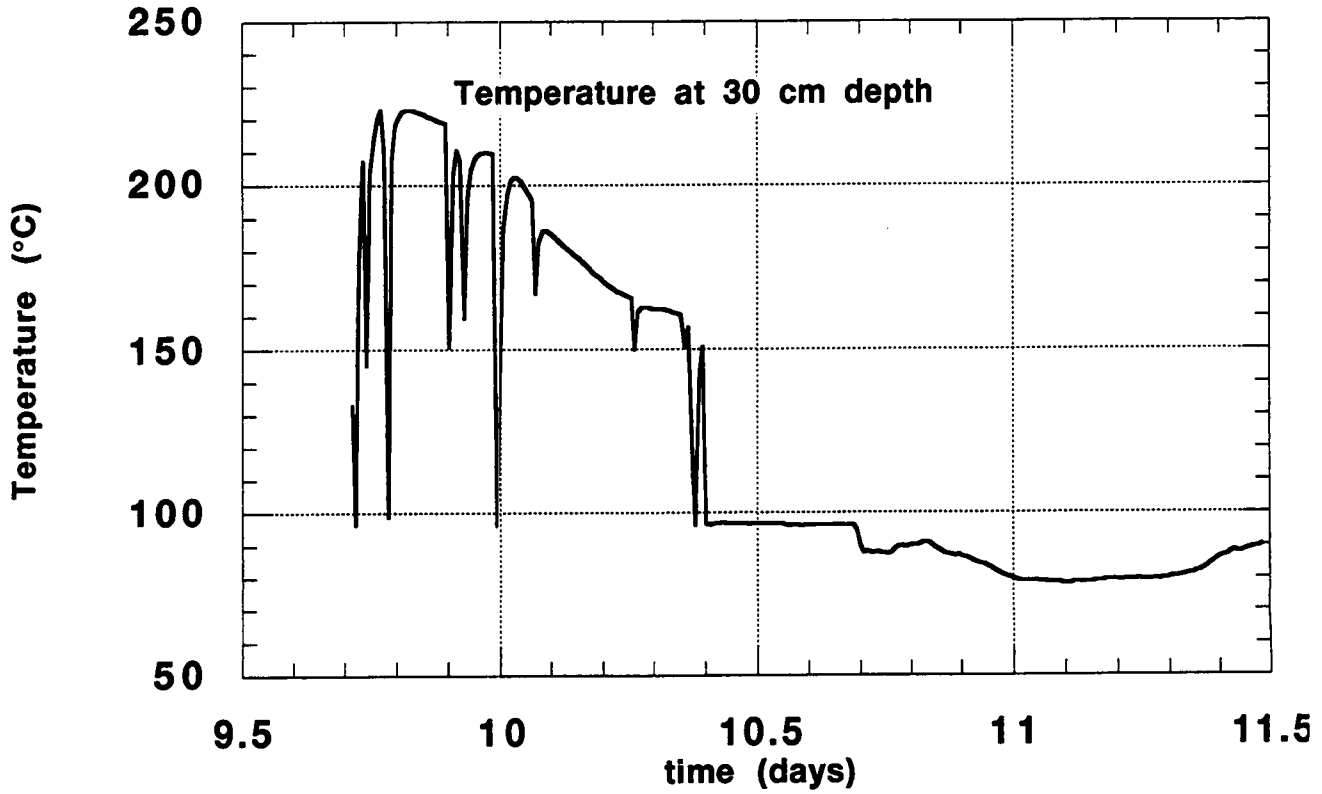

Temperatures at shallow depths (30 cm) were strongly effected by the rain. Initially, temperatures at 30 cm were about 220°C. Several spikes occur on days 9 and 10, when the termocouple temperature drops to just below 100°C. This probably results from water collecting in the tube, and the temperature decreases as a result of evaporation. During this time the temperature is dropping steadily until in reaches 150°C and then falls abruptly below 100°C. This is a combination of water collecting in the tube and infiltrating the soil (which is really cinder) - cooling the soil temperatures.

FIGURE 17. Temperature at 60cm (Cone I)

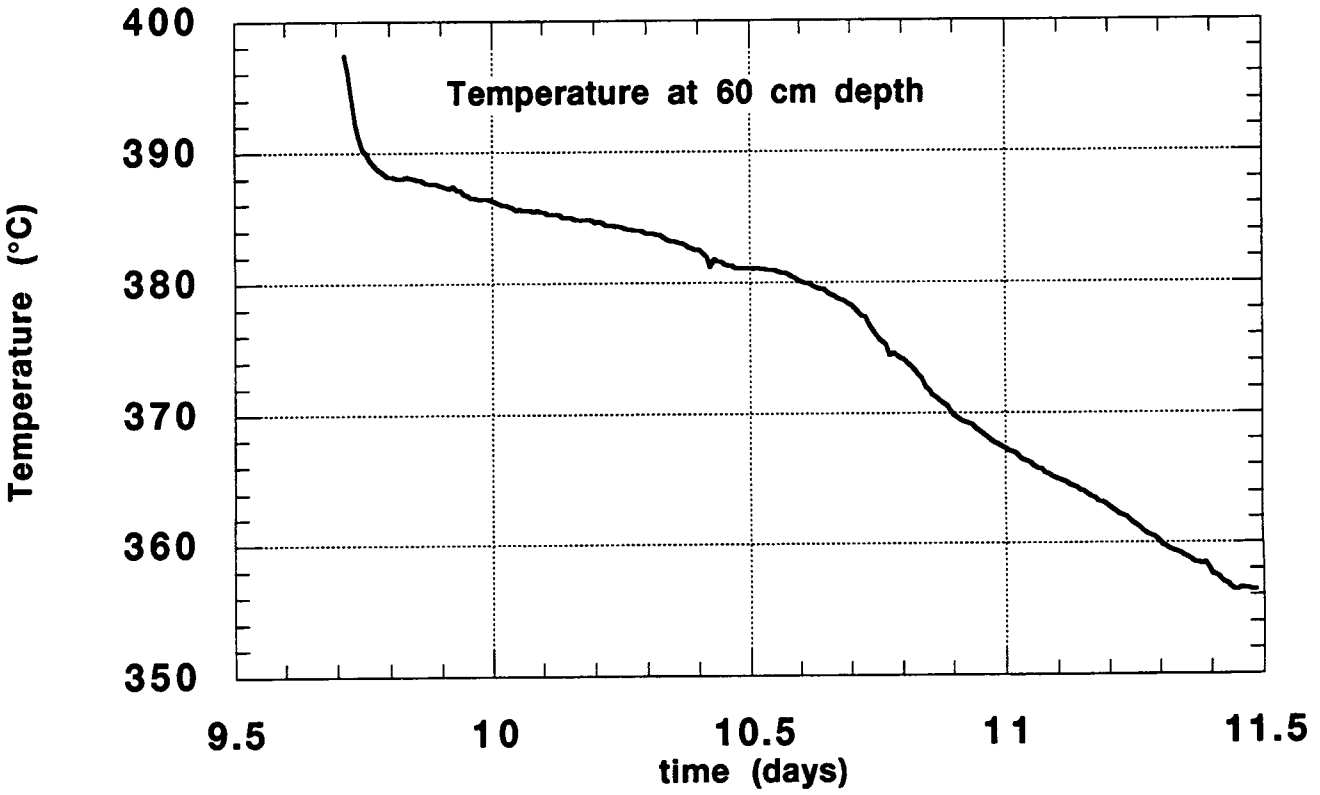

Temperatures are much higher at a depth of 60 cm. Over time the temperature decreases from 398°C to 356°C. No spikes occur in this thermocouple, indicating that the temperatures are high enough so that any water infiltrating the tube evaporated before reaching the thermocouple. The gradual cooling temperatures are thought to be related to cooling due to water infiltration (above 60 cm).

Temperatures are very steady a 90 cm depth during days 9 and 10, varying by less than 1°C about 433°C. At approximately 18:00 on day 10 the temprature begins to decrease, falling to 426°C in a steady fashion. It is clear that the rain had no effect on temperatures at 90 cm until heavy rain began on day 10, at which point temperatures decreased, but only slightly compared with changes at shallower depths.

FIGURE 18. Temperature at 90 cm (Cone I)

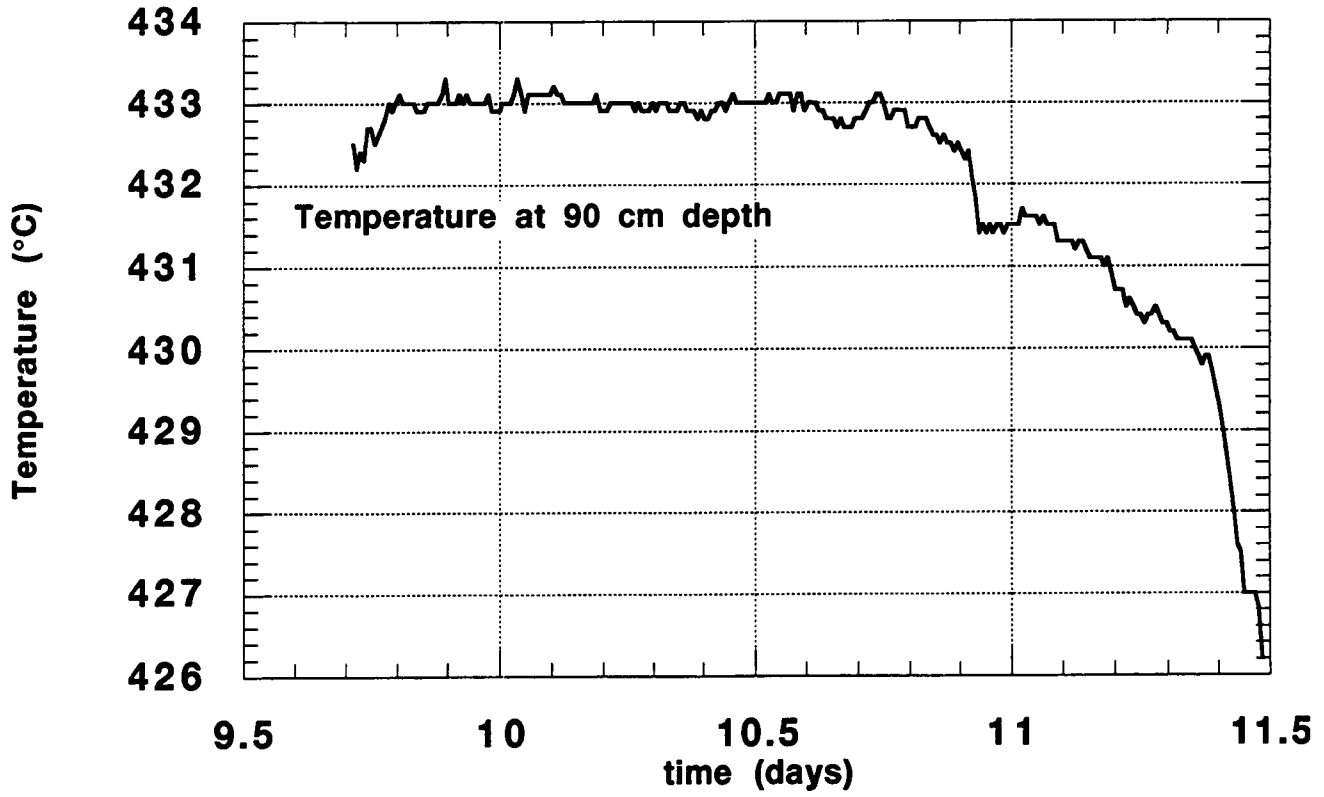

At 185 cm depth temperatures were steady at 469 - 470 °C during the entire sampling interval. No trends, associated with rain, occurred in temperature at this depth. The only variation is spikes in the temperature, espeicially on day 9. It is unknown what causes this spike.

FIGURE 19. Temperature at 185 cm (Cone I)

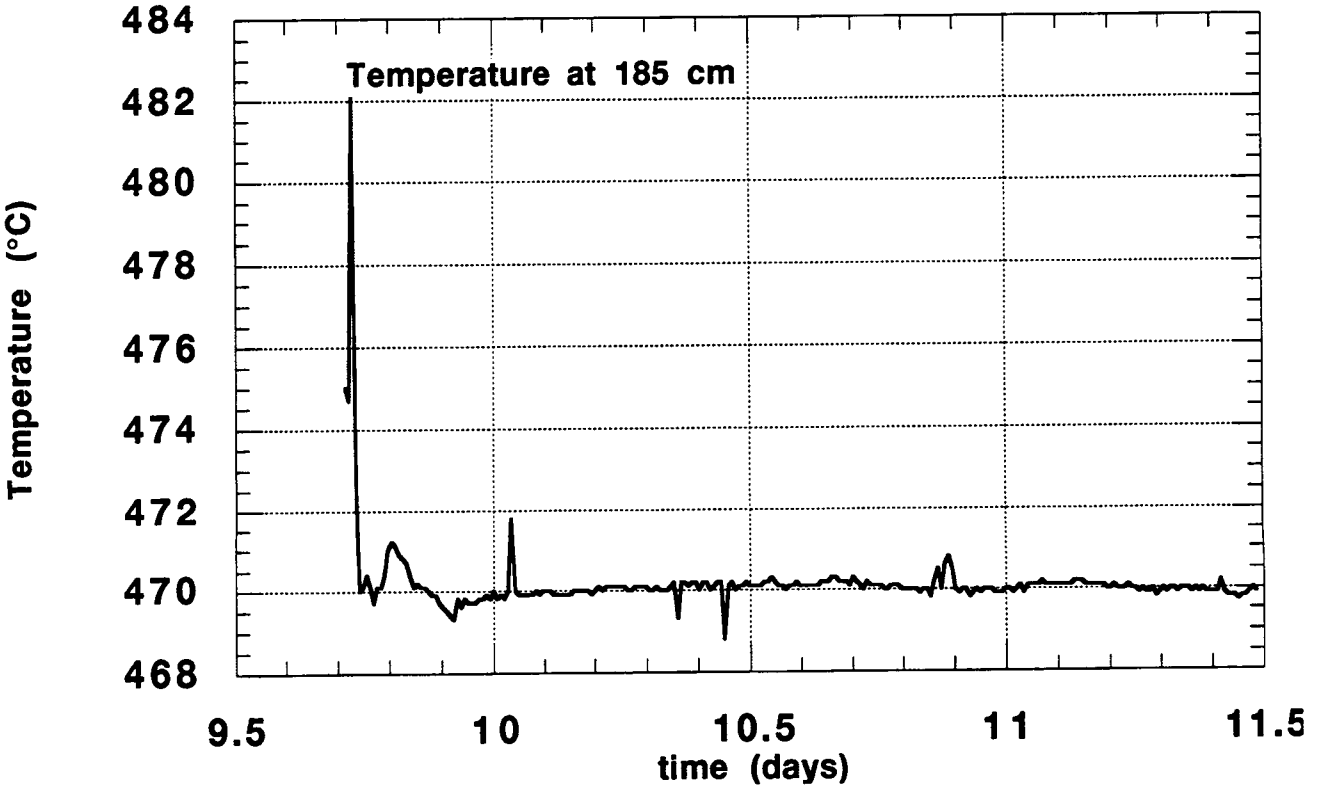

FIGURE 20. Atmospheric temperature measured at Cone I

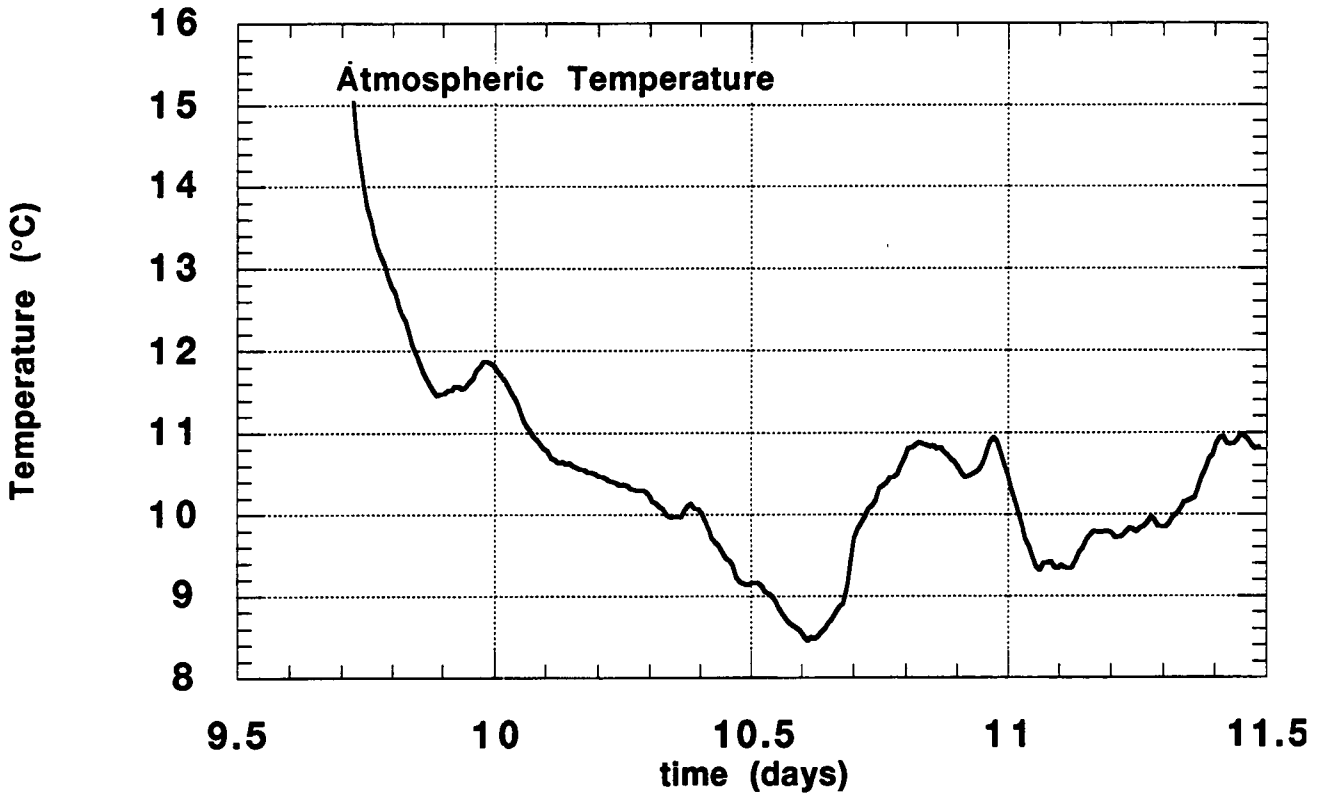

FIGURE 21. Atmospheric pressure measured at Cone I

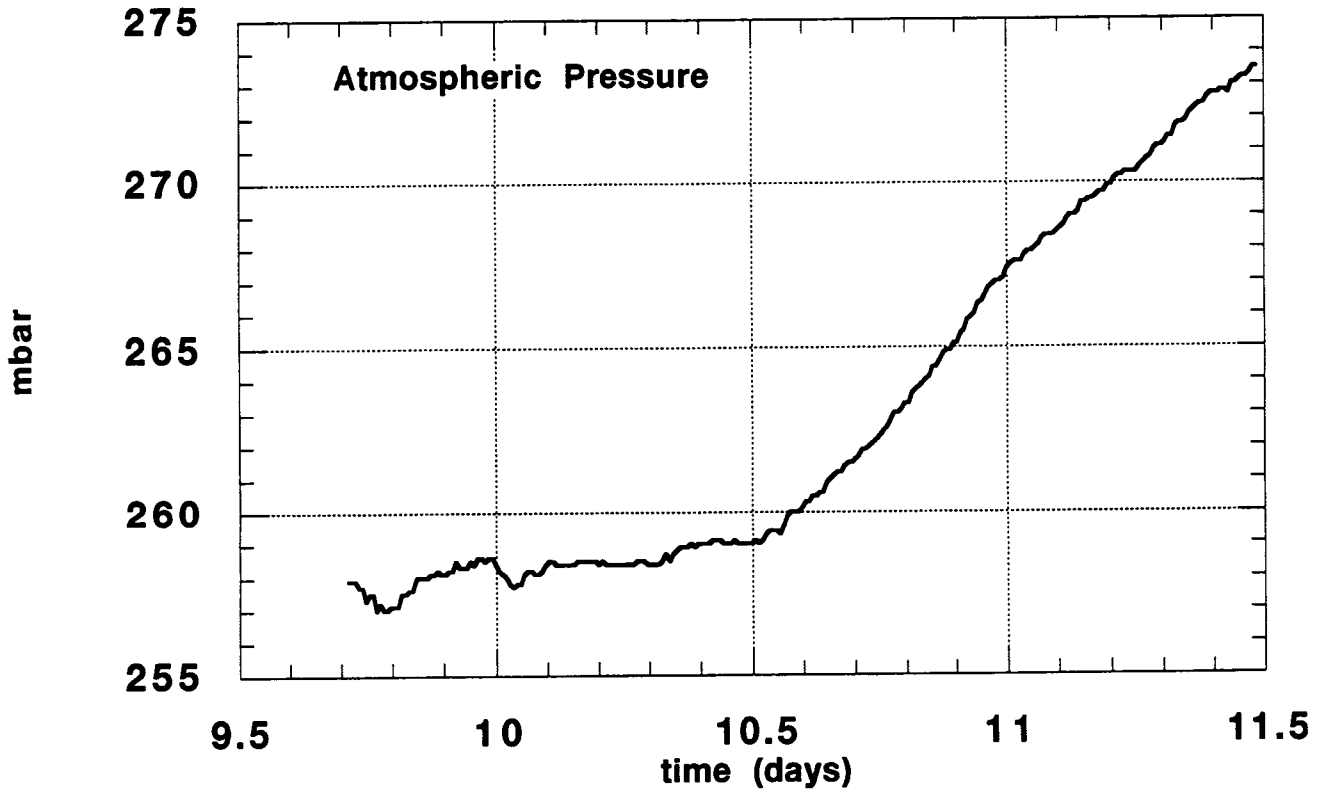

Summary of the continuous temperature gradient measurements

- The temperature gradient recorded between 185 cm and 90 cm varies from 38°C and 52°C per meter during the sampling interval. The temperature gradient recorded between 90 cm and 60 cm varies from 117 °C and 270°C during the sampling interval.
- temperatures at depth of 30 and 60 cm are strongly effected by weather conditions in this area, tempeatures at 90 cm and 185 cm are not, primarily because of the tremendous temperature gradient.
- The range of temperature gradients observed during the sampling period are plotted in Figure 22, "Temperature gradients on Cone I," on page 27.

FIGURE 22. Temperature gradients on Cone I

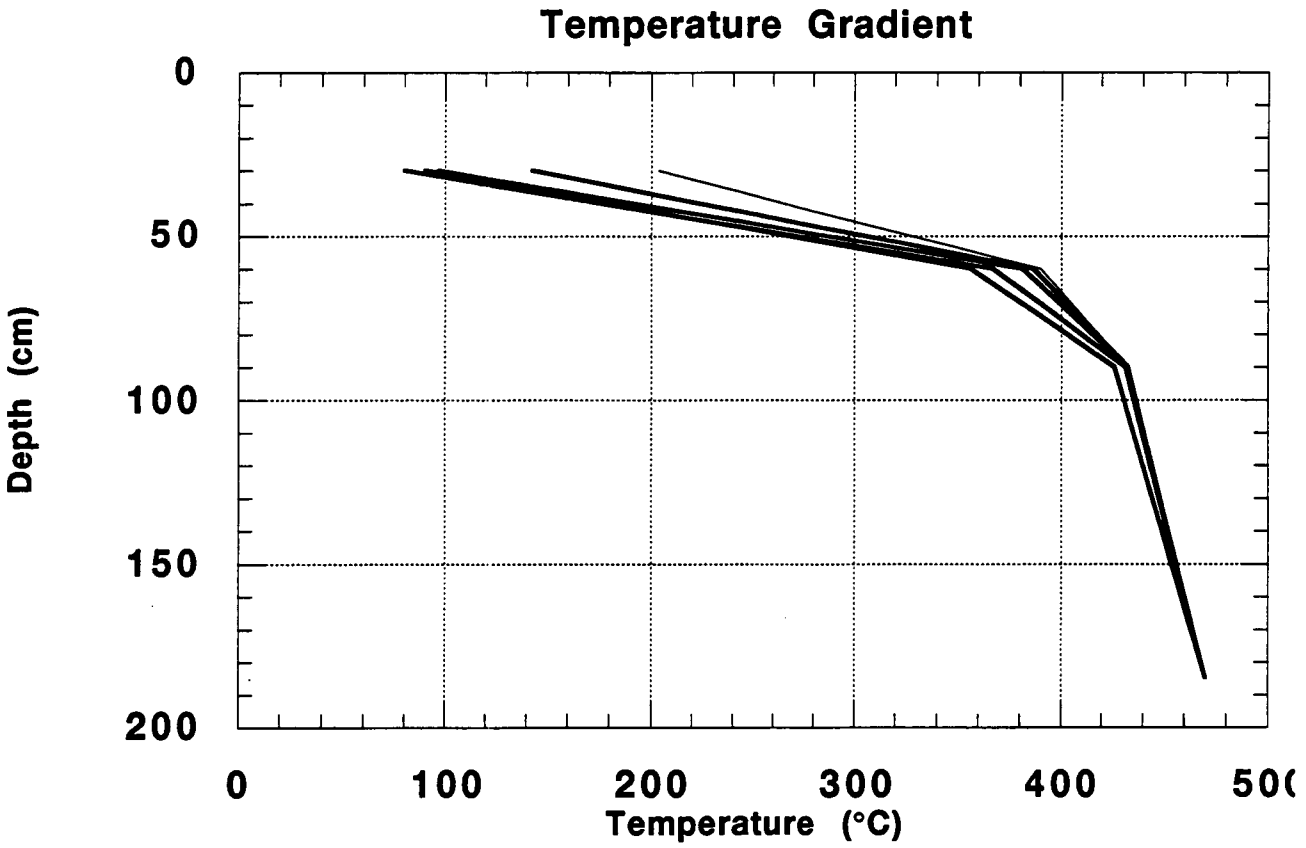

Crater Flat Magnetic Survey

Chuck Connor

Chuck Connor

A magnetic survey was conducted in two areas of Crater Flat: between Red and Black Cones and between the two Little Cones for the purpose of determining the ability of the method to identify shallow dikes in this area.

Summary

Ground magnetic data were collected in two areas of Crater Flat, immediately west of Yucca Mountain, Nevada, in order to determine the effectiveness of thes method for identifying shallow intrusive structures near the Crater Flat alignment. The basic problem is that the cinder cones and their associated lava flows likely produce large enough magnetic anomalies to obscure the comparatively small anomalies associated with dikes, especially on aeromagnetic maps. Ground magnetic surveys may be useful in identifying dikes, as long as the dikes are shallow compared to the map distance to lava flows.

The first survey was done on the approximately E-W road between Red and Black cones. Magnetic readings were collected every 5 m over a distance of 1.1 km. Data were drift corrected by reoccuppying a base station at 30 minute intervals. Significant drift was observed during one interval and stations were resurveyed to reduce the effects of this drift. The results of the survey showed a gradient that is identical to the one seen on aeromagnetic maps. There was no evidence of a shallow dike between the two cones based on the single traverse.

Ground magnetic data were also collected between the two Little Cones. 581 stations were occuppied on 8 traverse lines. Most lines were 400 ft long and trended 142° magnetic. Large amplitude (generally greater than 1,000 nT), short wavelength magnetic anomalies were identified between the two cones. However, the orientation and distribution of anomalies clearly indicates that at shallow levels dikes strike roughly N-S and are not continuous between the two cinder cones. The dikes identified intersect NE Little Cone and extend at least 350 ft south of the summit of NE Little Cone on a N-S

trend. It is noted that this dike orientation is consistent with mapped structural trends (faults and dikes) elsewhere in Crater Flat. Furthermore, a N-S structural control is consistent with the breaching of SW Little Cone, which occurred on the S side of that cinder cone. Additional ground magnetic mapping on Little Cones is recommended to determine if (i) the mapped N-S trending anomalies extend N of NE Little Cone, (ii) similar magnetic anomalies can be identified associated with SW Little Cone, and (iii) to map the buried edge of the lava flow from SW Little cone. Based on our preliminary survey, a very detailed magnetic map could be constructed in 7 - 9 days of field work in good weather.

Details of the Red Cone - Black Cone Traverse

A single ground magnetic traverse was made between Red and Black cones in Crater Flat Valley on Saturday, Sept. 10, 1994. Weather was clear and temperature was about

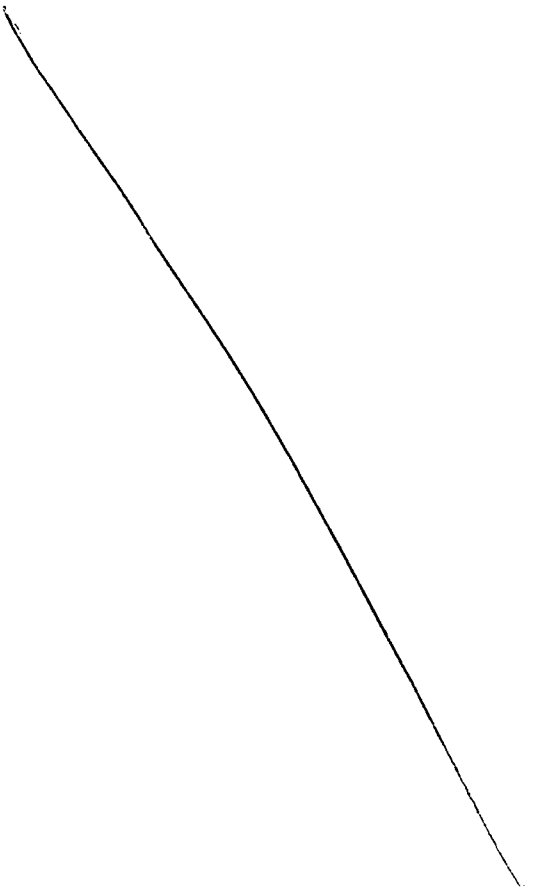

FIGURE 1. Ground Magnetic Traverse between Red and Black Cones

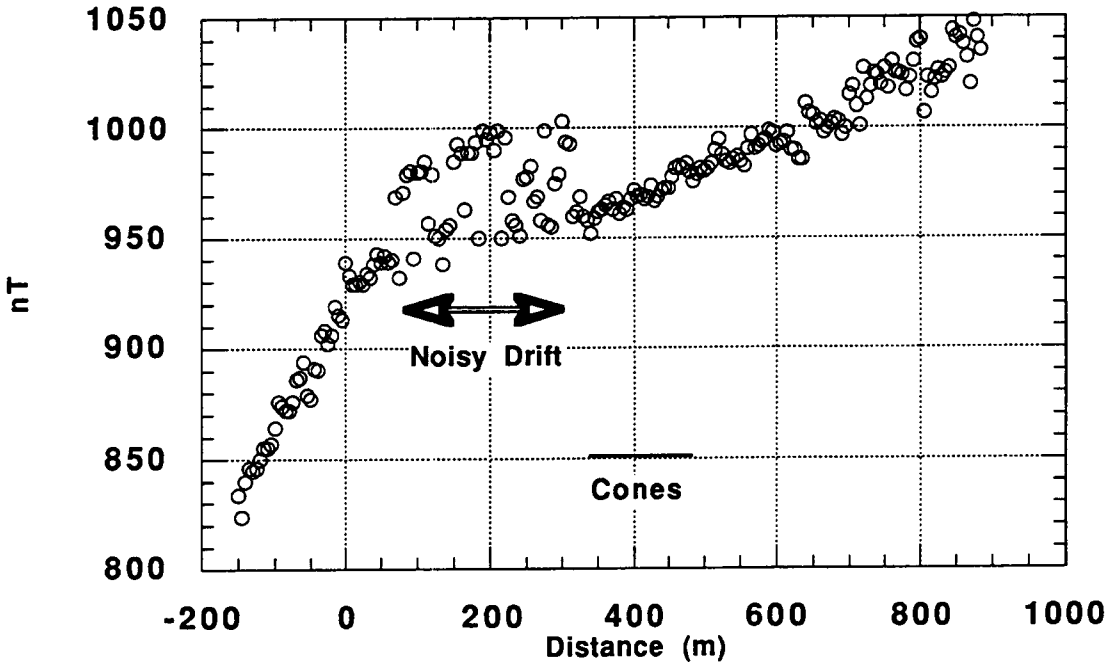

85°F. Winds were out of the SW at 10-20 mph. A base station was established at the SE corner of the intersection of the approximately E-W trending road between the two cones and the road which leads N to the drilling pad on the SW side of Black Cone. This station was reoccupied five times during the survey to check magnetic field drift. A proton -precession magnetometer (EG and G, Geometrics model G-856 total field magnetometer was used. Data were recorded digitally by the magnetometer and later transcribed. The sensor was carried on a two meter staff. A three meter staff was not used because of the wind.

Drift corrected results are shown in Figure 1, "Ground Magnetic Traverse between Red and Black Cones," on page 2. The base station is located at distance 0 and the traverse was from west to east along the road between the two cones. A line connecting the two cones is located at a distance of approximately 400 m.

Data were noisy between 75 and 100 m

The data are consistent with regional magnetic gradients shown on the aeromagnetic map of the area. The is no evidence of a shallow dike connecting the two cones on this particular traverse.

Little Cones Survey

A survey was done in the saddle between the two Little cones on Saturday Sept. 10 and on September 13. On Sept. 10 a single line was put in on a 142° azimuth in the saddle between the two cones. This line revealed a sharp, large amplitude, short wavelength anomaly. Based on this anomaly, it was decided that shallow dikes are present and a more detailed survey was done on Sept. 13. This survey consisted of seven additional lines, also trending 142° (magnetic) with stations every 5 ft. Each line was 400 ft long. The lines were parallel and spacing between lines was either 30 ft or 60 ft. A base station was established in the center of the area and measurments were collected at this base station at 15 minute intervals for drift correction. Total measured drift during the survey was less than 20 nT. A proton -precession magnetometer (EG and G, Geometrics model G-856 total field magnetometer was used. Data were recorded digitally by the magnetometer and later transcribed. The sensor was carried on a three meter staff. Data were collected by Chuck Connor, Britt Hill, and Steve Lynton of CNWRA.

Survey lines are shown inFigure 2, "Location of traverses between the Little Cones," on page 4. Profiles corresponding to these survey lines are shown inFigure 3, "Line -1, Little Cones," on page 5 through Figure 8, "Line 4, Little Cones," on page 7.

Review of these profiles yields several basic observations:

- The most direct line between the cones is magnetically quiet.
- Nice anomalies are found in the SE portion of the survey area
- In general, these anomalies are complex, of variable amplitude and wavelength, and consists of varying numbers of maxima and minima.
- the cleanest looking anomalies, such as on line 2, are consistent wit hthe presence of shallow, reversely polarized igneous dikes.
- more complex anomalies may indicate the presence of more than one dike, or bifurcation of the dike at shallow depths.
- The anomalies are nearly absent on line -1 and 0 except at the extreme SE end. This may indicate that the dike is further SE of the end of these profile lines.

FIGURE 2. Location of traverses between the Little Cones

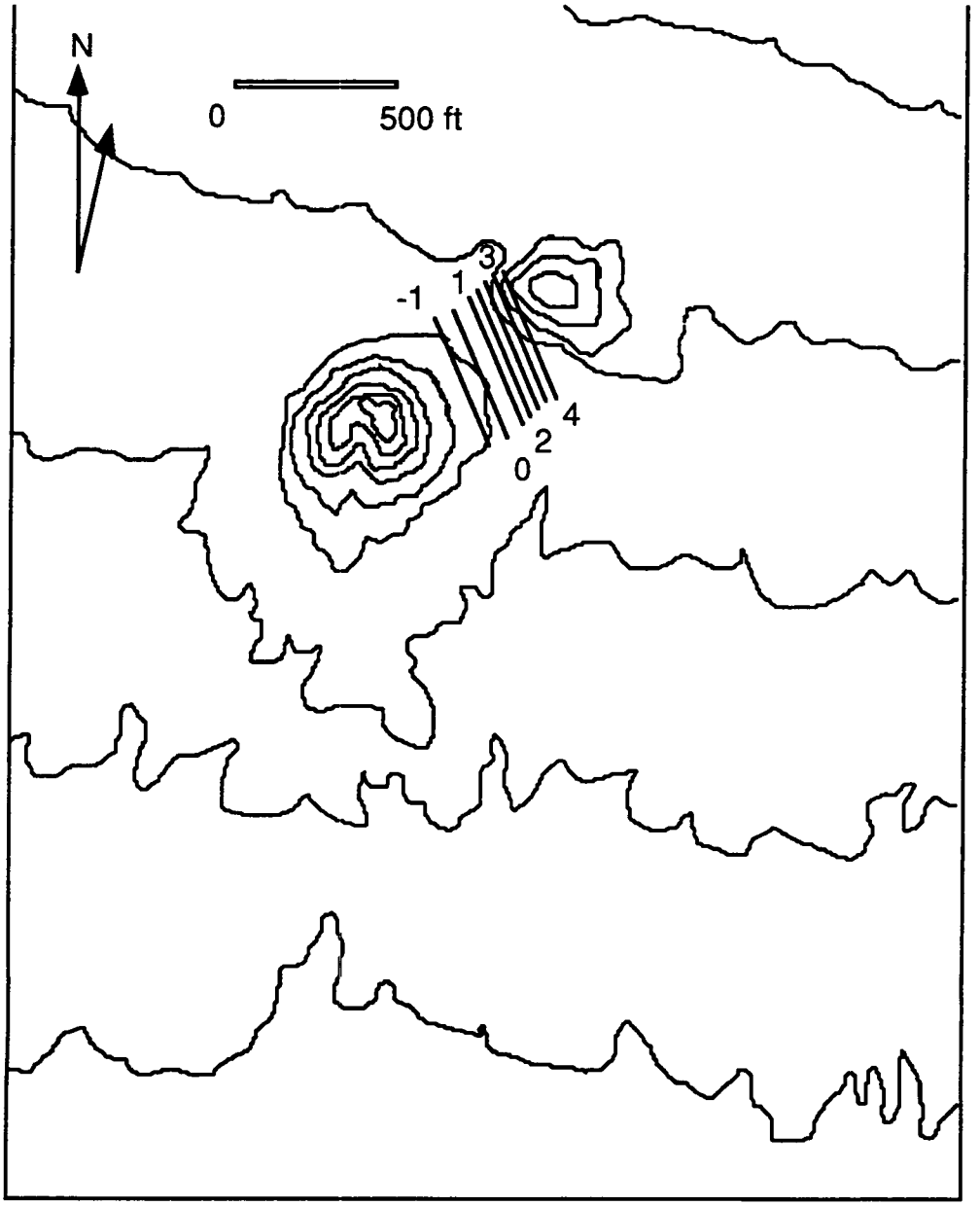

FIGURE 3. Line -1, Little Cones

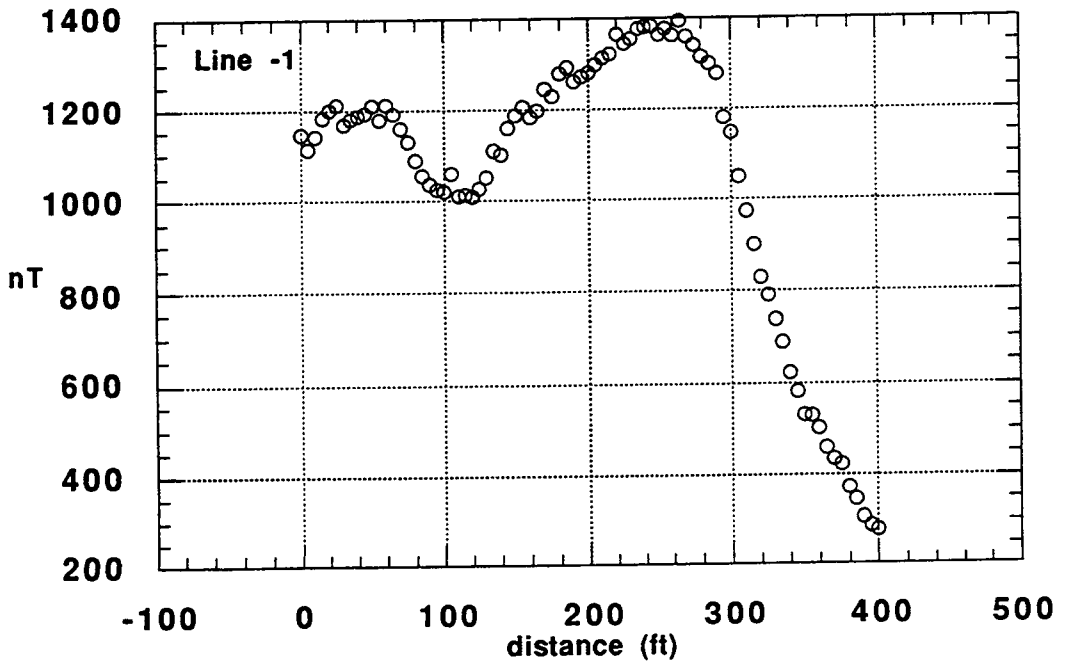

FIGURE 4. Line 0, Little Cones

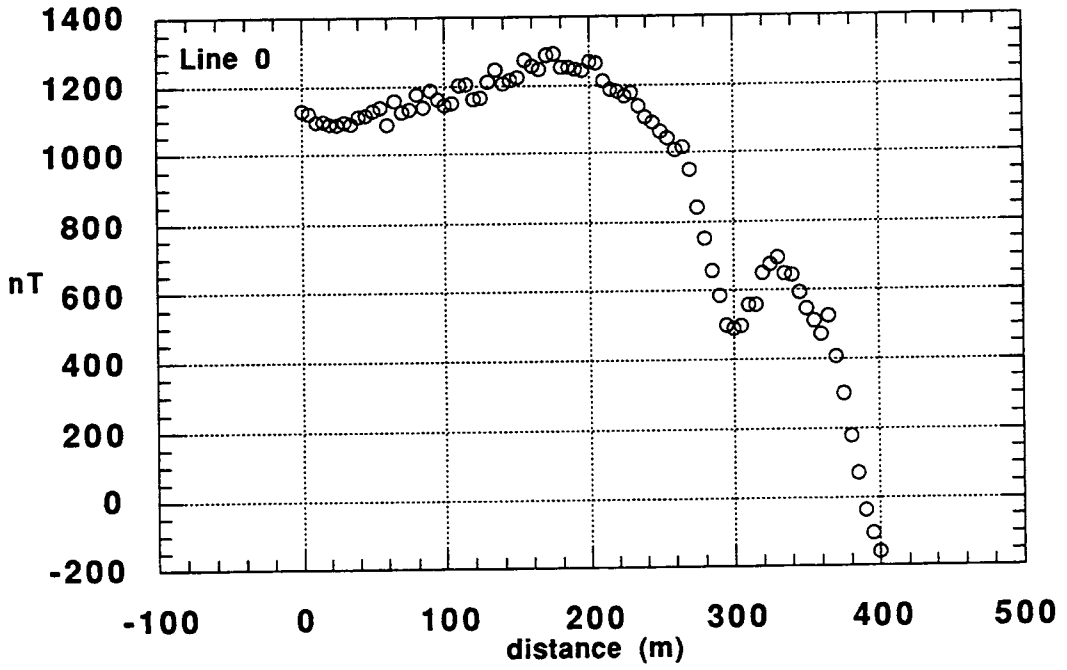

FIGURE 5. Line 1, Little Cones

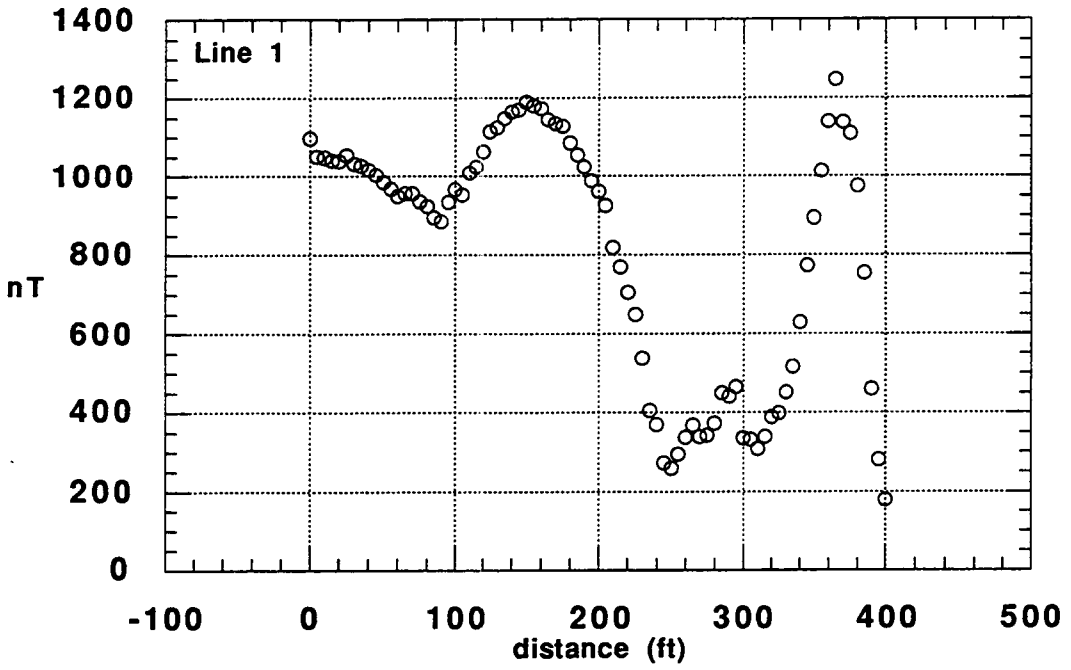

FIGURE 6. Line 2, Little Cones

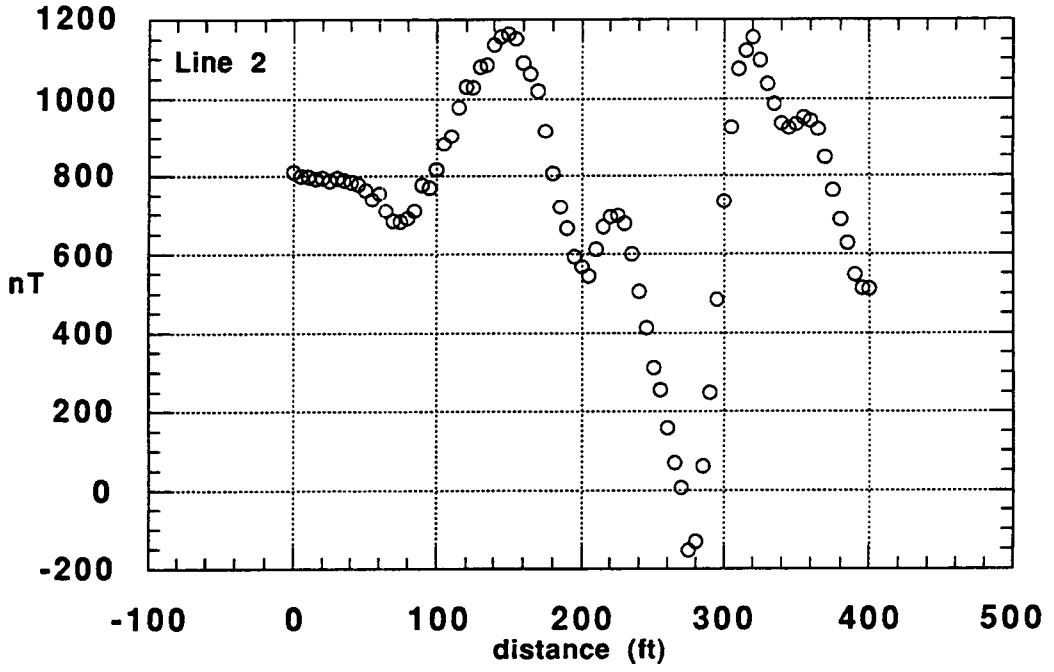

FIGURE 7. Line 3, Little Cones

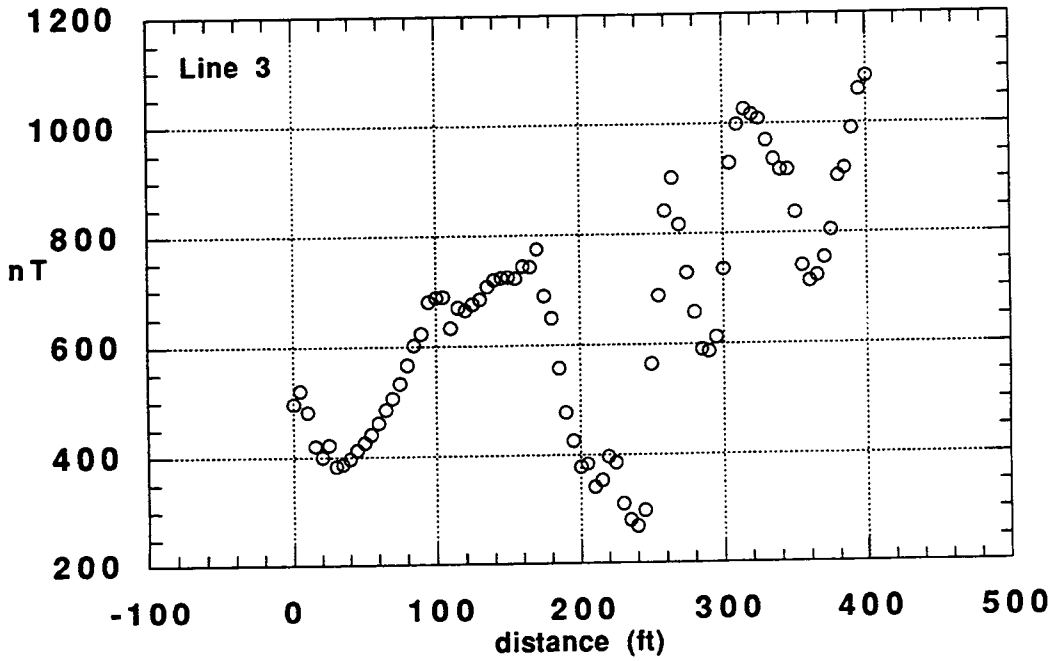

FIGURE 8. Line 4, Little Cones

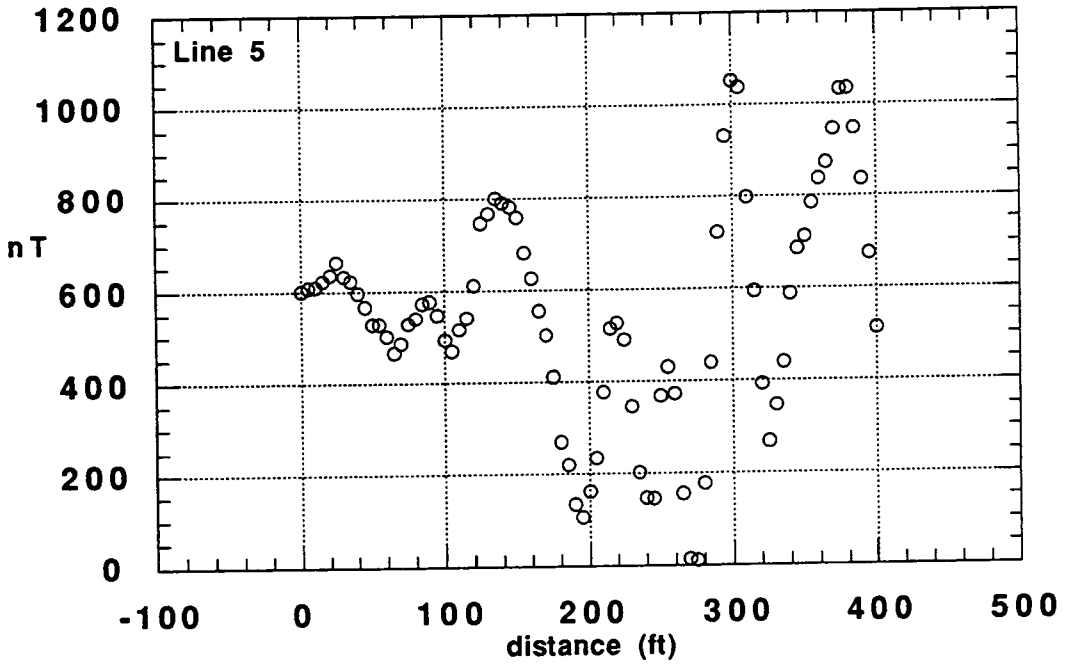

FIGURE 9. Shaded area shows the N-S trending zone of anomalies which is interpreted to be related to the presence of several dikes.

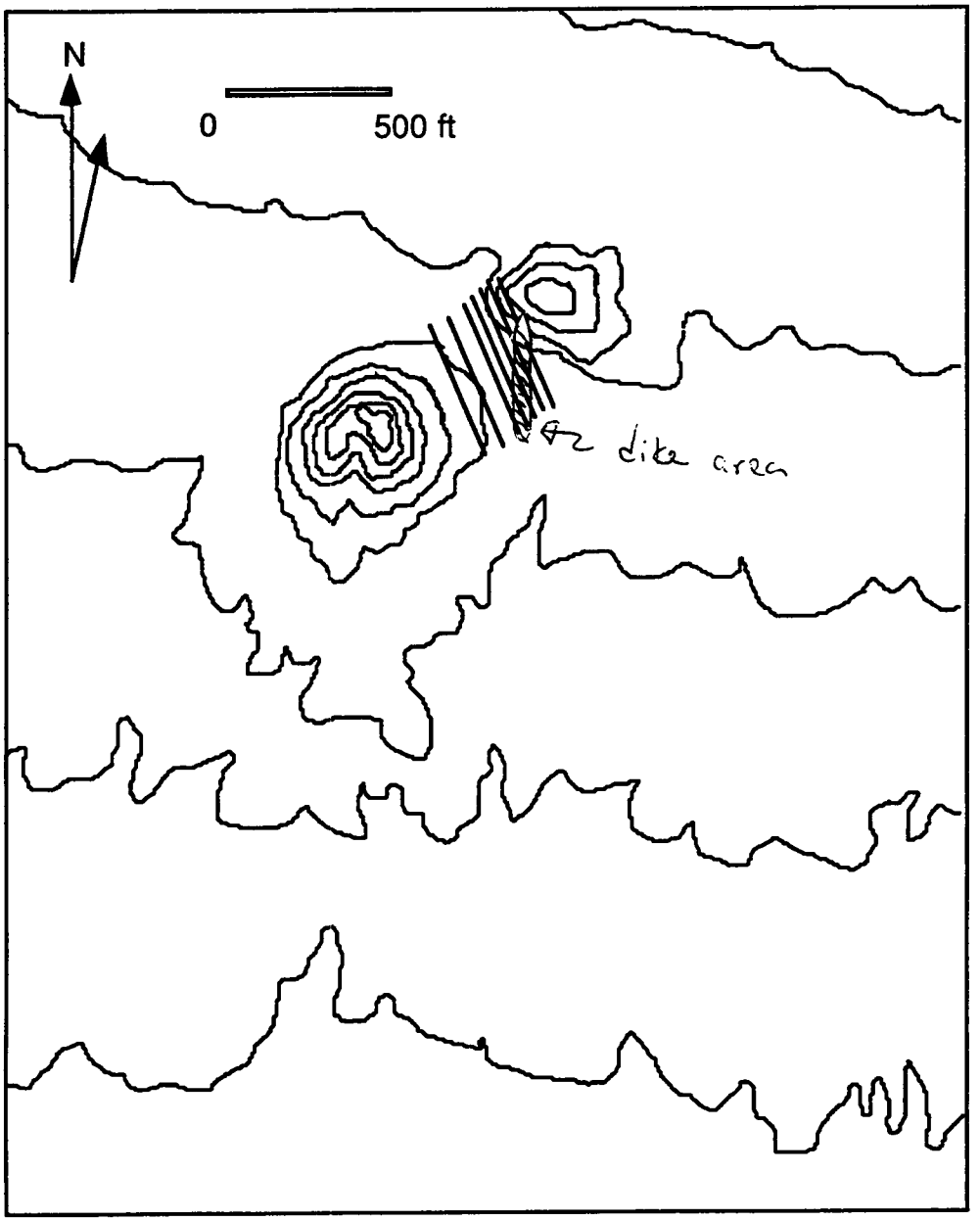

The interpretation shown in Figure 9, "Shaded area shows the N-S trending zone of anomalies which is interpreted to be related to the presence of several dikes.," on page 8 is simply derived by plotting the maxima and minima on the profiles in map view. The baest interpretation of these data are that a roughly N-S trending dike set is present

FIGURE 10. Detailed graph showing the trace of maxima and minima of magnetic anomalies in the survey area.

extending south of the NE Little Cone. This is not consistent with a simple dike connecting the two cones at shallow depth. However, the presence of N-S trending dikes is consistent with the overall geometry of mapped structures in Crater Flat, including dike trends and faults. Furthermore, the breached crater rim on the south side of SW Little Cone may indicate the presence of a similar structure beneath this cone.

The profiles are plotted together in Figure 10, "Detailed graph showing the trace of maxima and minima of magnetic anomalies in the survey area.," on page 10. Dashed lines on this figure connect minima. In reversely polarized basalts which trend roughly magnetic N, these minima probably show the axis of buried dikes.

The data are replotted in map view in Figure 11, "Interpretation of magnetic anomaly data. 20 foot contours on NE Little Cone are shown. The prominent magnetic minima are connected between profiles. The trend of the profile lines are shown.," on page 12. Note that the dike trends are roughly N-S, intersect the top of the cone where densely welded spatter outcrops, do not follow a direct line between the two cinder cones, and curve near the cinder cone. The curvature may indicate that close to the cone the dike pattern is radial - farther from the cone the dike pattern is closer to the regional stress pattern.

This type of survey helps place the cones in a structural context which is otherwise not possible. Clearly, further data collection arounf these cones is desirable. This will

- enable us to map out the anomalies to their fullest map extent
- place Little Cone dikes in a more reasonable (ie supportable) structural framework
- possibly determine the true thickness of lava flows on the south side of SW Little Cone, which would go a long way toward constraining volume measurements.

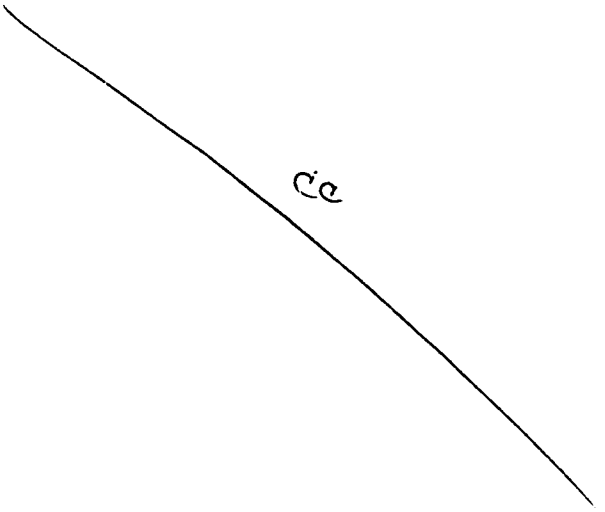

FIGURE 11. Interpretation of magnetic anomaly data. 20 foot contours on NE Little Cone are shown. The prominent magnetic minima are connected between profiles. The trend of the profile lines are shown.

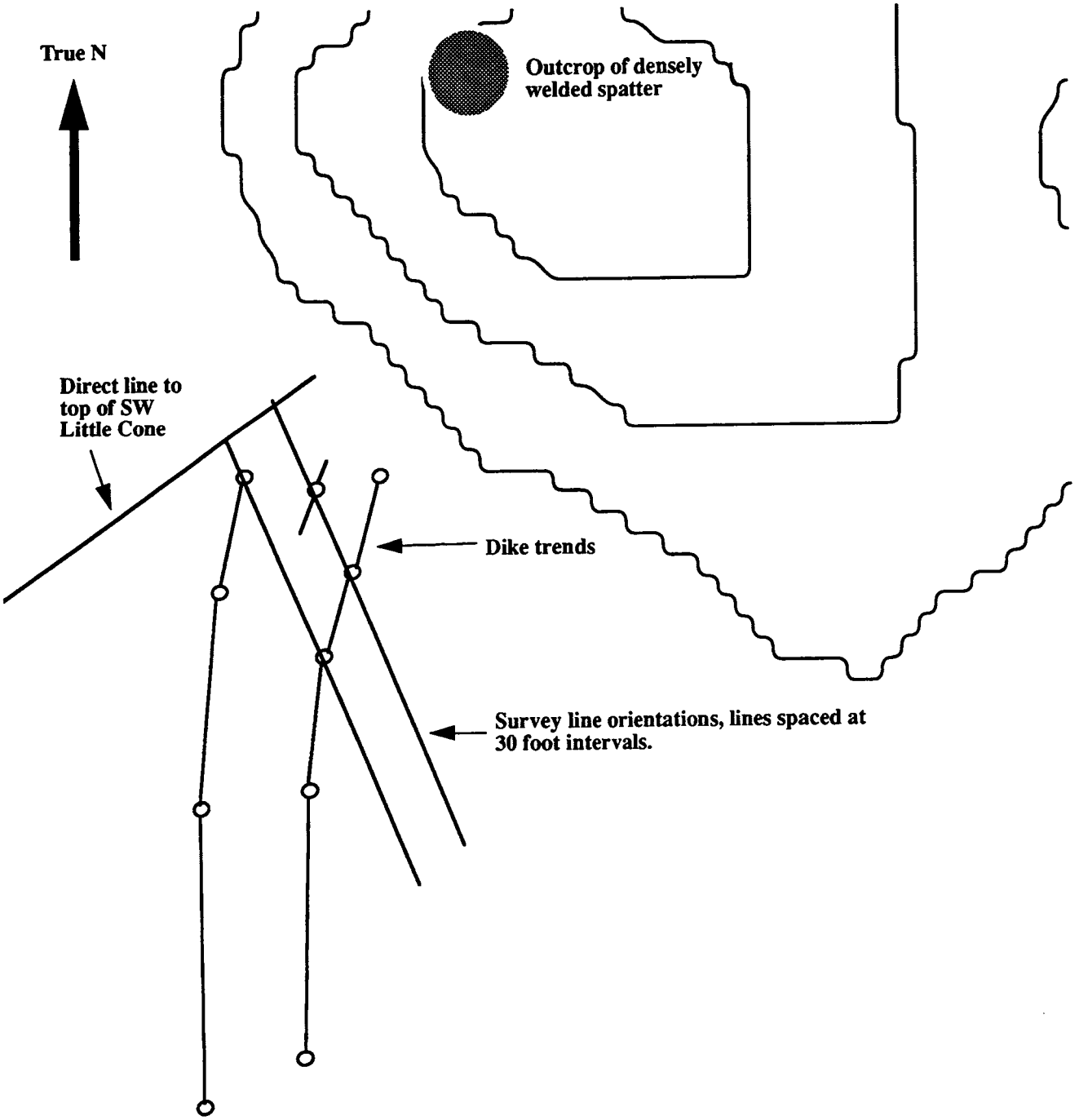

Recurrence Rate: SVF

Recurrence rate in the Springerville Volcanic field (SVF) is investigasted using near-neighbor techniques. The purpose is to test near-neighbor models in an area that has experienced a relatively large number of small-volume basaltic cinder cone eruptions compared with the YMR. In step 1, the actual recurrence rate of volcanism is estimated from avaialable data, in 2, the recurrence rate curve is modeled using near - neighbors, in 3 the spatial variablity in recurrence rate is estimated by plotting recurrence rate maps, in 4 the rate of change in recurrence rate is discussed in terms of tectonic and structural setting of the SVF.

1.0 Introduction

Problems with probability studies of the volcano disruption scenario include

- It is difficult to estimate recurrence rate
- It is difficult to assess the relatonship of the probability model to basic geological processes
- There are inadequate volcanic events in the YMR to test many probability models for sensitivity to geological processes.

Here, I use a near-neighbor model to estimate and describe recurrence rate of volcanism in a large, Colorado Plateau volcanic field. The Springerville filed (SVF) is selected for this analysis because

- There are a large number of cinder cones in the field
- The field is perhaps the best-mapped volcanic field in the U.S.
- A great deal of geochronology has been done in the SVF.

Summaries of the geological history of the field are found in Condit et al., 1989, Patterns of volcanism in the Springerville volcanic field, AZ, Journal of Geophysical Research) and Connor at el. (1992, Evidence of Structural control on vent distribution: Springerville volcanic field, AZ, Journal of Geophysical Research)

Briefly, the Springerville Volcanic Field (SVF), east-central Arizona, and is located on the southern margin of the Colorado Plateau and consists of 403 mapped basaltic (tholeiite to evolved alkaline) vents (Figure 1 on page 2). These vents include cinder cones, maars, spatter cones, and two shield volcanoes.

CC

FIGURE 1. Location of the Springerville Volcanic Field

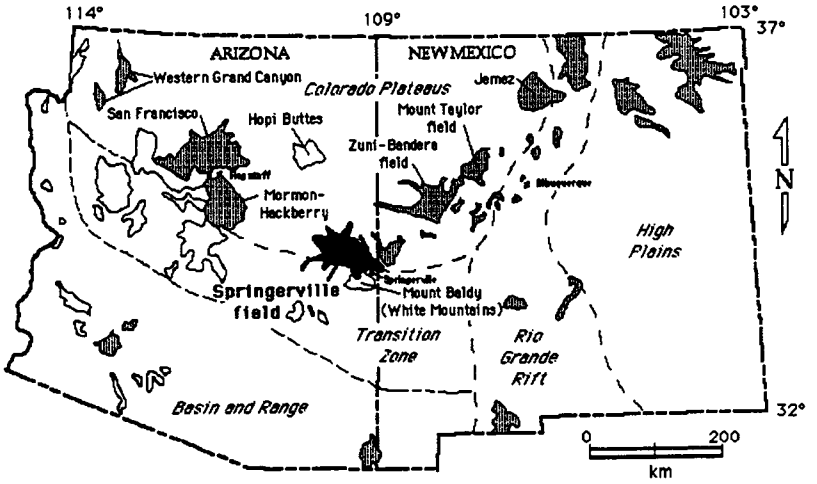

The Springerville volcanic field is located along the southern margin of the Colorado Plateaus in east-central Arizona. Physiographic provinces of the area delineated. The Mogollon Rim is a topographic escarpment which defineds the boundary between the Transition Zone and the Basin and Range provinces. Shaded areas indicate volcanic fields less than 5 m.y. old, outline areas show volcanic fields 5 to 16 m.y. old (from Wolfe et al., 1983).

Connor et al. (1992) identified vent clusters and vent alignments in the SVF using variaous statitstical techniques (cluster analysis, Hough transform, two-point azimuth analysis. The results of these analysis are shown in Figure 2 on page 3.

Basically, this analysis showed two things. First, vents show a statistical tendency to cluster in the SVF. Six large clusters are found in the field, accounting for all but 4 of the vents. Also, analysis of clusters for preferred alignment orientation demonstrated that regiona lalignments that are observed cutting across the field are statitstically significant. These alignments are oriented WNW in the western portion of the field and ENE in the eastern portion of the field. These orientations appear to mimic the boundary of the Colorado Plateau.

None of this work involved the ages of the flows or vents because in 1992 this information was not readily available. Since that time, Chris Condit has compiled the age data for the field and created a daatabase, which contains the age of the vent, the uncertainty in the age of the vent and the methods used to date the vent. These methods include K/Ar, paleomagnetics and stratigraphic relations.

CC

FIGURE 2. Results of cluster and vent alignment analysis of Connor et al., 1992

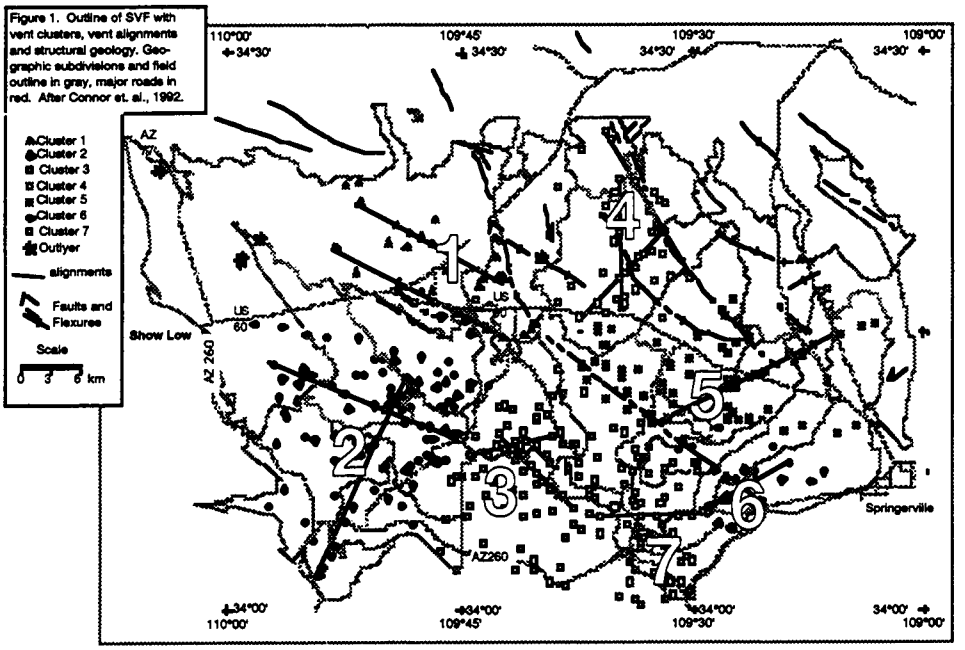

2.0 Age Determinations

Dated lava flows and their associated vents are given below.

2.1 Numerically dated Units

-705MC' Qhe 0.50±0.03 Cooper and others, 1990 ---

-706GP' Qph2 1.27±0.07 Cooper and others, 1990 Underlies unit Qpc8 (712GP, 1.30±0.04 Ma); suggests age >1.26 Ma.

-708WK' Qgh7 0.76±0.02 Cooper and others, 1990 Normal magnetic polarity of flow (two sites) suggests age <0.73 Ma.

-709WK' Qgb1 0.91±0.02 Cooper and others, 1990 ---

-712GP' Qpc8 1.30±0.04 Cooper and others, 1990 ---

-713SN' Qkc4 0.61±0.01 Cooper and others, 1990 ---

-716SM' Qmb6 1.01±0.02 Cooper and others, 1990 ---

-717MR' Qwg3 1.56±0.03 Cooper and others, 1990 ---

-719V' Qvc4 1.00±0.02 Cooper and others, 1990 Normal magnetic polarity of flow and date from sample UAKA 82-191 (1.30 ±0.05 Ma) cannot be reconciled with this date.

-801C' Tof 6.52±0.12 Cooper and others, 1990 aliquot has age of 6.66±0.12

-801C" Tof 6.66±0.12 Cooper and others, 1990 aliquot has age of 6.52±0.12

-2316-2 Twj 7.6±0.4 R.J. Miller, oral commun., Sample collected by C Conway, U.S. Geological Survey, Flagstaff, analyzed by R.J. Miller, U.S. Geological Survey, Menlo Park.

-AWL-40-74 (Trg) 2.94±0.14 Laughlin and others, 1979 Sample site 6.8 km east of Springerville along U.S. 60, off map

-AWL-41-74 (Qrg) 0.82±0.04 Laughlin and others, 1979 Sample site 6.8 km east of Springerville along U.S. 60, off map

-AWL-42-74 Tacl 3.06±0.08 Laughlin and others, 1979 ---

-AWL4-77 Qdh4 0.84±0.07 Laughlin and others, 1980 Normal polarity suggests age > 0.90 Ma

-AWL5-77 Qag 1.67±0.09 Laughlin and others, 1980 ---

-AWL6-77 Qkc6 0.75±0.13 Laughlin and others, 1980 Normal polarity; overlies Qkc4 (713SN, 0.61±.01 Ma) suggesting age of 0.62 Ma.

-UAKA 73-80 QTsf 1.62±0.08 Peirce and others, 1979 Sample from flow tongue near Carrizo 37 km southwest of Show Low, off map

-UAKA 73-137 QTsf 1.63±0.08 Peirce and others, 1979 --do--

-UAKA 74-136 QTsf 1.90±0.06 Peirce and others, 1979 --do--

-UAKA 75-52a QTsf 1.76±0.15 Peirce and others, 1979 --do--

-UAKA 80-131 Qsc5 1.53±0.21 Condit and Shafiqullah, 1985 ---

-UAKA 80-132 Qsg2 1.74±0.15 Condit and Shafiqullah, 1985 Stratigraphic and paleomagnetic constraints suggest age of 1.60 Ma.

-UAKA 80-133 QTsf 1.78±0.22 Condit and Shafiqullah, 1985 ---

-UAKA 80-134 Tbc3 1.83±0.21 Condit and Shafiqullah, 1985 ---

-UAKA 80-135 Tbl 8.66±0.19 Condit and Shafiqullah, 1985 Probable source Mount Baldy shield complex 20 km southeast of sample site (Condit, 1984).

-UAKA 80-136 Tbc1 8.97±0.19 Condit and Shafiqullah, 1985 Oldest dated volcanic unit in Springerville field; probable source Mount Baldy complex 20 km southeast of sample site (Condit, 1984).

-UAKA 82-95 Tnc 2.05±0.10 Condit and Shafiqullah, 1985 ---

-UAKA 82-96 Qnd 1.47±0.06 Condit and Shafiqullah, 1985 ---

-UAKA 82-183 Qbb2 1.65±0.09 Condit and Shafiqullah, 1985 Normal polarity suggests age >1.67 Ma.

-UAKA 82-184 Qme 0.486±0.029 Condit and Shafiqullah, 1985 ---

-UAKA 82-185 QTsf 2.00±0.11 Condit and Shafiqullah, 1985 ---

-UAKA 82-190 Qek 1.56±0.05 Aubele and others, 1986 ---

-UAKA 82-191 Qvc4 1.30±0.05 Aubele and others, 1986 Normal magnetic polarity from co-located site and date from sample 719V (1.00±0.02 Ma) cannot be reconciled with this date.

-UAKA 82-192 Qcb1 1.19±0.04 Aubele and others, 1986 ---

-UAKA 82-193 Qde3 1.05±0.04 Aubele and others, 1986 ---

-UAKA 82-194 Trc2 1.98±0.6 Aubele and others, 1986 ---

-UAKA 82-195 Qkb2 0.308±0.070 Aubele and others, 1986 ---

-UAKA 82-196 Quh4 1.04±0.05 Aubele and others, 1986 ---

-UAKA 82-197 Qgj2 0.67±0.022 Aubele and others, 1986 ---

2.2 Other Units

Clearly, most units in the field are not dated using numerical methods (K/Ar). Ages for other units have been determined by their stratigraphic position. Ages on these units are assumed to be between the ages of bounding dated units. Flows are assumed to have an age which is the average age of the bounding, dated units and uncertainty described by a uniform random probability distribution. For example, if a lava flow is stratigraphically between 0.45 Ma and 0.75 Ma lava flows, its age is assumed to be 0.6 Ma ± 0.15 Ma.

TABLE 1. Vent Ages Used in Analysis

cluster/ vent id	Latitude	Longitude	Mean Age (Ma)	Min Age (Ma)	Max Age (Ma)
1*0413	34.2645	250.2446	1.100	0.70	1.50
1*0520	34.2501	250.2775	1.230	0.85	1.61
1*0402	34.3015	250.2342	1.800	1.60	2.00
1*0528	34.2432	250.2953	1.00	0.85	1.15
1*0523	34.2504	250.3262	1.30	0.90	1.70
1*0504A	34.2961	250.2910	1.098	0.77	1.27
1*0504B	34.2955	250.2965	1.098	0.77	1.27
1*1529	34.3139	250.2889	1.098	0.77	1.27
1*0507B	34.2873	250.2690	1.001	0.75	1.25
1*0506	34.2945	250.2723	1.37	0.95	1.81
1*0522	34.2435	250.3186	1.215	0.91	1.53
1*1302	34.3803	250.1267	1.500	1.30	1.70
1*1327	34.3227	250.1168	1.500	1.30	1.70
1*1336	34.3006	250.1380	1.500	1.30	1.70
1*1428	34.3233	250.1923	1.500	1.30	1.70
1*0410A	34.2828	250.2087	1.400	1.00	1.80
1*0410B	34.2843	250.2183	1.400	1.00	1.80
1*1301	34.3813	250.1419	1.700	1.30	2.10
1*0405	34.2923	250.1862	1.740	1.54	1.94
1*1420	34.3427	250.1812	1.675	1.40	1.95
1*1422	34.3317	250.2076	1.675	1.40	1.95
1*1427	34.3253	250.2193	1.675	1.40	1.95
1*1414	34.3463	250.2224	1.560	1.53	1.59
1*1429	34.3274	250.1728	1.750	1.60	1.90
1*1421	34.3345	250.1964	1.300	1.00	1.60
1*1312	34.3635	250.1443	1.910	1.70	2.12
2*9308	34.1856	250.0758	1.61	1.42	1.80
2*8321	34.0777	250.0834	1.750	1.50	2.00
2*9335	34.1327	250.1171	1.71	1.67	1.74
2*9430A	34.1480	250.1595	1.650	1.56	1.74
2*9430B	34.1430	250.1541	1.650	1.56	1.74
2*8308	34.1065	250.0618	1.385	0.90	1.87
2*8311	34.1019	250.1152	1.385	0.90	1.87
2*9326	34.1541	250.1164	1.400	0.90	1.75

TABLE 1. Vent Ages Used in Analysis

cluster/ vent id	Latitude	Longitude	Mean Age (Ma)	Min Age (Ma)	Max Age (Ma)
2*8318	34.0920	250.0439	1.750	1.67	1.83
2*9328B	34.1538	250.0847	1.595	1.32	1.87
2*9328A	34.1502	250.0949	0.810	0.30	1.32
2*9317	34.1712	250.0653	1.725	1.58	1.87
2*9318	34.1752	250.0615	1.725	1.58	1.87
2*9330	34.1470	250.0520	1.165	0.73	1.60
2*0434	34.2241	250.2089	1.750	1.70	1.80
2*9402A	34.2114	250.2250	1.300	1.00	1.60
2*0424	34.2570	250.2555	1.200	0.80	1.60
2*9404A	34.2049	250.1924	1.725	1.55	1.90
2*0429	34.2285	250.1794	1.500	1.20	1.80
2*9403	34.2028	250.2046	1.350	1.05	1.65
2*0519	34.2450	250.2602	0.850	0.70	1.00
2*0432B	34.2182	250.1761	1.300	0.80	1.80
2*9401	34.2087	250.2429	1.115	0.73	1.50
2*9402B	34.2025	250.2341	1.115	0.73	1.50
2*0435	34.2201	250.2362	0.835	0.70	0.97
2*0432A	34.2210	250.1809	1.300	1.00	1.60
2*9404B	34.2027	250.1984	1.000	0.85	1.15
2*9411A	34.1979	250.2239	1.050	0.55	1.55
2*9411B	34.1852	250.2382	1.050	0.55	1.55
2*9412	34.1907	250.2469	1.050	0.55	1.55
2*9413	34.1795	250.2427	1.050	0.55	1.55
2*9414A	34.1801	250.2289	1.050	0.55	1.55
2*9414B	34.1789	250.2306	1.050	0.55	1.55
2*9506	34.2006	250.2607	1.680	1.56	1.80
2*8313	34.0912	250.1374	1.160	0.65	1.67
2*8407	34.1063	250.1590	1.750	1.65	1.85
2*8326	34.0552	250.1165	1.635	1.49	1.78
2*8324	34.0775	250.1284	0.950	0.30	1.60
2*9432	34.1276	250.1699	1.740	1.64	1.84
2*8408	34.0979	250.1740	1.260	0.65	1.87
2*9505	34.1990	250.2803	1.005	0.65	1.33
2*9434A	34.1322	250.2054	0.700	0.30	1.10
2*9435A	34.1315	250.2244	0.650	0.30	1.00

TABLE 1. Vent Ages Used in Analysis

cluster/ vent id	Latitude	Longitude	Mean Age (Ma)	Min Age (Ma)	Max Age (Ma)
2*9435B	34.1326	250.2324	1.250	0.80	1.70
2*9423	34.1587	250.2331	0.685	0.40	0.97
2*9425A	34.1544	250.2410	1.660	1.57	1.75
2*9434C	34.1332	250.2194	1.100	0.70	1.50
2*8410	34.1096	250.2003	1.000	0.80	1.20
2*8404A	34.1270	250.1968	0.970	0.77	1.17
2*8404B	34.1229	250.1933	0.970	0.77	1.17
2*9421	34.1670	250.1909	1.340	1.01	1.67
2*9422A	34.1620	250.2179	1.340	1.01	1.67
2*9422B	34.1642	250.2086	1.340	1.01	1.67
2*9424Q	34.1558	250.2467	1.340	1.01	1.67
2*9427A	34.1511	250.2213	1.340	1.01	1.67
2*9427B	34.1513	250.2134	1.340	1.01	1.67
2*9434B	34.1373	250.2134	0.815	0.73	0.90
2*9408B	34.1899	250.1771	1.600	1.40	1.80
2*9408C	34.1898	250.1857	1.600	1.40	1.80
2*9409C	34.1899	250.1918	1.600	1.40	1.80
2*9417C	34.1833	250.1837	1.600	1.40	1.80
2*0325	34.2405	250.1418	1.600	1.40	1.80
2*9416A	34.1798	250.1953	1.01	1.01	1.011
2*9416B	34.1771	250.1872	1.01	1.01	1.011
2*9417A	34.1821	250.1736	1.01	1.01	1.011
2*9417B	34.1788	250.1724	1.01	1.01	1.011
2*0327	34.2420	250.1075	1.600	1.40	1.80
2*9303	34.1991	250.1121	1.600	1.20	2.00
2*9301A	34.2090	250.1393	1.600	1.40	1.80
2*9313	34.1788	250.1316	1.200	0.73	1.67
2*9409A	34.1961	250.1953	1.200	0.73	1.67
2*9409B	34.1942	250.2010	1.200	0.73	1.67
2*9408A	34.1962	250.1772	1.200	0.73	1.67
2*9418	34.1810	250.1585	0.49	0.46	0.52
2*9311	34.1916	250.1267	1.250	1.01	1.49
2*0431A	34.2226	250.1596	1.255	1.01	1.50
2*0431B	34.2236	250.1674	1.255	1.01	1.50
2*9406	34.2118	250.1684	1.255	1.01	1.50

CC

TABLE 1. Vent Ages Used in Analysis

cluster/ vent id	Latitude	Longitude	Mean Age (Ma)	Min Age (Ma)	Max Age (Ma)
2*7303B	34.0304	250.1002	1.200	0.73	1.67
2*8327	34.0615	250.0932	1.365	0.73	2.00
2*8335A	34.0491	250.1142	1.560	1.44	1.68
2*8335B	34.0469	250.1123	1.560	1.44	1.68
2*0331	34.2194	250.0487	1.530	1.32	1.74
2*0224	34.2545	250.0285	1.565	1.53	1.60
2*9307	34.1886	250.0563	1.750	1.57	1.93
2*0321	34.2437	250.0865	1.600	1.40	1.80
2*0333	34.2137	250.0825	1.540	1.34	1.74
2*9304A	34.2085	250.0905	1.540	1.34	1.74
2*9304B	34.2074	250.0813	1.540	1.34	1.74
2*9306	34.2058	250.0590	1.53	1.32	1.74
2*9305	34.2002	250.0776	1.60	1.60	1.61
2*0319	34.2514	250.0602	1.800	1.60	2.00
2*9336A	34.1373	250.1444	1.91	1.90	1.92
2*9336B	34.1364	250.1400	1.91	1.90	1.92
2*0414	34.2598	250.2301	1.600	1.30	1.90
2*9325	34.1481	250.1409	1.995	1.87	2.12
2*8416	34.0927	250.1873	1.880	1.75	2.01
2*8422	34.0737	250.1988	1.995	1.87	2.12
2*9301B	34.2082	250.1471	1.855	1.61	2.10
2*7303A	34.0372	250.1032	1.905	1.67	2.14
3*9507	34.1973	250.2604	1.56	1.51	1.61
3*9621	34.1619	250.4146	0.89	0.89	0.93
3*8604	34.1147	250.3940	0.627	0.37	0.90
3*8607	34.1008	250.3599	1.275	0.90	1.66
3*9633	34.1333	250.3986	0.706	0.51	0.90
3*8609D	34.1073	250.3906	0.898	0.70	1.10
3*9631	34.1305	250.3787	0.728	0.56	0.90
3*8606	34.1254	250.3659	1.165	0.90	1.43
3*8609A	34.1020	250.3899	0.839	0.70	0.96
3*8609B	34.0981	250.3962	0.839	0.70	0.96
3*8609C	34.0700	250.3810	0.839	0.70	0.96
3*9629	34.1535	250.3917	0.942	0.53	1.35
3*9608	34.1941	250.3833	0.98	0.89	1.30

TABLE 1. Vent Ages Used in Analysis

cluster/ vent Id	Latitude	Longitude	Mean Age (Ma)	Min Age (Ma)	Max Age (Ma)
3*8605	34.1190	250.3775	0.77	0.50	1.05
3*8519	34.0817	250.2557	0.96	0.35	1.57
3*7401	34.0358	250.2450	1.700	1.40	2.00
3*8424	34.0808	250.2343	1.400	1.00	1.80
3*8435	34.0517	250.2277	1.660	1.35	1.97
3*9527A	34.1457	250.3140	1.330	0.90	1.76
3*9527B	34.1483	250.3211	1.330	0.90	1.76
3*9525B	34.1474	250.3600	0.86	0.73	0.90
3*9530	34.1477	250.3745	0.86	0.73	0.90
3*9630	34.1472	250.3728	0.86	0.73	0.90
3*9528A	34.1428	250.2971	0.86	0.73	0.90
3*9514A	34.1797	250.3352	1.208	0.91	1.51
3*9514C	34.1711	250.3317	1.208	0.91	1.51
3*9523	34.1676	250.3306	1.208	0.91	1.51
3*9520	34.1560	250.2901	1.301	0.85	1.75
3*9528B	34.1435	250.3052	0.838	0.55	1.20
3*9532	34.1384	250.2800	1.35	0.95	1.75
3*9516B	34.1820	250.2979	1.210	0.80	1.62
3*9517	34.1803	250.2917	1.063	0.90	1.22
3*9529	34.1456	250.2881	0.68	0.35	0.97
3*9535	34.1378	250.3423	1.142	0.91	1.39
3*9536	34.1299	250.3462	1.142	0.91	1.39
3*9525A	34.1546	250.3508	1.04	0.90	1.18
3*9525A	34.1547	250.3507	0.935	0.90	0.97
3*9525A	34.1572	250.3594	0.864	0.74	0.97
3*9516A	34.1773	250.3061	1.339	0.90	1.77
3*9521	34.1630	250.2997	1.339	0.90	1.77
3*9522	34.1576	250.3182	1.339	0.90	1.77
3*9526	34.1461	250.3330	1.08	0.79	1.38
3*9501	34.2124	250.3533	1.221	0.90	1.54
3*9514B	34.1723	250.3436	1.192	0.90	1.49
3*9525A	34.1547	250.3507	0.823	0.73	0.93
3*9512A	34.1888	250.3495	0.61	0.49	0.73
3*9512B	34.1922	250.3612	1.473	1.05	1.90
3*9533A	34.1367	250.3045	1.40	1.00	1.80

CC

TABLE 1. Vent Ages Used in Analysis

cluster/ vent id	Latitude	Longitude	Mean Age (Ma)	Min Age (Ma)	Max Age (Ma)
3*9534A	34.1385	250.3183	1.352	1.02	1.79
3*8506	34.1169	250.2502	0.650	0.30	1.00
3*9531A	34.1381	250.2604	1.550	1.35	1.75
3*8401A	34.1153	250.2380	0.815	0.73	0.90
3*8401B	34.1176	250.2445	0.700	0.30	1.10
4*0610A	34.2777	250.4277	.369	1.15	1.59
4*0611	34.2837	250.4380	.369	1.15	1.59
4*0601	34.2917	250.4583	1.19	1.15	1.23
4*1633	34.3011	250.4018	1.19	1.15	1.23
4*1622	34.3363	250.4220	0.697	0.31	1.09
4*1626A	34.3156	250.4474	0.548	0.30	0.79
4*1626B	34.3144	250.4415	0.517	0.30	0.74
4*0606	34.2868	250.3693	1.452	1.15	1.75
4*1624A	34.3365	250.4552	1.415	1.00	1.84
4*1624B	34.3358	250.4622	1.38	0.95	1.72
4*1719	34.3342	250.4685	1.372	1.23	1.56
4*1612B	34.3590	250.4508	1.305	0.90	1.70
4*0603	34.2942	250.4224	1.279	1.15	1.55
4*0615B	34.2682	250.4240	1.25	1.15	1.40
4*1635	34.3033	250.4386	1.516	1.14	1.90
4*1730	34.3162	250.4676	0.935	0.90	0.97
4*0615A	34.2723	250.4249	0.879	0.73	1.02
4*1609	34.3590	250.4065	0.822	0.50	1.15
4*1627	34.3276	250.4149	1.23	1.15	1.50
4*1613	34.3546	250.4526	1.148	0.70	1.60
4*1625	34.3202	250.4567	0.888	0.73	0.97
4*0609	34.2723	250.3974	1.40	1.15	1.66
4*0617	34.2602	250.3789	1.38	1.22	1.52
4*0616	34.2645	250.4065	1.320	0.95	1.69
4*1634	34.3007	250.4246	1.238	1.15	1.35
4*0512	34.2733	250.3548	0.825	0.55	1.10
4*0706	34.2963	250.4743	1.44	1.00	1.88
4*0610B	34.2758	250.4177	1.38	1.15	1.62
4*0705	34.2959	250.4970	1.271	0.90	1.63
4*0718	34.2591	250.4682	1.33	1.13	1.53

TABLE 1. Vent Ages Used in Analysis

cluster/ vent id	Latitude	Longitude	Mean Age (Ma)	Min Age (Ma)	Max Age (Ma)
4*1603	34.3840	250.4211	1.249	0.69	1.82
4*2621A	34.4276	250.4071	1.042	0.64	1.45
4*2621B	34.4203	250.4127	1.042	0.64	1.45
4*1610	34.3667	250.4167	1.568	1.05	2.09
4*1612A	34.3641	250.4644	1.450	1.00	1.90
4*1612C	34.3705	250.4581	1.450	1.00	1.90
4*1707	34.3614	250.4698	1.450	1.00	1.90
4*1602	34.3816	250.4373	0.881	0.65	1.11
4*2615	34.4292	250.4136	1.099	0.78	1.43
4*2629	34.4109	250.3812	1.10	0.90	1.30
4*1711	34.3272	250.5472	1.98	1.92	2.04
4*1601	34.3771	250.3544	1.22	1.00	1.44
5*0823	34.2457	250.6580	1.053	0.90	1.20
5*9823	34.1557	250.6523	1.745	1.60	1.89
5*0919A	34.2517	250.6808	0.93	0.78	1.09
5*0919B	34.2538	250.6943	0.85	0.75	1.00
5*0621B	34.2510	250.3990	1.372	1.23	1.56
5*0621C	34.2470	250.3990	1.372	1.23	1.56
5*0621A	34.2505	250.4135	0.82	0.73	0.90
5*0621D	34.2344	250.4058	1.148	0.95	1.29
5*0628	34.2350	250.4020	1.148	0.95	1.29
5*9705	34.2097	250.4963	1.312	0.87	1.76
5*0721	34.2424	250.5037	1.137	1.00	1.27
5*0724A	34.2423	250.5601	1.119	0.98	1.25
5*0731	34.2171	250.4760	1.66	1.32	2.00
5*0625	34.2380	250.4625	1.59	1.19	1.92
5*0726	34.2386	250.5452	1.205	0.85	1.56
5*9718A	34.1702	250.4724	1.262	1.13	1.39
5*9718B	34.1830	250.4797	1.451	1.17	1.73
5*0727	34.2319	250.5303	1.05	1.01	1.09
5*9716	34.1711	250.5058	1.039	0.79	1.29
5*0734	34.2276	250.5351	1.382	1.05	1.71
5*9717A	34.1772	250.4985	1.07	0.75	1.25
5*0732	34.2235	250.4973	0.84	0.77	0.91
5*0715A	34.2616	250.5326	1.320	1.01	1.63

CC

TABLE 1. Vent Ages Used in Analysis

cluster/ vent id	Latitude	Longitude	Mean Age (Ma)	Min Age (Ma)	Max Age (Ma)
5*0715B	34.2663	250.5310	1.320	1.01	1.63
5*9601	34.2011	250.4657	1.14	0.84	1.44
5*0711	34.2766	250.5423	1.453	1.06	1.85
5*9707A	34.1927	250.4800	1.453	1.06	1.85
5*0724B	34.2507	250.5567	1.230	0.87	1.58
5*9717B	34.1790	250.5284	1.230	0.87	1.58
5*9612	34.1897	250.4490	1.339	1.02	1.66
5*9613	34.1723	250.4565	1.322	0.90	1.70
5*9624	34.1664 250.4573	1.322	0.90	1.70	
5*0632A	34.2213 250.3957	1.008	0.90	1.25	
5*9605	34.2044	250.3862	1.055	0.98	1.25
5*9610	34.1929	250.4293	0.86	0.74	1.10
5*0633	34.2174	250.4067	0.856	0.73	0.93
5*9609	34.1871	250.4057	0.899	0.73	1.15
5*0634	34.2145	250.4244	0.838	0.73	0.93
5*9603	34.2074	250.4241	0.838	0.73	0.93
5*9615	34.1783	250.4308	1.19	0.99	1.45
5*9602	34.2122	250.4417	0.968	0.74	1.20
5*9707B	34.1945	250.4662	1.333	1.14	1.53
5*9707B	34.1958	250.4667	1.333	1.14	1.53
5*0632B	34.2169	250.3814	1.248	1.03	1.47
5*9821	34.1639	250.6184	0.972	0.63	1.32
5*0827	34.2358	250.6279	0.933	0.61	1.25
5*0833	34.2204	250.6081	0.3080	0.301	0.315
5*0829	34.2290	250.6025	0.838	0.62	1.04
5*0828	34.2289	250.6178	0.61	0.60	0.61
5*0833	34.2258	250.6169	0.61	0.61	0.611
5*9820	34.1595	250.5970	1.60	1.20	1.99
5*0714	34.2578	250.5472	0.990	0.70	1.28
5*9702	34.2041	250.5464	0.901	0.65	1.15
5*9703	34.2035	250.5353	1.478	1.04	1.91
5*9715	34.1703	250.5348	1.11	0.76	1.44
5*9806	34.2115	250.5770	0.95	0.80	1.09
5*9714A	34.1804	250.5370	1.18	0.99	1.38

TABLE 1. Vent Ages Used in Analysis

cluster/ vent id	Latitude	Longitude	Mean Age (Ma)	Min Age (Ma)	Max Age (Ma)
5*9710A	34.1963	250.5350	1.138	0.99	1.29
5*9710B	34.1842	250.5284	1.11	0.99	1.24
5*9702	34.2041	250.5464	0.90	0.71	1.09
5*9701B	34.2097	250.5648	0.85	0.60	1.09
5*9701C	34.2104	250.5708	0.85	0.60	1.09
5*9701A	34.2075	250.5594	0.85	0.60	1.09
5*9713	34.1693	250.5606	1.531	1.16	1.90
5*9818	34.1767	250.5790	1.441	1.05	1.85
5*9711	34.1958	250.5445	1.04	0.99	1.09
5*9723	34.1685	250.5477	1.599	1.25	1.95
5*9714B	34.1750	250.5414	1.115	0.77	1.46
6*8818A	34.0969	250.5725	1.175	1.05	1.30
6*8803	34.1130	250.6262	1.67	1.58	1.76
6*8714	34.0971	250.5327	1.77	1.67	1.89
6*8803	34.1132	250.6271	1.67	1.58	1.76
6*9729A	34.1480	250.4903	1.232	0.91	1.56
6*9730	34.1412	250.4842	1.102	0.70	1.30
6*9733	34.1301	250.5047	1.151	0.75	1.56
6*9729B	34.1447	250.4989	1.157	0.73	1.59
6*8701B	34.1238	250.5551	1.408	1.14	1.68
6*9830	34.1437	250.5851	1.79	1.50	2.08
6*8715A	34.0903	250.5181	1.78	1.35	2.21
6*8702	34.1164	250.5332	0.61	0.61	0.611
6*8701A	34.1162	250.5438	0.60	0.58	0.61
6*8702	34.1164	250.5332	0.60	0.58	0.61
6*8703	34.1230	250.5230	1.79	1.50	2.08
6*8723	34.0703	250.5416	1.369	1.26	1.70
6*8722	34.0753	250.5263	1.298	1.26	1.56
6*8804	34.1145	250.5957	1.80	1.58	2.03
6*9722	34.1607	250.5275	1.432	1.05	1.82
6*9727	34.1512	250.5232	1.79	1.53	2.05
6*8711	34.1000	250.5361	1.970	1.89	2.05
6*8806B	34.1148	250.5680	1.882	1.78	1.98
6*8818B	34.0945	250.5643	1.882	1.78	1.98
6*8806A	34.1219	250.5647	1.968	1.79	2.05

TABLE 1. Vent Ages Used in Analysis

cluster/ vent Id	Latitude	Longitude	Mean Age (Ma)	Min Age (Ma)	Max Age (Ma)
6*8711	34.0960	250.5351	1.82	1.62	1.98
6*8714	34.0977	250.5370	1.88	1.78	1.97
6*9832	34.1300	250.6028	1.948	1.81	2.09
7*9623	34.1663	250.4433	1.159	0.97	1.40
7*9622	34.1584	250.4255	0.89	0.89	0.93
7*8707	34.1003	250.4695	0.962	0.90	1.20
7*8718B	34.0953	250.4649	0.962	0.90	1.20
7*8613B	34.0835	250.4448	0.953	0.90	1.20
7*8602	34.1215	250.4364	1.028	0.77	0.97
7*8614B	34.0925	250.4374	0.89	0.71	0.97
7*8611B	34.0969	250.4354	0.84	0.73	0.97
7*8614A	34.1047	250.4376	0.84	0.73	0.97
7*8613A	34.0958	250.4431	0.94	0.90	0.97
7*8623	34.0762	250.4298	0.84	0.73	0.97
7*8615	34.0911	250.4159	0.823	0.72	0.97
7*8611A	34.1109	250.4254	0.78	0.78	0.781
7*9626	34.1408	250.4390	0.67	0.67	0.671
7*8718A	34.0833	250.4625	1.05	0.65	1.45
7*8704	34.1222	250.5033	1.15	0.90	1.40
7*8708	34.1083	250.4833	1.12	0.90	1.35
7*8627	34.0542	250.4139	0.891	0.73	1.10
7*8603	34.1243	250.4233	0.819	0.70	0.94
7*9625	34.1444	250.4538	1.25	0.67	1.83
7*9731	34.1312	250.4785	1.04	0.70	1.30
7*9635A	34.1285	250.4442	1.00	0.73	1.27
7*8706	34.1252	250.4709	1.42	0.90	1.38
7*8601	34.1198	250.4520	0.974	0.73	1.21
7*9635B	34.1356	250.4502	1.30	0.90	1.38
7*9636	34.1356	250.4410	1.30	0.90	1.38
7*9732	34.1310	250.5000	1.158	0.90	1.41
7*8715B	34.0859	250.5093	1.78	1.35	2.21
7*8625B	34.0629	250.4540	1.34	1.26	1.34
7*8719	34.0757	250.4680	1.351	0.97	1.63
7*8624	34.0724	250.4412	1.334	0.97	1.34
7*7706	34.0316	250.4587	1.311	1.05	1.34

TABLE 1. Vent Ages Used in Analysis

cluster/ vent id	Latitude	Longitude	Mean Age (Ma)	Min Age (Ma)	Max Age (Ma)
7*8717	34.0837	250.4827	1.295	0.97	1.62
7*7709A	34.0109	250.4994	1.292	1.26	1.54
7*7709B	34.0163	250.4978	1.292	1.26	1.54
7*7705	34.0242	250.4862	1.265	1.26	1.56
7*8732A	34.0423	250.4877	1.26	1.26	1.34
7*8716	34.0829	250.4992	1.497	1.23	1.77
7*7708A	34.0121	250.4795	1.360	1.07	1.65
7*8625A	34.0647	250.4475	1.175	0.97	1.34
7*8730	34.0565	250.4686	1.34	1.34	1.341
7*7707	34.0233	250.4677	1.316	1.26	1.56
7*8635A	34.0526	250.4322	1.303	1.05	1.34
7*8635B	34.0417	250.4319	1.303	1.05	1.34
7*8733	34.0435	250.4993	1.273	1.26	1.52
7*8625C	34.0589	250.4434	1.188	0.97	1.34
7*8732B	34.0477	250.4915	1.461	1.26	1.63
7*8720	34.0677	250.4400	1.485	1.15	1.84
7*7708B	34.0242	250.4740	1.291	1.26	1.56
7*8729	34.0677	250.4774	1.15	0.97	1.26

These data (Table 1) are then plotted at 0.25 Ma intervals on a series of maps (Figure 3, "Vent locations formed between 1.0 Ma and 0.5 Ma," on page 17; Figure 4, "Vent Locations 1.0 to 1.5 Ma," on page 18; Figure 5, "Vent locations 1.5 to 2.0 Ma," on page 19). These maps show the distribution of vent locations upon which subsequent analyses are based.

Note: the vent locations are plotted on Figures 3-5 accurately. However, vent locations are referenced to roads (red lines) and faults (solid black lines) using a draw program and some shifting may have occurred. This does not impact the analysis in any way.

FIGURE 3. Vent locations formed between 1.0 Ma and 0.5 Ma

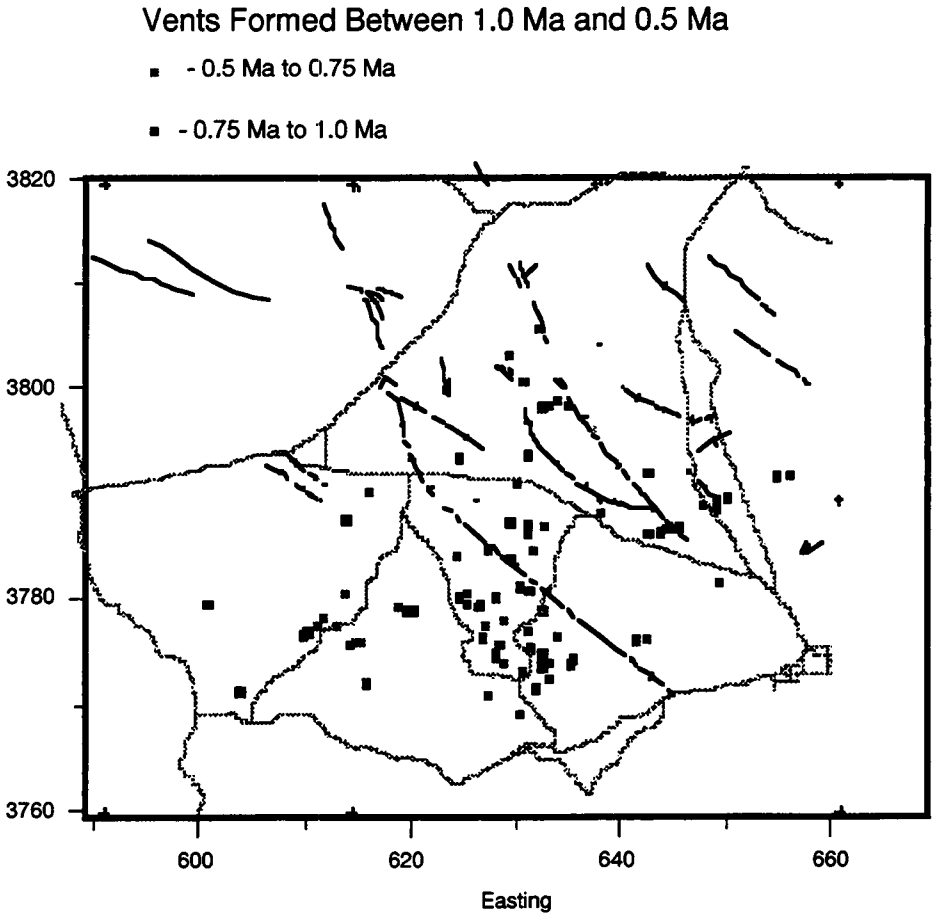

FIGURE 4. Vent Locations 1.0 to 1.5 Ma

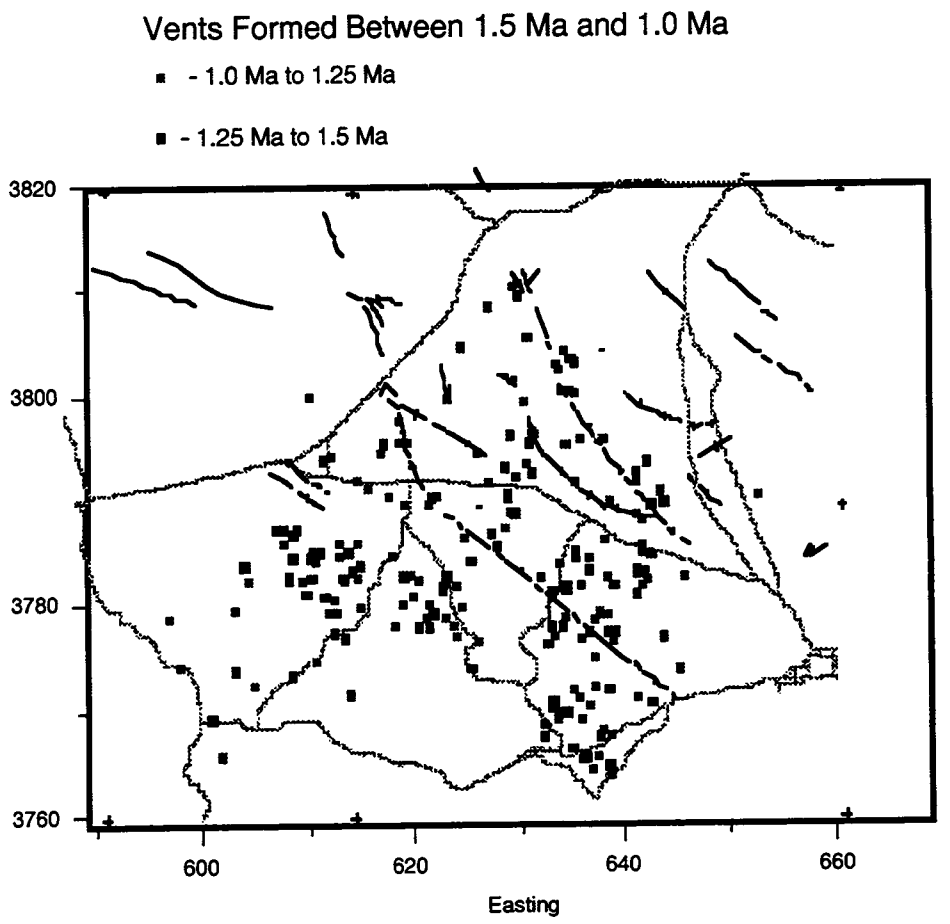

FIGURE 5. Vent locations 1.5 to 2.0 Ma

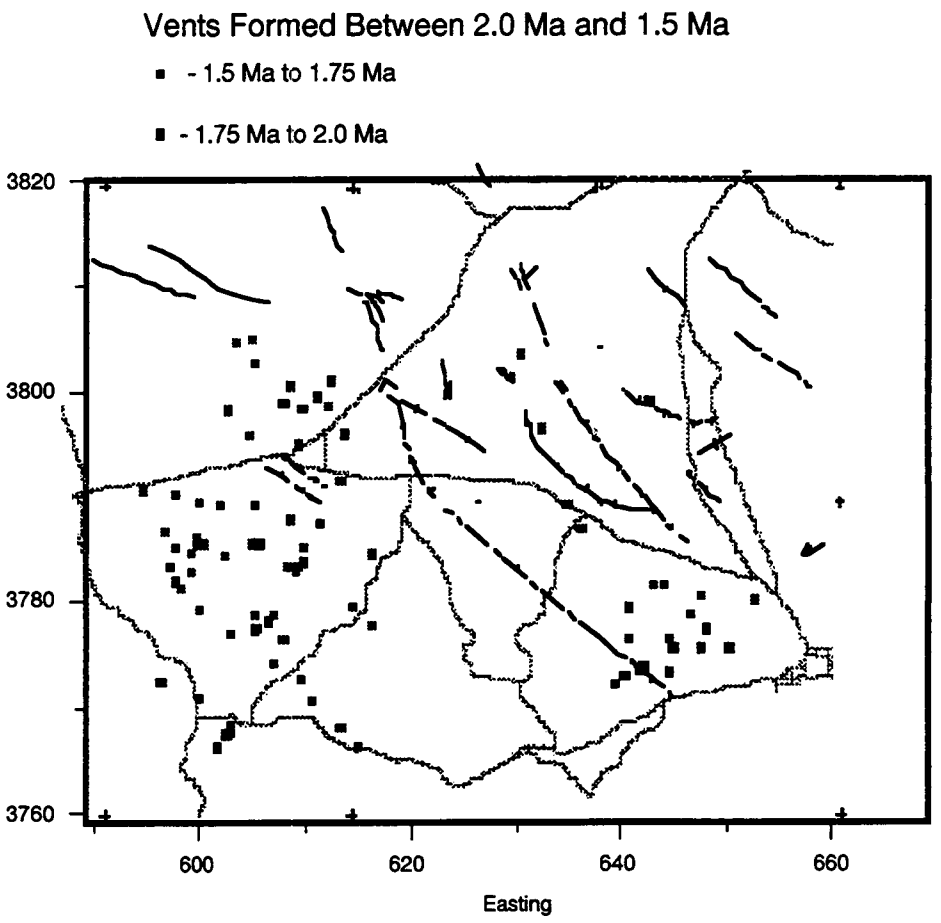

The data were then used to construct cumulative vent curves. These show the cumulative number of vents through time.

FIGURE 6. Cumulative Number of Vents in the SVF

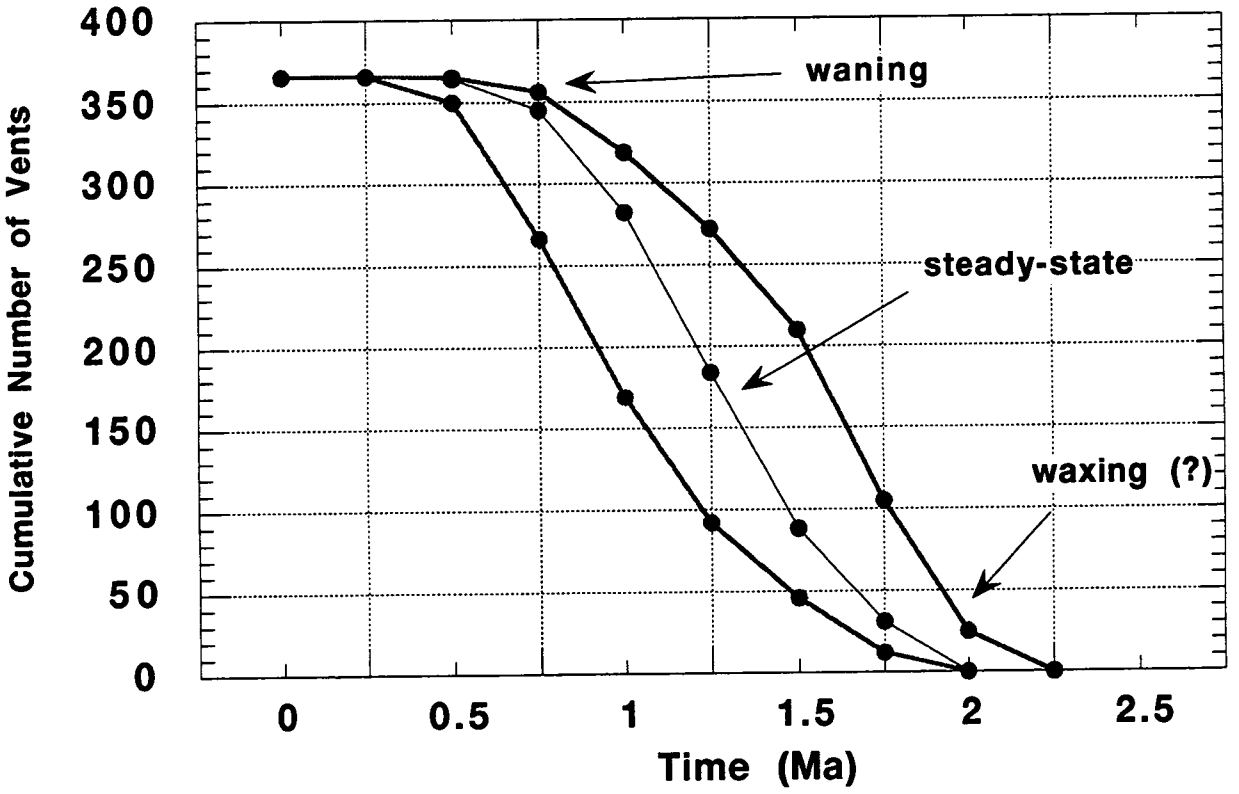

The cumulative number of vents graph (Figure 6, "Cumulative Number of Vents in the SVF," on page 20) shows a curve based on mean ages from Table 1, and a 90% confidence envelope. The envelope is constructed using the 2 sigma uncertainty on age determinations. In the case of vents which have K/Ar dates, this is done using analytical uncertainty. In the case of vents whose ages are estimated from stratigraphic position, this is done by assuming that the uncertainty is ditributed uniformly between the bounded, dated units.

2.3 Observations about the Cumulative vent frequency distribution

The following observations can be made based on the cumulative vent frequency distribution:

- the frequency of new vent formation appears to go through simple waxing, steady-state, and waning phases

- volcanism was initiated between 2.0 and 2.5 Ma
- a steady-state condition, in which vents formed at a steady rate, was achieved by 1.5 Ma and continued through about 1 Ma. About 50% of the vents in the field were formed during this 0.5 m.y. period.
- about 100 vents formed in the waning stages of volcanism in the SVF, after about 1 Ma. Frequency of volcanism exihibits a steady decrease since about 1 Ma
- Waxing stages ogf volcanism are much less constrained than the waning stages of volcanism. This is because the early formed volcanoes are much more likely to be buried by subsequent events. Lava flows can do a good job of eroding older cones, etc.

The observed curve was then modeled using near-neighbor analysis.

3.0 Near-Neighbor Analysis

The following introduction to n-n analysis techniques is exerpt and modified from Connor and Hill, 1993 - American Nuclear Society Focus paper on model validation.

Expected recurrence rate per unit area at an arbitrary point within the SVF canbe estimated using varying numbers of near neighbors vents:

$$\lambda_r = \frac{m}{\sum_{i=1}^{m} u_i t_i} \qquad (8)$$

where near-neighbor volcanoes are determined as the minimum, uiti, ti is the time elapsed since the formation of the ith nearest neighbor volcano, and ui is defined as before, with ui $\geq$ 1 km2. We differentiate between various near-neighbor models by comparing the observed recurrence rate for the region with the expected regional recurrence rate calculated using near-neighbor methods, defined by:

$$\lambda_t = \int_X \int_Y \lambda_r(x, y)\, dydx \qquad (9)$$

where λt is the estimated SVF recurrence rate, based on the near-neighbor model. In practice, recurrence rates, λr, are calculated on a grid and these values are summed over the region of interest:

$$\lambda_t = \sum_{i=0}^{m}\sum_{j=0}^{n}\lambda_r(i,j)\,\Delta x \Delta y \qquad (10)$$

where, in this case, Δx and Δy are 2000 m, the grid spacing used in the calculations, and m and n are the number of grid points used in the X and Y directions, respectively.

3.1 Computer Program to Calculate Recurrence Rates

These equations are implmented using the following computer program

```
! PROGRAM: recurmap
! Language: TrueBasic
! Author: Chuck Connor
!       Center for nuclear waste Regulatory Analysis
!       Southwest Research Institute
!       San Antonio Texas, 78238-5166
!Date: Dec 13, 1992
!
!Summary: This program calculates recurrence rates (point intensity)
!from vent location data.
!
!       Ripley, B.D., 1981, Spatial Statistics
!          Wiley series in probability and statistics
!          John Wiley and Sons, New York, 252 pp.
!          see pages 134-138.
```

```
!

!Library "sglib.trc"
DIM pts(400,3),grid(1600,2),lambda(1600),mtx(40,40),id$(400)
Dim venloc(400,3),young_vent(400,3),venlocid$(400),young_id$(400)

! mat pts is the matrix which holds point locations located
! within the selected area.
!

CLEAR
PRINT " type the name of the file containing the observed"
PRINT " data points"
!INPUT input_file$
!OPEN #1: name input_file$
Print "all (merc)"
OPEN #1: name "all (merc)"

OPEN #10: screen .25,1,.25,1
OPEN #13: screen 0,1,0,1

LET ymax = -1e30
LET ymin = 1e30
LET xmin = 1e30
LET xmax = -1e30
```

```
LET age_max = -1e30

LET age_min = 1e30


DO while more #1

  INPUT #1: ventid$, x,y, age, age2,age3

  IF x> xmax then LET xmax = x

  IF x < xmin then LET xmin = x

  IF y > ymax then LET ymax = y

  IF y< ymin then LET ymin = y

  IF age_max < age then LET age_max = age

  IF age_min > age then LET age_min = age


  LET num_volc = num_volc + 1

  LET venloc(num_volc,1) = x

  LET venloc(num_volc,2) = y

  LET venloc(num_volc,3) = age

  LET venlocid$(num_volc) = ventid$

LOOP


RESET #1: begin

WINDOW #13


PRINT "The maximum age of a volcano in this data set is: ";age_max

PRINT "The minimum age of a volcano in this data set is: ";age_min

PRINT "The maximum and minimum Easting and Northing are:"
```

```
PRINT xmin,xmax,ymin,ymax
PRINT
PRINT "type in the dimensions of the area you want to use "
PRINT "in this analysis: xmin, xmax, ymin, ymax"
!INPUT s1,s2,s3,s4
Print " 590000,660000,3760000,3830000"
let s1 = 590000
let s2 = 660000
let s3 = 3760000
let s4 = 3830000
PRINT
PRINT "type in the xmin, ymin of your calculation grid"
!INPUT gridx, gridy
print "590000,3760000"
let gridx = 590000
let gridy = 3760000

PRINT "type in the grid spacing (the grid will be square)"
!INPUT grid_space
print "2000"
let grid_space = 2000

PRINT "input the number of grid points in a given row and column"
PRINT "no more than 40!"
!INPUT gmax
```

cc

```
print "40"
let gmax = 40

LET gmax2 = gmax*gmax
MAT redim grid(gmax2,2)
MAT redim lambda(gmax2)
MAT redim mtx(gmax,gmax)

PRINT "age range you want to consider"
PRINT "(all volcanoes between oldest,youngest ..m.y. old)"
INPUT old_age,young_age

PRINT
PRINT "input the time of local recurrence rate estimate"
PRINT "for example, if your youngest age is 1.0 Ma, you might want"
PRINT "to estimate recurrence rate now (enter 0), or just after 1 MA"
PRINT "(enter 0.9)."
INPUT est_time

PRINT "input the number of near-neighbor volcanoes"
PRINT "used to estimate the local recurrence rate"
PRINT "no more than 50, but no more than 15 recommended"
PRINT "it really slows down the calculation"
INPUT num_neigh
```

```
PRINT "Do you want the output grid in:"

PRINT "    Local recurrence rate (type 1)"

PRINT "    Probability (type 2)"

INPUT output_flag


IF output_flag = 2 then


  ! tim_int is time interval for probability calculation

  ! prob_area is the probability of an event within prob_area units is calculated at each
grid point

  PRINT

  PRINT "type in the time interval and area term"

  PRINT " of the probability calculation (tim_int,prob_area)"

  INPUT tim_int,prob_area

END IF


CLEAR


WINDOW #10


SET COLOR "red"

SET TEXT justify "center", "half"


LET scrfix=s2-s1

SET WINDOW s1-(scrfix*28/128),s2+(scrfix*28/128),s3,s4
```

```
!now get the data set we'll use in this analysis

DO while more #1

  INPUT #1: ventid$,x,y,age,age1,age2

  IF x<=s2 and x=>s1 and y=>s3 and y<=s4 and age <=old_age and age => young_age
then

    PLOT TEXT, AT x,y: "*"


    LET totpts = totpts + 1

    LET pts(totpts,1) = x

    LET pts(totpts,2) = y

    LET pts(totpts,3) = age - est_time

    LET id$(totpts) = ventid$

  END IF

LOOP

SET TEXT justify "right", "top"


SET COLOR "cyan"

!plot the frame

PLOT s1,s3;s1,s4;s2,s4;s2,s3;s1,s3


RESET #1: begin

WINDOW #13

SET COLOR "black"

print "Volcanoes used in calculation"

!where are the next five volcanoes to form, and when?

FOR i = 1 to num_volc
```

```
  LET venloc(i,3)  = young_age - venloc(i,3)
  IF venloc(i,3) > 0 then                !then the volcano formed after the est_time
    LET sort_count = sort_count + 1
    LET young_vent(sort_count,1) = venloc(i,1)
    LET young_vent(sort_count,2) = venloc(i,2)
    LET young_vent(sort_count,3) = venloc(i,3)
    let young_id$(sort_count) = venlocid$(i)

    IF young_vent(sort_count,3) < (young_age - est_time) then  ! a new volcano forms
before recurrence time
      PRINT "Careful!"
      PRINT  young_id$(sort_count);" forms in this area after the"
      Print " cut-off for age calculations but before the"
      PRINT " time of the local recurrence rate estimate"
    END IF

  END IF
NEXT i

MAT redim young_vent(sort_count,3)
MAT redim young_id$(sort_count)

!sort the vents younger than est_time into ascending order
CALL piksr2(sort_count,young_vent,young_id$)
```

```
!make the grid


LET kount = 0
FOR x = 0 to gmax-1
  FOR y = 0 to gmax-1
    LET kount = kount + 1
    LET grid(kount,1) = gridx + x*grid_space
    LET grid(kount,2) = gridy + y*grid_space
  NEXT y
NEXT x
LET gridpts = kount



PRINT "calculating point-vent distances"
CALL lambdap(pts,grid,gridpts,totpts,lambda,num_neigh)


PRINT "Writing recurrence grid to Recur.out"
OPEN #11: name "recur.out", create newold
ERASE #11


LET maxlam = -1e30
LET minlam = 1e30
LET kount = 0
LET sum_space = grid_space/1000   !convert from m to km
```

```
FOR x = 1 to gmax
  FOR y = 1 to gmax

    LET kount = kount + 1
    LET mtx(x,y) = lambda(kount)

    IF output_flag <>2 then
      PRINT #11:grid(kount,1);" , ";grid(kount,2);" , ";lambda(kount)
    ELSE                !if output_flag = 2
      LET prob = 1 - exp(-tim_int*prob_area*lambda(kount))     ! probability calcula-
tion
      PRINT #11:grid(kount,1);" , ";grid(kount,2);" , ";prob
    END IF

    !This is the integration of recurrence rate over the area, the result is the
    !regional recurrence rate
    ! multiply by grid_space  because this is the sample spacing
    ! units of suml in volcanoes/(km2*yr)
    LET suml = suml + lambda(kount)*sum_space

    LET sumlam = sumlam + lambda(kount)
    LET sumlam2 =sumlam + lambda(kount)^2
    IF lambda(kount) > maxlam then
      LET maxlam = lambda(kount)
      LET maxlam_x = grid(kount,1)
      LET maxlam_y = grid(kount,2)
```

```
    END IF

    IF lambda(kount) < minlam then
      LET minlam = lambda(kount)
      LET minlam_x = grid(kount,1)
      LET minlam_y = grid(kount,2)
    END IF

  NEXT y
NEXT x

LET meanlam = sumlam/gmax2
LET stdlam = sqr((sumlam2 - (sumlam^2)/gmax2)/(gmax2-1))
LET grid_area = (GMAX-1)^2 * SUM_SPACE
LET naive_lam = suml/grid_area

PRINT "Writing summary to Recur.log"
OPEN #12: name "recur.log", create newold
ERASE #12
PRINT #12: "LOG OF RECURRENCE MAPPING"
PRINT #12: "Date: ";date$, "Time: ";time$
PRINT #12:
PRINT #12: "**********INPUT DATA**********"
PRINT #12:
```

```
PRINT #12: "INPUT DATA FILE: ";input_file$

PRINT #12: "NUMBER OF VOLCANOES IN INPUT FILE: ";num_volc

PRINT #12: "The maximum age of a volcano in this data set is: ";age_max

PRINT #12: "The minimum age of a volcano in this data set is: ";age_min

PRINT #12:

PRINT #12: "DATA INCLUDED IN CALCULATIONS WITHIN AREA: "; S1;" -
";S2;"E"

PRINT #12: "                                    "; S3;" - ";S4;"N"

PRINT #12: "AGE RANGE USED: ";OLD_AGE;" - ";YOUNG_AGE;" Ma"

PRINT #12: "TIME OF THE RECURRENCE RATE ESTIMATE: ";est_time;" Ma"

PRINT #12: "NUMBER OF NEAR-NEIGHBOR VOLCANOES USED: ";num_neigh

PRINT #12: "The next five vents to form are: "


WHEN exception in

   FOR i = 1 to 5

      PRINT #12: young_id$(i);young_vent(i,1);"E ";young_vent(i,2);"N
";young_vent(i,3);"Ma "

   NEXT i

USE

   PRINT #12: "     **no other younger vents**"

END WHEN


PRINT #12:

PRINT #12: "          GRID DATA"

PRINT #12: "NUMBER OF GRID POINTS: ";GMAX2

PRINT #12: "MINIMUM GRID COORDINATES: ";GRIDX;"E"
```

```
PRINT #12: "                    ";GRIDY;"N"

PRINT #12: "MAXIMUM GRID COORDINATES: ";grid(GMAX,1);"E"

PRINT #12: "                    ";grid(GMAX,2);"N"

PRINT #12: "GRID SPACING: ";grid_space;" m"

PRINT #12: "AREA OF THE GRID: ";grid_area;" km2"

PRINT #12:

PRINT #12: "***************OUTPUT DATA***************"

PRINT #12:

IF OUTPUT_FLAG = 1 THEN

  PRINT #12: "LOCAL RECURRENCE RATE GRID PRINTED TO RECUR.OUT"

  PRINT #12: "UNITS IN volcanoes/(km2*yr)"

ELSE

  PRINT #12: "PROBABILITY GRID PRINTED TO RECUR.OUT"

  PRINT #12: "     Time interval = ";tim_int

  PRINT #12: "     Area of probability calculation = ";prob_area

END IF

PRINT #12:

PRINT #12: "***************FUN FACTS ABOUT THESE CALCULA-
TIONS***************"

PRINT #12:

PRINT #12: "NUMBER OF VOLCANOES USED IN THE CALCULATION: ";totpts

PRINT #12: "LOCAL RECURRENCE RATE AT THE CORNERS OF THE GRID"

PRINT #12: "     "; grid(1,1);"E,";grid(1,2);"N: ";lambda(1);" v/(km2*yr)"

PRINT #12: "     "; grid(gmax,1);"E,";grid(gmax,2);"N: ";lambda(gmax);" v/
(km2*yr)"

PRINT #12: "     "; grid(gmax2-gmax+1,1);"E,";grid(gmax2-gmax+1,2);"N:
";lambda(gmax2-gmax+1);" v/(km2*yr)"
```

```
PRINT #12: "        "; grid(gmax2,1);"E,";grid(gmax2,2);"N: ";lambda(gmax2);" v/
(km2*yr)"

PRINT #12:

PRINT #12: "REGIONAL RECURRENCE RATE (integral of the local recurrence rate
over the grid)"

PRINT #12: "                ";suml;" v/yr"

PRINT #12: "MEAN LOCAL RECURRENCE RATE: ";MEANLAM;" v/(km2*yr)"

PRINT #12: "STANDARD DEVIATION OF LOCAL RECURRENCE RATE: ";STD-
LAM;" v/(km2*yr)"

PRINT #12: "MAXIMUM LOCAL RECURRENCE RATE:"

PRINT #12: "    ";maxlam;" v/(km2*yr) AT: ";maxlam_x;"E ";maxlam_y;"N"

PRINT #12: "MINIMUM LOCAL RECURRENCE RATE:"

PRINT #12: "    ";minlam;" v/(km2*yr) AT: ";minlam_x;"E ";minlam_y;"N"

PRINT #12: "NAIVE ESTIMATE OF RECURRENCE RATE: ";naive_lam;" v/
(km2*yr)"

PRINT #12:

PRINT #12: "***************VOLCANOES USED IN THESE CALCULA-
TIONS***************"

PRINT #12: "(ID, Easting, Northing, Age)"


FOR i = 1 to totpts

  PRINT #12: id$(i),pts(i,1), pts(i,2),pts(i,3)+est_time

NEXT i


print "WRITING VENT LOCATION TO recur.ven"

PRINT "press a key to continue to"

PRINT "view contour plot"

GET KEY uuu
```

```
CALL topograph(mtx,grid(1,1),grid(gridpts,1),grid(1,2),grid(gridpts,2),"black black
black")

SET COLOR "white"

CALL gotocanvas


open #16:name "recur.ven", create newold

erase #16


FOR x = 1 to totpts

 CALL graphpoint(pts(x,1),pts(x,2),2)

  print #16: pts(x,1),",";pts(x,2),",";2

NEXT x


FOR x = 1 to num_volc

  CALL graphpoint(venloc(x,1),venloc(x,2),4)

NEXT x


WHEN exception in

   FOR i = 1 to 5

     CALL graphpoint(young_vent(i,1),young_vent(i,2),10)

     Call graphtext (young_vent(i,1),young_vent(i,2),young_id$(i))

     print #16: young_vent(i,1),",";young_vent(i,2),",";10

   NEXT i

USE
```

```
   !no younger vents to plt
   print #16: 0,",";0,",";1

END WHEN

WHEN exception in
   FOR i = 6 to num_volc
      print #16: young_vent(i,1),",";young_vent(i,2),",";4
   NEXT i
USE
   !no younger vents to plt
   print #16: 0,",";0,",";1

END WHEN
close #16
stop
END

EXTERNAL

SUB lambdap(pts(,),rndpts(,),num_rnd_pts,totpts,lambda(),num_neigh)

  !This subroutine calculates the intensity based on distances from random points
  ! to nearest neighboring vents, equivalent to u(i) in Ripley, 1981
  ! "spatial statistics", page 135.
```

```
!pts(,) is the matrix containing the x,y coordinates of the vents
!rndpts(,) is the mtx containing x,y coordinates of random points
! pts and rndpts should both be dimensioned (totpts,2)

! totpts is the total number of points in pts() and rndpts()
! sumarea is the sum of areas swept out between a random point and
! the nearest vent = sum(minimum distance^2*pi)
! lambda is the intensity based on this calculation
DIM minarea(50), nearpt(50,3)


FOR numpt = 1 to num_rnd_pts

  LET sumarea = 0

  LET i1 = rndpts(numpt,1)/1000
  LET i2 = rndpts(numpt,2)/1000

  FOR nearneigh = 1 to num_neigh

    LET minrate = 1e20   !initialize with a very large number
    FOR j = 1 to totpts

      LET j1 = pts(j,1)/1000     !convert from meters to km
```

```
        LET j2 = pts(j,2)/1000      ! convert from meters to km
        LET j3 = pts(j,3)*1e6  !take age into account, convert from millions of years
to years
        !       let j3 = 1 !don't take age into account
        LET flag = 0
        IF nearneigh > 1 then
          FOR xx = 1 to nearneigh-1
            IF nearpt(xx,1) = j1 and nearpt(xx,2) = j2 then
              LET flag = 1
              !exit for
            END IF
          NEXT xx
        END IF

        IF flag = 0  then      !this point has not been used yet
          LET reck_rate = (((i1-j1)^2 + (i2-j2)^2))*pi*j3   !this is the area*time

          IF reck_rate < minrate then

            LET minrate = reck_rate
            LET nearpt(nearneigh,1) = j1
            LET nearpt(nearneigh,2) = j2
            LET nearpt(nearneigh,3) = pts(j,3)
          END IF
        END IF
```

```
    NEXT j
    ! sum the minimum areas
    LET minarea(nearneigh) = minrate
    !print nearpt(nearneigh,1),nearpt(nearneigh,2)
  NEXT nearneigh

  LET sumarea = 0
  FOR nearneigh = 1 to num_neigh

    LET sumarea = sumarea + minarea(nearneigh)
    !print nearneigh ,nearpt(nearneigh,3)
  NEXT nearneigh

  LET lambda(numpt) = nearneigh/sumarea

NEXT numpt

END SUB

SUB piksr2 (n, arr(,), brr$())

  FOR j = 2 to n
    LET a3 = arr(j,3)
```

```
    LET a2 = arr(j,2)
    LET a1 = arr(j,1)
    LET b$ = brr$(j)

    FOR i = j - 1 to 1 step -1
      IF arr(i,3) <= a3 then EXIT FOR

      LET arr(i + 1,3) = arr(i,3)
      LET arr(i + 1,2) = arr(i,2)
      LET arr(i + 1,1) = arr(i,1)
      LET brr$(i + 1) = brr$(i)
    NEXT i
    LET arr(i + 1,3) = a3
    LET arr(i + 1,2) = a2
    LET arr(i + 1,1) = a1
    LET brr$(i + 1) = b$
  NEXT j

END SUB
```

3.2 Example of output of Computer program

The program produces several forms of output, including a log of the run, and files containing the gridded recurrence rate data.

An example of the output log is provided below:

cc

LOG OF RECURRENCE MAPPING

Date: 19940401 Time: 15:50:44

**********INPUT DATA**********

INPUT DATA FILE:

NUMBER OF VOLCANOES IN INPUT FILE: 366

The maximum age of a volcano in this data set is: 1.995

The minimum age of a volcano in this data set is: .308

DATA INCLUDED IN CALCULATIONS WITHIN AREA: 590000 - 660000 E

3760000 - 3830000 N

AGE RANGE USED: 2 - .75 Ma

TIME OF THE RECURRENCE RATE ESTIMATE: .75 Ma

NUMBER OF NEAR-NEIGHBOR VOLCANOES USED: 6

The next five vents to form are:

*9631 627132 E 3777290 N .022 Ma

*9633 628963 E 3777620 N .044 Ma

*9434A 611149 E 3777280 N .05 Ma

*8401B 614774 E 3775700 N .05 Ma

*1622 630807 E 3800170 N .053 Ma

GRID DATA

NUMBER OF GRID POINTS: 1600

MINIMUM GRID COORDINATES: 590000 E

3760000 N

MAXIMUM GRID COORDINATES: 590000 E

3838000 N

GRID SPACING: 2000 m

AREA OF THE GRID: 3042 km2

**********OUTPUT DATA**********

LOCAL RECURRENCE RATE GRID PRINTED TO RECUR.OUT

UNITS IN volcanoes/(km2*yr)

**********FUN FACTS ABOUT THESE CALCULATIONS**********

NUMBER OF VOLCANOES USED IN THE CALCULATION: 343

LOCAL RECURRENCE RATE AT THE CORNERS OF THE GRID

590000 E, 3760000 N: 6.37024e-9 v/(km2*yr)

590000 E, 3838000 N: 1.54976e-9 v/(km2*yr)

668000 E, 3760000 N: 3.57177e-9 v/(km2*yr)

668000 E, 3838000 N: 1.55671e-9 v/(km2*yr)

REGIONAL RECURRENCE RATE (integral of the local recurrence rate over the grid)

2.51682e-4 v/yr

MEAN LOCAL RECURRENCE RATE: 7.86505e-8 v/(km2*yr)

STANDARD DEVIATION OF LOCAL RECURRENCE RATE: 2.80535e-4 v/(km2*yr)

MAXIMUM LOCAL RECURRENCE RATE:

2.57299e-6 v/(km2*yr) AT: 632000 E 3774000 N

MINIMUM LOCAL RECURRENCE RATE:

1.54976e-9 v/(km2*yr) AT: 590000 E 3838000 N

NAIVE ESTIMATE OF RECURRENCE RATE: 8.27356e-8 v/(km2*yr)

**********VOLCANOES USED IN THESE CALCULATIONS**********

(ID, Easting, Northing, Age)

*0413	614585	3791990	1.1
*0520	617634	3790430	1.23
*0402	613577	3796080	1.8
*0528	619283	3789690	1
*0523	622118	3790520	1.3
*0504A	618812	3795550	1.098

(Note: not all of the volcanoes used in the calculations are listed here)

3.3 Testing the Near Neighbor Program

The near - neighbor program was tested using magntite grain data in Cressie (1991, Statistics for Spatial Data) and Ripley (1982, Spatial statistics). The results are identical to those reported by Ripley.

3.4 Near - Neighbor Maps

Maps were produced using the N-N methods for the SVF, using the 7 near-neighbor model. The map grids were produced using the above program. These grids were then contoured in Spyglass Transform. Vent locations were then superimposed on the plot in transofrm and the enitre image was shipped to FrameMaker.

The maps are made at intervals of 0.25 Ma. This is considered the best resolution given uncertainty in the age data. Maps shown by age interval are given in Figure 7 on page 45 through Figure 12 on page 50.

FIGURE 7. Recurrence rate at 1.75 Ma

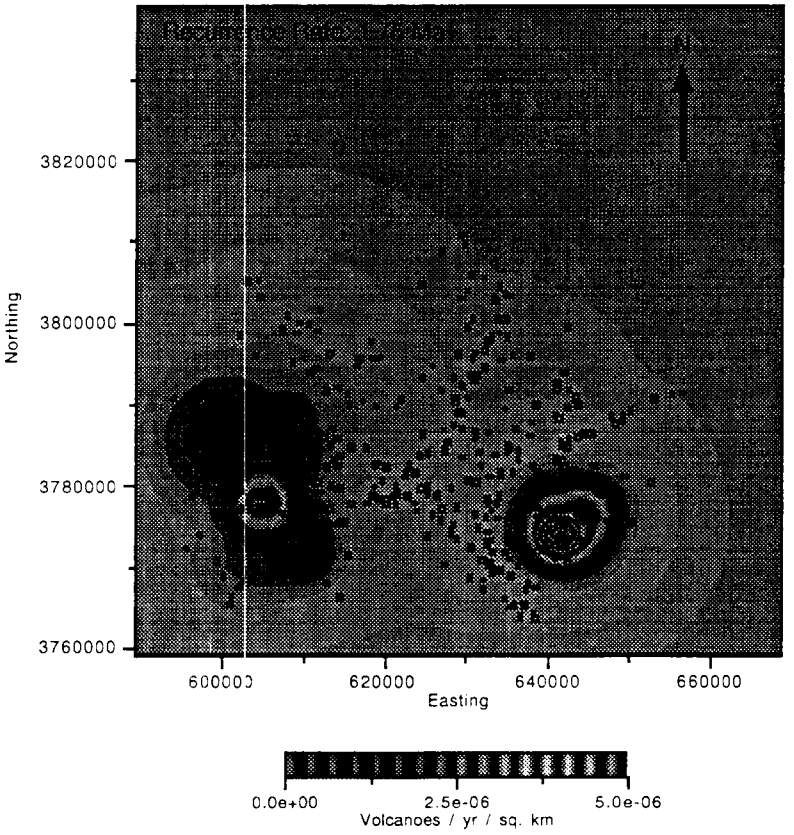

FIGURE 8. Recurrence Rate at 1.5 Ma

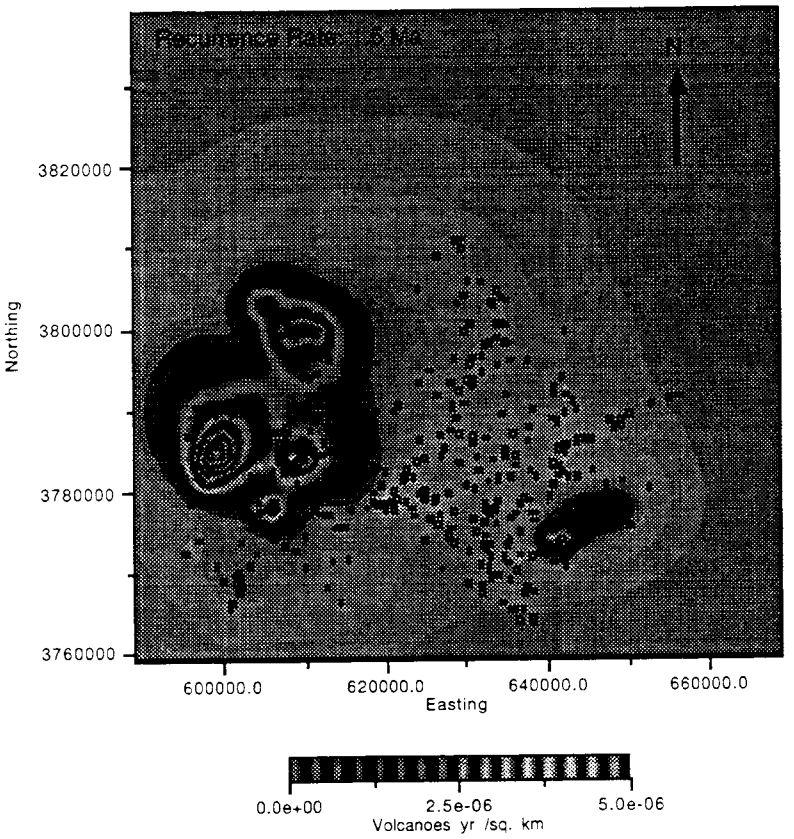

FIGURE 9. Recurrence Rate at 1.25 Ma

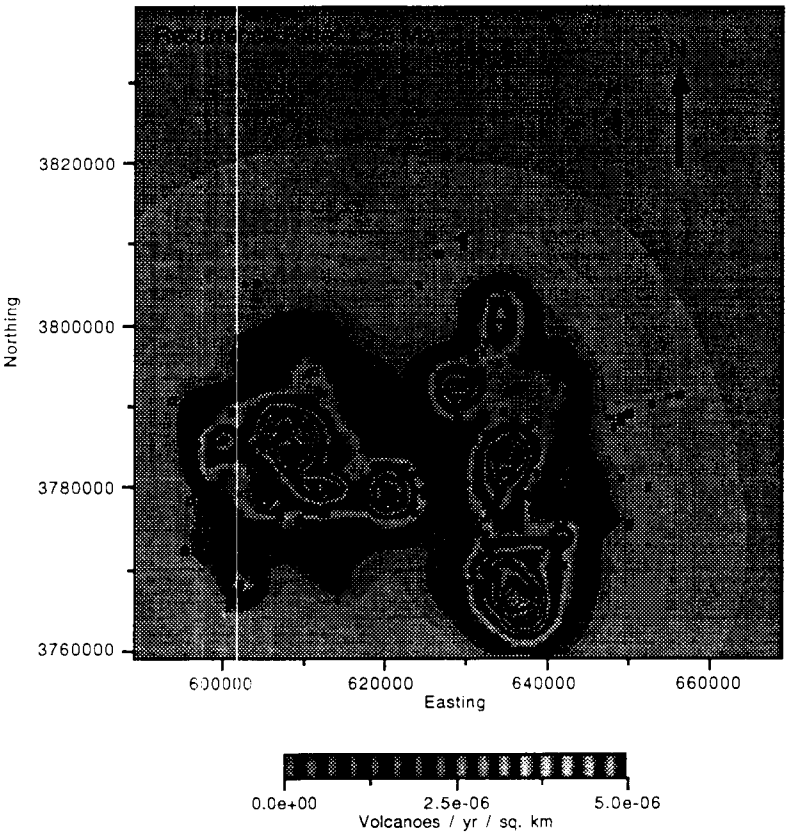

FIGURE 10. Recurrence Rate 1 Ma

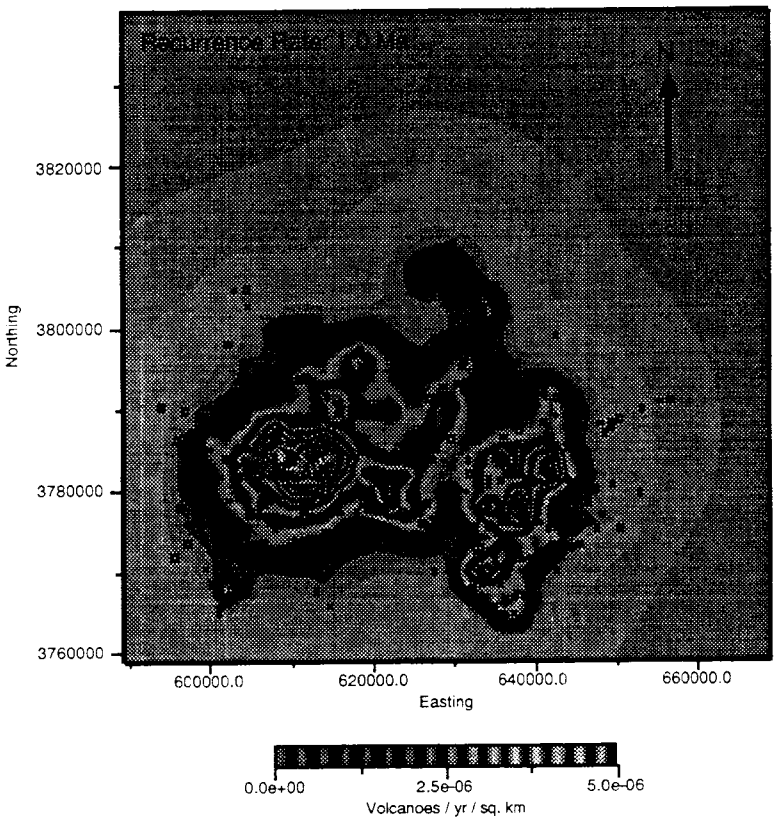

FIGURE 11. Recurrence Rate at 0.75 Ma

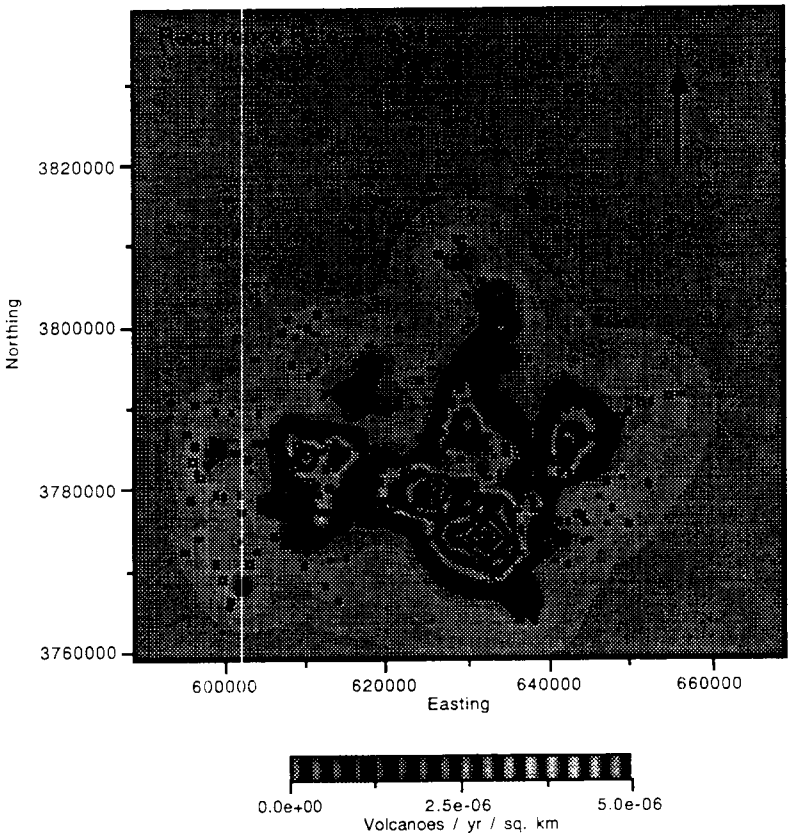

FIGURE 12. Recurrence Rate at 0.5 Ma

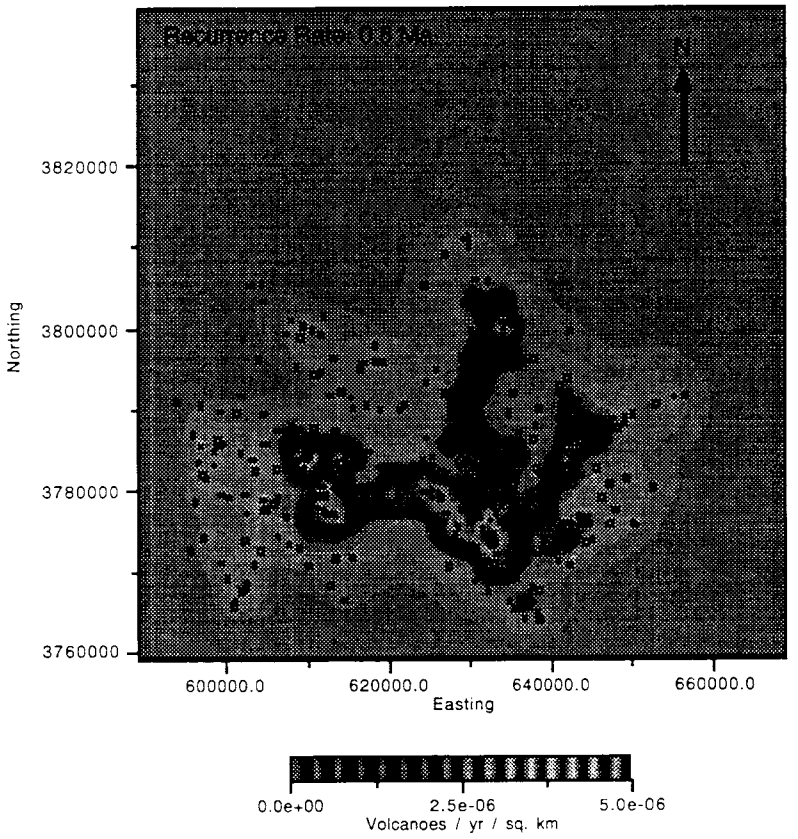

Observations about recurrence rate maps shown:

- Overall, the scenario of waxing, steady - state and waning magmatism is represented on the recurrence rate maps
- Different parts of the filed are active at different times. This is especially clear comparing maps of 1.25 Ma and 1.0 Ma, but it is also clear on othr maps
- The earliest map, 1.75 Ma shows acitvity in two distinct areas, but not in the center of the field. This may reflect overpringting by later eruptive events.

3.5 Change in Recurrence Rate Maps

Change in recurrerence rate is calculated by differencing the recurrence rate maps. For example, the change in recurrence rate between 1.25 Ma and 1.0 Ma is determined by substracting the 1.25 Ma map from the 1.0 Ma map. Areas that are waning over this period of time will show up on the resultant map with neagative change in recurrence rate. Areas that are waxing over this interval will show up with positive recurrence rates.

Change in recurrence rate maps are shown in Figure 13 on page 51 through Figure 17 on page 55.

Basic observations about these maps:

- As inferred from the recurrence rate maps, different areas of the field are waxing and waning through time.
- In general, areas experiencing volcanism move across the Springerville field from west to east through time. This is most clear in the southern half of the field where areas of high recurrence rate begin, early, in the western portion of the field and move steadily to the central and eastern portion of the field through time (and on successive maps).
- The resulting map pattern is that waning areas frequently are located WNW of waxing areas.
- Calculating the rate of shift. It turns out that this rate of migration is on the order of 1.5 to 2.0 cm per year. This is consistent with plate velocities.
- Comparing the change in recurrence rate figures gives a sense of the longevity of activity associated with a single episode of volcanism. This varies from 0.25 Ma to about 0.75 Ma
- The area affected in roughly circular and ususally on the order of 10 to 30 km in diameter.

FIGURE 13. Change in recurrence rate (1.75 - 1.5 Ma)

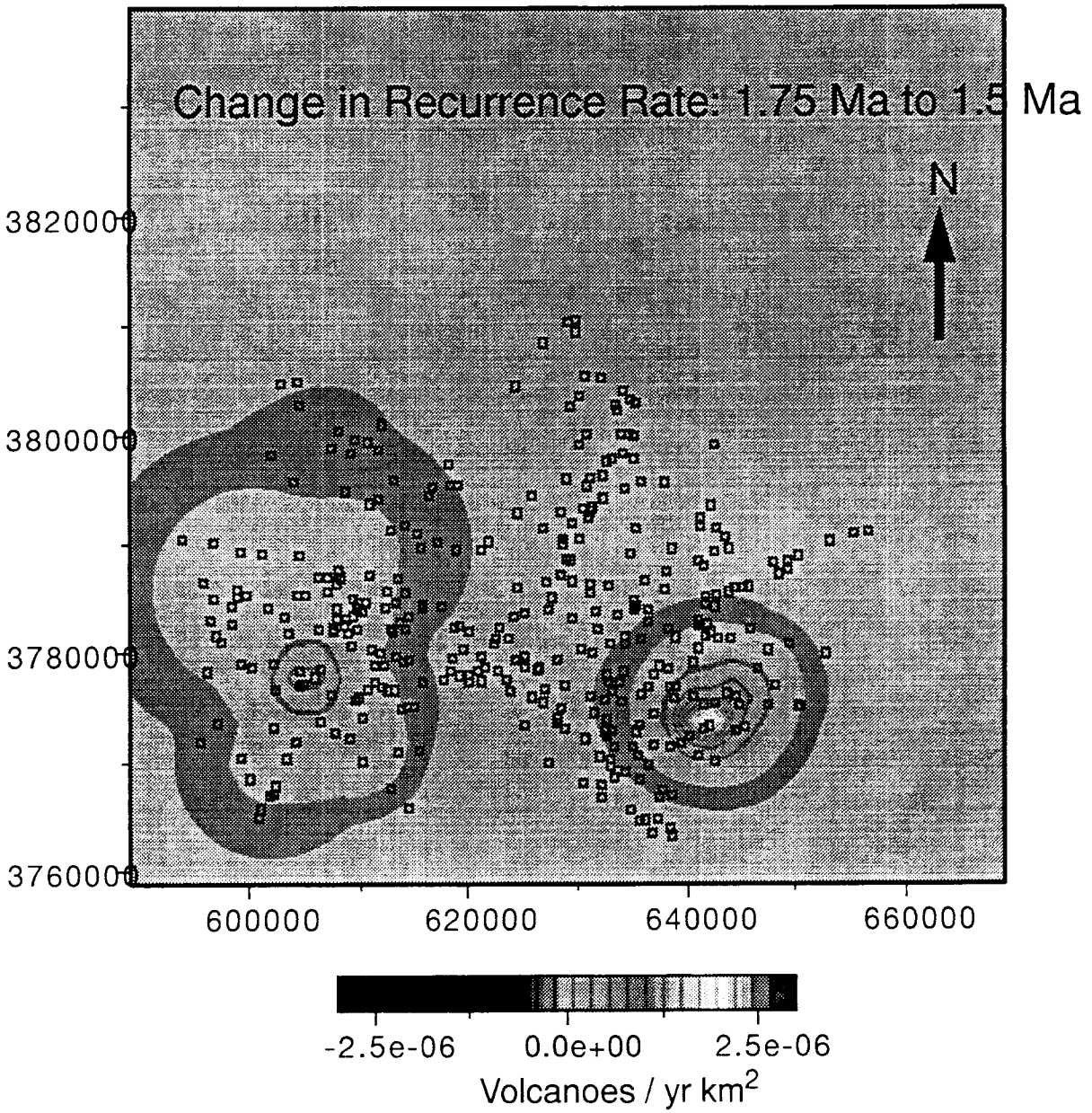

FIGURE 14. change in recurrence rate (1.5 - 1.25 Ma)

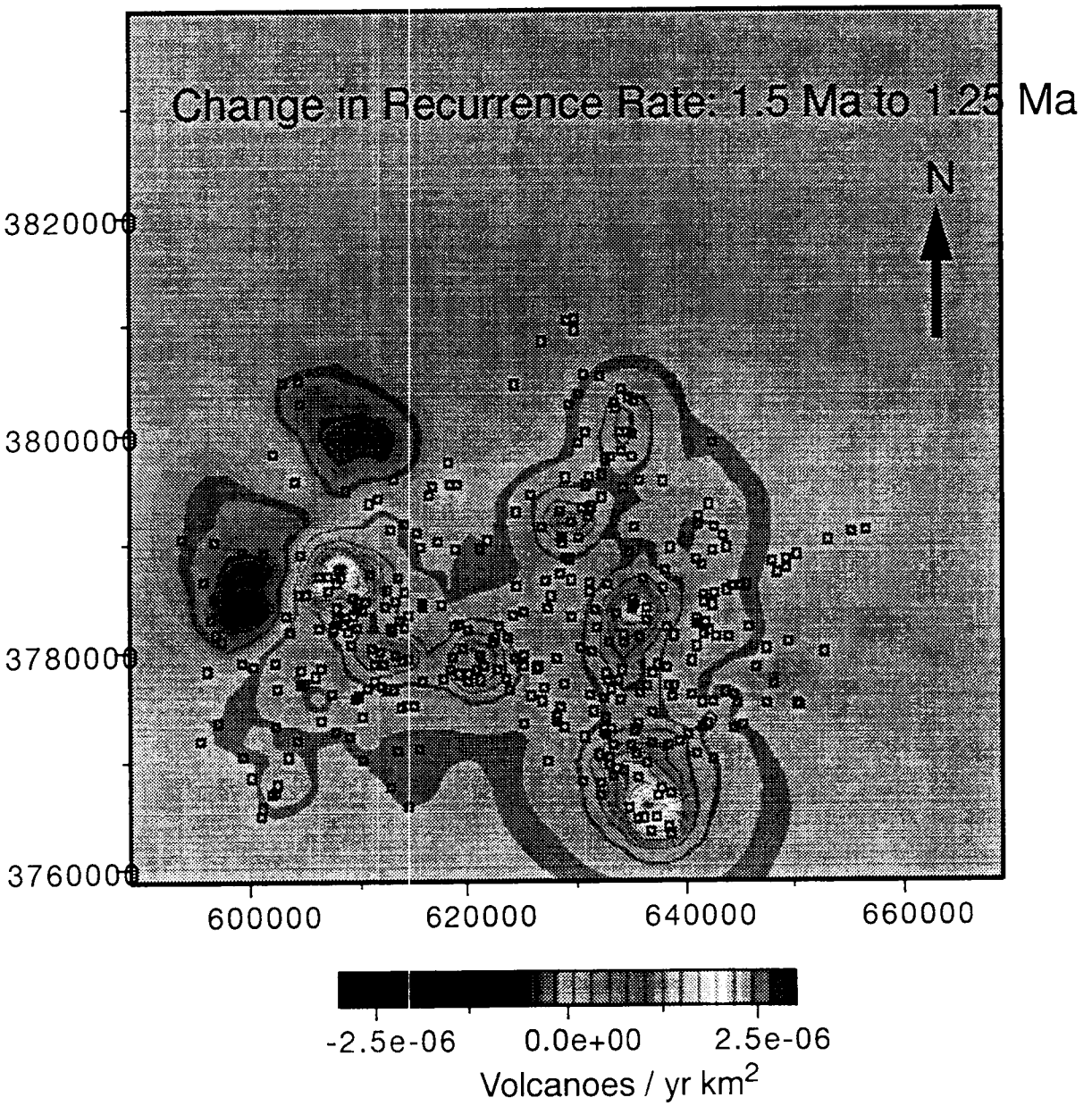

FIGURE 15. Change in recurrence rate (1.25 to 1.0 Ma)

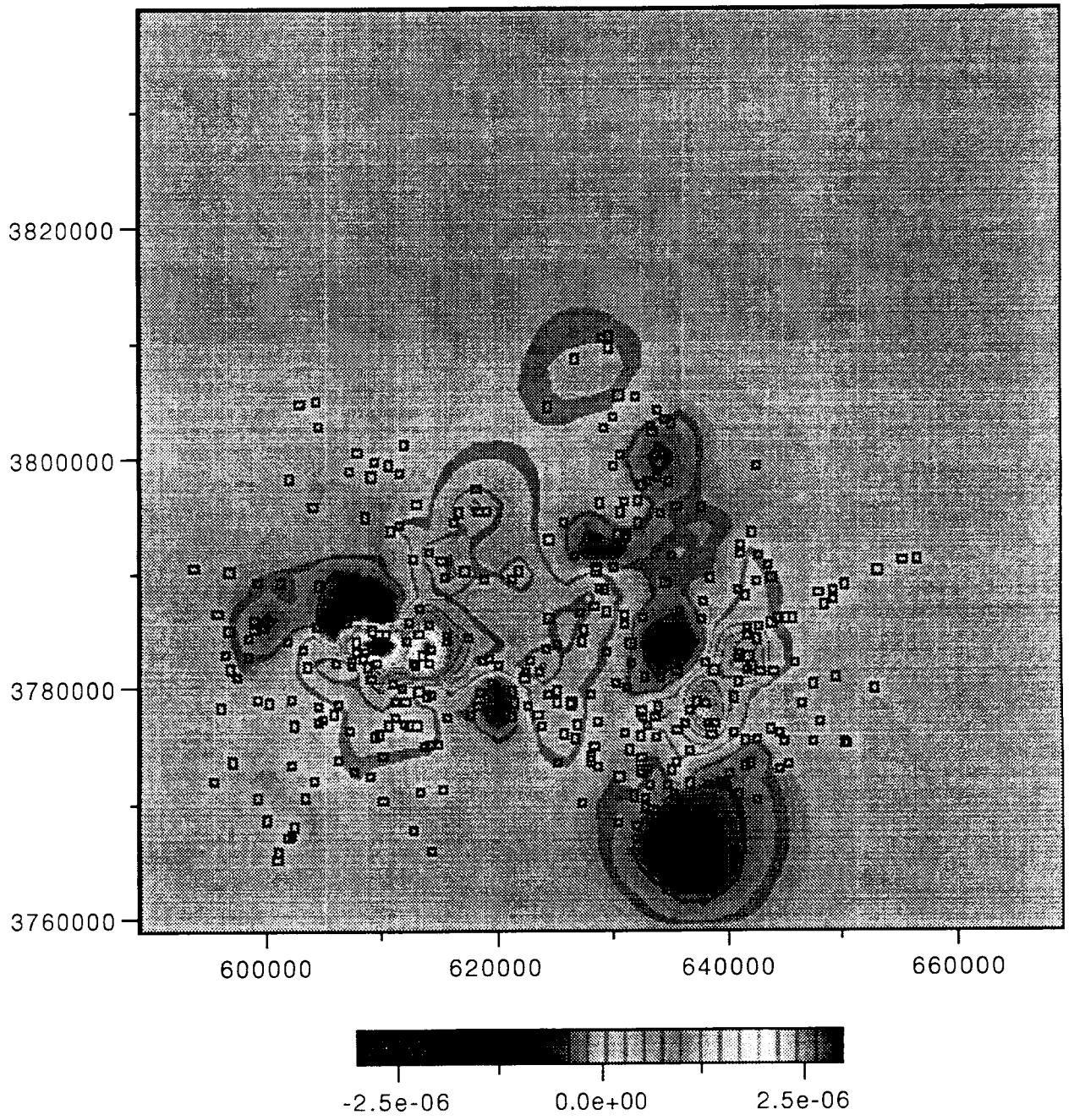

FIGURE 16. change in recurrence rate (1.0 - 0.75 ma)

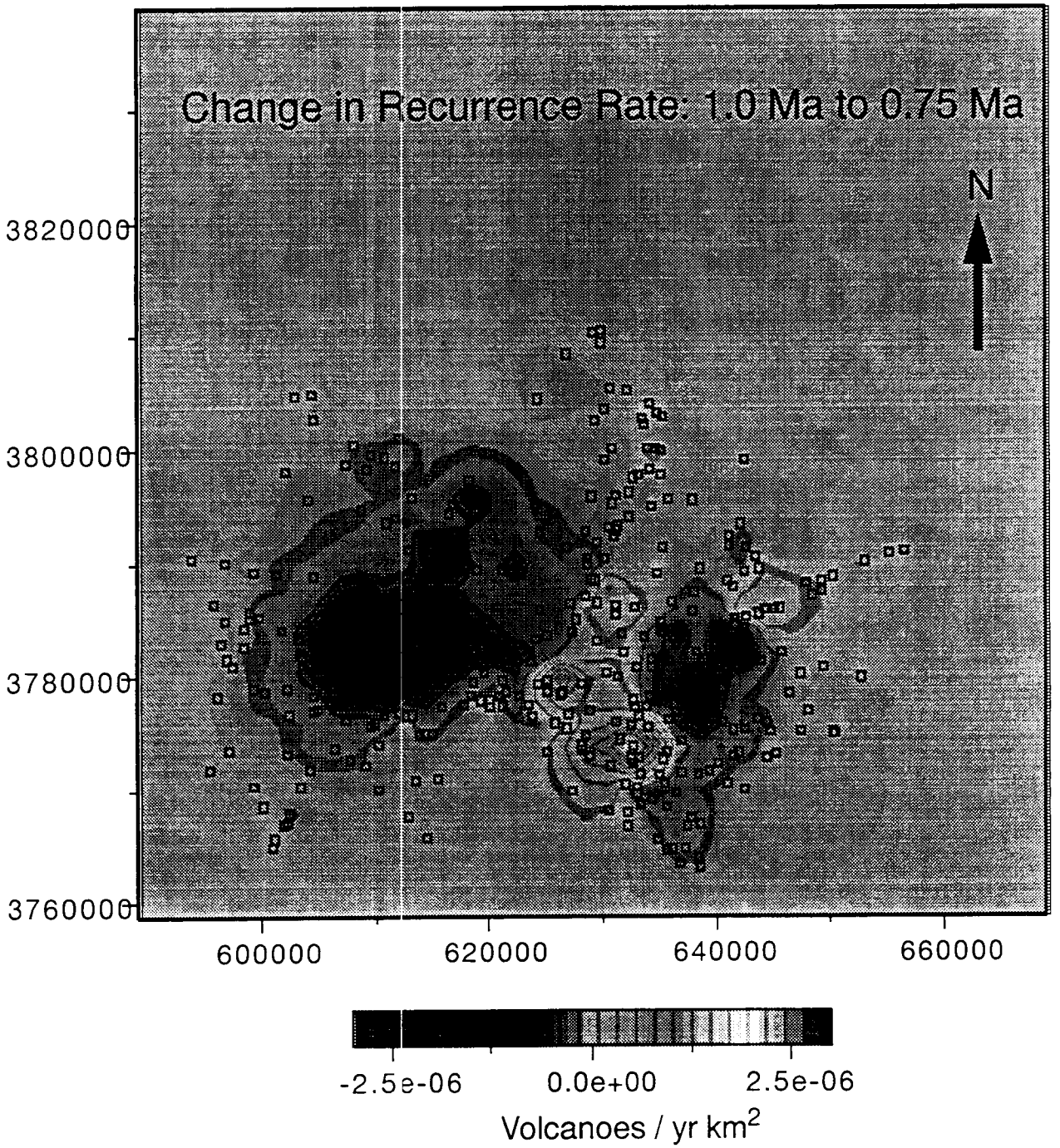

FIGURE 17. change in recurrence rate (0.75 to 0.5 Ma)

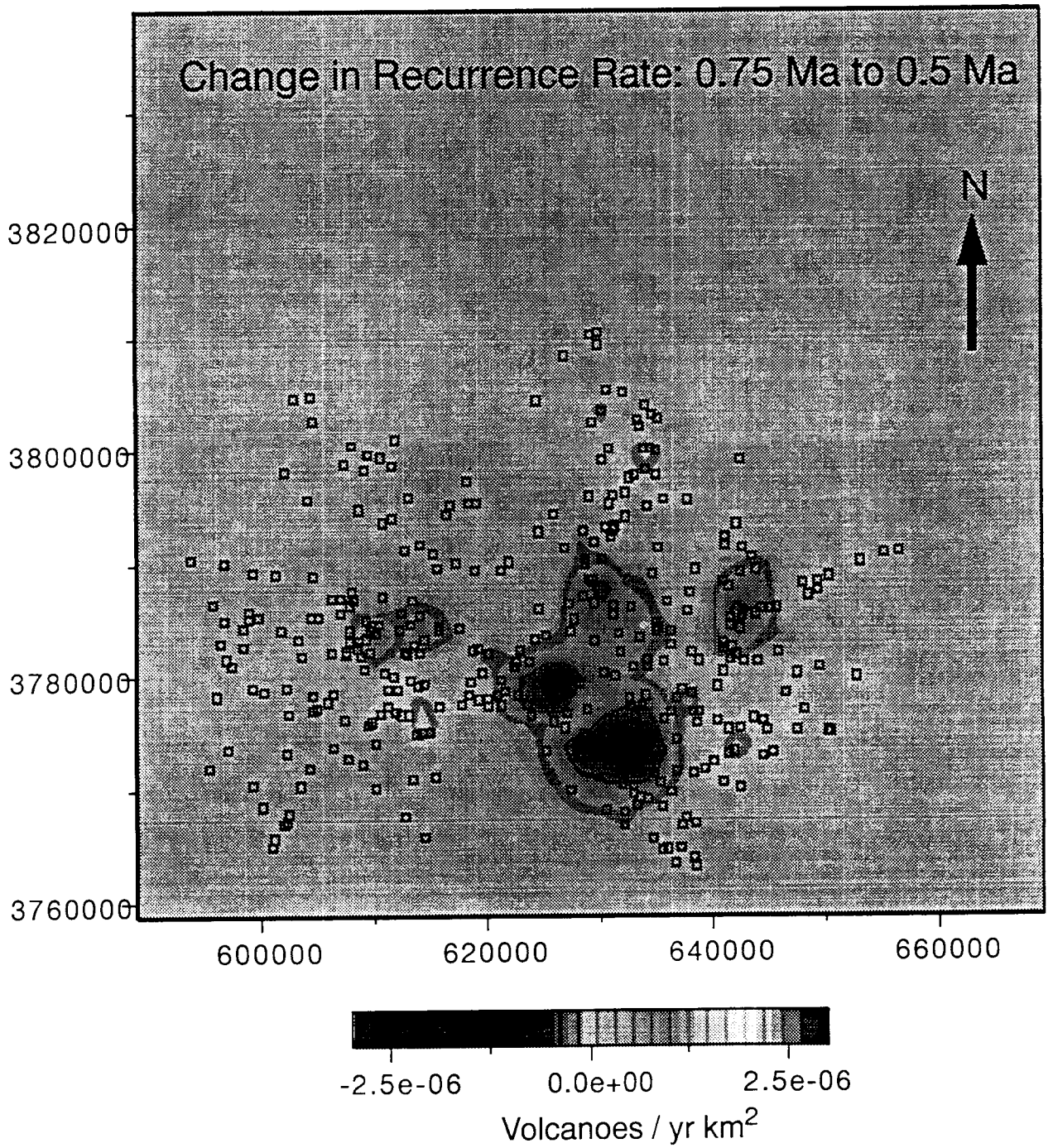

3.6 Interpretation of the results

The following abstract summarizes interpretation of the results. This abstract was presented at the Geological Society of America Meeting, in Seattle, Washington, October 23, 1994.

Estimating Recurrence Rate of Volcanism in the Springerville Volcanic Field, Arizona

C.B. Connor (Center for Nuclear Waste Regulatory Analyses, Southwest Research Institute, 6220 Culebra Rd., San Antonio, TX, 78228)

C.D. Condit (Department of Geology, University of Massachusetts, Amherst, MA)

Information potentially subject to copyright protection was redacted from pages 57 of 59 and 58 of 59 of this scientific notebook. The redacted material is from the reference listed above.

See previous page for redacted material reference information.

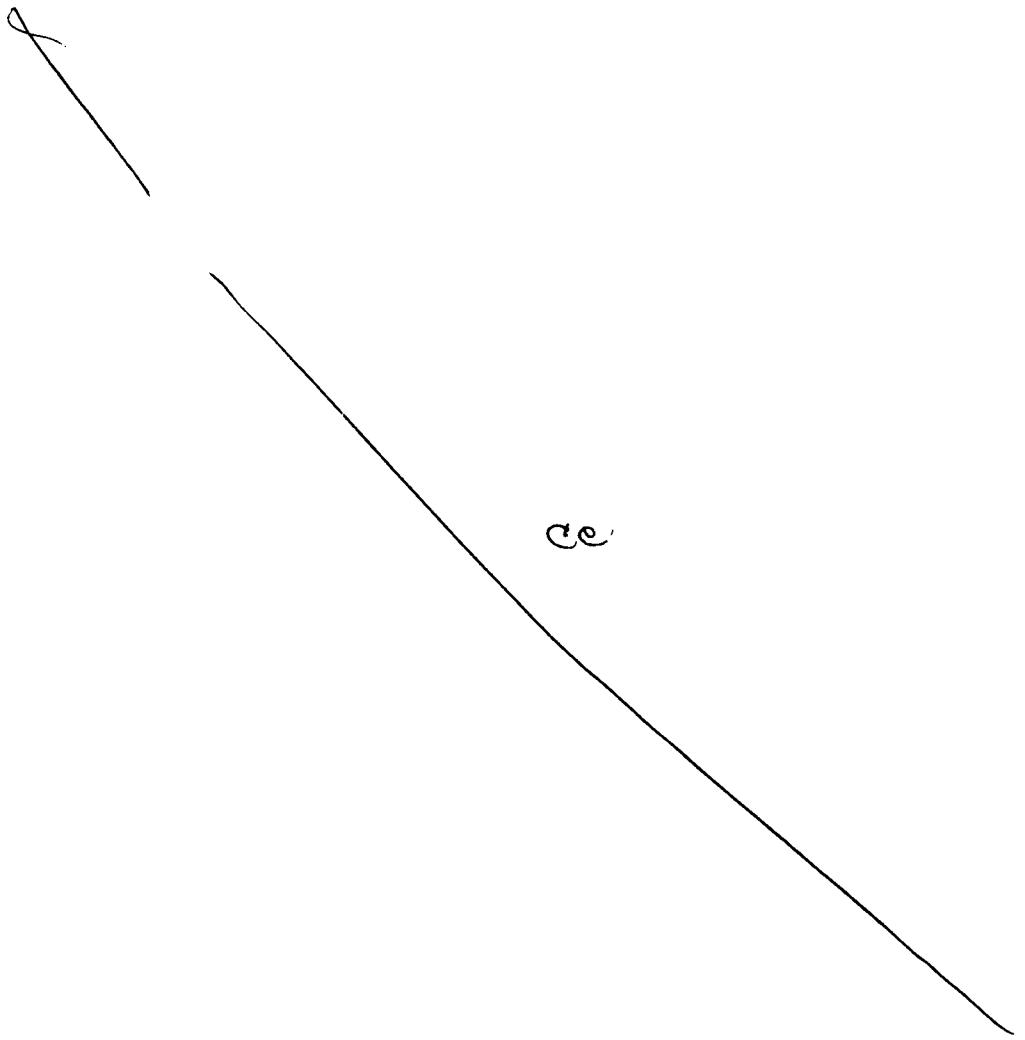

Cluster Analysis of Volcanoes in the YMR

Chuck Connor

Chuck Connor

A spatial cluster analysis of the distribution of volcanoes in the YMR shows that several distinct clusters can be identified and characterized. This helps (i) determine the size and longevity of individual clusters in a quantitative way and (ii) provides a means of estimating a smoothing parameter for kernel density estimates.

1.0 Purpose of the Cluster Analysis

The primary goal of any cluster analysis is to identify similarity between objects in a quantitiative manner. Here, I apply standard cluster analysis techniques to the volcanoes of the YMR. The purpose of this analysis is to:

- identify geographic clusters of vents in the YMR in a quantitative way
- differentiate between vent pairs, clusters, and groups of clusters systematically
- learn more about cluster size and volcano density within clusters
- learn more about the differences in ages of volcanoes between clusters.
- use the cluster analysis to estimate the best value of h - a smoothing parameter used in kernel intensity estimation techniques.
- determine how "different" in terms of geographic position a volcanic eruption at the repository would be compared with volcanoes that already form the Crater Flat cluster.

2.0 Procedure

Data used in the cluster analyses shown here are summarized in the following table.

TABLE 1. Summary of volcanoes used in the cluster analysis

Easting	Northing	age (Ma)	Name
548920	4133270	7.5	pm
554090	4134530	7.5	pm
562370	4132680	7.5	pm
594860	4107970	8.3	pr
595780	4106340	8.3	pr
592810	4105890	8.3	pr
593411	4105540	8.3	pr
591480	4105170	8.3	pr
603230	4095790	6.6	ncy
602170	4088960	6.6	ncy
600950	4085920	6.6	ncy
600550	4085450	6.6	ncy
599160	4085820	6.6	ncy
598030	4090090	6.6	ncy
597930	4082470	6.6	ncy
577860	4093930	8.1	yf
554680	4108970	2.9	bb
556060	4107580	2.9	bbse
536110	4109120	7.5	rw
529390	4112330	4.5	tm
523230	4112530	0.36	hc
522130	4110340	0.29	lb
540330	4079130	1.02	nc
538840	4073990	0.71	bc
537450	4071470	0.90	rc
535500	4069490	0.77	lcne
535131	4069220	0.77	lcsw
543780	4060380	0.05	lw
540232	4071610	3.5	cfa
540330	4070050	3.5	cfb
540365	4068790	3.5	cfc
540696	4067830	3.5	cfd
540300	4068390	3.5	cfe

TABLE 1. Summary of volcanoes used in the cluster analysis

Easting	Northing	age (Ma)	Name
540660	4067470	3.5	cff
553720	4052990	3.8	avb
546130	4054260	3.7	ava
538300	4047200	3.7	ave
547050	4042950	3.8	avc
549430	4040080	3.7	avd

In the first step of each analysis, the distance matrix is calculated. In practice, this was done using the following Perl code. The input file consisted of x and y locations of volcanoes. The data set was filtered by age. So, for example, it was possible to do the cluster analysis using only volcanoes less than 5 Ma.

```
#!/usr/bin/perl

print STDERR "\nEnter filename of x-y locations --> ";

$file = <STDIN>;

open(FILE, $file) || die "Couldn,t open $file: $!\n";

@lines = <FILE>;

print STDERR "\nEnter cutoff value --> ";

$val = <STDIN>;

foreach $elem (@lines){

@test = split(/ /, $elem);

if ($test[2] <= $val){

push(@line, $elem);

}

}

print STDERR "\nEligible locations -->\n";
```

```
print STDERR @line;

while($i < $#line){

@line1 = split(/ /,$line[$i]);

$j = ++$i;

while($j <= $#line){

@line2 = split(/ /,$line[$j++]);

$dist = sqrt(($line1[0]-$line2[0])**2 + ($line1[1]-$line2[1])**2);

print $dist, "\n";

}

}
```

This Perl code was tested by using a small input matrix, for which the distance values were calculated independently by calculator.

The Perl code outputs the distance matrix. This matrix is then read by the program cluster.c, listed below, which is written in C. This program was taken from S (1980, Clustering Algorithms) and is translated from Fortran. The program takes the distance matrix as input and outputs results suitable for plotting as a dendrogram. The program performs the cluster analysis using one of seven algorithms in the code, chosen by the user.

The algorithms are:

1. single linkage cluster analysis
2. complete linkage
3. average linkage
4. centroid
5. weighted centroid
6. Ward's method (1)
7. Ward's method (2)

Cluster.c was checked by inputing a distance matrix that Speth used as an example in his textbook. The output was identical to the output given in the text, for all seven clustering algorithms.

A listing of Cluster.c follows

```
/* cluster.c -- */

#include <stdio.h>
#include <string.h>
#include <math.h>

enum {no, yes};
floatdist[60][60];

void hiercl(int num_of_pts, int, int *, int *, float *);

void main(void){

enum {no, yes};

floatout_h[60];

intout_a[60],
out_b[60],
num_of_pts,
kenn,
choice = no,
row,
col;
```

```
charstr[25];

FILE*input;

do {
fprintf(stderr,"\nEnter number of points [1-60] --> ");
scanf("%d", &num_of_pts);
} while (num_of_pts > 60 || num_of_pts < 0);
if (num_of_pts == 0) exit(0);
gets(str);
fprintf(stderr,"\nSquare values? Enter [y] --> ");
gets(str);
if (!strncmp(str, "y", 1) || !strncmp(str, "Y", 1))
choice = yes;
do{
fprintf(stderr,"\nEnter your cluster algorithm number [1-7] --> ");
scanf("%d", &kenn);
} while (kenn > 7 || kenn < 0);
if (kenn == 0) exit(0);
fprintf(stderr,"\nEnter your inputfile name --> ");
scanf("%s",str);
if ((input = fopen(str, "r")) == NULL){
fprintf(stderr, "Error opening %s!! Quitting!!\n", str);
exit(1);
}
```

```
for(row=0; row < num_of_pts-1; row++){
for(col=row+1; col < num_of_pts; col++){
if (fscanf(input, "%f", &dist[row][col]) == EOF){
fprintf(stderr, "Ran out of input, quitting!");
exit(1);
}
if (choice)
dist[row][col] *= dist[row][col];
/*dist[col][row] = dist[row][col];    */
}
}
hiercl(num_of_pts, kenn, out_a, out_b, out_h);
printf("Clustering algorithm:%d\n", kenn);
for(row=0; row < num_of_pts-1; row++)
printf("%d %f %d %d\n",row,out_h[row],out_a[row],out_b[row]);
}
void hiercl(int num_of_pts, int kenn, int *a, int *b, float *h){

  intp[5000],/* P */
q[5000],/* Q */
row,/* I */
col,/* J */
row_val,/* IC */
col_val,/* JC */
```

```
q_row,/* QIC */
q_col,/* QJC */
qr,/* QI */
minr,/* J */
maxr,/* L */
minc,/* K1 */
maxc,/* K2 */
k = num_of_pts;/* K */

doubledmax;
floatdistj,/* DJ */
distk,/* DK */
f;

for (row=0; row < num_of_pts; row++){
p[row] = 0;
q[row] = 1;
}

while(k){
dmax = 1e30;
for(row=0; row < num_of_pts-1; row++){
if (!p[row]){
for(col = row+1; col < num_of_pts; col++){
if (!p[col]){
```

```
if (dist[row][col] <= dmax){
row_val = row;
col_val = col;
dmax = dist[row][col];
}
}
}
}
}
p[col_val] = 1;
*a++ = row_val;
*b++ = col_val;
*h++ = dmax;

if (kenn >= 5){
q_row = q[row_val];
q_col = q[col_val];
if (kenn < 7)
f = 1.0/(q_row + q_col);
}
for(row=0; row < num_of_pts; row++){
if (row != row_val && !p[row])
if (kenn == 7){
qr = q[row];
f = 1.0/(qr+q_row+q_col);
```

```
}
minr = (row_val < row) ? row_val : row;
maxr = (row_val > row) ? row_val : row;
minc = (col_val < row) ? col_val : row;
maxc = (col_val > row) ? col_val : row;
distj = dist[minr][maxr];
distk = dist[minc][maxc];

switch (kenn){
case 1:
dist[minr][maxr] = (distj < distk) ? distj : distk;
break;
case 2:
dist[minr][maxr] = (distj > distk) ? distj : distk;
break;
case 3:
dist[minr][maxr] = .5*(distj + distk);
break;
case 4:
dist[minr][maxr] = .5*(distj + distk) - .25*dmax;
break;
case 5:
dist[minr][maxr] = f*(q_row*distj + q_col*distk);
break;
case 6:
```

```
dist[minr][maxr] = f*(q_row*distj + q_col*distk -
  q_row*q_col*f*dmax);
break;
case 7:
dist[minr][maxr] = f*((q_row+qr)*distj + (q_col+qr)*
  distk - qr*dmax);
break;
}
}
q[row_val] += q[col_val];
--k;
}
return;
}
```

3.0 Results of the Cluster Analysis

The volcano locations were run using all seven clustering algorithms and plotted as dendrograms. All of the centroid methods (including Ward's method) give essentailly identical results. Slight variations exist between the averaging method and the centroid methods. Most variation is found between the single linkage algorithm and the others.

Dendrograms for single linkage, average linkage, and centroid methods are shown below (Figure 1, "Single Linkage Dendrogram for YMR," on page 12; Figure 2, "Average Linkage Dendrogram for YMR," on page 13; Figure 3, "Centroid (Method 5) Dendrogram for the YMR," on page 14).

The single linkage analysis joins clusters based on the minimum distance between and two points in the two clusters. This means that the single linkage technique is good at identifying long lines of vents - these will tend to cluster readily (at shorter distances). For example, the Pliocene crater flat vents all link at short distances. It is interesting to not that the Quaternary Crater Flat alignment links together with the Pliocene Crater Flat alignment before linking with northern cone (nc). The Crater Flat vents are joined into a single cluster at about 6.5 km. Lathrop Wells joins first with two Amargosa Valley magnetic anomalies, A and B; then these three volcanoes join with the rest of Craetr Flat. Similarly, the southern Amargosa Valley volcanoes join, then group with the rest. All this takes place at linkage distances of less than 11 km. Thirsty Mesa, and the Sleeping Butte volcanoes form a tight group and eventually link with Buckboard Mesa, but only at long distances. Then these two clusters link with the Crater Flat - Amargosa Val-

ley group. Based on a single linkage model, it is best to divide volcanoes into three

TABLE 2. Results of the single linkage cluster analysis

Iteration Number	Linkage Distance (m)	First point or Cluster linked	Second point or cluster linked
0	361.8	14	16
1	405.2	13	15
2	457.2	8	9
3	685	13	14
4	1260	12	13
5	1563	11	12
6	1958	0	1
7	2450	3	4
8	2757	6	11
9	2779	7	8
10	2950	6	7
11	3728	20	21
12	5351	5	6
13	6163	2	3
14	6555	10	18
15	7695	10	17
16	7946	5	10
17	9727	19	20
18	10542	5	19
19	25512	0	2
20	32509	0	5

major clusters, The BB, Sleeping Buttes, and Crater Flat - Amargosa Valley.

FIGURE 1. Single Linkage Dendrogram for YMR

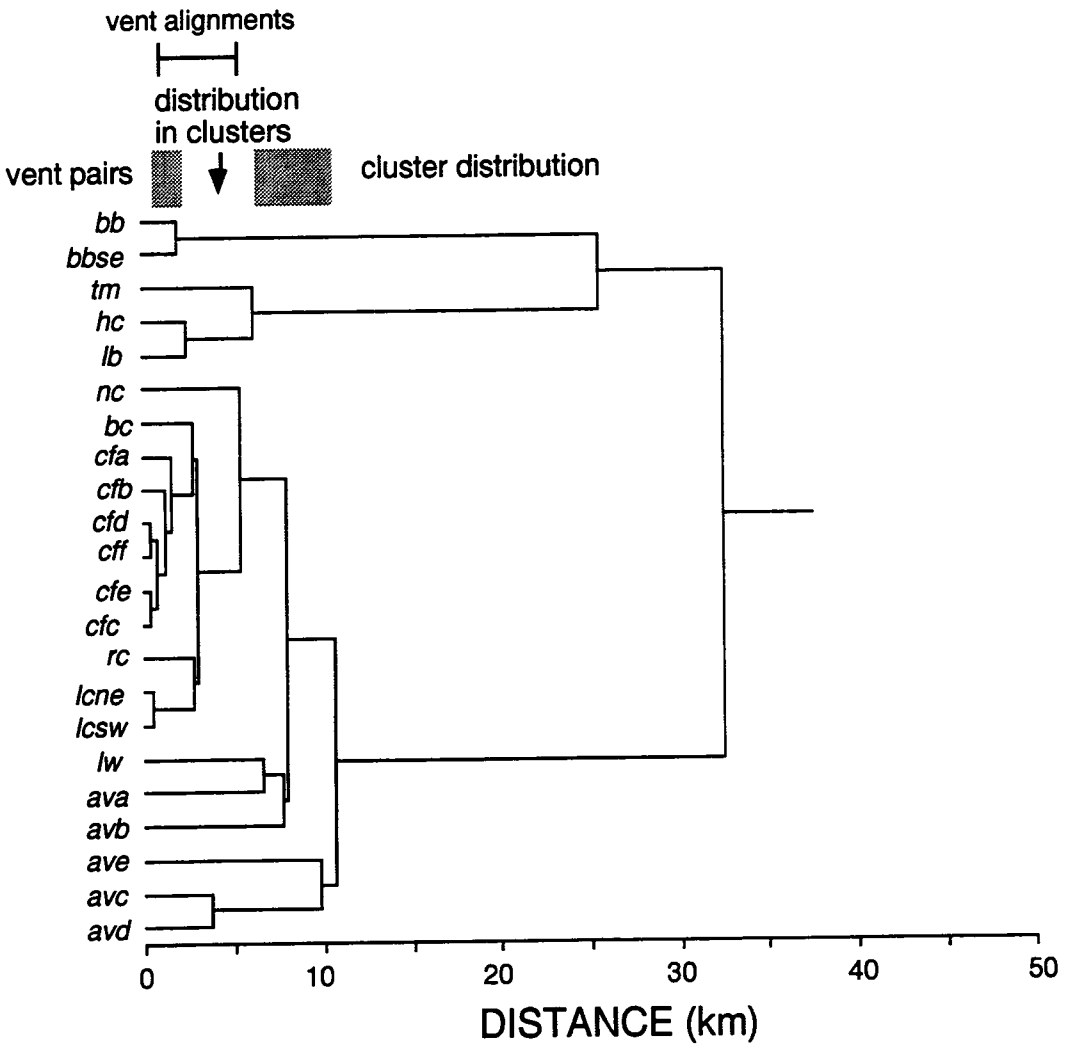

The results are much the same with the average linkage method with one important difference: the Amargosa Valley and Crater Flat clusters are clearly differentiated. This makes four major clusters in the region. Linkage distances in this dendrogram (Figure 2, "Average Linkage Dendrogram for YMR," on page 13) are longer because the linkages are calculated based on the "average" vent location in the cluster, rather than the closest vent position. The centroid method (Figure 3, "Centroid (Method 5) Dendrogram for the

YMR," on page 14) gives results but the location of the centroid is weighted by the number of vents in the cluster.

TABLE 3. Average Linkage results

Iteration Number	Linkage Distance (m)	First point or Cluster linked	Second point or cluster linked
0	361.8	14	16
1	405.2	13	15
2	457.2	8	9
3	1010	13	14
4	1563	11	12
5	1958	0	1
6	2450	3	4
7	2723	11	13
8	2877	6	7
9	3728	20	21
10	4281	6	11
11	4855	6	8
12	6555	10	18
13	6845	2	3
14	9599	5	6
15	10040	10	17
16	11470	19	20
17	14471	10	19
18	26899	5	10
19	29584	0	2
20	50573	0	5

FIGURE 2. Average Linkage Dendrogram for YMR

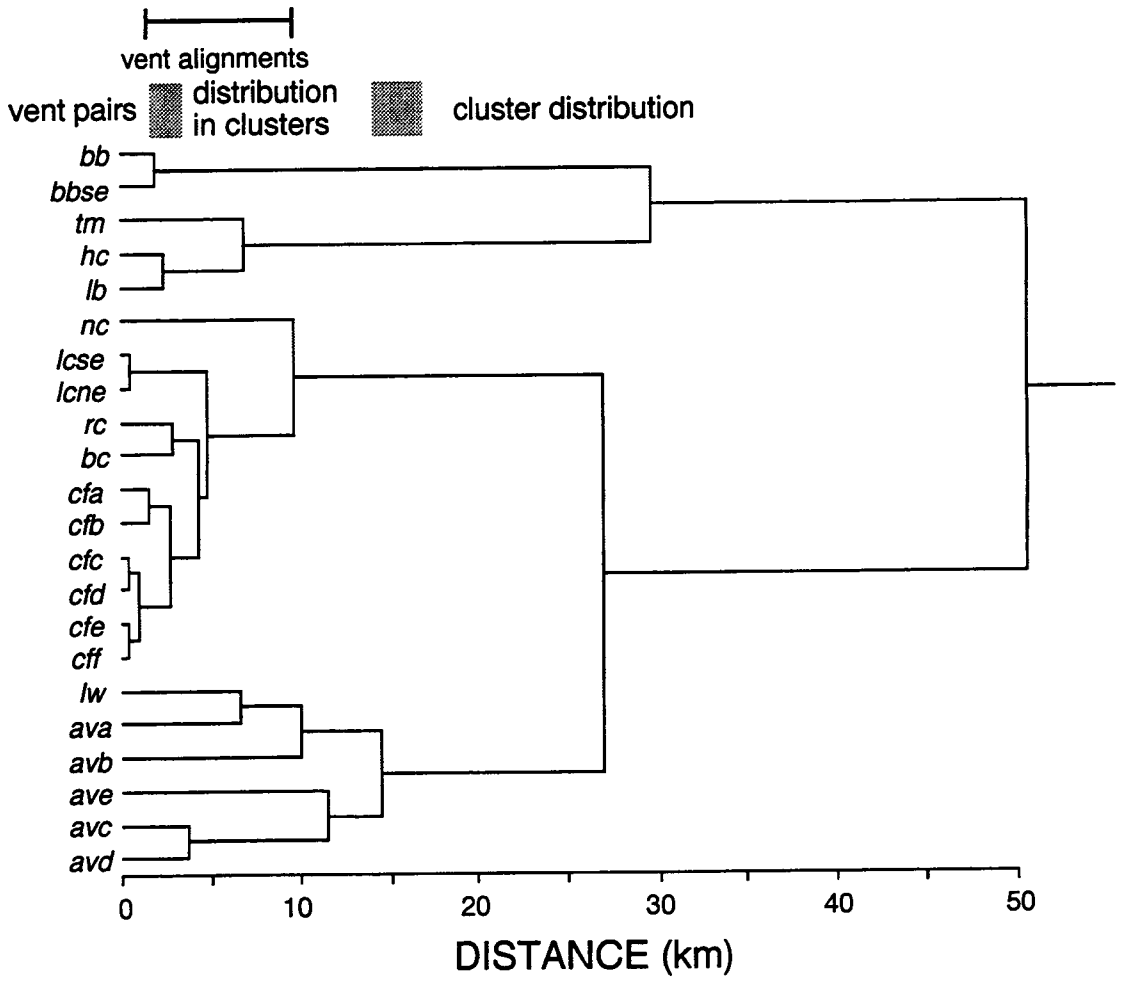

TABLE 4. Weighted Centroid results

Iteration Number	Linkage Distance (m)	First point or Cluster linked	Second point or cluster linked
0	361	14	16
1	405	13	15

TABLE 4. Weighted Centroid results

Iteration Number	Linkage Distance (m)	First point or Cluster linked	Second point or cluster linked
2	457	8	9
3	1010	13	14
4	1563	11	12
5	1958	0	1
6	2450	3	4
7	2723	11	13
8	2877	6	7
9	3728	20	21
10	4414	6	8
11	4972	6	11
12	6555	10	18
13	6845	2	3
14	9615	5	6
15	10040	10	17
16	11470	19	20
17	14628	10	19
18	22913	5	10
19	30679	0	2
20	49925	0	5

FIGURE 3. Centroid (Method 5) Dendrogram for the YMR

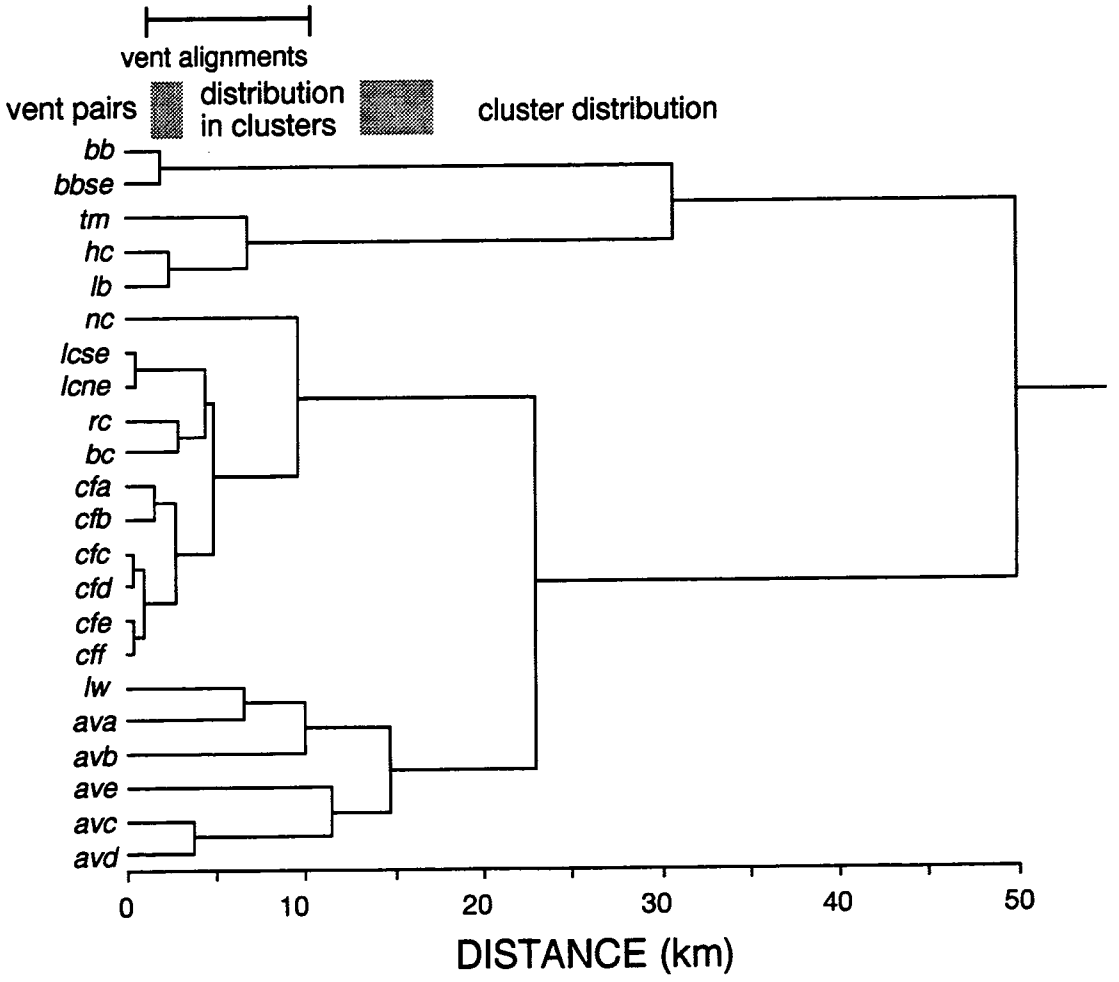

General observations about the results of the weighted centroid and average linake methods are:

- vent pairs and short vent alignments, some of which might be related to a single eruption episode, all group at distances of h = 3000 m or less. Good examples are the Pliocene Crater Flat alignment and the Little Cones.
- not including these vent pairs and short alignments, most grouping of vents within clusters occurs at 4 km < h < 15 km. For example, the six volcanoes in th Amargosa

Valley cluster link between 4 and 15 km. The Crater Flat cluster is more compact, with most linkage occrring at less than 6 km, except for northern cone, which links with the cluster at about h = 11 km.

- The four main clusters are distinct to varying degrees. The Crater Flat - and Amargosa Valley groups link at 27 km in the average method and at 23 km in the weighted centroid method. This is the closest linkage between the clusters.
- all of the clusters contain young vents - they have to be considered active.

3.1 Adding in the repository

In the next step in the analysis I added a point located roughly in the center of the repository to the distance matrix. This is equivalent to looking at the impact on the dendrogram of a volcano forming in the location of the center of the repository. The coordinate for the point added to the distance matrix is:

FIGURE 4. repository outline, showing the locations of hypothetical events used in the calculation

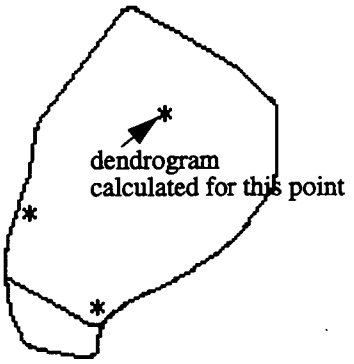

548500E , 40785000N

The dendrograms were then recalculated using the same algorithms (Figure 4, "Average linkage dendrogram plotted using the data in Table 1 + the location of the center of the repository (shown as solid circle)," on page 16; Figure 5, "Weighted centroid lnkage dendrogram using the data in Table 1 and the location of the center of the repository (shown as solid circle)," on page 17).

Observations about the results:

- the reposiotry clusters with northern cone at a linkage distance of 8.2 km
- this sub-cluster then links with the reset of the crater flat cluster at a linkage distance of about 11 km (in average linkage and centroid linkage methods.
- the linkage distance for a volcano at the center of the repository in comparable to the linkage distances for many cones in the YMR

So, it is concluded from this analysis that a volcano forming in the repository would not be between clusters, rather, it would be part of the Crater Flat cluster. Another way to say this is that the probability of volcanism in the Crater Falt cluster, or the Crater Flat - Amargosa Valley cluster, is what controls the probability of volcanism disrupting the repository, rather than the probability of a new cluster forming.

FIGURE 5. Average linkage dendrogram plotted using the data in Table 1 + the location of the center of the repository (shown as solid circle)

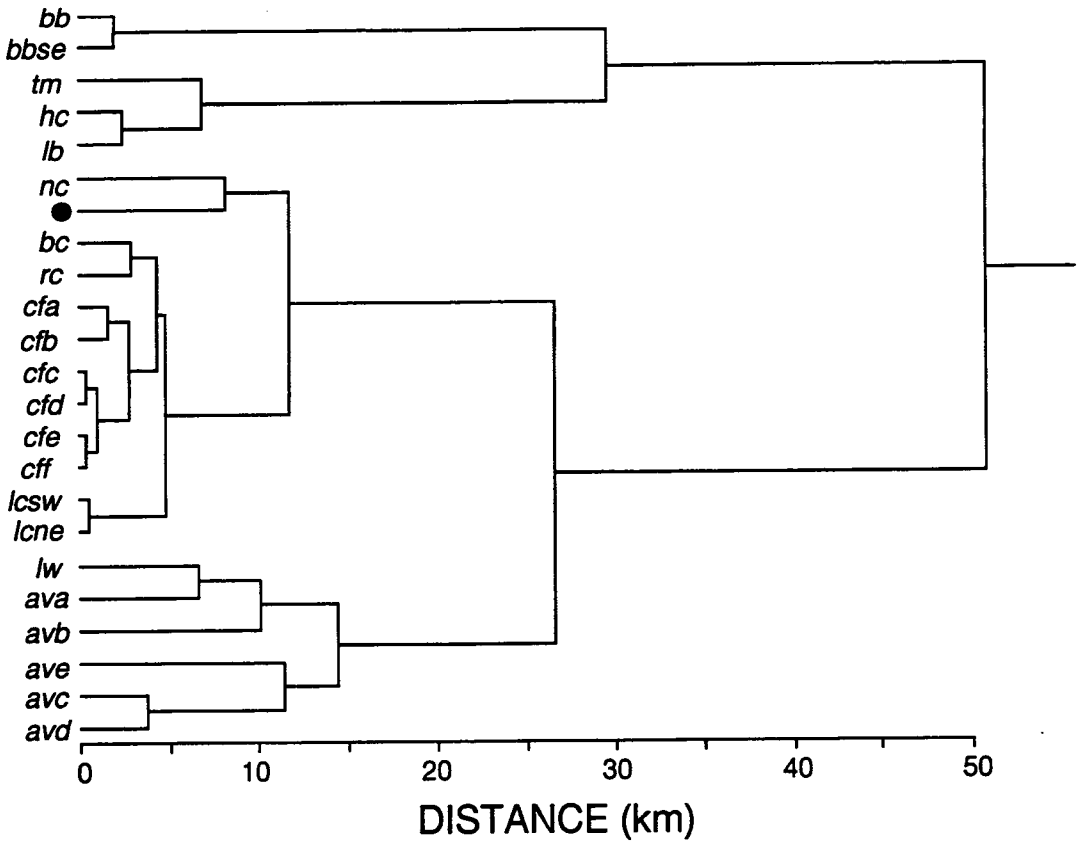

FIGURE 6. Weighted centroid Inkage dendrogram using the data in Table 1 and the location of the center of the repository (shown as solid circle)

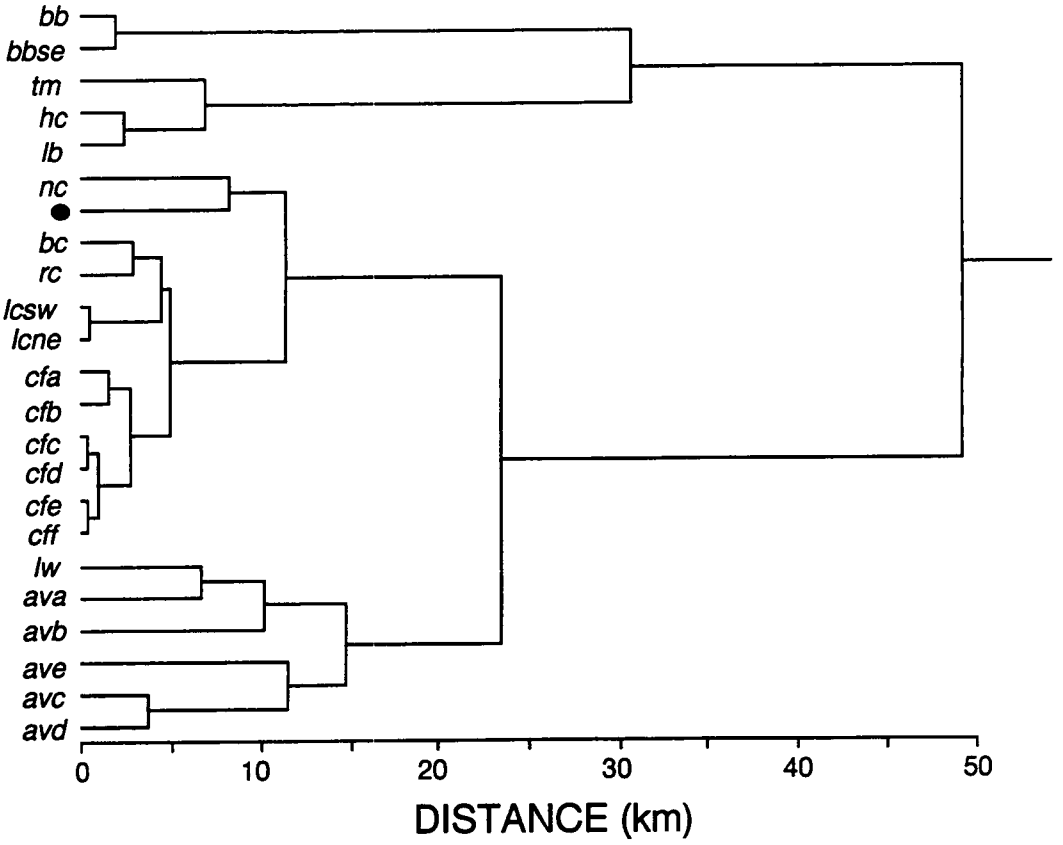

Cluster Analyses were also run for these points:

547900,4076500

547300,4077500

also shown on Figure 4, "repository outline, showing the locations of hypothetical events used in the calculation," on page 15. These give identical results except that the linkage distance changes slightly. The minimum linkage distance, for the southernmost point in the repository is about 7 km.

4.0 Including the Miocene

TABLE 5. Results of weighted centroid method using the Miocene also

Iteration Number	Linkage Distance (m)	First point or Cluster linked	Second point or cluster linked
0	361.795990	31	33
1	405.247009	30	32
2	457.231995	25	26
3	617.171021	10	11
4	695.486023	5	6
5	1010.453979	30	31
6	1563.079956	28	29
7	1615.594971	10	12
8	1739.255005	5	7
9	1871.709961	3	4
10	1958.699951	16	17
11	2450.729980	20	21
12	2723.253662	28	30
13	2877.929932	23	24
14	3349.905029	3	5
15	3728.439941	37	38
16	3830.386719	9	10
17	4414.134766	23	25
18	4769.822266	9	13
19	4972.507812	23	28
20	5321.330078	0	1
21	5498.928223	9	14
22	6555.680176	27	35
23	6845.524902	19	20
24	9615.977539	22	23
25	10040.809570	27	34
26	10090.558594	8	9
27	10973.530273	0	2
28	11470.019531	36	37
29	11601.402344	18	19
30	14628.644531	27	36
31	19864.662109	3	8

TABLE 5. Results of weighted centroid method using the Miocene also

Iteration Number	Linkage Distance (m)	First point or Cluster linked	Second point or cluster linked
32	22117.167969	3	15
33	22913.617188	22	27
34	25838.785156	0	16
35	32665.318359	0	18
36	56883.078125	0	22
37	63113.796875	0	3

Cluster analysis using the Miocene aged roks shows an identical situation in terms of cluster shape and density

5.0 Conclusions of the Cluster Analysis

The original goals of the analysis were:

- identify geographic clusters of vents in the YMR in a quantitative way

  Four clusters of vents younger than 5 ma are found in the YMR. These are the Crater Flat, Amargosa Valley, Sleeping Butte, and Buckboard Mesa clusters Linkage distances between these clusters are on the order of 25 km (Crater Flat - Amargosa Valley) or more.

- differentiate between vent pairs, clusters, and groups of clusters systematically

  The cluster analysis indicates that short vent alignments and vent pairs are separated by distances of less than 3 km. The most closely spaced vent pairs are: Little Cones, three vent pairs in Pliocene Crater Flat (two pairs of which form a short alignment), and buckboard. These could be considered to be single events(?) The Red Cone and Blackcone and Sleeping Buttes are more widely spaced, between 2.5 and 3 km. Vents within clusters group at distances of 15 km or less. Clusters don't begin to group until greater than 25 km.

- learn more about cluster size and volcano density within clusters

  single linkages within clusters: the Crater Flat cluster has the highest density of volcanoes. Northern cone is the most outlying vent in this cluster. It links with its nearest neighbor at a distance of 5.1 km, other nearest-neighbor linkage distances are on the order of 3 km or less. These short linkage distances reflect the fact that all of the vents in this cluster are aligned. Volcanoes are less closely spaced in the Amargosa Valley cluster. Single Linkage distances in this cluster are on the order of 3 to 10 km.

I wonder if this is a bias in the sampling. Vent density appears to be lower in the Amargosa valley cluster because the low resolution of aeromagnetic methods makes it impossible to id smaller vents (lacking substantial lava flows).

centroid linkages within clusters: In Crater Flat, the two alignments link together at 5.0 km, and northern cone links with this combined group at 9.6 km

- learn more about the differences in ages of volcanoes between clusters.

  All of the three major clusters contain Quaternary aged vents. Also, there are periods of inactivity in each cluster on the order of 2 - 3 Ma, followed by episodes of volcanism within the cluster again. This makes it tough to assign a true meaning to the recurrence rate!

- use the cluster analysis to estimate the best value of h - a smoothing parameter used in kernel intensity estimation techniques.

  h should be chosen so that recurrence rate is smooth within clusters, where there appears to a random chance of volcanism within the cluster, then tapers off substantially or completely between clusters. To do this h must be about 10 - 15 km, in order to link all the cones related to an individual cluster. If Amargosa Valley and Crtaer Flat were considered a single cluster, then h would have to be larger accourdingly, on the order of 25 km. It doesn't make sense for h to be any larger, because clusters arent that big.

- determine how "different" in terms of geographic position a volcanic eruption at the repository would be compared with volcanoes that already form the Crater Flat cluster.

  The cluster analysis including a completely hypothetical event at the repository indicates that such an event would occur within the Crater Flat Cluster, rather than outside an existing cluster.

  However, the essential character of the Cluster needs to be considered. The data used here indicates that, unlike the Amargosa Valley, the Crater Flat cluster occurs along two alignments only. If this is true, h might be smaller in this area?

Springerville Alkalinity

Chuck Connor

Investigate the dependence of alkalinity index on spatio-temporal recurrence rate in the Springerville volcanic field

Springerville Alkalinity

Chuck Connor

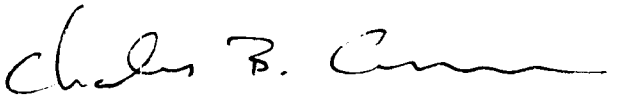

Investigate the dependence of alkalinity index on spatio-temporal recurrence rate in the Springerville volcanic field

1.0

In classifying rocks, petrologists see two major trends -

1) an alkalic trend - those that have a large concentration of incompatible elements in them for a given wt% SiO2, presumably if melted from the same source, a result of lower degrees of partial melting/and or high degrees of crystal fractionation. the incompat elements are those cations which have a charge/ionic radii that makes them "uncomfortable" in a crystal; these elements tend to be concentrated in the liquid, and excluded from the crystal - alkalies (Na2O & K2O).

2) a subalkaline trend - those that have a low concentration of incompatible elements in them for a given wt% SiO2, presumably if melted from the same source, a result of HIGHER degrees of partial melting/and or LOW degrees of crystal fractionation. the compat elements are those cations which have a charge/ionic radii that makes them enter into in a crystal easily; these elements tend to be depleted in the liquid, and concentrated in crystals.

Now back about 1972, Irvine & Baragar put a large file of analyses together, worldwide, and computed a line that compares SiO2 vs alkalies (Na2O + K2O). Those rocks falling above this line are alkalic, those below it are subalkalic (two groups of rocks in the IUGS classifications system, the tholeiitic basalts and calc-alkaline series).

To get this Alkali Index is to compare the alkalic elements (Na2O + K2O) found in the SVF rocks, to what would be expected in them at a similar SiO2 value on I &B's line. If these rocks fall above the line, they have + (positive) Alkali Index values (in IUGS terms, are"alkalic"), if they fall below the line, they have - (negative) AI values (are "subalkalic" in the IUGS scheme of things). -

This is what I think might be a pretty good tool as a petrologic indicator for our purposes. The reason we can't use normative ne & hy is that first, they are artificial, in that they rely on a normative calculation, which has a bunch of assumptions, some of which I think can really mess up what we're working on (like Fe++ vs Fe+++ ratio). to name one. Also, when we do a norm for the evolved alkali rocks (HAW, MUG, BEN), we get high hy values, for reason I won't get into - which could be misleading if we're using that as an indicator of how much partial melting or crystal farctionation we have.

Bottom line: use this one, and let's see what falls out.

A total of 256 samples were analyzed for alkalinity index. The unitvariate statics for these samples are shown in Table 1 on page 2.

TABLE 1. Univasriate Statistics for alkalinity index

	alkalinity
Minimum	-1.27
Maximum	2.95
Sum	224.48
Points	256
Mean	0.876
Median	0.861
RMS	1.12
Std Deviation	0.70
Variance	0.49
Std Error	0.043
Skewness	0.031
Kurtosis	-0.057

The distribution of alkalinity index is shown in the cumulative probability plot (Figure 1 on page 3) and histogram (Figure 2 on page 4). Alkalinity has a normal distribution.

Together the table and figuresd indicate that most sampled basalts in the Springerville volcanic field are alkaline (alkalinity index greater than 0). About 10% of the samples are subalkaline (alkalinity index is less than 0).

FIGURE 1. Cumulative Probability plot of alkalinity index

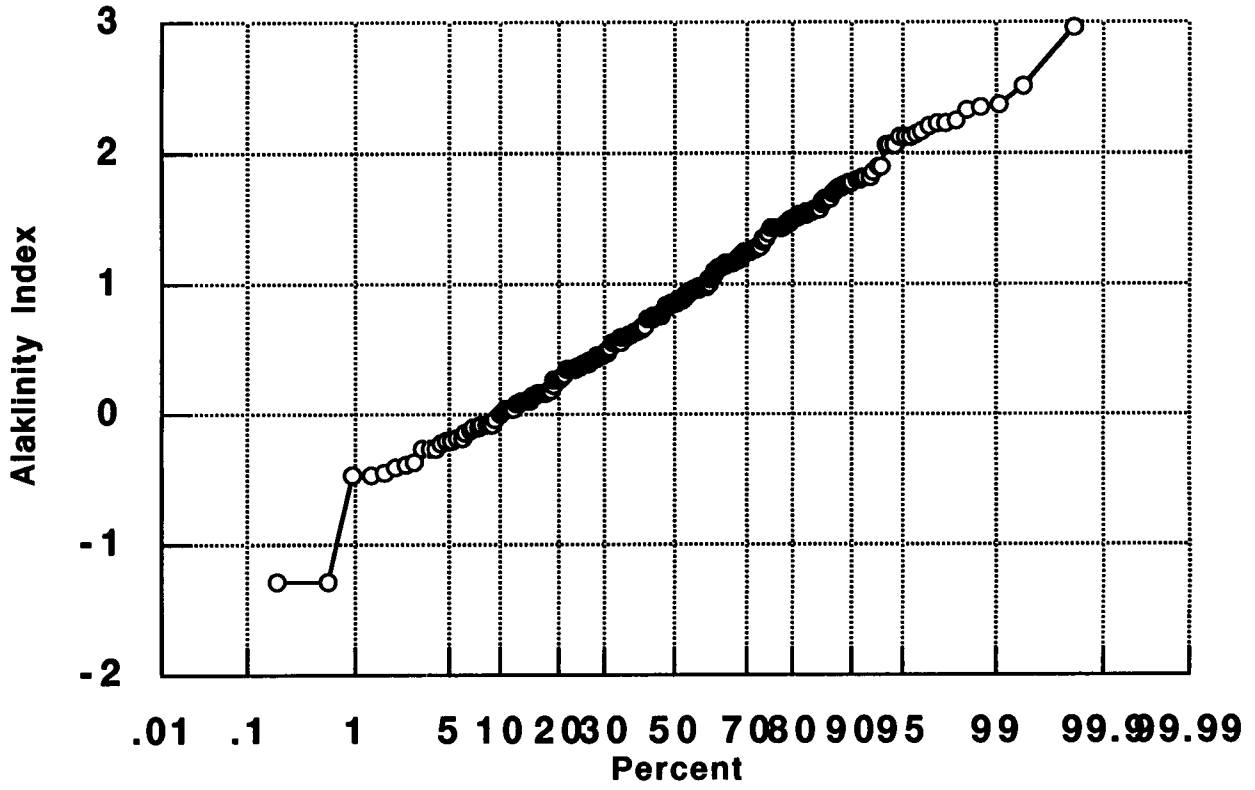

FIGURE 2. Histogram of Alkalinity Index

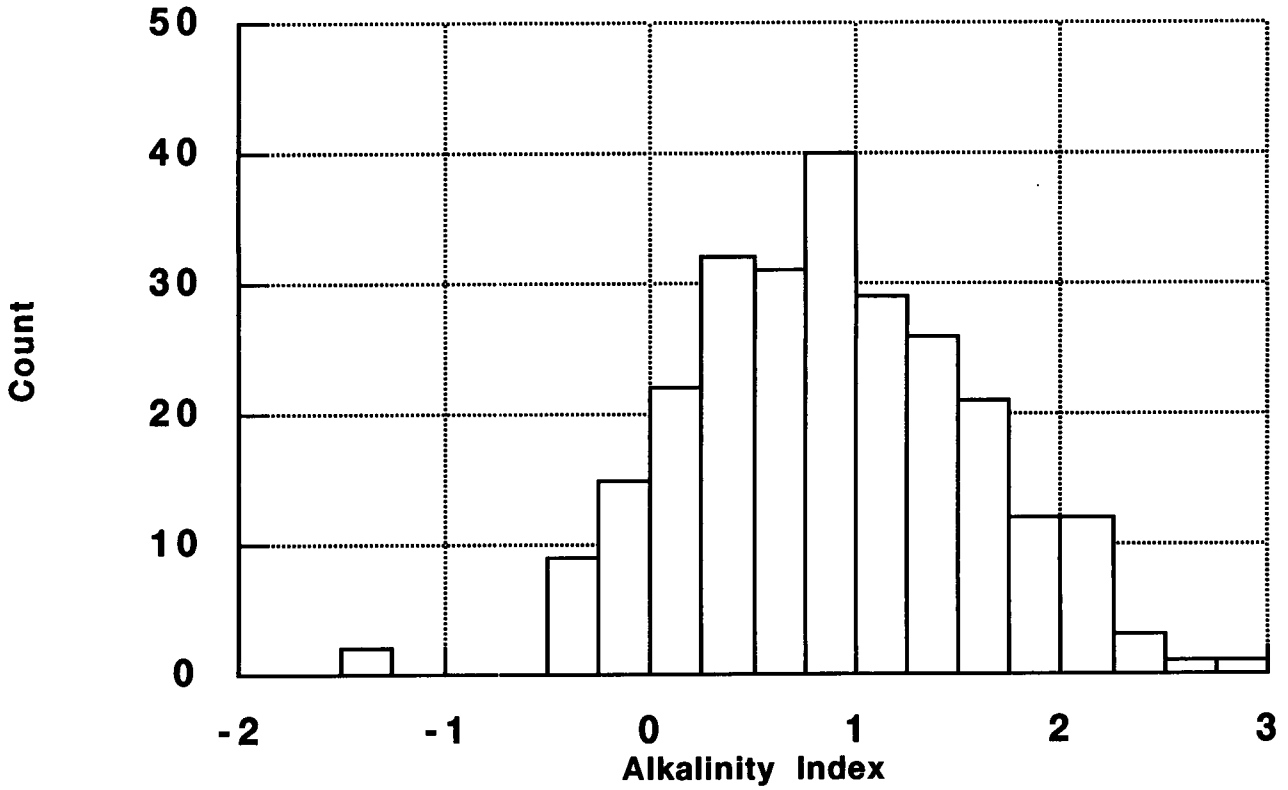

Plotting the alkalinity index vs age (using mean ages), it is clear that there is no relationship between mean age and alakalinity. There is a slight tendency for the oldest rocks in the field to be subalkaline, but this trend is very weakly developed.

FIGURE 3. Alkalinity index vs mean age of basalts

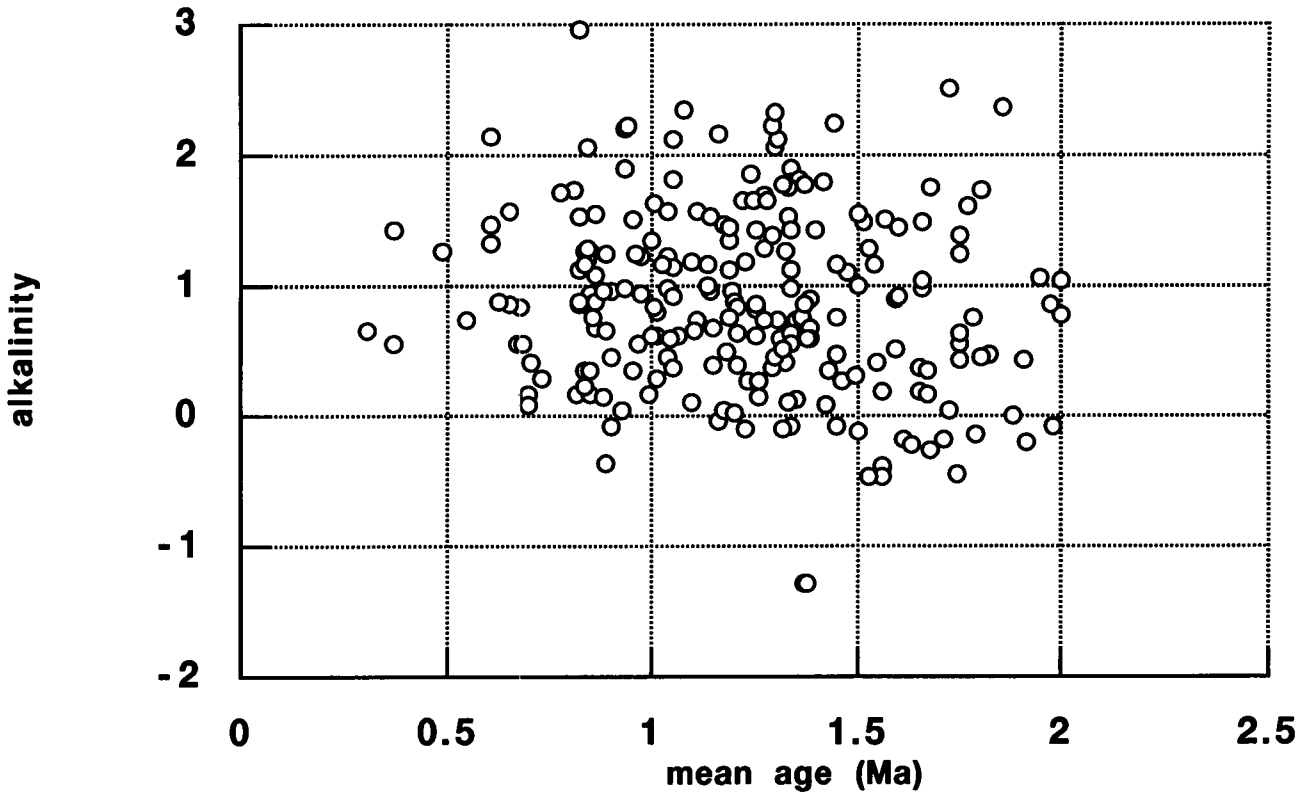


```
library "mactools*", "pictlib*"
open #1:name "alkalinity (merc)"
open #4: name "date_out", create newold
erase #4
open #3: screen .32,.9,.1,.9
call mactextfont(3)
call mactextsize(10)
```

```
clear


!you must change this line
set window 590000,668000,3760000,3838000
set text justify "center","half"


! delete next comment when ready to print
!call copy_printer(1)
do while more #1


let n = n + 1
!
input #1:dum$,x,y,z,z2,z3, alkalinity


set color "black"



if z < .75 and z => 0.5 then  ! this line is changed to filter by age
let samp = samp + 1
print #4:dum$;",";x;",";y;",";z;",";z2;",";z3;","; alkalinity
if alkalinity => 0 and alkalinity < 1 then
!set color "red"
box circle x-500,x+500, y-500, y+ 500
let alk1 = alk1+1
```

```
elseif alkalinity >= 1 and alkalinity < 1.75 then
!set color "green"
box lines x-500,x+500, y-500, y+ 500
let alk2 = alk2 + 1

elseif alkalinity >= 1.75 and alkalinity < 5 then
!set color "green"
box area x-500,x+500, y-500, y+ 500
let alk3 = alk3 + 1

elseif alkalinity < 0 then
!set color "cyan"
plot text, at x,y: "+"
let alk4 = alk4 + 1
else
!set color "black"
plot text, at x,y : "*"
let alk5 = alk5+1
end if

end if

loop
```

```
set text justify "left","bottom"

let text1$ = "age = 2.0 to 1.75   " & "number of vents = " & str$(samp)
let text2$ = "solid square - x => 1.75   " & "n = " & str$(alk3)
let text3$ = "square - 1 <= x < 1.75    " & "n = " & str$(alk2)
let text4$ = "circle - 0 <= x < 1       " & "n = " & str$(alk1)
let text5$ = "cross - -1 <= x < 0       " & "n = " & str$(alk4)
let text6$ = "asterisk - no analysis    " & "n = " & str$(alk5)

plot text, at 600000,3835000: text1$
plot text, at 600000,3830000: "alkalinity index"
plot text, at 600000,3827500: text2$
plot text, at 600000,3825000: text3$
plot text, at 600000,3820000: text4$
plot text, at 600000,3817500: text5$
plot text, at 600000,3815000: text6$
let n = 0

box lines 590000,668000,3760000,3810000
set color "cyan"
for x = 600000 to 660000 step 10000
plot x,3760000;x, 3810000
next x
for y = 3770000 to 3800000 step 10000
```

```
plot 590000,y;668000,y

next y

! delete comment when ready to print

!call copy_done



end
```

age = 2.0 to 1.75 number of vents = 31

alkalinity index
solid square - x => 1.75 n = 1
square - 1 <= x < 1.75 n = 6

circle - 0 <= x < 1 n = 10
cross - -1 <= x < 0 n = 5
asterisk - no analysis n = 9

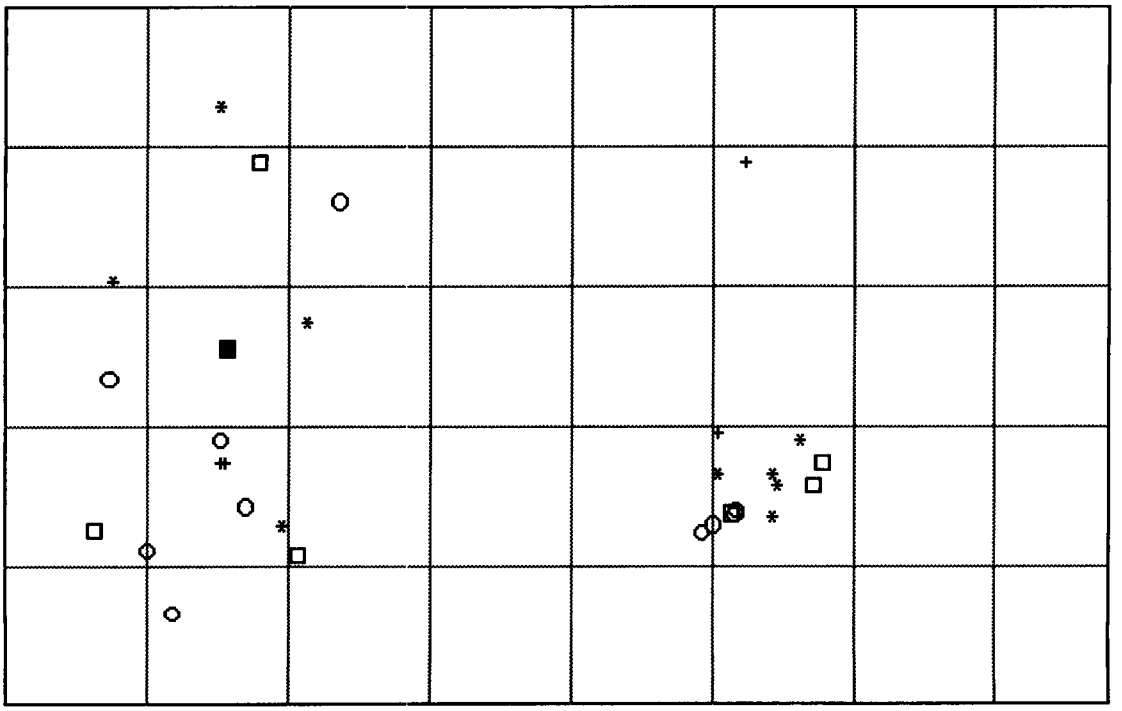

age = 1.75 to 1.5 number of vents = 56

alkalinity index
solid square - x => 1.75 n = 2
square - 1 <= x < 1.75 n = 11

circle - 0 <= x < 1 n = 12
cross - -1 <= x < 0 n = 12
asterisk - no analysis n = 19

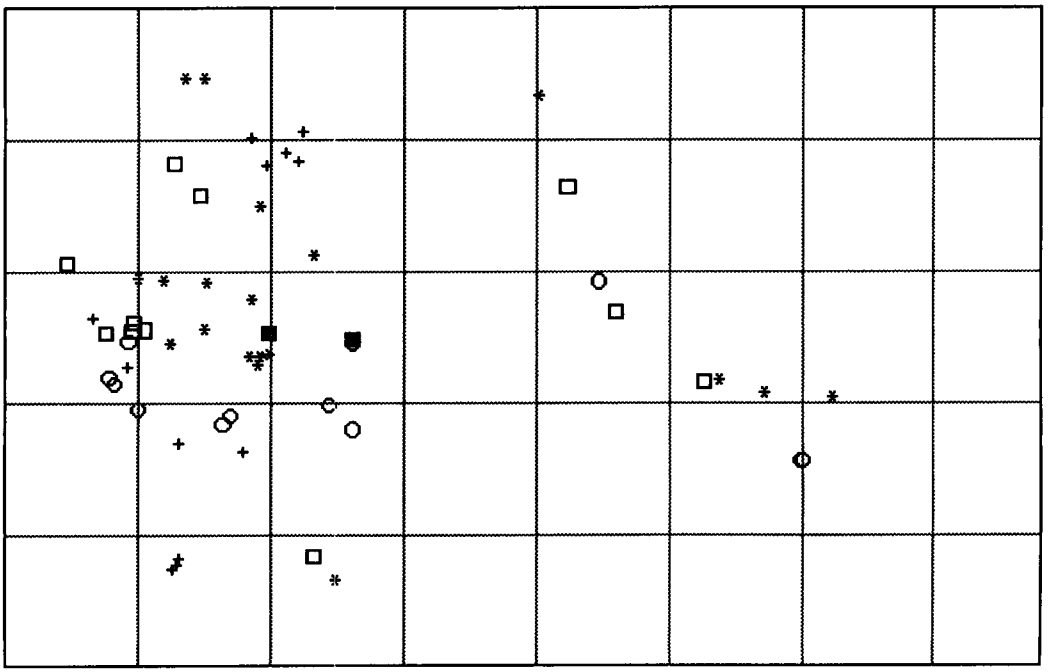

age = 1.5 to 1.25 number of vents = 98

alkalinity index
solid square - x => 1.75 n = 14
square - 1 <= x < 1.75 n = 16

circle - 0 <= x < 1 n = 32
cross - -1 <= x < 0 n = 5
asterisk - no analysis n = 31

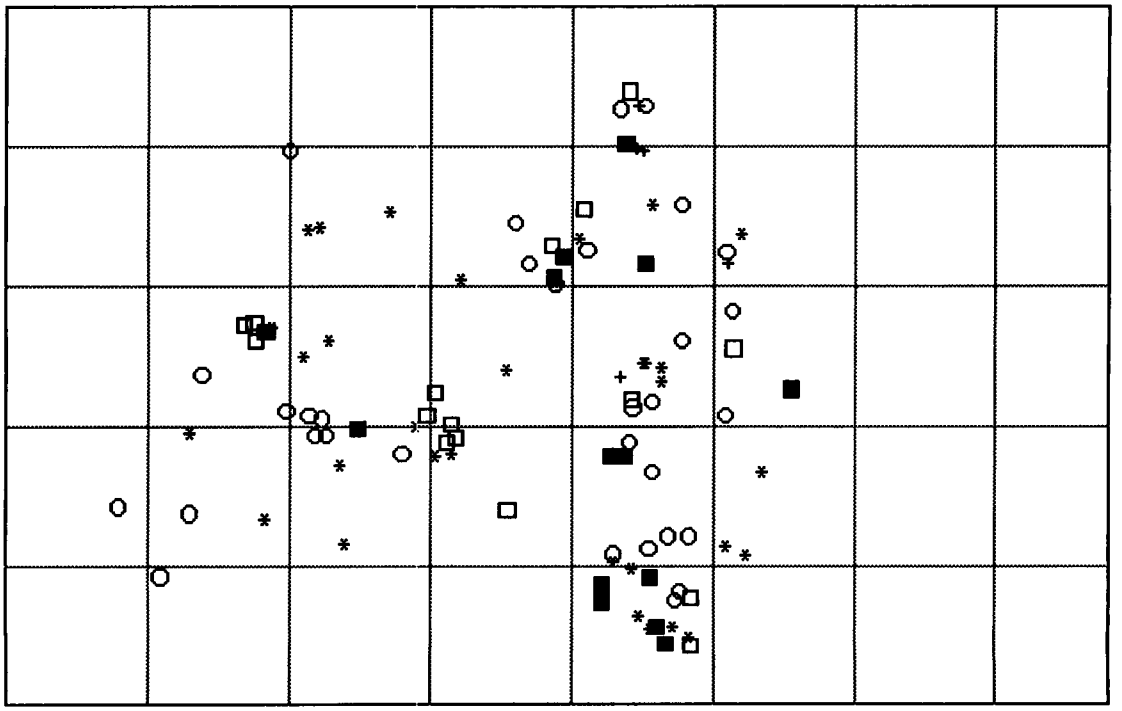

age = 1.25 to 1.0 number of vents = 93

alkalinity index
solid square - x => 1.75 n = 6
square - 1 <= x < 1.75 n = 20

circle - 0 <= x < 1 n = 34
cross - -1 <= x < 0 n = 2
asterisk - no analysis n = 31

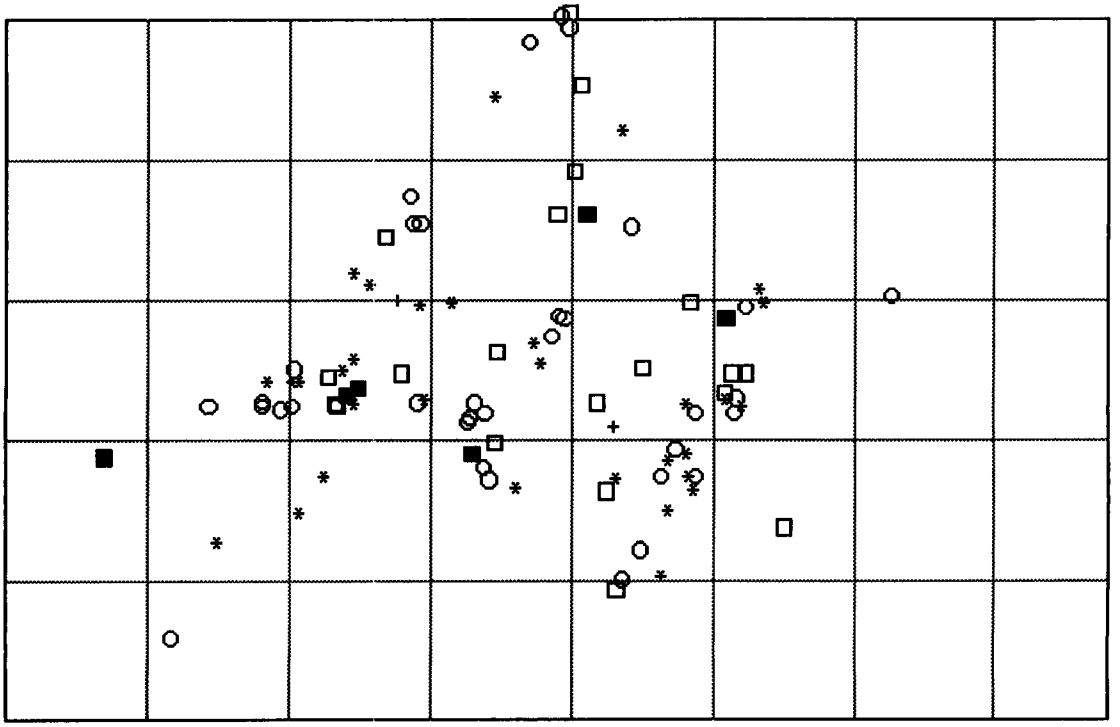

age = 1.0 to 0.75 number of vents = 65

alkalinity index
solid square - x => 1.75 n = 5
square - 1 <= x < 1.75 n = 18

circle - 0 <= x < 1 n = 25
cross - -1 <= x < 0 n = 2
asterisk - no analysis n = 15

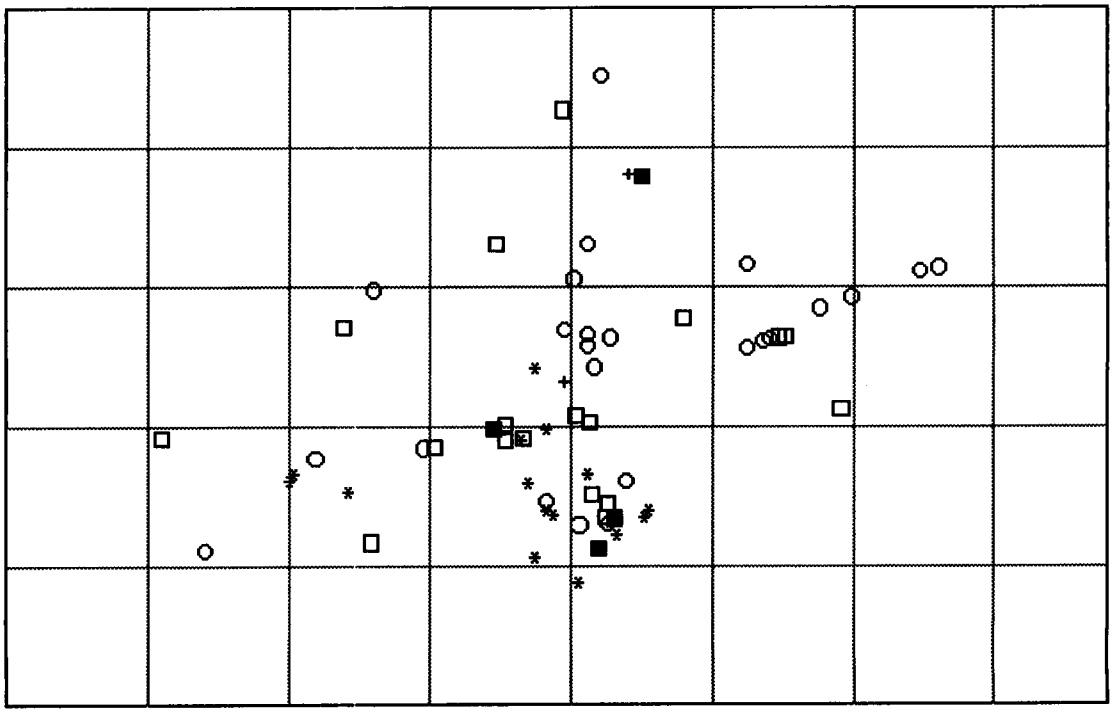

age = 0.75 to 0.5 number of vents = 19

alkalinity index
solid square - x => 1.75 n = 1
square - 1 <= x < 1.75 n = 3

circle - 0 <= x < 1 n = 10
cross - -1 <= x < 0 n = 0
asterisk - no analysis n = 5

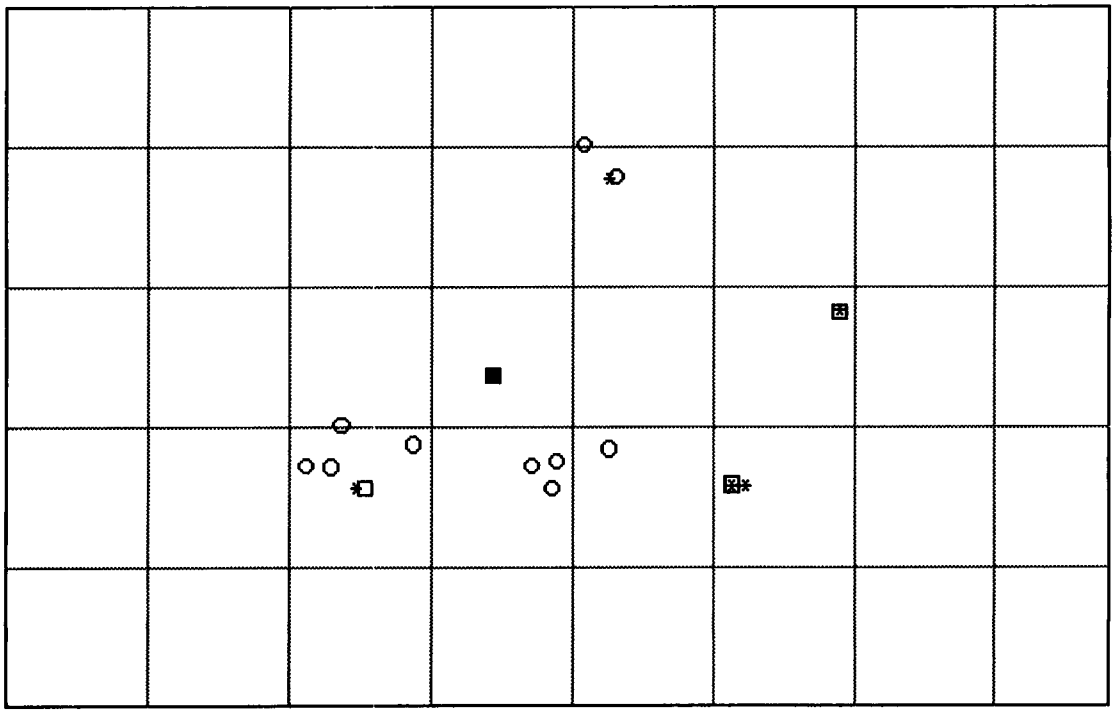

age = 0.5 to 0.25 number of vents = 4

alkalinity index
solid square - x => 1.75 n = 0
square - 1 <= x < 1.75 n = 2

circle - 0 <= x < 1 n = 2
cross - -1 <= x < 0 n = 0
asterisk - no analysis n = 0

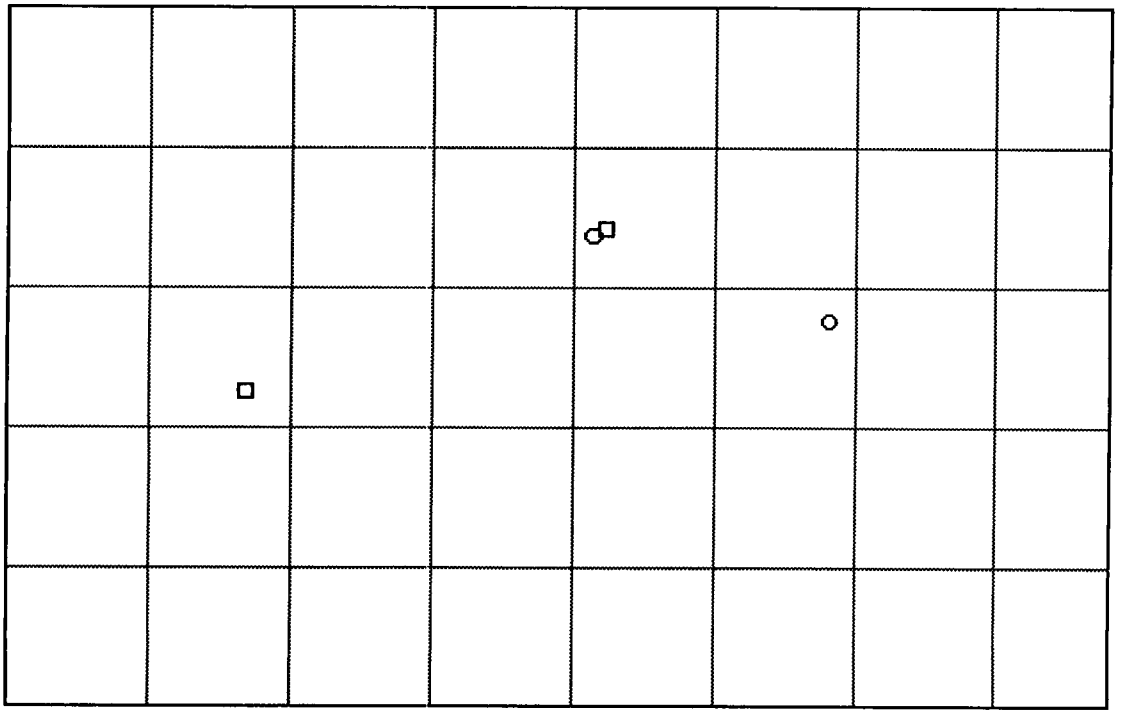

TABLE 2. Change in number ov vents, volume, and alkalinity index with time

Time (Ma)	# vents	volume (km3)	cum. vol (km3)	Alkalinity Index (percent of analyzed samples			
				> 1.75	1 to 1.75	0 to 1	-1 to 0
2.0-1.75	31	69	70	4.5	27.3	45.5	22.7
1.75-1.5	56	46	116	5.4	29.7	32.4	32.4

TABLE 2. Change in number ov vents, volume, and alkalinity index with time

Time (Ma)	# vents	volume (km3)	cum. vol (km3)	Alkalinity Index (percent of analyzed samples			
				> 1.75	1 to 1.75	0 to 1	-1 t
1.5-1.25	98	55	171	20.9	23.9	47.8	7.4
1.25-1.0	93	73	244	9.7	32.3	54.8	3.2
1.0-0.75	65	36	280	10	36	50	4
0.75-0.5	19	17	297	7.1	21.4	71.4	0
0.5-0.25	4	0.7	298	0	50	50	0

2.0 Intensity and Clustering in the Springerviller field by age

```
! PROGRAM: Intensity - SVF
! Language: TrueBasic
! Author: Chuck Connor
!       Center for nuclear waste Regulatory Analysis
!       Southwest Research Institute
!       San Antonio Texas, 78238-5166
!Date: April, 1995
!
!Summary: This program calculates recurrence rates (point intensity)
!from vent location data. This version runs specifically for the
!Springerville region data set, for which age data are available
!
!       Ripley, B.D., 1981, Spatial Statistics
!          Wiley series in probability and statistics
!          John Wiley and Sons, New York, 252 pp.
!          see pages 134-138.
!
! In this program, the coordinates of points are input from
! a file. The user then defines the area s/he wishes to
! analyze, inputting vertex corrdinates using the mouse. Only
```

```
! data points falling within the area selected are used in
! the analysis.  Several factors concerning this area are important:
!
! 1) the verticies must be input in a clockwise manner.  If
!    the verticies are input in a counter-clockwise manner,
!    the program will use points only found OUTSIDE the
!    polygon in the analysis.
!
! 2) the polygon will be rectilinear and concave inwards.
!    This is because of the algorithm uses the orientation
!    of line segments to discriminate between points within
!    and outside the area selected.
!
! 3) the area selected will close automatically.  For
!    instance, if you select 5 verticies, 5 line segments
!    will be drawn, connecting the verticies.  The last line
!    segment will be drawn connecting the first and last
!    verticies.
!
! Once the area of analysis is selected, the program
! takes a minute to find random points within the area.
! The reucurrence rate is then calculated in several ways.
!    1) a naive recurrence rate calculation is done
!           = #pts/total area the user selects
!    2) a recurrence rate based on minimum vent to vent distances
!           = #pts/ sum(minimum distance to nearest other vent^2*pi)
!    3) a recurrence rate based on minimum distances between randomly
!           selected points in the area chosen by the user and
!           vents
!           = #pts/sum(minimum point-vent distance^2*pi)
! measures 2 and 3 (above) can be used to test a distribution with the
! null hypothesis being that it is a homogeneous Poisson distribution.
! Divide recurrence rate point-vent by recurrence rate vent-vent and
! test with a F(2*total pts,2*total points) distribution. If the
! null hypothesis is rejected then the vents cluster.
! this is call the Hopkins F-test. (see Ripley page 136).

DIM pts(375,2), moncar(375,2), vert(30,2)

! mat pts is the matrix which holds point locations located
! within the selected area.
!
! mat moncar is the matrix that holds random points generated
! by the monte carlo subroutine. this matrix is scratched after
! each simulation
!
! mat vert holds the coordinated of the vertices selected by the user while
! the program is running
!
```

```
CLEAR
PRINT " type the name of the file containing the observed"
PRINT " data points"
INPUT file$

PRINT "input age cut off"
INPUT ager

OPEN #1: name file$
OPEN #10: screen .25,1,.25,1
OPEN #11: screen 0,1,0,.25
OPEN #12: screen 0,.24,.75,.8
OPEN #13: screen 0,.24,.6,.74
Open #5: name "intensity ouput", create newold
erase #5

LET ymax = -10000000
LET ymin = 100000000
LET xmin = 100000000
LET xmax = -100000000
DO while more #1
  INPUT #1: dum$,x,y, age, ag2, ag3, alk
  IF x> xmax then LET xmax = x
  IF x < xmin then LET xmin = x
  IF y > ymax then LET ymax = y
  IF y< ymin then LET ymin = y
LOOP
RESET #1: begin
WINDOW #11

!plot all the points
PRINT xmin,xmax,ymin,ymax
PRINT "type in the dimensions of the area you want to see"
PRINT "xmin, xmax, ymin, ymax"
INPUT s1,s2,s3,s4

!dimension the window to be square
WINDOW #10

SET TEXT justify "center", "half"

LET scrfix=s2-s1
SET WINDOW s1-(scrfix*28/128),s2+(scrfix*28/128),s3,s4
DO while more #1
  INPUT #1: dum$,x,y, age, ag2, ag3, alk

  IF x<=s2 and x=>s1 and y=>s3 and y<=s4 and age <=ager then
    PLOT TEXT, AT x,y: "*"
  END IF
LOOP
```

```
SET COLOR 15
!plot the frame
PLOT s1,s3;s1,s4;s2,s4;s2,s3;s1,s3

RESET #1: begin


WINDOW #11
PRINT
PRINT
PRINT " how many vertices will you select"
INPUT numvts

PRINT "click in the vertex coordinates using the mouse"
MAT vert = zer(numvts, 2)

! the routine below locates the verticies when the
! mouse is clicked, and plots the line segments
! between verticies.

WINDOW #10
LET count = 0
DO
  LET count = count + 1
  DO

    GET MOUSE vert(count,1), vert(count,2), state
  LOOP until state = 2
  PLOT vert(count,1),vert(count,2);
LOOP until count = numvts
PLOT vert(1,1),vert(1,2);
PLOT

!this routine now locates those observations within the
! area selected (enclosed in the polygon just defined
! by the verticies

!find the extreme x and y coordinates to speed the search
LET ymin2  = 10000000
LET xmin2 = 10000000
LET xmax2 = -10000000
LET ymax2 = -10000000

FOR look = 1 to numvts

   IF xmax2 < vert(look,1) then LET xmax2 = vert(look,1)
   IF xmin2 > vert(look,1) then LET xmin2 = vert(look,1)
   IF ymax2 < vert(look,2) then LET ymax2 = vert(look,2)
   IF ymin2 > vert(look,2) then LET ymin2 = vert(look,2)
```

```
NEXT look

! count the number of points in file$
DO while more #1

  INPUT #1: dum$,xpt,ypt, age, ag2, ag3, alk

  !the logical statement eliminates points located outside
  ! the smallest rectangle that completely encloses the
  ! polygon (this speeds the search)
  IF ypt => ymin2 and ypt <= ymax2 and xpt => xmin2 and xpt <= xmax2 then


    !this curvt loop finds points inside the polygon by
    !rejecting points found outside the polygon
    FOR curvt = 1 to numvts

      IF curvt = numvts then

        LET x1 = vert(curvt,1)
        LET x2 = vert(1,1)
        LET y1 = vert(curvt,2)
        LET y2 = vert(1,2)

      ELSE

        LET x1 = vert(curvt,1)
        LET x2 = vert(curvt + 1,1)
        LET y1 = vert(curvt,2)
        LET y2 = vert(curvt + 1,2)

      END IF
      WHEN error in          ! error when x2-x1 = 0
        LET m = (y2-y1)/(x2-x1)      !slope of line bet. vertices
        LET b = y1 - m*x1  !intercept of line

        LET ytest = m*xpt + b   ! point on line

        ! don't want points outside line segments: use
        ! the following tests

        IF x1 > x2 and y1 > y2 and ytest > ypt then EXIT FOR
        IF x1 > x2 and y1 < y2 and ytest > ypt then EXIT FOR
        IF x1 < x2 and y1 > y2 and ytest < ypt then EXIT FOR
        IF x1 < x2 and y1 < y2 and ytest < ypt then EXIT FOR

      USE
        !use this test instead if vertical line
        IF y2<y1 and xpt>x1 then EXIT FOR
        IF y2>y1 and xpt<x1 then EXIT FOR
```

```
      END WHEN

      !if the random point has passed the above tests for
      ! every line segment, the point lines within
      ! the selected area

      IF curvt = numvts then

        LET totpts = totpts + 1
        LET pts(totpts,1) = xpt
        LET pts(totpts,2) = ypt

      END IF

    NEXT curvt

  END IF
LOOP
PRINT totpts
get key aaa
!replot the area of interest
CLEAR
LET scrx=xmax2-xmin2
LET scry = ymax2-ymin2

IF scrx>scry then
  SET WINDOW xmin2,xmax2,ymin2,ymin2+scrx
ELSE
  SET WINDOW xmin2,xmin2+scry,ymin2,ymax2
END IF

FOR co = 1 to totpts
   PLOT TEXT, AT  pts(co,1), pts(co,2): "*"

NEXT co

LET count = 0
DO
  LET count = count + 1
  PLOT vert(count,1),vert(count,2);
LOOP until count = numvts
PLOT vert(1,1),vert(1,2);
PLOT

!redimension the point matrices
MAT moncar = zer(totpts,2)

!lineseg is the total number of line segments
LET lineseg = totpts*(totpts-1)/2
```

```
LET count = 0

CLOSE #1

LET count = 0
WINDOW #10
!clear the window
CLEAR
!replot the vertex coordinates
LET count = 0
DO
  LET count = count + 1
  PLOT vert(count,1),vert(count,2);
LOOP until count = numvts
PLOT vert(1,1),vert(1,2);
PLOT

FOR xercize = 1 to 25
  !find totpts randome points inside the area
  CALL findrnd(vert, moncar, numvts, totpts)

  !plot the points inside the area

  IF xercize = 1 then
    FOR alp = 1 to totpts
      PLOT moncar(alp,1), moncar(alp,2)
    NEXT alp
    OPEN #99: screen 0,1,0,1
    PRINT
    !PRINT "calculating the vent-vent distances"
  END IF
  CALL lambda_v(pts,totpts,sumareav,lambdav)

  !PRINT "calculating point-vent distances"
  CALL lambda_p(pts,moncar,totpts,sumareap,lambdap)

  ! this routine calculates the area inside the polygon
  FOR i = 1 to numvts-1
    LET ss = ss + (vert(i,1)-vert(i+1,1))*(vert(i,2)+vert(i+1,2))
  NEXT i
  LET ss = ss + (vert(numvts,1)-vert(1,1))*(vert(numvts,2)+vert(1,2))
  LET totarea = -ss/2


  !if all distances are in meters to begin with, (UTM) convert to
  !kilometers

  LET conv = 1e6
  LET totarea = totarea/conv
```

```
    LET sumareav = sumareav/conv
    LET sumareap = sumareap/conv
    LET lambdav = lambdav*conv
    LET lambdap = lambdap*conv
    LET hopf = sumareap/sumareav

    IF xercize = 1 then
      PRINT #5
      PRINT #5: "Input in meters (UTM) - - output in kilometers"
      PRINT #5: "# vents: ";totpts
      PRINT #5: "Total area in polygon: ";totarea
      PRINT #5: "naive lambda = ";totpts/totarea
      PRINT #5: "v(i) (vent-vent) = ";sumareav
      PRINT #5: "u(i) (point-vent) = ";sumareap
      PRINT #5: "lambda v-v = ";lambdav
      PRINT #5: "lambda p-v = ";lambdap
    END IF

    PRINT #5: "Hopkins F-test: ";hopf
    LET sumhopf = sumhopf + hopf
    LET sum2hopf = sum2hopf + hopf^2
NEXT xercize

let n = xercize-1
PRINT #5: "N = ";n
PRINT #5: "sum hopf =";sumhopf
PRINT #5: "sum squaured hopf = ";sum2hopf
PRINT #5: "mean = ";sumhopf/n

let sx = sqr(1/(n-1) * (sum2hopf - (sumhopf)^2/n))
print #5: "standard deviation = "; sx
let error_mean = sx/sqr(n)
print #5: "standard error on mean = ";error_mean

END


EXTERNAL

SUB FINDRND(vert(,), moncar(,), numvts, rndtot)
    RANDOMIZE
    !this subroutine finds random points within a known
    !area defined by a definite number of vertices
    !vert() is the input matrix of vertex coordinates
    !moncar() is the output matrix of random points found
    ! by the subroutine, which lie within the area defined by
    ! vert()
    ! numvts is the number of vertices (input)
    !rndtot is the number of random points to be found
```

```
! with in the area (input)

LET curvt = 0
LET rndct = 0
MAT moncar = zer(rndtot, 2)   ! make sure this mtx is empty
LET x1 = 0
LET x2 = 0
LET y1 = 0
LET y2 = 0

!find the extreme x and y coordinates to speed the search
LET ymin2  = 1000000
LET xmin2 = 1000000
LET xmax2 = -1000000
LET ymax2 = -1000000

FOR look = 1 to numvts

   IF xmax2 < vert(look,1) then LET xmax2 = vert(look,1)
   IF xmin2 > vert(look,1) then LET xmin2 = vert(look,1)
   IF ymax2 < vert(look,2) then LET ymax2 = vert(look,2)
   IF ymin2 > vert(look,2) then LET ymin2 = vert(look,2)

NEXT look

!now select random points within this range
DO
  LET xrndpt = (xmax2-xmin2)*rnd + xmin2
  LET yrndpt = (ymax2-ymin2)*rnd + ymin2
  !now that we have found likely random points,
  ! check to see if they are in the specified area

  FOR curvt = 1 to numvts

    IF curvt = numvts then

      LET x1 = vert(curvt,1)
      LET x2 = vert(1,1)
      LET y1 = vert(curvt,2)
      LET y2 = vert(1,2)

    ELSE

      LET x1 = vert(curvt,1)
      LET x2 = vert(curvt + 1,1)
      LET y1 = vert(curvt,2)
      LET y2 = vert(curvt + 1,2)

    END IF
    WHEN ERROR IN        !X2-X1 =0
```

```
        LET m = (y2-y1)/(x2-x1)     !slope of line bet. vertices
        LET b = y1 - m*x1       !intercept of line

        LET ytest = m*xrndpt + b    ! point on line

        ! don't want points outside line segments: use
        ! the following tests

        IF x1 > x2 and y1 > y2 and ytest > yrndpt then EXIT FOR
        IF x1 > x2 and y1 < y2 and ytest > yrndpt then EXIT FOR
        IF x1 < x2 and y1 > y2 and ytest < yrndpt then EXIT FOR
        IF x1 < x2 and y1 < y2 and ytest < yrndpt then EXIT FOR

      USE
        IF y1<y2 and yrndpt < y2 then EXIT FOR
        IF y1>y2 and yrndpt > y2 then EXIT FOR
      END WHEN
      !if the random point has passed the above tests for
      ! every line segment, the point lines within
      ! the selected area

      IF curvt = numvts then

        LET rndct = rndct + 1
        LET moncar(rndct,1) = xrndpt
        LET moncar(rndct,2) = yrndpt

      END IF

    NEXT curvt

  LOOP UNTIL rndct = rndtot

END SUB


SUB lambda_v(pts(,),totpts,sumarea,lambda)

  !This subroutine calculates the intensity based on distances from points
  ! to nearest neighboring points, equivalent to v(i) in Ripley, 1981
  ! "spatial statistics", page 135.

  !pts() is the matrix containing the x,y coordinates of the points
  ! totpts is the total number of points in pts()
  ! sumarea is the sum of areas swept out between a point and
  ! its nearest neighbor = sum(minimum distance^2*pi)
  ! lambda is the intensity based on this calculation


  LET sumarea = 0
```

```
  FOR i = 1 to totpts

    LET mindis = 1000000000

    FOR j = 1 to totpts

      LET i1 = pts(i,1)
      LET i2 = pts(i,2)
      LET j1 = pts(j,1)
      LET j2 = pts(j,2)

      IF i1 <> j1 and i2 <> j2 then   !it isn't the same vent
        LET dist = ((i1-j1)^2 + (i2-j2)^2)^0.5
        IF dist < mindis then LET mindis = dist
      END IF
    NEXT j

    ! sum the minimum areas
    LET sumarea = sumarea + mindis^2*pi
  NEXT i

  LET lambda = totpts/sumarea
END SUB

SUB lambda_p(pts(,),rndpts(,),totpts,sumarea,lambda)

  !This subroutine calculates the intensity based on distances from random points
  ! to nearest neighboring vents, equivalent to u(i) in Ripley, 1981
  ! "spatial statistics", page 135.

  !pts(,) is the matrix containing the x,y coordinates of the vents
  !rndpts(,) is the mtx containing x,y coordinates of random points
  ! pts and rndpts should both be dimensioned (totpts,2)

  ! totpts is the total number of points in pts() and rndpts()
  ! sumarea is the sum of areas swept out between a random point and
  ! the nearest vent = sum(minimum distance^2*pi)
  ! lambda is the intensity based on this calculation


  LET sumarea = 0

  FOR numpt = 1 to totpts

    LET i1 = rndpts(numpt,1)
    LET i2 = rndpts(numpt,2)
    LET mindis = 1000000000

    FOR j = 1 to totpts
```

```
      LET j1 = pts(j,1)
      LET j2 = pts(j,2)

      IF i1 <> j1 and i2 <> j2 then  ! vent and sample point are not in same spot
        LET dist = ((i1-j1)^2 + (i2-j2)^2)^0.5
        IF dist < mindis then LET mindis = dist
      ELSE              !vent and sample point are in same spot
        LET mindis = 0
        EXIT FOR
      END IF

    NEXT j

    ! sum the minimum areas
    LET sumarea = sumarea + mindis^2*pi

  NEXT numpt

  LET lambda = totpts/sumarea
END SUB
```

The program Intensity - SVF was rumn on the springerville data at 0.25 Ma intevals.

2.1 Interval 2.0-1.75

Input in meters (UTM) - - output in kilometers
vents: 31
Total area in polygon: 1586.47
naive lambda = 1.95402e-2
v(i) (vent-vent) = 2364.85
u(i) (point-vent) = 4499.72
lambda v-v = 1.31086e-2
lambda p-v = 6.88932e-3
Hopkins F-test: 1.90275
Hopkins F-test: 2.68915
Hopkins F-test: 3.44307
Hopkins F-test: 1.72746
Hopkins F-test: 1.08015
Hopkins F-test: 1.82969
Hopkins F-test: 2.59101
Hopkins F-test: 2.40298
Hopkins F-test: 2.45891
Hopkins F-test: 1.69169
Hopkins F-test: 2.39243
Hopkins F-test: 2.51245

Hopkins F-test: 2.28793
Hopkins F-test: 2.60866
Hopkins F-test: 2.26697
Hopkins F-test: 2.42978
Hopkins F-test: 2.40002
Hopkins F-test: 1.82114
Hopkins F-test: 2.5357
Hopkins F-test: 1.36698
Hopkins F-test: 2.67412
Hopkins F-test: 2.55924
Hopkins F-test: 2.53938
Hopkins F-test: 2.1894
Hopkins F-test: 2.89276
N = 25
sum hopf = 57.2938
sum squaured hopf = 137.406
mean = 2.29175
standard deviation = .504244
standard error on mean = .100849

2.2 1.75-1.5 Ma

Input in meters (UTM) - - output in kilometers
vents: 56
Total area in polygon: 1730.01
naive lambda = 3.23698e-2
v(i) (vent-vent) = 1336.53
u(i) (point-vent) = 3786.26
lambda v-v = 4.18997e-2
lambda p-v = 1.47903e-2
Hopkins F-test: 2.83291
Hopkins F-test: 4.04944
Hopkins F-test: 3.66936
Hopkins F-test: 3.90063
Hopkins F-test: 3.89766
Hopkins F-test: 2.57001
Hopkins F-test: 4.15965
Hopkins F-test: 4.93399
Hopkins F-test: 4.10493
Hopkins F-test: 5.68616
Hopkins F-test: 3.26352
Hopkins F-test: 3.87188
Hopkins F-test: 3.63424
Hopkins F-test: 5.04167
Hopkins F-test: 4.33326
Hopkins F-test: 2.69336
Hopkins F-test: 4.41294

Hopkins F-test: 4.13656
Hopkins F-test: 5.07174
Hopkins F-test: 4.20046
Hopkins F-test: 4.63366
Hopkins F-test: 3.53255
Hopkins F-test: 2.6989
Hopkins F-test: 3.0109
Hopkins F-test: 2.71368
N = 25
sum hopf = 97.0541
sum squaured hopf = 393.643
mean = 3.88216
standard deviation = .838247
standard error on mean = .167649

2.3 1.75-1.5 Ma

Input in meters (UTM) - - output in kilometers
vents: 56
Total area in polygon: 1730.01
naive lambda = 3.23698e-2
v(i) (vent-vent) = 1336.53
u(i) (point-vent) = 3786.26
lambda v-v = 4.18997e-2
lambda p-v = 1.47903e-2
Hopkins F-test: 2.83291
Hopkins F-test: 4.04944
Hopkins F-test: 3.66936
Hopkins F-test: 3.90063
Hopkins F-test: 3.89766
Hopkins F-test: 2.57001
Hopkins F-test: 4.15965
Hopkins F-test: 4.93399
Hopkins F-test: 4.10493
Hopkins F-test: 5.68616
Hopkins F-test: 3.26352
Hopkins F-test: 3.87188
Hopkins F-test: 3.63424
Hopkins F-test: 5.04167
Hopkins F-test: 4.33326
Hopkins F-test: 2.69336
Hopkins F-test: 4.41294
Hopkins F-test: 4.13656
Hopkins F-test: 5.07174
Hopkins F-test: 4.20046
Hopkins F-test: 4.63366
Hopkins F-test: 3.53255

Hopkins F-test: 2.6989
Hopkins F-test: 3.0109
Hopkins F-test: 2.71368
N = 25
sum hopf = 97.0541
sum squaured hopf = 393.643
mean = 3.88216
standard deviation = .838247
standard error on mean = .167649

2.4 1.5-1.25 Ma

Input in meters (UTM) - - output in kilometers
vents: 98
Total area in polygon: 1494.95
naive lambda = 6.55542e-2
v(i) (vent-vent) = 1861.24
u(i) (point-vent) = 2530.01
lambda v-v = .052653
lambda p-v = .038735
Hopkins F-test: 1.35931
Hopkins F-test: 1.56018
Hopkins F-test: 1.4635
Hopkins F-test: 1.55221
Hopkins F-test: 1.52357
Hopkins F-test: 1.36032
Hopkins F-test: 1.48837
Hopkins F-test: 1.16427
Hopkins F-test: 1.23974
Hopkins F-test: 1.09851
Hopkins F-test: 1.33935
Hopkins F-test: 1.27115
Hopkins F-test: 1.15002
Hopkins F-test: 1.49046
Hopkins F-test: 1.56073
Hopkins F-test: 1.40092
Hopkins F-test: 1.53178
Hopkins F-test: 1.35277
Hopkins F-test: 1.536
Hopkins F-test: 1.43852
Hopkins F-test: 1.42858
Hopkins F-test: 1.30467
Hopkins F-test: 1.25454
Hopkins F-test: 1.24653
Hopkins F-test: 1.32011
N = 25
sum hopf = 34.4361
sum squaured hopf = 47.8898

mean = 1.37744
standard deviation = .137834
standard error on mean = 2.75669e-2

2.5 1.25-1.0 Ma

Input in meters (UTM) - - output in kilometers
vents: 93
Total area in polygon: 1605.65
naive lambda = 5.79205e-2
v(i) (vent-vent) = 1825.72
u(i) (point-vent) = 3799.21
lambda v-v = 5.09387e-2
lambda p-v = 2.44787e-2
Hopkins F-test: 2.08094
Hopkins F-test: 2.34279
Hopkins F-test: 1.98841
Hopkins F-test: 1.80885
Hopkins F-test: 1.95408
Hopkins F-test: 1.4865
Hopkins F-test: 1.67509
Hopkins F-test: 1.84556
Hopkins F-test: 2.29165
Hopkins F-test: 2.29892
Hopkins F-test: 2.38318
Hopkins F-test: 1.54864
Hopkins F-test: 1.98643
Hopkins F-test: 1.44315
Hopkins F-test: 1.87058
Hopkins F-test: 1.88772
Hopkins F-test: 2.3504
Hopkins F-test: 1.96524
Hopkins F-test: 2.2387
Hopkins F-test: 2.27628
Hopkins F-test: 1.99714
Hopkins F-test: 1.53837
Hopkins F-test: 1.88055
Hopkins F-test: 2.1912
Hopkins F-test: 1.83908
N = 25
sum hopf = 49.1694
sum squaured hopf = 98.6454
mean = 1.96678
standard deviation = .284317
standard error on mean = 5.68634e-2

2.6 1.0-0.75

Input in meters (UTM) - - output in kilometers
vents: 65
Total area in polygon: 1307.68
naive lambda = 4.97065e-2
v(i) (vent-vent) = 1455.93
u(i) (point-vent) = 2133.96
lambda v-v = 4.46451e-2
lambda p-v = 3.04598e-2
Hopkins F-test: 1.46571
Hopkins F-test: 2.03167
Hopkins F-test: 1.82312
Hopkins F-test: 1.70662
Hopkins F-test: 1.45968
Hopkins F-test: 1.85314
Hopkins F-test: 1.35274
Hopkins F-test: 1.23521
Hopkins F-test: 1.43127
Hopkins F-test: 1.67159
Hopkins F-test: 1.79556
Hopkins F-test: 1.50262
Hopkins F-test: 1.71292
Hopkins F-test: 1.82166
Hopkins F-test: 1.58046
Hopkins F-test: 1.72165
Hopkins F-test: 1.65294
Hopkins F-test: 1.71059
Hopkins F-test: 1.81084
Hopkins F-test: 1.50828
Hopkins F-test: 1.49287
Hopkins F-test: 1.50165
Hopkins F-test: 1.67073
Hopkins F-test: 1.65451
Hopkins F-test: 1.71199
N = 25
sum hopf = 40.88
sum squaured hopf = 67.6274
mean = 1.6352
standard deviation = .180334
standard error on mean = 3.60668e-2

2.7 0.75-0.5 Ma

Input in meters (UTM) - - output in kilometers
vents: 19
Total area in polygon: 627.219

naive lambda = 3.02925e-2
v(i) (vent-vent) = 1222.82
u(i) (point-vent) = 1526.62
lambda v-v = 1.55379e-2
lambda p-v = 1.24458e-2
Hopkins F-test: 1.24845
Hopkins F-test: 1.47115
Hopkins F-test: 1.22658
Hopkins F-test: 1.02379
Hopkins F-test: 1.54294
Hopkins F-test: .846072
Hopkins F-test: 1.66657
Hopkins F-test: .892653
Hopkins F-test: .918992
Hopkins F-test: 1.5037
Hopkins F-test: 1.22548
Hopkins F-test: .87147
Hopkins F-test: 1.49027
Hopkins F-test: 1.4087
Hopkins F-test: 1.09218
Hopkins F-test: 1.09749
Hopkins F-test: 1.40882
Hopkins F-test: 1.10254
Hopkins F-test: 1.92746
Hopkins F-test: 1.34522
Hopkins F-test: 1.59538
Hopkins F-test: 1.46949
Hopkins F-test: 1.35662
Hopkins F-test: 1.23285
Hopkins F-test: 1.26979
N = 25
sum hopf = 32.2347
sum squaured hopf = 43.3184
mean = 1.28939
standard deviation = .270452
standard error on mean = 5.40903e-2

2.8 0.5 - 0.25 MA

Not enough vents to run analysis

2.9 all data

Input in meters (UTM) - - output in kilometers
vents: 366
Total area in polygon: 2371.53
naive lambda = .154331
v(i) (vent-vent) = 2105.

u(i) (point-vent) = 6427.28
lambda v-v = .173871
lambda p-v = 5.69447e-2
Hopkins F-test: 3.05333
Hopkins F-test: 2.88987
Hopkins F-test: 3.00357
Hopkins F-test: 3.08819
Hopkins F-test: 2.91346
Hopkins F-test: 3.43277
Hopkins F-test: 2.74064
Hopkins F-test: 2.96243
Hopkins F-test: 2.73132
Hopkins F-test: 3.55443
Hopkins F-test: 2.89156
Hopkins F-test: 3.36203
Hopkins F-test: 3.38139
Hopkins F-test: 3.21893
Hopkins F-test: 2.5384
Hopkins F-test: 2.93685
Hopkins F-test: 3.69601
Hopkins F-test: 3.18774
Hopkins F-test: 3.31187
Hopkins F-test: 3.14132
Hopkins F-test: 3.01878
Hopkins F-test: 2.63498
Hopkins F-test: 2.73274
Hopkins F-test: 3.13497
Hopkins F-test: 2.27578
N = 25
sum hopf = 75.8334
sum squaured hopf = 232.604
mean = 3.03333
standard deviation = .327615
standard error on mean = 6.55229e-2

2.10 for all vents in the field

Input in meters (UTM) - - output in kilometers
vents: 366
Total area in polygon: 2411.61
naive lambda = .151766
v(i) (vent-vent) = 2105.
u(i) (point-vent) = 6669.78
lambda v-v = .173871
lambda p-v = 5.48744e-2
Hopkins F-test: 3.16853
Hopkins F-test: 2.87486
Hopkins F-test: 3.5993

Hopkins F-test: 2.78121
Hopkins F-test: 3.38664
Hopkins F-test: 3.0598
Hopkins F-test: 3.37556
Hopkins F-test: 3.1836
Hopkins F-test: 2.78239
Hopkins F-test: 2.54675
Hopkins F-test: 3.15154
Hopkins F-test: 2.81209
Hopkins F-test: 2.93573
Hopkins F-test: 3.742
Hopkins F-test: 3.08992
Hopkins F-test: 2.87064
Hopkins F-test: 3.26509
Hopkins F-test: 3.00652
Hopkins F-test: 3.12
Hopkins F-test: 2.78031
Hopkins F-test: 3.12003
Hopkins F-test: 2.7296
Hopkins F-test: 2.95945
Hopkins F-test: 3.01318
Hopkins F-test: 2.65362
N = 25
sum hopf = 76.0083
sum squaured hopf = 233.062
mean = 3.04033
standard deviation = .286583
standard error on mean = 5.73166e-2

3.0 Conclusions

1. Rocks in the Springerville filed may be classified by alkalinity index. Based on an analysis of the alkalinity index for sampled rocks, they are classified as follows.

   sub-alkaline: A.I. of less than 0

   mildly alkaline - AI => 0 and AI < 1

   alkaline - AI => 1 and AI < 1.75

   highly alkaline AI => 1.75

   This classification follows Condit et al. (1989) except that highly alkaline rocks are broken out as being the highest alkalinity (uppermost 10%) of the sample distribuiton.

2. The volume production rate of basalt in the SVF is roughly constant over time from 2 Ma to 1 Ma. After 1 Ma volume production rate waned. This is in contrast to the number of vents formed with time. The frequency of new vent formation was greates

1.5 - 1.0 Ma and reamined high until 0.75 Ma compared to the frequency of vent formation prior to 1.5 Ma. Frequency of vent formation was low before 1.75 Ma.

Two explanations for this seem reasonable. First, it is possible that vent formation rate was the same 2.0-1.5 Ma as later in the history of the field, but that these vents have been buried or eroded. A second explanation is that there is a real shift in the stlye of volcanism in the SPF from high volume eruptions to lower volume eruptions. This latter explanation is supported by a shift in the alkalinity of basaltics in the field. Certainly some over-printing or erosion of older basalts may occur in the SVF, but this does not account for the overall trends observed.

A problem with this is that there is a clear decrease in volume production at 1.5 Ma but not such a clear decrease in frequency of vent formation. This indictes real changes in the ratio of vents to volume occurr - ie these two variables are not necessarily linked directly.

FIGURE 4. Volume remains realitively steady-state from 2 to 1 Ma. In contrast, the number of vents increases with time, then remains steady form 1.5 to 1.0 Ma.

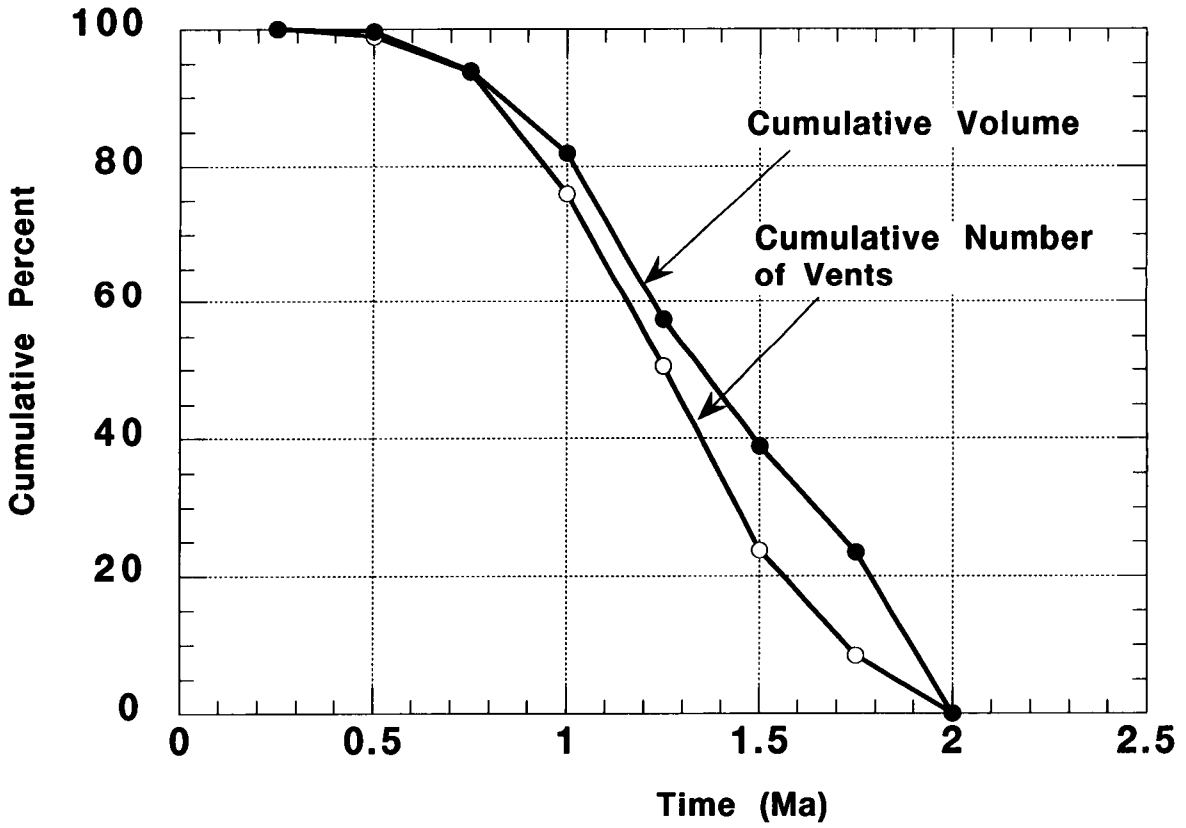

3. The rate of formation of new vents varies by alkalinity index. Sub-alkaline rocks erupt early. A total of 65% of the sub-alkaline vents form before 1.5 Ma. Most of these vents form between 1.75 and 1.5 Ma. These are distributed in the western part of the SVF.

   Highly alkaline rocks show a very different pattern in cumulative frequency of vent formation. Few highly alkaline rocks erupt before 1.5 Ma, then 50% pf the total number erupt between 1.5 and 1.25 Ma. Most of these erupt in the eastern part of the field.

   The vast majority of the vents in the field are mildly alkaline to alkaline (AI = 0 to 1.75). So the cumulative vent formation rate for the entire field tracks the cumulative vent formation curves for these types closely. There is vitually no difference in rate of vent formation for 0<= x < 1 and 1<= x < 1.75 alkalinity index rocks.

FIGURE 5. Cumulative percent of vents formed by alkalinity index

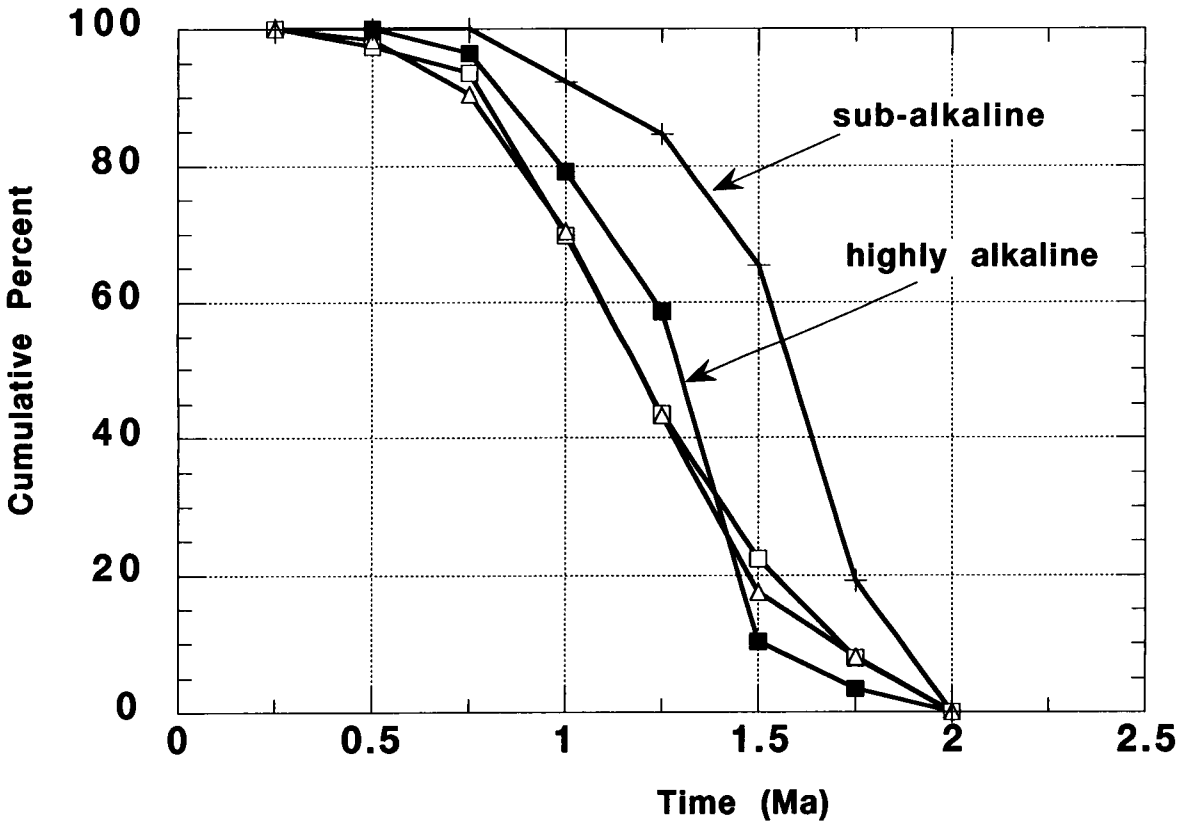

4. Clustering is statistically significant in all time slices of the analysis (250ky intervals). But, clustering is best developed in the early (sub-alkaline) stage of the field - before 1.5 Ma. This is because two main clusters occur at this time - one in the eastern part of the field and one in the west.

Springerville Alkalinity (continued)

Chuck Connor

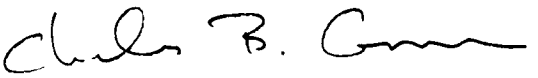

Variation in vent distribution in the Springerville volcanic field is explored using kernel density estimators.

Several studies in cinder cone volcanism have concentrated on patterns of activity and development in volcanic fields. These include early work by

Vent density, age, and geochemistry are studied in the Springerville volcanic field for several purposes. These are:

1. The Springerville field has gone through a period of intense magmatism during the last 2 Ma when compared with many basaltic volcanic fields. Cumulatively, the SVF has a relatively simple hisotry of waxing, steady-state, and waning volcanism. This makes the field ideally suited for the study of models of the recurrence rate of volcano formation in similar fields. One of the primary goals is to test models of the recurrence rate of cinder cone volcanism using data collected in the SVF.
2. The timing of volcanism in the Springerville volcanic field is better known than literally in all other volcanic fields in the western United States. Virtually every vent within the field can be placed in a time frame relative to other vents. Coupled with geochronolgical studies, each vent can be placed in a time interval of 250,000 uears.
3.

Previous experiments indicate that the Springerville basalts have a simple cumulative vent frequency dominated by a period of waxing - steady-state - then waning magmatism. However, the picture is more complex when volumes and variation in geochemistry - characterized by the alkalinity index - are considered. A summary of observations are:

1.
2. 2) These vents form over time and are spatially distributed over about 2,000 km^2. Earliest vents in the field formed at about 2.0 Ma and youngest vents are

Overall conclusions are:

1. We are able to show the pattern of development of the SVF with a high degree of confidence. Fundemental aspects of this pattern of development include: steady-state magma output from the earliest magmatism in the field 2 Ma to 1 Ma. Exponential waning in volume magma output after 1 Ma through about 0.5 Ma and very little output since that time. We infer from this that the volume of magma genrated from 2.0 Ma to 1.0 Ma was steady.
2. In contrast, the frequency of formation of new vents shows a different temporal pattern. Comparatively few vents formed prior to 1.5 Ma. Fully 50% of the vents in the entire field formed between 1.5 and 1.0 Ma, followed by a decline in the rate of new vent formation. In comparison with the volume magma output, the frequency of new vent formation is out of sync. Relatively few eruptions early in the history of the field This is especially clear comparing volumes produced between 1.75 and 1.5 Ma (km^3) by ** vents and between 1.5 Ma and 1.25 Ma (km^3) by ** vents. This is in good agreement with findings by Bacon (1982) and Kuntz et al. (1986) on the time-volume prdictability of basaltic volcanism in volcanic fields. The basic concept is that in many volcanic fields the volume production rate of basalt is constant. Over short periods of time, this basalt may erupt in single voluminous events, or a several discrete eruptions. The volume of the last eruption providing some indiation of the timing of the next. Smaller volume activity leads to more frequenct erutpion, a higher recurrence rate. Bacon (1982) found that basaltic volcanism in the Coso volcanic field has been volume-time predictable since 0.4 Ma; Kuntz et al. found volume-time predictability over the last 15,000 yr in the high-volume Snake River Plain volcanic field.

   The SVF provides an excellent example of this same relation extending over a period of one million years and where numerous volcanic events are involved. This may be the most robust indicator of volume-time predicibility yet. Also, study of the SVF provides an indication of departure from the volume-time predictible model during the waning stages of magmatism.
3. Basalts of different geochemical type erupted at different times in the field. In particular, most sub-alkaline rocks erupted early (2.0-1.5 Ma), followed by a pulse of highly alkaline magmatism between 1.5 and 1.25 Ma. Fully 65% of the subalkaline vents formed before 1.5 Ma and 50% of the highly alkaline vents formed between 1.5 and 1.25 Ma. Mildly alkaline and alkaline rocks erupted in a steady-state manner between 1.75 and 1.0 Ma. These account for 80% of the vents in the field. Thus, there is a major change in petrogenesis in the field around 1.75 Ma without there being a major change in magma supply. This implies that the change in petrogenesis is not due to a change in the thermal setting of the field (i.e., there is not change in the total amount of heat available to make basalt).
4. Vents cluster with greater than 95% confidence in the Springerville volcanic field. This was demonstrated using a Hopkins F-test (HopF = 3.03 ± 0.05, where the error is standard error on the mean).
5. One of the most intriguing aspects of volcanism in the SVF is the spatial nature of variation in recurrence rate. Although the total magma output in the field is steady-state, the area over which volcanism occurs changes through time. During a given

0.25 m.y. interval, volcanism occurs across the entire area of the field at a low level of output, but is much more intense in particular locations.

Some basic observations about this are:

0.0.1 2.0 - 1.75 Ma

Earliest volcanism in the SVF before 1.75 Ma occurred over a large area (** km2) in the western protion of the field. In this area the overall density of vents was low (generally less than 0.05 vents / km^2). At the same time, a tight cluster of volcanism developed in the SE portion of the field. At that time, vent intensity was highest in this area (>0.15 vents/ km2). A single sub-alkaline vent is located in the NE portion of the field at this time. A total of 11 vents (sub-alkaline to alkaline) formed in this area. This is cluster ** of Connor et al. (1992). Together, these groups are distributed over nearly the entire area of the field that eventually formed. This is different from many western great basin volcanic fields, in which shifts in the location of volcanism through time is a dominant characteristic of volcanism (Bergmann and Foland; Duffield et al., etc.).

0.0.2 1.75-1.5 Ma

Volcanism intensitfied in the western portion of the field between 1.75 and 1.5 Ma. During this time interval volcanism was essentially restricted to the same ** km2 area in the western portion of the field that it had occurred in during the previous 0.25 m.y. However, loccally the intensity of volcanism is much greater during this interval. In the area of greatest intensity, density of vents formed during this interval is >0.15 vents/km2 in the westernmost part of the field. Two groups of sub-alkaline basalts erupted during this time, one located at the northern end of the western area and one at the southern end. By contrast, volcanism in the eastern SVF decreased dramatically between 1.75 Ma and 1.5 Ma, with fewer, more dispersed vents forming. Analyzed samples in the eastern portion of the field erupted at this time are mildly alkaline to alkaline. These form an arcuate alignment.

1.5-1.25 Ma

A remarkable change in the distribution and intensity of volcanism occurs in the SVF after 1.5 Ma. Although the volume of magma output remains constant, the number of vents formed in a 0.25 Ma interval nearly doubles. This is accompanied by a dramatic increase in the number of highly alkaline vents formed - fully 50% of the highly alkaline vents in the SVF erupted bertween 1.5 and 1.25 Ma.

Kernel Analysis of the Probability of Volcanic Eruptions in the YMR

Chuck Connor

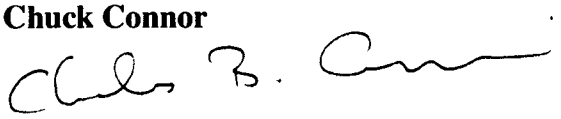

Probability of volcanic eruptions occurring in the YMR is estimated using the kernel analysis. This is a near-neighbor method applied to volcano distributions to estimate the probability density function for new volcano distribution. The model is run using several volcano data sets.

1.0 Introduction

Calculation of the probability of volcanic eruptions occurring in the YMR, and the probability of volcanic disruption of the candidate repository is a primary goal of the Volcanic Systems of the Basin and Range Research Project (Task 20-5704-124). Here, I apply a new method to the calculation of the probability of volcanic disruption of the repository: kernel intensity estimation. This technique has been developed in the statistics literature to estimate the intensity function for inhomogeneous point pattern distributions (Diggle, P.J., 1985, A kernel method for smoothing point process data, Applied Statistics 34: 138-147). Also see Silverman (B.W., 1986, Density Estimation, Chapman and Hall, NY, and Cressie, N. Statistics for Spatial Data, 1991, John Wiley and Sons, 899 pp). The method was first suggested to me by Tim Lutz.

2.0 ABSTRACT

The distribution and timing of areal basaltic volcanism are modeled using three nonhomogeneous methods: spatio-temporal nearest-neighbor, kernel, and nearest-neighbor kernel. These models give nonparametric estimates of spatial or spatio-temporal recurrence rate based on the positions and ages of cinder cones and related vent structures, and can account for migration and shifts in locus, volcano clustering, and development of regional vent alignments. The three methods are advantageous because: (i) recurrence rate and probability maps can be made, facilitating comparison with other geological information; (ii) the need to define areas or zones of volcanic activity, required in homogeneous approaches, is eliminated; and, (iii) the impact of uncertainty in the timing and distribution of individual events is particularly easy to assess. The models are

applied to the Yucca Mountain region (YMR), Nevada, the site of a proposed high-level radioactive waste repository. Application of the Hopkins F-test, Clark-Evans test, and K-function indicates volcanoes cluster in the YMR at the > 95% confidence level. Weighted-centroid cluster analysis indicates that Plio-Quaternary volcanoes are distributed in four clusters: three of these clusters include cinder cones formed < 1 Ma. Probability of disruption within the 8 km^2 area of the proposed repository by formation of a new basaltic vent is calculated to be between 1 x 10^{-4} and 5 x 10^{-4} in 10^4 yr (the kernel and nearest-neighbor kernel methods give a maximum probability of 5 x 10^{-4} in 10^4 yr), assuming regional recurrence rates of 5-10 volcanoes/million years. An additional finding, illustrating the strength of nonhomogeneous methods, is that maps of the probability of volcanic eruption for the YMR indicate the proposed repository lies on a steep probability gradient: volcanism recurrence rate varies by more than 2 orders of magnitude within 20 km. Insight into this spatial scale of probability variation is a distinct benefit of application of these methods to hazard analysis in areal volcanic fields.

3.0 INTRODUCTION

The distribution and timing of volcanism in areal basaltic volcanic fields has been the focus of numerous studies, primarily with the aim of better understanding the processes that govern magma supply and the role of crustal structure in influencing magma ascent [*Settle*, 1979; *Nakamura*, 1977; *Wadge and Cross*, 1988; *Connor*, 1990; *Lutz and Gutmann*, 1995]. Three basic aspects of cinder cone distribution have been described through these and related studies: (i) shifts in the locus of cinder cone volcanism are a common phenomenon in volcanic fields; (ii) cinder cones cluster within these fields, often on several scales; and (iii) vent alignments are ubiquitous, including short local alignments of several vents and more regional alignments that are usually more than 20 km in length and consist of numerous vents. Patterns in the distribution and timing of basaltic volcanism also have been used to assess hazards. For example, *Wadge et al.* [1994] made a quantitative analysis of the distribution of lava boccas on Mt. Etna as part of their assessment of lava flow hazards.

Here, three spatial and spatio-temporal nearest-neighbor models are presented to describe areal patterns in basaltic volcanism. These models are applied to the probability of volcanic eruption occurring in the Yucca Mountain region (YMR), Nevada. This approach features several characteristics of nearest-neighbor methods which make them amenable to volcano distribution studies and hazard analysis in areal volcanic fields. First, volcanic eruptions, such as the formation of a new cinder cone, are discrete in time and space. Using nearest-neighbor methods, the probability surface is estimated directly from the location and timing of these past, discrete volcanic events. As a result, nearest-neighbor models are sensitive to the patterns generally recognized in cinder cone distributions. Furthermore, the resulting probability surfaces are continuous, rather than consisting of abrupt changes in probability that must be introduced in spatially homogeneous models. Continuous probability surfaces can be readily compared to other

geologic data, such as fault location, that may influence volcano distribution. Nearest-neighbor methods also eliminate the need to define areas or zones of volcanic activity as is required by all spatially homogeneous Poisson models. Finally, uncertainties in the ages of individual volcanic events and the distribution of Neogene volcanoes are important limitations on the usefulness of all probability approaches. The impact of these uncertainties in the timing and distribution of individual events is relatively easy to assess using nearest-neighbor models.

Basaltic volcanism in the YMR has been the topic of numerous previous studies focusing on the probability of volcanic disruption of a proposed high-level radioactive waste repository [*Crowe et al.*, 1982; *Ho*, 1991; *Ho et al.*, 1991; *Crowe et al.*, 1992a; *Sheridan*, 1992]. These studies are pursued largely because the proposed waste repository is located within 10 to 20 km of at least five Quaternary cinder cones (Figure 1) and the high-level radioactive waste must be isolated from the surrounding environment for a period of at least 10,000 yr. Most models assessing the probability of future volcanism in the YMR and the likelihood of a repository-disrupting event rely on the assumption that Plio-Quaternary basaltic volcanoes are distributed in a spatially uniform random manner over some bounded area [e.g., *Crowe et al.*, 1982; *Crowe et al.*, 1992a; *Ho et al.*, 1991; *Margulies et al.*, 1992]. However, as in many other volcanic fields, patterns in the distribution and age of basaltic volcanoes in the YMR make the choice of these bounded areas somewhat subjective. Spatial variations in the YMR volcanic field are shown by shifts in the locus of basaltic volcanism from E to W since the cessation of caldera-forming volcanism in the Miocene Southern Nevada Volcanic Field [*Crowe and Perry*, 1989]. *Crowe et al.* [1992a] and *Sheridan* [1992] also noted that basaltic vents appear to cluster in the YMR. *Sheridan* [1992] suggests that one parametric method of accounting for spatial heterogeneity in vent distribution is to assume that post 4-Ma volcanoes located close to the proposed repository are formed as a result of steady-state activity and that the dispersion of these vents represents two standard deviations on an elliptical Gaussian probability surface. Using this assumption, *Sheridan* [1992] modeled the probability of repository disruption by Monte Carlo simulation for both volcanic events and dike intrusions, noting that variations in the shape of the probability surface significantly alter the probability of igneous disruption of the proposed repository. An alternative approach used to assess volcanic hazards in the YMR has been to define specific areas in which the recurrence rate of igneous events is increased. *Smith et al.* [1990] and *Ho* [1992] define NNE-trending zones within which average recurrence rates exceed that of the surrounding region. These zones correspond to cinder cone alignment orientations that *Smith et al.* [1990] and *Ho* [1992] hypothesize may occur as a result of structural control. The objectives of our application of nearest-neighbor methods in the YMR are to: (i) account for observed heterogeneities in volcano distribution in our estimate of the probability of volcanism in the area and within the boundaries of the proposed repository; (ii) use these methods to map variation in probability of volcanism across the region for the first time, thus placing the probability of volcanic eruption occurring at or near the repository in a more regional context; and (iii) compare the

three nearest-neighbor estimates, and previous estimates, of the probability of volcanic eruption in the area.

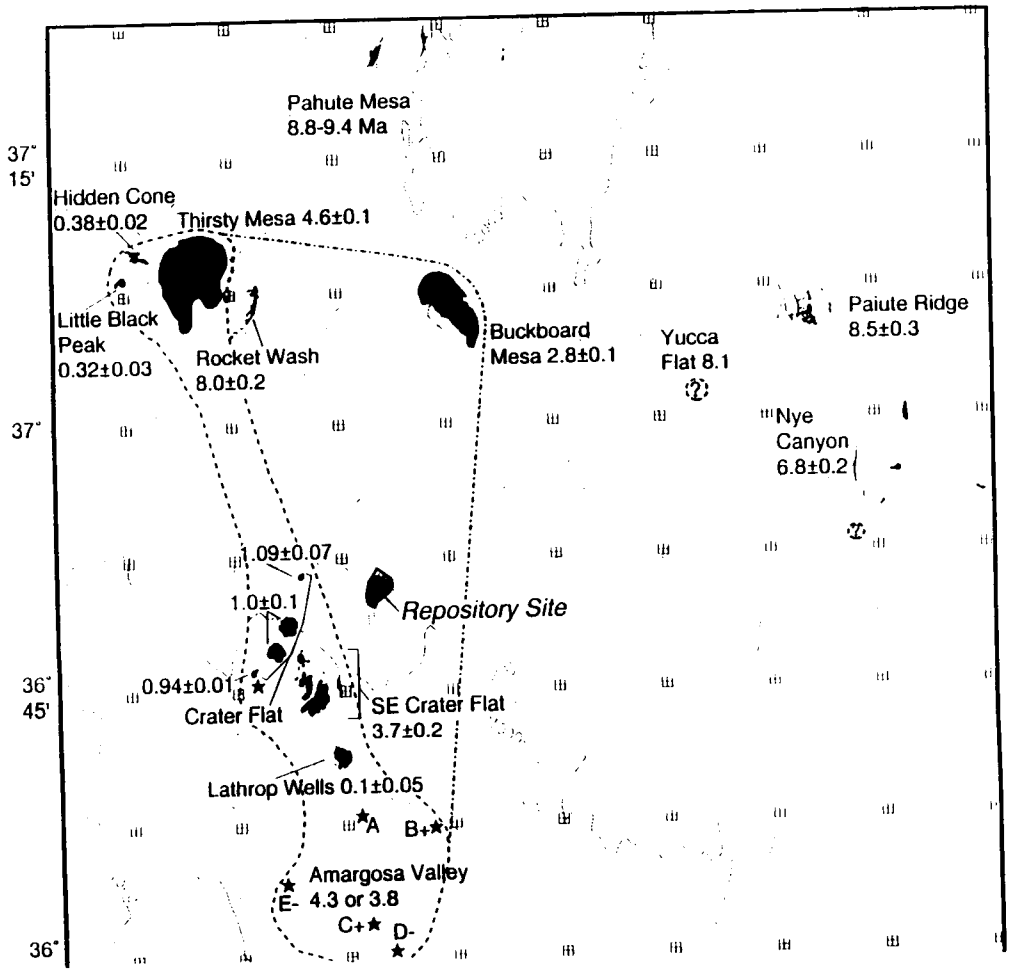

4.0 PATTERNS IN CINDER CONE VOLCANISM

Patterns in the distribution and timing of cinder cone volcanism in the YMR are similar to patterns identified in other, often more voluminous volcanic fields. For example, shifts or migration in the location of volcanism over periods of millions of years have been documented in many basaltic volcanic fields. In the Coso Volcanic Field, California, *Duffield et al.* [1980] found that basaltic volcanism has taken place in essentially two stages. Eruption of basalts occurred over a broad area in what is now the northern and western portions of the Coso Volcanic Field from approximately 4 to 2.5 Ma. In the Quaternary the locus of volcanism shifted to the southern portion of the Coso field. *Condit et al.* [1989] noted the tendency for basaltic volcanism to gradually migrate from west to east in the Springerville Volcanic Field between 2.5 and 0.3 Ma. Other examples of continental basaltic volcanic fields in which the location of cinder cone volcanism has migrated include the San Francisco Volcanic Field, Arizona [*Tanaka et al.*, 1986], the Lunar Crater Volcanic Field, Nevada [*Foland and Bergman*, 1992], the Michoacán-Guanajuato Volcanic Field, Mexico [*Hasenaka and Carmichael*, 1985], and the Cima Volcanic Field, California [*Dohrenwend et al.*, 1984; *Turrin et al.*, 1985]. In some areas, such as the San Francisco and Springerville Volcanic Fields, migration is readily explained by plate movement [*Tanaka et al.*, 1986; *Condit et al.*, 1989; *Connor et al.*, 1992]. In other areas, the direction of migration or shifts in the locus of volcanism does not correlate with the direction of plate movement. In either case, models developed to describe the recurrence rate of volcanism or to predict locations of future eruptions in volcanic fields need to be sensitive to these shifts in the location of volcanic activity.

On a slightly finer scale, cinder cones are known to cluster within many volcanic fields [*Heming*, 1980; *Hasenaka and Carmichael*, 1985; *Tanaka et al.*, 1986]. Spatial clustering can be recognized through field observation, or through the use of exploratory data analysis or cluster analysis techniques [*Connor*, 1990]. Clusters identified using the latter approach in the Michoacán-Guanajuato and the Springerville Volcanic Fields were found to consist of 10 to 100 individual cinder cones. Clusters in these fields are roughly circular to elongate in shape with diameters of 10 to 50 km. The simplest explanation for the occurrence, size, and geochemical differences between many of these clusters is that these areas have higher magma supply rates from the mantle. Factors affecting magma pathways through the upper crust, such as fault distribution, appear to have little influence on cluster formation [*Connor*, 1990; *Connor and Condit*, 1994]. In some volcanic fields, such as Coso, the presence of silicic magma bodies in the crust may influence cinder cone distribution by impeding the rise of denser mafic magma [*Eichelberger and Gooley*, 1977; *Bacon*, 1982], resulting in the formation of mafic volcano clusters peripheral to the silicic magma bodies.

Tectonic setting, strain-rate and fault distribution all may influence the distribution of basaltic vents within clusters, and sometimes across whole volcanic fields [*Nakamura*, 1977; *Smith et al.*, 1990; *Parsons and Thompson*, 1991; *Takada*, 1994]. *Kear* [1964] discussed local vent alignments, in which vents are the same age and easily explained by a single episode of dike injection, and regional alignments, in which vents of varying

age and composition are aligned over distances of 20 to 50 km or more. Numerous mathematical techniques have been developed to identify and map vent alignments on different scales, including the Hough transform [*Wadge and Cross*, 1988], two-point azimuth analysis [*Lutz*, 1986], and frequency-domain map filtering techniques [*Connor*, 1990]. Regional alignments identified using these techniques are commonly colinear or parallel to mapped regional structures. For example, *Draper et al.* [1994] mapped vent alignments in the San Francisco Volcanic Field which are parallel to, or colinear with, segments of major fault systems in the area. About 30% of the cinder cones and maars in the San Francisco Volcanic Field are located along these regional alignments [*Draper et al.*, 1994]. *Lutz and Gutmann* [1995] identified similar patterns in the Pinacate Volcanic Field, Mexico. Although alignments can clearly form due to episodes of dike injection [*Nakamura*, 1977] and therefore are sensitive to stress orientation [*Zoback*, 1989], there are also examples of injection along pre-existing faults [e.g., *Kear*, 1964; *Draper et al.*, 1994] oblique to maximum horizontal compressional stress.

Cumulatively, these studies indicate that models describing the recurrence rate, or probability, of basaltic volcanism should reflect the clustered nature of basaltic volcanism and shifts in the locus of basaltic volcanism through time. Models also should be amenable to comparison with basic geological data, such as fault patterns and neotectonic stress information, which may impact vent distributions on a comparatively more detailed scale. In addition, probability models should incorporate uncertainties in the distribution and timing of volcanism. Uncertainty in the distribution of volcanoes is particularly important for Neogene volcanoes. These volcanoes may be buried as a result of subsequent volcanic activity [e.g., *Condit et al.*, 1989] or sedimentation [e.g., *Langenheim et al.*, 1993], or have been so deeply eroded that vent locations can not be recognized. Uncertainty in the ages of volcanoes is due to variations in the precision and accuracy of different techniques used to date volcanic events and to open-system movement of radiogenic components.

Finally, it is possible to define a volcanic event in various ways. A simple definition that can be applied to young cinder cones, spatter mounds, and maars is based on morphology: an individual edifice represents an individual volcanic event. Volcanic events used in distribution analyses are commonly defined as mapped vents [*Condit et al.*, 1989; *Connor et al.*, 1992; *Lutz and Gutmann*, 1995; *Wadge et al.*, 1994], or volcanic edifices of a minimum size [*Hasenaka and Carmichael*, 1985; *Connor*, 1990; *Bemis and Smith*, 1993]. In older, eroded systems, evidence for the occurrence of vents, such a near-vent breccias or radial dikes, is required. However, several edifices can form in single, essentially continuous, eruptive episodes. For example, three closely spaced cinder cones formed during the 1975 Tolbachik fissure eruption [*Tokarev, 1983; Magus'kin et al., 1983*]. In this case, the three cinder cones represent a single eruptive event that is distributed over a larger area than is represented by a single cinder cone. The three 1975 Tolbachik cinder cones have very different morphologies and erupted adjacent to three older (late? Holocene) cinder cones [*Braytseva et al.*, 1983]. Together this group forms a 5 km-long N-trending alignment. Without observing the formation of this alignment, it likely would be difficult to resolve the number of volcanic events represented by these

six cones. This type of eruptive activity results in uncertainty in the number of volcanic events represented by individual cones, even where these vents are well-preserved.

These uncertainties represent a serious problem in most, if not all volcanic fields, because often there is no clear way to resolve them. An alternative approach is to ascertain the impact of these uncertainties on the probability model. This approach is adopted by developing several data sets for basaltic volcanism in the YMR that likely bound the uncertainties associated with the age, distribution, and number of volcanic events in the area.

5.0 MODELING VENT DISTRIBUTION

Aherne and Diggle [1978] define two measures of intensity [expected number of points (i.e., volcanoes) per unit area]:

$$\lambda_p = \frac{m}{\sum_{i=1}^{m} u_i}$$

$$\lambda_v = \frac{m}{\sum_{i=1}^{m} v_i}$$

where u_i and v_i are areas of circles whose radii are the distance from the i^{th} randomly chosen point to the nearest volcano, and the i^{th} volcano to its nearest neighbor, respectively; m is the number of nearest neighbors and in this case is equal to the number of volcanoes; λ_p is the intensity estimated from m point-to-volcano measurements; and λ_v is the intensity estimated from m volcano-to-volcano measurements. *Aherne and Diggle* [1978] used these measures of intensity to distinguish between homogeneous Poisson point distributions, for which λ_p and λ_v should be approximately equal, and clustered distributions, for which λ_v tends to measure the intensity within clusters and λ_p is a measure of cluster intensity [*Ripley*, 1981]. The Hopkins *F*-test [*Ripley*, 1981] uses the ratio:

$$Hop_F = \frac{\lambda_p}{\lambda_v}$$

tested against a Fisher *F(2m,2m)* distribution [*Byth and Ripley*, 1980], the null hypothesis being that $Hop_F = 1$ and volcanoes have a homogeneous Poisson distribution. Assuming that some area can be identified in which all points, *p*, are located, Hop_F provides one means of distinguishing clustered and random volcano distributions. Numerous similar tests exist, including the Clark-Evans test [*Clark and Evans*, 1955] and the K-function [*Ripley*, 1977]. Calculation of these statistics, coupled with a spatial cluster analysis [*Späth*, 1980; *Connor*, 1990], provides an effective means of characterizing the spatial distribution of volcanoes.

The expected recurrence rate per unit area [*Diggle*, 1977; 1978; *Ripley*, 1977; 1981; *Cressie*, 1991], must be estimated in most volcanic fields because clustering causes a marked departure of recurrence rate per unit area from the average recurrence rate. Here, three nearest-neighbor estimates of recurrence rate and their assumptions are described. All three methods are nonparametric and the recurrence rate estimates are controlled by the distribution and timing of past volcanism.

Method 1: Spatio-temporal nearest-neighbor estimate

The first method provides a spatial and temporal estimate of recurrence rate:

$$\lambda_n(x, y) = \frac{m}{\sum_{i=1}^{m} u_i t_i}$$

where nearest-neighbor volcanoes are determined as the minimum, $u_i t_i$, t_i is the time elapsed since the formation of the i^{th} nearest-neighbor volcano, and u_i is defined as before [Eq. 1], with $u_i \geq 1$ km^2.

The relationship between this estimate of recurrence rate and homogeneous Poisson models, in which the recurrence rate is a constant over time and within a specified area, can be illustrated by describing the behavior of $\lambda_n(x,y)$ when a completely spatially and temporally random process is sampled. Modifying equation 4 slightly:

$$z_i = u_i t_i$$

$$\lambda_n(x, y) = \frac{m}{\sum_{i=1}^{m} z_i} = \frac{1}{E(Z)}$$

where $E(Z)$ is the expected value of z. If volcanoes form as the result of a completely spatially and temporally random process, $E(Z)$ can be thought of as the expected time and area within which n volcanoes will form, and z must have a gamma density distribution [*Ripley*, 1981]. Therefore the probability density function for z is:

$$f_z(z) = \frac{\lambda^n}{(n-1)!} z^{n-1} e^{-\lambda z}$$

where λ is the average recurrence rate within some specified area and over some specified time interval. The expected value of z, given this probability density function, becomes:

$$E(Z) = \frac{\lambda^n}{(n-1)!} \int_0^\infty z^n e^{-\lambda z} dz$$

$$E(Z) = \frac{\lambda^n}{(n-1)!} \frac{n!}{\lambda^{n+1}} = \frac{n}{\lambda}$$

In order to compare $E(Z)$ with the recurrence rate per unit area, as defined in equation 6, $E(Z)$ is evaluated for $n = 1$, that is, the expected time and area within which one new volcano will form. Combining equations 6 and 9,

$$\lambda_n(x, y) = \lambda$$

for completely spatially and temporally random distributions. The nearest-neighbor estimate of recurrence rate, $\lambda_n(x,y)$, becomes a constant equal to the average recurrence rate over some specified area if the underlying distribution is completely spatially and

temporally random. This nearest-neighbor nonhomogeneous Poisson model thus is simply a general form of homogeneous Poisson models. One distinct advantage of using the more general nearest-neighbor nonhomogeneous Poisson models rather than homogeneous Poisson models is that regions within which λ is taken to be constant need not be defined.

Therefore, it is reasonable to compare the expected regional recurrence rate calculated using various nearest-neighbors [equation 4]:

$$\lambda_t = \iint_{XY} \lambda_n(x, y)\, dydx$$

with the observed regional recurrence rate. In practice, recurrence rates, $\lambda_n(x,y)$, are calculated on a grid and these values are summed over the region of interest:

$$\lambda_t = \sum_{i=0}^{q} \sum_{j=0}^{n} \lambda_n(i, j)\, \Delta x \Delta y$$

where, in this case, Δx and Δy are the grid spacing used in the calculations, and q and n are the number of grid points used in the X and Y directions, respectively.

Summarizing the first method, several assumptions are made in the application of equation 4 to estimate the intensity of volcanism and the probability of volcanic eruption in a particular volcanic field. The most important assumption is that the appropriate number of nearest-neighbor volcanoes can be estimated from the regional recurrence rate. In areas of concentrated volcanism, such as the Springerville Volcanic Field, the frequency of vent-forming eruptions is high enough to make recurrence-rate estimates fairly straightforward [*Connor and Condit*, 1994]. In other areas, such as the YMR, greater uncertainty exists in recurrence rate estimates because of the comparatively small number of events [*Crowe et al.*, 1982; *Ho et al.*, 1991]. In addition, the use of equation 4 assumes that u_i and t_i have been adequately determined for each volcano. Here, t_i is taken to represent the time since the formation of the volcano. Finally, it is assumed that each volcano is adequately represented as a point. However, as described below, various area terms may be used to alleviate this assumption. In practice, it is relatively simple to test the sensitivity of the model results to both uncertainty in the ages of volcanoes and

estimates of the regional recurrence rate of volcanism by computing the recurrence rate using a range of parameters.

Method 2: Kernel estimate

Lutz and Gutmann [1995] applied a kernel method [*Silverman*, 1986] for estimation of the spatial recurrence rate of volcanism in their study of vent alignment distribution in the Pinacate Volcanic Field. In the kernel estimation technique, spatial variation in estimated recurrence rate is a function of distance to nearby volcanoes and a smoothing constant, h. The kernel function is a probability density function which is symmetric about the locations of individual volcanoes. Following the example of *Lutz and Gutmann* [1995], an Epanechnikov kernel is used [*Cressie*, 1991]. For a purely spatial, bivariate distribution:

$$\kappa_i = \frac{2}{\pi}\left[1 - \left(\frac{d_i}{h}\right)^2\right], \qquad \text{if } \left(\frac{d_i}{h}\right)^2 < 1$$

$$\kappa_i = 0, \qquad \text{otherwise}$$

where h is the smoothing constant used to normalize the distance, d_i, between the location for which recurrence rate is estimated and the i^{th} volcano. The spatial recurrence rate at point (x,y) is then:

$$\lambda_h(x, y) = \frac{1}{e_h}\sum_{i=1}^{n} h^{-2}\kappa_i$$

where n volcanoes are used in the analysis and e_h is an edge correction [*Diggle*, 1985; *Cressie*, 1991]. In the case of a volcanic field, integrating $\lambda_h(x,y)$ over some large area, A, relative to the size of the field and the smoothing constant, h, should yield n. Therefore, if $e_h = n$ then $\int_A \lambda_h(x, y)\, da = 1$, where the units of $\lambda_h(x, y)$ are volcanoes/km^2. Using this value for e_h, $\lambda_h(x,y)$ can be multiplied by an estimate of the temporal recurrence rate, λ_t, to calculate the expected number of volcanoes per unit area per time. The value of $\lambda_h(x,y)$ at a given point (x, y) depends on the number of volcanoes found within a distance h of the point. If no volcanoes are located within h of the point, then $\lambda_h(x, y) = 0$.

Eruptions will have a high probability close to existing volcanoes if h is chosen to be small. Conversely, a large value of h will result in a more uniform probability distribution. Clearly, utility of the kernel model depends on the assumption that the smoothing constant can be estimated in a geologically meaningful way. *Silverman* [1986] recommends using a wide range of smoothing constants in density calculations, an approach adopted by *Lutz and Gutmann* [1995]. An identical approach is used here. However, the range of reasonable smoothing constants is further constrained by using a spatial cluster analysis. The shape of the kernel function is an additional assumption in the model. Alternative kernel functions include uniform random and normal density distributions. Although *Cressie* [1991] and *Lutz and Gutmann* [1995] indicate that the choice of the kernel function is not as important as the choice of an appropriate smoothing constant, we used several different kernels in our analysis of volcano distribution in the YMR. Even with this limited number of volcanic events, we also found that the kernel function has a trivial impact on probability calculations compared with the choice of a smoothing constant.

Method 3: Nearest-neighbor kernel estimate

In method 3 a value $r_m(x, y)$ is substituted for the smoothing constant, h, in equation 14, where $r_m(x,y)$ is the distance between point (x, y) and the m^{th} nearest-neighbor volcano [*Silverman*, 1986]. In this case, the nearest-neighbor is determined on the basis of distance only, rather than using the measure $u_i t_i$ used in method 1. For $m \geq 1$, $\lambda_r(x, y) > 0$ everywhere. Thus, this nearest-neighbor kernel method produces smoother variation in the probability surface than is calculated for all but the largest values of a smoothing constant in method 2. Nonetheless, the estimated recurrence rate will be higher near the center of clusters than is estimated using the large values for the smoothing constant in method 2. As in method 1, the number of nearest neighbors used to estimate $\lambda_r(x, y)$ will strongly impact the results and experimentation using a range of nearest neighbors is necessary to identify the resulting variation in $\lambda_r(x,y)$. Unlike method 2, e_h will not always equal n in application of the nearest-neighbor kernel method [*Silverman*, 1986]. The simplest approach to determination of e_h is to first integrate estimates of $\lambda_r(x,y)$ over the entire region using $e_h = n$, then chose a value of e_h such that

$\int_A \lambda_r(x, y)\, da = 1$. The value of e_h typically varies from $0.9n$ to n when estimated using this approach.

The three methods yield three different measures of recurrence rate, which are distinguished by subscript (method 1: $\lambda_n(x,y)$; method 2: $\lambda_h(x,y)$; method 3: $\lambda_r(x,y)$). Commonality between the three methods lies in the fact that each method depends fundamentally on the distribution of past volcanic events in order to estimate the probable locations of future volcanism. In the case of methods 1 and 3, the m nearest-neighbor volcanoes are used, defined by the distance to, or distance to and time since, past

eruptions in the area. In method 2, only nearby volcanoes are used in the estimate of recurrence rate, where "nearby" is defined by the smoothing constant. Furthermore, in all three methods the calculation of a probability of future volcanism at a given location within a volcanic field depends on an estimate of the regional recurrence rate, λ_t, which is generally not known with certainty [*McBirney*, 1992; *Ho*, 1991].

APPLICATION TO THE YUCCA MOUNTAIN REGION

The proposed geological repository for high-level radioactive waste at Yucca Mountain, Nevada, provides one example of the increasing need to evaluate hazards due to areal basaltic volcanism. The objective of the repository is to isolate high-level radioactive waste from the accessible environment for at least the next 10,000 years, through deep (about 300 m) burial in Tertiary ignimbrites situated in the unsaturated zone several hundred meters above the local water table [*DOE*, 1988]. Volcanic eruptions at or near the repository could potentially release high-level radioactive waste into the accessible environment [*DOE*, 1988]. Therefore, determining the probability of a volcanic eruption in the repository area during the next 10,000 years is an important step in evaluating the potential risks associated with the Yucca Mountain site. The nearest-neighbor models described above provide one means of calculating these probabilities and evaluating their uncertainties.

Basaltic Volcanism in the Yucca Mountain area

The YMR contains more than 30 Late Miocene to Quaternary basaltic volcanoes distributed over approximately 2500 km^2. The region has been the site of recurring basaltic volcanism since the cessation of Late Miocene caldera-forming activity in the Southwestern Nevada Volcanic Field [e.g., *Sawyer et al.*, 1994]. Basalts younger than about 9 Ma appear petrogenetically distinct from older basalts and better represent the mafic system that produced Quaternary eruptions in the YMR [*Crowe et al.*, 1983; 1986]. Figure 1 illustrates the location of mapped and inferred basaltic vents younger than about 9 Ma. Several subdivisions have been proposed for YMR post-caldera basaltic volcanism. The Crater Flat Volcanic Zone (CFVZ) of *Crowe and Perry* [1989] is a NNW-trending zone that includes all YMR Quaternary volcanoes, most Pliocene volcanoes, and the Amargosa Valley aeromagnetic anomalies. The Area of Most Recent Volcanism (AMRV) of *Smith et al.* [1990] includes all Pliocene and younger YMR volcanoes. Both the CFVZ and AMRV are expanded from their original boundaries to include all of the aeromagnetic anomalies of Amargosa Valley [*Langenheim et al.*, 1993].

Vent locations in Table 1 were generally reported as such on geologic maps and in reports [*Byers et al.*, 1966; *Ekren et al.*, 1966; *Carr and Quinlivan*, 1966; *Byers and*

Barnes, 1967; *Byers and Cummings*, 1967; *Hinrichs et al.*, 1967; *Noble et al.*, 1967; *Tschanz and Pampeyan*, 1970; *Cornwall*, 1972; *Crowe and Perry*, 1991; *Crowe et al.*, 1983, 1986; 1988; *Carr*, 1984; *Swadley and Carr*, 1987; *Faulds et al.*, 1994], or interpreted in the field from the presence of feeder dikes, vent agglutinate, or cinder cone remnants. Some of the Miocene volcanic centers have been eroded to hundreds of meters below the paleosurface, removing most of the evidence for vent locations. The number of vents reported for Pliocene and older volcanic centers should be regarded as a minimum estimate. Difficulty in recognizing older volcanic vents may impact estimated cluster size, shape and longevity, but has little impact on spatial or spatio-temporal recurrence rates when data are weighted by age.

Over 200 isotopic age determinations have been published for YMR basaltic rocks younger than about 9 Ma. Many of the older analyses have relatively low degrees of precision and are occasionally inaccurate. For example, dates as old as 10.4±0.4 Ma are reported for the basalt of Pahute Mesa [*Crowe et al.*, 1983], which overlies the 9.40±0.03 Ma Rocket Wash Tuff [*Sawyer et al.*, 1994]. Following the example of *Crowe* [1994], age estimates reported in Table 1 were selected from more recent analyses, which are generally regarded as more precise and accurate than older analyses [*Sinnock and Easterling*, 1983; *Vaniman and Crowe*, 1981; *Vaniman et al.*, 1982]. For units with multiple analyses, the age estimates represent the mean and one standard deviation of the data set and in cases where there is apparent discrepancy between two recent dates, both are incorporated in the analyses.

Several of the age estimates reported in Table 1 require further explanation. The dipolar aeromagnetic anomalies in Amargosa Valley [*Kane and Bracken*, 1983; *Langenheim et al.*, 1993] have both normal (Figure 1, sites D and E) or reversed (Figure 1, sites B and C) magnetic polarities. Anomaly B has been drilled and samples of this basalt dated at 4.3±0.1 [*Turrin*, 1992] and 3.8±0.1 Ma [*Perry*, 1994]. Magnetic polarities are used to constrain the ages of the other anomalies, which have not been drilled but are interpreted to be caused by buried basaltic centers [*Langenheim et al.*, 1993]. The aeromagnetic anomaly in southern Crater Flat (Figure 1) likely represents a buried basalt with normal magnetic polarity [*Kane and Bracken*, 1983; *Crowe et al.*, 1986]. The age of this unit is problematic, as all of the other basalts in Crater Flat have reversed magnetic polarities [*Crowe et al.*, 1986]. This possible volcanic center is not included in our analyses. Over 100 age determinations are published for the Lathrop Wells volcano, which range from about 0.4 Ma to younger than 0.01 Ma and represent numerous analytical methods such as $^{40}Ar/^{39}Ar$ [*Turrin et al.*, 1991], U-series disequilibrium [*Crowe et al.*, 1992b], and cosmogenic isotopes [*Poths and Crowe*, 1992; *Zreda et al.*, 1993; *Poths et al.*, 1994]. In an attempt to encompass many of the higher-precision age determinations for Lathrop Wells, we use an estimated age of 0.1±0.05 for this volcano. *A posteriori* experimentation indicates that the age of Lathrop Wells may vary from 0.01 to 0.4 Ma with little impact on the probability of establishing a new volcano at the location of the repository.

Data Used in Models

Based on the abundant geological and geochronological data available for the YMR, we use two data sets throughout the following analyses. These two data sets are meant to encompass most of the uncertainty in the number and timing of volcanoes formed in the YMR. Data set 1 [Table 1] maximizes the number of events in the YMR. For example, closely spaced cinder cones, like Little Cone NE and Little Cone SW are treated as distinct events in data set 1. Furthermore, minimum ages are used in data set 1. These minimum ages are defined by the one-sigma uncertainty reported for age determinations. In cases where there is no overlap between two recent age determinations, such as is the case for Black Cone [Table 1], we use the younger of the dates in data set 1. Data set 2 excludes several mapped vents from the analysis because these vents are closely spaced and therefore may represent a single eruptive event. For example, Little Cone NE is not included in data set 2 because of its proximity to Little Cone SW. Also, several undrilled aeromagnetic anomalies are not included in data set 2. Older volcano ages are used in data set 2 [Table 1]. These two data sets bound current estimates of the timing and distribution of post-caldera basaltic volcanic events in the YMR, noting that alternative data sets may certainly be developed and ages may be revised as additional geochronological analyses are published.

The type of event modeled using these two data sets is formation of a new volcano. Individual cones, isolated lava boccas, or mappable remnants of these structures represent events. In data set 1, these events include the construction of any Quaternary edifice by volcanic eruption. In data set 2, events include individual cones and cone pairs separated by < 1 km. Events in this data set imply that vent pairs may be fed by the same intrusions at shallow levels during an eruption. *Champion* [1991] has argued that the Quaternary Crater Flat alignment and similar cone alignments in the area formed during single episodes of volcanism. Thus, all five cones in the Quaternary Crater Flat alignment may represent one eruptive event. One way to think of the two data sets is that they weight episodes of alignment formation by the number of volcanoes formed in each. This approach is consistent with the use of spatially nonhomogeneous models.

These two data sets are not appropriate for modeling the probability of reactivation of an existing cinder cone, a process that some investigators have suggested occurs in the YMR [e.g., *Wells et al.*, 1990; *Bradshaw and Smith*, 1994]. The probability models in this paper are used to determine the probability of formation of a new volcano, a spatial or spatio-temporal process. Reactivation of an existing vent is essentially a temporal process and should be modeled accordingly.

In addition, these two data sets are further divided by volcano age throughout the analyses that follow. Each analysis is made for all volcanoes in the data set (i.e., all mapped post-caldera basalts), volcanoes less than 5 Ma, and volcanoes less than 2 Ma. This is done in recognition of the nonstationary character of YMR cinder cone volcanism. Inspection of Figure 1, for example, reveals that Late Miocene clusters have little spatial

relationship to Pliocene and Quaternary cluster distribution [*Crowe and Perry*, 1989]. However, most Pliocene clusters have reactivated in the Quaternary. Thus, further division of the two data sets preferentially weights the distribution of younger volcanoes.

Estimate of the regional recurrence rate of new volcano formation, λ_t, in the YMR during the Quaternary has received a great deal of study. These estimates range from about 1 volcano per million years (v/my) to 8 v/my [e.g., *Ho*, 1991; *Ho et al.*, 1991; *Crowe et al.*, 1992a]. This range of estimates is based on the application of various averaging techniques and statistical estimators. For example, one approach has been to consider that 7-8 volcanoes have formed in the last 1.8 m.y., yielding $\lambda_t \approx 4$ v/my [*Crowe et al.*, 1982]. However, the YMR Quaternary volcanoes are all less than approximately 1 Ma, so averaging over the last one million years, $\lambda_t \approx 7$ - 8 v/my. For all post-caldera basalts, $\lambda_t \approx 3$ v/my. Using a maximum likelihood estimator, *Ho et al.* [1991] calculated $\lambda_t \approx 5$ - 6 v/my. Finally, based on a Poisson-Weibull model, *Ho* [1992] calculated that $\lambda_t \approx 2$ - 13 v/my with 90% confidence. We do not attempt to refine these estimates here. Rather, our probability estimates assume $\lambda_t = 5$ - 10 v/my. This range encompasses the known recurrence rate of volcano formation over the last one million years and allows for some variation about this value.

Probability Models

As a first step in analysis of volcano distribution in the YMR, the presence of volcano clusters is tested using data sets 1 and 2 [Table 1] and Equations 1 and 2. Random points within the AMRV are used to calculate volcano intensity, λ_p [equation 1]. The value of λ_p may change depending on the position of the m random points. So, λ_p and Hop_F are calculated averaging the results of 100 simulations [*Cressie*, 1991] and reported with the standard error on the mean. Considering all volcanoes in the AMRV (i.e., data set 1), $Hop_F = 2.6 \pm 0.1$. Considering only Quaternary volcanoes within the AMRV (data set 2), $Hop_F = 7.1 \pm 0.3$. In either case, the null hypothesis that volcanoes are randomly distributed in the AMRV is rejected with greater than 95% confidence. Hopkins F-test may be applied to smaller regions also. The CFVZ (Figure 1) is approximately 70 km long and 20 km wide and is a minimum area which includes Quaternary cinder cones of the YMR and the Amargosa Valley vents. Even using areas as small as the CFVZ, $Hop_F = 3.1 \pm 0.2$ (data set 1) and clustering is significant with greater than 95% confidence. Application of similar measures of clustering, including the Clark-Evans test [*Clark and Evans*, 1955] and the *K*-function [*Ripley*, 1977] shows that volcanoes in these areas are not randomly distributed at similar confidence levels. Consequently, we conclude that the recurrence rate of volcanism varies across the YMR, and therefore application of nearest-neighbor estimates of spatial and spatio-temporal variation in recurrence rate are appropriate.

A weighted-centroid cluster analysis [*Späth*, 1980] of vent distribution in the YMR helps illustrate vent clustering and provides additional insight into vent distribution. The

results of the cluster analysis are shown by a dendrogram [Figure 2], which plots the distance at which individual cones and cluster centers link [*Späth*, 1980]. The dendrogram shown was calculated using data set 1 and volcanoes less than 5 Ma. The cluster analysis was repeated using both data sets, subdivided by age and a variety of clustering algorithms, with very similar results to those plotted [Figure 2]

FIGURE 1. Weighted-centroid cluster analysis of volcano distribution in the YMR, calculated using data set 1 [Table 1] and volcanoes less than 5 Ma. Vent pairs group at distances of less than 2 km, clusters are completely formed at linkage distances of 15 km or less, and clusters begin to group at distances of greater than 23 km. Volcano abbreviations are given in Table 1.

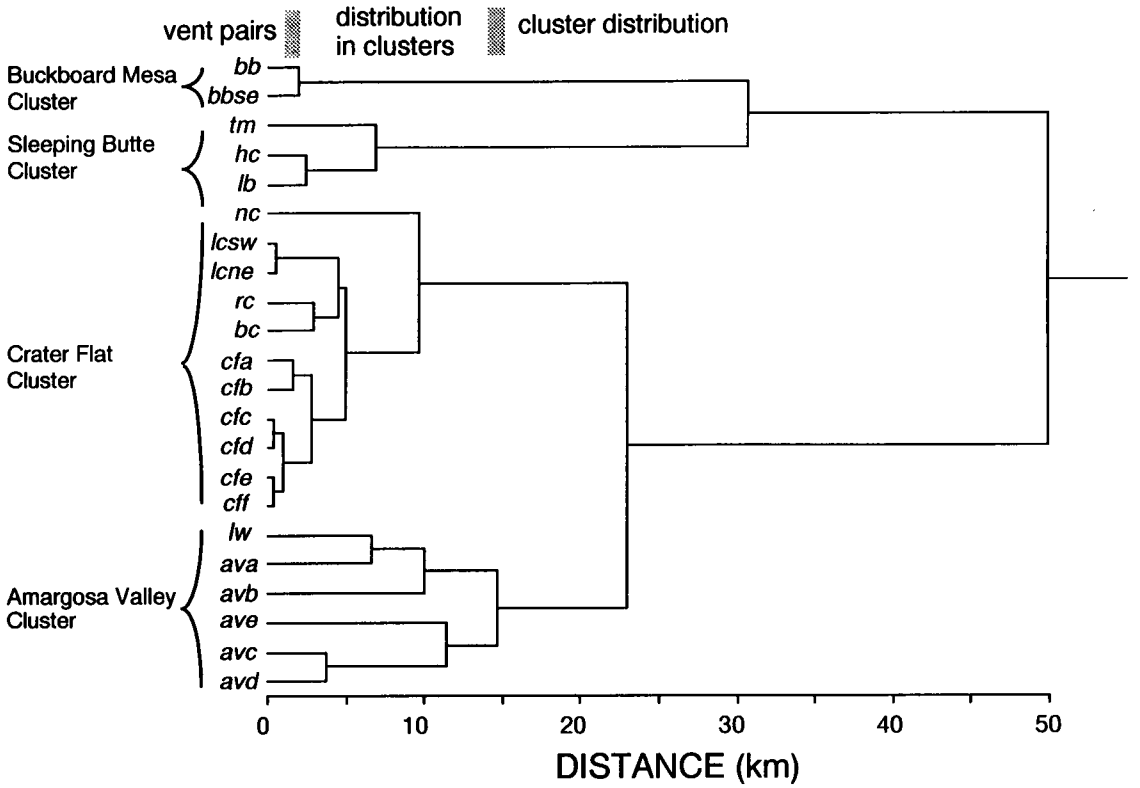

The dendrogram shows that volcanoes form pairs and then larger clusters at short linkage distances. Cluster membership changes rapidly until a linkage distance of 15 km, at which point four clusters occur. These are named the Amargosa Valley cluster, including Lathrop Wells, the Crater Flat Cluster, Sleeping Butte Cluster, including Hidden Cone, Little Black Peak, and Thirsty Mountain [Figure 1], and the Buckboard Mesa Cluster,

which consists of only two closely spaced vents. Each of these four clusters are complete and self-contained at linkage distances of 15 km or less and do not group with other clusters until linkage distances of ≥ 23 km, comparatively large changes in linkage distances. At 23 km, the Amargosa Valley and Crater Flat Valley Clusters form a single group [Figure 2]. Together these volcanoes are isolated from the Sleeping Butte and Buckboard Mesa Clusters. The Amargosa Valley and Crater Flat Clusters are less distinct using a single linkage clustering algorithm because of the comparatively intermediate position of Lathrop Wells [Figure 1].

Vent pairs that are grouped as single events in data set 2, such as the Little Cones, link at distances of less than 1 km. The absence of these vent pairs in the Amargosa Valley Cluster is evident comparing linkage distances in this cluster with Crater Flat. This may indicate the comparatively low resolution of aeromagnetic methods for the delineation of buried vent pairs, or reflect a difference in the style of volcanism between the two clusters.

Adding a hypothetical volcanic event at the location of the candidate repository [Figure 1] alters the cluster analysis very little. The hypothetical repository event links with Northern Cone at a distance of 8.2 km; this group then links with the rest of the Crater Flat Cluster at a distance of approximately 11 km.

In summary, the analysis of volcano distribution yields several observations that are useful for interpretation of the nearest-neighbor analyses. First, vents form statistically significant clusters in the YMR. Spatially, volcanoes less than 5 Ma form four clusters, the Crater Flat and Amargosa Valley Clusters overlapping somewhat due to the position of Lathrop Wells volcano and aeromagnetic anomaly A. Second, a volcanic event located at the repository would be spatially part of, albeit near the edge of, the Crater Flat Cluster, rather than forming between or far from clusters in the YMR. Third, three of the four clusters contain Quaternary basalt, indicating that these clusters are long-lived and provide some indication of the likely areas of future volcanism. Finally, the cluster analysis provides one means of estimating the smoothing constant, h, used in method 2. If h is chosen to be less than 15 km, then significant, perhaps unwarranted, variation in recurrence rate will be predicted within clusters. If h is chosen to be greater than 25 to 30 km, recurrence rate will be comparatively high between clusters. Choosing h between 15 km and 25 km, therefore, will best capture the clustered nature of volcano distribution in the YMR.

Application of Method 1. Regional recurrence rate is calculated using equation [3] and then compared with expected regional recurrence rate, λ_t using equation [12]. The calculations are repeated using the two data sets, further subdivided by age [Figure 3]. For data set 1, 6 to 11 nearest-neighbor volcanoes give regional recurrence rates of 5 to 10 v/

my. Data set 2 models this range of recurrence rates with 6 to 8 nearest-neighbor volcanoes. Limiting the analysis to younger volcanoes results in lower regional recurrence rates at a given number of nearest neighbors because Quaternary volcanoes are tightly clustered. Ten to thirteen nearest-neighbor volcanoes are required to model recurrence rates similar to the estimated post-caldera recurrence rate of <4 v/my.

In equation 7, the gamma density distribution was introduced to determine the expected time and area over which a new volcano will form. The Poisson distribution is used to determine the number of volcanoes that can be expected to form over a given time and area. In this case the probability of one or more volcanoes, $P[N(t) \geq 1]$, is of interest. The probability of volcanic disruption of the potential repository site is calculated for various estimates of $\lambda_n(x,y)$ [equation 4],

$$P[N(t) \geq 1] = 1 - \exp\left[-t \int_X \int_Y \lambda_n(x, y)\, dy dx\right]$$

where the limits of integration define the area of the repository. This relation is closely approximated in discretized form:

$$P[N(t) \geq 1] = 1 - \exp\left[-t \sum_a \lambda_n(x, y)\, \Delta x \Delta y\right]$$

where Δx and Δy each are one kilometer and a is the area within which a volcanic eruption may occur and intersect the repository. These probabilities are very close to the probability of one volcanic event because the probability of two or more events is vanishingly small ($P[N(10{,}000\ \text{yr}) > 1] \approx 1 \times 10^{-9}$), although it is noted that a single event using data set 2 may form more than one volcanic vent. Note that independence of events is always assumed in the application of the Poisson distribution. Because there is significant variation in $\lambda_n(x,y)$ and other estimates of recurrence rate of volcano formation across the region, the area, $\Delta x \cdot \Delta y$, and time interval, t, must be small enough to be reasonably assured of independence. The application of equations 15 and 16 assumes that $\lambda_n(x,y)$ does not vary in a significant way within the area $\Delta x \cdot \Delta y$ or over the time interval t.

The probabilities of volcanic disruption of the repository using a range of nearest-neighbor models are given in Figure 4, calculated of t = 10,000 yr and a = 8 km^2. The area of the actual repository is currently undetermined, but is estimated to be approximately 6

km^2. Larger area terms (i.e., 8 km^2) are presented to indicate the effects of an increase in repository size, and, more importantly, to account for the subsurface area directly affected by the emplacement of a new volcanic center. For example, emplacement of a cinder cone 500 m outside the repository boundary may result in dike injection within the repository itself. Using λ_t = 5 v/my to 10 v/my, a = 8 km^2, and both data sets in Table 1, the probability of disruption during a 10,000 year isolation period is between 9.0 x 10^{-5} and 3.3 x 10^{-4} [Figure 4]. Altering the area term a from 6 km^2 to 10 km^2 has little impact on these probabilities. The probability of volcanic disruption of the proposed repository is greater than 1 x 10^{-4} for all but the lowest proposed values of λ_t (< 3 v/my).

One way to illustrate spatial variation in estimated recurrence rate in the YMR, and hence the probability of volcanic eruption, is to map probabilities calculated from non-homogeneous Poisson models. Applying equation 4, the expected recurrence rate is estimated at points on a grid (grid-node spacing 2 km) using varying numbers of nearest neighbors. Probabilities of at least one event occurring within one repository area (8 km^2) about each grid point during the next 10,000 years are then calculated (equation 16). Four such maps are illustrated in Figures 5a-5d. Using m = 9 nearest-neighbor volcanoes and data set 1 (Figure 5a) the clustered nature of volcanism in the YMR is captured by the probability surface, with the most significant mode in probability being centered on the Crater Flat Cluster. Modes in probability are also preserved at Late Miocene clusters in the eastern part of the YMR, although probabilities of eruption are estimated to be more than one order of magnitude lower than in Crater Flat. None of the maps shown indicate increased probability of volcanic eruption in the Sleeping Butte Cluster because of the few vents that comprise this cluster. Probability contours on all four maps [Figures 5a-5d] are elongate NNW-SSE, reflecting the overall distribution of Quaternary cones in the CFVZ [*Crowe and Perry*, 1989]. This elongation is more subdued in Figures 5c-5d because of uncertainty in the origin of several aeromagnetic anomalies in Amargosa Valley, which are not included in data set 2.

FIGURE 2. Recurrence rate for the formation of new volcanoes in the YMR is estimated using method 1 [equations 4 and 12], calculated using data from Table 1. Solid triangles - data set 1, open triangles - data set 2. These data sets are further subdivided and calculations repeated for all volcanoes < 10 Ma, < 5 Ma, and < 2 Ma.

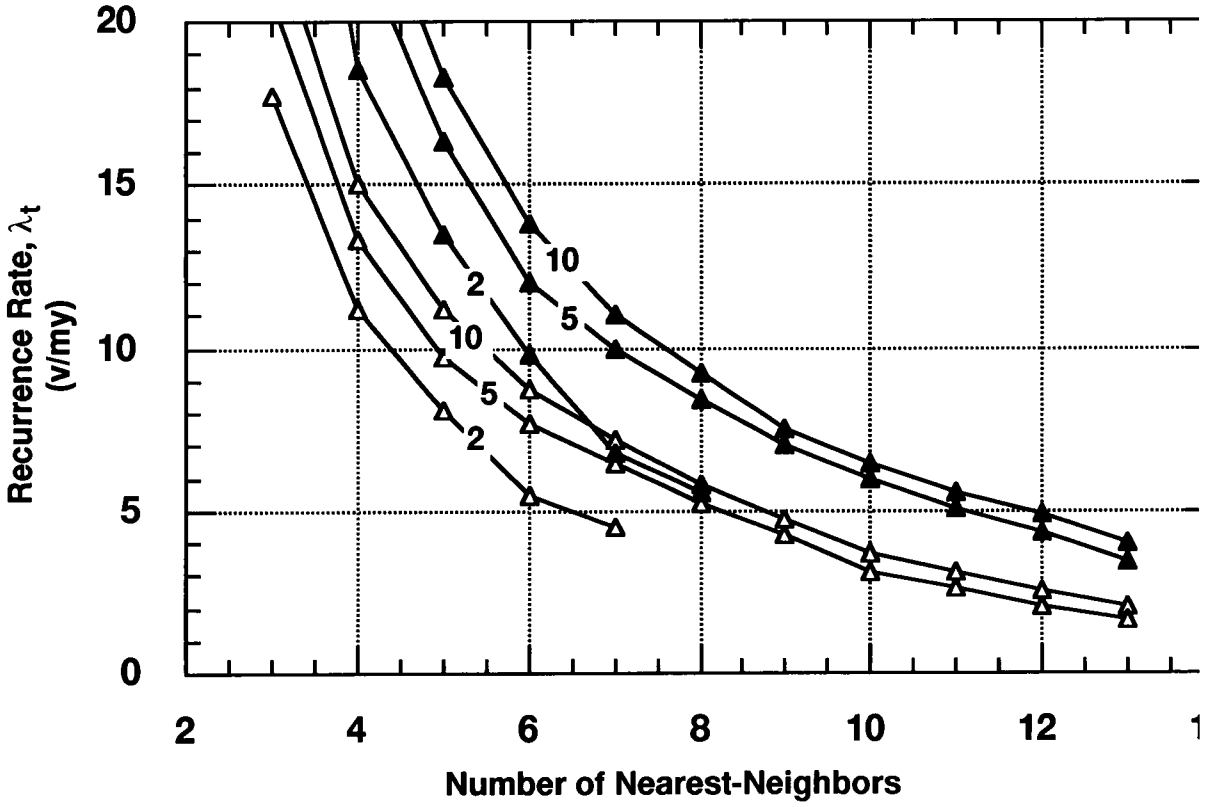
20
15
10
5
0
Recurrence Rate, λ_t (v/my)
2
4
6
8
10
12
Number of Nearest-Neighbors
10
5
2
10
5
2

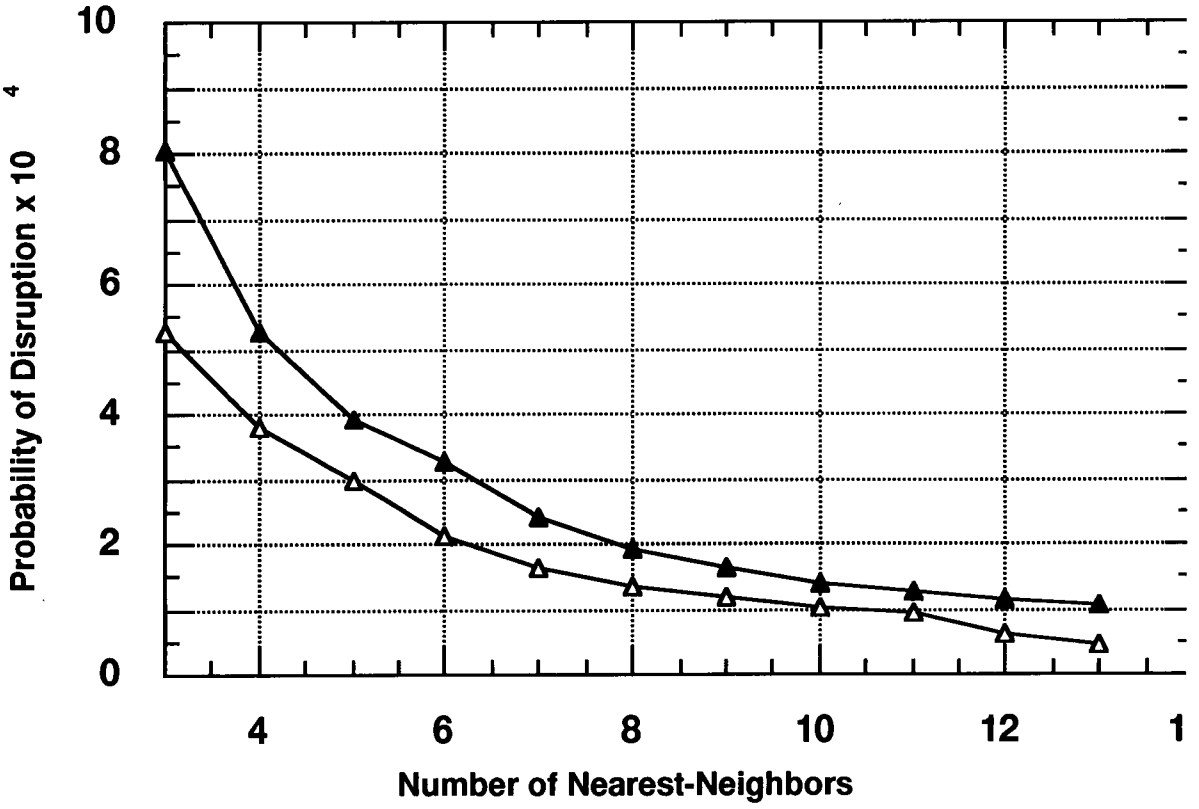
Probability of Disruption x 10 4
10
8
6
4
2
0
4
6
8
10
12
1
Number of Nearest-Neighbors

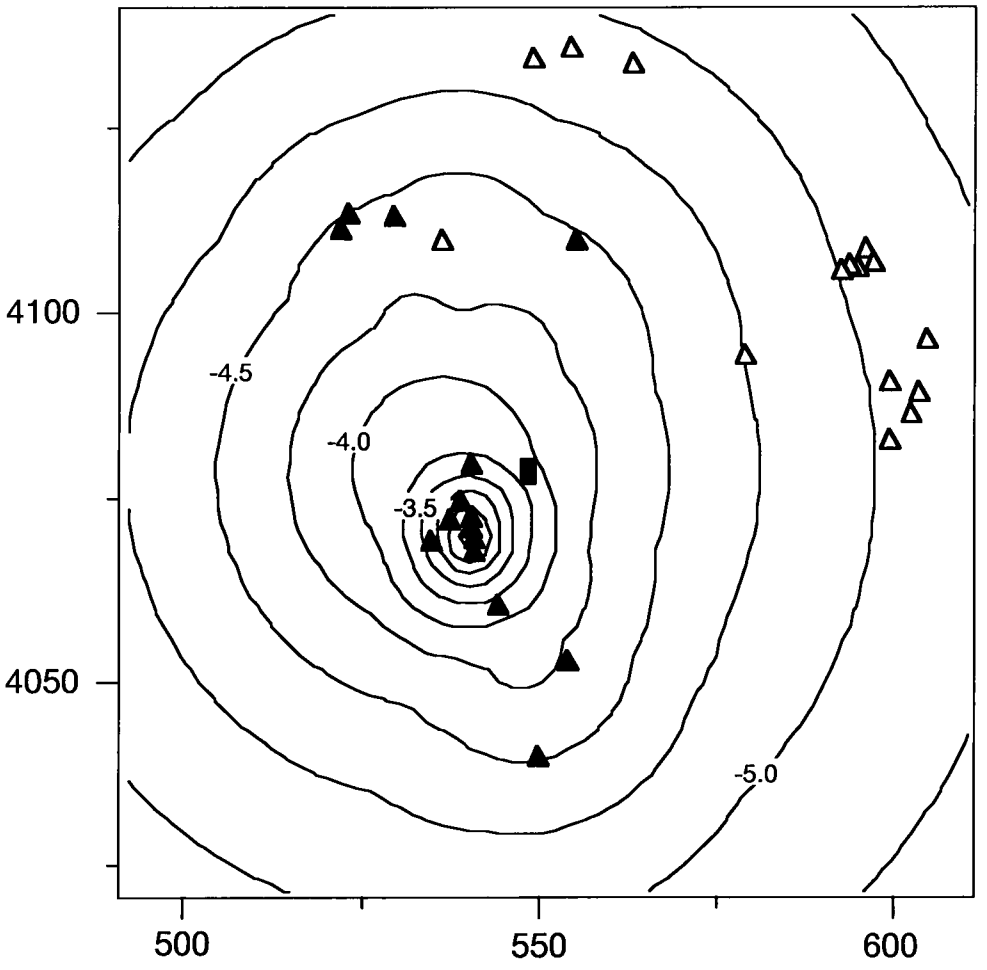
4100
4050
500
550
600
-4.5
-4.0
-3.5
-5.0

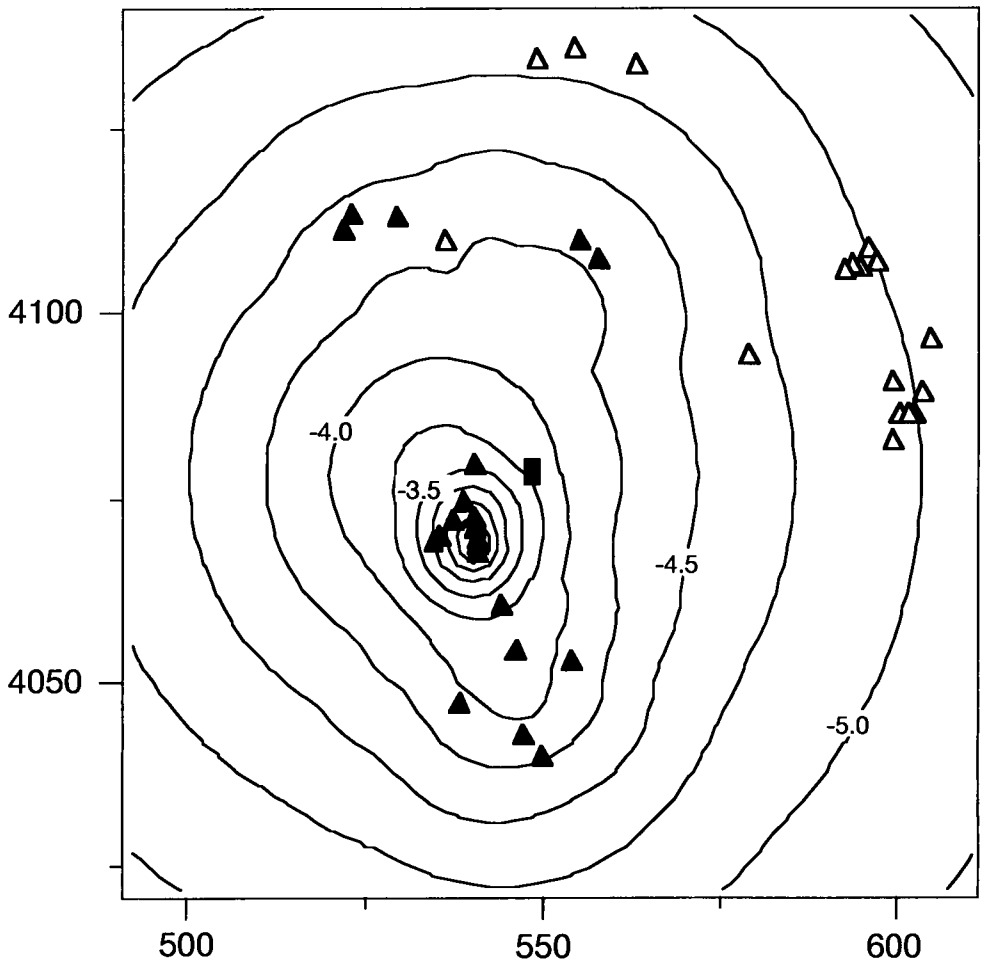

Here are additional maos that illustrate the point that by variying the number of volcanoes used and the number of neighbors, the shape of the map changes, but overall is not much different.

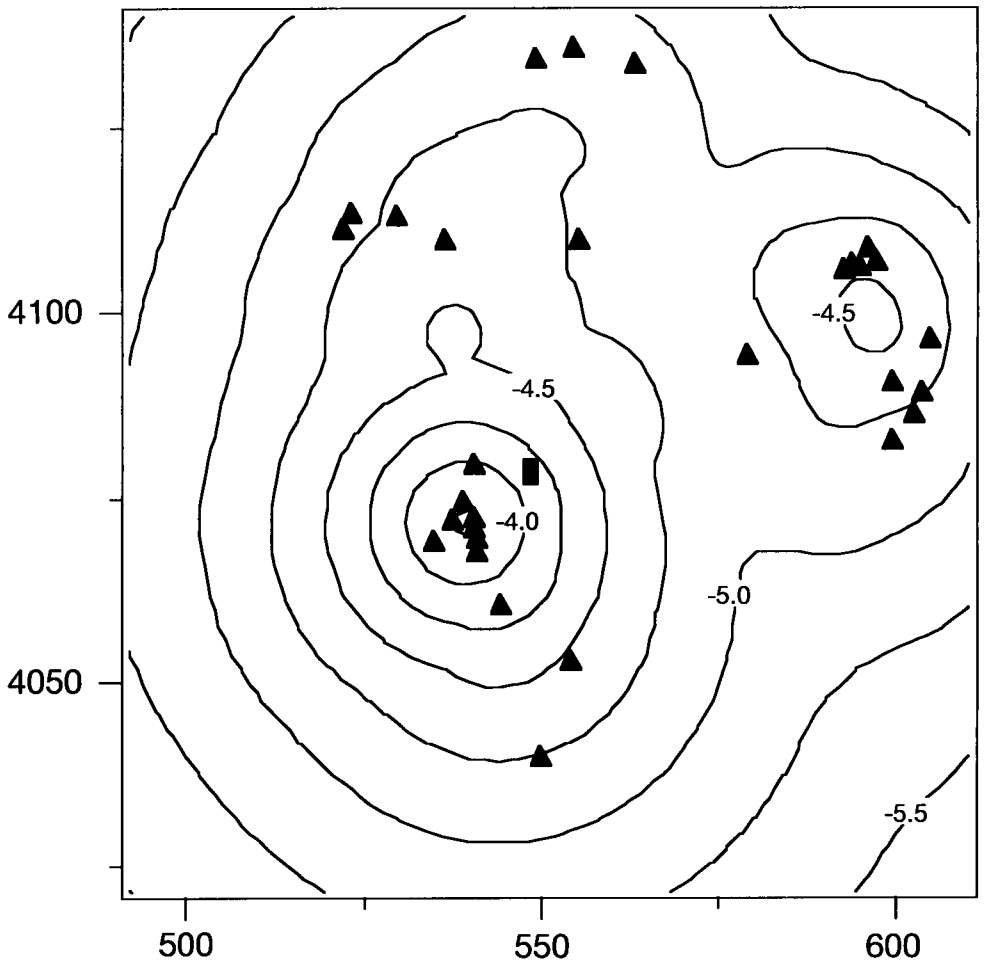

Above is 11 near neighbors, 10 million years, using data set 2

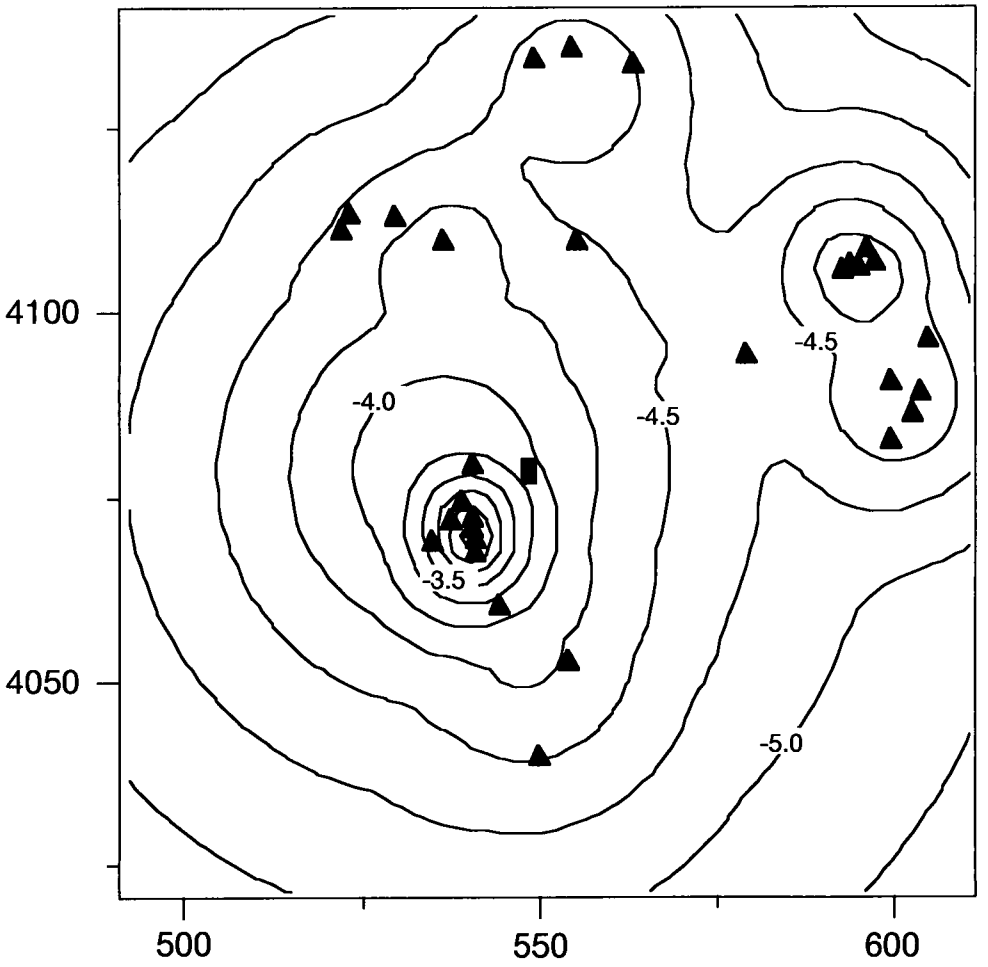

above is 7 nn , 10 Ma, data set 2

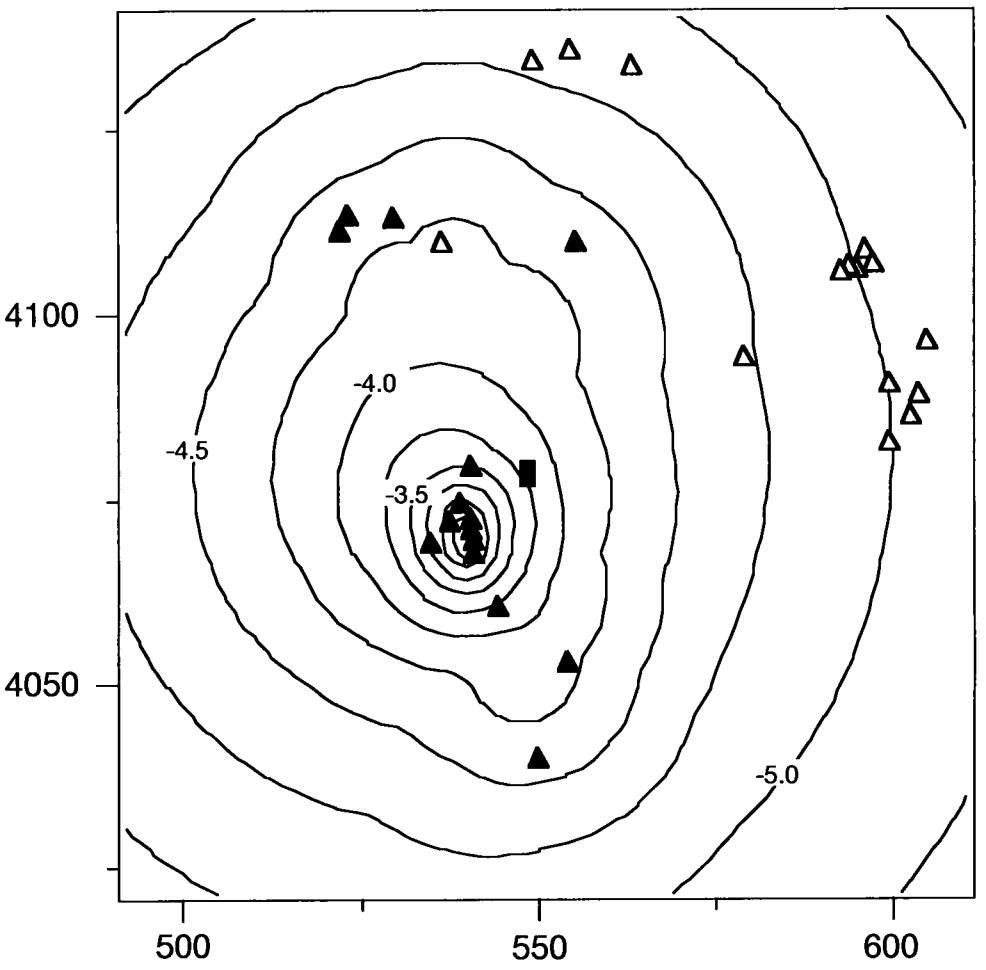

above is 6 nn, 5 Ma, data set 2

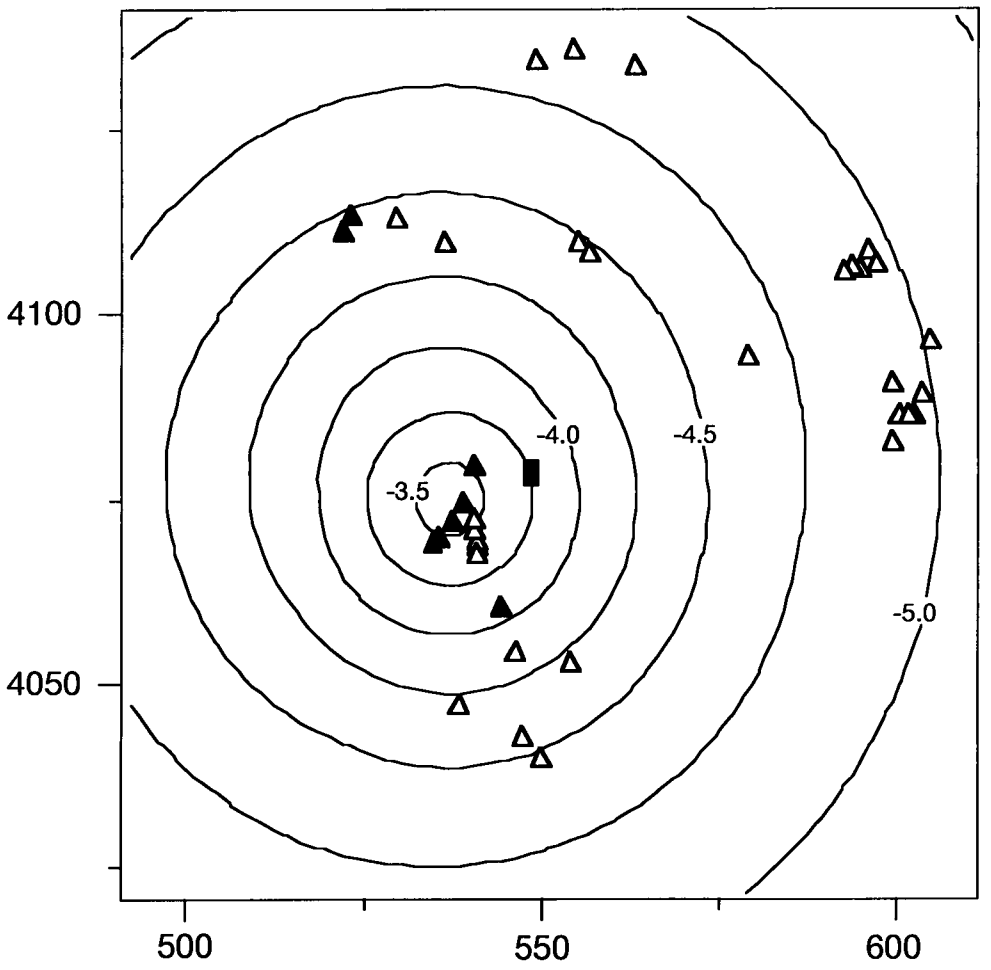

7 nn, 2 Ma, data set 1

Numerous additional maps were made with the same basic results

```
! PROGRAM: Yuccadist
! Language: TrueBasic
! Author: Chuck Connor
!       Center for nuclear waste Regulatory Analysis
!       Southwest Research Institute
!       San Antonio Texas, 78238-5166
```

```
!Date: Dec 13, 1992
!
!Summary: This program calculates recurrence rates (point intensity)
!from vent location data.
!
!       Ripley, B.D., 1981, Spatial Statistics
!          Wiley series in probability and statistics
!          John Wiley and Sons, New York, 252 pp.
!          see pages 134-138.
!
! In this program, the coordinates of points are input from
! a file. The user then defines the area s/he wishes to
! analyze, inputting vertex corrdinates using the mouse. Only
! data points falling within the area selected are used in
! the analysis. Several factors concerning this area are important:
!
! 1) the verticies must be input in a clockwise manner. If
!    the verticies are input in a counter-clockwise manner,
!    the program will use points only found OUTSIDE the
!    polygon in the analysis.
!
! 2) the polygon will be rectilinear and concave inwards.
!    This is because of the algorithm uses the orientation
!    of line segments to discriminate between points within
!    and outside the area selected.
```

```
!
! 3) the area selected will close automatically. For
!    instance, if you select 5 verticies, 5 line segments
!    will be drawn, connecting the verticies.  The last line
!    segment will be drawn connecting the first and last
!    verticies.
!
! Once the area of analysis is selected, the program
! takes a minute to find random points within the area.
! The reucurrence rate is then calculated in several ways.
!    1) a naive recurrence rate calculation is done
!           = #pts/total area the user selects
!    2) a recurrence rate based on minimum vent to vent distances
!           = #pts/ sum(minimum distance to nearest other vent^2*pi)
!    3) a recurrence rate based on minimum distances between randomly
!           selected points in the area chosen by the user and
!           vents
!           = #pts/sum(minimum point-vent distance^2*pi)
! measures 2 and 3 (above) can be used to test a distribution with the
! null hypothesis being that it is a homogeneous Poisson distribution.
! Divide recurrence rate point-vent by recurrence rate vent-vent and
! test with a F(2*total pts,2*total points) distribution. If the
! null hypothesis is rejected then the vents cluster.
! this is call the Hopkins F-test. (see Ripley page 136).
```

```
!Library "sglib.trc"
DIM pts(75,3),grid(1600,2),lambda(1600),mtx(40,40), a(15)

! mat pts is the matrix which holds point locations located
! within the selected area.
!
! mat moncar is the matrix that holds random points generated
! by the monte carlo subroutine. this matrix is scratched after
! each simulation

CLEAR
PRINT " type the name of the file containing the observed"
PRINT " data points"
!INPUT file$
let file$ = "yucca.dat2"
OPEN #1: name file$

OPEN #10: screen .25,1,.25,1
OPEN #13: screen 0,1,0,1

LET ymax = -10000000
LET ymin = 100000000
LET xmin = 100000000
LET xmax = -100000000
DO while more #1
```

```
  INPUT #1: x,y, id$, age$
  IF x> xmax then LET xmax = x
  IF x < xmin then LET xmin = x
  IF y > ymax then LET ymax = y
  IF y< ymin then LET ymin = y
LOOP
RESET #1: begin
WINDOW #13

!plot all the points
PRINT xmin,xmax,ymin,ymax
PRINT "type in the dimensions of the area you want to see"
PRINT "xmin, xmax, ymin, ymax"
!INPUT s1,s2,s3,s4
let s1 = 520000
let s2 =620000
let s3 = 4040000
let s4 = 4140000
!dimension the window to be square
print "age range you want to consider (all volcanoes less than...m.y. old)"
input ager

WINDOW #10
SET COLOR 15
SET TEXT justify "center", "half"
```

```
SET COLOR 15
LET scrfix=s2-s1
SET WINDOW s1-(scrfix*28/128),s2+(scrfix*28/128),s3,s4
DO while more #1
  INPUT #1: x,y,age,id$
  IF x<=s2 and x=>s1 and y=>s3 and y<=s4 and age <=ager then
    PLOT TEXT, AT x,y: "*"

let totpts = totpts + 1
let pts(totpts,1) = x
let pts(totpts,2) = y
let pts(totpts,3) = age
  END IF
LOOP
set color 15
box area 547300,549200,4077000,4080000     ! roughly the repository

!plot the frame
PLOT s1,s3;s1,s4;s2,s4;s2,s3;s1,s3
get key dum
RESET #1: begin
!make the grid

let grid(1,1) = 548500
let grid(2,1) = 548500
```

```
let grid(3,1) = 547500

let grid(4,1) = 549500

let grid(5,1) = 548500

let grid(6,1) = 547500

let grid(7,1) = 547500

let grid(8,1) = 548500

let grid(9,1) = 547750 !add for ten km

let grid(10,1) = 549250 !add for 10 km

let grid(11,1) = 546750

let grid(12,1) = 546750

let grid(13,1) = 549500

let grid(14,1) = 546750

let grid(15,1) = 548250

let grid(1,2) = 4079500

let grid(2,2) = 4078500

let grid(3,2) = 4078500

let grid(4,2) = 4078500

let grid (5,2) =4077500

let grid(6,2) = 4077500

let grid(7,2) = 4076500

let grid(8,2) = 4080250

let grid(9,2) = 4079500  !add for te nkm

let grid(10,2) = 4079500 !add for ten km

let grid(11,2) = 4078500

let grid(12,2) = 4077500
```

```
let grid(13,2) = 4077500

let grid(14,2) = 4076500

let grid(15,2) = 4076500

let gridpts = 15


for xx = 1 to 9

let a(xx)=1

next xx

let a(8) = .2

let a(9) = .5

let a(10) = .5

let a(11) = .15

let a(12) = .25

let a(13) = .7

let a(14) = .1

let a(15) = .5


!let kount = 0

!for x = 1 to 40

!for y = 1 to 40

!let kount = kount + 1

!let grid(kount,1) = 510000 + x*2000

!let grid(kount,2) = 4040000 + y*2000

!next y

!next x
```

```
!let gridpts =kount
                    ! this is the number of volcanoes

for num_neigh = 1 to 13
let sumlam = 0
!PRINT "calculating point-vent distances"
CALL lambdap(pts,grid,gridpts,totpts,lambda,num_neigh)

window #13
clear
set color 15
!open #11: name "recur.out", create newold
!erase #11
!
!let kount = 0
!for x = 1 to 40
!for y = 1 to 40
!let kount = kount + 1

!let mtx(x,y) = lambda(kount)
!print #11:lambda(kount)
!let suml = suml + lambda(kount)*4          ! multiply 4 km2 because this is the sample
spacing
!
!next y
!next x
```

```
!

!print "the sum is:";suml

!get key uuu


!call topograph(mtx,grid(1,1),590000,grid(1,2),4080000,"")


for xx = 1 to gridpts


let sumlam = sumlam + lambda(xx)*a(xx)

print lambda(xx)


next xx

let probxx = 1 - exp(-sumlam*10000)

print

print "near neighbor = "; num_neigh

print "prob ="; probxx

get key uuu

next num_neigh

!call topograph(mtx,grid(1,1),grid(gridpts,1),grid(1,2),grid(gridpts,2),"black black
black")

!set color "white"

!call gotocanvas

!call graphpoint(570000,4100000,2)

!for x = 1 to totpts

!call graphpoint(pts(x,1),pts(x,2),2)

!next x
```

```
!
!box area 547300,549200,4077000,4080000     ! roughly the repository

END

EXTERNAL

SUB lambdap(pts(,),rndpts(,),num_rnd_pts,totpts,lambda(),num_neigh)

   !This subroutine calculates the intensity based on distances from random points
   ! to nearest neighboring vents, equivalent to u(i) in Ripley, 1981
   ! "spatial statistics", page 135.

   !pts(,) is the matrix containing the x,y coordinates of the vents
   !rndpts(,) is the mtx containing x,y coordinates of random points
   ! pts and rndpts should both be dimensioned (totpts,2)

   ! totpts is the total number of points in pts() and rndpts()
   ! sumarea is the sum of areas swept out between a random point and
   ! the nearest vent = sum(minimum distance^2*pi)
   ! lambda is the intensity based on this calculation
dim minarea(50), nearpt(50,3)

   FOR numpt = 1 to num_rnd_pts
```

```
LET sumarea = 0

    LET i1 = rndpts(numpt,1)/1000

    LET i2 = rndpts(numpt,2)/1000

for nearneigh = 1 to num_neigh

    LET minrate = 1e20   !initialize with a very large number

    FOR j = 1 to totpts

        LET j1 = pts(j,1)/1000      !convert from meters to km

        LET j2 = pts(j,2)/1000      ! convert from meters to km

      let j3 = pts(j,3)*1e6      !take age into account, convert from millions of years to
years

 !       let j3 = 1 !don't take age into account

let flag = 0

if nearneigh > 1 then

for xx = 1 to nearneigh-1

if nearpt(xx,1) = j1 and nearpt(xx,2) = j2 then

let flag = 1

!exit for

end if

next xx

end if

        IF flag = 0  then  !this point has not been used yet
```

```
LET reck_rate = (((i1-j1)^2 + (i2-j2)^2))*pi*j3  !this is the area*time


IF reck_rate < minrate then



  LET minrate = reck_rate

  let nearpt(nearneigh,1) = j1

  let nearpt(nearneigh,2) = j2

  let nearpt(nearneigh,3) = pts(j,3)

 end if

END IF


NEXT j

! sum the minimum areas

if minrate < j3 then let minrate = j3     !the 1/ut (ie, 1/minrate) term cannot be greater
than 1/t (ie, 1/j3)

let minarea(nearneigh) = minrate

!print nearpt(nearneigh,1),nearpt(nearneigh,2)

next nearneigh


let sumarea = 0

for nearneigh = 1 to num_neigh


let sumarea = sumarea + minarea(nearneigh)

!print nearneigh ,nearpt(nearneigh,3)

next nearneigh
```

```
let lambda(numpt) = nearneigh/sumarea

  NEXT numpt

END SUB
```

Application of Method 2. Spatial recurrence rate $\lambda_h(x, y)$ [equation 14] is calculated for the 8 km^2 area about the repository using the same data sets for a range of smoothing constants [Figure 6]. For h = 15 to 30 km, $\lambda_h(x,y) = 2.3 \times 10^{-4}$ to 6.0×10^{-4} volcanoes per square kilometer (v/km^2) at the repository with a maximum at h = 17-20 km for most data sets. At h < 15 km the recurrence rate drops with decreasing h to 0 at h = 8 km, the approximate distance between Northern Cone and the repository site. Letting λ_t = 5 v/my to 10 v/my, the probability of volcanic disruption of the repository (a = 8 km^2 and t = 10,000 yr) is calculated in Figure 7 for data set 1 (volcanoes formed < 5 Ma) and data set 2 (volcanoes formed < 2 Ma), with other calculations falling at intermediate values. Taking 15 km < h < 25 km, based on interpretation of the cluster analysis (Figure 2), the probability of volcanic disruption of the repository in 10,000 yr is between 1.6×10^{-4} and 4.6×10^{-4}. Maps of the probability of volcanic eruption throughout the region are plotted in Figures 8a and 8b. The clustered nature of volcanism in the YMR is clearly illustrated on these maps, as is the overall NNW-trend in post-5 Ma vent distribution. The probability of volcanic eruption drops to zero very close to the log P[n = 1, a = 8km^2, t = 10,000yr] = -4.5 contour, for h = 20 km.

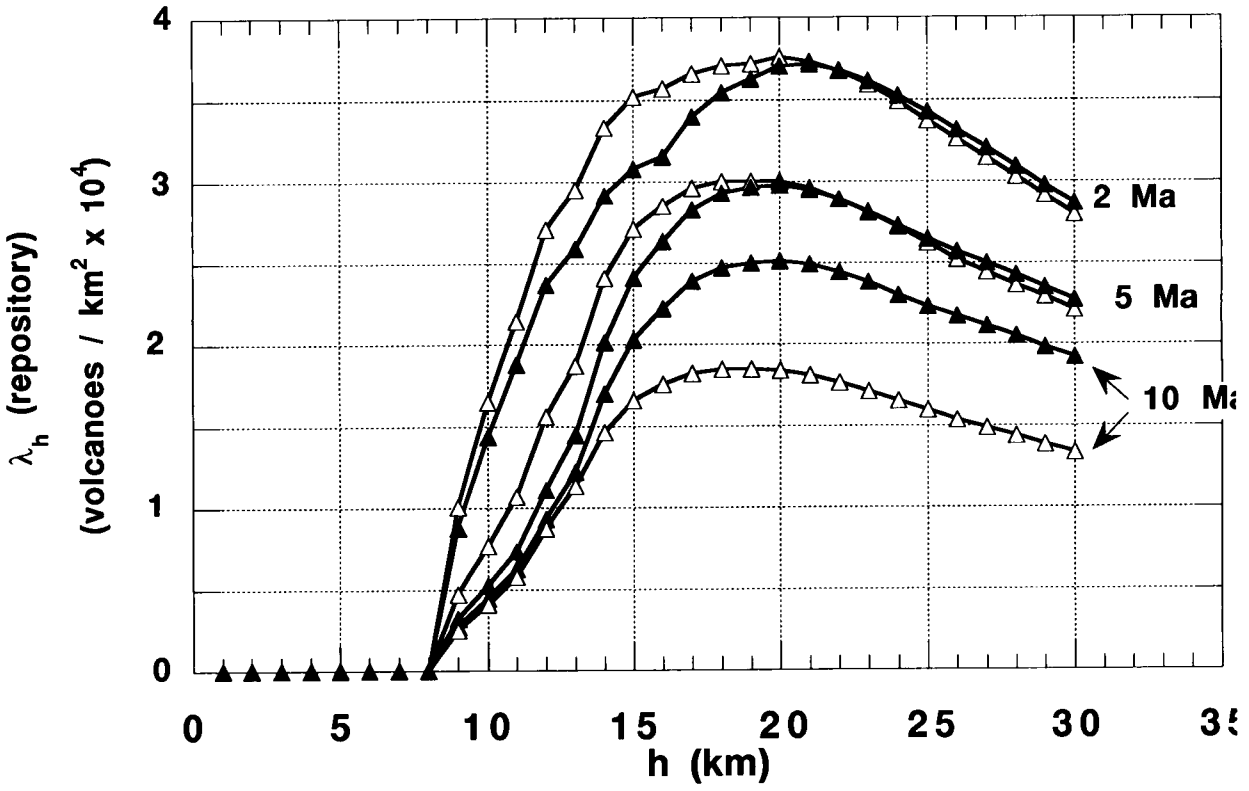
4
3
2
1
0
0
5
10
15
20
25
30
35
h (km)
λh (repository)
(volcanoes / km2 x 10-4)
2 Ma
5 Ma
10 Ma

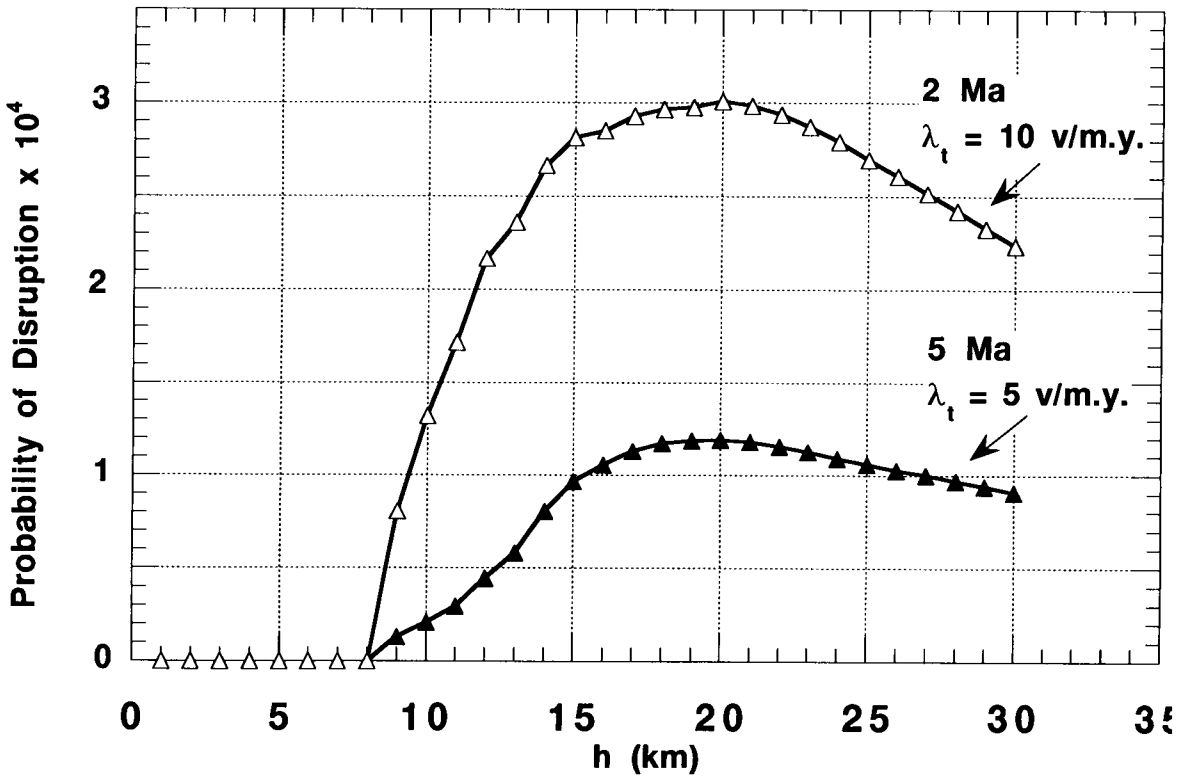
Probability of Disruption x 10^4
3
2
1
0
0
5
10
15
20
25
30
35
h (km)
2 Ma
λ_t = 10 v/m.y.
5 Ma
λ_t = 5 v/m.y.

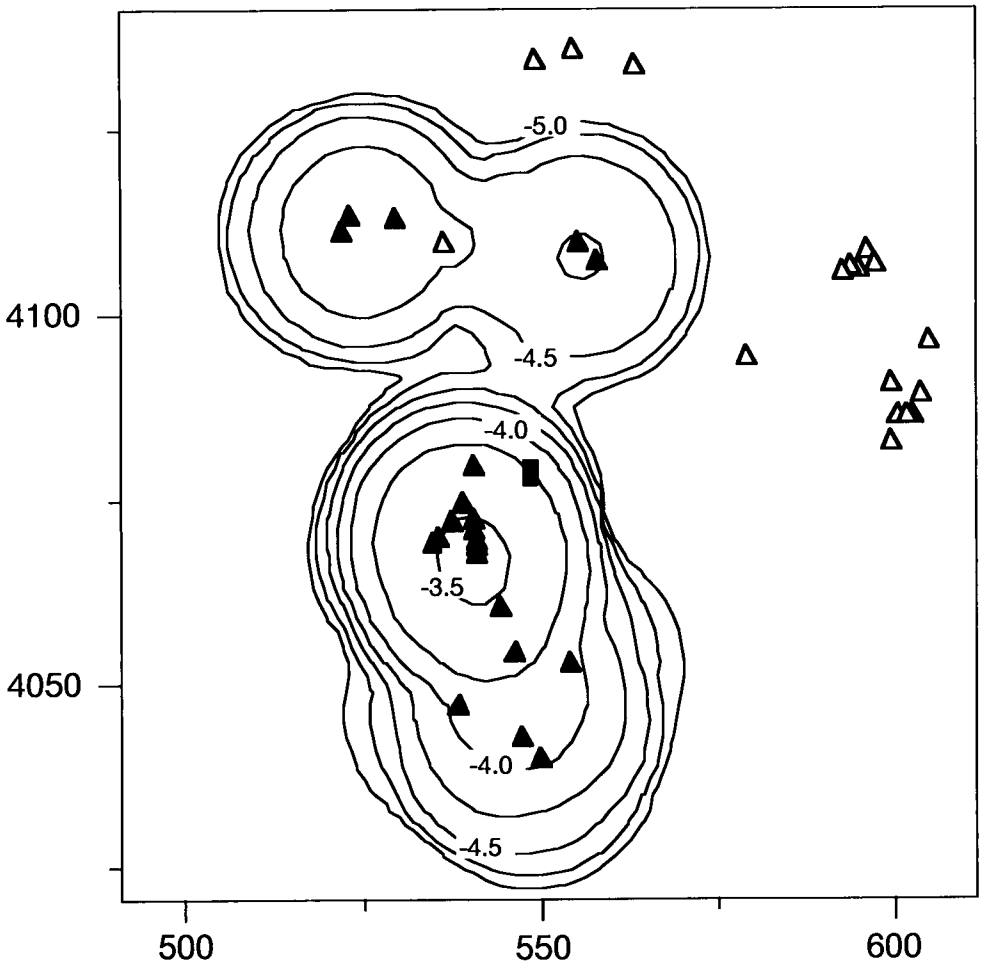
-5.0
-4.5
-4.0
-3.5
-4.0
-4.5
4100
4050
500
550
600

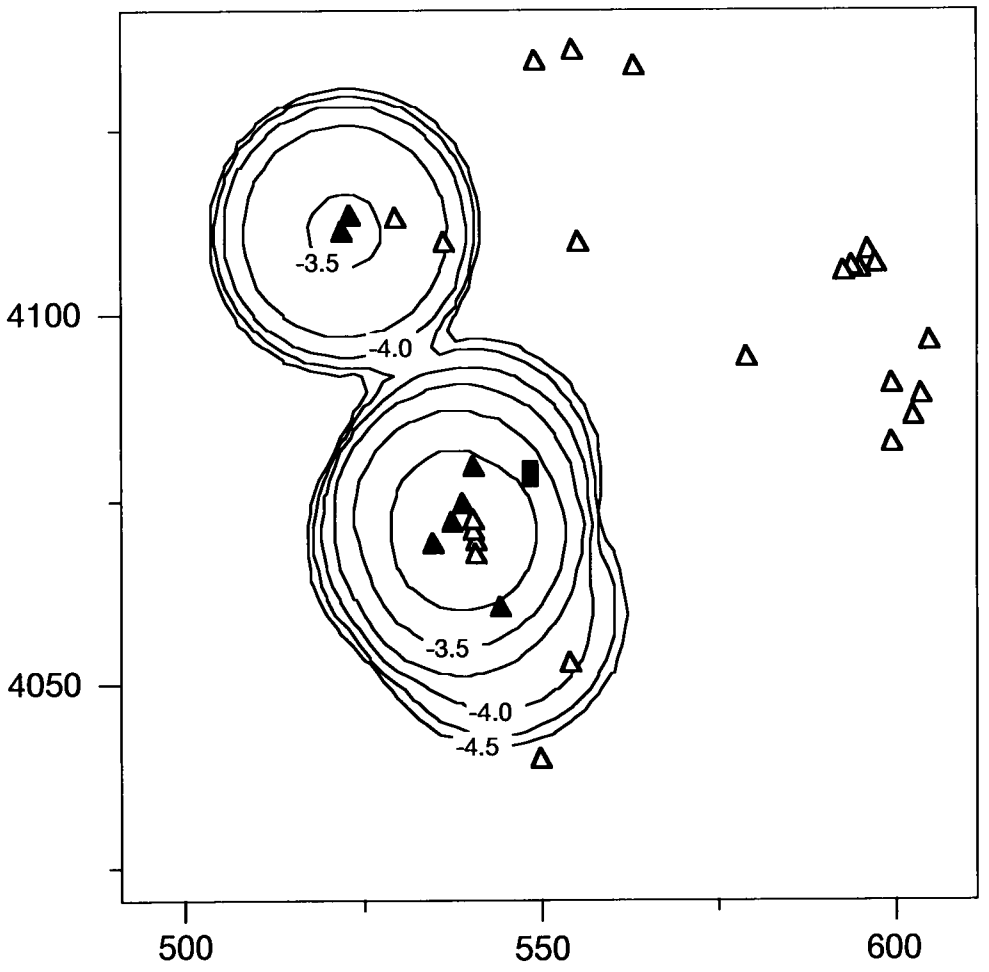

Application of Method 3. Spatial recurrence rate, $\lambda_r(x,y)$, is calculated at the repository site using equation 14 where the smoothing constant h is replaced by the distance to the m^{th} nearest-neighbor volcano. The maximum value of $\lambda_r(x,y)$ at the repository is estimated to be 4.2 x 10^{-4} v/km^2, for data set 2, using volcanoes less than 2 Ma and the fifth nearest-neighbor [Figure 9]. Each of the data sets goes through a maximum, the value of $\lambda_r(x,y)$ at the maximum depending on the number of volcanoes included in the analysis. Data sets of volcanoes less than 5 Ma and 10 Ma have maxima at the same number of nearest-neighbors because the nearest-neighbors to the repository are all less than 5 Ma. Nearly all estimates of $\lambda_r(x,y) > 1 \times 10^{-4}$ v/km^2 (Figure 9). Using volcanoes < 5 Ma, the probability of volcanic disruption of the repository site varies from P[$n = 1$, $a = 8$km^2, $t = 10{,}000$yr] = 5 x 10^{-5} to 1.5 x 10^{-4}. A maximum probability of 3.3 x 10^{-4} [Figure 10] is calculated using volcanoes < 2 Ma and $\lambda_t = 10$ v/my. Maps showing the variation in probability of volcanic eruption across the YMR calculated using $\lambda_r(x,y)$ are plotted in Figures 11a and 11b.

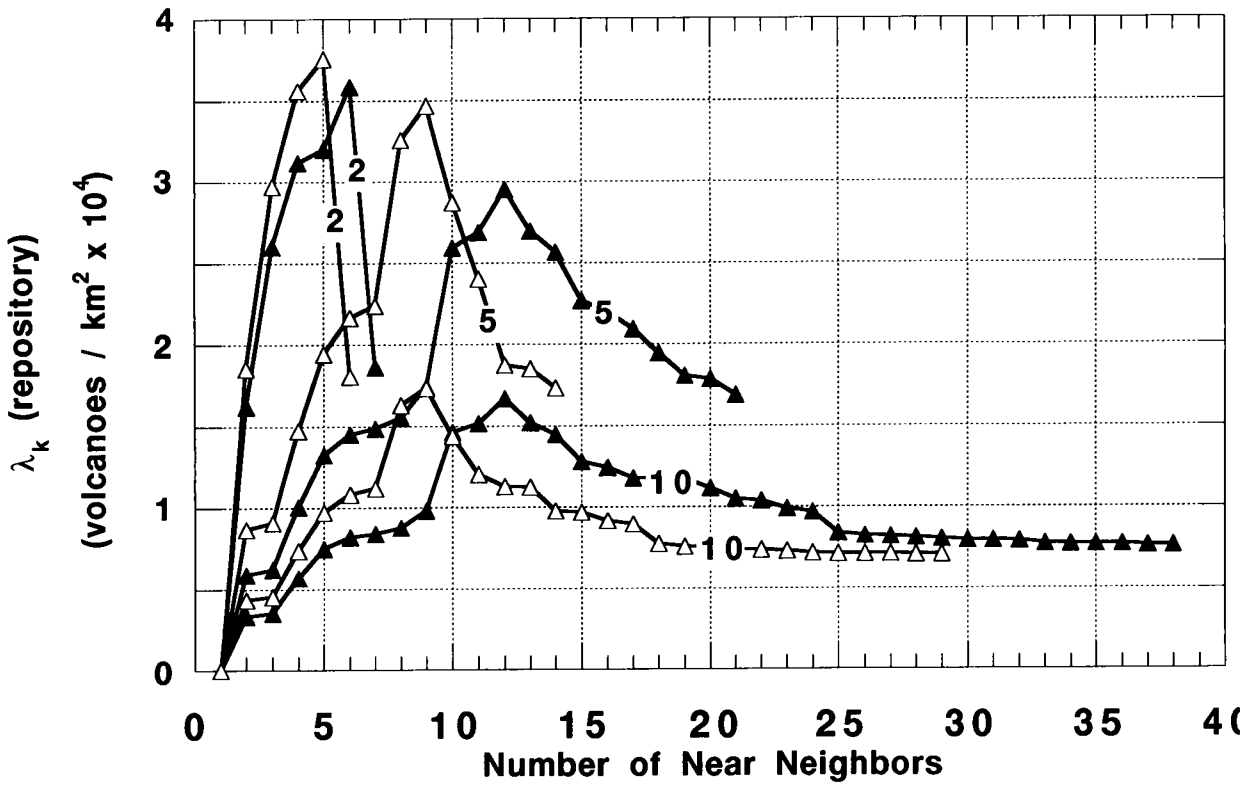
4
3
2
1
0
0
5
10
15
20
25
30
35
40
λ_k (repository)
(volcanoes / km^2 x 10^4)
Number of Near Neighbors
2
2
5
5
10
10

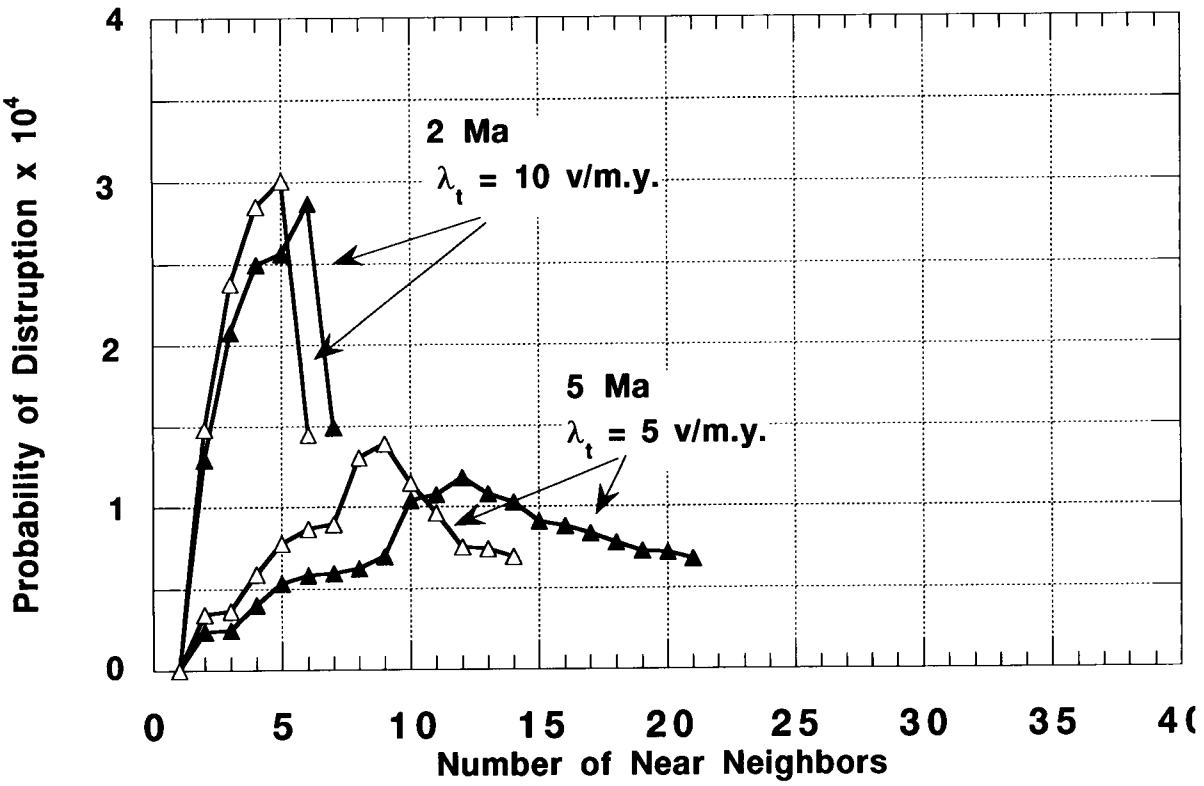
Probability of Distruption x 10^4
4
3
2
1
0
2 Ma
λ_t = 10 v/m.y.
5 Ma
λ_t = 5 v/m.y.
0
5
10
15
20
25
30
35
Number of Near Neighbors

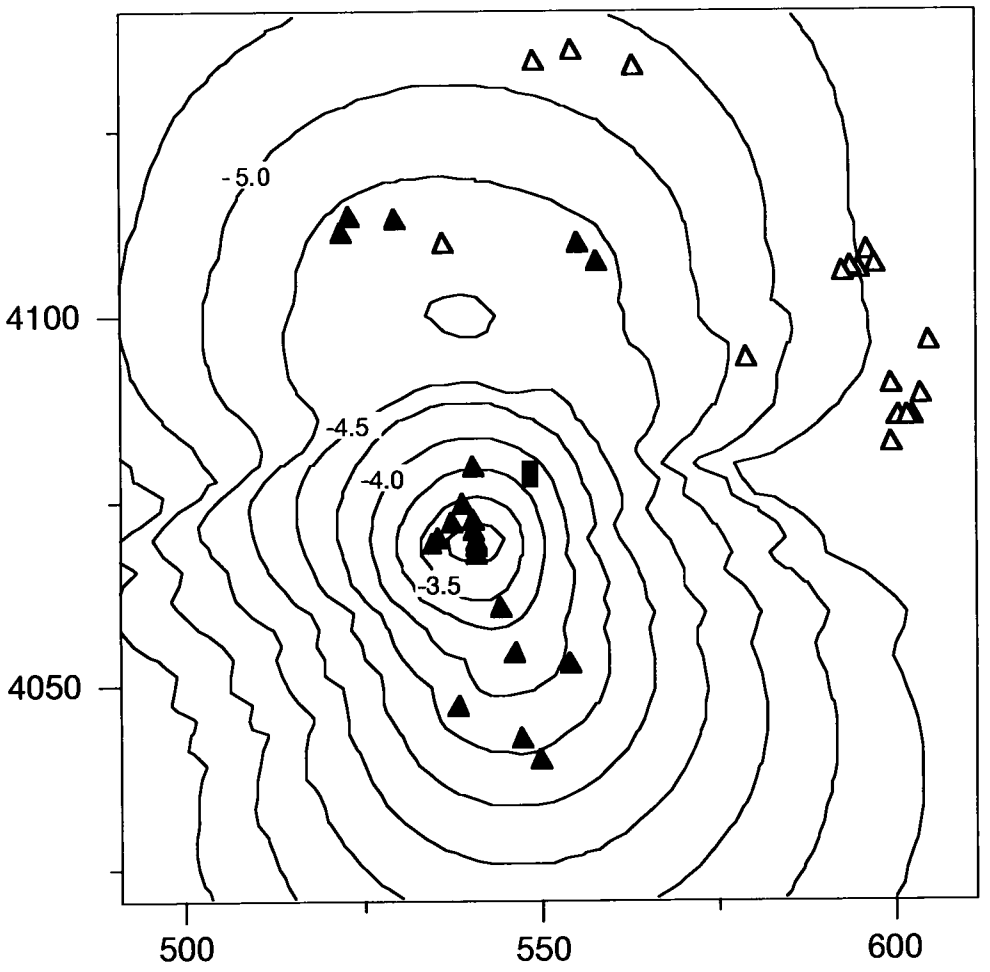
-5.0
-4.5
-4.0
-3.5
4100
4050
500
550
600

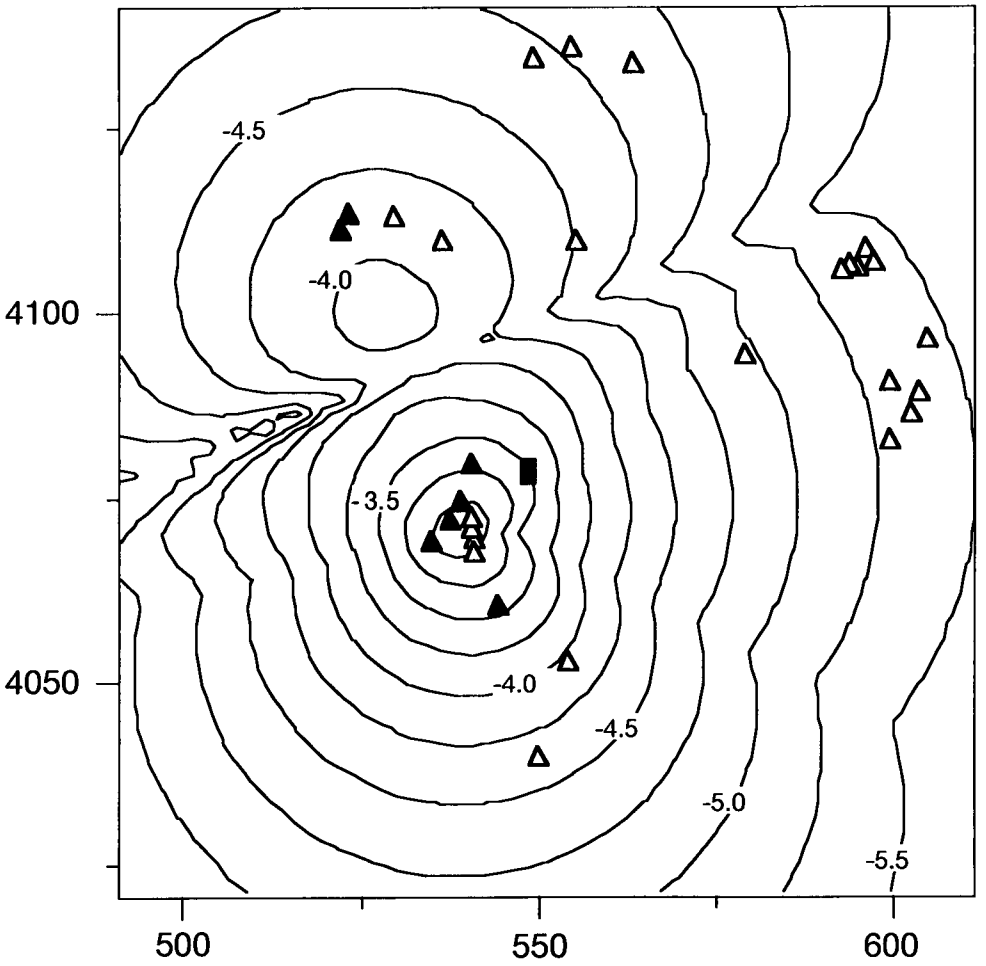

ISCUSSION

The three nonhomogeneous methods are sensitive to basic patterns in cinder cone distribution to varying degrees. These patterns include shifts in the location of cinder cone volcanism in time, cinder cone clustering, and the presence of vent and regional volcano alignments. These features of areal volcanic fields make nonhomogeneous models very useful for modeling volcano distributions and calculating the probability of future volcanic eruption within these areas.

Comparison of the Three Methods

Method 1 is most sensitive to shifts in the locus of cinder cone volcanism through time because equation [4] incorporates time since volcano formation directly into the recurrence rate estimate. Thus, using all post-caldera basalts in the calculation of probability of future volcanic eruption in the YMR, method 1 produces a small mode in probability

at Late Miocene clusters, but this mode is distinctly smaller than the Crater Flat mode [Figure 5a]. Using methods 2 and 3 and the same data, modes at Crater Flat and in Late Miocene clusters are of nearly equal amplitude. However, application of method 1 to many other volcanic fields is also more difficult because the ages of all volcanoes in the region must be known with reasonable precision. In areas where shifts in the locus of volcanism are as temporally distinct as they are in the YMR, methods 2 and 3 are easily adapted by subdividing the volcano data set on the basis of age, as was done for the YMR. Method 2 is least sensitive to shifts in the location of volcanism because the probability of volcanic eruption is zero at distances greater than the smoothing constant if the Epanechnikov kernel is used [equation 13].

Cinder cone clusters are common and well-documented in basaltic volcanic fields [e.g., *Heming*, 1980; *Connor*, 1990]. This clustering may be the result of various geologic controls on cinder cone emplacement, including the size, distribution, and longevity of partial melt zones, or possibly the heterogeneity of extension rates within the crust [*Heming*, 1980; *Connor*, 1990]. Geological factors such as these suggest a mechanistic basis for application of temporally and spatially nonhomogeneous Poisson probability models. The three nonhomogeneous methods treat clusters using different criteria, with varying results. Method 2 presupposes that volcano density and distance between volcanoes best defines clustering. As a result, for example, method 2 effectively identifies the Sleeping Butte area as a cluster of three volcanoes (Hidden Cone, Little Black Peak, and Thirsty Mountain), in a manner quite consistent with the cluster analysis [Figures 8a and 8b]. Methods 1 and 3 presuppose that the number of volcanoes, or volcanic events, is the predominant characteristic defining clusters. Therefore, these methods weight rates of volcanic activity between clusters much more heavily than does method 2. For example, methods 1 and 3 do not identify a separate cluster in the Sleeping Butte area, because only three volcanoes define the cluster [e.g., Figures 5a and 11a]. Rather, contour lines tend to elongate between the Sleeping Butte Cluster and the Crater Flat Cluster when recurrence rate is determined using methods 1 and 3, and probability of volcanic eruption in the center of the Crater Flat Cluster is calculated to be comparatively high.

All three methods respond to the presence of regional volcano alignments. In the YMR, the NNW trend of the CFVZ is reflected in the overall shape of the probability surfaces calculated using the three methods [Figures 5b, 8a, and 11a]. It is possible to model existing local vent alignments, such as the vent alignments within the Crater Flat Cluster, by decreasing the smoothing constant, h, in method 2 [*Lutz and Gutmann*, 1995] or decreasing the number of nearest-neighbors used in methods 1 and 3. In the case of the YMR, this is achieved by choosing $h < 5$ km or $m \leq 3$ nearest-neighbor volcanoes.

Probability of Volcanic Disruption of the Proposed Yucca Mountain Repository

Volcano clustering in the YMR is statistically significant at the 95% confidence level. Probability models based on a homogeneous Poisson density distribution will overesti-

mate the likelihood of future igneous activity in parts of the YMR far from Quaternary centers and underestimate the likelihood of future igneous activity within and close to Quaternary volcano clusters.

The probability of volcanic disruption of the proposed HLW repository site, calculated using the three nearest-neighbor methods, is consistently between 1×10^{-4} and 5×10^{-4} in 10,000 yr for an 8 km^2 area. This range is close to, or slightly higher than, ranges indicated by most calculations based on homogeneous Poisson models. For example, *Crowe et al.* [1982] propose a range of probability of disruption between 3.3×10^{-6} and 4.7×10^{-4} in 10,000 yr, noting that only a "worst case" model leads to probabilities in excess of 1×10^{-4}. Other reported ranges between 1×10^{-6} and 1×10^{-4} in 10,000 yr [*Crowe et al.*, 1992a] are close to the probabilities calculated using nearest-neighbor nonhomogeneous models. Differences, especially at the lower bound, arise because the candidate repository site is relatively close to the youngest large volcano cluster in the YMR. More recently, *Crowe et al.* [1993] proposed a range of models using various area terms and calculated probabilities of disruption between 9×10^{-5} and 2.6×10^{-4} in 10,000 yr. "Worst case" homogeneous Poisson models of repository disruption in which structural controls, such as those that may have resulted in the alignment of cinder cones in Crater Flat, are assumed to focus magmatism [*Smith et al.*, 1990; *Ho*, 1992] and result in probabilities as high as 1×10^{-3} in 10,000 yr. The nonhomogeneous models developed here do not support such high probabilities for the candidate repository site, because they do not include this kind of mechanistic control. It is noted that the nonhomogeneous methods do, however, give probabilities as high as 1×10^{-3} in 10,000 yr near the center of the Crater Flat Cluster.

The basic agreement between many of these estimates of the probability of volcanic disruption of the proposed repository site must be tempered, however, by a fundamental result of the spatial and spatio-temporal nonhomogeneous techniques developed here. All three nonhomogeneous methods indicate that the proposed repository is positioned on a probability gradient due to its proximity to Crater Flat. Immediately west of the proposed site, the probability of volcanism within the next 10,000 years increases to at least 1×10^{-3} in 10,000 yr due to the presence of Quaternary volcanoes in Crater Flat Valley. However, the probability of volcanism within the next 10,000 years decreases east of the proposed repository site.The probability of a new volcano forming within an 8 km^2 area located 20 km east of the site is on the order of 1×10^{-5} in 10,000 yr or less. This rapid change in probability, resulting from clustering in volcano distribution, has important implications for the uncertainty associated with the use of probability models. Within 20 km of the proposed site, the probability of volcanism during the next 10,000 yr and within a given 8 km^2 area varies by more than two orders of magnitude. Given the rapid change in probability across the area, it seems likely that additional geologic information, such as the role of pre-existing structure [*Smith et al.*, 1990; *McDuffie et al.*, 1994] or strain rate [*Parsons and Thompson*, 1991], may alter estimates of the probability of future volcanic activity at the proposed repository site.

The use of the estimates of regional recurrence rate, λ_t, and the area term for repository disruption, a [equations 15 and 16], and the effect of these assumed values on probability values warrants further discussion. Values of regional recurrence rate of new volcano formation used in the calculations presented here are 5 -10 v/my. It is a simple matter to recalculate probabilities using different regional recurrence rates. For example, using the range of spatial recurrence rates found using the kernel method (Figure 6), $a = 8$ km^2, and $t = 10{,}000$ yr, the probability of volcanic eruption at the repository site varies from 4.5×10^{-5} to 5.8×10^{-4} for $\lambda_t = 2$ to 12 v/my.

Throughout the preceding calculations, λ_t represents the estimated recurrence rate of new volcano formation in the YMR. Some of the geochemical, geomorphological and geochronological variation present at some YMR Quaternary volcanoes is thought to represent reactivation of these volcanoes after more than 10,000 yr quiescence [*Wells et al.*, 1990; *Crowe et al.*, 1992b; *Bradshaw and Smith*, 1994]. However, results from some other studies appear to contradict this interpretation [*Champion*, 1991; *Turrin et al.*, 1991], which remains controversial [*Whitney and Shroba*, 1991; *Wells et al.*, 1991; 1992; *Turrin et al.*, 1992]. Given the possibility of cinder cone reactivation, the range of λ_t of 5 - 10 v/my may underestimate the rate of volcanic eruptions that will occur in the future in the YMR. However, λ_t is only intended to represent an estimate of the rate of new volcano formation. This is the same as the eruption rate in a monogenetic model but less than the eruption rate in a reactivated volcano model. In the context of volcanic hazards for the proposed repository, the spatially dispersed character of volcanism gives rise to hazards, rather than the reactivation of an existing cinder cone, and λ_t is defined accordingly.

Variation in the repository area term also results in variation in probability estimates. As mentioned above, the total area of the repository is currently estimated to be about 6 km^2. The area radioactive waste occupies within repository depends on design, but varies from about 2.3 km^2 for a high thermal load repository to 4.6 km^2 for a lower thermal load repository [*Wilson et al.*, 1994]. Our calculations have been for 8 km^2, which includes the total area of the repository and a buffer zone extending 500 m out from the repository perimeter. This is done in recognition that satellite vents and other direct disruptive effects commonly extend for about 500 m from the central vent. In addition, this buffer accounts for some of the possible deleterious effects of volcanism within a short distance of the repository, such as adverse impact on the hydrological and geochemical setting of the repository. Changing the area term from $a = 8$ km^2 to $a = 4$ km^2 will decrease the range of probability estimates by about a factor of two. Using $a = 4$ km^2 (i.e., low thermal load design) to calculate probability of volcanic disruption implies that volcanism is a point source, and that volcanism close to, but not within, a waste storage area has no impact on the isolation of radionuclides. Such assumptions do not seem conservative; consequently a larger area term is used.

In a similar way, increasing the value of a will increase probability estimates. This is particularly important when probability estimates are made assuming distributed volcanoes represent a single event. This was done in data set 2 by treating NE and SW Little Cones as single events. As a further example, it is possible to consider episodes of cone-alignment formation, such as the formation of the Quaternary Crater Flat alignment, to be single events. Of course, this reduces both the total number of volcanic events in the region and the regional recurrence rate, λ_t. However, the value of a must be increased to reflect the area impacted by the entire cone alignment.

Experimentation with values of λ_t and a indicates that they have a very limited effect on probability calculations when considered together. Although these variables are important, spatial variation dominates uncertainty in the probability analysis. This salient point illustrates the basic advantages of applying spatially nonhomogeneous methods to volcanic hazards problems.

CONCLUSIONS

Nearest-neighbor estimates of spatial and spatio-temporal variation in the recurrence rate of basaltic volcanism can account, to varying degrees, for several basic features of volcano distribution in areal basaltic fields. These features include spatial shifts in the locus of volcanism, clustering of volcanoes within the field, and the occurrence of volcano alignments. A strength of nearest-neighbor methods is that uncertainty can be estimated, both by mapping variation in the probability surface across the region of interest and through experimentation encompassing the precision and accuracy of geochronological information.

Application of the Hopkins F-test and related methods shows that cinder cones cluster in the YMR with greater than 95% confidence. Assuming a regional Quaternary recurrence rate of 5 to 10 v/my, these models estimate probabilities of disruption are generally between 1×10^{-4} and 5×10^{-4} in 10,000 yr, in close agreement with some other recent estimates. However, spatial variation in estimated recurrence rate is substantial across the YMR, with the probability of volcanic eruption varying by more than two orders of magnitude within 20 km of the proposed repository site. This variation indicates that refinement of models, primarily through the incorporation of additional geological information, may alter these probability estimates significantly.

Acknowledgments: Budhi Sagar and William M. Murphy made important contributions to this work. Thorough reviews by Bruce Crowe, Ken Foland, Tim Lutz, Bill Melson,

Eugene Smith, and two anonymous reviewers are greatly appreciated. Tim Lutz first suggested the use of method 2. Careful C and PERL programming by Laura Connor and DEM work by Brent Henderson and Ron Martin is gratefully acknowledged. This manuscript is the result of work performed at the Center for Nuclear Waste Regulatory Analyses (CNWRA) for the U.S. Nuclear Regulatory Commission (NRC) under contract No. NRC-02-93-005. This report is an independent product of the CNWRA and does not necessarily reflect the views or regulatory position of the NRC.

REFERENCES

Aherne, W.A., and P.J. Diggle, The estimation of neuronal population density by a robust distance method, *J. of Microscopy, 114*, 285—293, 1978.

Bacon, C.R., Time-predictable bimodal volcanism in the Coso Range, California, *Geology, 10*, 65—69, 1982.

Bemis, K.G., and D.K. Smith, Production of small volcanoes in the Superswell region of the South Pacific, *Earth Planet. Sci. Lett., 118*, 251—262, 1993.

Bradshaw, T.K., and E.I. Smith, Polygenetic Quaternary volcanism at Crater Flat, Nevada, *J. Volcanol. Geotherm. Res., 63,* 165—182, 1994.

Braytseva, O.A., I.V. Melekestev, and V.V. Ponomareva, Age divisions of the Holocene volcanic formations of the Tolbachik Valley, in *The Great Tolbachik Fissure Eruption, Geological and Geophysical data, 1975-1976*, edited by S.A. Fedotov and Ye. K. Markhnin, pp. 83—95, Cambridge University Press, Cambridge, 1983.

Byers, F.M., and H. Barnes, Geologic map of the Paiute Ridge Quadrangle, Nye County, Nevada, *U.S. Geol. Surv. Geological Quadrangle Map GQ-577*, 1967.

Byers, F.M., and D. Cummings, Geologic map of the Scrugham Peak Quadrangle, Nye County, Nevada, *U.S. Geol. Surv. Geological Quadrangle Map GQ-695*, 1967.

Byers, F.M., C.L. Rogers, W.J. Carr, and S.J. Luft, Geologic map of the Buckboard Mesa Quadrangle, Nye County, Nevada, *U.S. Geol. Surv. Geological Quadrangle Map GQ-552*, 1966.

Byth, K., and B.D. Ripley, On sampling spatial patterns by distance methods, *Biometrics, 36*, 279—284, 1980.

Carr, W.J., Regional and structural setting of Yucca Mountain, Southwestern Nevada, and late Cenozoic rates of tectonic activity in part of the southwestern Great Basin, Nevada and California, *U.S. Geol. Surv. Open File Rep. 84-854*, 1984.

Carr, W.J., and W.D. Quinlivan, Geologic map of the Timber Mountain Quadrangle, Nye County, Nevada, *U.S. Geol. Surv. Geological Quadrangle Map GQ-503*, 1966.

Champion, D.E., Volcanic episodes near Yucca Mountain as determined by paleomagnetic studies at Lathrop Wells, Crater Flat, and Sleeping Butte, Nevada, *Second International Conference on High-Level Radioactive Waste Management,* Las Vegas, NV, American Nuclear Society, 61-67, 1991.

Clark, P.J., and F.C. Evans, On some aspects of spatial pattern in biological populations, *Science, 121*, 397—398, 1955.

Condit, C.D., L.S. Crumpler, J.C. Aubele, and W.E. Elston, Patterns of volcanism along the southern margin of the Colorado Plateau: the Springerville Field. *J. Geophys. Res., 94*, 7,975—7,986, 1989.

Connor, C.B, Cinder cone clustering in the TransMexican volcanic belt: structural and petrologic implications, *J. Geophys. Res., 95*, 19,395—19,405, 1990.

Connor, C.B., and C.D. Condit, Estimating recurrence rate of volcanism in the Springerville volcanic field, Arizona, *Geol. Soc. Am. Abstr. Programs,* Seattle, Washington, A-115, 1994.

Connor, C.B., C.D. Condit, L.S. Crumpler, and J.C. Aubele, Evidence of regional structural controls on vent distribution: Springerville volcanic field, Arizona. *J. Geophys. Res., 97*, 12,349—12,359, 1992.

Cornwall, H.R., Geology and mineral deposits of Southern Nye County, Nevada, *Nevada Bur. Mines and Geo. Bull. 77*, 1972.

Cressie, N.A.C., *Statistics for Spatial Data*, 900 pp., John Wiley and Sons, New York, 1991.

Crowe, B.M., Probabilistic volcanic risk assessment, *Presentation to the Advisory Committee on Nuclear Waste*, Bethesda, Maryland, 1994.

Crowe, B.M., and F.V. Perry, Volcanic probability calculations for the Yucca Mountain site: estimation of volcanic rates, *Proceedings Nuclear Waste Isolation in the Unsaturated Zone, Focus '89*, American Nuclear Society, 326—334, 1989.

Crowe, B., and F. Perry, Preliminary geologic map of the Sleeping Butte Volcanic Centers, *Los Alamos National Laboratory Report LA-12101-MS*, 1991.

Crowe, B.M., M.E. Johnson, and R.J. Beckman, Calculation of the probability of volcanic disruption of a high-level nuclear waste repository within southern Nevada, USA, *Radioactive Waste Management and the Nuclear Fuel Cycle, 3*, 167—190, 1982.

Crowe, B.M., D.T. Vaniman, and W.J. Carr, Status of volcanic hazard studies for the Nevada nuclear waste storage investigations, *Los Alamos National Laboratory Report LA-9325-MS*, 1983.

Crowe, B.M., K.H. Wohletz, D.T. Vaniman, E. Gladney, and N. Bower, Status of volcanic hazard studies for the Nevada nuclear waste storage investigations, *Los Alamos National Laboratory Report LA-9325- MS, Vol. II*, 1986.

Crowe, B.M., C. Harrington, L. McFadden, F. Perry, S. Wells, B. Turrin, and D. Champion, Preliminary geologic map of the Lathrop Wells Volcanic Center, *Los Alamos National Laboratory Report LA-UR-88- 4155*, 1988.

Crowe, B.M., R. Picard, G. Valentine, and F.V. Perry, Recurrence models for volcanic events: Applications to volcanic risk assessment, *Third International Conference on High-Level Radioactive Waste Management*, Las Vegas, NV, American Nuclear Society, 2344—2355, 1992a.

Crowe, B., R. Morley, S. Wells, J. Geissman, E. McDonald, L. McFadden, F. Perry, M. Murrell, J. Poths, and S. Forman, The Lathrop Wells volcanic center: Status of field and geochronology studies, *Third International Conference on High-Level Radioactive Waste Management*, Las Vegas, NV, American Nuclear Society, 1997—2,013, 1992b.

Crowe, B.M., F.V. Perry, G.A. Valentine, P.C. Wallmann, and R. Kossik, Simulation modeling of the probability of magmatic disruption of the potential Yucca Mountain site, *Proceedings, Site Characterization and Model Validation, Focus '93,* Las Vegas, NV, American Nuclear Society, 182—191, 1993.

Diggle, P.J., A note on robust density estimation for spatial point patterns, *Biometrika, 64,* 91—95, 1977.

Diggle, P.J., On parameter estimation for spatial point patterns, *J. Royal Statistical Soc., B 40,* 178—181, 1978.

Diggle, P.J., A kernel method for smoothing point process data, *Applied Statistics 34,* 138—147, 1985.

DOE, Site Characterization Plan: Yucca Mountain Site, Nevada Research and Development Area, Nevada, *DOE/RW-0199,* U.S. Department of Energy, Office of Radioactive Waste Management, Washington D.C., 1988.

Dohrenwend, J.C., L.D. MacFadden, B.D. Turrin, and S.G. Wells, K-Ar dating of the Cima volcanic field, eastern Mojave Desert, California: Late Cenozoic volcanic history and landscape evolution, *Geology, 12,* 163—167, 1984.

Draper, G., Z. Chen, M. Conway, C.B. Connor, and C.D. Condit, Structural control on magma pathways in the upper crust: insights from the San Francisco volcanic field, Arizona, *Geol. Soc. Am. Abstr. Programs,* Seattle, Washington, *A-115,* 1994.

Duffield, W.A., C.R. Bacon, and G.B. Dalrymple, Late Cenozoic volcanism, geochronology, and structure of the Coso Range, Inyo County, California, *J. Geophys. Res., 85,* 2381—2404, 1980.

Eichelberger, J.C., and R. Gooley, Evolution of silicic magma chambers and their relationship to basaltic volcanism, in *The Earth's Crust,* edited by J.G. Heacock, American Geophysical Union Monograph, 20, 57—77, 1977.

Ekren, E.B., R.E. Anderson, P.P. Orkild, and E.N. Hinrichs, Geologic map of the Silent Butte Quadrangle, Nye County, Nevada, *U.S. Geol. Surv. Geological Quadrangle Map GQ-493*, 1966.

Faulds, J.E., J.W. Bell, D.L. Feuerbach, and A.R. Ramelli, Geologic map of the Crater Flat Area, Nevada, *Nevada Bur. Mines Geol. Map 101*, 1994.

Fleck, R.J., B.D. Turrin, D.A. Sawyer, R.G. Warren, D.E. Champion, M.R. Hudson, and S.A. Minor, Age and character of basaltic rocks of the Yucca Mountain region, southern Nevada, *J. Geophys. Res.*, submitted, 1994.

Foland, K.A., and S.C. Bergman, Temporal and spatial distribution of basaltic volcanism in the Pancake and Reveille ranges north of Yucca Mountain, High-Level Radioactive Waste Management, *Third International Conference on High-Level Radioactive Waste Management,* Las Vegas, NV, American Nuclear Society, 2366—2371, 1992.

Hasenaka, T., and I.S.E. Carmichael, The cinder cones of Michoacán-Guanajuato, central Mexico, their age, volume, distribution, and recharge rate, *J. Volcanol. Geotherm. Res., 25*, 195—204, 1985.

Heizler, M.T., W.C. McIntosh, F.V. Perry, and B.M. Crowe, $^{40}Ar/^{39}Ar$ results of incompletely degassed sanidine: age of Lathrop Wells volcanism, *U.S. Geol. Surv. Circular, 1107*, 133, 1994.

Heming, R.F., Patterns of Quaternary basaltic volcanism in the northern North Island, New Zealand, *New Zealand J. Geol. Geophys., 23*, 335—344, 1980.

Hinrichs, E.N., Krushensky, R.D., and S.J. Luft, Geologic map of the Ammonia Tanks Quadrangle, Nye County, Nevada. *U.S. Geol. Surv. Geological Quadrangle Map GQ-638*, 1967.

Ho, C.-H., Risk assessment for the Yucca Mountain high-level nuclear waste repository site: estimation of volcanic disruption, *Math. Geol., 24*, 347—364, 1992.

Ho, C.-H., Time trend analysis of basaltic volcanism at the Yucca Mountain site, *J. Volcanol. Geotherm. Res., 46*, 61—72, 1991.

Ho, C.-H., E.I. Smith, D.L. Feuerbach, and T.R. Naumann, Eruptive probability calculation for the Yucca Mountain site, USA: statistical estimation of recurrence rates, *Bull. Volcanol., 54*, 50—56, 1991.

Kane, M.F., and R.E. Bracken, Aeromagnetic map of Yucca Mountain and surrounding regions, southwest Nevada, *U.S. Geol. Surv. Open-File Report 83-616*, 19 pp., 1983.

Kear, D., Volcanic alignments north and west of New Zealand's central volcanic region, *New Zealand J. Geol. Geophys., 7*, 24—44, 1964.

Langenheim, V.E., K.S. Kirchoff-Stein, and H.W. Oliver, Geophysical investigations of buried volcanic centers near Yucca Mountain, southwestern Nevada. *Fourth International Conference on High-Level Radioactive Waste Management*, Las Vegas, NV, American Nuclear Society, 1840—1846, 1993.

Lutz, T.M., An analysis of the orientations of large scale crustal structures: A statistical approach based on areal distributions of pointlike features, *J. Geophys. Res., 91*, 421—434, 1986.

Lutz, T.M., and J.T. Gutmann, An improved method of determining alignments of pointlike features and its implications for the Pinacate volcanic field, Mexico, *J. Geophys. Res.*, in press, 1995.

Magus'kin, V.B. Enman, and V.S. Tselishchev, Changes in the height, volume, and shape of the New Tolbachik volcanoes of the Northern Breakthrough, in *The Great Tolbachik Fissure Eruption, Geological and Geophysical data, 1975-1976*, edited by S.A. Fedotov and Ye. K. Markhnin. Cambridge University Press, Cambridge, 307—315, 1983.

Margulies, T., L. Lancaster, N. Eisenberg, and L. Abramson, Probabilistic analysis of magma scenarios for assessing geologic waste repository performance, *92-WA/SAF-11*, American Society of Mechanical Engineers, New York, 1992.

McBirney, A.R., Volcanology, in *Techniques for Determining Probabilities of Geologic Events and Processes*, edited by R.L. Hunter and C.J. Mann, Studies in Mathematical Geology No. 4, Oxford University Press, New York, 167—184, 1992.

McDuffie, S., C.B. Connor, and K.D. Mahrer, A simple model of fault-dike interaction, *EOS Trans. AGU 75 (16)*, 345, 1994.

Nakamura, K., Volcanoes as possible indicators of tectonic stress orientation - principles and proposal, *J. Volcanol. Geotherm. Res., 2*, 1—16, 1977.

Noble, D.C., R.D. Krushensky, E.J. McKay, and J.R. Ege, Geologic Map of the Dead Horse Flat Quadrangle, Nye County, Nevada, *U.S. Geol. Surv. Geological Quadrangle Map GQ-614*, 1967.

Parsons, T., and G.A. Thompson, The role of magma overpressure in suppressing earthquakes and topography: worldwide examples, *Science, 253*, 1399—1402, 1991.

Perry, F.M., Update on characterization of volcanic features, *Presentation to the Advisory Committee on Nuclear Waste*, Bethesda, MD, 1994.

Poths, J., and Crowe, B.M., Surface exposure ages and noble gas components of volcanic units at the Lathrop Wells volcanic center, Nevada. *EOS Trans. AGU, 73*, 610, 1992.

Poths, J., F. Perry, and B.M. Crowe, ^{3}He surface exposure ages at the Lathrop Wells, NV, volcanic center, *U.S. Geol. Surv. Circular 1107*, 255, 1994.

Ripley, B.D., Modelling spatial patterns, *J. Royal Stat. Soc., B39,* 172—212, 1977.

Ripley, B.D., Spatial statistics, in *Wiley Series in Probability and Mathematics*, John Wiley and Sons, New York, 252 pp., 1981.

Sawyer, D.R., R.J. Fleck, M.A. Lanphere, R.G. Warren, D.E. Broxton, and M.R. Hudson, Episodic caldera volcanism in the Miocene southwestern Nevada volcanic field: Revised stratigraphic framework, $^{40}Ar/^{39}Ar$ geochronology, and implications for magmatism and extension, *Geol. Soc. Am. Bull., 106,* 1304—1318, 1994.

Settle, M., The structure and emplacement of cinder cone fields, *Am. J. Sci., 279,* 1089—1107, 1979.

Sheridan, M.F., A Monte Carlo technique to estimate the probability of volcanic dikes, *Third International Conference on High-Level Radioactive Waste Management*, Las Vegas, NV, American Nuclear Society, 2033—2038, 1992.

Silverman, B.W., *Density Estimation for Statistics and Data Analysis*, Chapman and Hall, London, 175 pp., 1986.

Sinnock, S., and R.G. Easterling, Empirically determined uncertainty in potassium-argon ages for Plio- Pleistocene basalts from Crater Flat, Nye County, Nevada, *Sandia National Laboratory Report SAND 82- 2441*, 1983.

Smith, E.I., T.R. Naumann, D.L. Feuerbach, and J.E. Faulds, The area of most recent volcanism near Yucca Mountain, Nevada: implications for volcanic risk assessment, *International Meeting on High-level Radioactive Waste Management*, Las Vegas, NV, American Nuclear Society, 81—90, 1990.

Späth, H., *Clustering Algorithms*, John Wiley and Sons, New York, 226 pp., 1980.

Swadley, W.C., and W.J. Carr, Geologic map of the Quaternary and Tertiary deposits of the Big Dune Quadrangle, Nye County, Nevada, and Inyo County, California, *U.S. Geol. Surv. Misc. Invest. Series Map I-1767*, 1987.

Takada, A., The influence of regional stress and magmatic input on styles of monogenetic and polygenetic volcanism, *J. Geophys. Res., 99*, 13,563—13,574, 1994.

Tanaka, K.L., E.M. Shoemaker, G.E. Ulrich, and E.W. Wolfe, Migration of volcanism in the San Francisco volcanic field, Arizona, *Geol. Soc. Am. Bull., 97*, 129—141, 1986.

Tokarev, P.I., Calculation of the magma discharge, growth in the height of the cone and dimensions of the feeder channel of Crater I in the Great Tolbachik Fissure Eruption, July 1975, in *The Great Tolbachik Fissure Eruption, Geological and Geophysical data, 1975-1976*, edited by S.A. Fedotov and Ye. K. Markhnin, Cambridge University Press, Cambridge, 27—35, 1983.

Tschanz, C.M, and E.H. Pampeyan, Geology and mineral deposits of Lincoln County, Nevada, *Nevada Bur. Mines Geol. Bull. 73*, 1970.

Turrin, B., New high-precision $^{40}Ar/^{39}Ar$ step heating results from basalts near Yucca Mountain, *U.S. Nuclear Waste Technical Review Board, Panel on Structural Geology and Engineering Meeting on Volcanism*, Las Vegas, NV, 1992.

Turrin, B.D., J.C. Dohrenwend, R.E. Drake, and G.H. Curtis, K-Ar ages from the Cima volcanic field, eastern Mojave Desert, California, *Isochron West, 44*, 9—16, 1985.

Turrin, B.D., D. Champion, and R.J. Fleck, $^{40}Ar/^{39}Ar$ age of the Lathrop Wells volcanic center, Yucca Mountain, Nevada, *Science, 253*, 654—657, 1991.

Turrin, B.D., D. Champion, and R.J. Fleck, Measuring the age of the Lathrop Wells volcanic center at Yucca Mountain: Response, *Science 257*, 556—558, 1992.

6.0 Additional method 2 figures

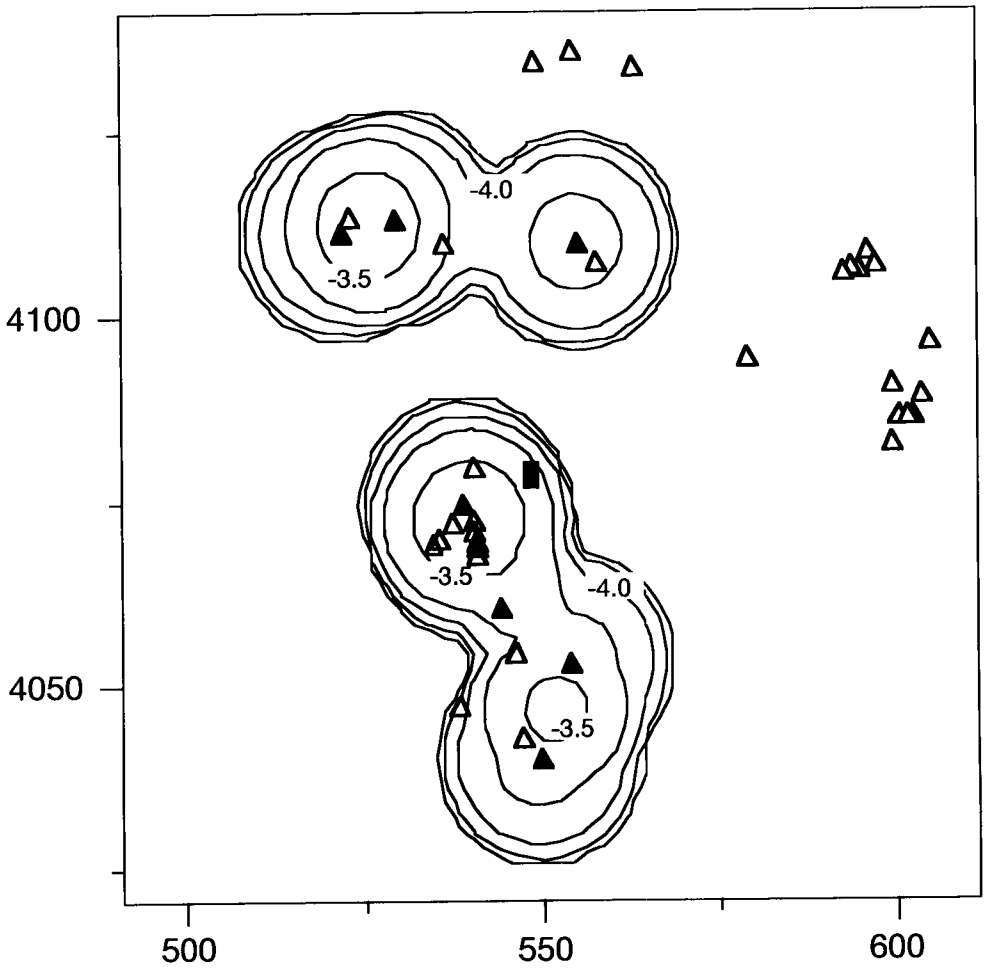

Above figure uses h = 20 km and only episodes of volcanism (less than 5 Ma). In other words, the crater flat alignment is treated as one event.

Table 1: Data used in the Analyses

Volcano (abbreviation)	UTM Coordinate	Age Estimate (Ma)	Source	Explanation	Data Set 1 (Ma)	Data Set 2 (Ma)
Quaternary						
Hidden Cone (hc)	523230E 4112530N	0.38±0.02	*Turrin* [1992]	Ar/Ar step-heating, 1 sample	0.36	0.4
Little Black Peak (lb)	522130E 4110340N	0.32±0.03	*Fleck et al.* [1994]	K-Ar, best estimated age from 4 measurements	0.29	0.35
Northern Cone (nc)	540330E 4079130N	1.09±0.07	*Faulds et al.* [1994]	K-Ar on plagioclase separate, 1 sample	1.02	1.16
Black Cone (bc)	538840E 4073990N	1.0±0.1 0.71±0.06	*Perry* [1994] *Faulds et al.* [1994]	Ar/Ar, average of 4 samples K-Ar on plagioclase separates, 1 sample	0.71	1.1
Red Cone (rc)	537450E 4071470N	1.0±0.1	*Faulds et al.* [1994]	K-Ar on plagioclase separates, average of 3 samples	0.90	1.1
Little Cone NE (lcne)	535500E 4069490N	0.77±0.04	*Faulds et al.* [1994]	K-Ar on plagioclase separate, 1 sample	0.77	—
Little Cone SW (lcsw)	535131E 4069220N	0.94±0.01 0.77±0.04	*Heizler et al.* [1994] *Faulds et al.* [1994]	Ar/Ar step heating of sanidine xenocyrsts, 1 sample K-Ar on plagioclase separate, 1 sample	0.77	0.94
Lathrop Wells (lw)	543780E 4060380N	0.1±0.05	*Crowe et al.* [1992] *Zreda et al.* [1991] *Poths et al.* [1994] *Turrin et al.* [1991]	U/Th series and Ar/Ar dates generally > 100 ka, ^{36}Cl and ^{3}He cosmogenic exposure dates generally < 90 ka	0.05	0.15
Pliocene						
Buckboard Mesa (bb)	554680E 4108970N	2.87±0.06	*Fleck et al.* [1994]	K/Ar, best estimated age from 4 samples	2.8	2.9

Table 1: Data used in the Analyses (continued)

Volcano (abbreviation)	UTM Coordinate	Age Estimate (Ma)	Source	Explanation	Data Set 1 (Ma)	Data Set 2 (Ma)
Buckboard Mesa SE (bbse)	556060E 4107580N	2.87±0.06		Assumed to correlate with main Buckboard Mesa vent	2.8	—
Crater Flat A (cfa)	540232E 4071610N	3.7±0.2	*Perry et al.* [1994]	Average of 3 Ar/Ar step-heating measurements, for undifferentiated Pliocene Crater Flat. All events in Pliocene Crater Flat are assumed to be relatively synchronous based on paleomagnetic work by *Champion* [1991]	3.5	3.9
Crater Flat B (cfb)	540330E 4070050N	3.7±0.2			3.5	3.9
Crater Flat C (cfc)	540365E 4068790N	3.7±0.2			3.5	3.9
Crater Flat D (cfd)	540696E 4067830N	3.7±0.2			3.5	3.9
Crater Flat E (cfe)	540300E 4068390N	3.7±0.2			3.5	—
Crater Flat F (cff)	540660E 4067470N	3.7±0.2			3.5	—
Amargosa Valley B (avb)	553720E 4052990N	4.3±0.1 3.8±0.1	*Turrin* [1992] *Perry* [1994]	Aeromagnetic anomaly [*Langenheim et al.*, 1993]; drilled and dated by Ar/Ar step-heating; *reversed* magnetic polarity	3.8	4.4
Amargosa Valley A (ava)	546130E 4054260N	3.8±0.1		Aeromagnetic anomaly [*Langenheim et al.*, 1993], not drilled; assumed to correlate with anomaly B	3.7	—
Amargosa Valley E (ave)	538300E 4047200N	3.8±0.1		Aeromagnetic anomaly [*Langenheim et al.*, 1993], not drilled; assumed to correlate roughly with anomaly B; *normal* polarity	3.7	—
Amargosa Valley C (avc)	547050E 4042950N	3.8±0.1		Aeromagnetic anomaly [*Langenheim et al.*, 1993], not drilled; assumed to correlate roughly with anomaly B; *reversed* polarity	3.8	—

Table 1: Data used in the Analyses (continued)

Volcano (abbreviation)	UTM Coordinate	Age Estimate (Ma)	Source	Explanation	Data Set 1 (Ma)	Data Set 2 (Ma)
Amargosa Valley D (avd)	549430E 4040080N	4.3±0.1 3.8±0.1		Aeromagnetic anomaly, not drilled; assumed to correlate roughly with anomaly B; *reversed* polarity; basalt found in nearby well [*Langenheim et al.*, 1993]	3.7	4.5
Thirsty Mesa (tm)	529390E 4112330N	4.6±0.1	*Fleck et al.* [1994]	K/Ar estimate based on 3 samples	4.5	4.7
Miocene						
Rocket Wash	536110E 4109120N	8.0±0.2	*Crowe et al.* [1983]	K/Ar date	7.8	8.2
Pahute Mesa A	548920E 4133270N	9.8±0.8	*Crowe et al.* [1983] *Sawyer et al.* [1994]	Overlies 9.40±0.03 Pahute Mesa Member of Thirsty Canyon Tuff, 2 K/Ar dates	9.0	9.4
Pahute Mesa B	554090E 4134530N	8.8±0.1	*Crowe et al.* [1983]	Single K/Ar date	8.7	8.9
Pahute Mesa C	562370E 4132680N	9.8±0.8	*Crowe et al.* [1983]	Correlative with Pahute Mesa A	9.0	9.4
Paiute Ridge A	594860E 4107970N	8.5±0.3	*Crowe et al.* [1983]	Average of three K/Ar dates, undifferentiated Paiute Ridge. Vent locations marked by exposed vent breccia, feeder dikes, or cones remnants	8.3	8.8
Paiute Ridge B	595780E 4106340N	8.5±0.3			8.3	8.8
Paiute Ridge C	592810E 4105890N	8.5±0.3			8.3	8.8
Paiute Ridge D	593411E 4105540N	8.5±0.3			8.3	8.8
Paiute Ridge E	591480E 4105170N	8.5±0.3			8.3	8.8

Table 1: Data used in the Analyses (continued)

Volcano (abbreviation)	UTM Coordinate	Age Estimate (Ma)	Source	Explanation	Data Set 1 (Ma)	Data Set 2 (Ma)
Nye Canyon A	603230E 4095790N	6.8±0.2	*Crowe et al.* [1983]	Average of three K/Ar dates, for undifferentiated Nye Canyon	6.6	7.0
Nye Canyon B	602170E 4088960N	6.8±0.2			6.6	7.0
Nye Canyon C	600950E 4085920N	6.8±0.2			6.6	7.0
Nye Canyon D	600550E 4085450N	6.8±0.2			6.6	—
Nye Canyon E	599160E 4085820N	6.8±0.2			6.6	—
Nye Canyon F	598030E 4090090N	6.8±0.2			6.6	7.0
Nye Canyon G	597930E 4082470N	6.8±0.2	*Carr* [1984]	Drillhole in Frenchman Flat, assumed correlation with Nye Canyon	6.6	7.0
Yucca Flat	577860E 4093930N	8.1	*Carr* [1984]	Basalt in drillholes UE1H and UE6D, 1 K/Ar date, no reported uncertainty	8.1	8.1

3 of 17

Cerro Negro SP Data

Cerro Negro SP Data

Chuck Connor

Self-potential data were collected at Cerro Negro cinder cone during the 1995 eruption. These data include a tranverse across the Cerro La Mula ridge and data collected over time at the SP anomaly. The data are interpreted in terms of the pattern of ground water flow. No change due to phreatic activity at the volcano was discerned.

Scientific Notebook No. 115 CCC 6/26/98

1.0 Introduction

Self-potential data is used to map ground water flow, especially in hydrothermal areas. We mapped an SP anomaly in a thermal area on the Cerro La Mula ridge, 750 m north of Cerro Negro volcano, during phreatic eruptive activity at Cerro Negro. We monitored radon flux and soil Hg along the same traverse.

The goal was to

- identify and map possible SP anomalies
- determine the relationship of these anomalies to the thermal areas on the Cerro La Mula ridge
- monitor change in the anomaly over time and correlate with changes in volcanic activity

2.0 Thermal area on Cerro La Mula ridge

The thermal area on Cerro La Mula ridge occurs high on the East side of the ridge. The closest point of the ridge is about 500 m North of the crater of Cerro Negro and the ridge trends north of Cerro Negro. The ridge itself appears to be constructional and is likely the result of cinder cones coalescing on a N-S fracture zone. Three phreatic pits trend N-S on the East flank of the ridge. These pits are approximately 50 - 100 m in diameter. Thermal activity on the ridge is above these pits and consists of low temperature fumaroles that form a N-S trending zone. Alteration is pronounced and is most abundant in the third phreatic pit (furthest form Cerro Negro). Trees have been filled in the thermal

area, indicating that the thermal area originated long after the formation of the phreatic pits.

3.0 Self-Potential Traverse

An E-W traverse was made across cerro La Mula ridge. The base station for the traverse was at radon station 8 on the top of the ridge. This station was fixed and the potential difference between a CuSO4 electrode at this location and one located at some distance was measured using a high impedance voltmeter.

The main thermal area was interested at +50 m (east) of the base station at radon station number 7.

The total anomaly was approximately 100 mV. The maximum anomaly was measured between the base station and the thermal area. The results of the traverse are summarized in the following graph.

FIGURE 1. SP traverse across the Cerro La Mula Ridge

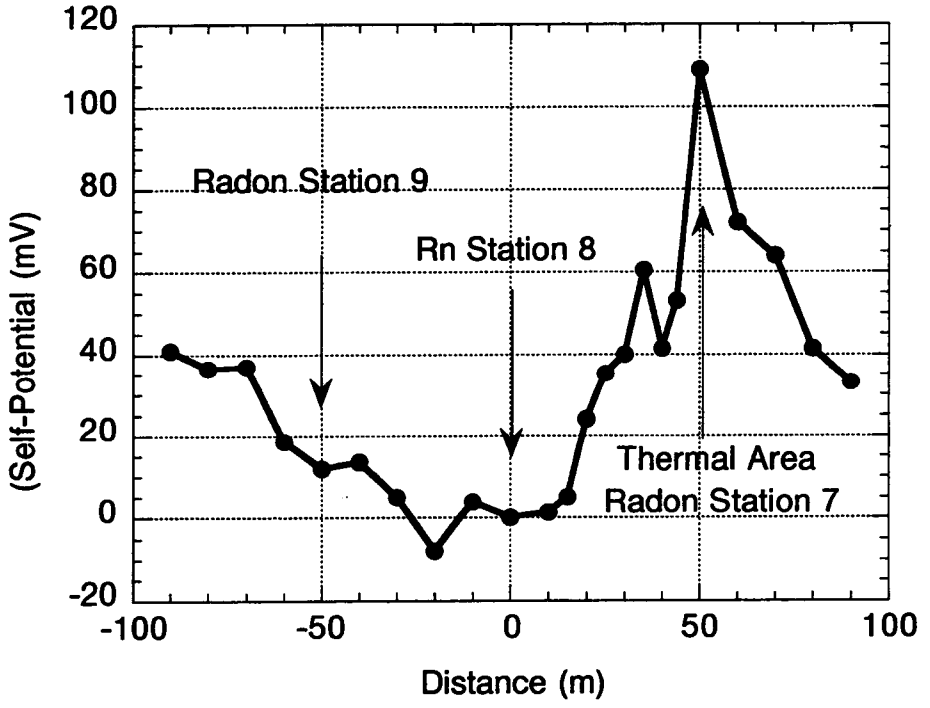

The results show flow away from the base station on the crest of the ridge and significant discharge at the thermal area (radon station 8)The anomaly is slightly dipolar.

4.0 Temporal Change in SP anomaly

The SP anomaly observed on the traverse was monitored over a period of about 48 hours using a campbell scientific datalogger. The potential difference between the electrodes was recorded at three minute intervals using the data logger. The data logger has a dynamic range of ±5000 mV and precision of much better than 0.1 mV. Voltage was compared in the field between the datalogger and the millivolt meter. The difference was 0.1 mV.

One electrode was placed at radon station 8 and the other at radon station 7, located 50 m east and in the thermal area. The ground temperature in the thermal area was measured with a K-type thermocouple and was 67°C at a depth of 15 cm, the approximate depth of the electrode.

Air temperature and the temperature of the ground at a depth of 15 cm 25 m east of the base station were recorded using the datalogger at 3 minute intervals.

FIGURE 2. SP and ground temperature

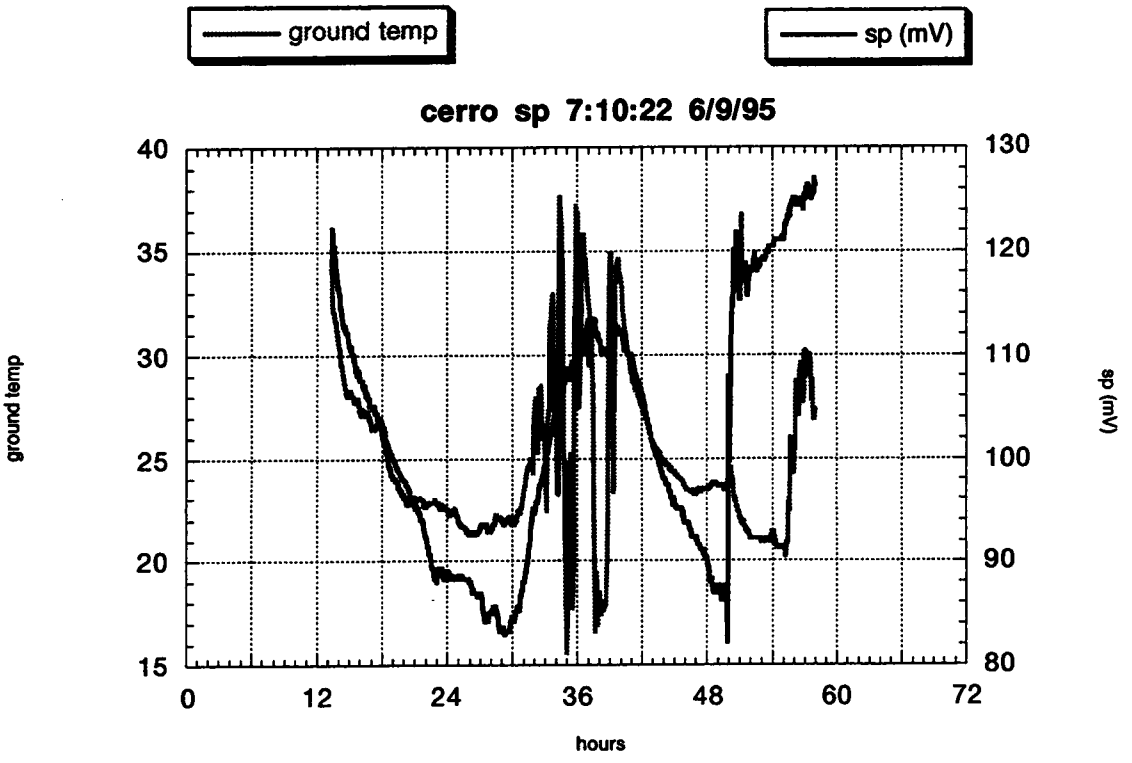

FIGURE 3. SP and Air Temperature

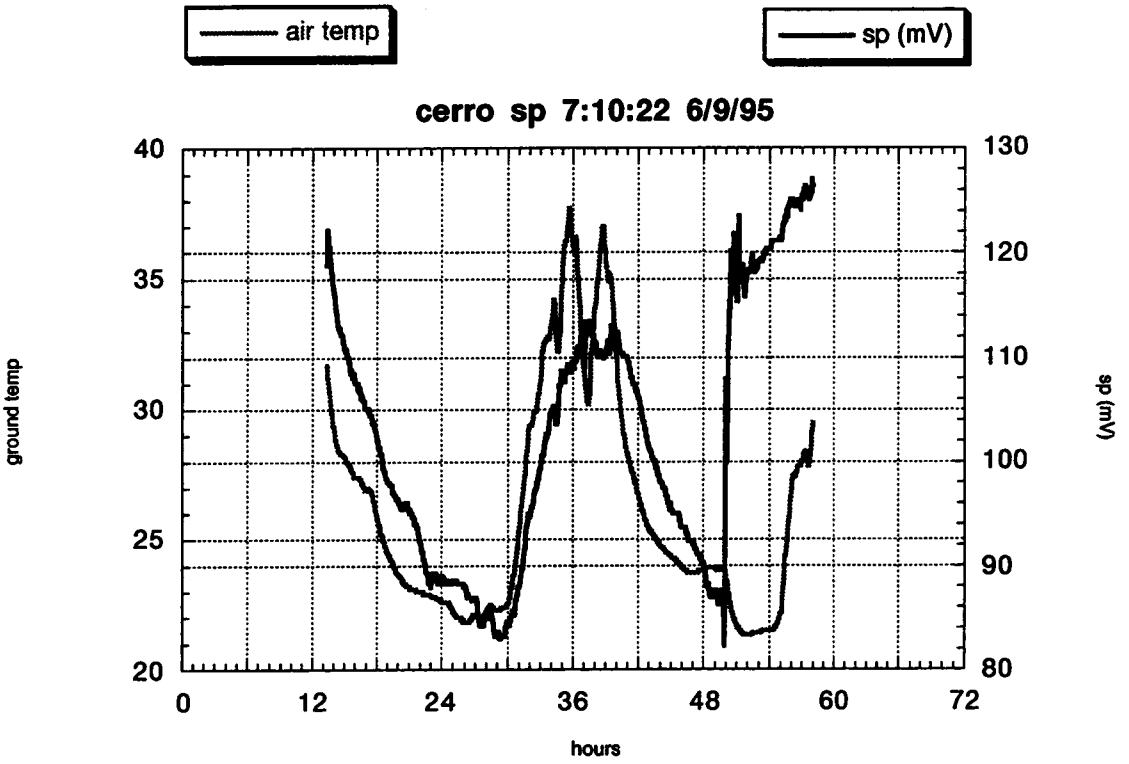

The SP anomaly varied by more than 40 mV during the sampling interval. This variation tracks the change in air temperature, lagging air temperature by about 2 hour. The SP anomaly variation correlates very well with ground temperature.

The correlation is not good at 50 hours, when a heavy rain storm occurred. At this time SP changed very rapidly but temperature did not change very much. There was a kick (increase) in ground temperature at this time.

FIGURE 4. Detail of SP anomaly and ground temperature around 50 hr (during heavy rain)

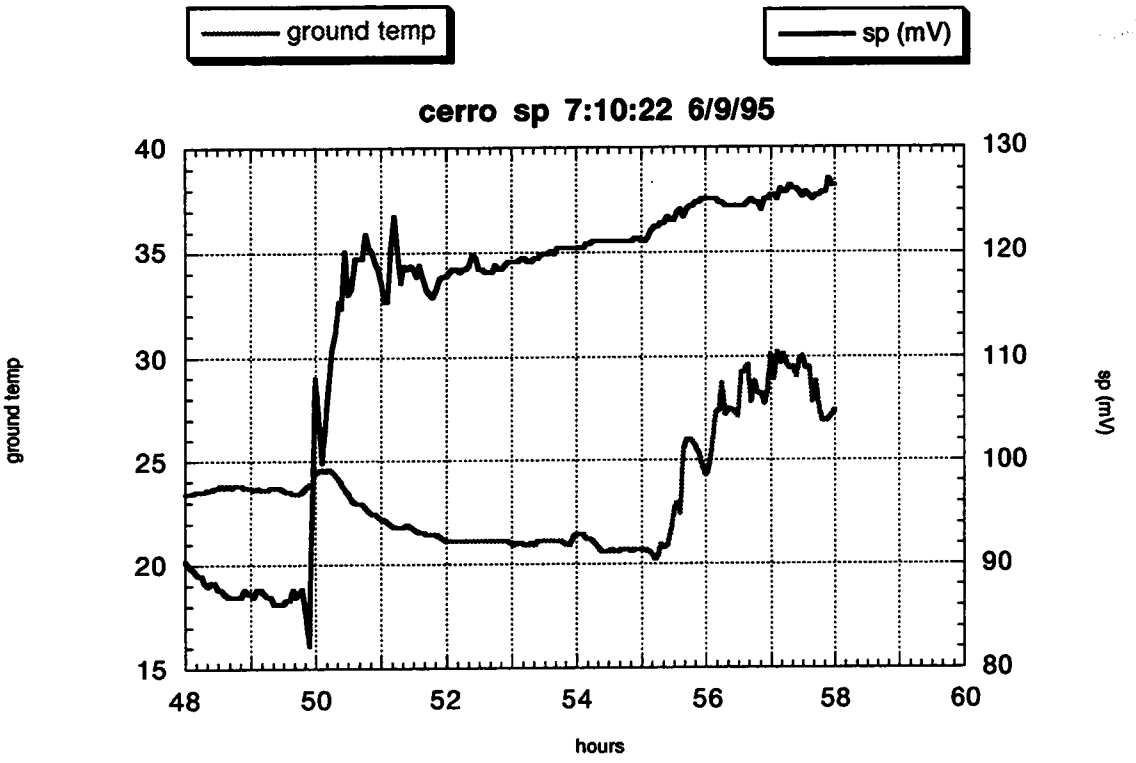

The above figure shows the 1 degree C temperature increase during and 40 mV SP increase during the rain storm. Air temperature dropped during the same period (Figure 3, "SP and Air Temperature," on page 4).An interpretation of this is that the change in ground (and air) temperature effected the electrodes differentially. This makes sense since the temperature in the thermal area did not change substantially, but the temperature at radon station 7 changed diurnally. This resulted in a change in electrical potential between the two electrodes.A simple diagram explaining the SP anomaly is:

FIGURE 5. Flow lines interpreted from SP data

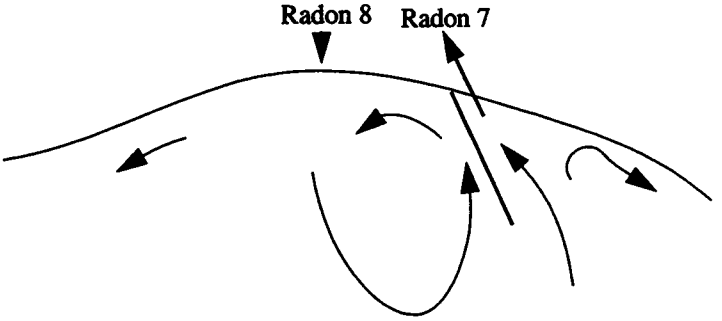

The interpretation is that a fracture exists in permeable rock (cinders). Most flow is from depth and creates a net positive anomaly in the thermal area. Some heated water moves out of the fracture into the permeable cinders as the ascending water cools and looses buoyancy. Some of this water flows down hill away from the thermal area. A small convection cell is set up between the fracture zone (thermal area) and the crest of the hill.

During the rainstorm at hour 50, the ground temperature increased and the SP anomaly increased. This implies that the source of the anomaly is shallow (due to the rapid response) and that convection was more vigorous as a result of the recharge.

5.0 Conclusions

- A large SP anomaly exists over the Cerro La MUla ridge corresponding to the thermal anomalies
- Total amplitude of the anomaly was 100 mV on June 4, 1995
- The anomaly shows significant diurnal variation and change with rainfall.
- The traverse and temporal changes in the anomaly can be explained in terms of a simple convection model.
- No change was observed during the short period of observation

6.0 Recommendations

- continued monitoring of the anomaly in this area may show whether there is long term variation related to volcanic activity. For example, the anomaly may be much larger during this sampling period than in normal.
- In the long term, it is worthwhile to map this anomaly across Cerro La MUla ridge in mode detail.

7.0 SP Data

7.1 Traverse data

TABLE 1. Traverse across the Cerro La Mula ridge

Distance (m)	SP (mV)
-90.000	41.000
-80.000	36.500
-70.000	37.000
-60.000	18.500
-50.000	12.000
-40.000	13.500
-30.000	5.0000
-20.000	-8.0000
-10.000	4.0000
0.0000	0.0000
10.000	1.4000
15.000	5.0000
20.000	24.000
25.000	35.300
30.000	40.000
35.000	60.500
40.000	41.500
44.000	53.000
50.000	109.00
60.000	72.000
70.000	64.000
80.000	41.500
90.000	33.000

Distance 0 is radon station 8, distance 50 is radon station 7

7.2 Output from the Data Logger for temporal monitoring

01+id tag

02+ julian day

03+hour/min

04+air temp (C)

05+ ground temperature (C)

06+ sp (mvolt)

01+0104. 02+0155. 03+1319. 04+31.76 05+34.22 06+118.8
01+0104. 02+0155. 03+1321. 04+31.64 05+34.01 06+119.2
01+0104. 02+0155. 03+1324. 04+31.37 05+32.92 06+122.2
01+0104. 02+0155. 03+1327. 04+31.14 05+32.46 06+121.9
01+0104. 02+0155. 03+1330. 04+30.96 05+32.27 06+120.5
01+0104. 02+0155. 03+1333. 04+30.77 05+32.08 06+120.5
01+0104. 02+0155. 03+1336. 04+30.60 05+31.92 06+120.5
01+0104. 02+0155. 03+1339. 04+30.41 05+31.88 06+119.5
01+0104. 02+0155. 03+1342. 04+30.22 05+31.70 06+119.2
01+0104. 02+0155. 03+1345. 04+30.04 05+31.52 06+118.2
01+0104. 02+0155. 03+1348. 04+29.88 05+31.27 06+117.9
01+0104. 02+0155. 03+1351. 04+29.72 05+31.11 06+117.2
01+0104. 02+0155. 03+1354. 04+29.57 05+31.05 06+117.2
01+0104. 02+0155. 03+1357. 04+29.43 05+30.74 06+116.5
01+0104. 02+0155. 03+1400. 04+29.30 05+30.53 06+116.5
01+0104. 02+0155. 03+1403. 04+29.20 05+30.35 06+115.8
01+0104. 02+0155. 03+1406. 04+29.07 05+30.22 06+115.8
01+0104. 02+0155. 03+1409. 04+28.98 05+30.05 06+115.2
01+0104. 02+0155. 03+1412. 04+28.88 05+29.79 06+114.5
01+0104. 02+0155. 03+1415. 04+28.77 05+29.59 06+114.5
01+0104. 02+0155. 03+1418. 04+28.69 05+29.43 06+113.8
01+0104. 02+0155. 03+1421. 04+28.62 05+29.35 06+113.2
01+0104. 02+0155. 03+1424. 04+28.55 05+29.13 06+113.2
01+0104. 02+0155. 03+1427. 04+28.49 05+28.90 06+112.8
01+0104. 02+0155. 03+1430. 04+28.46 05+28.70 06+112.8
01+0104. 02+0155. 03+1433. 04+28.43 05+28.67 06+112.5
01+0104. 02+0155. 03+1436. 04+28.41 05+28.49 06+112.8
01+0104. 02+0155. 03+1439. 04+28.38 05+28.46 06+112.5
01+0104. 02+0155. 03+1442. 04+28.36 05+28.28 06+112.2
01+0104. 02+0155. 03+1445. 04+28.35 05+28.10 06+112.2
01+0104. 02+0155. 03+1448. 04+28.33 05+28.09 06+112.2
01+0104. 02+0155. 03+1451. 04+28.33 05+28.09 06+111.8
01+0104. 02+0155. 03+1454. 04+28.30 05+28.22 06+111.5
01+0104. 02+0155. 03+1457. 04+28.27 05+28.19 06+111.5
01+0104. 02+0155. 03+1500. 04+28.23 05+28.31 06+110.8
01+0104. 02+0155. 03+1503. 04+28.21 05+28.29 06+110.8
01+0104. 02+0155. 03+1506. 04+28.16 05+28.33 06+110.5
01+0104. 02+0155. 03+1509. 04+28.10 05+28.27 06+110.8
01+0104. 02+0155. 03+1512. 04+28.06 05+28.22 06+110.8
01+0104. 02+0155. 03+1515. 04+28.02 05+28.19 06+110.1

01+0104. 02+0155. 03+1518. 04+27.99 05+28.08 06+110.1
01+0104. 02+0155. 03+1521. 04+27.96 05+28.04 06+110.1
01+0104. 02+0155. 03+1524. 04+27.92 05+28.00 06+110.1
01+0104. 02+0155. 03+1527. 04+27.90 05+27.90 06+109.5
01+0104. 02+0155. 03+1530. 04+27.87 05+27.79 06+109.5
01+0104. 02+0155. 03+1533. 04+27.84 05+27.76 06+108.5
01+0104. 02+0155. 03+1536. 04+27.79 05+27.88 06+108.8
01+0104. 02+0155. 03+1539. 04+27.75 05+27.83 06+108.8
01+0104. 02+0155. 03+1542. 04+27.70 05+27.95 06+108.8
01+0104. 02+0155. 03+1545. 04+27.66 05+27.90 06+108.1
01+0104. 02+0155. 03+1548. 04+27.61 05+27.94 06+108.1
01+0104. 02+0155. 03+1551. 04+27.55 05+27.88 06+108.1
01+0104. 02+0155. 03+1554. 04+27.49 05+27.74 06+108.5
01+0104. 02+0155. 03+1557. 04+27.46 05+27.46 06+108.1
01+0104. 02+0155. 03+1600. 04+27.46 05+27.30 06+107.5
01+0104. 02+0155. 03+1603. 04+27.44 05+27.20 06+107.5
01+0104. 02+0155. 03+1606. 04+27.44 05+27.12 06+107.5
01+0104. 02+0155. 03+1609. 04+27.44 05+27.12 06+107.5
01+0104. 02+0155. 03+1612. 04+27.43 05+27.18 06+107.5
01+0104. 02+0155. 03+1615. 04+27.43 05+27.18 06+107.1
01+0104. 02+0155. 03+1618. 04+27.40 05+27.48 06+106.8
01+0104. 02+0155. 03+1621. 04+27.37 05+27.37 06+107.1
01+0104. 02+0155. 03+1624. 04+27.35 05+27.27 06+106.8
01+0104. 02+0155. 03+1627. 04+27.34 05+27.17 06+107.1
01+0104. 02+0155. 03+1630. 04+27.32 05+27.24 06+106.1
01+0104. 02+0155. 03+1633. 04+27.29 05+27.38 06+106.1
01+0104. 02+0155. 03+1636. 04+27.26 05+27.35 06+106.4
01+0104. 02+0155. 03+1639. 04+27.20 05+27.37 06+106.4
01+0104. 02+0155. 03+1642. 04+27.16 05+27.32 06+105.8
01+0104. 02+0155. 03+1645. 04+27.10 05+27.18 06+105.8
01+0104. 02+0155. 03+1648. 04+27.05 05+26.97 06+105.8
01+0104. 02+0155. 03+1651. 04+27.01 05+27.01 06+105.1
01+0104. 02+0155. 03+1654. 04+26.98 05+26.98 06+105.1
01+0104. 02+0155. 03+1657. 04+26.95 05+26.87 06+105.1
01+0104. 02+0155. 03+1700. 04+26.95 05+26.62 06+105.1
01+0104. 02+0155. 03+1703. 04+26.96 05+26.55 06+105.1
01+0104. 02+0155. 03+1706. 04+26.99 05+26.42 06+105.1
01+0104. 02+0155. 03+1709. 04+26.99 05+26.50 06+105.1
01+0104. 02+0155. 03+1712. 04+26.99 05+26.42 06+104.8
01+0104. 02+0155. 03+1715. 04+27.01 05+26.43 06+105.1
01+0104. 02+0155. 03+1718. 04+26.99 05+26.58 06+104.4
01+0104. 02+0155. 03+1721. 04+26.98 05+26.57 06+104.4
01+0104. 02+0155. 03+1724. 04+26.96 05+26.55 06+104.4
01+0104. 02+0155. 03+1727. 04+26.93 05+26.69 06+104.4
01+0104. 02+0155. 03+1730. 04+26.87 05+26.79 06+104.4
01+0104. 02+0155. 03+1733. 04+26.82 05+26.90 06+103.7
01+0104. 02+0155. 03+1736. 04+26.74 05+26.99 06+103.8
01+0104. 02+0155. 03+1739. 04+26.65 05+27.06 06+103.8
01+0104. 02+0155. 03+1742. 04+26.56 05+26.98 06+103.8
01+0104. 02+0155. 03+1745. 04+26.46 05+27.04 06+103.4

01+0104. 02+0155. 03+1748. 04+26.37 05+26.95 06+103.1
01+0104. 02+0155. 03+1751. 04+26.27 05+26.93 06+103.1
01+0104. 02+0155. 03+1754. 04+26.17 05+26.91 06+103.1
01+0104. 02+0155. 03+1757. 04+26.08 05+26.82 06+102.7
01+0104. 02+0155. 03+1800. 04+25.99 05+26.74 06+102.1
01+0104. 02+0155. 03+1803. 04+25.89 05+26.64 06+102.1
01+0104. 02+0155. 03+1806. 04+25.79 05+26.53 06+102.1
01+0104. 02+0155. 03+1809. 04+25.69 05+26.43 06+101.4
01+0104. 02+0155. 03+1812. 04+25.61 05+26.51 06+101.4
01+0104. 02+0155. 03+1815. 04+25.52 05+26.43 06+101.4
01+0104. 02+0155. 03+1818. 04+25.44 05+26.26 06+101.4
01+0104. 02+0155. 03+1821. 04+25.35 05+26.09 06+100.7
01+0104. 02+0155. 03+1824. 04+25.28 05+25.94 06+100.7
01+0104. 02+0155. 03+1827. 04+25.24 05+25.81 06+100.7
01+0104. 02+0155. 03+1830. 04+25.17 05+25.74 06+100.1
01+0104. 02+0155. 03+1833. 04+25.11 05+25.69 06+100.1
01+0104. 02+0155. 03+1836. 04+25.04 05+25.70 06+099.4
01+0104. 02+0155. 03+1839. 04+24.97 05+25.55 06+099.4
01+0104. 02+0155. 03+1842. 04+24.91 05+25.49 06+099.1
01+0104. 02+0155. 03+1845. 04+24.84 05+25.42 06+099.1
01+0104. 02+0155. 03+1848. 04+24.77 05+25.35 06+098.7
01+0104. 02+0155. 03+1851. 04+24.72 05+25.29 06+098.4
01+0104. 02+0155. 03+1854. 04+24.66 05+25.24 06+098.4
01+0104. 02+0155. 03+1857. 04+24.61 05+25.10 06+098.4
01+0104. 02+0155. 03+1900. 04+24.56 05+25.06 06+098.0
01+0104. 02+0155. 03+1903. 04+24.52 05+25.02 06+098.0
01+0104. 02+0155. 03+1906. 04+24.49 05+24.99 06+098.0
01+0104. 02+0155. 03+1909. 04+24.45 05+24.95 06+098.0
01+0104. 02+0155. 03+1912. 04+24.41 05+24.91 06+098.0
01+0104. 02+0155. 03+1915. 04+24.35 05+24.77 06+097.7
01+0104. 02+0155. 03+1918. 04+24.31 05+24.73 06+097.7
01+0104. 02+0155. 03+1921. 04+24.26 05+24.67 06+097.7
01+0104. 02+0155. 03+1924. 04+24.22 05+24.63 06+097.7
01+0104. 02+0155. 03+1927. 04+24.16 05+24.58 06+097.7
01+0104. 02+0155. 03+1930. 04+24.11 05+24.52 06+097.0
01+0104. 02+0155. 03+1933. 04+24.05 05+24.47 06+097.0
01+0104. 02+0155. 03+1936. 04+24.01 05+24.42 06+097.0
01+0104. 02+0155. 03+1939. 04+23.97 05+24.30 06+097.0
01+0104. 02+0155. 03+1942. 04+23.93 05+24.26 06+096.7
01+0104. 02+0155. 03+1945. 04+23.89 05+24.22 06+096.7
01+0104. 02+0155. 03+1948. 04+23.86 05+24.19 06+096.7
01+0104. 02+0155. 03+1951. 04+23.82 05+24.07 06+096.4
01+0104. 02+0155. 03+1954. 04+23.79 05+24.04 06+096.4
01+0104. 02+0155. 03+1957. 04+23.77 05+24.01 06+096.4
01+0104. 02+0155. 03+2000. 04+23.73 05+23.97 06+096.4
01+0104. 02+0155. 03+2003. 04+23.69 05+23.93 06+096.0
01+0104. 02+0155. 03+2006. 04+23.67 05+23.92 06+096.0
01+0104. 02+0155. 03+2009. 04+23.63 05+23.88 06+096.0
01+0104. 02+0155. 03+2012. 04+23.60 05+23.85 06+096.0
01+0104. 02+0155. 03+2015. 04+23.58 05+23.74 06+095.7

01+0104. 02+0155. 03+2018. 04+23.54 05+23.70 06+095.4
01+0104. 02+0155. 03+2021. 04+23.51 05+23.67 06+095.7
01+0104. 02+0155. 03+2024. 04+23.47 05+23.63 06+095.4
01+0104. 02+0155. 03+2027. 04+23.43 05+23.59 06+095.4
01+0104. 02+0155. 03+2030. 04+23.39 05+23.47 06+095.7
01+0104. 02+0155. 03+2033. 04+23.36 05+23.36 06+096.0
01+0104. 02+0155. 03+2036. 04+23.35 05+23.18 06+096.0
01+0104. 02+0155. 03+2039. 04+23.35 05+23.18 06+096.0
01+0104. 02+0155. 03+2042. 04+23.32 05+23.16 06+096.0
01+0104. 02+0155. 03+2045. 04+23.29 05+23.13 06+096.1
01+0104. 02+0155. 03+2048. 04+23.27 05+23.10 06+096.0
01+0104. 02+0155. 03+2051. 04+23.25 05+23.01 06+096.1
01+0104. 02+0155. 03+2054. 04+23.25 05+23.01 06+095.4
01+0104. 02+0155. 03+2057. 04+23.25 05+22.92 06+095.4
01+0104. 02+0155. 03+2100. 04+23.23 05+22.98 06+095.4
01+0104. 02+0155. 03+2103. 04+23.21 05+22.97 06+095.0
01+0104. 02+0155. 03+2106. 04+23.19 05+22.94 06+095.4
01+0104. 02+0155. 03+2109. 04+23.19 05+22.94 06+095.0
01+0104. 02+0155. 03+2112. 04+23.17 05+22.93 06+095.0
01+0104. 02+0155. 03+2115. 04+23.17 05+23.01 06+095.0
01+0104. 02+0155. 03+2118. 04+23.17 05+23.01 06+094.7
01+0104. 02+0155. 03+2121. 04+23.16 05+22.99 06+094.7
01+0104. 02+0155. 03+2124. 04+23.16 05+22.99 06+094.7
01+0104. 02+0155. 03+2127. 04+23.17 05+23.01 06+094.4
01+0104. 02+0155. 03+2130. 04+23.15 05+22.98 06+094.0
01+0104. 02+0155. 03+2133. 04+23.13 05+22.97 06+094.0
01+0104. 02+0155. 03+2136. 04+23.11 05+22.94 06+094.0
01+0104. 02+0155. 03+2139. 04+23.09 05+22.93 06+094.0
01+0104. 02+0155. 03+2142. 04+23.07 05+22.90 06+093.7
01+0104. 02+0155. 03+2145. 04+23.04 05+22.87 06+093.7
01+0104. 02+0155. 03+2148. 04+23.01 05+22.85 06+093.3
01+0104. 02+0155. 03+2151. 04+23.00 05+22.75 06+093.0
01+0104. 02+0155. 03+2154. 04+23.00 05+22.67 06+092.7
01+0104. 02+0155. 03+2157. 04+23.00 05+22.67 06+092.3
01+0104. 02+0155. 03+2200. 04+23.00 05+22.67 06+092.3
01+0104. 02+0155. 03+2203. 04+23.01 05+22.76 06+092.3
01+0104. 02+0155. 03+2206. 04+23.00 05+22.83 06+092.0
01+0104. 02+0155. 03+2209. 04+23.00 05+22.83 06+091.3
01+0104. 02+0155. 03+2212. 04+23.00 05+22.83 06+091.3
01+0104. 02+0155. 03+2215. 04+23.00 05+22.83 06+091.3
01+0104. 02+0155. 03+2218. 04+22.99 05+22.82 06+090.6
01+0104. 02+0155. 03+2221. 04+22.99 05+22.82 06+090.6
01+0104. 02+0155. 03+2224. 04+22.99 05+22.74 06+090.6
01+0104. 02+0155. 03+2227. 04+22.99 05+22.82 06+090.0
01+0104. 02+0155. 03+2230. 04+22.99 05+22.82 06+090.0
01+0104. 02+0155. 03+2233. 04+22.99 05+22.82 06+089.6
01+0104. 02+0155. 03+2236. 04+22.97 05+22.81 06+089.3
01+0104. 02+0155. 03+2239. 04+22.97 05+22.81 06+089.3
01+0104. 02+0155. 03+2242. 04+22.97 05+22.81 06+089.3
01+0104. 02+0155. 03+2245. 04+22.97 05+22.89 06+088.6

01+0104. 02+0155. 03+2248. 04+22.96 05+22.88 06+088.6
01+0104. 02+0155. 03+2251. 04+22.96 05+22.96 06+088.3
01+0104. 02+0155. 03+2254. 04+22.95 05+22.95 06+088.3
01+0104. 02+0155. 03+2257. 04+22.93 05+22.85 06+088.3
01+0104. 02+0155. 03+2300. 04+22.92 05+22.75 06+088.6
01+0104. 02+0155. 03+2303. 04+22.91 05+22.82 06+087.9
01+0104. 02+0155. 03+2306. 04+22.89 05+22.89 06+088.9
01+0104. 02+0155. 03+2309. 04+22.88 05+22.88 06+088.9
01+0104. 02+0155. 03+2312. 04+22.87 05+22.78 06+089.3
01+0104. 02+0155. 03+2315. 04+22.85 05+22.60 06+089.3
01+0104. 02+0155. 03+2318. 04+22.85 05+22.60 06+089.3
01+0104. 02+0155. 03+2321. 04+22.84 05+22.51 06+088.6
01+0104. 02+0155. 03+2324. 04+22.84 05+22.51 06+088.6
01+0104. 02+0155. 03+2327. 04+22.83 05+22.58 06+088.6
01+0104. 02+0155. 03+2330. 04+22.83 05+22.66 06+088.9
01+0104. 02+0155. 03+2333. 04+22.80 05+22.72 06+089.3
01+0104. 02+0155. 03+2336. 04+22.79 05+22.79 06+088.9
01+0104. 02+0155. 03+2339. 04+22.77 05+22.69 06+088.6
01+0104. 02+0155. 03+2342. 04+22.76 05+22.59 06+088.3
01+0104. 02+0155. 03+2345. 04+22.75 05+22.58 06+088.3
01+0104. 02+0155. 03+2348. 04+22.75 05+22.58 06+088.3
01+0104. 02+0155. 03+2351. 04+22.75 05+22.58 06+088.3
01+0104. 02+0155. 03+2354. 04+22.75 05+22.58 06+088.3
01+0104. 02+0155. 03+2357. 04+22.72 05+22.55 06+088.6
01+0104. 02+0156. 03+0000. 04+22.69 05+22.53 06+089.0
01+0104. 02+0156. 03+0003. 04+22.68 05+22.52 06+088.9
01+0104. 02+0156. 03+0006. 04+22.67 05+22.42 06+089.0
01+0104. 02+0156. 03+0009. 04+22.67 05+22.34 06+088.6
01+0104. 02+0156. 03+0012. 04+22.65 05+22.24 06+088.9
01+0104. 02+0156. 03+0015. 04+22.65 05+22.24 06+088.3
01+0104. 02+0156. 03+0018. 04+22.65 05+22.32 06+088.3
01+0104. 02+0156. 03+0021. 04+22.67 05+22.34 06+088.3
01+0104. 02+0156. 03+0024. 04+22.67 05+22.34 06+088.3
01+0104. 02+0156. 03+0027. 04+22.65 05+22.41 06+088.3
01+0104. 02+0156. 03+0030. 04+22.67 05+22.34 06+088.3
01+0104. 02+0156. 03+0033. 04+22.65 05+22.32 06+088.6
01+0104. 02+0156. 03+0036. 04+22.64 05+22.39 06+088.3
01+0104. 02+0156. 03+0039. 04+22.61 05+22.45 06+088.3
01+0104. 02+0156. 03+0042. 04+22.58 05+22.49 06+088.3
01+0104. 02+0156. 03+0045. 04+22.52 05+22.52 06+088.3
01+0104. 02+0156. 03+0048. 04+22.48 05+22.40 06+088.3
01+0104. 02+0156. 03+0051. 04+22.44 05+22.28 06+088.3
01+0104. 02+0156. 03+0054. 04+22.40 05+22.24 06+088.3
01+0104. 02+0156. 03+0057. 04+22.35 05+22.19 06+088.3
01+0104. 02+0156. 03+0100. 04+22.31 05+22.07 06+088.6
01+0104. 02+0156. 03+0103. 04+22.27 05+21.94 06+088.6
01+0104. 02+0156. 03+0106. 04+22.23 05+21.90 06+088.6
01+0104. 02+0156. 03+0109. 04+22.18 05+21.85 06+088.6
01+0104. 02+0156. 03+0112. 04+22.16 05+21.83 06+088.6
01+0104. 02+0156. 03+0115. 04+22.13 05+21.72 06+088.6

01+0104. 02+0156. 03+0118. 04+22.12 05+21.79 06+088.6
01+0104. 02+0156. 03+0121. 04+22.09 05+21.76 06+088.6
01+0104. 02+0156. 03+0124. 04+22.09 05+21.76 06+088.3
01+0104. 02+0156. 03+0127. 04+22.08 05+21.75 06+088.3
01+0104. 02+0156. 03+0130. 04+22.08 05+21.75 06+088.3
01+0104. 02+0156. 03+0133. 04+22.06 05+21.73 06+088.3
01+0104. 02+0156. 03+0136. 04+22.05 05+21.72 06+088.3
01+0104. 02+0156. 03+0139. 04+22.01 05+21.68 06+088.3
01+0104. 02+0156. 03+0142. 04+22.00 05+21.59 06+088.3
01+0104. 02+0156. 03+0145. 04+21.97 05+21.48 06+088.3
01+0104. 02+0156. 03+0148. 04+21.95 05+21.45 06+088.3
01+0104. 02+0156. 03+0151. 04+21.92 05+21.42 06+088.3
01+0104. 02+0156. 03+0154. 04+21.90 05+21.40 06+088.3
01+0104. 02+0156. 03+0157. 04+21.88 05+21.39 06+088.3
01+0104. 02+0156. 03+0200. 04+21.87 05+21.37 06+087.9
01+0104. 02+0156. 03+0203. 04+21.87 05+21.37 06+087.9
01+0104. 02+0156. 03+0206. 04+21.87 05+21.37 06+088.0
01+0104. 02+0156. 03+0209. 04+21.87 05+21.46 06+087.6
01+0104. 02+0156. 03+0212. 04+21.87 05+21.46 06+087.6
01+0104. 02+0156. 03+0215. 04+21.87 05+21.46 06+087.3
01+0104. 02+0156. 03+0218. 04+21.88 05+21.39 06+086.9
01+0104. 02+0156. 03+0221. 04+21.88 05+21.39 06+087.3
01+0104. 02+0156. 03+0224. 04+21.88 05+21.39 06+086.9
01+0104. 02+0156. 03+0227. 04+21.88 05+21.39 06+086.9
01+0104. 02+0156. 03+0230. 04+21.88 05+21.47 06+086.9
01+0104. 02+0156. 03+0233. 04+21.90 05+21.40 06+086.9
01+0104. 02+0156. 03+0236. 04+21.91 05+21.41 06+086.9
01+0104. 02+0156. 03+0239. 04+21.93 05+21.35 06+086.9
01+0104. 02+0156. 03+0242. 04+21.97 05+21.31 06+086.9
01+0104. 02+0156. 03+0245. 04+22.03 05+21.36 06+086.6
01+0104. 02+0156. 03+0248. 04+22.06 05+21.40 06+086.9
01+0104. 02+0156. 03+0251. 04+22.10 05+21.44 06+086.9
01+0104. 02+0156. 03+0254. 04+22.14 05+21.56 06+086.9
01+0104. 02+0156. 03+0257. 04+22.17 05+21.59 06+086.9
01+0104. 02+0156. 03+0300. 04+22.18 05+21.68 06+086.9
01+0104. 02+0156. 03+0303. 04+22.18 05+21.68 06+086.9
01+0104. 02+0156. 03+0306. 04+22.17 05+21.84 06+086.9
01+0104. 02+0156. 03+0309. 04+22.16 05+21.82 06+086.6
01+0104. 02+0156. 03+0312. 04+22.14 05+21.89 06+086.3
01+0104. 02+0156. 03+0315. 04+22.12 05+21.87 06+085.6
01+0104. 02+0156. 03+0318. 04+22.10 05+21.85 06+085.2
01+0104. 02+0156. 03+0321. 04+22.08 05+21.83 06+084.9
01+0104. 02+0156. 03+0324. 04+22.06 05+21.82 06+084.6
01+0104. 02+0156. 03+0327. 04+22.05 05+21.80 06+084.2
01+0104. 02+0156. 03+0330. 04+22.04 05+21.79 06+084.2
01+0104. 02+0156. 03+0333. 04+22.03 05+21.86 06+084.2
01+0104. 02+0156. 03+0336. 04+22.01 05+21.85 06+084.2
01+0104. 02+0156. 03+0339. 04+22.00 05+21.75 06+084.2
01+0104. 02+0156. 03+0342. 04+22.01 05+21.60 06+084.2
01+0104. 02+0156. 03+0345. 04+22.04 05+21.54 06+084.2

01+0104. 02+0156. 03+0348. 04+22.06 05+21.40 06+084.2
01+0104. 02+0156. 03+0351. 04+22.10 05+21.52 06+084.9
01+0104. 02+0156. 03+0354. 04+22.14 05+21.65 06+084.9
01+0104. 02+0156. 03+0357. 04+22.18 05+21.52 06+084.9
01+0104. 02+0156. 03+0400. 04+22.22 05+21.48 06+084.9
01+0104. 02+0156. 03+0403. 04+22.27 05+21.53 06+084.9
01+0104. 02+0156. 03+0406. 04+22.31 05+21.65 06+085.2
01+0104. 02+0156. 03+0409. 04+22.35 05+21.69 06+084.9
01+0104. 02+0156. 03+0412. 04+22.39 05+21.73 06+084.9
01+0104. 02+0156. 03+0415. 04+22.43 05+21.77 06+085.2
01+0104. 02+0156. 03+0418. 04+22.47 05+21.81 06+085.6
01+0104. 02+0156. 03+0421. 04+22.49 05+21.83 06+085.6
01+0104. 02+0156. 03+0424. 04+22.51 05+21.93 06+085.6
01+0104. 02+0156. 03+0427. 04+22.51 05+22.18 06+085.6
01+0104. 02+0156. 03+0430. 04+22.50 05+22.25 06+085.6
01+0104. 02+0156. 03+0433. 04+22.47 05+22.22 06+085.2
01+0104. 02+0156. 03+0436. 04+22.44 05+22.20 06+084.9
01+0104. 02+0156. 03+0439. 04+22.43 05+22.18 06+084.6
01+0104. 02+0156. 03+0442. 04+22.40 05+22.16 06+084.2
01+0104. 02+0156. 03+0445. 04+22.39 05+22.14 06+083.9
01+0104. 02+0156. 03+0448. 04+22.38 05+22.13 06+083.6
01+0104. 02+0156. 03+0451. 04+22.37 05+22.12 06+083.2
01+0104. 02+0156. 03+0454. 04+22.34 05+22.09 06+083.6
01+0104. 02+0156. 03+0457. 04+22.34 05+22.09 06+083.6
01+0104. 02+0156. 03+0500. 04+22.34 05+22.09 06+083.6
01+0104. 02+0156. 03+0503. 04+22.34 05+22.01 06+083.6
01+0104. 02+0156. 03+0506. 04+22.33 05+21.91 06+083.6
01+0104. 02+0156. 03+0509. 04+22.34 05+21.92 06+083.6
01+0104. 02+0156. 03+0512. 04+22.35 05+21.85 06+083.6
01+0104. 02+0156. 03+0515. 04+22.36 05+21.87 06+083.2
01+0104. 02+0156. 03+0518. 04+22.37 05+21.87 06+082.9
01+0104. 02+0156. 03+0521. 04+22.39 05+21.90 06+082.9
01+0104. 02+0156. 03+0524. 04+22.40 05+21.99 06+083.2
01+0104. 02+0156. 03+0527. 04+22.42 05+22.00 06+083.2
01+0104. 02+0156. 03+0530. 04+22.44 05+22.03 06+083.2
01+0104. 02+0156. 03+0533. 04+22.46 05+22.04 06+083.2
01+0104. 02+0156. 03+0536. 04+22.46 05+22.04 06+083.2
01+0104. 02+0156. 03+0539. 04+22.47 05+22.06 06+083.2
01+0104. 02+0156. 03+0542. 04+22.47 05+22.14 06+083.2
01+0104. 02+0156. 03+0545. 04+22.47 05+22.06 06+083.6
01+0104. 02+0156. 03+0548. 04+22.47 05+22.06 06+083.9
01+0104. 02+0156. 03+0551. 04+22.48 05+21.99 06+084.2
01+0104. 02+0156. 03+0554. 04+22.50 05+21.92 06+084.2
01+0104. 02+0156. 03+0557. 04+22.52 05+21.86 06+084.6
01+0104. 02+0156. 03+0600. 04+22.58 05+21.91 06+084.6
01+0104. 02+0156. 03+0603. 04+22.63 05+21.80 06+084.6
01+0104. 02+0156. 03+0606. 04+22.71 05+21.80 06+084.6
01+0104. 02+0156. 03+0609. 04+22.80 05+21.81 06+084.2
01+0104. 02+0156. 03+0612. 04+22.89 05+21.82 06+084.6
01+0104. 02+0156. 03+0615. 04+23.00 05+21.92 06+084.6

01+0104. 02+0156. 03+0618. 04+23.10 05+22.03 06+084.9
01+0104. 02+0156. 03+0621. 04+23.22 05+21.98 06+085.2
01+0104. 02+0156. 03+0624. 04+23.35 05+22.11 06+085.2
01+0104. 02+0156. 03+0627. 04+23.48 05+22.24 06+085.2
01+0104. 02+0156. 03+0630. 04+23.60 05+22.36 06+085.6
01+0104. 02+0156. 03+0633. 04+23.67 05+22.43 06+085.2
01+0104. 02+0156. 03+0636. 04+23.78 05+22.37 06+085.2
01+0104. 02+0156. 03+0639. 04+23.93 05+22.36 06+085.9
01+0104. 02+0156. 03+0642. 04+24.09 05+22.36 06+086.6
01+0104. 02+0156. 03+0645. 04+24.27 05+22.54 06+086.6
01+0104. 02+0156. 03+0648. 04+24.46 05+22.65 06+086.9
01+0104. 02+0156. 03+0651. 04+24.66 05+22.76 06+087.2
01+0104. 02+0156. 03+0654. 04+24.85 05+22.95 06+087.2
01+0104. 02+0156. 03+0657. 04+25.05 05+22.99 06+087.9
01+0104. 02+0156. 03+0700. 04+25.26 05+23.20 06+087.9
01+0104. 02+0156. 03+0703. 04+25.48 05+23.41 06+087.9
01+0104. 02+0156. 03+0706. 04+25.69 05+23.54 06+088.2
01+0104. 02+0156. 03+0709. 04+25.89 05+23.75 06+088.6
01+0104. 02+0156. 03+0712. 04+26.08 05+23.94 06+088.9
01+0104. 02+0156. 03+0715. 04+26.28 05+24.14 06+088.9
01+0104. 02+0156. 03+0718. 04+26.47 05+24.33 06+089.6
01+0104. 02+0156. 03+0721. 04+26.65 05+24.51 06+089.6
01+0104. 02+0156. 03+0724. 04+26.81 05+24.67 06+090.3
01+0104. 02+0156. 03+0727. 04+26.99 05+24.68 06+090.3
01+0104. 02+0156. 03+0730. 04+27.17 05+24.53 06+090.9
01+0104. 02+0156. 03+0733. 04+27.38 05+24.75 06+091.6
01+0104. 02+0156. 03+0736. 04+27.59 05+24.79 06+091.6
01+0104. 02+0156. 03+0739. 04+27.79 05+24.99 06+092.3
01+0104. 02+0156. 03+0742. 04+27.99 05+25.03 06+092.9
01+0104. 02+0156. 03+0745. 04+28.24 05+24.94 06+093.6
01+0104. 02+0156. 03+0748. 04+28.47 05+24.77 06+093.9
01+0104. 02+0156. 03+0751. 04+28.74 05+24.70 06+094.3
01+0104. 02+0156. 03+0754. 04+28.98 05+24.36 06+095.0
01+0104. 02+0156. 03+0757. 04+29.21 05+25.02 06+094.9
01+0104. 02+0156. 03+0800. 04+29.34 05+26.88 06+094.6
01+0104. 02+0156. 03+0803. 04+29.41 05+27.27 06+094.6
01+0104. 02+0156. 03+0806. 04+29.44 05+27.80 06+094.9
01+0104. 02+0156. 03+0809. 04+29.44 05+27.96 06+095.3
01+0104. 02+0156. 03+0812. 04+29.42 05+27.78 06+095.6
01+0104. 02+0156. 03+0815. 04+29.47 05+27.33 06+095.6
01+0104. 02+0156. 03+0818. 04+29.58 05+27.12 06+095.6
01+0104. 02+0156. 03+0821. 04+29.73 05+25.37 06+095.9
01+0104. 02+0156. 03+0824. 04+29.88 05+27.41 06+096.3
01+0104. 02+0156. 03+0827. 04+29.94 05+28.46 06+096.6
01+0104. 02+0156. 03+0830. 04+29.93 05+28.45 06+097.0
01+0104. 02+0156. 03+0833. 04+29.94 05+28.14 06+097.3
01+0104. 02+0156. 03+0836. 04+29.98 05+28.50 06+097.3
01+0104. 02+0156. 03+0839. 04+30.02 05+28.05 06+097.6
01+0104. 02+0156. 03+0842. 04+30.12 05+27.99 06+097.9
01+0104. 02+0156. 03+0845. 04+30.27 05+26.66 06+097.6

01+0104. 02+0156. 03+0848. 04+30.45 05+26.02 06+098.3
01+0104. 02+0156. 03+0851. 04+30.60 05+26.66 06+098.3
01+0104. 02+0156. 03+0854. 04+30.72 05+26.61 06+099.0
01+0104. 02+0156. 03+0857. 04+30.82 05+26.55 06+099.0
01+0104. 02+0156. 03+0900. 04+30.99 05+25.81 06+099.3
01+0104. 02+0156. 03+0903. 04+31.18 05+25.01 06+099.3
01+0104. 02+0156. 03+0906. 04+31.47 05+23.49 06+100.0
01+0104. 02+0156. 03+0909. 04+31.81 05+22.43 06+100.3
01+0104. 02+0156. 03+0912. 04+32.13 05+23.33 06+100.6
01+0104. 02+0156. 03+0915. 04+32.36 05+24.55 06+100.6
01+0104. 02+0156. 03+0918. 04+32.50 05+27.00 06+100.6
01+0104. 02+0156. 03+0921. 04+32.55 05+27.38 06+101.3
01+0104. 02+0156. 03+0924. 04+32.60 05+27.35 06+101.6
01+0104. 02+0156. 03+0927. 04+32.66 05+29.63 06+101.9
01+0104. 02+0156. 03+0930. 04+32.68 05+31.69 06+101.9
01+0104. 02+0156. 03+0933. 04+32.71 05+29.43 06+102.6
01+0104. 02+0156. 03+0936. 04+32.78 05+31.96 06+102.3
01+0104. 02+0156. 03+0939. 04+32.82 05+32.66 06+102.6
01+0104. 02+0156. 03+0942. 04+32.78 05+32.46 06+102.6
01+0104. 02+0156. 03+0945. 04+32.75 05+32.91 06+102.6
01+0104. 02+0156. 03+0948. 04+32.71 05+32.22 06+103.3
01+0104. 02+0156. 03+0951. 04+32.80 05+27.88 06+104.0
01+0104. 02+0156. 03+0954. 04+33.04 05+26.23 06+104.6
01+0104. 02+0156. 03+0957. 04+33.18 05+27.19 06+104.6
01+0104. 02+0156. 03+1000. 04+33.29 05+27.80 06+104.6
01+0104. 02+0156. 03+1003. 04+33.36 05+27.62 06+104.6
01+0104. 02+0156. 03+1006. 04+33.53 05+25.24 06+105.0
01+0104. 02+0156. 03+1009. 04+33.84 05+23.25 06+105.0
01+0104. 02+0156. 03+1012. 04+34.14 05+23.38 06+105.3
01+0104. 02+0156. 03+1015. 04+34.29 05+26.83 06+104.6
01+0104. 02+0156. 03+1018. 04+34.08 05+36.53 06+104.3
01+0104. 02+0156. 03+1021. 04+33.71 05+37.55 06+104.3
01+0104. 02+0156. 03+1024. 04+33.31 05+37.64 06+104.3
01+0104. 02+0156. 03+1027. 04+32.93 05+37.18 06+103.6
01+0104. 02+0156. 03+1030. 04+32.59 05+36.18 06+103.6
01+0104. 02+0156. 03+1033. 04+32.36 05+35.30 06+103.6
01+0104. 02+0156. 03+1036. 04+32.25 05+33.40 06+104.6
01+0104. 02+0156. 03+1039. 04+32.25 05+31.76 06+105.3
01+0104. 02+0156. 03+1042. 04+32.43 05+27.51 06+106.7
01+0104. 02+0156. 03+1045. 04+32.73 05+25.42 06+107.3
01+0104. 02+0156. 03+1048. 04+33.04 05+24.25 06+107.3
01+0104. 02+0156. 03+1051. 04+33.44 05+22.26 06+107.3
01+0104. 02+0156. 03+1054. 04+33.86 05+19.96 06+108.3
01+0104. 02+0156. 03+1057. 04+34.36 05+18.16 06+108.7
01+0104. 02+0156. 03+1100. 04+34.93 05+16.75 06+108.7
01+0104. 02+0156. 03+1103. 04+35.50 05+15.66 06+108.6
01+0104. 02+0156. 03+1106. 04+35.99 05+18.07 06+108.6
01+0104. 02+0156. 03+1109. 04+36.27 05+21.00 06+108.0
01+0104. 02+0156. 03+1112. 04+36.37 05+23.99 06+107.9
01+0104. 02+0156. 03+1115. 04+36.45 05+24.98 06+107.6

01+0104. 02+0156. 03+1118. 04+36.47 05+24.92 06+108.3
01+0104. 02+0156. 03+1121. 04+36.57 05+25.27 06+108.6
01+0104. 02+0156. 03+1124. 04+36.61 05+24.24 06+108.6
01+0104. 02+0156. 03+1127. 04+36.71 05+21.87 06+108.6
01+0104. 02+0156. 03+1130. 04+37.00 05+18.69 06+109.3
01+0104. 02+0156. 03+1133. 04+37.37 05+17.74 06+108.6
01+0104. 02+0156. 03+1136. 04+37.66 05+20.19 06+108.6
01+0104. 02+0156. 03+1139. 04+37.77 05+24.75 06+108.6
01+0104. 02+0156. 03+1142. 04+37.60 05+29.67 06+108.6
01+0104. 02+0156. 03+1145. 04+37.35 05+32.29 06+108.6
01+0104. 02+0156. 03+1148. 04+37.10 05+32.61 06+108.6
01+0104. 02+0156. 03+1151. 04+36.87 05+37.20 06+109.2
01+0104. 02+0156. 03+1154. 04+36.65 05+37.14 06+109.2
01+0104. 02+0156. 03+1157. 04+36.49 05+36.98 06+109.6
01+0104. 02+0156. 03+1200. 04+36.31 05+36.80 06+109.6
01+0104. 02+0156. 03+1203. 04+36.15 05+32.15 06+108.9
01+0104. 02+0156. 03+1206. 04+36.05 05+31.47 06+108.9
01+0104. 02+0156. 03+1209. 04+36.03 05+27.52 06+109.6
01+0104. 02+0156. 03+1212. 04+36.67 05+27.75 06+109.6
01+0104. 02+0156. 03+1215. 04+36.51 05+28.82 06+109.6
01+0104. 02+0156. 03+1218. 04+36.11 05+30.22 06+109.9
01+0104. 02+0156. 03+1221. 04+35.75 05+35.10 06+110.3
01+0104. 02+0156. 03+1224. 04+35.42 05+35.58 06+110.6
01+0104. 02+0156. 03+1227. 04+35.07 05+35.89 06+111.0
01+0104. 02+0156. 03+1230. 04+34.69 05+35.75 06+110.6
01+0104. 02+0156. 03+1233. 04+34.33 05+35.80 06+110.3
01+0104. 02+0156. 03+1236. 04+33.93 05+35.57 06+110.3
01+0104. 02+0156. 03+1239. 04+33.56 05+35.20 06+110.7
01+0104. 02+0156. 03+1242. 04+33.22 05+34.61 06+111.7
01+0104. 02+0156. 03+1245. 04+32.89 05+34.36 06+112.4
01+0104. 02+0156. 03+1248. 04+32.59 05+33.90 06+112.4
01+0104. 02+0156. 03+1251. 04+32.32 05+33.47 06+112.0
01+0104. 02+0156. 03+1254. 04+32.06 05+33.37 06+112.7
01+0104. 02+0156. 03+1257. 04+31.78 05+33.09 06+112.7
01+0104. 02+0156. 03+1300. 04+31.54 05+32.77 06+113.4
01+0104. 02+0156. 03+1303. 04+31.31 05+32.38 06+109.0
01+0104. 02+0156. 03+1306. 04+31.09 05+32.00 06+112.4
01+0104. 02+0156. 03+1309. 04+30.92 05+31.83 06+112.1
01+0104. 02+0156. 03+1312. 04+30.74 05+31.72 06+112.1
01+0104. 02+0156. 03+1315. 04+30.56 05+31.54 06+112.4
01+0104. 02+0156. 03+1318. 04+30.39 05+31.29 06+112.4
01+0104. 02+0156. 03+1321. 04+30.24 05+30.57 06+112.4
01+0104. 02+0156. 03+1324. 04+30.21 05+29.63 06+112.8
01+0104. 02+0156. 03+1327. 04+30.29 05+27.66 06+113.4
01+0104. 02+0156. 03+1330. 04+30.59 05+23.51 06+113.5
01+0104. 02+0156. 03+1333. 04+31.02 05+19.90 06+113.4
01+0104. 02+0156. 03+1336. 04+31.52 05+17.67 06+113.4
01+0104. 02+0156. 03+1339. 04+32.02 05+16.60 06+112.8
01+0104. 02+0156. 03+1342. 04+32.36 05+18.85 06+112.1
01+0104. 02+0156. 03+1345. 04+32.59 05+19.42 06+112.1

01+0104. 02+0156. 03+1348. 04+32.86 05+18.03 06+112.1
01+0104. 02+0156. 03+1351. 04+33.20 05+17.22 06+111.7
01+0104. 02+0156. 03+1354. 04+33.55 05+16.91 06+112.1
01+0104. 02+0156. 03+1357. 04+33.80 05+17.67 06+111.4
01+0104. 02+0156. 03+1400. 04+33.97 05+18.50 06+111.4
01+0104. 02+0156. 03+1403. 04+34.18 05+18.38 06+111.4
01+0104. 02+0156. 03+1406. 04+34.36 05+17.91 06+111.0
01+0104. 02+0156. 03+1409. 04+34.59 05+17.56 06+110.7
01+0104. 02+0156. 03+1412. 04+34.84 05+17.40 06+110.3
01+0104. 02+0156. 03+1415. 04+35.07 05+17.63 06+110.0
01+0104. 02+0156. 03+1418. 04+35.26 05+18.08 06+110.0
01+0104. 02+0156. 03+1421. 04+35.48 05+18.05 06+110.3
01+0104. 02+0156. 03+1424. 04+35.69 05+17.60 06+110.3
01+0104. 02+0156. 03+1427. 04+35.95 05+17.70 06+110.6
01+0104. 02+0156. 03+1430. 04+36.21 05+17.80 06+110.6
01+0104. 02+0156. 03+1433. 04+36.43 05+17.86 06+110.3
01+0104. 02+0156. 03+1436. 04+36.67 05+18.02 06+110.3
01+0104. 02+0156. 03+1439. 04+36.92 05+18.60 06+110.3
01+0104. 02+0156. 03+1442. 04+37.04 05+19.72 06+110.3
01+0104. 02+0156. 03+1445. 04+37.08 05+22.49 06+109.9
01+0104. 02+0156. 03+1448. 04+36.90 05+26.58 06+109.9
01+0104. 02+0156. 03+1451. 04+36.63 05+29.27 06+110.3
01+0104. 02+0156. 03+1454. 04+36.35 05+30.79 06+110.3
01+0104. 02+0156. 03+1457. 04+36.03 05+34.97 06+110.3
01+0104. 02+0156. 03+1500. 04+35.71 05+34.90 06+110.3
01+0104. 02+0156. 03+1503. 04+35.42 05+34.93 06+111.0
01+0104. 02+0156. 03+1506. 04+35.13 05+34.15 06+111.0
01+0104. 02+0156. 03+1509. 04+34.97 05+30.07 06+111.6
01+0104. 02+0156. 03+1512. 04+34.93 05+27.57 06+111.3
01+0104. 02+0156. 03+1515. 04+34.99 05+24.91 06+111.6
01+0104. 02+0156. 03+1518. 04+35.13 05+23.32 06+111.6
01+0104. 02+0156. 03+1521. 04+35.26 05+23.62 06+111.6
01+0104. 02+0156. 03+1524. 04+35.22 05+26.71 06+110.3
01+0104. 02+0156. 03+1527. 04+35.07 05+33.11 06+111.0
01+0104. 02+0156. 03+1530. 04+34.82 05+33.51 06+113.0
01+0104. 02+0156. 03+1533. 04+34.63 05+33.57 06+112.0
01+0104. 02+0156. 03+1536. 04+34.38 05+34.30 06+112.0
01+0104. 02+0156. 03+1539. 04+34.05 05+34.54 06+112.3
01+0104. 02+0156. 03+1542. 04+33.71 05+34.61 06+112.7
01+0104. 02+0156. 03+1545. 04+33.38 05+34.69 06+112.3
01+0104. 02+0156. 03+1548. 04+33.05 05+34.28 06+112.4
01+0104. 02+0156. 03+1551. 04+32.77 05+33.91 06+112.4
01+0104. 02+0156. 03+1554. 04+32.50 05+33.81 06+112.0
01+0104. 02+0156. 03+1557. 04+32.18 05+33.74 06+112.4
01+0104. 02+0156. 03+1600. 04+31.88 05+33.60 06+112.4
01+0104. 02+0156. 03+1603. 04+31.56 05+33.19 06+112.4
01+0104. 02+0156. 03+1606. 04+31.28 05+32.84 06+112.4
01+0104. 02+0156. 03+1609. 04+30.99 05+32.47 06+112.1
01+0104. 02+0156. 03+1612. 04+30.76 05+32.07 06+111.4
01+0104. 02+0156. 03+1615. 04+30.54 05+31.77 06+111.1

01+0104. 02+0156. 03+1618. 04+30.34 05+31.57 06+110.4
01+0104. 02+0156. 03+1621. 04+30.14 05+31.37 06+110.4
01+0104. 02+0156. 03+1624. 04+29.98 05+31.13 06+110.4
01+0104. 02+0156. 03+1627. 04+29.80 05+30.95 06+110.4
01+0104. 02+0156. 03+1630. 04+29.64 05+30.70 06+110.4
01+0104. 02+0156. 03+1633. 04+29.47 05+30.54 06+110.4
01+0104. 02+0156. 03+1636. 04+29.33 05+30.40 06+110.4
01+0104. 02+0156. 03+1639. 04+29.18 05+30.25 06+110.1
01+0104. 02+0156. 03+1642. 04+29.04 05+30.11 06+110.1
01+0104. 02+0156. 03+1645. 04+28.92 05+29.98 06+110.1
01+0104. 02+0156. 03+1648. 04+28.80 05+29.79 06+110.1
01+0104. 02+0156. 03+1651. 04+28.68 05+29.66 06+110.1
01+0104. 02+0156. 03+1654. 04+28.57 05+29.47 06+110.1
01+0104. 02+0156. 03+1657. 04+28.46 05+29.28 06+110.1
01+0104. 02+0156. 03+1700. 04+28.37 05+29.19 06+109.8
01+0104. 02+0156. 03+1703. 04+28.27 05+29.09 06+109.5
01+0104. 02+0156. 03+1706. 04+28.19 05+28.93 06+109.5
01+0104. 02+0156. 03+1709. 04+28.12 05+28.77 06+109.5
01+0104. 02+0156. 03+1712. 04+28.04 05+28.70 06+108.8
01+0104. 02+0156. 03+1715. 04+27.95 05+28.61 06+108.8
01+0104. 02+0156. 03+1718. 04+27.87 05+28.53 06+108.4
01+0104. 02+0156. 03+1721. 04+27.79 05+28.45 06+108.1
01+0104. 02+0156. 03+1724. 04+27.72 05+28.38 06+108.1
01+0104. 02+0156. 03+1727. 04+27.66 05+28.32 06+108.1
01+0104. 02+0156. 03+1730. 04+27.57 05+28.31 06+107.4
01+0104. 02+0156. 03+1733. 04+27.50 05+28.25 06+107.4
01+0104. 02+0156. 03+1736. 04+27.43 05+28.17 06+107.4
01+0104. 02+0156. 03+1739. 04+27.35 05+28.09 06+107.4
01+0104. 02+0156. 03+1742. 04+27.28 05+28.02 06+107.4
01+0104. 02+0156. 03+1745. 04+27.19 05+27.93 06+106.8
01+0104. 02+0156. 03+1748. 04+27.11 05+27.85 06+106.8
01+0104. 02+0156. 03+1751. 04+27.02 05+27.77 06+106.8
01+0104. 02+0156. 03+1754. 04+26.94 05+27.68 06+106.8
01+0104. 02+0156. 03+1757. 04+26.86 05+27.60 06+106.4
01+0104. 02+0156. 03+1800. 04+26.79 05+27.53 06+106.1
01+0104. 02+0156. 03+1803. 04+26.74 05+27.48 06+106.1
01+0104. 02+0156. 03+1806. 04+26.65 05+27.39 06+106.1
01+0104. 02+0156. 03+1809. 04+26.58 05+27.32 06+105.8
01+0104. 02+0156. 03+1812. 04+26.49 05+27.40 06+105.4
01+0104. 02+0156. 03+1815. 04+26.40 05+27.31 06+105.1
01+0104. 02+0156. 03+1818. 04+26.33 05+27.15 06+104.8
01+0104. 02+0156. 03+1821. 04+26.24 05+27.07 06+104.4
01+0104. 02+0156. 03+1824. 04+26.17 05+26.91 06+104.4
01+0104. 02+0156. 03+1827. 04+26.10 05+26.92 06+103.8
01+0104. 02+0156. 03+1830. 04+26.02 05+26.77 06+103.8
01+0104. 02+0156. 03+1833. 04+25.95 05+26.69 06+103.8
01+0104. 02+0156. 03+1836. 04+25.89 05+26.55 06+103.4
01+0104. 02+0156. 03+1839. 04+25.84 05+26.41 06+103.1
01+0104. 02+0156. 03+1842. 04+25.76 05+26.34 06+103.1
01+0104. 02+0156. 03+1845. 04+25.71 05+26.28 06+102.4

01+0104. 02+0156. 03+1848. 04+25.66 05+26.08 06+102.4
01+0104. 02+0156. 03+1851. 04+25.61 05+26.02 06+102.4
01+0104. 02+0156. 03+1854. 04+25.56 05+25.98 06+101.7
01+0104. 02+0156. 03+1857. 04+25.52 05+25.93 06+101.7
01+0104. 02+0156. 03+1900. 04+25.49 05+25.82 06+101.4
01+0104. 02+0156. 03+1903. 04+25.45 05+25.78 06+101.1
01+0104. 02+0156. 03+1906. 04+25.42 05+25.75 06+101.1
01+0104. 02+0156. 03+1909. 04+25.38 05+25.71 06+101.1
01+0104. 02+0156. 03+1912. 04+25.35 05+25.60 06+100.7
01+0104. 02+0156. 03+1915. 04+25.32 05+25.57 06+100.4
01+0104. 02+0156. 03+1918. 04+25.28 05+25.53 06+100.4
01+0104. 02+0156. 03+1921. 04+25.25 05+25.50 06+100.4
01+0104. 02+0156. 03+1924. 04+25.21 05+25.46 06+100.1
01+0104. 02+0156. 03+1927. 04+25.19 05+25.44 06+100.1
01+0104. 02+0156. 03+1930. 04+25.14 05+25.39 06+100.1
01+0104. 02+0156. 03+1933. 04+25.12 05+25.37 06+099.7
01+0104. 02+0156. 03+1936. 04+25.09 05+25.34 06+099.7
01+0104. 02+0156. 03+1939. 04+25.05 05+25.30 06+099.4
01+0104. 02+0156. 03+1942. 04+25.02 05+25.27 06+099.4
01+0104. 02+0156. 03+1945. 04+25.00 05+25.24 06+099.0
01+0104. 02+0156. 03+1948. 04+24.95 05+25.12 06+099.0
01+0104. 02+0156. 03+1951. 04+24.93 05+25.09 06+098.7
01+0104. 02+0156. 03+1954. 04+24.90 05+25.06 06+098.7
01+0104. 02+0156. 03+1957. 04+24.86 05+24.94 06+098.4
01+0104. 02+0156. 03+2000. 04+24.83 05+24.91 06+098.0
01+0104. 02+0156. 03+2003. 04+24.81 05+24.90 06+098.0
01+0104. 02+0156. 03+2006. 04+24.79 05+24.87 06+098.0
01+0104. 02+0156. 03+2009. 04+24.77 05+24.86 06+098.0
01+0104. 02+0156. 03+2012. 04+24.74 05+24.83 06+097.7
01+0104. 02+0156. 03+2015. 04+24.72 05+24.80 06+097.4
01+0104. 02+0156. 03+2018. 04+24.70 05+24.79 06+097.4
01+0104. 02+0156. 03+2021. 04+24.67 05+24.76 06+097.4
01+0104. 02+0156. 03+2024. 04+24.66 05+24.74 06+097.4
01+0104. 02+0156. 03+2027. 04+24.65 05+24.73 06+097.4
01+0104. 02+0156. 03+2030. 04+24.62 05+24.70 06+097.0
01+0104. 02+0156. 03+2033. 04+24.59 05+24.67 06+096.7
01+0104. 02+0156. 03+2036. 04+24.58 05+24.58 06+096.7
01+0104. 02+0156. 03+2039. 04+24.55 05+24.63 06+096.7
01+0104. 02+0156. 03+2042. 04+24.55 05+24.63 06+096.0
01+0104. 02+0156. 03+2045. 04+24.51 05+24.59 06+096.0
01+0104. 02+0156. 03+2048. 04+24.49 05+24.49 06+096.0
01+0104. 02+0156. 03+2051. 04+24.47 05+24.47 06+096.0
01+0104. 02+0156. 03+2054. 04+24.47 05+24.47 06+095.3
01+0104. 02+0156. 03+2057. 04+24.44 05+24.44 06+096.0
01+0104. 02+0156. 03+2100. 04+24.42 05+24.42 06+095.7
01+0104. 02+0156. 03+2103. 04+24.40 05+24.40 06+095.3
01+0104. 02+0156. 03+2106. 04+24.38 05+24.38 06+095.3
01+0104. 02+0156. 03+2109. 04+24.37 05+24.29 06+095.3
01+0104. 02+0156. 03+2112. 04+24.35 05+24.27 06+095.0
01+0104. 02+0156. 03+2115. 04+24.34 05+24.26 06+095.0

01+0104. 02+0156. 03+2118. 04+24.33 05+24.24 06+095.0
01+0104. 02+0156. 03+2121. 04+24.30 05+24.22 06+095.0
01+0104. 02+0156. 03+2124. 04+24.27 05+24.19 06+095.0
01+0104. 02+0156. 03+2127. 04+24.24 05+24.16 06+095.0
01+0104. 02+0156. 03+2130. 04+24.23 05+24.15 06+095.0
01+0104. 02+0156. 03+2133. 04+24.20 05+24.12 06+095.0
01+0104. 02+0156. 03+2136. 04+24.18 05+24.09 06+095.0
01+0104. 02+0156. 03+2139. 04+24.15 05+24.07 06+095.0
01+0104. 02+0156. 03+2142. 04+24.12 05+23.96 06+095.0
01+0104. 02+0156. 03+2145. 04+24.09 05+23.93 06+094.7
01+0104. 02+0156. 03+2148. 04+24.07 05+23.90 06+094.3
01+0104. 02+0156. 03+2151. 04+24.05 05+23.89 06+094.7
01+0104. 02+0156. 03+2154. 04+24.03 05+23.78 06+094.0
01+0104. 02+0156. 03+2157. 04+24.01 05+23.76 06+093.7
01+0104. 02+0156. 03+2200. 04+23.97 05+23.64 06+093.7
01+0104. 02+0156. 03+2203. 04+23.94 05+23.61 06+093.7
01+0104. 02+0156. 03+2206. 04+23.93 05+23.52 06+093.7
01+0104. 02+0156. 03+2209. 04+23.90 05+23.49 06+093.7
01+0104. 02+0156. 03+2212. 04+23.89 05+23.48 06+093.7
01+0104. 02+0156. 03+2215. 04+23.88 05+23.46 06+093.7
01+0104. 02+0156. 03+2218. 04+23.85 05+23.44 06+093.7
01+0104. 02+0156. 03+2221. 04+23.85 05+23.44 06+093.7
01+0104. 02+0156. 03+2224. 04+23.83 05+23.42 06+093.3
01+0104. 02+0156. 03+2227. 04+23.82 05+23.41 06+093.0
01+0104. 02+0156. 03+2230. 04+23.81 05+23.39 06+093.0
01+0104. 02+0156. 03+2233. 04+23.79 05+23.38 06+093.0
01+0104. 02+0156. 03+2236. 04+23.78 05+23.45 06+092.7
01+0104. 02+0156. 03+2239. 04+23.78 05+23.37 06+092.3
01+0104. 02+0156. 03+2242. 04+23.77 05+23.44 06+092.3
01+0104. 02+0156. 03+2245. 04+23.75 05+23.34 06+092.3
01+0104. 02+0156. 03+2248. 04+23.75 05+23.34 06+092.3
01+0104. 02+0156. 03+2251. 04+23.75 05+23.34 06+092.3
01+0104. 02+0156. 03+2254. 04+23.75 05+23.26 06+092.3
01+0104. 02+0156. 03+2257. 04+23.77 05+23.35 06+092.3
01+0104. 02+0156. 03+2300. 04+23.77 05+23.27 06+092.3
01+0104. 02+0156. 03+2303. 04+23.77 05+23.27 06+092.0
01+0104. 02+0156. 03+2306. 04+23.74 05+23.33 06+092.3
01+0104. 02+0156. 03+2309. 04+23.74 05+23.33 06+092.0
01+0104. 02+0156. 03+2312. 04+23.74 05+23.41 06+091.6
01+0104. 02+0156. 03+2315. 04+23.75 05+23.50 06+091.6
01+0104. 02+0156. 03+2318. 04+23.75 05+23.42 06+091.6
01+0104. 02+0156. 03+2321. 04+23.75 05+23.42 06+091.6
01+0104. 02+0156. 03+2324. 04+23.77 05+23.35 06+091.3
01+0104. 02+0156. 03+2327. 04+23.77 05+23.35 06+091.0
01+0104. 02+0156. 03+2330. 04+23.79 05+23.38 06+091.0
01+0104. 02+0156. 03+2333. 04+23.79 05+23.46 06+091.0
01+0104. 02+0156. 03+2336. 04+23.82 05+23.49 06+091.0
01+0104. 02+0156. 03+2339. 04+23.82 05+23.49 06+091.0
01+0104. 02+0156. 03+2342. 04+23.83 05+23.42 06+090.6
01+0104. 02+0156. 03+2345. 04+23.83 05+23.50 06+091.0

01+0104. 02+0156. 03+2348. 04+23.82 05+23.41 06+090.6
01+0104. 02+0156. 03+2351. 04+23.82 05+23.41 06+090.3
01+0104. 02+0156. 03+2354. 04+23.83 05+23.42 06+090.3
01+0104. 02+0156. 03+2357. 04+23.85 05+23.44 06+090.3
01+0104. 02+0157. 03+0000. 04+23.86 05+23.45 06+090.3
01+0104. 02+0157. 03+0003. 04+23.88 05+23.46 06+089.9
01+0104. 02+0157. 03+0006. 04+23.88 05+23.46 06+089.6
01+0104. 02+0157. 03+0009. 04+23.88 05+23.55 06+089.3
01+0104. 02+0157. 03+0012. 04+23.89 05+23.56 06+088.9
01+0104. 02+0157. 03+0015. 04+23.92 05+23.59 06+088.9
01+0104. 02+0157. 03+0018. 04+23.92 05+23.59 06+088.3
01+0104. 02+0157. 03+0021. 04+23.94 05+23.69 06+087.9
01+0104. 02+0157. 03+0024. 04+23.93 05+23.60 06+088.3
01+0104. 02+0157. 03+0027. 04+23.94 05+23.70 06+088.3
01+0104. 02+0157. 03+0030. 04+23.94 05+23.70 06+087.6
01+0104. 02+0157. 03+0033. 04+23.94 05+23.86 06+087.6
01+0104. 02+0157. 03+0036. 04+23.96 05+23.79 06+087.2
01+0104. 02+0157. 03+0039. 04+23.97 05+23.80 06+086.9
01+0104. 02+0157. 03+0042. 04+23.96 05+23.79 06+086.9
01+0104. 02+0157. 03+0045. 04+23.96 05+23.87 06+086.9
01+0104. 02+0157. 03+0048. 04+23.94 05+23.86 06+086.9
01+0104. 02+0157. 03+0051. 04+23.96 05+23.87 06+086.9
01+0104. 02+0157. 03+0054. 04+23.94 05+23.78 06+087.6
01+0104. 02+0157. 03+0057. 04+23.93 05+23.77 06+087.2
01+0104. 02+0157. 03+0100. 04+23.92 05+23.75 06+087.2
01+0104. 02+0157. 03+0103. 04+23.93 05+23.68 06+086.9
01+0104. 02+0157. 03+0106. 04+23.90 05+23.74 06+087.6
01+0104. 02+0157. 03+0109. 04+23.89 05+23.64 06+087.6
01+0104. 02+0157. 03+0112. 04+23.89 05+23.64 06+087.2
01+0104. 02+0157. 03+0115. 04+23.89 05+23.64 06+086.9
01+0104. 02+0157. 03+0118. 04+23.89 05+23.72 06+086.9
01+0104. 02+0157. 03+0121. 04+23.91 05+23.75 06+086.2
01+0104. 02+0157. 03+0124. 04+23.91 05+23.75 06+086.2
01+0104. 02+0157. 03+0127. 04+23.90 05+23.74 06+086.2
01+0104. 02+0157. 03+0130. 04+23.90 05+23.66 06+086.2
01+0104. 02+0157. 03+0133. 04+23.90 05+23.57 06+086.6
01+0104. 02+0157. 03+0136. 04+23.91 05+23.58 06+086.6
01+0104. 02+0157. 03+0139. 04+23.90 05+23.49 06+087.6
01+0104. 02+0157. 03+0142. 04+23.89 05+23.48 06+086.9
01+0104. 02+0157. 03+0145. 04+23.89 05+23.48 06+087.2
01+0104. 02+0157. 03+0148. 04+23.89 05+23.56 06+087.6
01+0104. 02+0157. 03+0151. 04+23.89 05+23.72 06+085.2
01+0104. 02+0157. 03+0154. 04+23.85 05+23.85 06+082.2
01+0104. 02+0157. 03+0157. 04+23.82 05+23.99 06+094.3
01+0104. 02+0157. 03+0200. 04+23.75 05+24.41 06+107.9
01+0104. 02+0157. 03+0203. 04+23.60 05+24.51 06+104.5
01+0104. 02+0157. 03+0206. 04+23.49 05+24.65 06+099.8
01+0104. 02+0157. 03+0209. 04+23.36 05+24.52 06+103.5
01+0104. 02+0157. 03+0212. 04+23.23 05+24.63 06+107.5
01+0104. 02+0157. 03+0215. 04+23.08 05+24.57 06+110.9

01+0104. 02+0157. 03+0218. 04+22.93 05+24.34 06+112.3
01+0104. 02+0157. 03+0221. 04+22.79 05+24.19 06+115.3
01+0104. 02+0157. 03+0224. 04+22.64 05+23.97 06+114.7
01+0104. 02+0157. 03+0227. 04+22.52 05+23.68 06+120.1
01+0104. 02+0157. 03+0230. 04+22.42 05+23.41 06+116.0
01+0104. 02+0157. 03+0233. 04+22.34 05+23.17 06+116.7
01+0104. 02+0157. 03+0236. 04+22.25 05+22.99 06+119.4
01+0104. 02+0157. 03+0239. 04+22.16 05+22.98 06+119.4
01+0104. 02+0157. 03+0242. 04+22.08 05+22.99 06+119.4
01+0104. 02+0157. 03+0245. 04+22.01 05+22.76 06+121.8
01+0104. 02+0157. 03+0248. 04+21.96 05+22.54 06+120.4
01+0104. 02+0157. 03+0251. 04+21.91 05+22.49 06+120.1
01+0104. 02+0157. 03+0254. 04+21.86 05+22.44 06+119.1
01+0104. 02+0157. 03+0257. 04+21.81 05+22.38 06+118.4
01+0104. 02+0157. 03+0300. 04+21.76 05+22.25 06+117.0
01+0104. 02+0157. 03+0303. 04+21.73 05+22.14 06+115.3
01+0104. 02+0157. 03+0306. 04+21.69 05+22.02 06+115.3
01+0104. 02+0157. 03+0309. 04+21.66 05+21.91 06+120.4
01+0104. 02+0157. 03+0312. 04+21.64 05+21.89 06+123.5
01+0104. 02+0157. 03+0315. 04+21.61 05+21.86 06+120.1
01+0104. 02+0157. 03+0318. 04+21.59 05+21.84 06+117.1
01+0104. 02+0157. 03+0321. 04+21.56 05+21.89 06+118.7
01+0104. 02+0157. 03+0324. 04+21.52 05+21.94 06+118.4
01+0104. 02+0157. 03+0327. 04+21.48 05+21.82 06+118.7
01+0104. 02+0157. 03+0330. 04+21.45 05+21.78 06+118.4
01+0104. 02+0157. 03+0333. 04+21.42 05+21.67 06+117.7
01+0104. 02+0157. 03+0336. 04+21.41 05+21.57 06+118.8
01+0104. 02+0157. 03+0339. 04+21.38 05+21.55 06+117.4
01+0104. 02+0157. 03+0342. 04+21.37 05+21.45 06+116.4
01+0104. 02+0157. 03+0345. 04+21.36 05+21.44 06+116.0
01+0104. 02+0157. 03+0348. 04+21.34 05+21.43 06+115.7
01+0104. 02+0157. 03+0351. 04+21.33 05+21.41 06+116.4
01+0104. 02+0157. 03+0354. 04+21.32 05+21.32 06+117.4
01+0104. 02+0157. 03+0357. 04+21.33 05+21.25 06+117.7
01+0104. 02+0157. 03+0400. 04+21.33 05+21.17 06+117.7
01+0104. 02+0157. 03+0403. 04+21.34 05+21.10 06+118.1
01+0104. 02+0157. 03+0406. 04+21.36 05+21.11 06+118.4
01+0104. 02+0157. 03+0409. 04+21.36 05+21.11 06+118.4
01+0104. 02+0157. 03+0412. 04+21.37 05+21.12 06+118.1
01+0104. 02+0157. 03+0415. 04+21.37 05+21.12 06+118.4
01+0104. 02+0157. 03+0418. 04+21.38 05+21.13 06+118.4
01+0104. 02+0157. 03+0421. 04+21.38 05+21.13 06+118.8
01+0104. 02+0157. 03+0424. 04+21.39 05+21.15 06+119.8
01+0104. 02+0157. 03+0427. 04+21.39 05+21.15 06+119.4
01+0104. 02+0157. 03+0430. 04+21.41 05+21.16 06+118.4
01+0104. 02+0157. 03+0433. 04+21.41 05+21.16 06+118.4
01+0104. 02+0157. 03+0436. 04+21.41 05+21.16 06+118.1
01+0104. 02+0157. 03+0439. 04+21.41 05+21.16 06+118.1
01+0104. 02+0157. 03+0442. 04+21.41 05+21.16 06+118.1
01+0104. 02+0157. 03+0445. 04+21.42 05+21.17 06+118.8

01+0104. 02+0157. 03+0448. 04+21.41 05+21.16 06+118.4
01+0104. 02+0157. 03+0451. 04+21.42 05+21.17 06+118.4
01+0104. 02+0157. 03+0454. 04+21.42 05+21.17 06+118.8
01+0104. 02+0157. 03+0457. 04+21.42 05+21.17 06+119.1
01+0104. 02+0157. 03+0500. 04+21.41 05+21.08 06+119.1
01+0104. 02+0157. 03+0503. 04+21.41 05+20.99 06+119.1
01+0104. 02+0157. 03+0506. 04+21.42 05+21.01 06+119.1
01+0104. 02+0157. 03+0509. 04+21.43 05+21.02 06+119.4
01+0104. 02+0157. 03+0512. 04+21.46 05+20.96 06+119.4
01+0104. 02+0157. 03+0515. 04+21.48 05+20.90 06+119.1
01+0104. 02+0157. 03+0518. 04+21.51 05+21.01 06+119.1
01+0104. 02+0157. 03+0521. 04+21.52 05+20.94 06+119.4
01+0104. 02+0157. 03+0524. 04+21.55 05+21.13 06+119.4
01+0104. 02+0157. 03+0527. 04+21.55 05+21.13 06+119.8
01+0104. 02+0157. 03+0530. 04+21.55 05+21.13 06+119.8
01+0104. 02+0157. 03+0533. 04+21.55 05+21.13 06+119.8
01+0104. 02+0157. 03+0536. 04+21.55 05+21.13 06+120.1
01+0104. 02+0157. 03+0539. 04+21.55 05+21.13 06+119.8
01+0104. 02+0157. 03+0542. 04+21.55 05+21.13 06+120.4
01+0104. 02+0157. 03+0545. 04+21.55 05+21.13 06+120.4
01+0104. 02+0157. 03+0548. 04+21.55 05+21.05 06+120.4
01+0104. 02+0157. 03+0551. 04+21.55 05+20.97 06+120.4
01+0104. 02+0157. 03+0554. 04+21.56 05+20.90 06+120.4
01+0104. 02+0157. 03+0557. 04+21.59 05+21.34 06+120.4
01+0104. 02+0157. 03+0600. 04+21.57 05+21.49 06+120.4
01+0104. 02+0157. 03+0603. 04+21.56 05+21.48 06+120.4
01+0104. 02+0157. 03+0606. 04+21.55 05+21.47 06+120.4
01+0104. 02+0157. 03+0609. 04+21.54 05+21.29 06+120.8
01+0104. 02+0157. 03+0612. 04+21.52 05+21.27 06+120.8
01+0104. 02+0157. 03+0615. 04+21.52 05+21.11 06+121.1
01+0104. 02+0157. 03+0618. 04+21.51 05+20.93 06+121.1
01+0104. 02+0157. 03+0621. 04+21.52 05+20.78 06+121.1
01+0104. 02+0157. 03+0624. 04+21.54 05+20.62 06+121.1
01+0104. 02+0157. 03+0627. 04+21.56 05+20.65 06+121.1
01+0104. 02+0157. 03+0630. 04+21.60 05+20.69 06+121.1
01+0104. 02+0157. 03+0633. 04+21.64 05+20.73 06+121.1
01+0104. 02+0157. 03+0636. 04+21.68 05+20.68 06+121.1
01+0104. 02+0157. 03+0639. 04+21.73 05+20.65 06+121.1
01+0104. 02+0157. 03+0642. 04+21.79 05+20.72 06+121.1
01+0104. 02+0157. 03+0645. 04+21.84 05+20.77 06+121.1
01+0104. 02+0157. 03+0648. 04+21.87 05+20.79 06+121.1
01+0104. 02+0157. 03+0651. 04+21.92 05+20.68 06+121.1
01+0104. 02+0157. 03+0654. 04+21.96 05+20.72 06+121.4
01+0104. 02+0157. 03+0657. 04+22.03 05+20.78 06+121.4
01+0104. 02+0157. 03+0700. 04+22.12 05+20.71 06+121.1
01+0104. 02+0157. 03+0703. 04+22.18 05+20.77 06+121.1
01+0104. 02+0157. 03+0706. 04+22.26 05+20.69 06+121.4
01+0104. 02+0157. 03+0709. 04+22.40 05+20.50 06+122.1
01+0104. 02+0157. 03+0712. 04+22.65 05+20.25 06+122.5
01+0104. 02+0157. 03+0715. 04+22.97 05+20.49 06+122.5

01+0104. 02+0157. 03+0718. 04+23.28 05+20.96 06+122.8
01+0104. 02+0157. 03+0721. 04+23.60 05+20.87 06+122.8
01+0104. 02+0157. 03+0724. 04+23.95 05+20.98 06+123.4
01+0104. 02+0157. 03+0727. 04+24.30 05+21.65 06+123.1
01+0104. 02+0157. 03+0730. 04+24.49 05+22.67 06+123.1
01+0104. 02+0157. 03+0733. 04+24.56 05+22.99 06+123.8
01+0104. 02+0157. 03+0736. 04+24.73 05+22.41 06+124.1
01+0104. 02+0157. 03+0739. 04+24.99 05+25.57 06+123.4
01+0104. 02+0157. 03+0742. 04+25.25 05+26.07 06+124.1
01+0104. 02+0157. 03+0745. 04+25.50 05+26.00 06+124.4
01+0104. 02+0157. 03+0748. 04+25.75 05+25.91 06+124.4
01+0104. 02+0157. 03+0751. 04+25.99 05+25.66 06+124.8
01+0104. 02+0157. 03+0754. 04+26.21 05+25.30 06+124.8
01+0104. 02+0157. 03+0757. 04+26.43 05+24.78 06+125.1
01+0104. 02+0157. 03+0800. 04+26.66 05+24.36 06+125.1
01+0104. 02+0157. 03+0803. 04+26.92 05+24.53 06+125.1
01+0104. 02+0157. 03+0806. 04+27.13 05+25.56 06+125.1
01+0104. 02+0157. 03+0809. 04+27.31 05+27.31 06+125.1
01+0104. 02+0157. 03+0812. 04+27.41 05+27.41 06+124.7
01+0104. 02+0157. 03+0815. 04+27.47 05+28.79 06+124.7
01+0104. 02+0157. 03+0818. 04+27.50 05+27.26 06+124.4
01+0104. 02+0157. 03+0821. 04+27.50 05+27.59 06+124.4
01+0104. 02+0157. 03+0824. 04+27.47 05+27.47 06+124.4
01+0104. 02+0157. 03+0827. 04+27.49 05+27.32 06+124.4
01+0104. 02+0157. 03+0830. 04+27.52 05+27.19 06+124.4
01+0104. 02+0157. 03+0833. 04+27.61 05+29.25 06+124.4
01+0104. 02+0157. 03+0836. 04+27.72 05+29.36 06+124.4
01+0104. 02+0157. 03+0839. 04+27.81 05+29.62 06+124.7
01+0104. 02+0157. 03+0842. 04+27.88 05+27.80 06+125.0
01+0104. 02+0157. 03+0845. 04+27.88 05+28.87 06+124.7
01+0104. 02+0157. 03+0848. 04+27.82 05+28.23 06+124.7
01+0104. 02+0157. 03+0851. 04+27.81 05+28.22 06+124.0
01+0104. 02+0157. 03+0854. 04+27.87 05+27.79 06+125.0
01+0104. 02+0157. 03+0857. 04+27.96 05+28.37 06+125.0
01+0104. 02+0157. 03+0900. 04+28.05 05+30.19 06+125.4
01+0104. 02+0157. 03+0903. 04+28.05 05+28.96 06+125.4
01+0104. 02+0157. 03+0906. 04+28.07 05+30.21 06+125.0
01+0104. 02+0157. 03+0909. 04+28.19 05+29.75 06+126.0
01+0104. 02+0157. 03+0912. 04+28.27 05+30.16 06+125.7
01+0104. 02+0157. 03+0915. 04+28.39 05+29.71 06+125.7
01+0104. 02+0157. 03+0918. 04+28.46 05+29.44 06+126.4
01+0104. 02+0157. 03+0921. 04+28.36 05+29.51 06+126.0
01+0104. 02+0157. 03+0924. 04+28.32 05+29.06 06+126.0
01+0104. 02+0157. 03+0927. 04+28.25 05+29.82 06+125.7
01+0104. 02+0157. 03+0930. 04+28.10 05+30.07 06+125.3
01+0104. 02+0157. 03+0933. 04+27.96 05+29.44 06+125.7
01+0104. 02+0157. 03+0936. 04+27.85 05+29.50 06+125.4
01+0104. 02+0157. 03+0939. 04+27.81 05+27.81 06+125.0
01+0104. 02+0157. 03+0942. 04+27.98 05+28.80 06+125.4
01+0104. 02+0157. 03+0945. 04+28.22 05+27.57 06+125.4

```
01+0104. 02+0157. 03+0948. 04+28.50 05+26.94 06+125.7
01+0104. 02+0157. 03+0951. 04+28.75 05+26.95 06+125.7
01+0104. 02+0157. 03+0954. 04+29.01 05+27.03 06+127.0
01+0104. 02+0157. 03+0957. 04+29.23 05+27.26 06+126.4
01+0104. 02+0157. 03+1000. 04+29.58 05+27.45 06+126.4


!Program to read the datalogger format and output
! self-potential and temperature data for plotting
!The format of the input file is....
!0....+....1....+....2....+....3....+....4....+....5....+....6
!01+0104. 02+0157. 03+0821. 04+27.50 05+27.59 06+124.4
!01+0104. 02+0157. 03+0824. 04+27.47 05+27.47 06+124.4
!01+0104. 02+0157. 03+0827. 04+27.49 05+27.32 06+124.4
!01+0104. 02+0157. 03+0830. 04+27.52 05+27.19 06+124.4
!01+0104. 02+0157. 03+0833. 04+27.61 05+29.25 06+124.4

open #1: name "cerrosp.dat"
open #2: name "cerro sp", create newold
erase #2
do while more #1

line input #1: dum$

let day = val(dum$[15:18])
let hour = val(dum$[24:26])
let min = val(dum$[27:29])
let airtemp = val(dum$[34:38])
let grdtemp = val(dum$[44:48])
let mv = val(dum$[54:60])
!print day,hour,min,mV
let hour = day*24 + hour + min/(60) - 155*24

print #2: hour,airtemp,grdtemp,mv

loop

end
```

Soil ^{222}Rn Pulse During the Initial Phase of the June-August Eruption of Cerro Negro, Nicaragua

Charles Connor

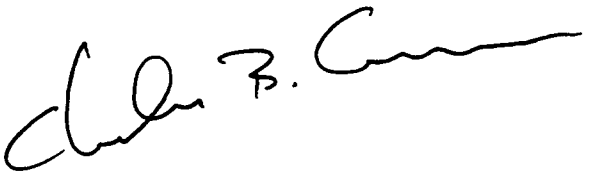

The June 1995 phreatic eruption of Cerro Negro, a small-volume basaltic cinder cone in Nicaragua, provided a unique opportunity to quantify ^{222}Rn degassing from soils in response to explosive volcanic activity. ^{222}Rn was monitored at 28 stations distributed north and southeast of the volcano. A pulse of elevated ^{222}Rn degassing occurred early in the eruption along a >1 km-long zone, extending at least 750 m beyond the base of the cinder cone. These observations demonstrate that degassing pulses through volcanoes and surrounding rock can be coherent over large areas in response to low-energy phreatic eruptions.

1.0 Introduction

Radon concentrations in soils and fumarole gases are used to identify areas of convective upwelling and to monitor changes in degassing through time (Chirkov, 1976; Crenshaw et al., 1982; LeCloarec et al., 1994). Monitoring of degassing (Braubon et al., 1990) through soils on and around volcanoes can document the response of the volcano-hydrothermal system to changing magmatic activity. Because degassing through soils can be monitored far from the active crater, this method is often a practical and less hazardous alternative to direct fumarole sampling during volcanic crises. However, the response of soil gases is less direct than the response of fumaroles to changing magmatic activity and eruptions because of the added complexities of gas transport through the volcano's edifice and surrounding rock. In June 1995, ^{222}Rn gas flow was monitored during explosive volcanic activity at Volcán Cerro Negro, Nicaragua, employing electrostatically charged teflon (E-perm®) detectors (Kotrappa et al., 1988; 1990). Changes in soil ^{222}Rn concentration were monitored at 24 to 48 hour intervals at stations deployed around the volcano. These observations show for the first time that large changes in soil ^{222}Rn concentration can occur simultaneously at widely separated stations in response to volcanic eruption. Frequent ^{222}Rn sampling at multiple stations provides a sense of the magnitude, time scales and area affected by convective gas transport during volcanic eruptions.

Cerro Negro is a small-volume basaltic cinder cone that has erupted 22 times since its formation in 1850 (Taylor and Stoiber, 1973; Rose et al.; 1973; Simkin and Siebert, 1994; McKnight et al., 1994) and is part of a cluster of small shields, cinder cones, and maars of the La Hoya complex (Figure 1). Cinder cones and maars of this complex form a broad NNW-trending alignment. At Cerro Negro, this alignment is manifested by the positions of nearby cinder cones, phreatic pit craters, and lava boccas. Thermal features are limited to superheated fumaroles in the crater (≈ 350 °C), and low temperature (<100 °C) fumaroles located in arcuate fractures on the crater rim and near phreatic pit craters between Cerro Negro and the cinder cone Cerro La Mula. The last eruption prior to 1995 was in April, 1992. Plinian activity during this eruption widened the crater to approximately 400 m and decreased the volume of the cone (Connor et al., 1993). Degassing did not persist after this eruption. No gas plume was visible even days after the end of explosive activity and fumarole temperatures in the crater and arcuate fractures on the crater rim rapidly returned to pre-eruption temperatures (90–350°C).

FIGURE 1. Location of Cerro Negro, Nicaragua and nearby volcanoes. Dashed lines indicate the 1 mm and 0.5 mm isopachs for the phreatic eruption in early June, 1995.

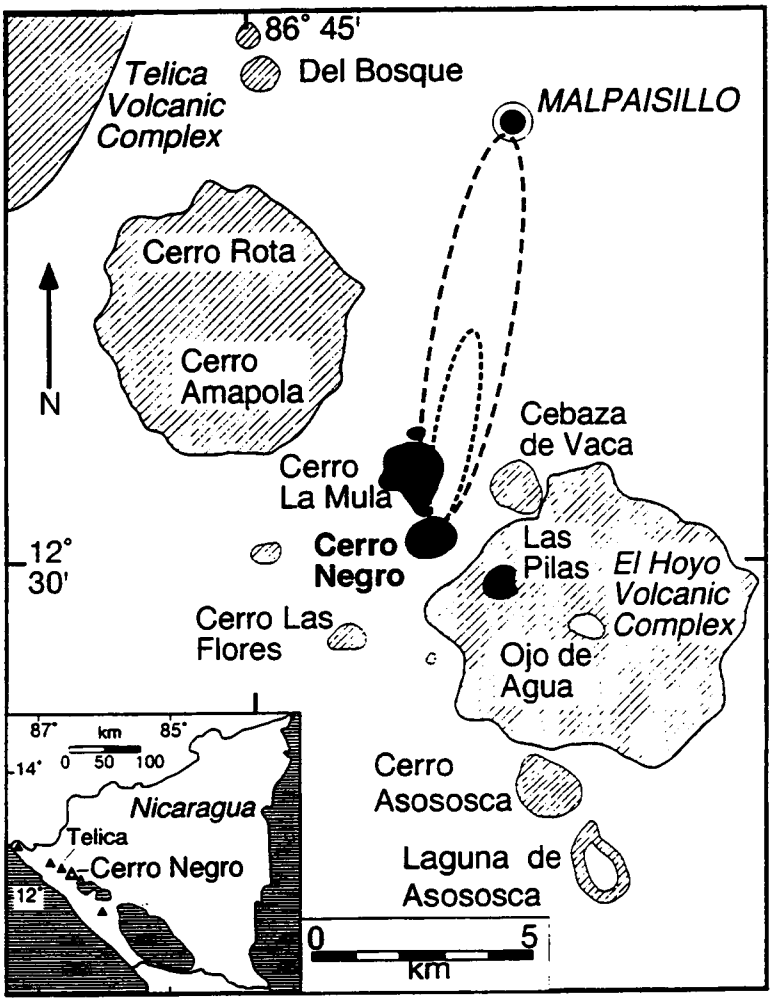

2.0 The 1995 Eruption

Activity in 1995 began with seismic swarms on 24 May followed by explosive eruptions on 28 May and continued until 15 August (GVN, 1995). During early June, eruptive activity consisted of discrete explosions at 8±5 minute intervals. These explosions produced convective ash columns that commonly reached heights of 200 m before drift-

ing downwind (Figure 2). Ballistic ejecta up to ≈1 m in diameter reached the lower cone slope during some of these eruptions (ejection velocities of 100 ms^{-1}). The most intense activity was observed 2 June, when a dilute, low-energy pyroclastic flow was observed on the NW cone flank. Integration of the ash isopach (Figure 1) indicates an average eruption rate from 2–6 June of 100 m^3hr^{-1}. Between explosions, little or no degassing from the crater was visible.

FIGURE 2. Typical phreatic eruption at Cerro Negro.This photo was taken at 11:20 am, on June 3, 1995, approximately 20 s after the explosion. Column height is ≈100 m. The volcanic-bomb field in the foreground is a result of the 1992 eruption.

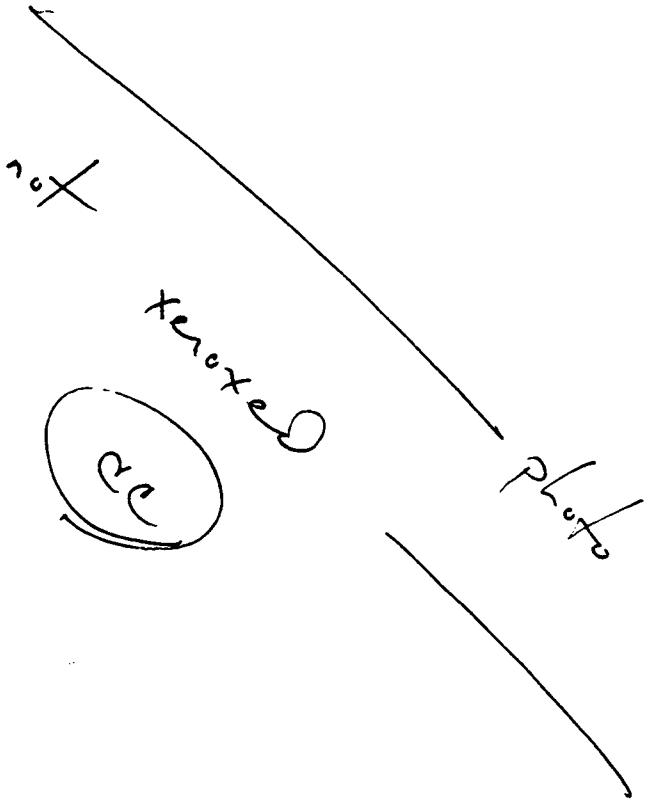

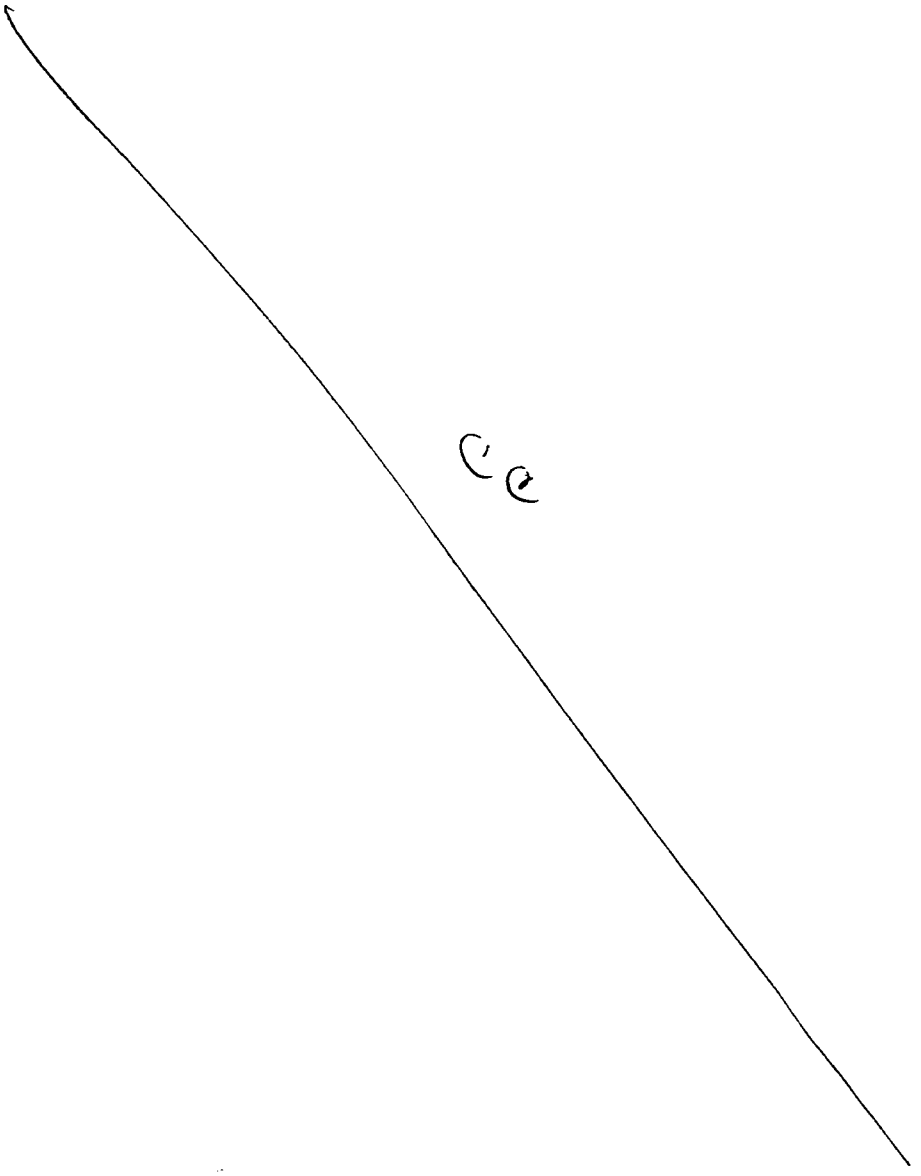

The primary eruption product was very fine lithic-crystal ash, consisting of angular fragments of olivine, pyroxene, clinopyroxene, and plagioclase, with lesser amounts of finer grained basalt. The character of this ash, lack of a juvenile component, and low eruption rate are characteristic of a phreatic eruption (Cas and Wright, 1988), possibly initiated by dike injection during late May seismic activity.

3.0 Radon Measurements

^{222}Rn concentration is ideally suited for identification and monitoring convective gas and fluid flow because of the limited distance of ^{222}Rn diffusion through soils due to its short half-life (3.823 days). ^{222}Rn in soils results from decay of ^{226}Ra. In areas where ^{222}Rn flux is diffusive, the mean depth from which ^{222}Rn escapes from soils is 1.75–2.25 m. The mean diffusion length in water is approximately 1 mm (Graustein and Turekian, 1990; Appleby and Oldfield, 1992). Near active volcanoes, ^{222}Rn concentrations are observed to be 100 - 1000 times regional background values and fluctuate on time scales of hours to days during passive degassing episodes (Baubron et al., 1991). Radon concentrations increased by a factor of 3 to 9 during dike injection at Long Valley Caldera, California (Williams, 1985). Given the diffusivity of ^{222}Rn in water and pore gases, the anomalous concentrations associated with volcanism can be reached only by relatively fast convective transport in gas or hydrothermal fluids. Correlation of ^{222}Rn anomalies with thermal areas and soil Hg anomalies (e.g., Varekamp and Buseck, 1984; Williams, 1985) is further indication of convective transport. ^{222}Rn gas originates in both magma and the surrounding wallrock. Changes in ^{222}Rn concentration in soil gases may also occur as a result of groundwater temperature fluctuations.

Increases in ^{222}Rn flux may occur due to magmatic degassing as ^{222}Rn is released directly from magma or revolatilization of sublimates during intrusion. Hydrofracturing increases both permeability and the surface area that provides ^{222}Rn through alpha-recoil release. Changes in temperature result in changes in the aqueous solubility of ^{222}Rn. For example, $^{222}Rn_{(aq)} = 0.2$ pCil^{-1} is in equilibrium with $^{222}Rn_{(gas)} = 1$ pCil^{-1} at 25°C. This same concentration of $^{222}Rn_{(aq)}$ is in equilibrium with $^{222}Rn_{(gas)} = 2$ pCil^{-1} at 100°C. Thus, increases in temperature of the hydrothermal system can cause increases in soil ^{222}Rn concentration.

Soil ^{222}Rn concentrations were monitored at Cerro Negro in March and June 1994, during which time no eruptive activity occurred, and during the June 1995 eruption. Radon was monitored using E-perm® detectors, which consist of an electret dosimeter contained within a small chamber (Kotrappa et al., 1988).

In the Eperm® (electret passive environmental radon monitor) detection system, gases pass into this chamber through a filter and ^{222}Rn decay produces ions that cause a reduction in electrostatic charge on the electret. Measurement of the change in electrical potential results in a time-integrated measure of ^{222}Rn that is insensitive to humidity and gas temperature (Kotrappa et al., 1988). Electrets and chambers used in this study were produced by Rad Elec, Inc. Chambers were suspended within vertical tubes that are buried to a depth of 40–50 cm and change in electret voltage was measured at 24 or 48 hr intervals. Background gamma radiation effects on ^{222}Rn measurements were

monitored using sealed chambers, also deployed at field stations, and found to be negligible. Precision of the measurements is ≈1 $pCil^{-1}$ Total measurement errors are approximately 10% and result primarily from variation in chamber and electret dimensions. Instrument drift did not occur, evaluated using calibrated reference electrets.

Stations were located up to 1 km from the crater of Cerro Negro and were concentrated on the N-S-trending alignment of vents and near thermal features (Figures 3a–3c). Stations were positioned on the crater rim during 1994 surveys, particularly along arcuate fractures that emit low-temperature gases, but this was not possible due to eruptive activity in June 1995. The March 1994 study was conducted in the dry season during 12 days and included 35 radon stations. The June 1994 survey comprised 24 stations and was made during an 8 day period in wet field conditions. June 1995 conditions were comparatively dry, with occasional rainfall during the 6-day sampling period. Ground temperatures in thermal areas near phreatic pits north of Cerro Negro were 40–71°C in March and June 1994, and 70–84°C in June 1995.

FIGURE 3. Station locations and concentrations of soil-gas ^{222}Rn for (a) March 1994, (b) June 1994, and (c) June 1995 surveys. ^{222}Rn values shown in $pCil^{-1}$; black dots show anomalous ^{222}Rn concentrations. Hachured lines show craters and phreatic pits, black stars indicate

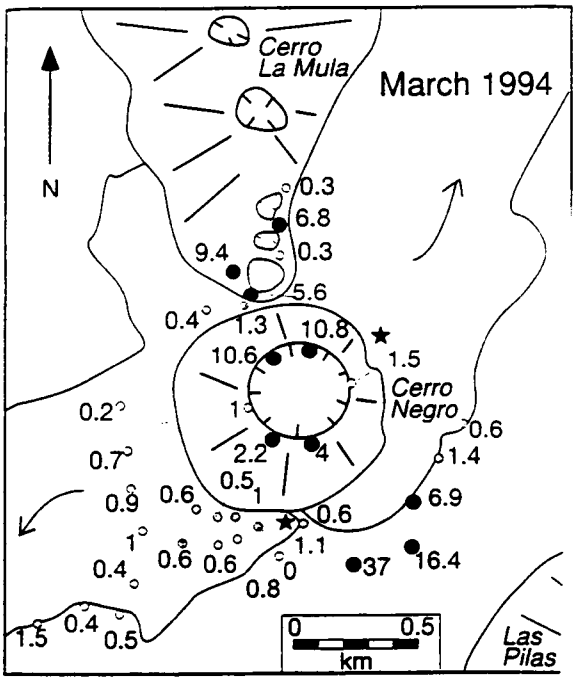

lava boccas, Radial lines indicate cinder cones. Cerro Negro lava flows are outlined and

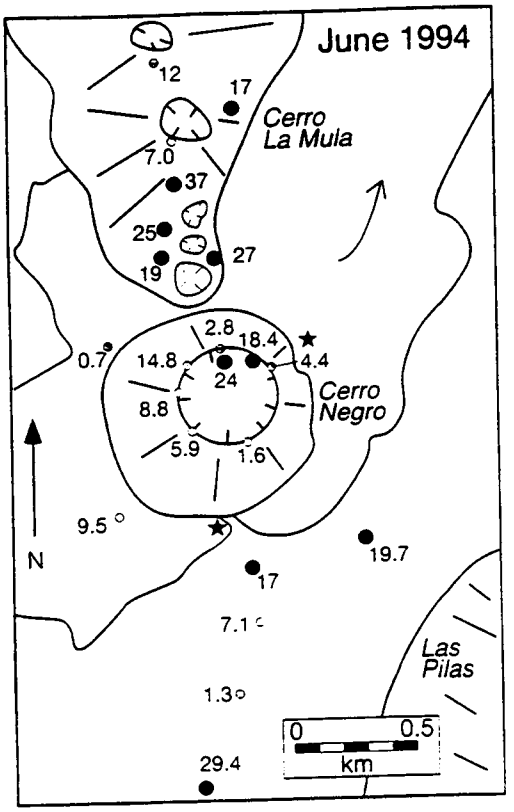

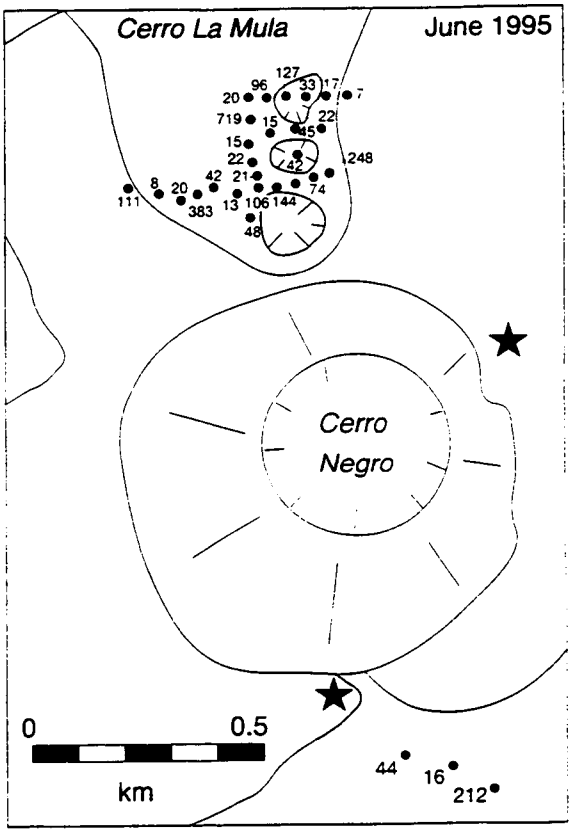

lava flow directions indicated by arrows.

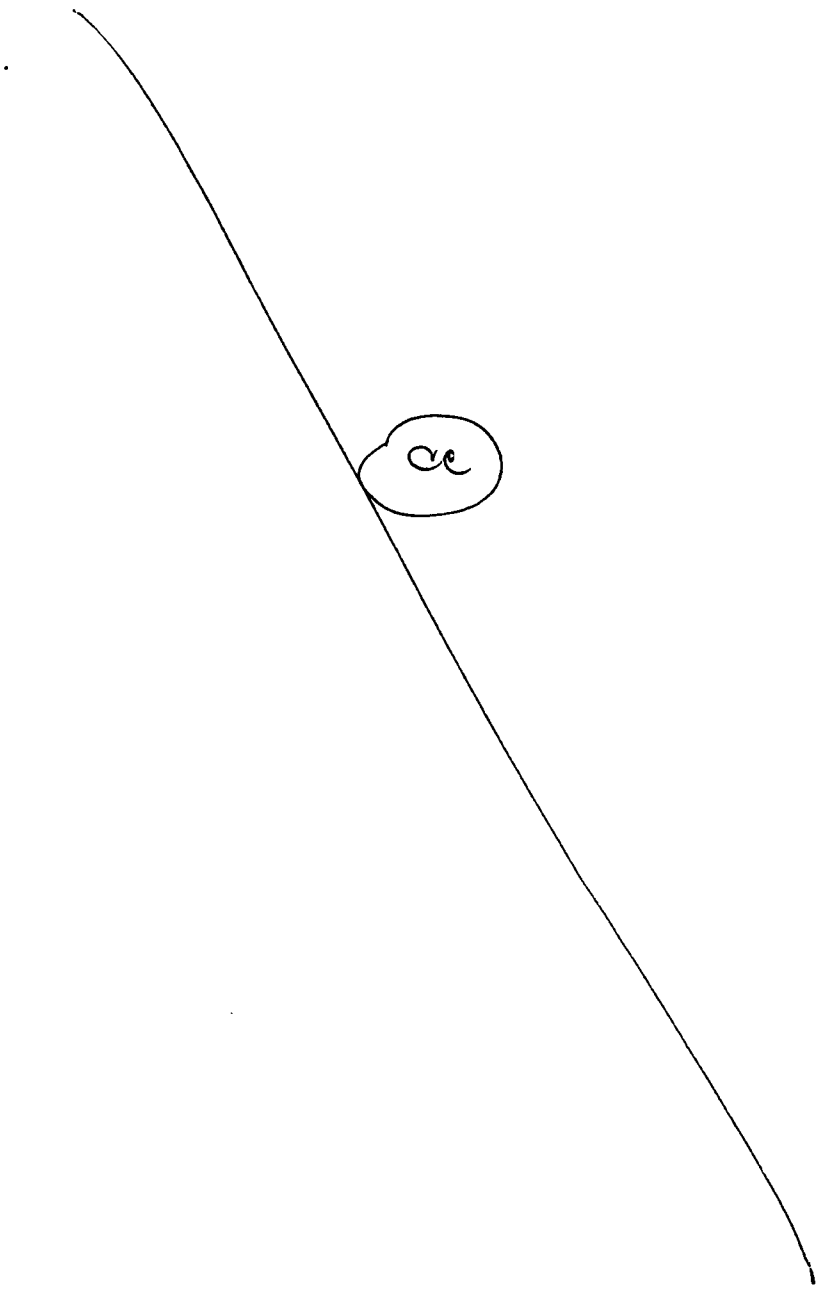

Mean soil ^{222}Rn concentrations during the survey periods were 1 $pCil^{-1}$ in March 1994, 10 $pCil^{-1}$ in June 1994, and 40 $pCil^{-1}$ in June 1995 (Figure 4). Maximum ^{222}Rn concentrations averaged over each sampling period were less than 40 $pCil^{-1}$ in both March and June 1994 and were 720 $pCil^{-1}$ in June 1995.

FIGURE 4. Comparison of the sample distribution of average ^{222}Rn concentration for surveys in March 1994 (squares), June 1994, (diamonds), and June 1995 (circles).

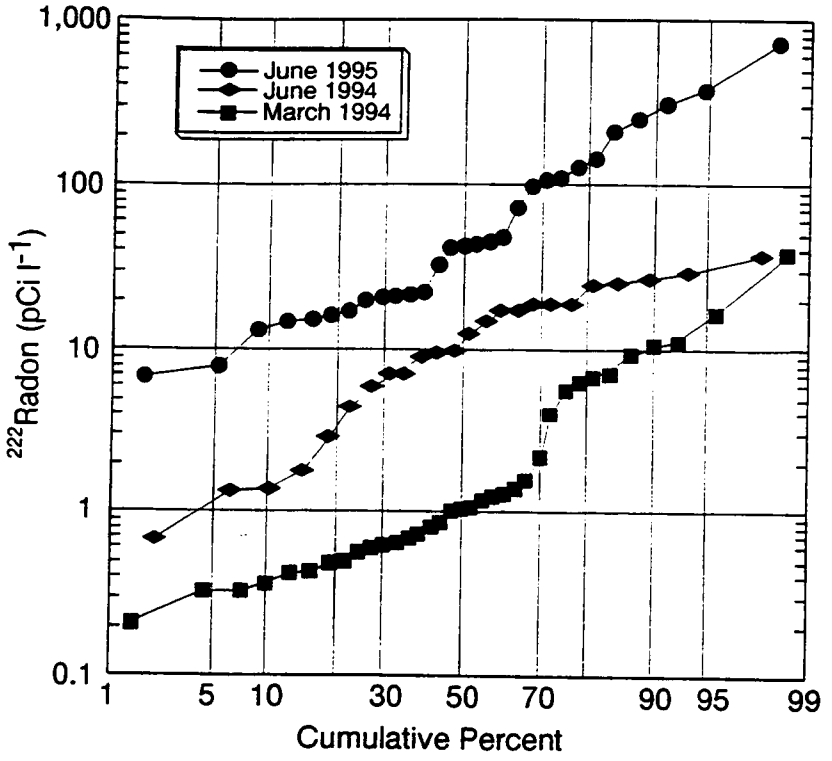

FIGURE 5.

Soil ^{222}Rn concentration was significantly greater on 2-3 June (solid circles) than on following days (3-4 June – open squares, 4-5 June – open circles, 5–6 June – open triangles). Concentrations remained high throughout early June compared to 1994 concentrations.

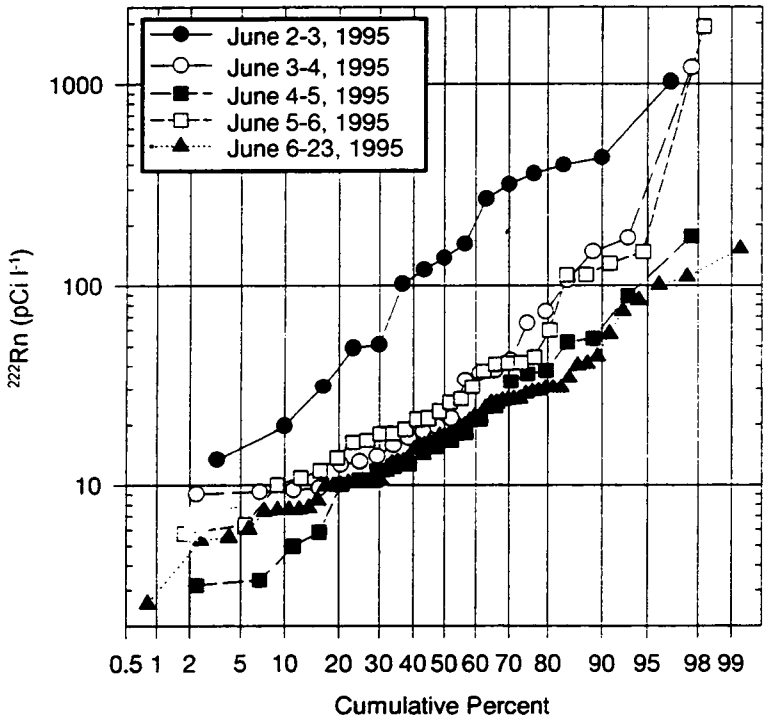

4.0 Discussion and Conclusions

A pattern of anomalous ^{222}Rn concentration in soils at Cerro Negro is evident in the March 1994 data. Offset in the cumulative distribution at the 70th percentile (Figure 4) indicates that ^{222}Rn concentrations greater than 5 pCi l^{-1} were anomalously high for the March 1994 survey. These ^{222}Rn anomalies occurred near thermal areas 400-800 m north of Cerro Negro, on the crater rim, and 500 m southeast of Cerro Negro.The March 1994 ^{222}Rn anomalies follow structural trends (e.g., McBirney, 1955), indicating convective transport of ^{222}Rn along structures.

Correlation of soil ^{222}Rn anomalies with soil Hg and electrical anomalies in these areas supports the hypothesis that ^{222}Rn is transported convectively to these thermal areas. Soil Hg anomalies (>50 ppb) were mapped in 1994 (Conway et al., 1994). A 100 mV dipolar self-potential electrical anomaly across the phreatic pit craters also indicates convective upwelling in this area. Del ^{13}C (-4.5 per mil) and del ^{18}O (-0.961), measured from gases collected on the crater rim in 1994, suggest a significant deep crustal or magmatic component to crater rim gases at that time.

Near-surface processes probably account for the change in the sample distribution of ^{222}Rn between March and June 1994 (Figure 4). Near-surface processes include increased mixing of air in shallow soils during the dry season or atmospheric pumping, both of which may dilute ^{222}Rn concentration above the groundwater table (Schery and Gaeddert, 1982), which is deeper in the dry season. Alternatively, increased vigor of convection in the geothermal system may occur seasonally, in response to increased recharge. However, similar ^{222}Rn concentration in anomalous areas in March and June 1994 argue against change in flow in the geothermal system. Thus, data collected in March and June 1994 represent the background activity of ^{222}Rn on and near Cerro Negro in the absence of active volcanism.

^{222}Rn concentrations were significantly elevated during the eruption relative to the March and June 1994 surveys (Figure 4). Ten stations had average concentrations >100 pCil^{-1} during the eruption. Most of these stations showed considerable change on daily intervals, with maximum values on 2-3 June and decreased ^{222}Rn activity after 3 June (Figure 5). For example, one ^{222}Rn station 0.5 km southeast of the crater had a ^{222}Rn concentration of 400 pCi l^{-1} 2-3 June, 180

pCil^{-1} 3-4 June, and 150 pCi l^{-1} 4-5 June. The same site had a ^{222}Rn concentration of 17 pCi l^{-1} in June 1994. All other stations on the south side of the volcano showed a similar pattern in ^{222}Rn concentration in June 1995 and order-of-magnitude increases in ^{222}Rn

between June 1994 and June 1995. The same pattern in ^{222}Rn activity was observed in the thermal area north of the volcano, where most stations had highest concentrations on 2-3 June and lower concentrations on following days. However, not every station followed this pattern. On June 3-6 three stations had ^{222}Rn concentrations greater than 1,000 $pCil^{-1}$, and the maximum observed concentration was

1,920 pCi l^{-1} on June 5-6.

These observations indicate that a pulse of ^{222}Rn-enriched gas occurred during the early stage of the June 1995 eruption. Elevated degassing was observed during the same time interval (2-3 June) throughout a >1 km-long zone. This zone extends north and southeast of Cerro Negro and correlates well with previously mapped ^{222}Rn anomalies, thermal anomalies, and structures. This observed spatial and temporal variation in soil ^{222}Rn concentration demonstrates that degassing pulses can be coherent over large areas during volcanic eruptions and can occur in response to low-energy phreatic volcanism. Recognition of this pulse depended on mapping anomalous ^{222}Rn zones during periods of quiescence and monitoring numerous ^{222}Rn stations distributed around the volcano at frequent intervals during the eruption.

As is often the case in volcano monitoring, measurements were made only after the beginning of the eruption. Thus, the timing of the initiation of the ^{222}Rn pulse with respect to the initiation of the eruption is unknown. Nonetheless, the ^{222}Rn measurements provide insight into the nature of the eruption as it progressed. Assuming that anomalous ^{222}Rn originated from hydrofracturing of rock, direct magma degassing, or both, these processes ceased or continued at a much reduced rate after 3 June. Although the frequency of explosions continued unchanged after 3 June, the ^{222}Rn data imply that magma injection and hydrofracturing did not continue at the same intensity. Such information could be useful in mitigating hazards and monitoring activity at other volcanoes.

5.0 References

Appleby, P.G. and Oldfield, F., 1992. Application of lead-210 to sedimentation studies, In M. Ivanovich and R.S. Harmon, editors. Uranium-series Disequilibrium: Applications to Earth, Marine, and Environmental Sciences: Clarendon Press, Oxford, England: 731-778.

Baubron, J.C., Allard, P., Sabroux, J.C., Tedesco, D., and Tountain, J.P., 1991. Soil gas emanations as precursory indicators of volcanic eruptions. J. Geol. Soc. London, 148: 571-576.

Baubron, J.C., Allard, P. , and Tountain, J.P., 1990. Diffuse volcanic emanations of carbon dioxide from Vulcano Island, Italy. Nature 344: 51-53.

Cas, R.A.F., and Wright, J.V., 1988. Volcanic Successions. Winchester, MA: Unwin Hyman Inc.

Chirkov, A.M., 1976. Radon as possible criterion for predicting eruptions as observed at Karymsky volcano. Bull. Volcanol. 38: 126-131.

Connor, C.B., Powell, L. , Strauch, W. , Navarro, M., Urbina, O., and Rose, W.I. , 1993. The 1992 eruption of Cerro Negro, Nicaragua: An example of Plinian-style activity at a small basaltic cinder cone. EOS, Trans. Am. Geophys. Union 74(43): 640. (abstract).

Conway, F.M., Macfarlane, A.W. , Connor, C.B., Lafemina, P.C. , and Reimer, M., 1994. Degassing at a young cinder cone: Volcan Cerro Negro. Geol. Soc. Am. Abstracts with Program–1994 Annual Meeting. Boulder, CO: Geol. Soc. Am.: 26(7): 435. (abstract).

Crenshaw, W.B., Williams, S.N., and Stoiber, R.E., 1982. Fault location by radon and mercury detection at an active volcano in Nicaragua. Nature 300: 345-346.

Graustein, W.C., and Turekian, K., 1990. Radon fluxes from soils to the atmosphere measured by ^{210}Pb–^{226}Ra disequilibrium in soils. Geophysical Research Letters 17: 841-844.

GVN. 1995. Bulletin of the Global Volcanism Network 20:5: 2.

Kotrappa, P., Dempsey, J.C., Hickey, J.R., and Stieff, L.R., 1988. An electret passive environmental ^{222}Rn monitor based on ionization measurement. Health Phys. 54: 47-56.

Kotrappa, P., Dempsey, J. C. ,Ramsey, R.W. , and Stieff, L.R., 1990. A practical E-perm (electret passive environmental monitor) system for indoor radon measurement. Health Phys. 58: 461-467.

LeCloarec, M.F., Pennisi, M., Corazza, E., and Lambert, G., 1994. Origin of fumarolic fluids emitted from a nonerupting volcano: Radionuclide constraints at Vulcano (Aeolian Islands, Italy). Geochim. Cosmochim. Acta 58: 4401-4410.

McKnight, S.B., Roggensack, K., and Williams, S.N., 1994. Historical eruption dynamics, volumes, and geochemistry of a young volcano, Cerro Negro Nicaragua. EOS, Trans. Am. Geophys. Union 75(44): 731. (abstract).

McBirney, A.R. 1955. Thoughts on the eruptions of the Nicaraguan volcano Las Pilas. Bull. Volcanol. 17:113—117.

Rose, W.I., Jr., Bonis, S., Stoiber, R.E., Keller, M., and Bickford, T., 1973. Studies of volcanic ash from two recent Central American eruptions. Bull. Volcanol. 37: 338—364.

Schery, S.D., and Gaeddert, D.H., 1982. Measurements of the effect of cyclic atmospheric pressure variation on the flux of ^{222}Rn from soil. Geophys. Res. Lett. 9: 835-838.

Simkin, T., and Siebert, L., 1994. Volcanoes of the World. Tucson, AZ: Geoscience Press.

Taylor, P.S., and Stoiber, R.E., 1973. Soluble material on ash from active Central America volcanoes. Geol. Soc. Am. Bull. 84:1,031—1,042.

Varekamp, J.C., and Buseck, P.R., 1984. Changing mercury anomalies in Long Valley, California. Geology 12: 283-286.

Williams, S.N., 1985. Soil radon and elemental mercury distribution in relation to magmatic resurgence at Long Valley caldera. Science 229: 551-553.

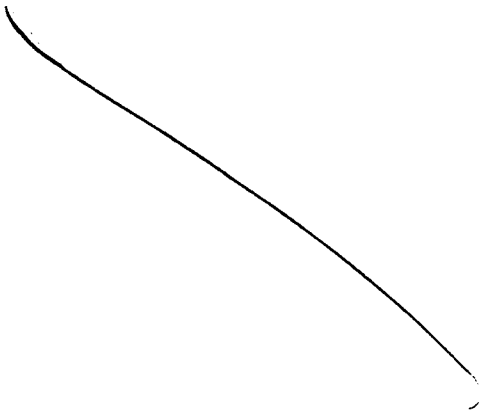

July 28, 1995

Solubility of Rn

Chuck Connor

The purpose is to calculate the change in radon concentration (pCi/l) in soil gases as a function of fluid temperature.

1.0 Introduction

Radon concentration neasr volcanoes may vary as a function of the temperature of fluids because solubility of Rn isa function of temperature. It is important to evaluate or estimate the magnitude of change in soil gas Rn concentration in response to small changes in temperature.

2.0 Calculation

From EQ3/6 tables (Dater0.com.R16)

$Rn\,(gas) = Rn\,(aq)$

$K = a_{Rn(aq)}/f_{Rn(gas)} \approx m_{Rn(aq)}/P_{Rn(gas)} \approx M_{Rn(aq)}/P_{Rn(gas)}$

25°C - log K = -2.05

100°C - log K = -2.44

$-dN/dt = \lambda N$

instantaeous change in total concentration of decaying element = decay constant *concentration

$\lambda = (\ln 2)/t_{1/2}$

t1/2 = 3.823 days

λ = ln2/3.823 days = 2.098×10^{-6} / sec

1 Curie = 3×10^{10} decays/sec

1 pCi/liter = .030 decays/sec/liter

30 (decaying atoms/sec/liter) = λ * N (atoms/liter)

N/liter = .030/2.098×10^{-6} = 1.43×10^{4} atoms/liter

Now, what is the partial pressure of Rn gas at a concentration of 1.43×10^{4} atoms / liter

Use the ideal gas law:

PV = nRT

T = 25°C = 298.15°K

1.43×10^{4} atoms/ liter * 1 mol/6.022×10^{23} atoms = 2.37×10^{-20} mols/liter

n/V = 2.37×10^{-20} mols/liter

R = 0.08206 Liters atmos / mol °K

P (Rn gas) = 5.8×10^{-19} atmos

K (25°C) = 0.0089

M Rn (aq) = P(Rn gas)*K = 5.162×10^{-21} mols/L

= 3.11×10^{3} atoms/liter = 0.22 pCi/Liter

So water at 25°C and 0.22 pCi/liter Radon is in equilibrium with gas with 1 pCi/liter partial pressure of radon.

K (100°C) = 0.0036

5.162×10^{-21} M (Rn aq) / K = 1.43×10^{-18} atmospheres

PV = nRT

P = 1.43×10^{-18} atmospheres

R = 0.08206

T = 100°C = 373.15°K

n/V = P/RT = 4.7×10^{-20} mols/liter

= 2.8×10^{6} atoms/liter

= 2.0 pCi/liter

So at 100°C the partial pressure of Rn gas above the same water is 2.0 pCi/l

This means that the temperature change from 25°C to 100°C would double the concentration of Rn in soil gases simply by changing the solubility of Rn in water.

Dike Intersection with the Repository

Chuck Connor

The goal of this study is to take existing probability models for volcanic disruption of the candidate reposiotry and add dike intersection probability

1.0 Introduction

Connor and Hill (1995) use several methods of calculating the probability of a volcanic event in the YMR, using the distributio of past volcanism as a guide. The resulting probabilities do not take the lengths or orientations of dikes into account for estimating the probabilitiy of magma intersection with the repository. In the following, a simple model is developed to account for variable dike lengths.

2.0 Assumptions made in the model

Several assumptions are necessary for creating a dike intersection model. In the current implementation, the following asumptions are made.

1. The program assumes that an Epanechnikov kernel function describes the distribution of volcanic events (see Connor and Hill, 1995), it is assumed that the distribution of mapped volcanoes represents the past distribution of volcanic events. But, definitions of independent volcanic events, and what they represent, can vary - this is explored using the model

2. A smoothing parameter for the Epanechnikov kernel must be assumed; this smoothing parameter can be estimated from the distribution of past volcanic events

3. A regional recurrence rate for volcanism must be assumed, and is generally inferred from the timing of past volcanic events.

4. The probability distribution for dike length must be assumed. In this assumed to be a uniform random distribution between a low value for the dike half-length (maybe 50m) and a high value for the dike half-length (maybe 5000 m).

5. It is assumed that the probability distribution for dike orientations is known. This might be estimated from fault orientations, or the orientations of high-dilation tendency faults, or the orientation of the current stress-ellipse, and the relative values of sigma 1 - 3.

3.0 Calculation procedure

The calculation proceeds as follows.

1. A set of volcano locations are read in. These are the volcanic events - but whatever definition used.

2. The probability surface for volcanic events is estimated - by estimating spatial recurrence rate on a grid.

3. For each grid point, the probability of a dike half-length intersecting the reposiotry is determined using the probability dike length distribution. For a given run, this is done assuming some fixed dike orientation.

4. the probability an event at point p is multiplied by the probability of a dike at point p interesecting the repository, for a given dike orientation.

The affect of the grid spacing is worth considering. Figure 1, "The problem with the grid approximation," on page 3 shows a sketch of the reposiotry outline and three grid cells. The cells in the figure are drawn to illustrate the effect of cell, or grid, spacing on the approximation. The calculation assumes that intersection for any point in the cell is well estimated by the intersection of the center of the cell with the repository. In most cases, if the center of the cell hits a repository boundary, lines at a specific orientation drawn from anywhere else in the cell will intersect the repository with the same probability. In some cases, a line drawn from the center of the cell will interesect the reposiotry, but parallel lines drawn from elsewhere in the cell would miss the repository. Conversely, some cell-center lines miss the repoistory, but the cell contains other lines that interest the repository (Figure 1, "The problem with the grid approximation," on page 3).

This problem is greatest for dike orientations that are close to N-S, or E-W because the grid begins to align (or aligns completely at E-W or N-S) and adjacent cells will interesect exactly the same spot on the repository boundary. Also, it is assumed tha there is a uniform random probability of the event occurring anywhere in the cell. For lines ori-

ented E-W or N-S, this means that there is an equal chance of a line "really" originating anywhere along cell wall orthogonal to the dike. If the dike is oriented at N45E, there is a triangluar distribution, centered on the cell center Figure 2, "Cell geometry, continued," on page 3).

FIGURE 1. The problem with the grid approximation

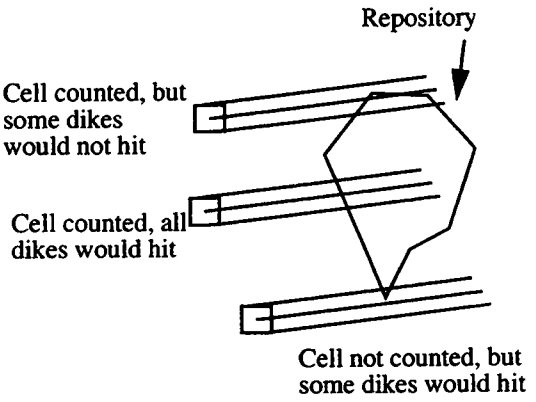

FIGURE 2. Cell geometry, continued

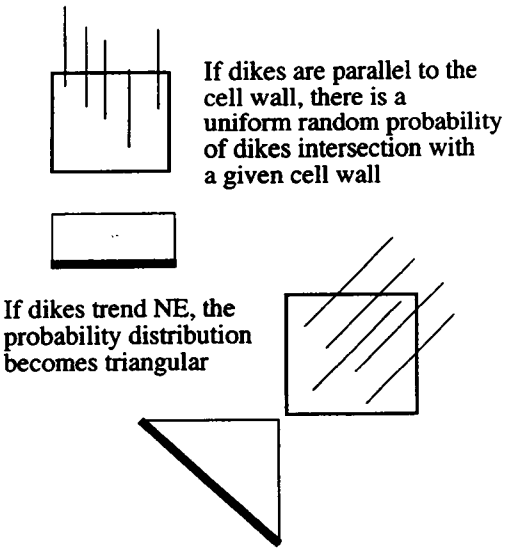

So, the cell center is a better approximation for NE-trending dikes than for N-S or E-W trending dikes.

4.0 Program

The following program is used to calculate the probability of sike intersection. First some explanation.

rep_x, rep_y - are the utm coordinates of the reposiotry boundary.

x_volcano, y_volcano are the UTM coordinates of the volcano event locations, normally is is simply the locations of cinder cones, and or aeromagnetic anomalies. The volcano event locations are read from a file, the name of which in this version is "yucca.dat3", but this can be changed.

The file yucca.dat3 looks like:

•554680,4108970, 2.9,bb
•529390,4112330, 4.6,tm
•522130,4110340, 0.32,lb
•538840,4073990, 0.99,bc
•540330,4070050, 3.8,cfb
•543780,4060380, 0.05,lw
•553720,4052990, 4.3,avb
•549430,4040080, 4.3,avd

where bb - buckboard Mesa, tm - thirsty mountain, lb - little black peak, bc - black cone (quaternary crater flat), cfb - crater flat vent b (pliocene), lw - lathrop wells, avb - amargosa valley aeromagnetic anomaly b, avd - amargosa valley aeromagentic anomaly d.

the first two numbers in each row are the UTM coordinate, the third number in each row is the approximate age of the center in millions of years before present. So, use of yucca.dat3 treats the formation of multiple cones, such as the Quaternary crater flat alignment as single events.

Two other files used are yucca.dat2, and yucca.dat1

yucca.dat2:

•548920,4133270, 7.5,pm
•554090,4134530, 7.5,pm
•562370,4132680, 7.5,pm
•594860,4107970, 8.8,pr
•595780,4106340, 8.8,pr
•592810,4105890, 8.8,pr
•593411,4105540, 8.8,pr
•591480,4105170, 8.8,pr

•603230,4095790, 7.0,ncy
•602170,4088960, 7.0,ncy
•600950,4085920, 7.0,ncy
•598030,4090090, 7.0,ncy
•597930,4082470, 7.0,ncy
•577860,4093930, 8.1,yf
•554680,4108970, 2.9,bb
•536110,4109120, 7.5,rw
•529390,4112330, 4.7,tm
•523230,4112530, 0.4,hc
•522130,4110340, 0.35,lb
•540330,4079130, 1.16,nc
•538840,4073990, 1.1,bc
•537450,4071470, 1.1,rc
•535500,4069490, 0.94,lcne
•543780,4060380, 0.15,lw
•540232,4071610, 3.9,cfa
•540330,4070050, 3.9,cfb
•540365,4068790, 3.9,cfc
•540696,4067830, 3.9,cfd
•553720,4052990, 4.4,avb
•549430,4040080, 4.5,avd

yucca.dat1:

•548920,4133270, 7.5,pm
•554090,4134530, 7.5,pm
•562370,4132680, 7.5,pm
•594860,4107970, 8.3,pr
•595780,4106340, 8.3,pr
•592810,4105890, 8.3,pr
•593411,4105540, 8.3,pr
•591480,4105170, 8.3,pr
•603230,4095790, 6.6,ncy
•602170,4088960, 6.6,ncy
•600950,4085920, 6.6,ncy
•600550,4085450, 6.6,ncy
•599160,4085820, 6.6,ncy
•598030,4090090, 6.6,ncy
•597930,4082470, 6.6,ncy
•577860,4093930, 8.1,yf
•554680,4108970, 2.9,bb
•556060,4107580, 2.9,bbse
•536110,4109120, 7.5,rw
•529390,4112330, 4.5,tm
•523230,4112530, 0.36,hc
•522130,4110340, 0.29,lb
•540330,4079130, 1.02,nc
•538840,4073990, 0.71,bc
•537450,4071470, 0.90,rc

•535500,4069490, 0.77,lcne
•535131,4069220, 0.77,lcsw
•543780,4060380, 0.05,lw
•540232,4071610, 3.5,cfa
•540330,4070050, 3.5,cfb
•540365,4068790, 3.5,cfc
•540696,4067830, 3.5,cfd
•540300,4068390, 3.5,cfe
•540660,4067470, 3.5,cff
•553720,4052990, 3.8,avb
•546130,4054260, 3.7,ava
•538300,4047200, 3.7,ave
•547050,4042950, 3.8,avc
•549430,4040080, 3.7,avd

The differences betwee these data files and yucca.dat3 are (a) the two files contain volcanic events older the 5 my, (b) individual cones are broken out as separate volcanic events. In yucca.dat2 some very closely spaced cones, such as the Little cones, are still lumped as single events.

So, use of the three different files implies different definitions of volcanic events. Other parameters, such as dike length, may have to change accordingly.

The program also allows assignment of:

agecut - only volcanoes from the files younger than agecut (in millions of years) are considered in the analysis

h - is the Epanechnikov smoothing constant (meters).

recur - is the estimated regional recurrence rate in volcanic evetns/yr

grid_step - is the spacing of the grid, experimatation indicates that the grid step ought to be 500 m or less. area - used in the probability calculations, depends on the grid_step used.

interval - is the time interval for whick probability is calculated. if interval is one - the calculation gives annual probability

north_angle - is the angle from north of the dike trends in degrees - this is constant for a given run

high_distribution - is the maximum dike half-length - assuming a uniform random probability distribution on length, low_distribution is the minimum dike half-length.

Altering any of the above parameters will altr the probability distribution of dike intersection.

```
•DIM rep_x(6),rep_y(6), x_volcano(50), y_volcano(50)
•LET s1 = 520000
•LET s2 =560000
•LET s3 = 4050000
•LET s4 = 4090000
•
•open #33: name "dike.out", create newold
•erase #33
•
•open #99: screen 0,.85,0,1
•SET WINDOW s1,s2,s3,s4
•
•let grid_step = 500
•
•Let volcano_file$ = "yucca.dat3"
•LET agecut = 5                ! age of volcanoes to consider or less
•LET h = 18000                 ! epan smoothing constant
•LET recur = 3e-6              ! annual regional recurrence rate
•LET area = grid_step^2            ! area of probabilty
•LET interval = 1              ! time interval for probability (annual if 1)
•
•LET north_angle = 30
•!uniform random distribution
•LET high_distribution = 10000
•LET low_distribution = 500
•
•
•OPEN #1: name volcano_file$
•DO while more #1
•
•  INPUT #1: xx,yy,age,dum2$
•
•  IF age <= agecut then
•    LET i = i + 1
•    LET x_volcano(i) = xx
•    LET y_volcano(i) = yy
•   plot text, at x_volcano(i), y_volcano(i):  "*"
•  END IF
•
•LOOP
•LET num_volcano = i
•
•
•
•!boundaries of the repository
•
•LET n_repo = 6
•LET rep_x(1) = 548216
```

```
•LET rep_x(2) = 549658
•LET rep_x(3) = 549180
•LET rep_x(4) = 547827
•LET rep_x(5) = 547065
•LET rep_x(6) = 547393
•
•LET rep_y(1) = 4079714
•LET rep_y(2) = 4078510
•LET rep_y(3) = 4077130
•LET rep_y(4) = 4075864
•LET rep_y(5) = 4076802
•LET rep_y(6) = 4078484
•
•Let repo_center_x = 548500
•let repo_center_y = 4078250
•
•FOR i = 1 to n_repo-1
•   PLOT rep_x(i),rep_y(i);
•NEXT i
•PLOT rep_x(n_repo), rep_y(n_repo); rep_x(1),rep_y(1)
•plot text, at repo_center_x, repo_center_y: "R"
•
•
•for angle = -90 to 90 step 5
•let north_angle = angle
•IF north_angle = 0 then LET north_angle = 0.001
•LET north_angle = 90 - north_angle
•LET theta = north_angle*pi/180
•
•LET prob_tot = 0
•FOR x_pt = 510000 to 580000 step grid_step
•   FOR y_pt = 4050000 to 4120000 step grid_step
•
•let trial_dist = sqr((x_pt-repo_center_x)^2 + (y_pt - repo_center_y)^2) -3000
•if trial_dist< high_distribution then
•      !**************************
•      LET sumn = 0
•
•      FOR i_vol = 1 to num_volcano
•
•         LET dist1 = (x_pt - x_volcano(i_vol))^2 + (y_pt-y_volcano(i_vol))^2
•         !if dist1> 0 then print dist1
•         LET dist2 = dist1/(h^2)
•
•
•         IF dist2 < 1 then
•            LET ku = 2/pi * (1-dist2)
•            LET sumn = sumn + (1/(h^2))*ku
•         END IF
•
```

```
•      NEXT i_vol
•
•      LET lambda = sumn/num_volcano
•
•      LET prob_spatial_temp = (1-exp(-area*recur*interval*lambda))
•      !*****************
•
•LET m1 = tan(theta)
•      LET b1 = y_pt - m1*x_pt
•      LET min_dist = 1e32
•
•
•      CALL convex_hull(rep_x, rep_y, x_pt,y_pt,n_repo, pt_state$)
•
•      IF pt_state$ = "true" then
•        LET min_dist = 0
•
•      ELSE                !find distance to repo
•
•        FOR i = 1 to n_repo
•
•          IF i < n_repo then
•            LET x1 = rep_x(i)
•            LET y1 = rep_y(i)
•            LET x2 = rep_x(i+1)
•            LET y2 = rep_y(i+1)
•
•          ELSE
•            LET x1 = rep_x(i)
•            LET y1 = rep_y(i)
•            LET x2 = rep_x(1)
•            LET y2 = rep_y(1)
•
•          END IF
•
•          LET m2 = (y2-y1)/(x2-x1)
•          LET b2 = y2- m2*x2
•
•          SET COLOR "red"
•
•          LET x_intersect = (b1-b2)/(m2-m1)
•          LET y_intersect = m1*x_intersect + b1
•
•
•          IF (x_intersect => x1 and x_intersect <= x2) or (x_intersect <= x1 and
x_intersect => x2) then
•
•            LET dist_inter = sqr((x_pt-x_intersect)^2 + (y_pt-y_intersect)^2)
•            IF dist_inter < min_dist then
•              LET min_dist = dist_inter
```

```
•                let inter_pt_x = x_intersect
•                let inter_pt_y = y_intersect
•              end if
•            END IF
•
•
•         NEXT i
•
•
•       END IF
•
•       IF min_dist > high_distribution then
•         LET prob_dist = 0
•       ELSE IF min_dist <= 1000 then
•         LET prob_dist = 1
•       ELSE
•         LET prob_dist = (high_distribution - min_dist)/(high_distribution -
low_distribution)
•         PLOT x_pt,y_pt; inter_pt_x, inter_pt_y
•         !print min_dist,x_pt,y_pt; x_intersect, y_intersect
•
•
•       END IF
•
•       ! ************************************
•
•
•       LET prob_tot = prob_tot + prob_dist*prob_spatial_temp
•end if
•   NEXT y_pt
•NEXT x_pt
•
•Print  angle,prob_tot
•Print #33: angle;",";prob_tot
•next angle
•!CLEAR
•END
•
•SUB convex_hull(x_vert(), y_vert(), xpt,ypt,numvts, pt_state$)
•
•   LET pt_state$ = "false"
•
•   FOR curvt = 1 to numvts
•     IF curvt = numvts then
•       LET x1 = x_vert(curvt)
•       LET x2 = x_vert(1)
•       LET y1 = y_vert(curvt)
•       LET y2 = y_vert(1)
•
•     ELSE
```

```
•
•       LET x1 = x_vert(curvt)
•       LET x2 = x_vert(curvt + 1)
•       LET y1 = y_vert(curvt)
•       LET y2 = y_vert(curvt + 1)
•
•     END IF
•
•     WHEN error in          ! error when x2-x1 = 0
•        LET m = (y2-y1)/(x2-x1)  !slope of line bet. vertices
•        LET b = y1 - m*x1    !intercept of line
•
•        LET ytest = m*xpt + b     ! point on line
•
•        ! don't want points outside line segments: use
•        ! the following tests
•
•        IF x1 > x2 and y1 > y2 and ytest > ypt then EXIT FOR
•        IF x1 > x2 and y1 < y2 and ytest > ypt then EXIT FOR
•        IF x1 < x2 and y1 > y2 and ytest < ypt then EXIT FOR
•        IF x1 < x2 and y1 < y2 and ytest < ypt then EXIT FOR
•
•     USE
•        !use this test instead if vertical line
•        IF y2<y1 and xpt>x1 then EXIT FOR
•        IF y2>y1 and xpt<x1 then EXIT FOR
•
•     END WHEN
•
•     !if the random point has passed the above tests for
•     ! every line segment, the point lines within
•     ! the selected area
•
•     IF curvt = numvts then
•
•       LET pt_state$ = "true"
•
•     END IF
•
•   NEXT curvt
•END SUB
```

5.0 Results

In the first set of calculations, the probability of dike intersection is determined using yucca.dat2, all volcanoes less than 5 my old, a regional recurrence rate of 8 volcanic events/million years, a minimum dike half-length of 50 m, a maximum dike half-length of 5000 m

FIGURE 3. Probability of dike intersection using yucca.dat2

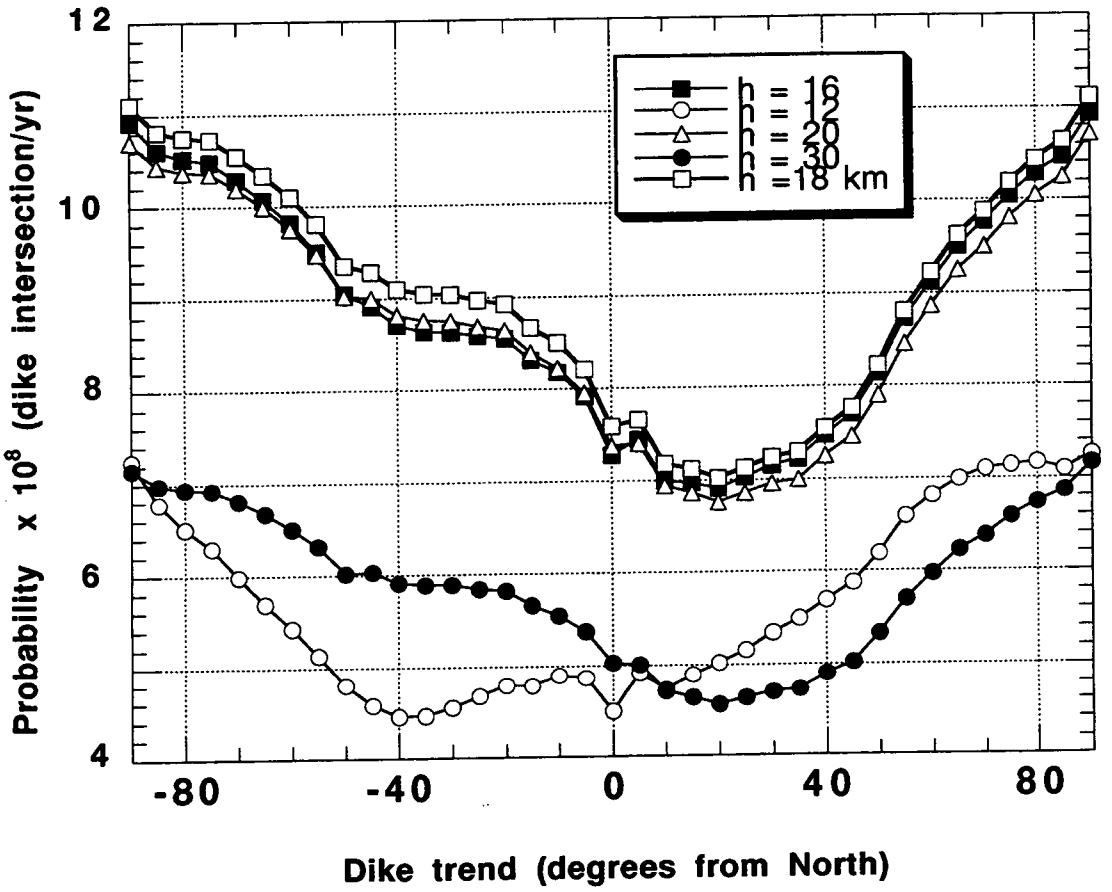

TABLE 1. Probability calculations made using yucca.dat2 and above parameters

North-angle	h= 16 km	h = 12 km	h = 20 km	h = 30 km	h = 18 km
-90.	1.0922e-07	7.2455e-08	1.0702e-07	7.1556e-08	1.1106e-07
-85.	1.0605e-07	6.7831e-08	1.0436e-07	6.9828e-08	1.0811e-07
-80.	1.0522e-07	6.5083e-08	1.0378e-07	6.9394e-08	1.0745e-07
-75.	1.0485e-07	6.3051e-08	1.0362e-07	6.9243e-08	1.0723e-07
-70.	1.0289e-07	5.9886e-08	1.0193e-07	6.8074e-08	1.0543e-07
-65.	1.0066e-07	5.6928e-08	9.9958e-08	6.6721e-08	1.0337e-07
-60.	9.8185e-08	5.4250e-08	9.7596e-08	6.5057e-08	1.0099e-07
-55.	9.5082e-08	5.1321e-08	9.4764e-08	6.3157e-08	9.8084e-08
-50.	9.0448e-08	4.7955e-08	9.0294e-08	6.0141e-08	9.3516e-08
-45.	8.9105e-08	4.5775e-08	8.9959e-08	6.0289e-08	9.2878e-08
-40.	8.7008e-08	4.4548e-08	8.8091e-08	5.9103e-08	9.0946e-08
-35.	8.6318e-08	4.4622e-08	8.7566e-08	5.8827e-08	9.0391e-08
-30.	8.6221e-08	4.5431e-08	8.7492e-08	5.8836e-08	9.0317e-08
-25.	8.5797e-08	4.6671e-08	8.6802e-08	5.8331e-08	8.9691e-08
-20.	8.5511e-08	4.7839e-08	8.6405e-08	5.8129e-08	8.9259e-08
-15.	8.3161e-08	4.7781e-08	8.3969e-08	5.6594e-08	8.6702e-08
-10.	8.1833e-08	4.8940e-08	8.2255e-08	5.5436e-08	8.5001e-08
-5.	07.917e-08	4.8594e-08	7.9489e-08	5.3705e-08	8.2095e-08
0.	7.2808e-08	4.4888e-08	7.3713e-08	5.0221e-08	7.5821e-08
5.	7.4436e-08	4.9103e-08	7.4010e-08	5.0027e-08	7.6583e-08
10.	6.9873e-08	4.7292e-08	6.9401e-08	4.7039e-08	7.1785e-08
15.	6.9708e-08	4.8911e-08	6.8600e-08	4.6359e-08	7.1151e-08
20.	6.9076e-08	5.0175e-08	6.7506e-08	4.5542e-08	7.0171e-08
25.	7.0288e-08	5.1533e-08	6.8540e-08	4.6245e-08	7.1265e-08
30.	7.1483e-08	5.3404e-08	6.9518e-08	4.6901e-08	7.2343e-08
35.	7.2214e-08	5.4929e-08	6.9975e-08	4.7164e-08	7.2897e-08
40.	7.4710e-08	5.6861e-08	7.2503e-08	4.8947e-08	7.5463e-08
45.	7.7036e-08	5.8702e-08	7.4546e-08	5.0186e-08	7.7682e-08
50.	8.1392e-08	6.1855e-08	7.9017e-08	5.3314e-08	8.2227e-08
55.	8.7244e-08	6.5886e-08	8.4570e-08	5.6912e-08	8.8064e-08
60.	9.1169e-08	6.8140e-08	8.8594e-08	5.9631e-08	9.2176e-08
65.	9.5005e-08	6.9929e-08	9.2523e-08	6.2248e-08	9.6194e-08
70.	9.7624e-08	7.0966e-08	9.5003e-08	6.3760e-08	9.8799e-08
75.	1.0041e-07	7.1339e-08	9.8084e-08	6.5856e-08	1.0186e-07

TABLE 1. Probability calculations made using yucca.dat2 and above parameters

North-angle	h= 16 km	h = 12 km	h = 20 km	h = 30 km	h = 18 km
80.	1.0280e-07	7.1631e-08	1.0049e-07	6.7358e-08	1.0435e-07
85.	1.0460e-07	7.0901e-08	1.0244e-07	6.8607e-08	1.0631e-07
90.	1.0922e-07	7.2455e-08	1.0702e-07	7.1556e-08	1.1106e-07

Suppose that any dike that forms in the region will be oriented N28E. This is the estimated orientation of sigma2, perpendicular to sigma- 1. Then for h = 16, 18, or 20, the probability of dike interestion is about 7×10^{-8} annually.

TABLE 2. Length of fault segments by orientation (given as fraction of total fault segments length)

North-angle	fraction faults
-90	0
-85	.0005
-80	.001
-75	.001
-70	.002
-65	.002
-60	.003
-55	.004
-50	.0115
-45	.019
-40	.02425
-35	.0295
-30	.03475
-25	.04
-20	.04525
-15	.0505
-10	.061
-5	.0714
0	.06725
5	.063
10	.06525

TABLE 2. Length of fault segments by orientation (given as fraction of total fault segments length)

North-angle	fraction faults
15	.0675
20	.056
25	.0445
30	.04
35	.0355
40	.0305
45	.0255
50	.02325
55	.021
60	.019
65	.017
70	.0105
75	.004
80	.003
85	.002
90	.002

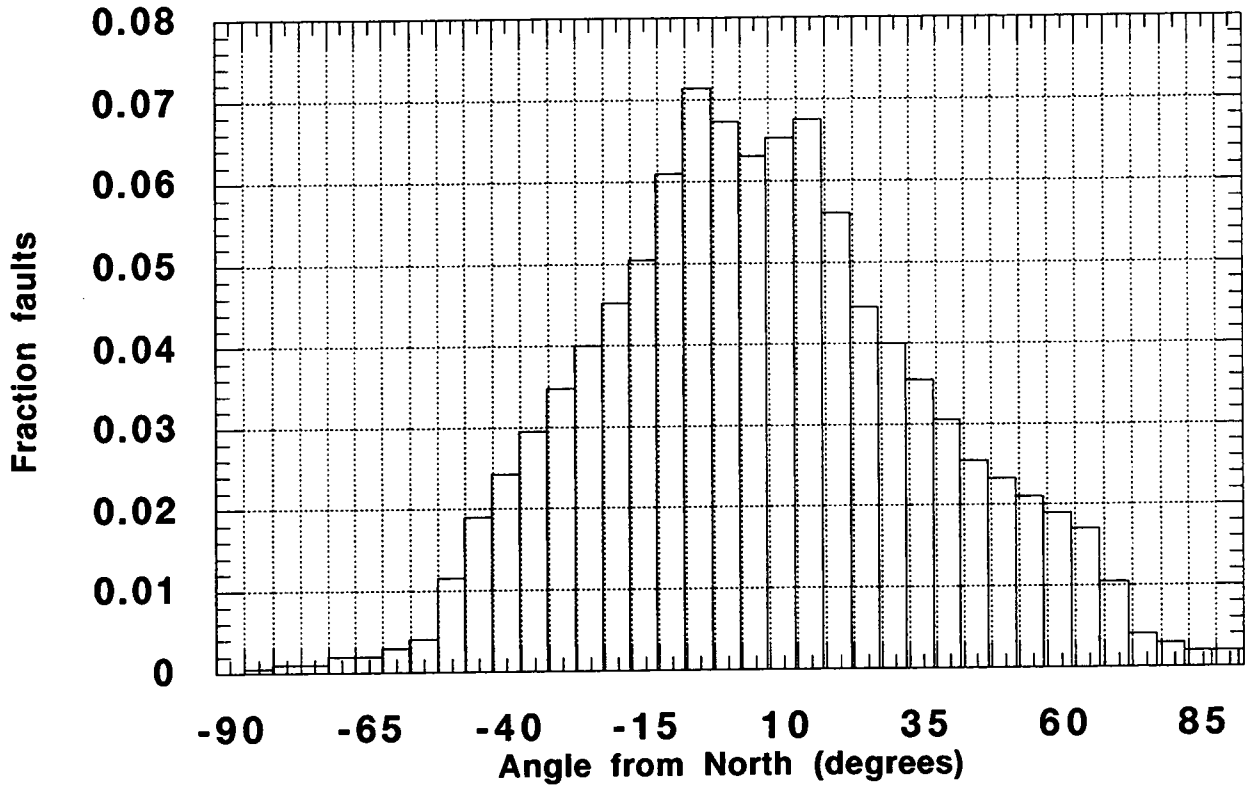

TABLE 3.

Data_set	age_cut (ma)	h (km)	Recur. Rate (v/ my)	grid spacing (m)	dike half-length (low, high)	dike orientation	annual probability (x 10^8)
yucca.dat2	5	12	8	500	50, 5000	28	5.2
yucca.dat2	5	16	8	500	50, 5000	28	7.0

TABLE 3.

Data_set	age_cut (ma)	h (km)	Recur. Rate (v/ my)	grid spacing (m)	dike half-length (low, high)	dike orientation	annual probability (x 10^{-8})
yucca.dat2	5	18	8	500	50, 5000	28	7.1
yucca.dat2	5	20	8	500	50, 5000	28	6.9
yucca.dat2	5	30	8	500	50, 5000	28	4.6
yucca.dat2	5	18	8	500	50,5000	faults	8.1
yucca.dat2	5	12	8	500	50,5000	faults	5.1
yucca.dat2	5	30	8	500	50,5000	faults	5.3
yucca.dat2	5	18	8	500	1,2 (pt hit)	28	
yucca.dat2	5	18	8	500	50,1000	28	
yucca.dat2	5	18	8	500	50,2000	28	
yucca.dat2	5	18	8	500	50,3000	28	

Lava Flow Models

Chuck Connor

Implement a model for lava flow simulation based on cellular automata, following the approach of Barca et al. 1994

1.0 Introduction

Lava flow geometry and morphology provide information about the rheological propoerties of the active flow and flow rates at the vent, long after the eruption. There are several cinder cones in crater flat valley surrounded by lava flow aprons. Using models to simulate lava flows, it may be possible to gain insight into eruption rates and rheological properties of the basalts by modeling the lava flows. This is important for characterizing volcanic events in the Yucca Mountain region and understanding the consequences of volcanism for repository performance.

The cellualr automate method was invented by John von Neumann for simulating the growth and development of complex systems. Barca et al. (1994) realized that lava flows are growing, complex systems and can be modeled using celluar automata. Celluar automata is simply a computational technique. The method simplifies the rheologic propoerties of the rock - greatly reducing the calculations. Calculation of lava flow movement from first principles requires a solution to the Navier-Stokes equations. Although this is doable - it isnt practical or necessary for this analysis. The full reference to the paper is:

Barca, D., G.M. Crisci, S. Di Gregorio, and F. Nicoletta, 1994. Cellular Automata for simulationd lava flows: a method and examples of the Etnean eruptions. Transport Theory and Statistical Physics, 23(1-3): 195-232.

Barca provides background on the theory of application of cellular automata and psuedo-code in the paper that document kay aspects of the approach.

2.0 Lava distribution without temperature

In the first step, lava flow distribution is considered withour temperature or other rheologic properties, except as they effect resistance to flow - a term Barca uses is adherence.

Suppose there is a topography (altitude) that consists of five cells:

where the number given in each cell is the elevation of the cell

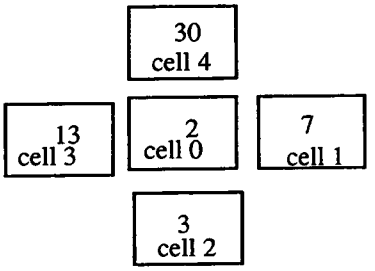

then lava is added to the middle cell. How will this lava be distributed?

Barca defines the matrix z where:

z(0) = altitude of cell 0 + adherence

z(1) = altitude of cell 1 + initial thickness of lava in cell 1

z(2) = altitude of cell 2 + initial thickness of lava in cell 2

z(2) = altitude of cell 3 + initial thickness of lava in cell 3

z(4) = altitude of cell 4 + initial thickness of lava in cell 4

and

La = the thickness of lava to be distributed, which is added to cell 0

In Barca's example:

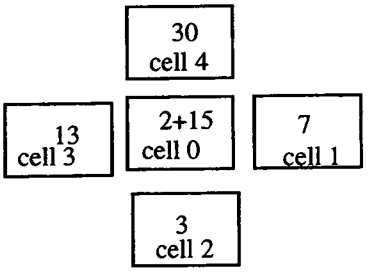

where La = 15, then the avg height is 70/5 = 14

because cell 4 has altitude 30, lava can not flow there from cell 0 and it is eliminated from the calculation:

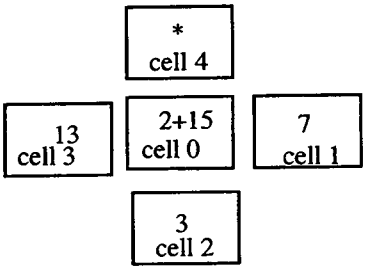

Now the average elevation is 40/4 = 10 and cell 3 should be eliminated:

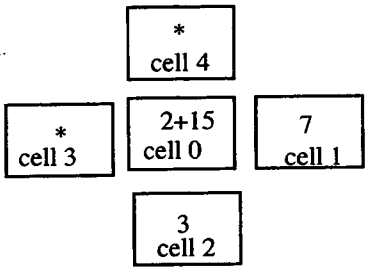

and the average elevation is 27/3 = 9. Since 9>7 or 3, lava flows into cells 1 and 2 from cell 0. The amount of lava that will flow into cell 1 from cell 0 is 2, and the amount of

lava that flows into cell 2 is 6; the lava remaining in cell 0 aftr this redistribution is 15-2-6 = 7 The following could reproduces Barca's results exactly:

```
•DIM z(0:4), fe(4), altitude(3,3),thickness(3,3)
•DIM source(3,3),adher(3,3), fe_tot(3,3)
•LET i = 2
•LET j = 2
•LET altitude(i,j) = 2
•LET altitude(i+1,j) = 7
•LET altitude(i,j-1) = 3
•LET altitude(i-1,j) = 13
•LET altitude(i,j+1) = 30
•LET thickness(i,j) = 0
•LET thickness(i+1,j) = 0
•LET thickness(i,j-1) = 0
•LET thickness(i-1,j) = 0
•LET thickness(i,j+1) = 0
•LET source(i,j) = 16
•LET source(i+1,j) =0
•LET source(i,j-1) =0
•LET source(i-1,j) =0
•LET source(i,j+1) =0
•LET adher(i,j) =1
•LET adher(i+1,j) =0
•LET adher(i,j-1) =0
•LET adher(i-1,j) =0
•LET adher(i,j+1) =0
•
•
•LET z(0) = altitude(i,j) + thickness(i,j) + source(i,j) - adher(i,j)
•LET z(1) = altitude(i+1,j) + thickness(i+1,j)
•LET z(2) = altitude(i,j-1) + thickness(i,j-1)
•LET z(3) = altitude(i-1,j) + thickness(i-1,j)
•LET z(4) = altitude(i,j+1) + thickness(i,j+1)
•
•
•CALL lava_distribute(z,fe)
•
•LET fe_tot(i,j) = fe(1) + fe(2) + fe(3) + fe(4)  ! total output from i,j
•
•MAT PRINT fe
•END
•
•SUB lava_distribute(z(), fe())
•
•  ! mat z is the altitude + adherence factor matrix
•
•  ! fe is the lava outflow toward cell i
•
•  DIM eliminated$(0:4)
```

```
•
• !initialize the eliminated$ so no cells
• ! are initially eliminated
• FOR i = 0 to 4
•    LET eliminated$(i) = "false"
• NEXT i
•
• !step through the averaging process 4 times
• ! once for each border cell
•
• DO
•   LET z_sum = 0          !initialize z_sum
•   LET count = 0          !initialize count
•   LET new_control$ = "false"
•
•   !find the average height in the group of 5 cells
•   !not including eliminated cells
•   FOR i = 0 to 4
•     IF eliminated$(i) <> "true" then
•       LET z_sum = z_sum + z(i)
•       LET count = count + 1
•     END IF
•   NEXT i
•   !find the average lava height in the cells
•   LET av_height = z_sum/count
•
•   !eliminate any cells that are higher than the average height
•   FOR i = 1 to 4
•     IF z(i) > av_height and eliminated$(i) <> "true" then
•       LET eliminated$(i) = "true"
•       LET new_control$ = "true"
•     END IF
•   NEXT i
•
•   ! if no cells eliminated then exit the loop
•   IF new_control$ = "false" then
•     EXIT DO
•   END IF
•   !iterate to calculate new average ht
•   !not including the eliminated cells
• LOOP
•
• ! the outflow to cell i = 0 if the cell was eliminated
• ! all other cells now have an average height - they
• ! get the outflow to make the heights uniform
•
• FOR i = 1 to 4
•    IF eliminated$(i) = "true" then
•      LET fe(i) = 0
•    ELSE
```

```
•       LET fe(i) = av_height - z(i)
•     END IF
•   NEXT i
•
•END SUB
```

the matrix fe gives the output to the ith adjacent cell.

Several modifications are made to the pseudo-code of barca. First , the term La is eliminated and

z(0) = altitude + thickness + source - adherence

where altitute is the elevation of the topography (solid) in the cell 0, thickness is the inital thickness of lava in the cell, source is the lava added to the cell (at a vent), and adherence is the factor that accounts for resistance to flow. Barca defines adherence as

adherence = A*exp(-B*T)

where A = 1e9m, B= 0.0154/°K, and T = temperature in °K

so the goal of adherence is to determine the thickness of lava that will not flow from cell to cell because of the rheologic propoerties of the rock. Barca says that this adherence is added to z(0), but this adds to the lava source that must be distributed - which doesn;t make sense. So adherence is the thickness of lava subtracted (not available to flow into adjacent cells because of the rheologic propoerties of the lava - which are strongly dependent on temperature.

A graph of adherence as a function of temperature using Barca's constants for A and B:

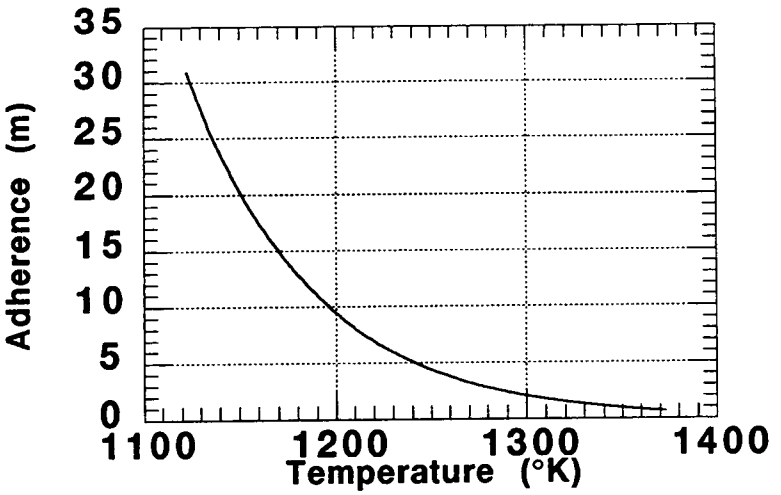

This graph implies that for a given thickness of lava in cell 0, about 1 m of lava is unavailable to flow out of cell 0 at temperature = 1350°K, and about 10 m is unavailable to flow out of the cell at 1200°K. Barca does not discuss estimates of A and B.

Barcas estimation technique also has to be modified for steep topography and low flow rates. If the unmodified algorithm is used, then more lava can be supplies to adjcent cells than is actually available in cell 0.

for example:

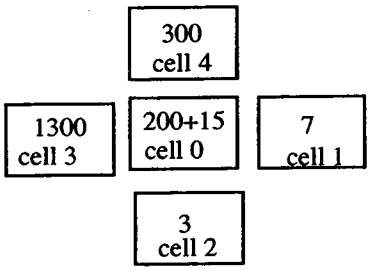

the available lava to flow into cell 1 and cell 2 is 15 m (thickness). Based on Barca's unmodified algorithm. 68 m of lava will accumulate in cell 1 and 72 m of lava will accumulate in cell 2. This is more than the 15 m avaialable, so the algorithm does not work where topographic changes are large compared to the lava input rate. The algorithm was modified to adjust for this change:

•DIM z(0:4), fe(4), altitude(3,3),thickness(3,3)
•DIM source(3,3),adher(3,3), fe_tot(3,3)
•LET i = 2
•LET j = 2
•LET altitude(i,j) = 300
•LET altitude(i+1,j) = 7
•LET altitude(i,j-1) = 3
•LET altitude(i-1,j) = 1300
•LET altitude(i,j+1) = 3000
•LET thickness(i,j) = 0
•LET thickness(i+1,j) = 0
•LET thickness(i,j-1) = 0
•LET thickness(i-1,j) = 0
•LET thickness(i,j+1) = 0
•LET source(i,j) = 16
•LET source(i+1,j) =0
•LET source(i,j-1) =0
•LET source(i-1,j) =0
•LET source(i,j+1) =0

```
•LET adher(i,j) =1
•LET adher(i+1,j) =0
•LET adher(i,j-1) =0
•LET adher(i-1,j) =0
•LET adher(i,j+1) =0
•
•let lava_available = thickness(i,j) + source(i,j) - adher(i,j)
•LET z(0) = altitude(i,j) + lava_available
•LET z(1) = altitude(i+1,j) + thickness(i+1,j)
•LET z(2) = altitude(i,j-1) + thickness(i,j-1)
•LET z(3) = altitude(i-1,j) + thickness(i-1,j)
•LET z(4) = altitude(i,j+1) + thickness(i,j+1)
•
•
•CALL lava_distribute(z,fe)
•
•LET fe_tot(i,j) = fe(1) + fe(2) + fe(3) + fe(4)  ! total output from i,j
•
•!make sure that Fe_tot does not exceed the available supply from
•! cell(i,j). If it does then ajust proportionately.
•
•if fe_tot(i,j) > lava_available then
•let old_fe_tot = fe_tot(i,j)
•let fe_tot(i,j) = lava_available
•for count = 1 to 4
•let fe(count) = fe(count)*fe_tot(i,j)/old_fe_tot
•next count
•end if
•
•MAT PRINT fe
•END
•
•SUB lava_distribute(z(), fe())
•
•  ! mat z is the altitude + adherence factor matrix
•
•  ! fe is the lava outflow toward cell i
•
•  DIM eliminated$(0:4)
•
•  !initialize the eliminated$ so no cells
•  ! are initially eliminated
•  FOR i = 0 to 4
•    LET eliminated$(i) = "false"
•  NEXT i
•
•  !step through the averaging process 4 times
•  ! once for each border cell
•
•  DO
```

```
    LET z_sum = 0          !initialize z_sum
    LET count = 0          !initialize count
    LET new_control$ = "false"
•
    !find the average height in the group of 5 cells
    !not including eliminated cells
    FOR i = 0 to 4
      IF eliminated$(i) <> "true" then
        LET z_sum = z_sum + z(i)
        LET count = count + 1
      END IF
    NEXT i
    !find the average lava height in the cells
    LET av_height = z_sum/count
•
    !eliminate any cells that are higher than the average height
    FOR i = 1 to 4
      IF z(i) > av_height and eliminated$(i) <> "true" then
        LET eliminated$(i) = "true"
        LET new_control$ = "true"
      END IF
    NEXT i
•
    ! if no cells eliminated then exit the loop
    IF new_control$ = "false" then
      EXIT DO
    END IF
    !iterate to calculate new average ht
    !not including the eliminated cells
  LOOP
•
  ! the outflow to cell i = 0 if the cell was eliminated
  ! all other cells now have an average height - they
  ! get the outflow to make the heights uniform
•
  FOR i = 1 to 4
    IF eliminated$(i) = "true" then
      LET fe(i) = 0
    ELSE
      LET fe(i) = av_height - z(i)
    END IF
  NEXT i
•
•END SUB
```

Using this modified code, all of the available lava flows from cell 0 to cells 1 and 2. 7.29m accumulates is cell 1 and 7.71 m accumulates in cell 2. The small difference in accumulation occurs because the difference in elevation between cell 0 and cell 1 is less than the difference in elevation between cell 0 and cell 2. The code divides the lava up based on this proportionate difference. This is realistic as long as average slopes charac-

terize the topography well. Alternatively, suppose there is a large cliff between cells 0 and cells 1 and 2. Then an equal amount of lava should flow into each - a condition not modelled by the code.

An additional problem comes up in that the flow geometry is different for a flow on a topographic surface that is slopes parallel with the cell axis and a topographic surface that slopes diagonal to the cell surface. With the 4 near-neighbor cell implementation, the lava flow is much wider when it flows diagonal to the cell grid.

A solution to this problem is to implement an eigth near-neighbor model for the lava flow.

now the cell geometry might look as follows:

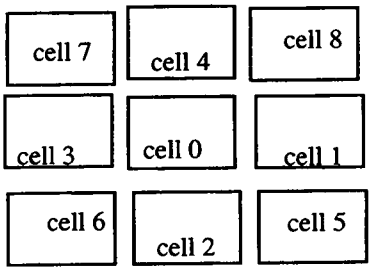

The matrix z has to include a weighting term because the average elevation of cells 5-8 represent an average state at a sqr(2)*distance greater than the elevations represented by cells 1-4.

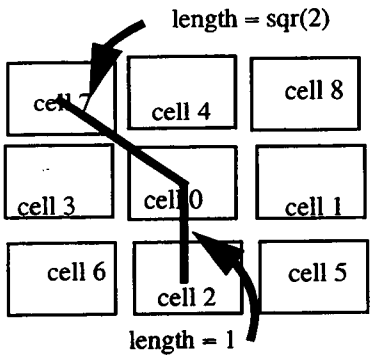

So the diagonal cells are weighted by the formula:

- for n = 5 to 8
- let z(n) = z(0) - (z(0)-z(n))/sqr(2)
- next n

and an eight near-neighbor cell is used.

The code is modified as follows:

```
•DIM z(0:8), fe(8), altitude(0:50,0:50),thickness(0:50,0:50)
•DIM source(0:50,0:50),adher(50,0:50), fe_tot(0:50,0:50)
•DIM new_thickness(0:50,0:50)
•
•open #99: screen 0,1,0,1
•SET WINDOW 0,50,0,50
•box lines 5,15,5,15
•get key dum
•LET adherence_dum = .6
•LET source(35,35) = 10
•LET adher(35,35) = adherence_dum
•LET nrow = 50
•LET ncol = 50
•
•FOR i = 0 to nrow
•   FOR j = 0 to ncol
•      !LET altitude(i,j) = (i+j)*10
• LET altitude(i,j) = (i)*20
•   NEXT j
•NEXT i
•
•FOR iteration = 1 to 100
•
•   MAT new_thickness = 0
•   MAT fe_tot = 0
•   FOR i = 1 to nrow-1
•      FOR j = 1 to ncol-1
•
•         LET lava_available = thickness(i,j) + source(i,j) - adher(i,j)
•         IF lava_available > 0 then
•
•           LET z(0) = altitude(i,j) + lava_available
•           LET z(1) = altitude(i+1,j) + thickness(i+1,j)
•           LET z(2) = altitude(i,j-1) + thickness(i,j-1)
•           LET z(3) = altitude(i-1,j) + thickness(i-1,j)
•           LET z(4) = altitude(i,j+1) + thickness(i,j+1)
•
•           let fudge_factor = 1  !/sqr(2)
•           LET z(5) = fudge_factor * altitude(i+1,j-1) + thickness(i+1,j-1)
•           LET z(6) = fudge_factor *altitude(i-1,j-1) + thickness(i-1,j-1)
•           LET z(7) = fudge_factor *altitude(i-1,j+1) + thickness(i-1,j+1)
•           LET z(8) = fudge_factor *altitude(i+1,j+1) + thickness(i+1,j+1)
•
•           for n = 5 to 8
```

```
•          let z(n) = z(0) - (z(0)-z(n))/sqr(2)
•          next n
•
•          CALL lava_distribute(z,fe)
•
•          LET fe_tot(i,j) = fe(1) + fe(2) + fe(3) + fe(4) + fe(5) + fe(6) + fe(7) + fe(8) !
total output from i,j
•
•          !make sure that Fe_tot does not exceed the available supply from
•          ! cell(i,j). If it does then adjust proportionately.
•
•          IF fe_tot(i,j) > lava_available then
•            LET old_fe_tot = fe_tot(i,j)
•            LET fe_tot(i,j) = lava_available
•            FOR count = 1 to 8
•              LET fe(count) = fe(count)*fe_tot(i,j)/old_fe_tot
•            NEXT count
•          END IF
•
•
•          LET new_thickness(i,j) = new_thickness(i,j) + lava_available + adher(i,j) -
fe_tot(i,j)
•          LET new_thickness(i+1,j) =  new_thickness(i+1,j) + fe(1)
•          LET new_thickness(i,j-1) = new_thickness(i,j-1)+ fe(2)
•          LET new_thickness(i-1,j) = new_thickness(i-1,j) + fe(3)
•          LET new_thickness(i,j+1) = new_thickness(i,j+1) + fe(4)
•          LET new_thickness(i+1,j-1) = new_thickness(i+1,j-1) + fe(5)
•          LET new_thickness(i-1,j-1) = new_thickness(i-1,j-1) + fe(6)
•          LET new_thickness(i-1,j+1) = new_thickness(i-1,j+1) + fe(7)
•          LET new_thickness(i+1,j+1) = new_thickness(i+1,j+1) + fe(8)
•
•        ELSE
•          LET new_thickness(i,j) = new_thickness(i,j) + thickness(i,j) + source(i,j)
•
•        END IF
•      NEXT j
•    NEXT i
•
•    FOR i = 1 to nrow-1
•      FOR j = 1 to ncol-1
•
•        LET thickness(i,j) = new_thickness(i,j)
•        IF thickness(i,j) > 0 then
•          LET adher(i,j) = adherence_dum
•        END IF
•      NEXT j
•    NEXT i
•
•    FOR i = 1 to nrow
•      FOR j = 1 to ncol
```

```
•         IF thickness(i,j) > 0 then
•
•           IF thickness(i,j) > 1 then
•             LET text$ = str$(thickness(i,j))
•             LET text$ = text$[1:4]
•            ! PLOT TEXT, AT i,j: text$
• BOX AREA i-0.5,i+0.5,j-0.5,j+0.5
•           ELSE
•             PLOT TEXT, AT i,j:"*"
•           END IF
•           LET tot_thick = tot_thick + thickness(i,j)
•         END IF
•       NEXT j
•   NEXT i
•   LET text$ = str$(tot_thick)
•   LET tot_thick = 0
•   PLOT TEXT, AT 16,16 :text$
•let i = 35
•set color "red"
•box area i-0.5,i+0.5,i-0.5,i+0.5
•set color "green"
•   GET KEY dum
•   CLEAR
•
•
•NEXT iteration
•
•
•END
•
•SUB lava_distribute(z(),fe())
•
•   ! mat z is the altitude + adherence factor matrix
•
•   ! fe is the lava outflow toward cell i
•
•   DIM eliminated$(0:8)
•   MAT fe = 0
•   !initialize the eliminated$ so no cells
•   ! are initially eliminated
•   FOR i = 0 to 8
•      LET eliminated$(i) = "false"
•   NEXT i
•
•   !step through the averaging process 4 times
•   ! once for each border cell
•
•   DO
•      LET z_sum = 0          !initialize z_sum
•      LET count = 0          !initialize count
```

```
    LET new_control$ = "false"
•
    !find the average height in the group of 5 cells
    !not including eliminated cells
    FOR i = 0 to 8
      IF eliminated$(i) <> "true" then
        LET z_sum = z_sum + z(i)
        LET count = count + 1
      END IF
    NEXT i
    !find the average lava height in the cells
    LET av_height = z_sum/count
•
    !eliminate any cells that are higher than the average height
    FOR i = 1 to 8
      IF z(i) > av_height and eliminated$(i) <> "true" then
        LET eliminated$(i) = "true"
        LET new_control$ = "true"
      END IF
    NEXT i
•
    ! if no cells eliminated then exit the loop
    IF new_control$ = "false" then
      EXIT DO
    END IF
    !iterate to calculate new average ht
    !not including the eliminated cells
  LOOP
•
  ! the outflow to cell i = 0 if the cell was eliminated
  ! all other cells now have an average height - they
  ! get the outflow to make the heights uniform
•
  FOR i = 1 to 8
    IF eliminated$(i) = "true" then
      LET fe(i) = 0
    ELSE
      LET fe(i) = av_height - z(i)
    END IF
  NEXT i
•
•END SUB
```

The following results were obtained by running the above program

-black box indicates source region 10 m thickness of lava added to at each time step.

- magenta boxes indicate lava accumulation in the cell of more than 1 m thickness

- magenta * indicates lava accumualtion in the cell of 0<lava<1 m thickness

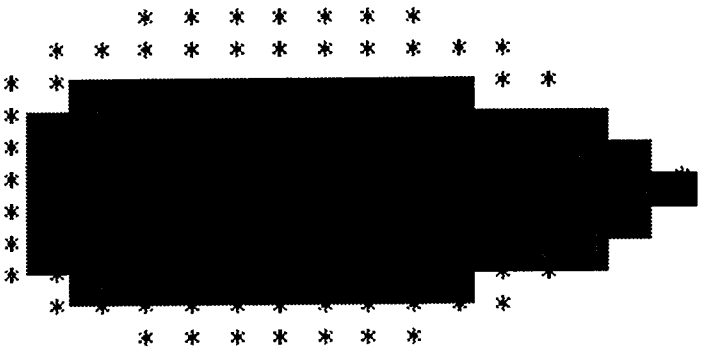

input parameters in the model are those used by Barca.

- cell wall length is 10 m

- cell area is $100m^2$

- adherence = 0.6 (assumed constant)

- source term = 10 m per iteration (= $1000m^3$ per iteration)

- and the slope of the preexisiting topographic surface is 45° to the west

in this example all conditions are the same as above except that the preexisting topo-

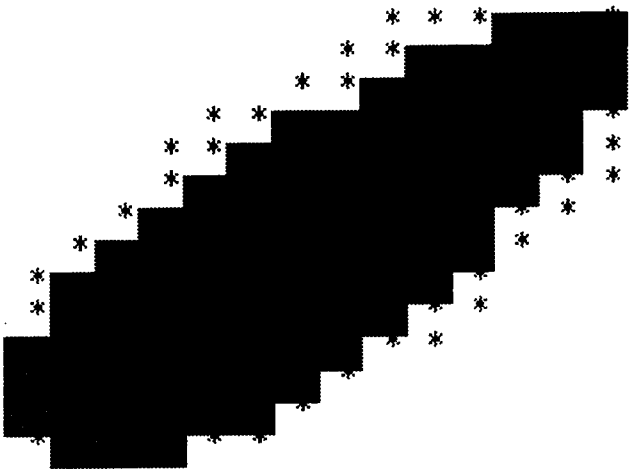

graphic surface is dipping at 45° to the SW. Note that the cells are not quite square.

So, differences in the lava flow geometries are entiriely attributed to differences in the cell geometry.

Thickness of flow (using square cells)

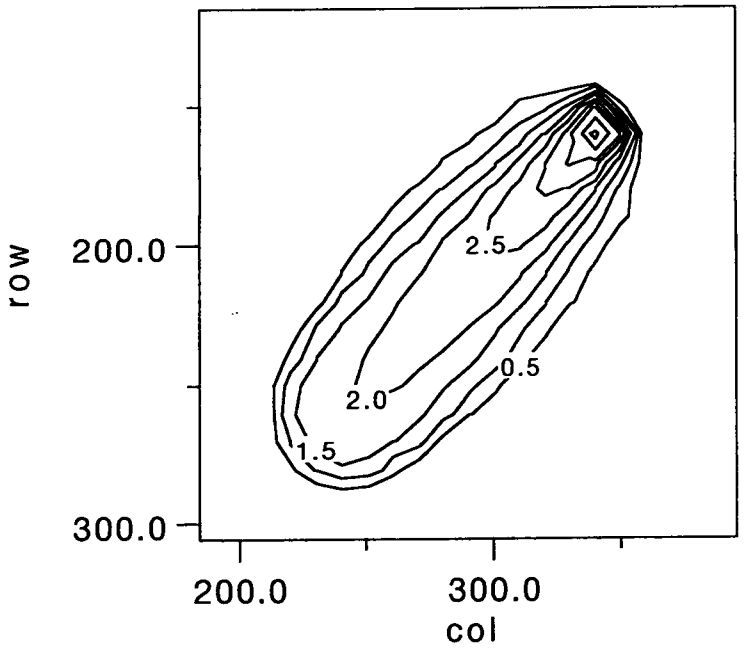

Ground Magnetic Survey of the Little Cones, Crater Flat Valley, Nevada

Chuck Connor

1.0 INTRODUCTION

The proposed High-Level Waste (HLW) repository at Yucca Mountain (YM), Nevada is located within a geologically active volcanic field. This volcanic field consists of eight basaltic cinder cones formed by volcanic activity within the last one million years, and numerous cinder cones and lava flows formed within the last 5 million years (Figure 1)(Faulds et al., 1994; Sawyer et al., 1994; Bradshaw and Smith, 1994; Champion, 1991; Heizler et al., 1994). As is typical for volcanic fields of this kind located throughout western North America, volcanic activity in the YM region is best characterized by the formation of new basaltic volcanoes at a low recurrence rate. Recent estimates of the probability of a new basaltic cinder cone forming within the area of the proposed repository are 1–5 x 10-4for a 10,000 yr period (Crowe and Perry, 1989; Ho et al., 1991; Smith et al., 1991; Margulies et al., 1992; Connor and Hill, 1995). Although probability estimates will likely be refined, current estimates are large enough to be of regulatory concern and must be addressed in performance assessment.

FIGURE 1. Basaltic vents, lavas, and known intrusions in the YM region younger than about 9 Ma. Geology compiled from Geology compiled from Byers et al. [1966]; Ekren et al. [1966]; Carr and Quinlivan [1966]; Byers and Barnes [1967]; Byers and Cummings [1967]; Hinrichs et al. [1967]; Noble et al. [1967]; Tschanz and Pampeyan [1970]; Cornwall [1972]; Crowe et al. [1983, 1986]; Carr [1984]; Swadley and Carr [1987]; and Faulds et al. [1994]. Locations of aeromagnetic anomalies [stars] from Kane and Bracken [1983] and Langenheim et al. [1993]. Little Cones are located in southern Crater Flat valley. Contours generated from regional a 3 arc-second Digital Elevation Model, 200 m contour

interval. UTM projection, Nevada zone 11, NAD 1983 datum. Modified from Connor and Hill (1995).

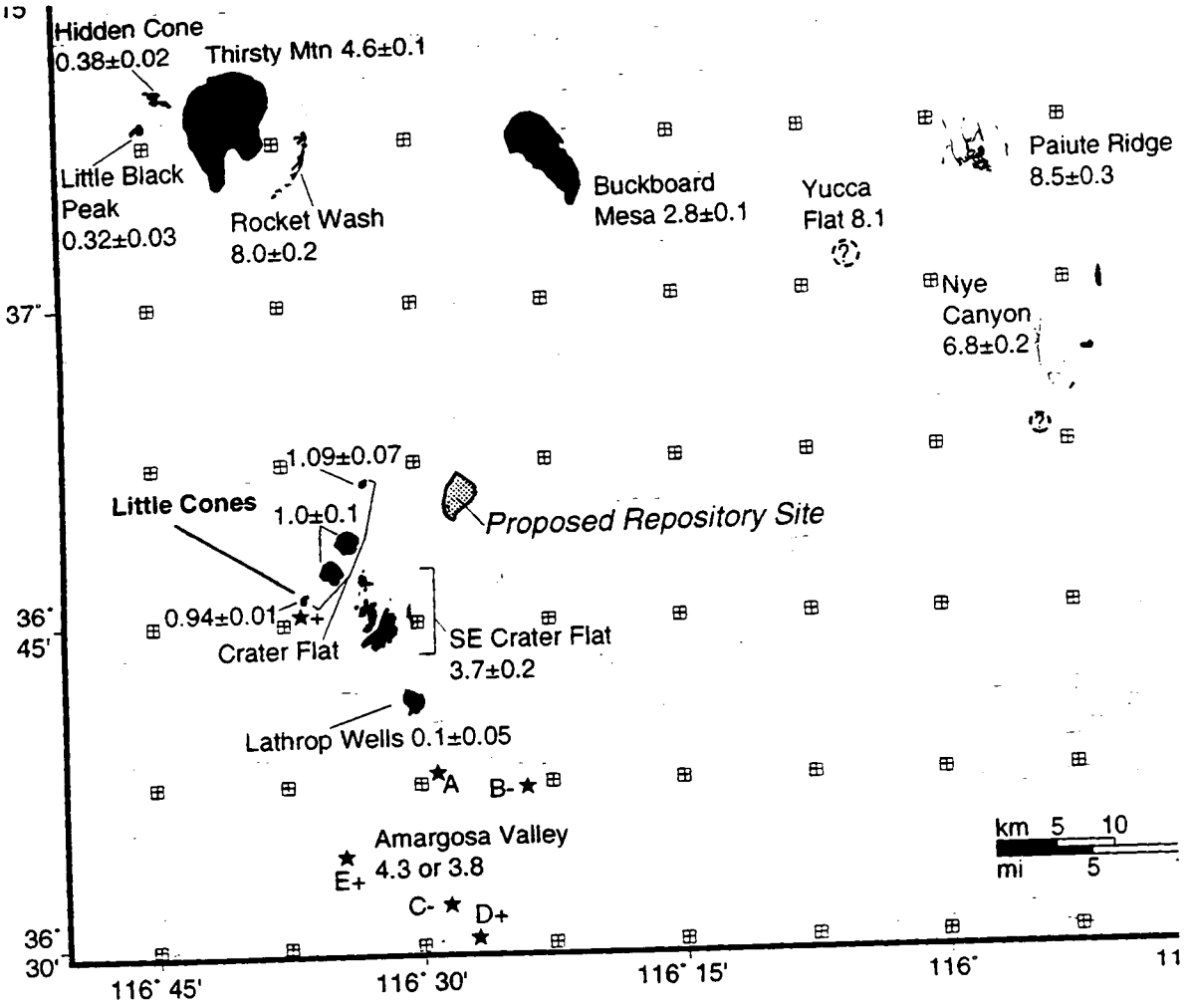

Estimates of the probability of volcanic disruption of the candidate repository are strongly effected by the volume, orientation, shape and frequency of intrusions associated with volcanic events. These factors are represented by an area term included in all probability models. If volcanic events are considered to be very spatially limited phenomenon, then the probability of volcanic disruption of the candidate repository is less for a given recurrence rate than if the area affected by an individual volcanic event is large. Consequently, it is important to estimate the area impacted by individual volcanic events in the YM region in as much detail as possible. Current estimates of this area term are based on assumptions about intrusion geometries that may not be conservative (e.g., Barr et al., 1992; Lin et al., 1993; Wilson et al., 1994).

This report presents results of a ground magnetic survey made at the Little Cones, two Quaternary basaltic cinder cones located in Crater Flat valley approximately 15 km southwest the proposed repository site (Figure 1). The goals of this survey were to:

•Evaluate the utility of ground magnetic data for characterizing intrusions and related structures at basaltic volcanoes.

•Identify intrusions and related volcanic features associated with the formation of the Little Cones

•Determine the relationship of these intrusions to more regional structural features

•If possible, estimate the subsurface area disrupted by the Little Cones eruption.

The results of this ground magnetic survey provide an indication of the utility of high-resolution ground magnetic surveys for elucidating the volcanic history of known volcanic features, such as the Little Cones. Furthermore, interpretation of the ground magnetic survey using a variety of map filtering and forward modeling techniques indicates that collection of these data is essential in order to assess the true extent of volcanism in the Yucca Mountain region. Results of such magnetic surveys and interpretation of these data can be used to refine estimates of area terms used in probability models for volcanic hazard assessment.

1.1 Regulatory Basis

Insight into the frequency, distribution, and volume of basaltic magmatism in the YM region, the repository and regional scales of volcanic effects, and the relationships between volcanism and regional tectonic and structural settings, form an integral part of license review. Volcanism must be reviewed in terms of site characterization as described in the License Application Review Plan (LARP). These activities include review of evidence of igneous activity as a potentially adverse condition (LARP Section 3.2.1.9), review of the impact of volcanism on groundwater movement (LARP Section 3.2.2.7), and description of overall system performance (LARP Section 6.1).

The Compliance Determination Strategy (CDS) associated with evidence of Quaternary igneous activity is of Type 5, indicating that independent research must be conducted to evaluate Key Technical Uncertainties (KTUs) associated with volcanism, and that volcanism poses a high risk to the NRC of researching unwarranted conclusions about compliance with 40 CFR Part 191 and 10 CFR Part 60.122(c)(15).

The magnetic survey of the Little Cones was made to partially address several KTUs. These are:

•Low resolution of exploration techniques to detect and evaluate igneous features (Type 4)

•Inability to characterize many igneous features and events (Type 5)

•Probability of igneous activity and resulting disruption of the candidate repository site (Type 5)

•Consequences of igneous activity for repository performance (Type 5).

Clearly each of these KTUs cannot be resolved based on the limited results obtained in this survey. However, the techniques used in this magnetic survey of the Little Cones provide significant insight into the ways in which commonly available geophysical techniques may be used to reduce the impact of uncertainty related to low resolution of exploration techniques to detect and evaluate igneous features , and inability to characterize many igneous features and events, on models of the probability and consequences of igneous activity.

1.2 Organization of this Report

The results and geological interpretation of the ground magnetic surveys are presented in Section 2 of this report. In Section 3 , the regulatory significance of the results of the field survey of Little Cones is discussed. In Section 4, conclusions drawn from the survey results are given. References cited throughout the text are given in Section 5. Much of the magnetic survey results are provided in Plate 1 (inside back cover). Drift-corrected magnetic data and the results of map filtering of these data are provided in Appendix 1.

2.0 Results of the Ground Magnetic Survey

The Little Cones were selected for the ground magnetic survey because the cones are small and are located in the most accessible part of Crater Flat Valley, simplifying survey logistics. As few lava flows crop out around the Little Cones, it was believed that magnetic surveys of these cones would provide the best possibility of identifying intrusions associated with Quaternary volcanism in Crater Flat, because lava flows associated with other cones produce substantial magnetic anomalies that mask anomalies produced by intrusions.

3.0 Geology of the Little Cones

The two Little Cones are small pyroclastic cones located in the southern part of Crater Flat Valley. These cones are the southernmost in a 12-km-long alignment of five Quaternary cinder cones that trends NNE across the valley and includes, Red Cone, Black Cone, and Northern Cone (Figure 1). This alignment is arcuate: the azimuth at the north end of the alignment, between Black Cone and Northern Cone, is approximately 025°; the azimuth at the southern end of the alignment, between the Little Cones and Red Cone is approximately 040°.

3.1 Geologic Setting of the Little Cones

NE and SW Little Cones are located near the main axis of deposition in Crater Flat Valley on a broad alluvial surface that slopes gently to the south (Figure 2). Faulds et al. (1994) referred to this alluvium as the Quaternary Little Cones Alluvium and described it as fan skirt and low basin remnants of Late Pleistocene to Holocene age. Faulds et al. (1994) report 14C rock varnish ages on alluvial material of this deposit of 6,645±245 and 11,135±105 yBP. Except for active washes, this alluvial surface is the youngest in Crater Flat Valley.

No faults have been mapped on this young alluvial surface (Faulds et al., 1994). The nearest mapped fault to the Little Cones is the NNW-tending Bare Mountain fault, located approximately 1.5 km west of SW Little Cone. Uplift rates along the Bare Mountain fault have been estimated to be approximately 0.24 mm/yr based on fission track thermochronometry and alluvial fan development (Ferrill et al., 1995). The Bare Mountain fault dips eastward beneath Crater Flat. Assuming an average dip of 60° along the shallow portion of the Bare Mountain fault (Ferrill et al., 1995), the fault crosses beneath the Little Cones at a depth of approximately 2.5 km, or less if the fault dip shallows over this distance. Numerous N-S-trending faults cut older alluvial surfaces in western Crater Flat (Faulds et al., 1994). These mapped faults are near-vertical or are steeply dipping and do not likely project beneath the Little Cones.

Aeromagnetic anomalies have a pronounced N–S trend in Crater Flat Valley (Kane and Bracken, 1983), consistent with the presence of buried N–S trending faults. The Quaternary Crater Flat cinder cone alignment is positioned at a transition from comparatively low magnetic gradients to the west and high magnetic gradients prodiced by shallow volcanic rocks to the east (Figure 2). This change in magnetic gradient, combined with the N–S trend of aeromagnetic anomalies and mapped structures elsewhere in the valley suggests that basement structure may influence the position and development of the cinder cone alignment.

FIGURE 2. Aeromagnetic data of Kane and Bracken (1983) is superimposed on a LandSat TM Band 3 image of Crater Flat Valley. Contour interval is 50 nT and contours are broken in areas with high magnetic gradients.

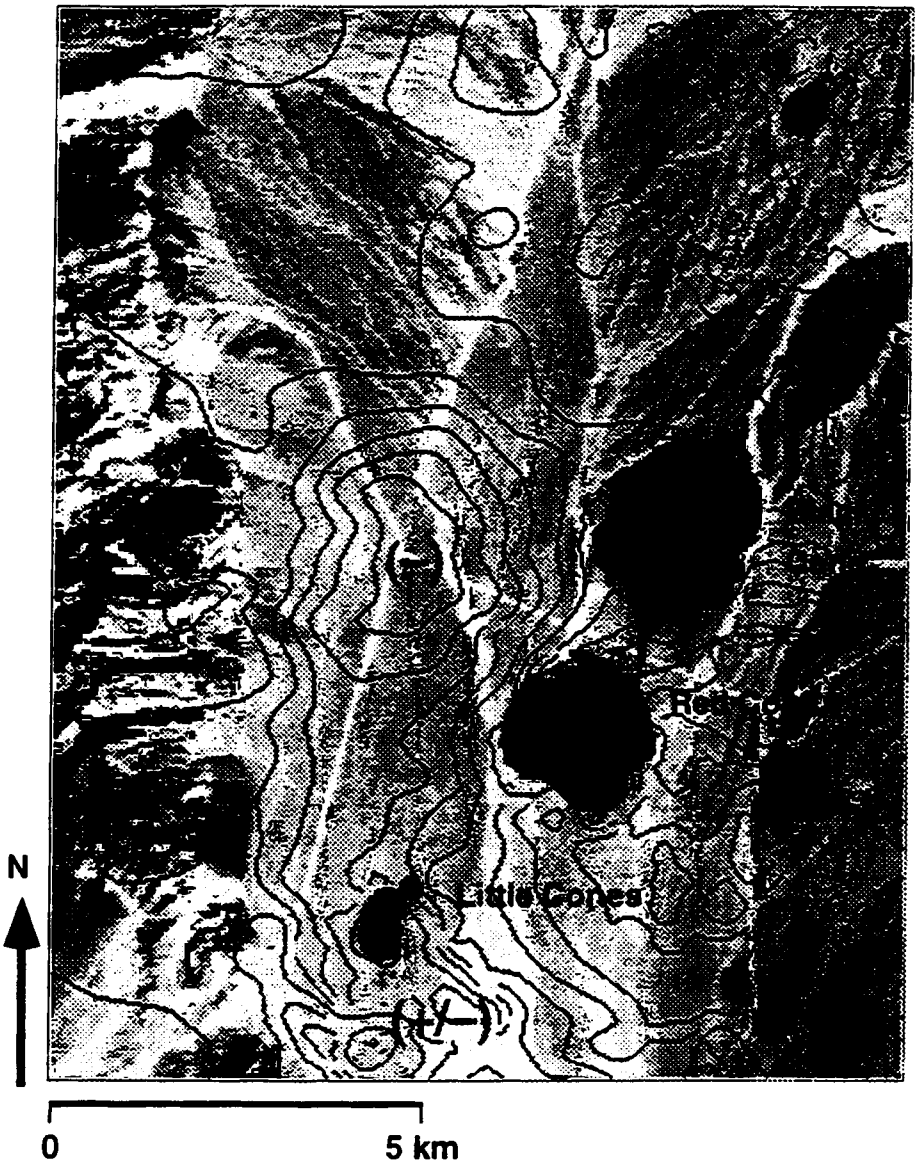

On local scales, very high gradients in the aeromagnetic data occur at Red Cone, Black Cone, and a set of Pliocene dikes and vents in southeast Crater Flat (Figure 2–1). Small–amplitude, reversely–polarized aeromagnetic anomalies are ampped at Northern Cone and SW Little Cone.

Other prominent magnetic anomalies in Crater Flat Valley are not associated with mapped basalts. A comparatively large–amplitude anomaly is mapped south of the Little Cones. This anomaly is of unknown origin, but given its steep magnetic gradient is produced by shallow, highly magnetized rock, possibly of volcanic origin. Several anomalies occur north of Black Cone, including an elongate magnetic low colinear with the alignment and sevearl dipolar anomalies. These anomalies are comparable is size

and amplitude to the aeromagnetic anomalies associated with SW Little Cone and Northern Cone, and may be produced by shallow dikes or buried volcanic rocks.

3.2 Physical Features and Age of the Little Cones

The highest points on the two cones are separated by 360 m along an azimuth of 052° (Figure 3). NE Little Cone is a low, undissected mound of cinders and bombs that is 230 m in diameter, 15 m in height, and 170,000 m3 in volume. NE cone is slightly elongate in a E-W direction. The western slope of the cone is the steepest; a small topographic depression occurs low on the south flank of NE Little Cone. A small outcrop of indurated lava caps NE Little Cone. SW Little Cone is larger, 24 m in height, 350 m in diameter, and 630,000 m3 in volume (Figure 3). Rill development is much more pronounced on SW Little Cone compared with NE Little Cone, especially on the north and west sides of the cone. SW Little Cone is breached on its south side. The lava flow associated with this breach crops out up to 0.5 km south of the cone but is almost completely covered by alluvial material.

SW Little Cone is quarried on its west flank. Cinder to block-sized angular pyroclasts are exposed in this quarry. Poorly developed bedding and the fragmented character of the pyroclasts indicates some downslope movement during or immediately after deposition. A lack of agglutinate or deformed pyroclastic material exposed in the quarry at SW Little Cone indicates that at least some stages of the eruption were sufficiently energetic for pyroclastic material to cool during transport within the eruption column.

FIGURE 3. Topographic map of the NE and SW Little Cones. Topography was surveyed using lane table and alidade methods and referenced to U.S. Geological Survey 30 m digital

elevation data. Contour interval is 2.5 m, dirt roads in the area of the two cones are indicated.

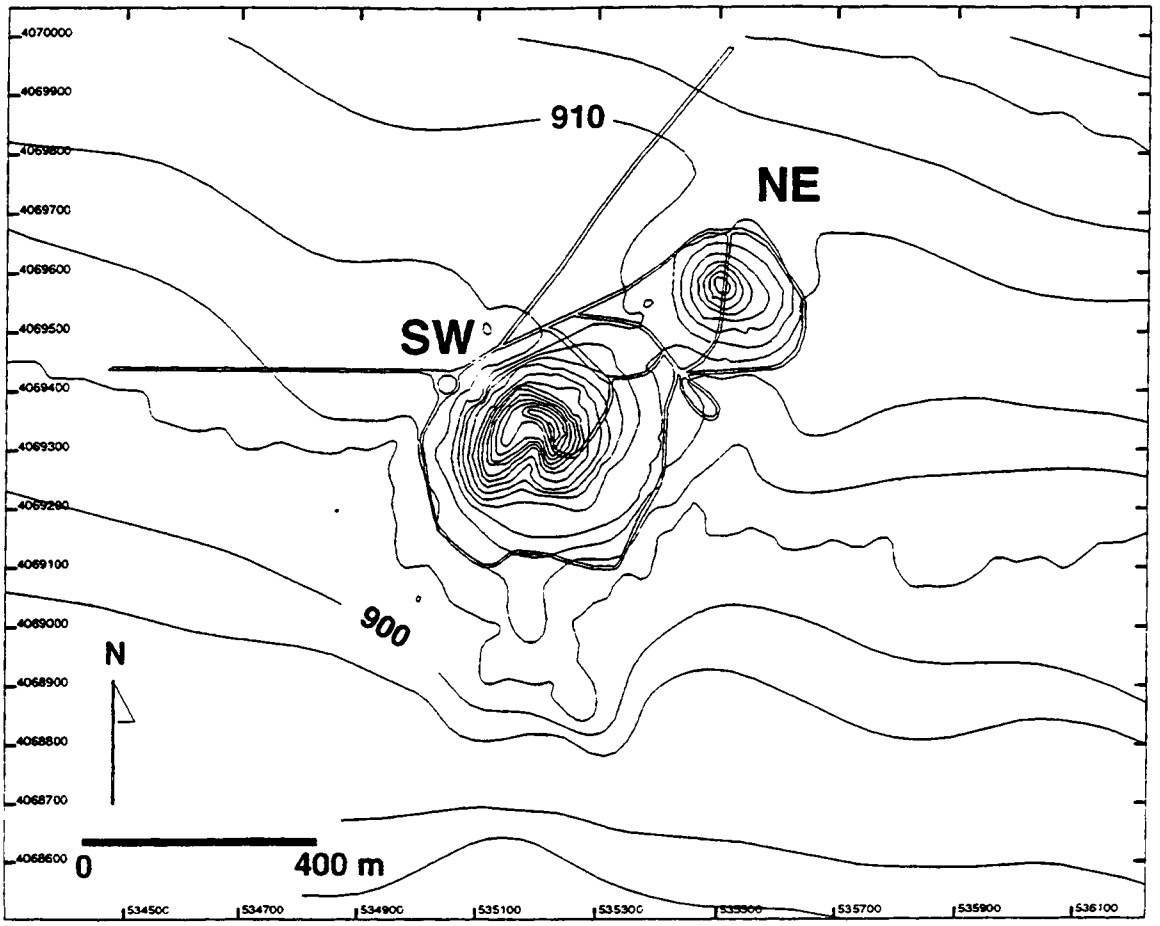

Faulds et al., (1994) report a K-Ar date of 0.77±0.04 Ma on a single plagioclase separate collected at the Little Cones. Heizler et al. (1994) dated a sample from SW Little Cone at 0.94±0.01 by Ar/Ar step heating of sanidine xenocrysts. Basaltic rock samples collected at the two cones have reversed magnetic polarity (Champion, 1991). D. Champion collected samples from three sites at the Little Cones for rock magnetic analysis1, located on the summit of NE Little Cone, SW Little Cone, and a lava outcrop south of SW Little Cone. Champion found a uniform vector of magnetization at the three sites of inclination -67° and declination of 177° (a95 = 6.3°). This high inclination suggests that, despite the differences in the two numeric age determinations, the Little Cones eruption occurred over a brief period of time during the late Matuyama epoch.

3.3 Background on the Ground Magnetic Method

Potential field methods are commonly used to develop a three-dimensional view of geologic structures. Identification of these structures is one of the primary goals of geophysical exploration in the YM region (Oliver et al., 1990). The principles and utility of magnetic methods for the identification of basaltic volcanic rocks in the YM region have recently been reviewed by Connor and Sanders (1994).

Clearly, magnetic methods have been among the most successful techniques for the identification of basalts in the YM region that do not crop out at the surface (Langenheim et al., 1993; Ponce et al., 1992). Magnetic methods are particularly suited for the exploration and mapping of basaltic rock in alluvial valleys because of the high contrast in magnetic properties between basalt and alluvium. Aeromagnetic surveys in the YM region (Kane and Bracken, 1983) have lead to the identification of five magnetic anomalies in the Amargosa Valley (Figure 1) that have been attributed to the presence of buried basaltic volcanoes (Langenheim et al., 1993). Recognition of these anomalies has led to revision of estimates of the extent and recurrence rate of basaltic volcanism in the YM region (Connor and Hill, 1995), and indicates that additional ground magnetic surveys may provide additional insight into volcanism in the region.

3.4 Survey Design and Results

A total of 2,891 ground magnetic observations were made during a five day sampling period using a Geometrics model G–856 proton–precession magnetometer. Survey point locations are shown in Figure 4. The magnetometer sensor height was three meters above the surface. Usually, drift in the magnetic field was monitored continuously using a model G-866 base station magnetometer. Amplitude of diurnal variations in the total magnetic field were always less than 60 nT and typically less than 40 nT during the survey. Occasionally, drift was monitored by reoccupying base stations at frequent intervals (less than 15 minutes). All magnetic data were drift corrected based on these observations. Drift corrected magnetic readings are listed in Appendix 1.

Based on the results of this survey, two areas were surveyed at a higher resolution using a Geometrics model G–858 optically-pumped cesium-vapor magnetometer (Figure 4). This magnetometer provides highly repeatable readings in areas of high magnetic gradient, such as those identified in the Little Cones area, and is capable of collecting data at a much greater sampling rate than proton-precession magnetometers. Sensor height for these detailed surveys was 1 m. High– and low–resolution surveys were not integrated into a single map because of differences in sensor height and survey point density.

Results of the low-resolution survey are presented on Plate 1 (inside back cover). The total magnetic field has a tremendous dynamic range within the survey area, from approximately 47,000 nT to 53,000 nT. This dynamic range reflects the high remanent magnetization of the Little Cones basalt.

FIGURE 4. Survey point locations. Data were collected using a proton-precession magnetometer except on grids A and B, where data were collected using a cesium-vapor magnetometer.

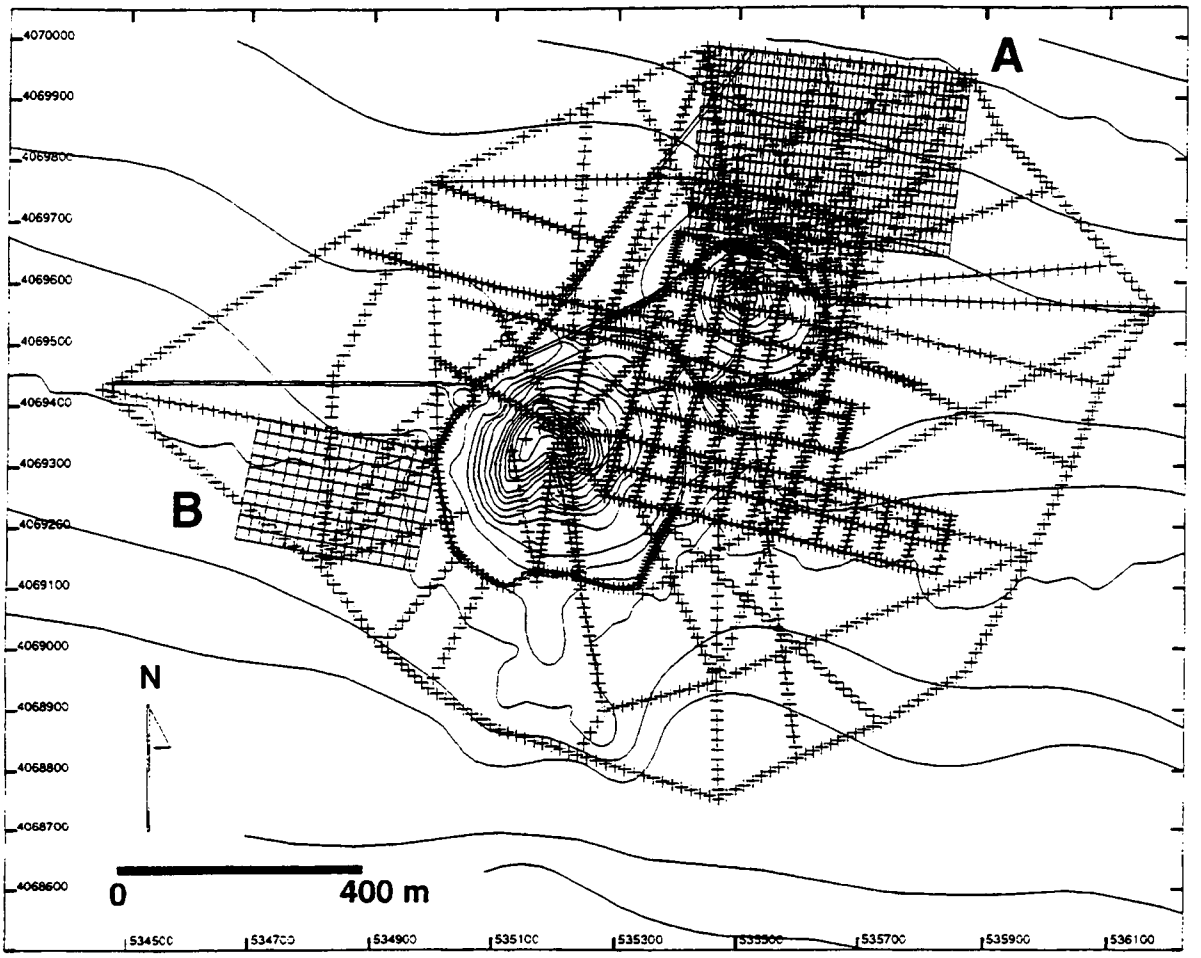

Short wavelength anomalies surround and extend outward from the two cones to distances of 300–600 m (Plate 1). These short-wavelength anomalies extend off the magnetic map area to the south. Short–wavelength anomalies are interpreted to be produced by lava flows that form an apron about the two cones. The survey was extended beyond these anomalies on the east, west, and north sides of the map, into the magnetically quiet alluvium. Typical horizontal gradients in the total magnetic field within this alluvium are <1 nT/m. In contrast, magnetic gradients in the area immediately around the cone often exceed 100 nT/m.

Large amplitude anomalies associated with the two cones dominate the magnetic map (Plate 1). A N-S trending negative anomaly correlates with the breach on the south side of SW Little Cone. High frequency, high-amplitude anomalies extend over lava flows that crop out on the south side of the SW Little Cone, reflecting the thick, shallow lava flows in this area. A prominent dipole south of SW Little Cone is associated with a basaltic lava outcrop associated with this flow.

Three aspects of the magnetic map (Plate 1) were investigated in detail. These are:

•A reversed, dipolar anomaly centered on NE Little Cone

•The areal extent of lava flows revealed by the magnetic map, particularly north of NE Little Cone

•An anomaly northeast of NE Little Cone that is interpreted to be related to a vent or shallow intrusion.

3.5 NE Little Cone Anomaly

A large number of measurements were made on NE Little Cone with the goal of determining the geometry of the internal cone structure. Details of the magnetic anomalies associated with NE Little Cone are shown in Figure 5a. Numerous short–wavelength anomalies are prevalent on and around the cone. These anomalies often have wavelengths of less than 10 m and amplitudes of >1,000 nT. These anomalies are clearly related to shallow magnetized blocks. A longer–wavelength reversely–polarized dipolar anomaly is centered on the cone itself (label A of Figure 5) This anomaly has an amplitude of about 3000 nT. Three other anomalies of interest on this map are a negative anomaly northeast of NE Cone (labeled B), a long, complex negative anomaly that extends southeast of the cone (labeled C) and a dipolar anomaly east of the cone (labelled D).

FIGURE 5. (a) Detailed map of the magnetic anomaly over NE Little Cone. A large dipolar anomaly occurs centered on the summit of the cone (labeled A), an elongate NE-trending anomaly occurs NE of the cone (labeled B). Negative anomalies southeast (labeled C) and east (labeled D) of the cone are interpreted to be related to shallow, massive flows.

(b) Low-pass filtering of the magnetic map enhanced each of these anomalies. Contour interval is 200 nT. Map coordinates are in meters (UTM, zone 11, Clarke 1866).

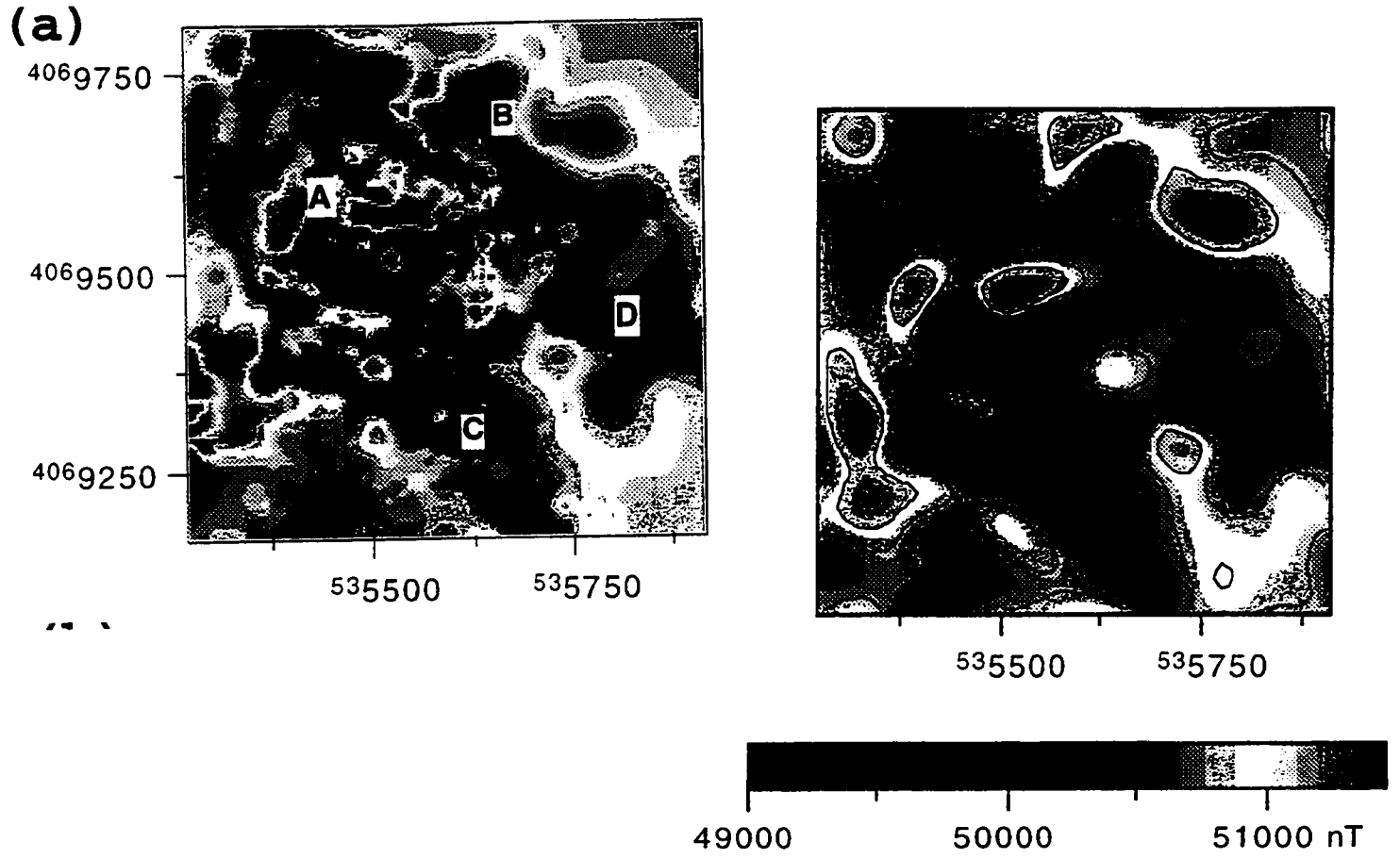

The NE Little Cones map was enhanced by frequency filtering, because of the large number of large–amplitude, short–wavelength anomalies present on the map. Map enhancement and filtering techniques are widely used to interpret aeromagnetic and ground magnetic data (e.g., Hildenbrand, 1985) and are described by Hildenbrand (1983) and Connor and Sanders (1994). In this case a low–pass filter was used to attenuate short-wavelength anomalies. This was accomplished by interpolating observed magnetic data within the NE Little Cone area on to a 64 x 64 grid, and filtering this grid in the frequency domain using a ramped low–pass filter. Anomalies with wavelengths greater than 50 m are passed through this filter unchanged. Anomalies with wavelengths less than 20 m are completely attenuated by the filter. Between 20 m and 50 m, anomalies are attenuated using a cumulative normal distribution, which provides a smooth

ramp. In general, anomalies enhanced by this low–pass filter will be produced by deeper and larger magnetized bodies than anomalies that are attenuated by this filter.

The low-pass filtered map (Figure 5b) reveals each of the magnetic anomalies (labeled A–D in Figure 5a) more clearly. The reversed, dipolar anomaly associated with the cone (labeled A) consists of a large negative anomaly and a smaller positive anomaly located to the north. A dipolar anomaly of this shape and amplitude is expected, given the high angle of inclination of the remanent magnetization vector (–67°), if it is related to the internal cone structure rather than surface features. Anomaly B of Figure 5a is also enhanced by the low–pass filter. This anomaly is more clearly a NE-trending magnetic low, extending NE of the cone. As discussed in more detail in the following, this anomaly is likely produced by a buried vent or shallow dike. The filtered map shows a nearly continuous magnetic low extending southeast from the cone for a distance of 400 m (labeled C). This anomaly is interpreted to be related to a shallow lava flow surface. This interpretation is supported by the topography of NE Little Cone. A shallow depression in the cone is located on the southeast side of the cone, associated with the southeast trending magnetic anomaly. This depression may have been produced by incipient breaching of the cone during a late-stage effusion of lavas which flowed to the southeast. Anomaly D of Figure 5a is also a broad negative anomaly and is enhanced by the filtering process. However, sample density is relatively low in this part of the map (Figure 4) and, therefore, the wavelength of this anomaly is less certain. A possible interpretation of this anomaly is that it is also related to shallow lavas.

In order to further interpret anomaly A (Figure 5a), several models were constructed based on the topography of the cone and the possible structure of the cone. These models include:

•A magnetized, 20-m-diameter circular conduit that extends vertically from the surface to great depth; the cone carries a small remanent magnetization and the conduit carries a large remanent magnetization (Figure 6a and 6b)

•Uniform magnetization of the entire cone; most of the cone carries a high remanent magnetization beneath a mantle of unconsolidated float and scoria (Figures 7a and 7b)

•An intermediate model, in which the central part of the cone carries a high remanent magnetization and most of the volume of the cone consists of unconsolidated float and scoria (Figures 7a and 7b).

In each of these models the geometry is approximated by vertical-sided polygons and the magnetic anomaly associated with the geometries is calculated based on the algorithm of Plouff (1976). The magnetic anomaly is calculated at points on a 20 m grid and at elevations corresponding to the sensor height for the proton-precession magnetometer survey, 3 m above the topographic surface.

This is the TrueBasic code used to model the magnetic anomalies:

```
CLEAR
DIM box(100,6), oldbox(100,6), exit(4), pt(1000,2)

LET ymin = 1e20
LET ymax = -1e20
LET xmin = 1e20
LET xmax = -1e20

PICTURE polygons(num_boxes,box(,))
  FOR i = 1 to num_boxes
    BOX AREA box(i,1),box(i,2),box(i,3),box(i,4)
    IF i>1 then
      PLOT box(i,5),box(i,6);box(i-1,5),box(i-1,6)
    END IF
  NEXT i
  PLOT box(1,5), box(1,6); box(num_boxes,5), box(num_boxes,6)
END PICTURE

PICTURE exit_box(exit())
  BOX LINES exit(1),exit(2),exit(3),exit(4)
  PLOT TEXT, AT exit(1),exit(3):"Quit"
END PICTURE

PICTURE line_dat(num_dats,delx,dely,pt(,))
  FOR n = 1 to num_dats
    LET lx = pt(n,1)
    LET ly = pt(n,2)
    LET lx1 = pt(n,1)-delx
    LET lx2 = pt(n,1)+delx
    LET ly1 = pt(n,2)-dely
    LET ly2 = pt(n,2)+dely
    PLOT lx,ly1;lx,ly2
    PLOT lx1,ly;lx2,ly
  NEXT n
END PICTURE
```

```
PRINT "TYPE IN THE NAME OF THE DATA POINT FILE"
PRINT "these points will be posted"
INPUT file$
OPEN #1: name file$
DO while more #1
  LET num_dats = num_dats+1
  INPUT #1: pt(num_dats,1),pt(num_dats,2),dum
  IF  pt(num_dats,1)<xmin then LET xmin =  pt(num_dats,1)
  IF  pt(num_dats,1)> xmax then LET xmax =  pt(num_dats,1)
  IF pt(num_dats,2)< ymin then LET ymin = pt(num_dats,2)
  IF pt(num_dats,2)>ymax then LET ymax = pt(num_dats,2)
LOOP
CLOSE #1

PRINT "Add a polygon to a file (1) or change a polygon file (2)"
INPUT choice

SELECT CASE choice

CASE 1

   PRINT "Name of output file"
   PRINT "polygon will be appended to the end of this file"
   INPUT file$
   OPEN #1: name file$, create newold

   DO until num_boxes => 3
     INPUT prompt "number of polygon vertices--> ": num_boxes
   LOOP

   INPUT prompt "polygon susceptibiliti (emu) --> ": sus
   INPUT prompt "declination of remanent mag (deg) --> ": rdec
   INPUT prompt "inclination of remanent mag (deg) --> ": rinc
   INPUT prompt "intensity of remanent mag (emu/cc) --> ": nrm
   INPUT prompt "elevation of polygon top (m) --> ": top
   INPUT prompt "elevation of polygon bottom (m) --> ": bottom
   DO while more #1
```

```
    INPUT #1: num_boxes, sus, rdec,rinc,nrm,top,bottom
    FOR i = 1 to num_boxes
      INPUT #1: box(i,6),box(i,5)
      IF box(i,6) > ymax then LET ymax = box(i,6)
      IF box(i,6) < ymin then LET ymin = box(i,6)
      IF box(i,5) > xmax then LET xmax = box(i,5)
      IF box(i,5) < xmin then LET xmin = box(i,5)

    NEXT i
  LOOP
  MAT oldbox = box
  MAT box = 0

  RESET #1: end


  LET diffx = xmax-xmin
  LET diffy = ymax-ymin
  LET delx = diffx*.01
  LET dely = diffy * .01

  IF diffy > diffx then
    LET xmax = xmax + diffy*.1
    LET xmin = xmin - diffy*.1
    LET ymax = ymax + diffy*.1
    LET ymin = ymin - diffy*.1
  ELSE
    LET xmax = xmax + diffx*.1
    LET xmin = xmin - diffx*.1
    LET ymax = ymax + diffx*.1
    LET ymin = ymin - diffx*.1
  END IF


  LET r = (diffx + diffy)/10

  LET theta = -2*pi/num_boxes
```

```
•
•     LET xcenter = xmin + diffx/2
•     LET ycenter = ymin + diffy/2
•
•     LET theta1 = theta
•     FOR i = 1 to num_boxes
•       LET box(i,5) = r*cos(theta1)+xcenter
•       LET box(i,6) = r*sin(theta1)+ycenter
•       LET theta1 = theta1 + theta
•     NEXT i
•
•     LET exit(1) = xmin+ diffx*.005
•     LET exit(2) = xmin + diffx* .06
•     LET exit(3) = ymin + diffy*.005
•     LET exit(4) = ymin + diffy* .06
•
•     FOR i = 1 to num_boxes
•       LET box(i,1) = box(i,5)-delx
•       LET box(i,2) = box(i,5)+delx
•       LET box(i,3) = box(i,6)-dely
•       LET box(i,4) = box(i,6)+dely
•     NEXT i
•
•
•  CASE 2
•
•     PRINT "Name of polygon file"
•     PRINT "this file will be overprinted"
•     INPUT file$
•     OPEN #1: name file$
•
•
•     DO while more #1
•       INPUT #1: num_boxes, sus, rdec,rinc,nrm,top,bottom
•       FOR i = 1 to num_boxes
•         INPUT #1: box(i,6),box(i,5)
•         IF box(i,6) > ymax then LET ymax = box(i,6)
```

```
•         IF box(i,6) < ymin then LET ymin = box(i,6)
•         IF box(i,5) > xmax then LET xmax = box(i,5)
•         IF box(i,5) < xmin then LET xmin = box(i,5)
•
•       NEXT i
•     LOOP
•
•     ERASE #1
•
•
•
•     LET diffx = xmax-xmin
•     LET diffy = ymax-ymin
•     LET delx = diffx*.01
•     LET dely = diffy * .01
•
•     IF diffy > diffx then
•       LET xmax = xmax + diffy*.1
•       LET xmin = xmin - diffy*.1
•       LET ymax = ymax + diffy*.1
•       LET ymin = ymin - diffy*.1
•     ELSE
•       LET xmax = xmax + diffx*.1
•       LET xmin = xmin - diffx*.1
•       LET ymax = ymax + diffx*.1
•       LET ymin = ymin - diffx*.1
•     END IF
•
•     LET exit(1) = xmin+ diffx*.005
•     LET exit(2) = xmin + diffx* .06
•     LET exit(3) = ymin + diffy*.005
•     LET exit(4) = ymin + diffy* .06
•
•     FOR i = 1 to num_boxes
•       LET box(i,1) = box(i,5)-delx
•       LET box(i,2) = box(i,5)+delx
•       LET box(i,3) = box(i,6)-dely
```

```
      LET box(i,4) = box(i,6)+dely
    NEXT i

    MAT oldbox = box

END SELECT

CLEAR

OPEN #44: screen .2,1,.15,1
SET WINDOW xmin,xmax,ymin,ymax


DRAW exit_box(exit)
DRAW line_dat(num_dats,delx,dely,pt)
DRAW polygons(num_boxes,box)
DO
  GET MOUSE x,y,state


  IF  x< exit(2) and y<exit(4) then
    IF state = 2 then
      EXIT DO
    END IF
  END IF

  IF state = 1 then

    FOR i = 1 to num_boxes
      LET x1 = box(i,1)
      LET x2 = box(i,2)
      LET y1 = box(i,3)
      LET y2 = box(i,4)

      IF x>x1 and x<x2 then
        IF y>y1 and y< y2 then
```

```
            DO
              GET MOUSE x,y,state
              IF state = 3 then
                CLEAR
                LET x1 = x-delx
                LET x2 = x + delx
                LET y1 = y -dely
                LET y2 = y + dely

                EXIT DO
              END IF


            LOOP

            LET box(i,1) = x1
            LET box(i,2) = x2
            LET box(i,3) = y1
            LET box(i,4) = y2
            LET box(i,5) = x1+delx
            LET box(i,6) = y1+dely

            DRAW line_dat(num_dats,delx,dely,pt)
            SET COLOR "blue"
            DRAW polygons(num_boxes, oldbox)
            SET COLOR "black"
            DRAW polygons(num_boxes,box)
            DRAW exit_box(exit)
          END IF
        END IF
      NEXT i
    END IF
  LOOP

  PRINT #1: num_boxes;",";sus;",";rdec;",";rinc;",";nrm;",";top;",";bottom
  FOR i = 1 to num_boxes
    PRINT #1: box(i,6),",";box(i,5)    ! north then east
```

- NEXT i
-
- END

These three model geometries correspond to volcanological models for the origin of NE Little Cone. In the simple conduit model, it is assumed that the cone consists of scoria and blocks that carry low bulk remanent magnetization. Of course, individual blocks of basalt carry high remanent magnetization. However, if the blocks and scoria are cooled below their Curie-blocking temperatures when deposited, vectors of remanent magnetization will not be consistently oriented between blocks, cummulatively leading to a low bulk remanent magnetization for the cone. Randomized vectors of magnetization of blocks and other pyroclasts will occur in pyroclastic eruptions in which the column height is high enough, or the accumulation rate is low enough, so that welding or reomorphism of pyroclasts does not occur. The central conduit is assumed to consist of massive basalt. A 20-m-diameter conduit is used. Even with this large diameter, the resulting magnetic anomaly is small and has a short wavelength (Figure 6a) relative to the observed anomaly (Figures 5a and 5b).

In contrast, uniformly high bulk magnetization of the cone produces a large amplitude long-wavelength anomaly (Figure7a). This calculated anomaly is similar in wavelength but larger in amplitude than the observed anomaly (Figures 5a and 5b). In this model, a thin ($\approx$1 m) mantle of unconsolidated material covers a massive cone interior. Such a geometry is produced if the cone consists of welded pyroclasts or agglutinated spatter, deposited at temperatures above the Curie–blocking temperatures for this basalt.

The third model (Figure s8a and 8b) consists of a thick mantle of pyroclastic material that constitutes much of the volume of the cone. A small, 10-m-high and 30-m-diameter spatter mound carries a high bulk remanent magnetization at the center of the cone. This spatter mound overlies a lava flow that extends outward radially under the weakly magnetized cone. The resulting magnetic map (Figure 8a) is more complicated than the others, but does produce an anomaly that is similar in wavelength and amplitude to the observed anomaly (Figure 5a and 5b).

FIGURE 6. Magnetic map calculated for a single magnetized vertical conduit centered on NE Little Cone on a 20 m grid (a). The model geometry consists of a single vertical-sided polygon extending to infinite depth. Sensor height is shown by the mesh and conforms to the

local topography (b). This model produces a magnetic anomaly that is similar in amplitude, but shorter in wavelength than the observed anomaly (Figure 5a and 5b).

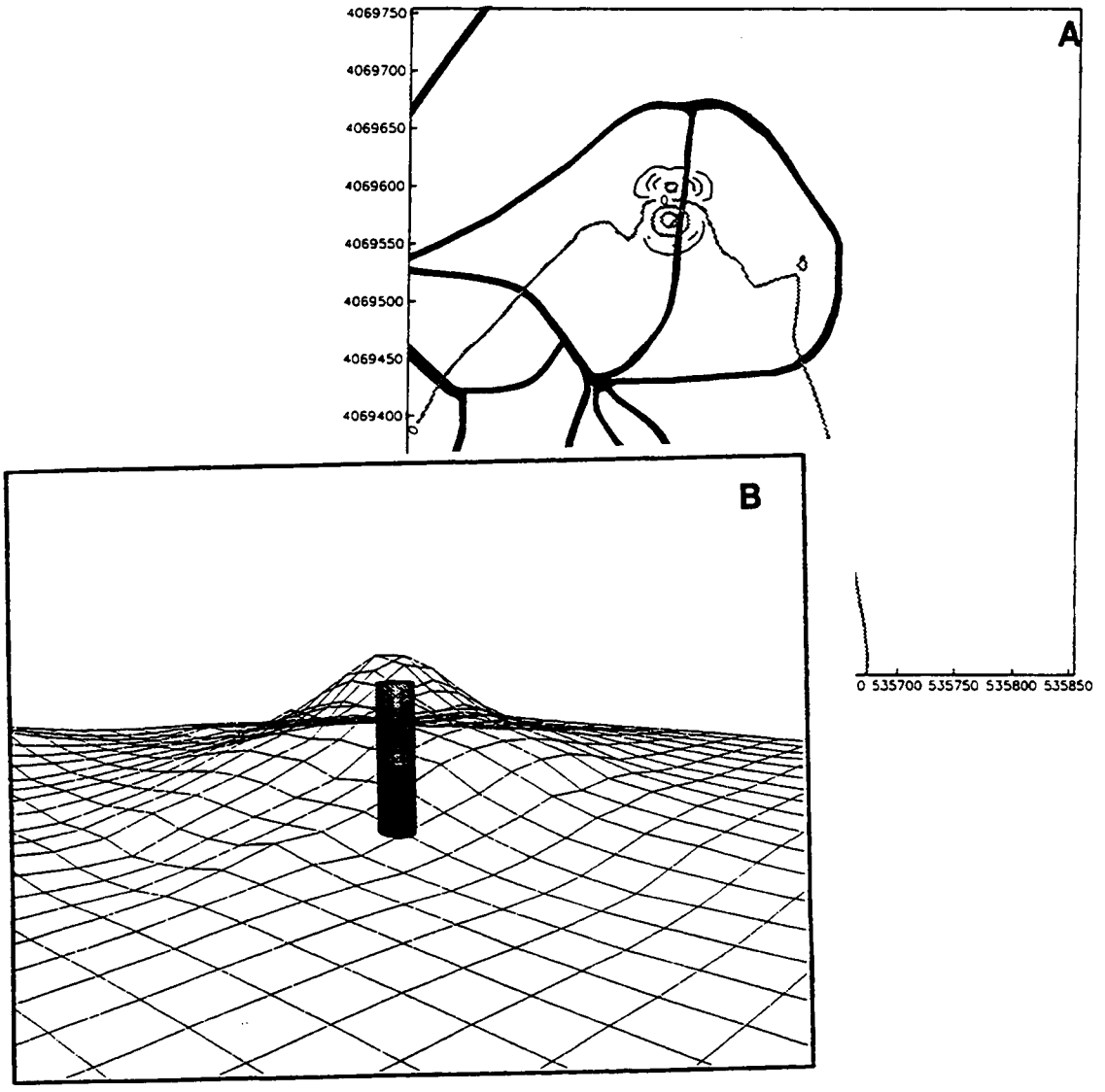

FIGURE 7. Magnetic map calculated on a 20 m grid assuming that NE Little Cone is a uniformly magnetized body, carrying a high remanent magnetization except for a thin carapace of surface material (a). The model geometry consists of multiple vertical sided polygons

that follow topography. Sensor height is shown by the mesh and conforms to topography (b).

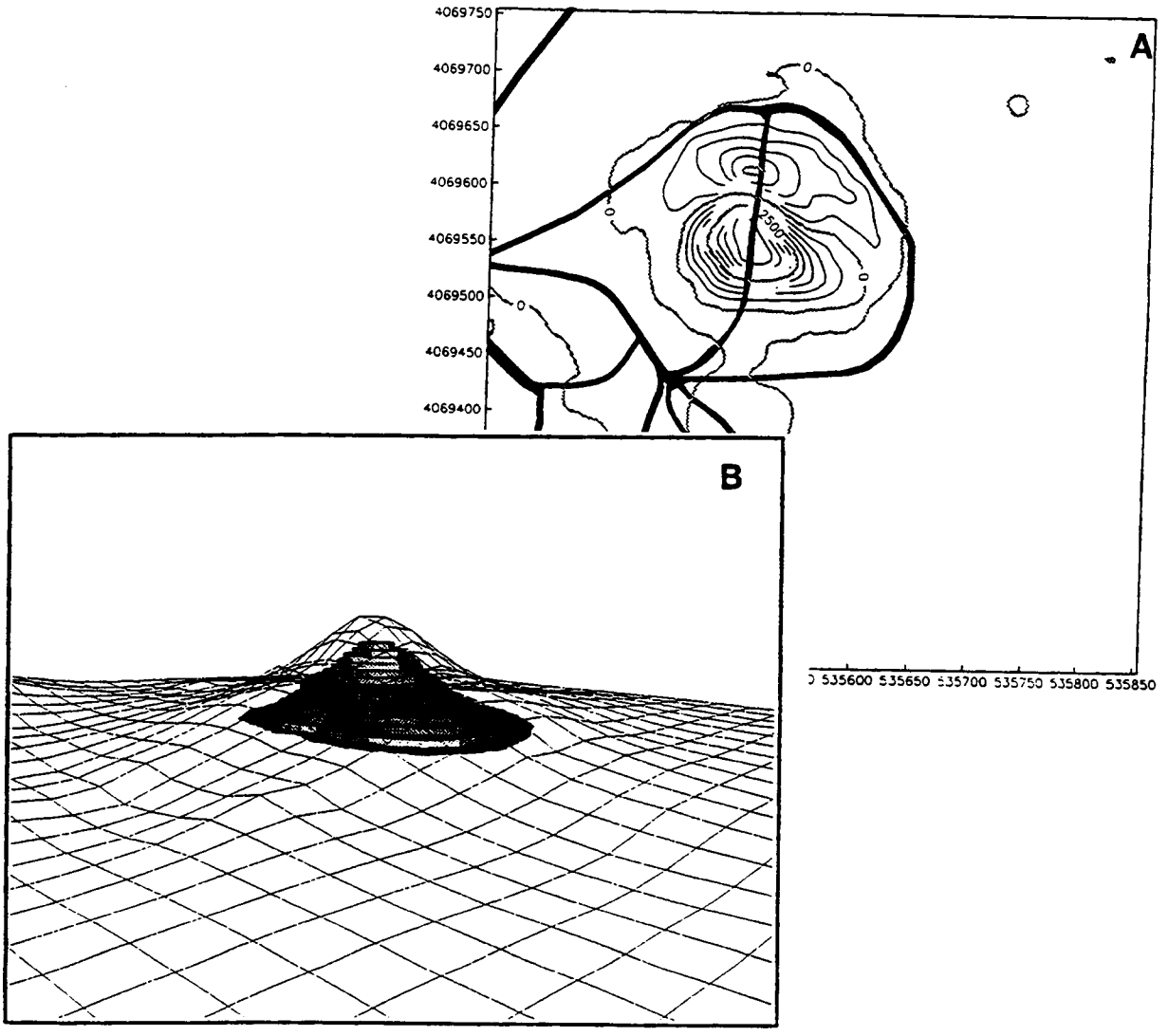

FIGURE 8. Magnetic map calculated on a 20 m grid assuming that NE Little Cone consists of a small, early-formed spatter mound that carries a high remanent magnetization and a thick carapace of unconsolidated rock that carries a low remanent magnetization (a). The model geometry consists of multiple vertical-sided polygons of varying thickness. Sensor height is shown by the mesh and conforms to topography (b).

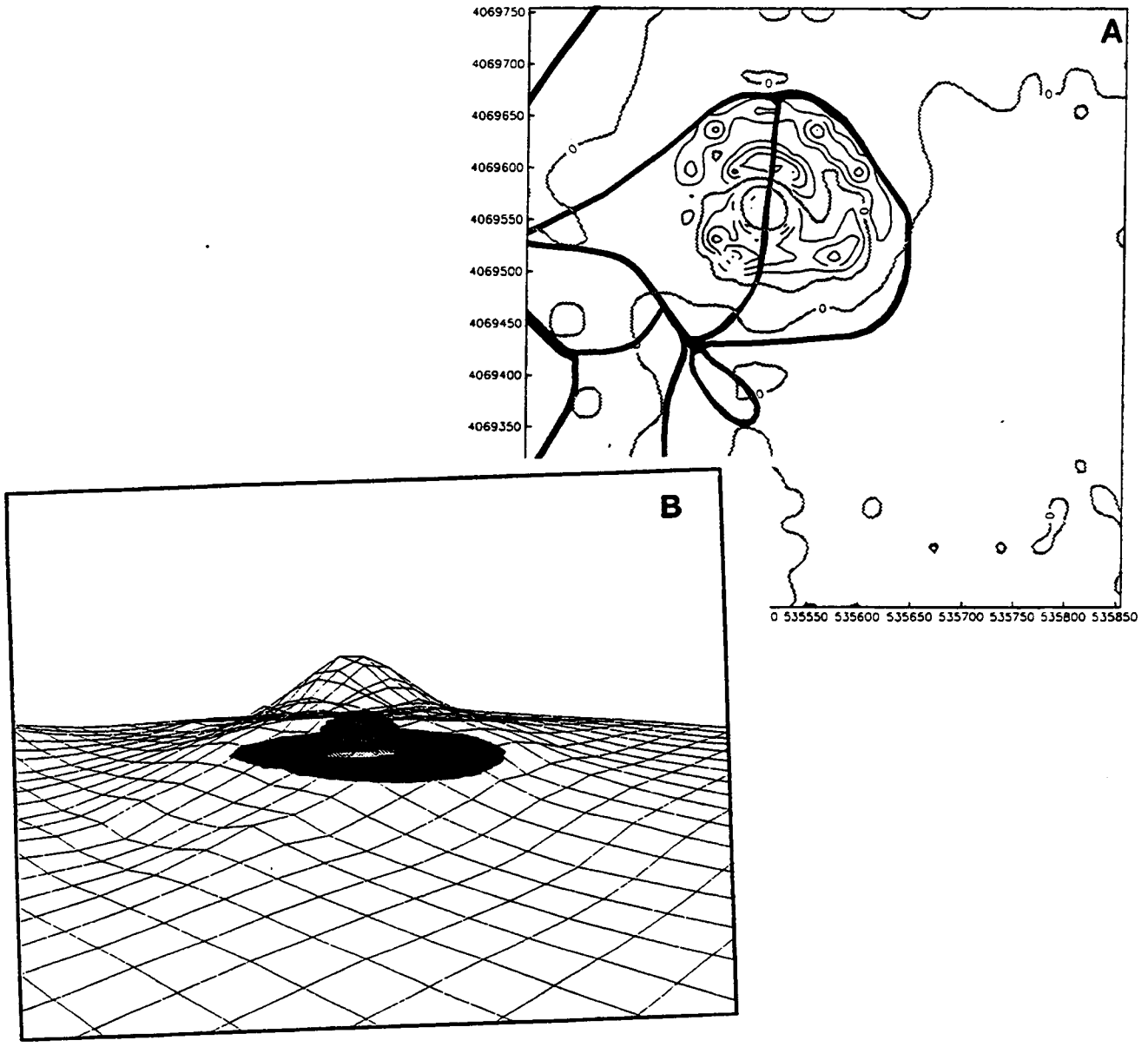

Based on these calculated magnetic maps, it is concluded that NE Little Cone consists of highly magnetized rock beneath a mantle of weakly magnetized rock. High bulk remanent magnetization of the cone indicates the presence of agglutinate spatter or welded scoria deposited above the Curie-point blocking temperature, beneath a mantle of unconsolidated pyroclastic material that is likely less than 5 m thick. Such spatter mounds are common and often form early in basaltic cinder cone eruptions (e.g., Tokerev, 1983). The magnetic anomalies associated with the NE Little Cone are not consistent with intrusion geometries, such as a large central conduit. Magnetic anomalies associated with intrusions that fed the NE Little cone are masked by anomalies produced by the cone itself.

3.6 Extent of lava flows

Possibly the most surprising result of the ground magnetic surveys is recognition of the extent of the lava flow field surrounding the Little Cones. Lava flows do not crop out around the Little Cones except south of SW Little Cone, yet it is clear from the extent of short wavelength anomalies that lava flows are present around both cones. Three lines of investigation help clarify the nature and distribution of flows in the area: (I) the high-resolution cesium vapor magnetometer survey made north of NE Little Cone; (ii) models of these high-resolution magnetic data; and (iii) a filtered map that shows the distribution of short wavelength, large amplitude anomalies, constructed using the low-resolution proton-precession magnetometer data.

The character of the lava flow and its margin is best elucidated by the high resolution survey north of NE Little Cone (Figure 9a and 9b). This survey shows the complex surface of the lava flow in detail. The high-resolution magnetic map (Figure 9a) was actually made in two surveys. The first survey consisted of 43 N-S trending lines spaced at 10 m intervals. The second survey consisted of E-W trending lines spaced at 20 m interval. Even very short wavelength anomalies correlate between these surveys, indicating a high degree of precision in the locations, amplitudes, and wavelengths of anomalies was achieved.

FIGURE 9. (a)High-resolution, cesium-vapor magnetic survey north of NE Little Cone, Survey grid is shown in Figure 2–3. Map is contoured using a 200 nT interval and colored using a variable area shading algorithm. (b) Shaded–relief map of the high-resolution magnetic survey north of NE Little Cone. Magnetic anomalies are illuminated from the north by a

light source 45° above the horizon. E-W trending lobate structures on the lava flow surface are enhanced.

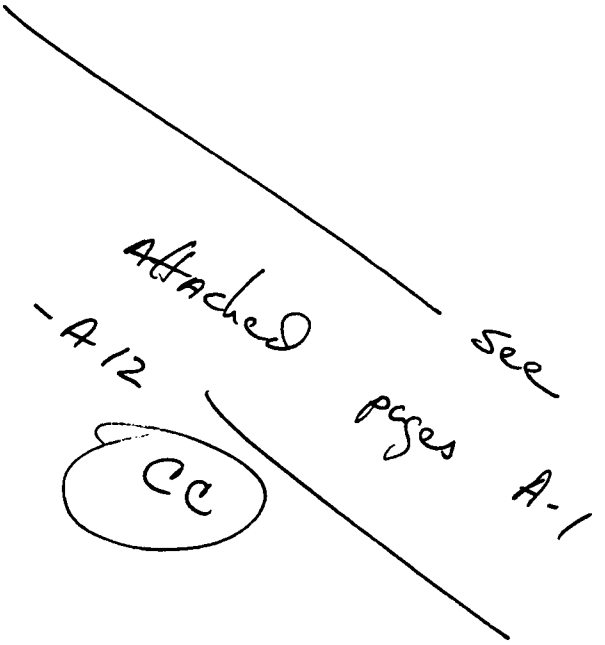

The most prominent anomaly on this map (Figure 9a) is a +500 nT anomaly that forms an arcuate band across the survey area. The wavelength of this anomaly is approximately 100 m. The anomaly separates the magnetically quiet alluvium to the north from the complex, large–amplitude, short–wavelength anomalies produced by the shallow lava flow surface in the southern portion of the map area. This type of long–wavelength, positive, total magnetic field anomaly is exactly what is expected a the northern margin of a thin, reversely polarized, horizontal sheet, such as lava flow.

Note: Additonal maps showing the reproducibility of anomalies are shown on the following pages Labelled A1 - A12. CC.

2.86 m to Pixels

Grd Pins

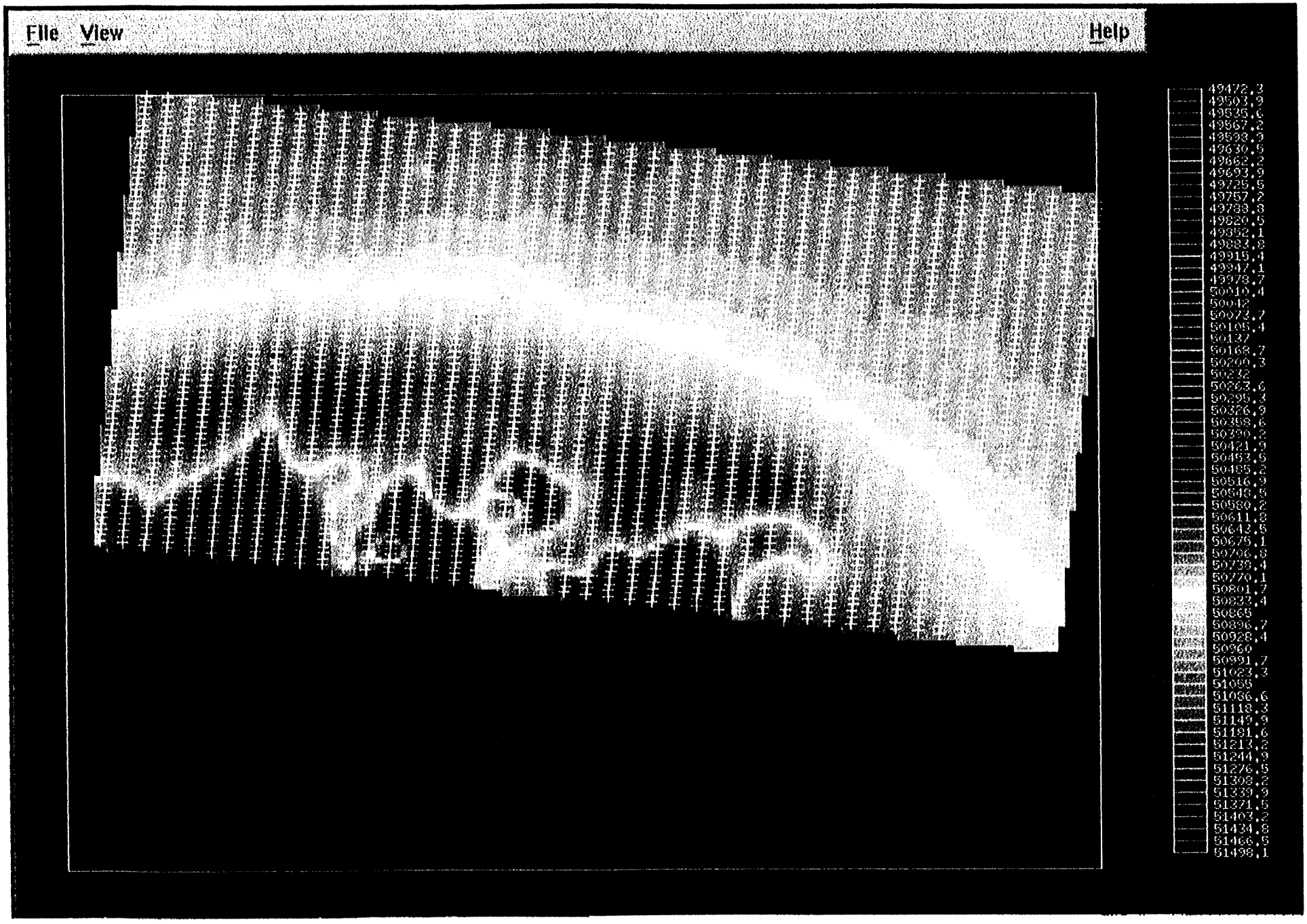

R. Martin

A-1 c2

2.86 MBR PIXELS

GRADIENTS

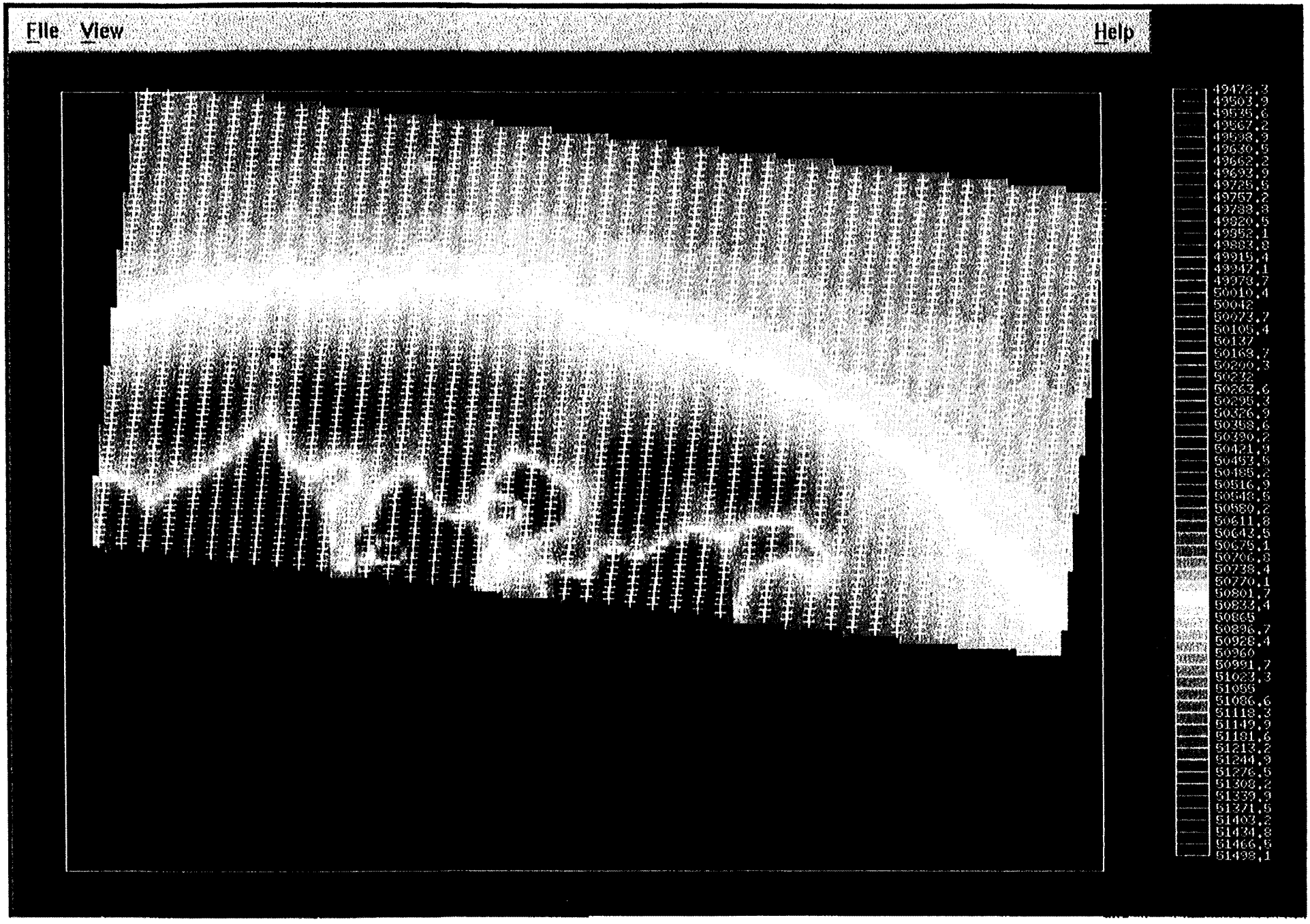

42 - 22

R. Marton

2.86 MR Peaks

GRAPHS

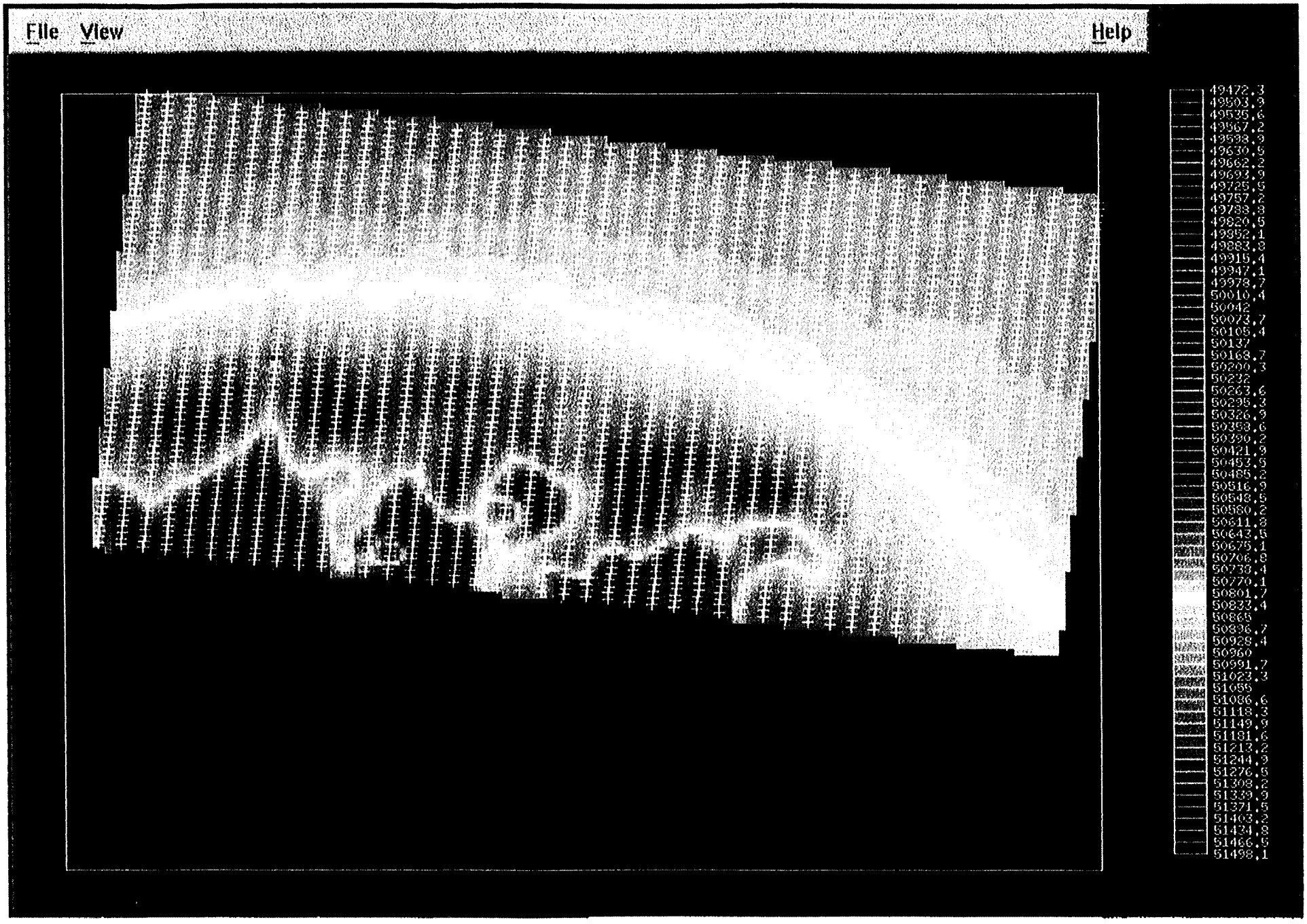

R. Marston

A3 - CC

1.86 MPa plane

GRDØ3EW

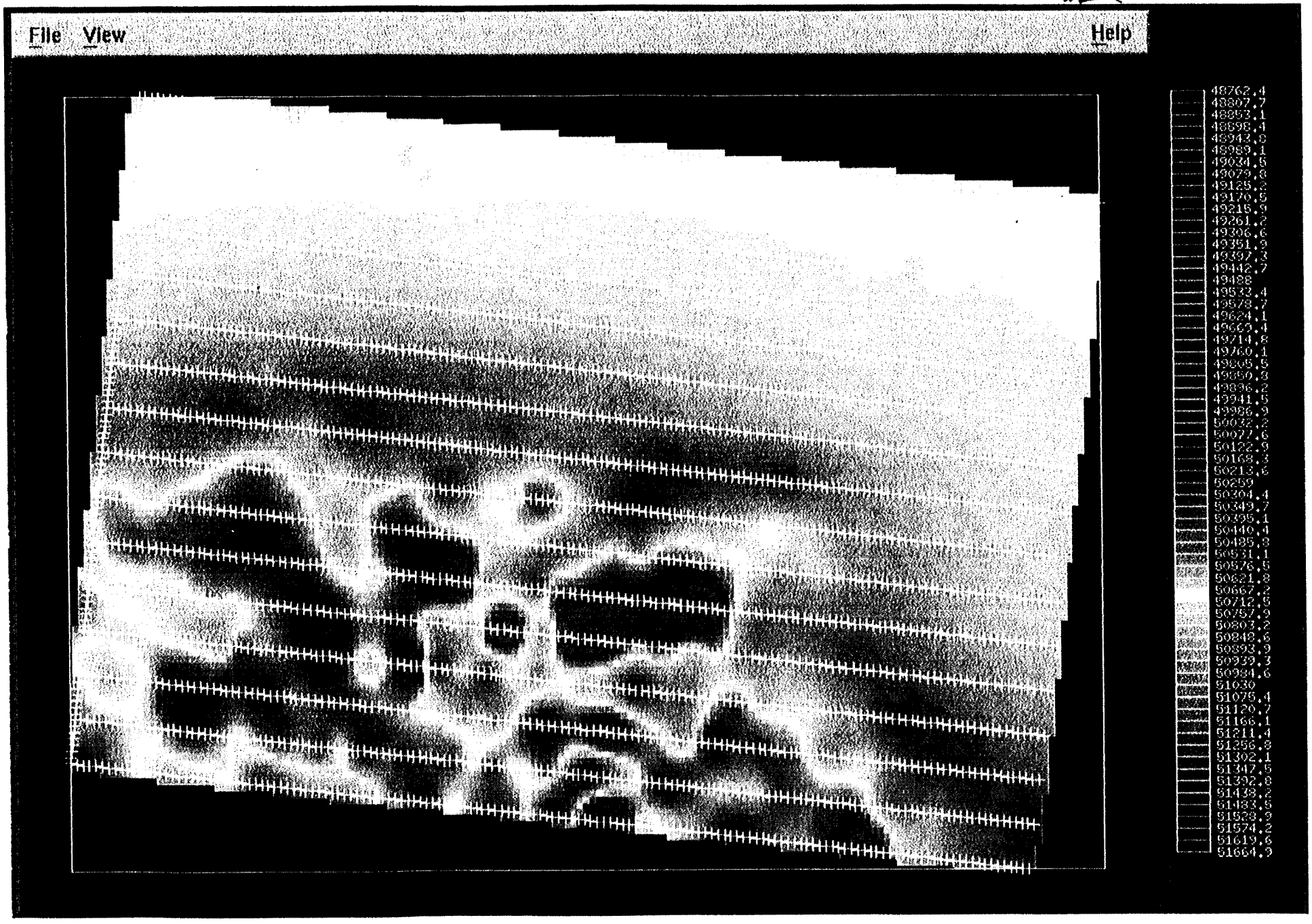

R. Marten

A4-02

GRID1_Ø2MS

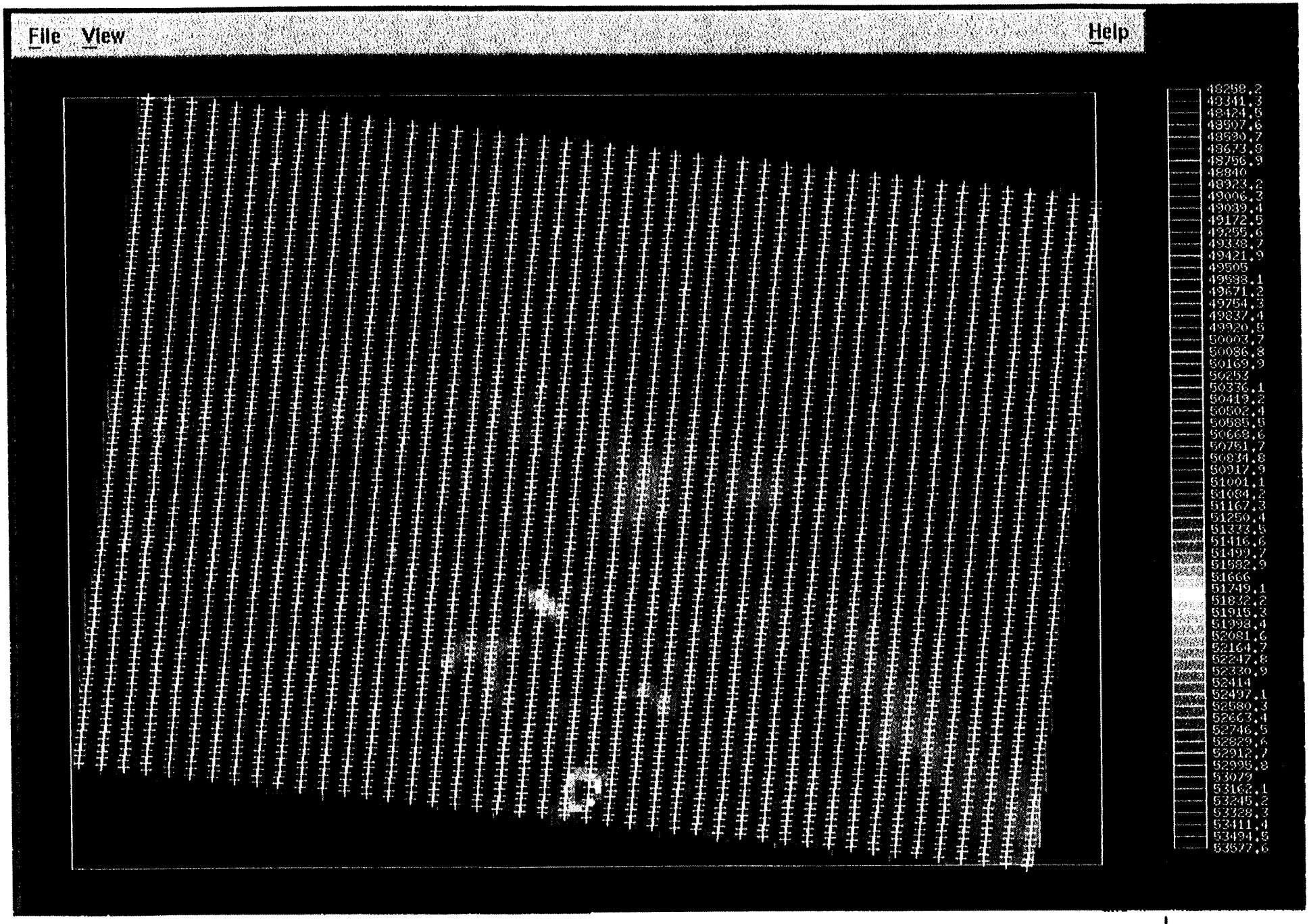

R. Marston

A5 cc

2.00 MIC (IXES)

GRDOI_OZNS

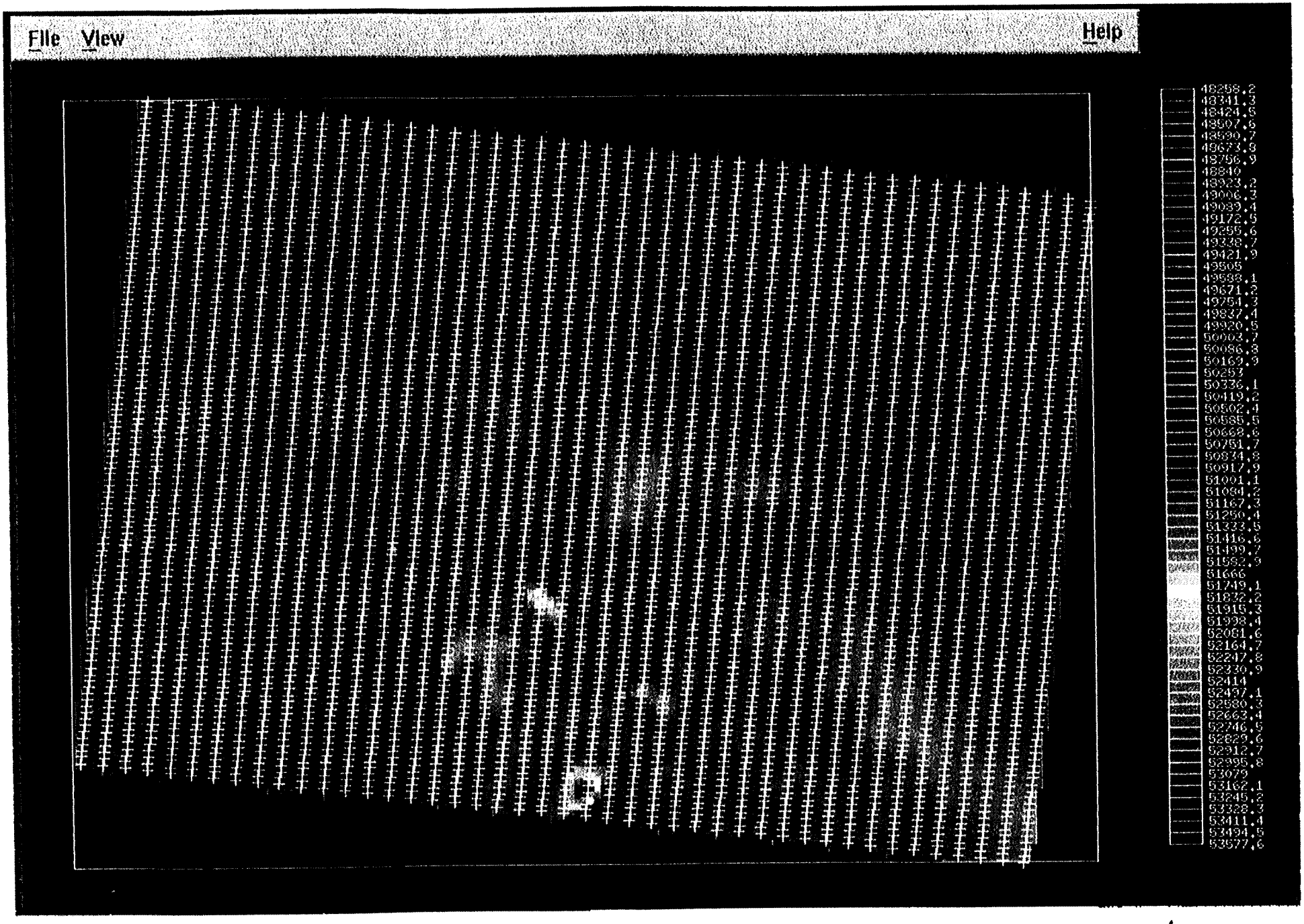

R. Morton

A6 - CC

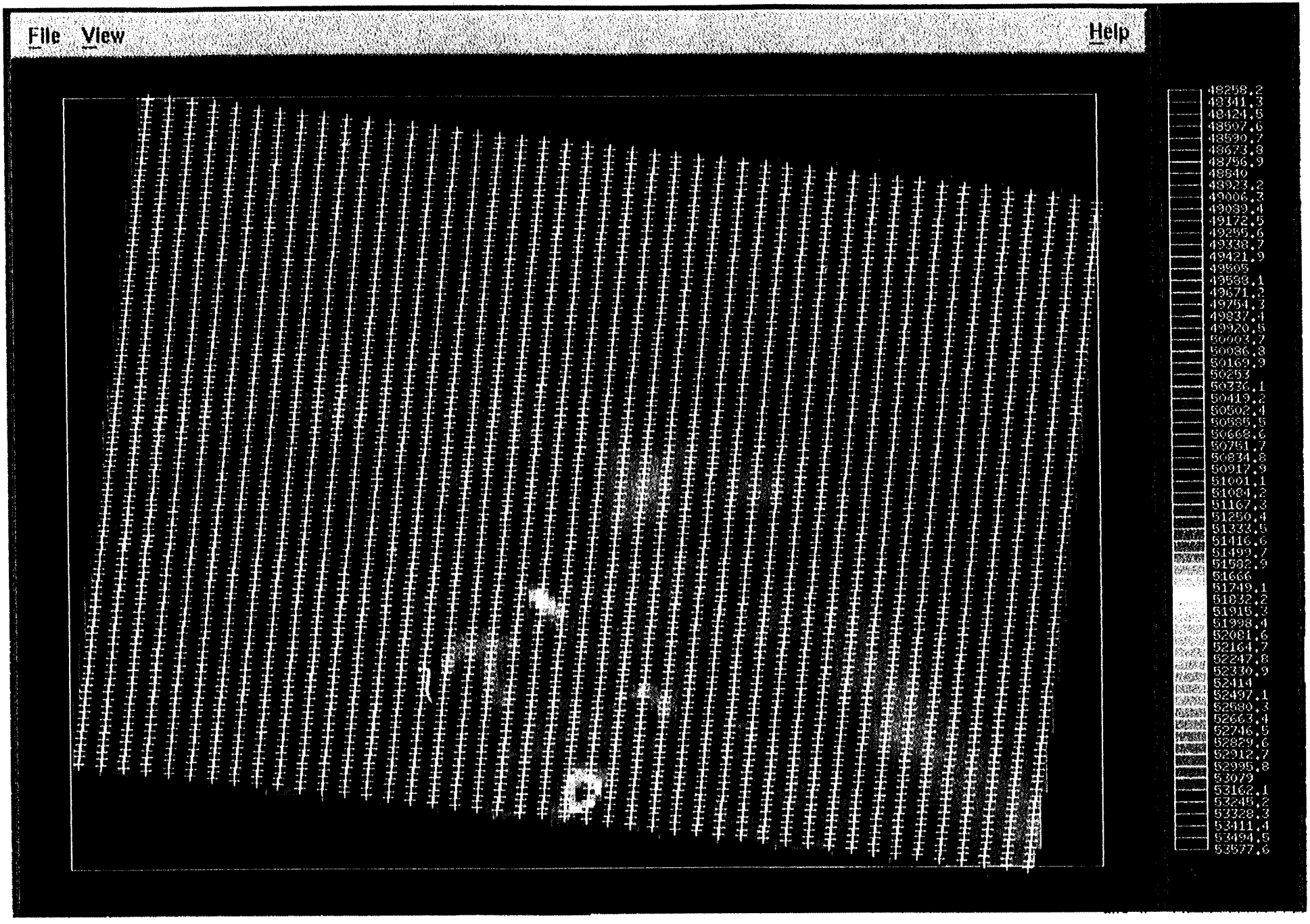
File View
Help
48258.2
48341.3
48424.5
48507.6
48590.7
48673.8
48756.9
48840
48923.2
49006.3
49089.4
49172.5
49255.6
49338.7
49421.9
49505
49588.1
49671.2
49754.3
49837.4
49920.5
50003.7
50086.8
50169.9
50253
50336.1
50419.2
50502.4
50585.5
50668.6
50751.7
50834.8
50917.9
51001.1
51084.2
51167.3
51250.4
51333.5
51416.6
51499.7
51582.9
51666
51749.1
51832.2
51915.3
51998.4
52081.6
52164.7
52247.8
52330.9
52414
52497.1
52580.3
52663.4
52746.5
52829.6
52912.7
52995.8
53079
53162.1
53245.2
53328.3
53411.4
53494.5
53577.6

R. Morton

2.86 mb pixels.

GRID SEW

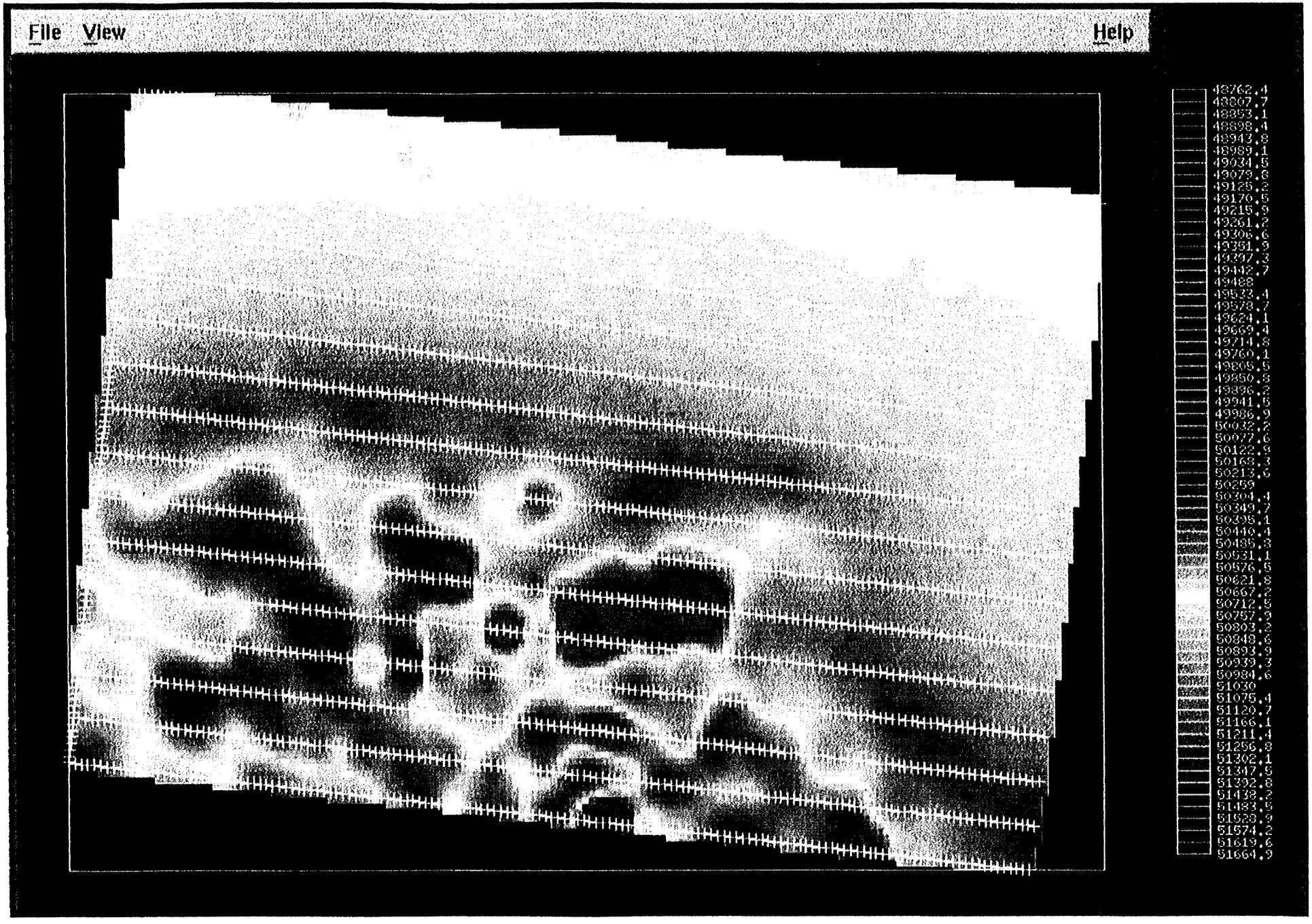

R. Martin

A8 - 88

2.86 mm pixels

Grd Ø2 NS

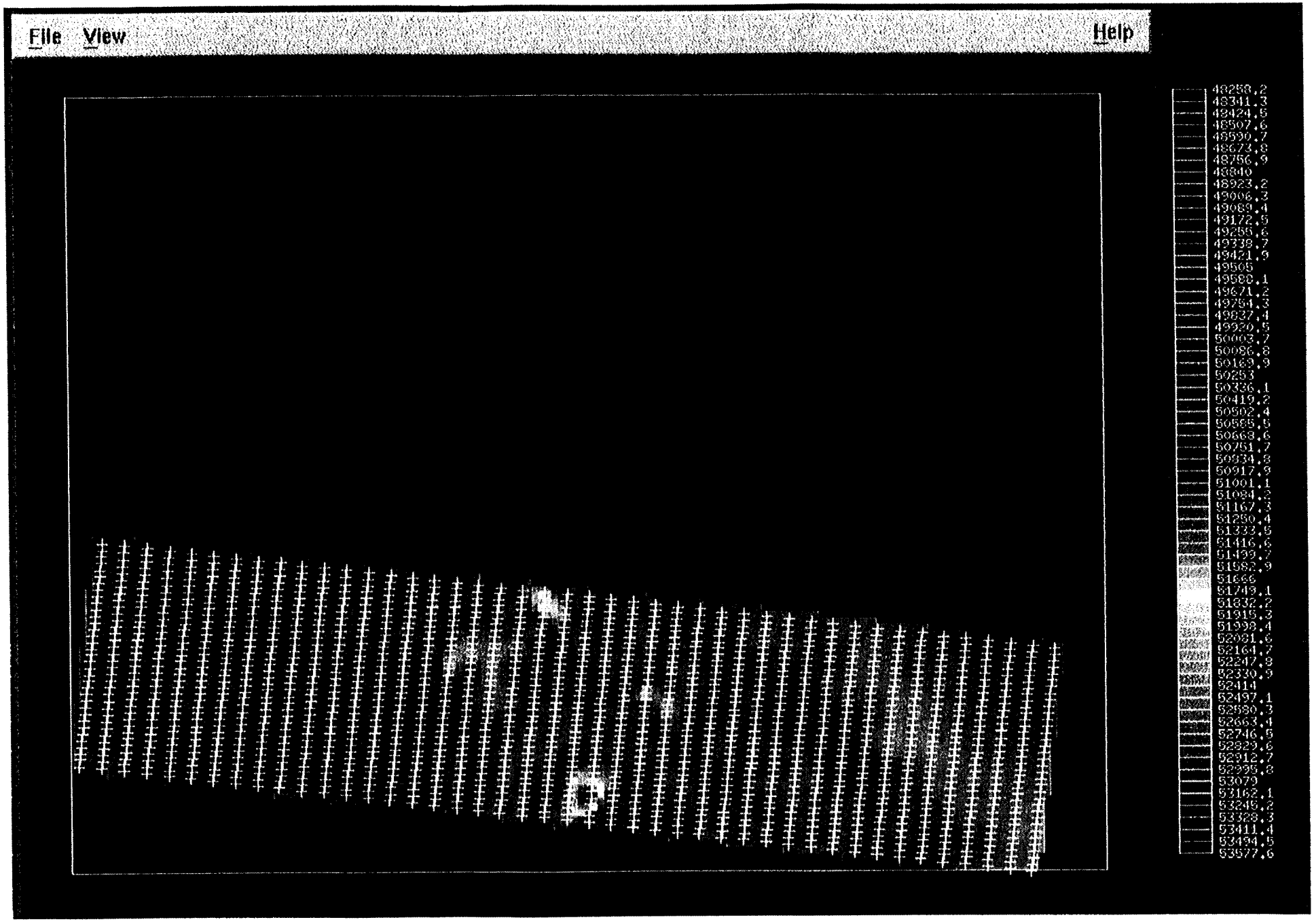

R. Martin

49 cc

2.86 atm pressure

GRIDLINES

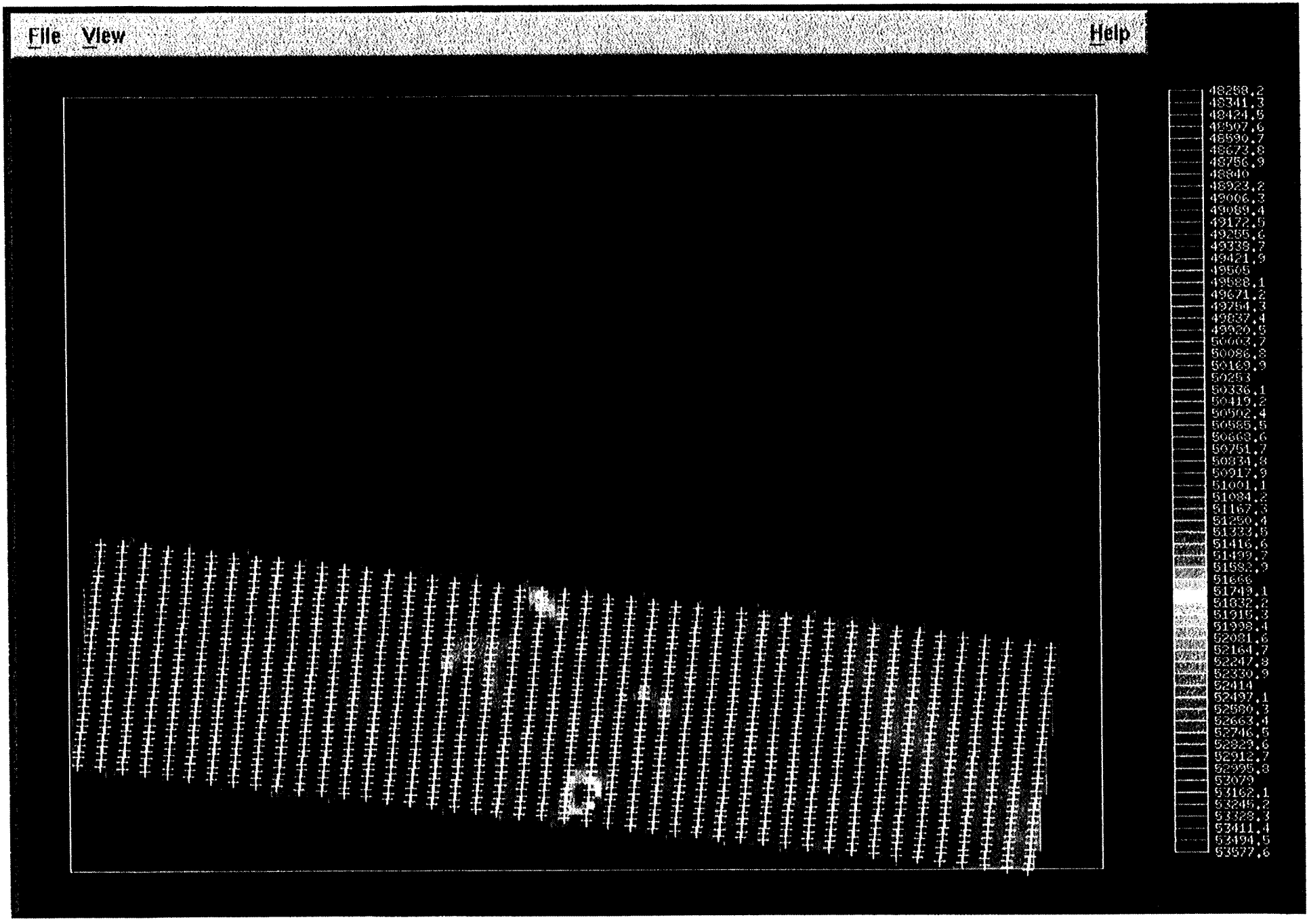

A16 - CC

R. MARTIN

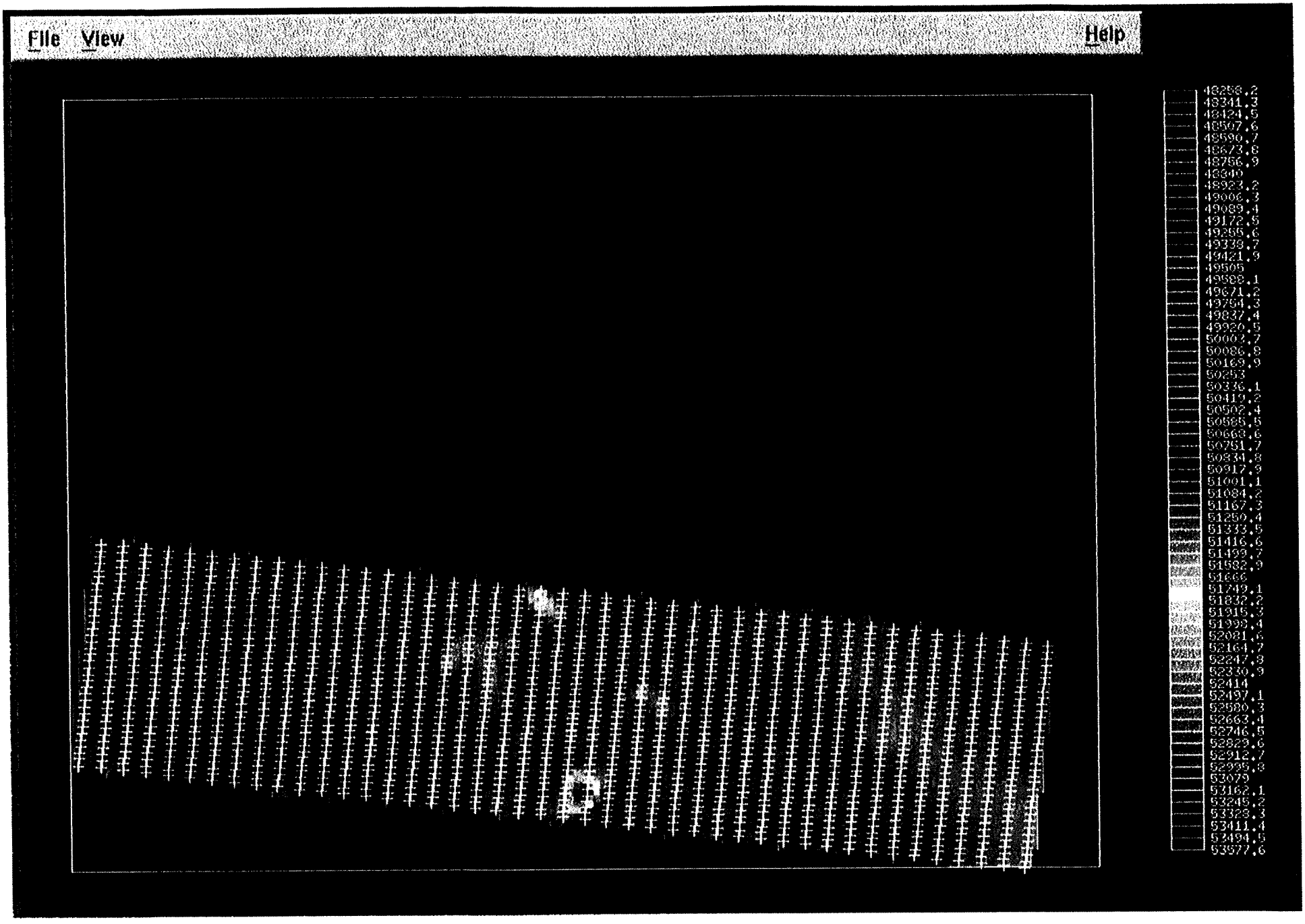

R. Martin

A11-CC

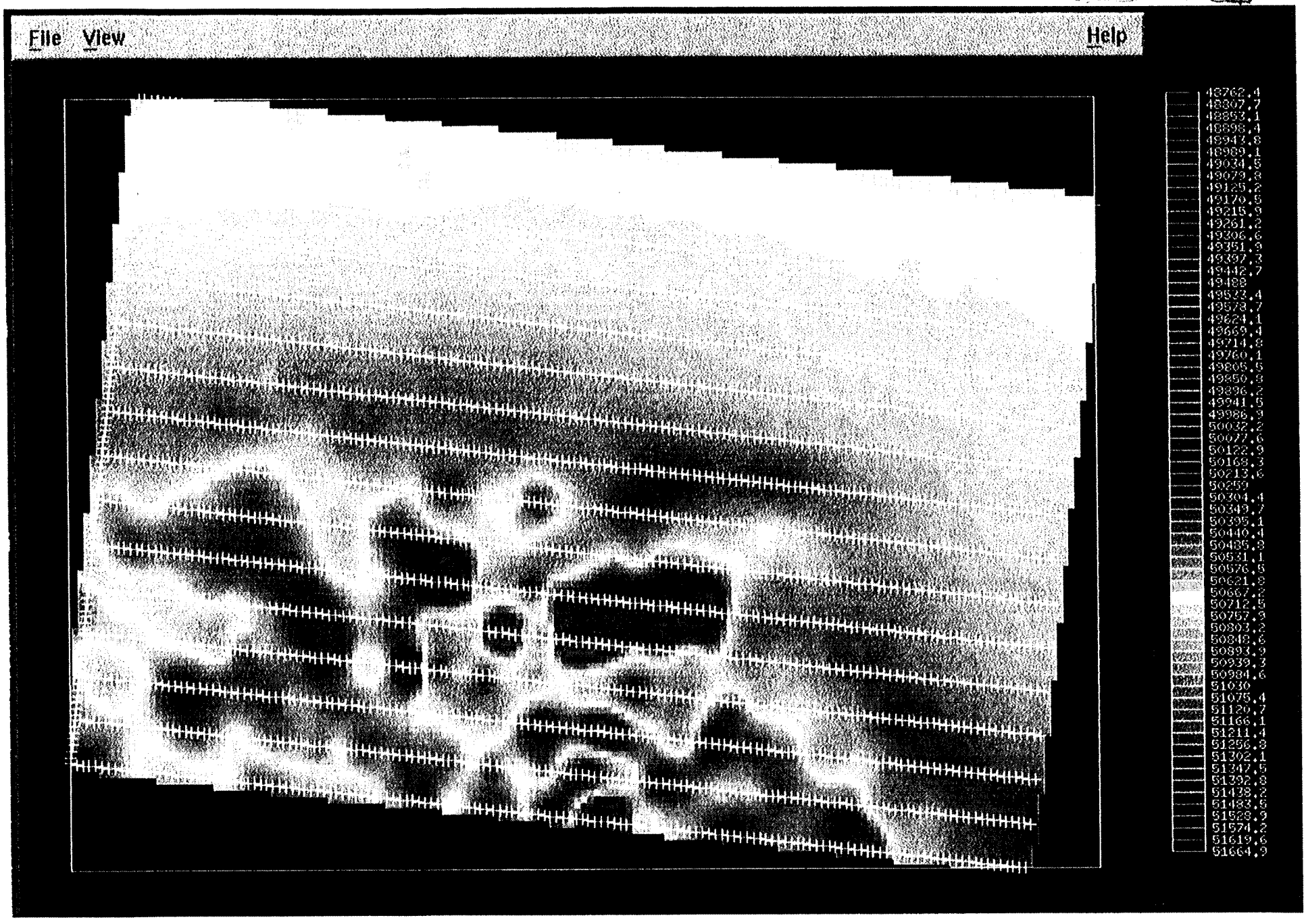

R. Marston

A12 - cc

Additional perspective on the complex anomalies mapped on the lava flow surface is provided by viewing the total magnetic field data as a shaded relief map, illuminated from a sun-angle of 45° above the horizon and from the north (Figure 9b). This sun-angle enhances E-W trending features on the flow surface. Although the anomalies produced by the rubbly flow top are complex, the shaded relief map suggests the lobate character of anomalies on the flow top. Lobate flow tops are common on cinder cones and are produced when successive flows produce a compound flow-field. In this case, the lobate character of the magnetic anomalies suggests flow from the NE Little Cone vent.

Data collected along four lines using the cesium-vapor magnetometer were modeled using a three-dimensional algorithm first developed by Plouff (1976). Figure 10 shows the positions of these lines within the survey area and the magnetic profiles are shown in Figures 11-14. The lava flow was modeled as two vertical-sided polygons that extend well beyond the map area to the south and west. The polygons are assumed to carry remanent magnetizations similar to those measured by Champion (1991). In all the models, the inclination and declination of the remanent magnetization vectors were held constant at I = –67° and D = 177°. Champion (1991) determined the magnitude of remanent magnetization, J, to be between 7.5 and 15 Am-1 for Crater Flat basalts. The models shown here use J = 20 Am-1. Using J = 20 Am-1 the modeled lava flows tend to be thinner than is the case using smaller values of J. However, it was found that the steep gradients observed on the map and profiles is better modeled using a higher remanent magnetization. Certainly, J = 20 Am-1 is reasonable, given the range of basaltic rock magnetic properties observed in Crater Flat. The lava flows are assumed have a low susceptibility compared to remanent magnetization. In this case, a susceptibility of 0.063 SI (0.005 emu) was used.

FIGURE 10. Model geometries for the high-resolution survey north of NE Little Cone. Two polygons are used to model the lava flow; each is 5 m thick and the tops of the polygons are at depths of 15 and 20 m beneath the surface. The two polygons extend far beyond the map area to the west and south. Four survey lines were modeled in detail — labelled 10–

40. Line 20 was modeled using additional polygons shown as solid boxes. Magnetic data are contoured using a 200 nT contour interval.

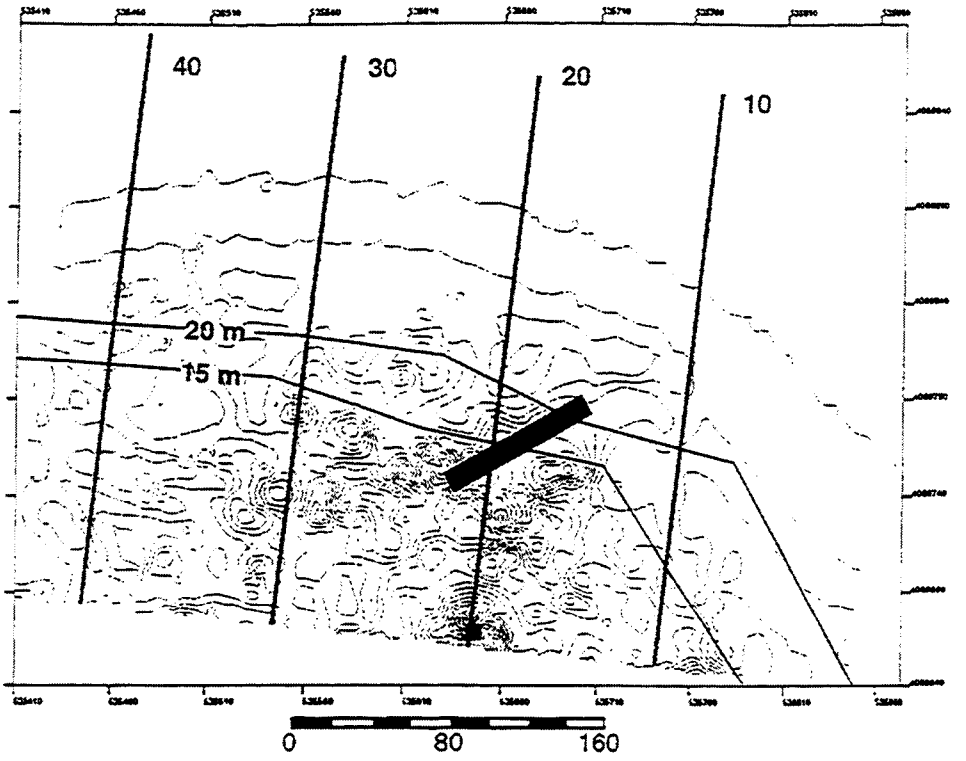

FIGURE 11. Observed magnetic anomaly along line 10 is shown by solid squares and calculated magnetic anomaly is shown by open circles. Distance is indicated from the southern end of the line and survey line trends NNE (Figure 10).

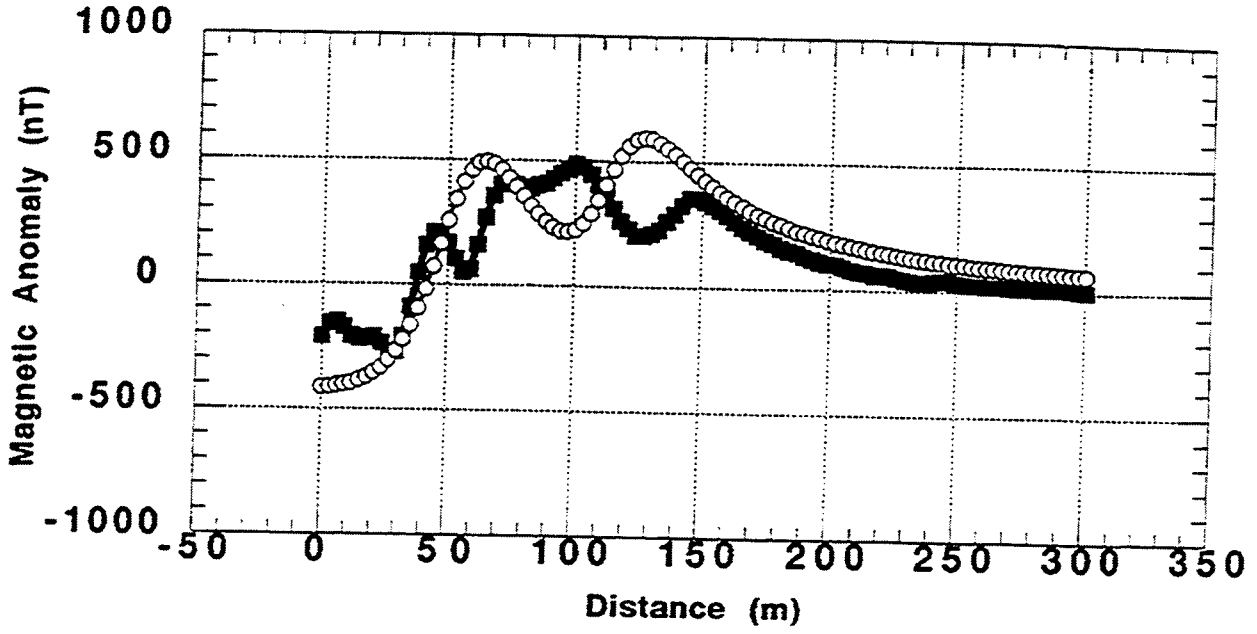

FIGURE 12. Observed magnetic anomaly along line 20 is shown by solid squares and calculated magnetic anomaly is shown by open circles. Distance is indicated from the southern end of the line and survey line trends NNE. The magnetic model includes both the flow

margin and two polygons representing magnetized rock beneath the flow and a smaller magnetized body on top of the flow (Figure 10).

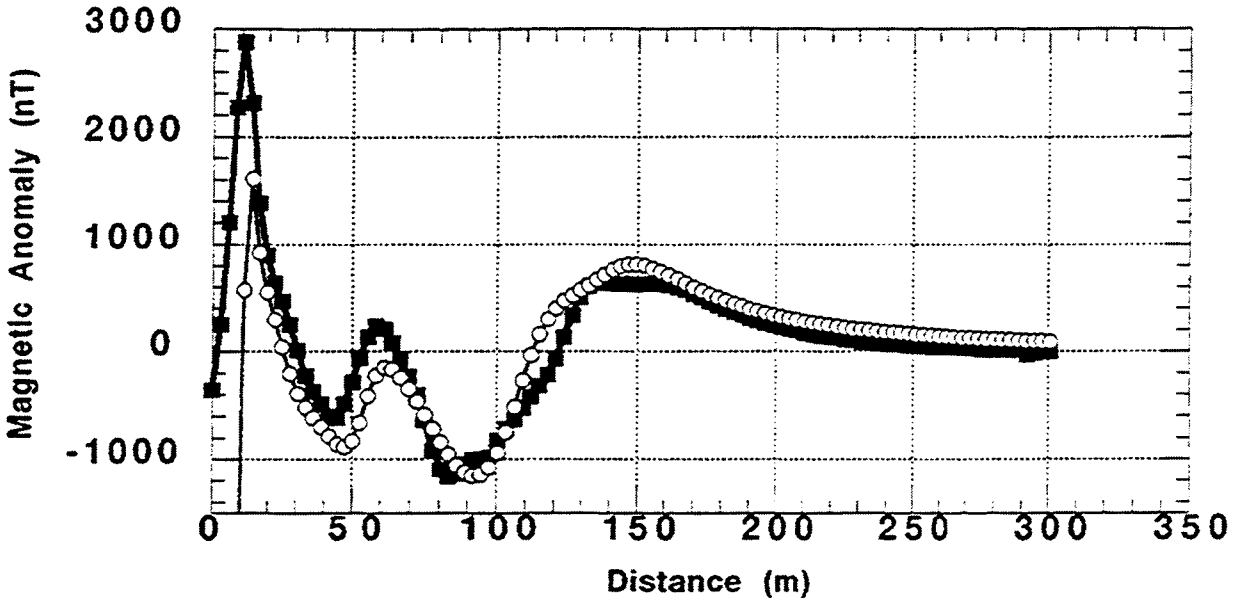

FIGURE 13. Observed magnetic anomaly along line 30 is shown by solid squares and calculated magnetic anomaly is shown by open circles. Distance is indicated from the southern end of the line and survey line trends NNE (Figure 10).

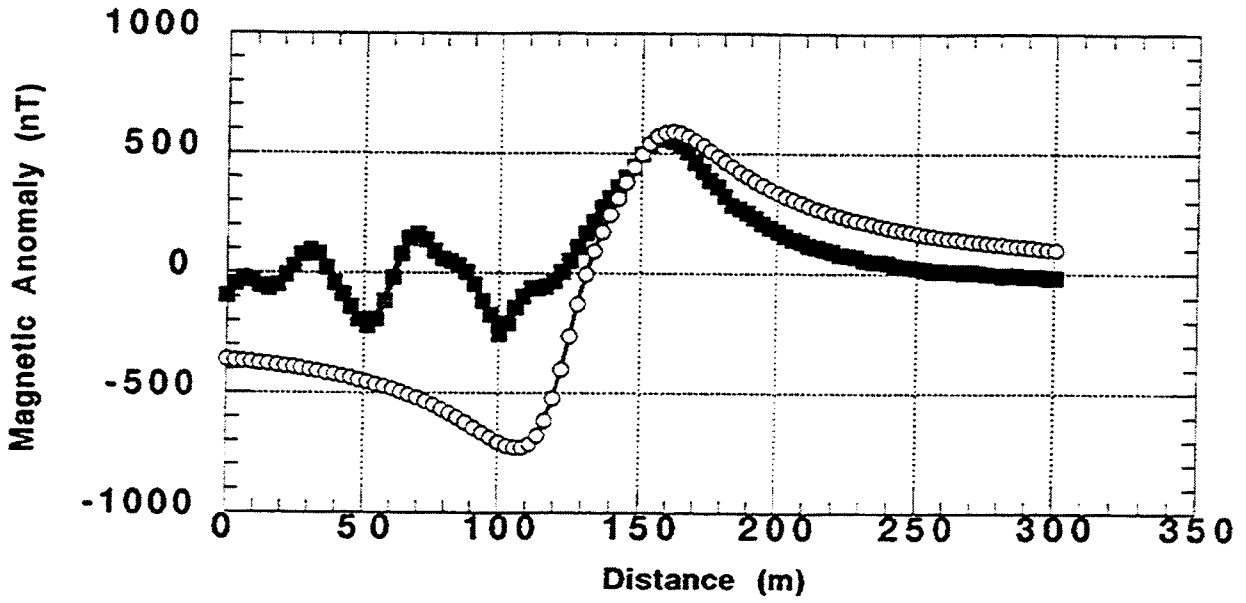

FIGURE 14. Observed magnetic anomaly along line 40 is shown by solid squares and calculated magnetic anomaly is shown by open circles. Distance is indicated from the southern end of the line and survey line trends NNE (Figure10).

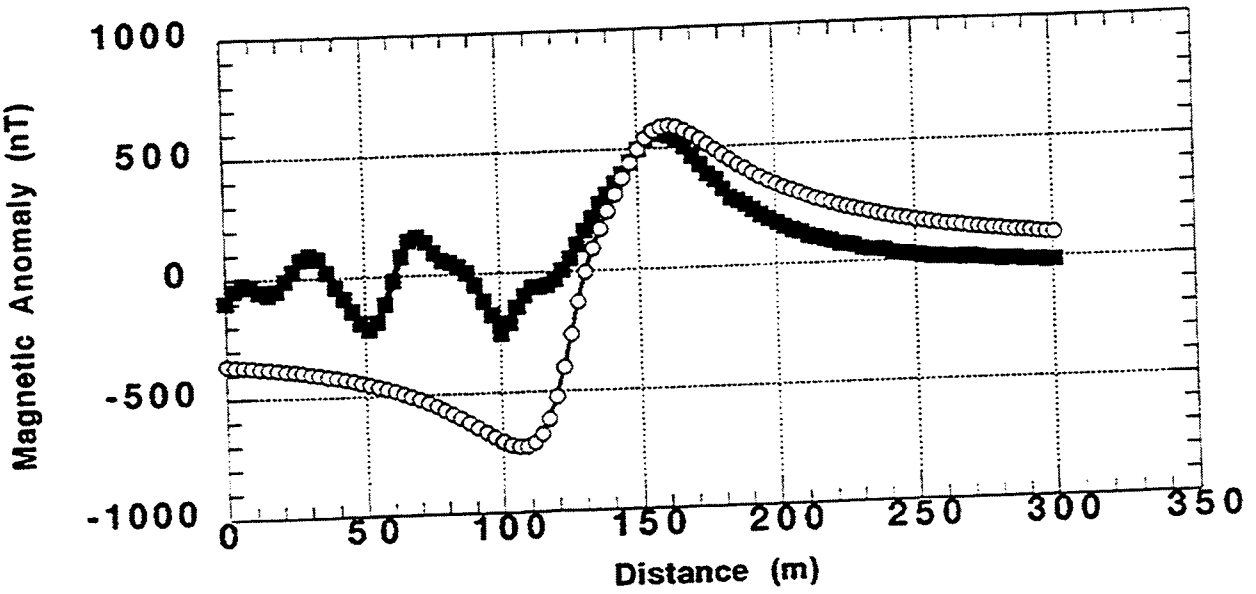

The modeled lava flow geometry is shown in map view in Figure 10 and in cross section in Figure15. The vertical-sided polygons are used to represent the indurated, massive flow interior. This part of the lava flow cooled in situ to produce a uniform vector of remanent magnetization. Blocky material caps the massive flow interior. This material represents the rubbly flow–top which formed as the exterior part of the flow cooled, solidified, and broke-up as the flow continued to move. Each block in this flow–top carries a remanent magnetization similar to that of the lava flow interior, locked in as the block cooled through its Curie temperature. Remanent magnetization vectors are addi-

tive and, because individual blocks are rotated, the net remanent magnetization of the rubbly flow–top is low. Nonetheless, large, shallow blocks within this carapace produce large-amplitude, short–wavelength anomalies of the type seen on the high-resolution map (Figure 9a). No attempt was made to model these very short–wavelength anomalies. Two vertical-sided polygons are used to represent the change in thickness of the lava flow at its margin.

FIGURE 15. Cross–section of the polygon model used to represent the lava flow margin. The model consists of two horizontal, vertically sided polygons, each 5 m thick. The lava flow is mantled by weakly magnetized rock representing the rubbly flow–top. Short wavelength anomalies are produced by magnetized blocks within this flow top. The inclination of the vector of remanent magnetization is indicated by vector J.

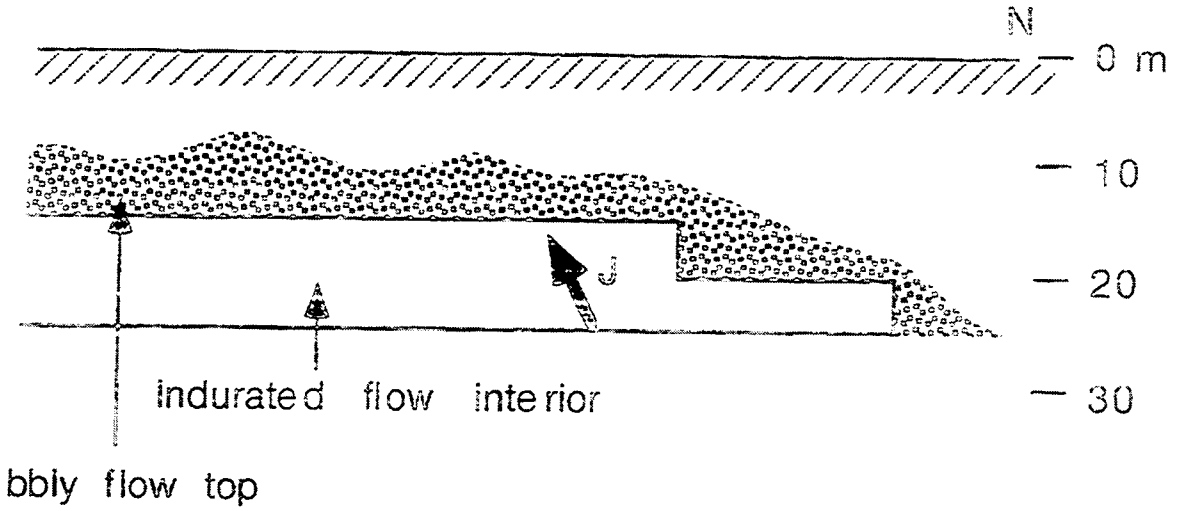

The magnetic field anomaly produced by this model geometry captures the amplitude of the long-wavelength anomaly associated with the flow margin in each map profile. For the calculated magnetic anomalies in Figures 11-14, the top of the massive flow interior is assumed to be 15 m beneath the surface and 10 m thick. Experimentation indicates that this massive flow interior is not likely greater than 20 m in total thickness and the top of the massive interior is not likely deeper than 20 m. Naturally the thickness of the rubbly flow–top may be quite variable and is poorly constrained by the magnetic data.

The high-resolution survey and modeling of these data indicates that the lava flow field extends approximately 300 m north of NE Little Cone. The extent of lava flows around the two cones can be determined using the low-resolution survey data. Magnetic data collected across the entire area (Plate 1) were filtered using a high–pass filter on a line-by-line basis. In this case, a ramped high–pass filter was used, passing anomalies with wavelengths shorter than 10 m unchanged, and completely attenuating anomalies with wavelengths greater than 40 m. The root-mean-square of the derivative of this map shows the locations of short-wavelength anomalies in the survey area (Figure16).

FIGURE 16. Distribution of short-wavelength anomalies in the Little Cones map area is indicated by dark shading. Anomalies are shaded by high-pass filtering original magnetic data, and calculating the root–mean–square of the derivative of this map. Short-wavelength

anomalies indicate the distribution of shallow lava flow surfaces, rubbly flow tops and cone material.

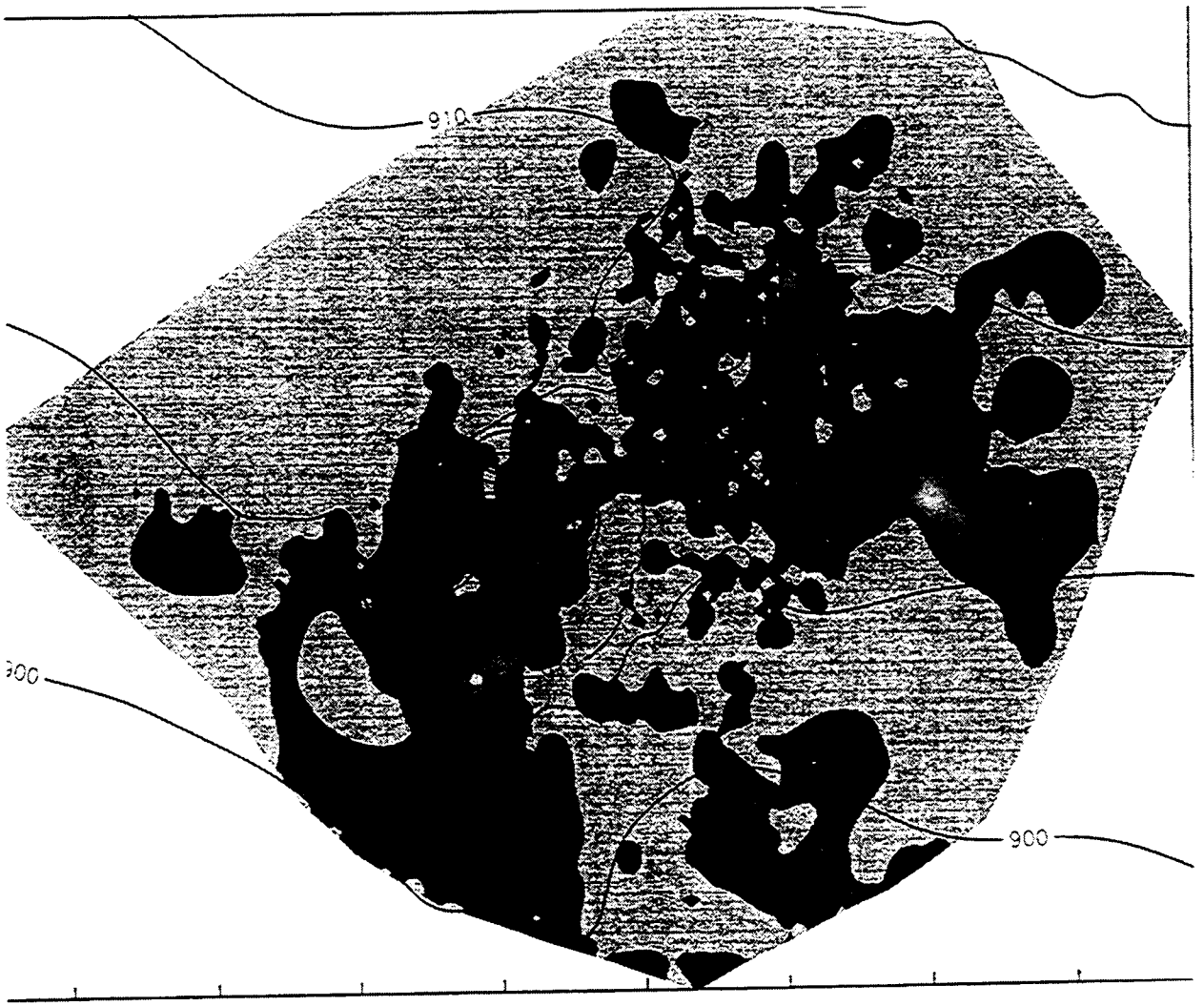

The most prominent areas of short-wavelength anomalies are on the south side of SW Little Cone, where lavas actually crop out, south and east of NE Little Cone, and to a lesser extent north and west of NE Little Cone. Sources of these anomalies must be highly magnetized rocks close to the surface as magnetic anomalies associated with the cones themselves cannot produce high frequency anomalies hundreds of meters from the cones.

The location of the flow margin was estimated throughout the survey area based on the extent of anomalies using Figure16 and Plate 1, together with models of the flow margin on the north side of the cone (Figure 10) . The low-resolution survey encompassed and extended beyond these anomalies everywhere except on the south side of the cones,

where lava flows clearly extend beyond the map area. The approximate flow margin is shown in Figure 17. The area within the outlined flow margin (Figure 17) is 970,000 m2. Given the uncertainty in locating the flow margin in low resolution survey areas, the area of the flow field within the survey area is taken to be 1±0.1 km2. If the lava flow averages 10 m in thickness, the volume of the flow field within the survey area is approximately 1 x 107 m3, or about 10 times the volume of the cones.

FIGURE 17.

Figure 17. The extent of buried lava flows in the survey area is indicated by shading, based on interpretation of magnetic data presented on Plate 1, modeling, and map enhancement. Position of a possible buried vent, northeast of NE Little Cone is also indicated. Lava flows extend beyond the survey area to the south.

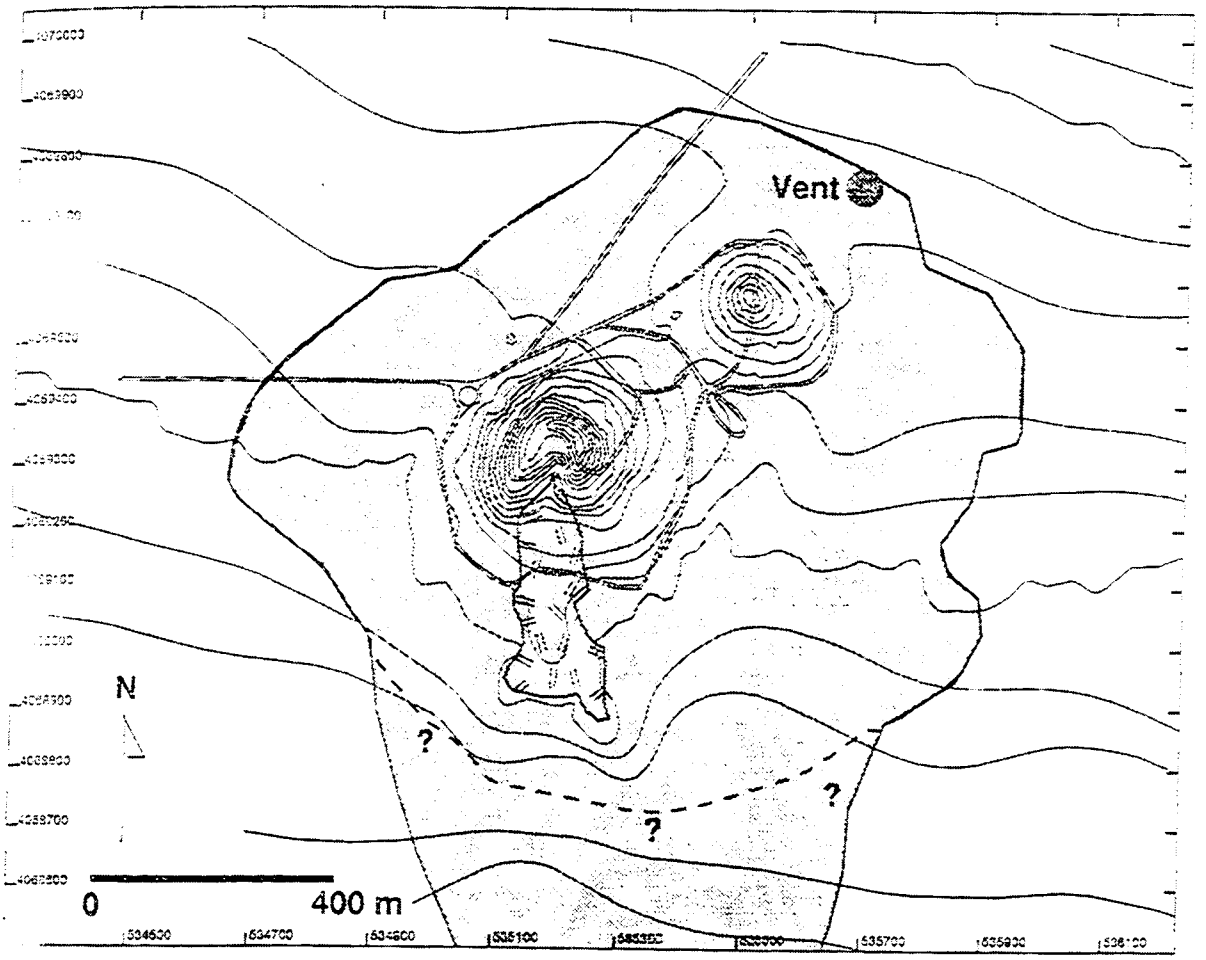

Unfortunately, it is uncertain how far the lava flow field extends south the Little Cones and therefore an eruptive volume cannot be calculated. Based on the known distribution of flows and the extent of outcrops south of the SW Little Cone, the eruptive volume is >0.01km3. In comparison, the volume of the exposed lava flow field at Black Cone, including the cinder cone, is approximately 0.07km3.

3.7 Anomaly northeast of NE Little Cone

Not all of the magnetic field variation identified in the high-resolution survey north of NE Little Cone is easily explained by the lava flow model. In particular, a negative anomaly, greater than 1000 nT in amplitude, is located near the edge of the flow in the central part of the map area (Figure 9a). This anomaly has a wavelength of approximately 80 m, much longer than other anomalies associated with the flow surface flow.

The shape of this anomaly is best revealed by filtering the magnetic data using a low-pass filter. The filter ramped-up using a normal distribution between wavelengths of 40 and 80 m, and anomalies with wavelengths greater than 80 m passed through the filter unchanged. The resulting map (Figure 2–18a) shows that the anomaly is enhanced by this filtering process, and therefore is not likely associated with variation on the flow top that produces large–amplitude, but short–wavelength anomalies.

FIGURE 18. Low–pass filtered magnetic map of the high-resolution survey area north of NE Little Cone (a), and calculated magnetic anomaly using a vertical–sided polygon extending

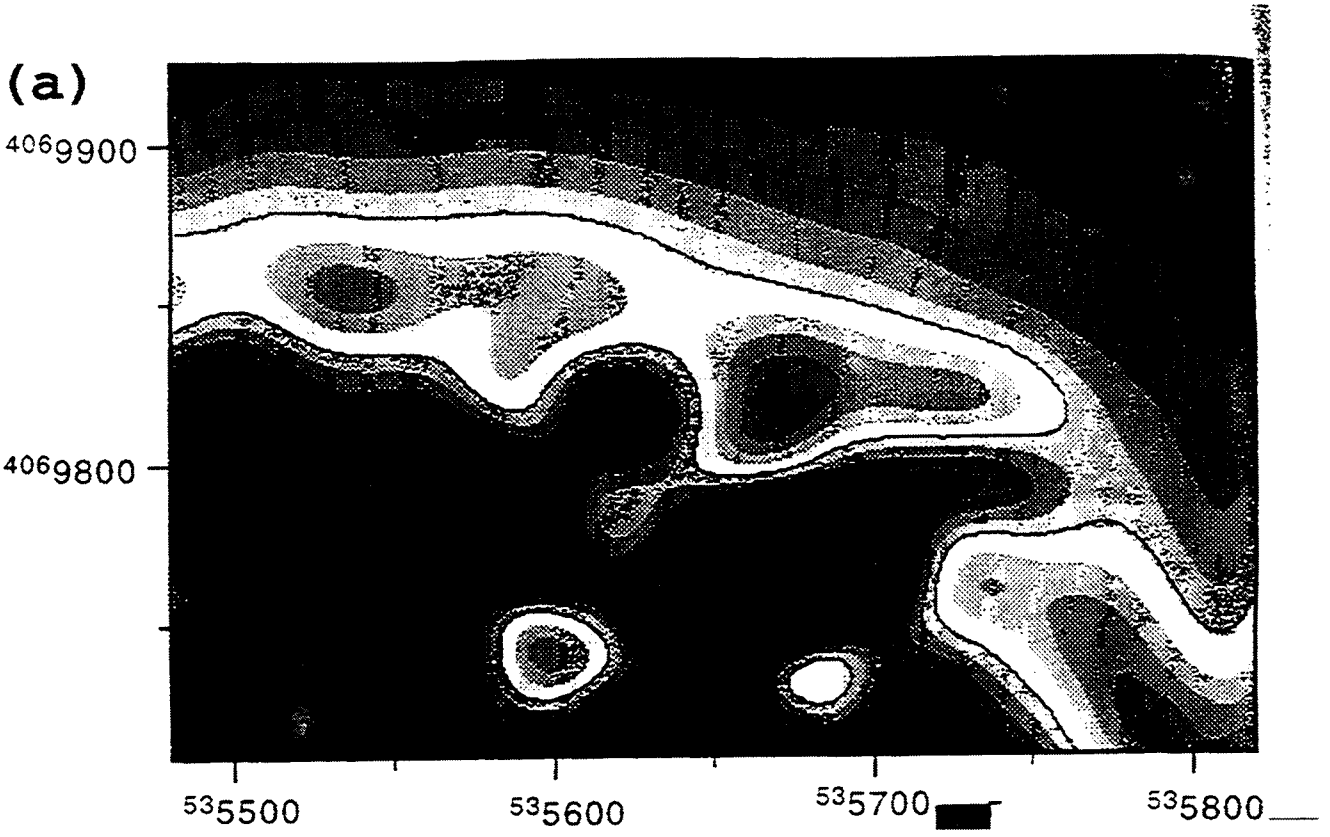

from the base of the lava flow to great depth (b). See Figure 10 for model geometry and Figure12 for fit between model geometry and observed magnetic data.

(b)

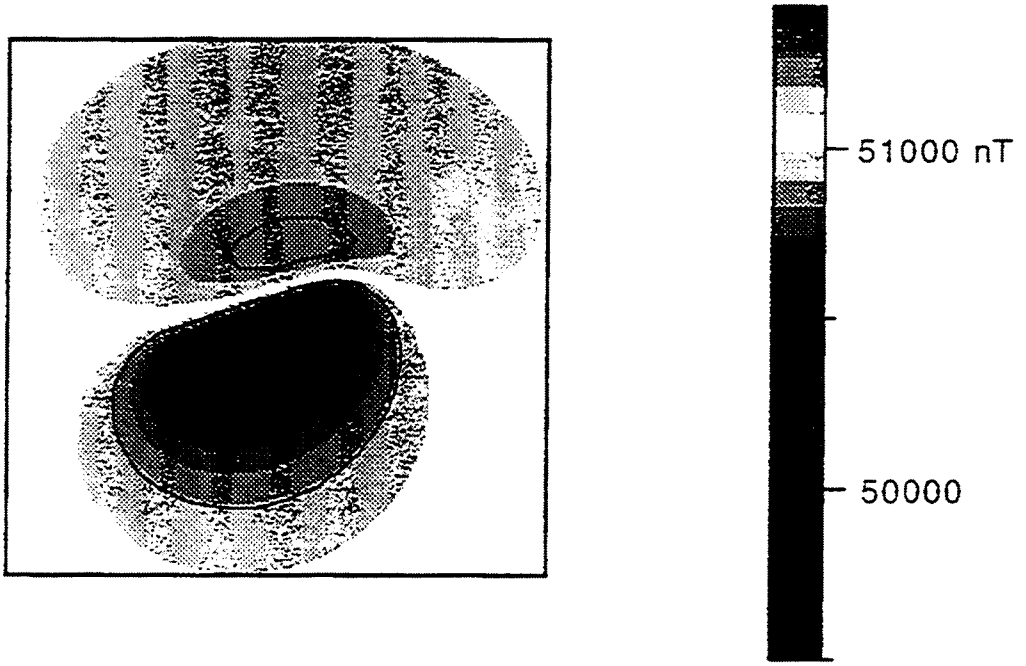

A vertically-sided prism is used to model this anomaly. This prism is 80 m in length. 15 m wide, and extends from the base of the lava flow to a model depth 100 m below the surface. The magnetic properties of the prism are the same as those of the lava flow (I = –67°, D = 177°, J = 20 Am-1). The map extent of this prism is shown in Figure 2–9. The calculated anomaly resulting from this body is shown in map view in Figure 2–17b and profile in Figure 2–11. Such a magnetized body explains the observed anomaly near the lava flow margin. One interpretation of this magnetized body is that it represents a buried vent or shallow dike.

4.0 Discussion of Results

Like other cinder cones in the YM region, the Little Cones are surrounded by a lava flow field. Where the lava flow was modeled north of NE Little Cone, the flow is buried at a depth of approximately 5–10 m and are 10–15 m thick. The magnetic survey bounds the areal extent of these flows on all but the south side of the cones. The volume of the Little Cones eruption is far greater than represented by the cones themselves

A large, >2000 nT, dipolar anomaly is located 250 m northeast of NE Little Cone along and azimuth of 042° (Figure 16). This anomaly has a wavelength and amplitude that are too large to be associated with the lava flow top or flow margin. A combination of map filtering and modeling indicates that a magnetized intrusion can account for the shape and dimensions of this anomaly. The modeled intrusion extends from the base of the lava flows to great depth is 15 m wide at its top and is 80 m in length. Such a geometry is consistent with the presence of a buried vent or shallow dike.

The location of this vent or shallow dike is consistent with the NE trend of the Crater Flat cinder cone alignment, and nearly doubles the length of the Little Cones segment of this alignment.

5.0 Summary

One of the primary goals of this magnetic survey was to evaluate the utility of ground magnetic data for characterizing igneous intrusions and related structures at small-volume basaltic volcanoes in the YM region. This activity was undertaken because two KTUs associated with volcanism,

•Low resolution of exploration techniques to detect and evaluate igneous features and

•Inability to characterize many igenous features and events,

will likely have a strong impact on assessment of volcanism studies and hazard assessments as part of license evaluation. These KTUs exist because surface geological studies of volcanism provide an incomplete and necessarily biased view of the extent of igneous activity in the YM region (Trapp and Justus, 1993). If investigations do not provide additional insight into the extent of igneous activity then conservative assumptions are required to compensate for lack of investigation in order to fulfill the siting criteria described in 60.122(a)(2)(ii).

Trapp and Justus (1993) point out that site investigations should seek a balance between the intensity of geophysical investigations and the assumptions made in volcano probability models. Failure to account for igneous features undetected by surface investigations will result in underestimation of volcanic hazards. Thus, current probility models based on the frequency of volcanic events (e.g., Crowe, 1995; Connor and Hill, 1995) are biased toward lower probabilities for igneous activity in the YM region and therefore do not meet the siting critieria of 60.122(a)(2)(ii). Conversely, assumptions about the volume of undetected igneous activity can be overly conservative, resulting in estimates of probability of volcanic disruption that are higher than warranted by the geology of the region. Geophysical investigations provide the empirical evidence required to formulate realistic and conservative volcanic hazard models that do meet siting critieria.

Ground magnetic surveys made at the Little Cones are one example of the type of investigation that can bound the extent of igneous activity near YM. The volcanological history of the Little Cones has been augmented by the magnetic survey in several ways:

•The volume of Little Cones magmatism is much greater than is represented by surface deposits and the cones are surrounded by a lava flow field

•NE Little cone is interpreted to consist of a spatter mound mantled by a weakly magnetized, unconsolidated layer of pyroclastic material; the presence of this spatter mound is consistent with both the presence of the surrounding lava flow field and observations of historically active cinder cones

•The vent or shallow dike northeast of NE Little Cone indicates that eruptive activity in the area may have been distributed among several vents separated by at least 600 m at the outset of the eruption, in an orientation consistent with the orientation of the entire Quaternary Crater Flat alignment, then localized at the two Little Cones in a manner consistent with observations made at historically active cinder cones; shallow dikes do not extend northeast of the survey area, based on the low magnetic gradients observed in that area.

Thus, volcanological information required to evaluate complicance with siting criteria was revealed using low-cost and fast ground magnetic surveys. Selective investigations at other volcanoes in the area, such as Northern Cone, would likely improve the basis for assumptions made in volcanic hazard assessment.

Insight into intrusion geometry was hampered at the Little Cones by the presence of the lava flow field discovered in the course of the survey. The magnetization of these lava flows prevented detection of intrusions associated with the cones. The area impacted by shallow intrusions will likely be best revealed by a combination of mapping and shallow geophysical investigations at eroded alignments, such as Pliocene Crater Flat

6.0 Appendix

Data are given on the enclosed disk

TOTAL MAGNETIC FIELD SURVEY OF THE LITTLE CONES, CRATER FLAT, NYE COUNTY, NEVADA

by Charles B. Connor, Ronald H. Martin, Peggy G. Hunka, Richard Klar, John Stamatakos, Brent Henderson
Center for Nuclear Waste Regulatory Analyses, Southwest Research Institute

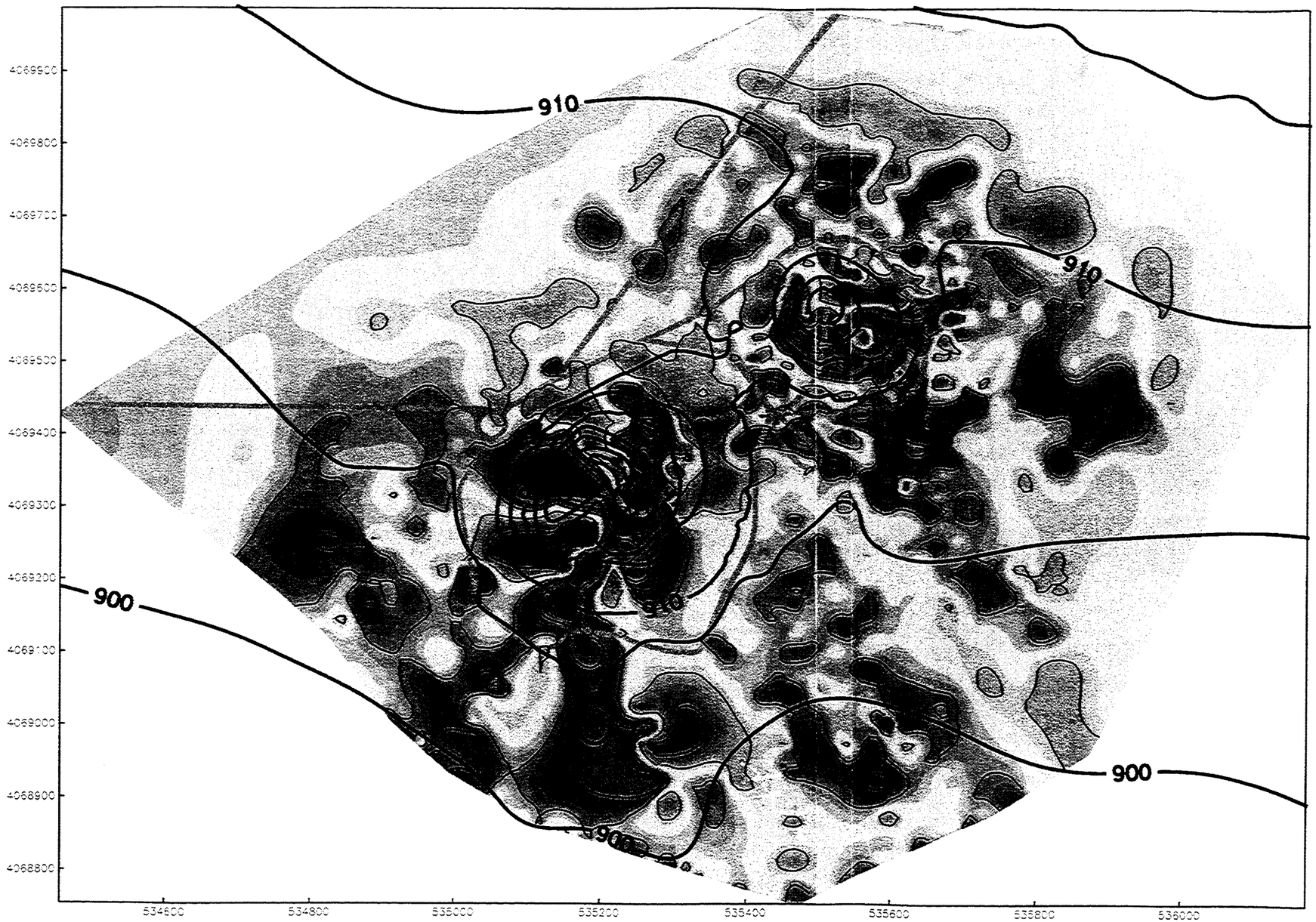

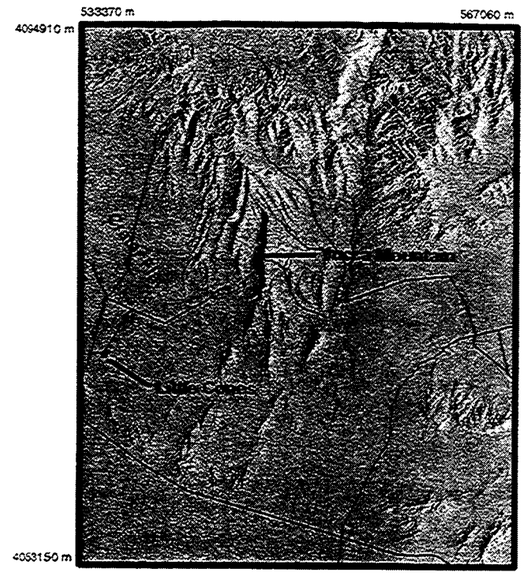

Location Map

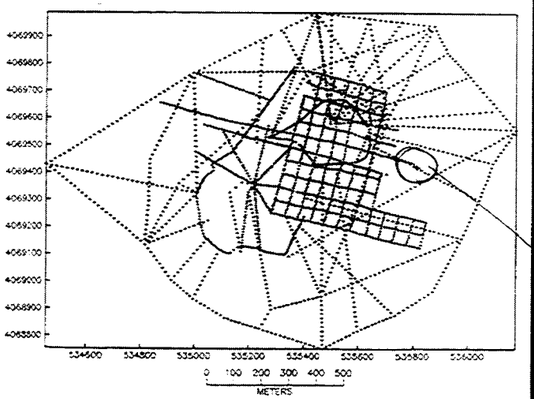

Survey Point Locations

TN
MN
14.2°
1995

Total Magnetic Intensity (nT)

47200 47800 48400 49000 49600 50200 50800 51400 52000 52600 53000

SCALE 1:6000 (approximately)

0 100 200 300 400 500
METERS

TOPOGRAPHIC CONTOUR INTERVAL: 5 METERS

Explanation

Ground magnetic survey of the Little Cones, Crater Flat, Nevada, showing intensity of the total magnetic field, based on measurements at 2,891 survey points. The total magnetic field was measured using a proto-precession magnetometer with 3 m sensor height. All magnetic data are drift corrected. International Geomagnetic Reference Field for Crater Flat is declination 14.2°, inclination 61.7°, and total intensity 50,827 nT, for January 1, 1995.

Dirt roads in the area are shown by solid gray lines. Topography was surveyed in the vicinity of the Little Cones and referenced to a U.S. Geological Survey 30 m digital elevation model (also see Crater Flat 7.5 min. quadrangle, U.S.G.S. map 36116-G5-TF-24). Map projection is UTM (m), zone 11, Clarke 1866.

This map is part of Center For Nuclear Waste Regulatory Analyses document CNWRA 96-002, Ground Magnetic Survey of the Little Cones, Crater Flat, Nevada, and was produced in cooperation with the U.S. Nuclear Regulatory Commission.

PLATE 1

Vent radius

Chuck Connor

Literature review control on column behavior and vent radius

Wilson et al. 1980 Geol. J. R. Astr. Soc., London 63: 117-148 discuss controls on explosive eruptions and the role and evolution of the vent radius.

Governing equations are

$$-\frac{dP}{\rho} = gdh + udu + \frac{fu^2}{4r}dh$$

where

P = pressure

u = velocity

rho = bulk density

f = friction factor (drag on wall)

g = gravity

r = vent radius

and h is the vertical coordinate (+upwards)

$$\dot{m} = \rho u \pi r^2$$

where m is the mass flow past a point

this is the same as

$$\frac{d\rho}{\rho} + \frac{du}{u} + 2\frac{dr}{r} = 0$$

also have the perfect gas law

$$P = \sigma RT$$

where sigma is the gas density in th erupting fluid

$$\frac{1}{\rho} = \frac{n}{\sigma} + \frac{(1-n)}{\sigma_r}$$

where sigma r is the density of the magma alone

Wilson et al derive the following equations from the above relation

$$\left(1 - \frac{u^2}{u_c^2}\right)\frac{du}{dh} = \left(\frac{u^2 f}{4r} + g\right)\frac{u}{u_c^2} - 2\frac{u}{r}\frac{dr}{dh}$$

$$\left(1 - \frac{u^2}{u_c^2}\right)\left(\frac{nRT}{P} + \frac{1-n}{\sigma_r}\right)\frac{dP}{dh} = 2\frac{u^2}{r}\frac{dr}{dh} - g - \frac{fu^2}{4r}$$

and

$$u_c = \sqrt{\frac{RT}{n}\left(n + \frac{(1-n)P}{\sigma_r RT}\right)}$$

if uc = u then

$\left(1 - \frac{u^2}{u_c^2}\right) = 0$ and du/dh and dP/dh are infinite unless

$$2\frac{u^2}{r}\frac{dr}{dh} - g - \frac{fu^2}{4r} = 0 \text{ and}$$

$$\left(\frac{u^2 f}{4r} + g\right)\frac{u}{u_c^2} - 2\frac{u}{r}\frac{dr}{dh} = 0$$

this occurs in both equations if

$$\left(\frac{dr}{dh}\right)_L = \frac{rg}{2u_c^2} + \frac{f}{8}$$

So, uc is a critical velocity . Wilson et al. rlate usc to the speed of sound in the magma (nongaseous fraction). If the flow velocity is greater than uc then the flow is supersonic

Recall that flow velocities increase as the magma approaches the surface, so

(i) if u<uc then $\left(1 - \frac{u^2}{u_c^2}\right) > 0$ if du/dh>0 then

to satisfy this

$$\left(\frac{u^2 f}{4r} + g\right)\frac{u}{u_c^2} - 2\frac{u}{r}\frac{dr}{dh} > 0$$

and

$\frac{dr}{dh} < \frac{rg}{2u_c^2} + \frac{fu^2}{8u_c^2}$: converging or slightly diverging conduit

this works if the conduit diameter shrinks toward the surface or for positive dr/dh that is less than (dr/dh)L.

(ii) If u>uc then

$\frac{dr}{dh} > \frac{rg}{2u_c^2} + \frac{fu^2}{8u_c^2}$, which means that the conduit must diverge fast enough for dr/dh>(dr/dh)L at all depths, so : rapidly diverging conduit.

Note that as the flow apporaches the surface, the value of uc will fall., as pressure falls. If u becomes slightly greater than uc - the conduit must diverge and flare toward the surface.

1.0 Physical properties

In order to investigate dh/dr as a function of u and uc, we need to know about T,R,sigma r, and f.

Also, there are local relationships, expected to change as a function of depth: P and n.

Wilson et al. use a constant liquid rhyolite density and a constant temperature.

n' = total water weight fraction

solubility of water =

$n_d = s\sqrt{P}$ if P is in bars s= 0.0013, or s = 4.1 x 10^{-6} $mN^{-1/2}$

if nd> n' then gas is totally dissolved

exsolution begins at depth De where nd=n'

Local pressure is talken to be lithostatic

$\sigma_{cr} g D_e = \left(\frac{n'}{s}\right)^2 - P_s$, where sigma cr is density of crustal rock and Ps is pressure at the Earth's surface.

exsolved gas fraction = n'– nd between the depth De and the surface

2.0 motion below the exsolution level

no gs solution at this level n=0 and rho = sigma r

the pressure gradient will equal the lithostatic pressure gradient

$dP = -\sigma_{cr} g dh$ where sigma cr is crustal rock density.

everything is constant and the velocity becomes

$$u = \left(\frac{16\eta}{f_o \sigma_r r}\right)\left(\sqrt{1 + \frac{g r^3 (\sigma_{cr} - \sigma_r)(f_o \sigma_r)}{64\eta^2}} - 1\right)$$

where η is the fluid viscosity and f_o is about 0.01

for laminar flow, this becomes

$$u = \frac{g(\sigma_{cr} - \sigma_r) r^2}{8\eta}$$

and

$$\dot{m} = \frac{\pi r^4 \sigma_r (\sigma_{cr} - \sigma_r) g}{8\eta}$$

3.0 Example

suppose viscosity = 10^5 PaS

gas content = 5%

given $\sigma_{cr} g D_e = \left(\frac{n'}{s}\right)^2 - P_s$, sigma cr = 2800 kgm3, g = 9.8 m/s2

between -1524 <H<11000 m elevation

T = 288.15-0.0065H

P = 1013.25*(288.15/T)^-5.255877 millibars =

1 millibar = 100 Pa

Ps (sealevel) = 10^5 Pa

De = 5.41 km, Wilson report 5.38 Km - they must have used a slightly higher density.

suppose $(\sigma_{cr} - \sigma_r)$ = 200 kg m3, and mass eruption rate of 10^7 kg/s.

using $\dot{m} = \frac{\pi r^4 \sigma_r (\sigma_{cr} - \sigma_r) g}{8\eta}$, the radius of the conduit at depths of greater than 5.4 km must be r = 26 m.

u = 1.65 m/s (laminar flow).

for tolbachik:

mass flow = 1 - 1.25 x 10^5 kg/s, 2% wt water and 1200°C, and 20 PaS (numbers from Britt)

feeder vent radius = 1 m

u = 12.2 m/s

De = 900 m

ADDITIONAL INFORMATION FOR SCIENTIFIC NOTEBOOK #: 115E (3 of 17)

Document Date:	06/09/1995
Availability:	Southwest Research Institute® Center for Nuclear Waste Regulatory Analyses 6220 Culebra Road San Antonio, Texas 78228
Contact:	Southwest Research Institute® Center for Nuclear Waste Regulatory Analyses 6220 Culebra Road San Antonio, Texas 78228 Attn.: Director of Administration 210.522.5054
Data Sensitivity:	■"Non-Sensitive" □ Sensitive □"Non-Sensitive - Copyright" ☐ Sensitive - Copyright
Date Generated:	03/20/1996
Operating System: (including version number)	MAC 98
Application Used: (including version number)	NA
Media Type: (CDs, 3 1/2, 5 1/4 disks, etc.)	1 - 3 ½ disks
File Types: (.exe, .bat, .zip, etc.)	txt
Remarks: (computer runs, etc.)	Media contains: Little cones magnetic data.

4 of 17

Ground Magnetic Data collected in Crater Flat and the Amargosa Desert

Chuck Connor

Ground Magnetic Data collected in Crater Flat and the Amargosa Desert

Chuck Connor

Charles B. Connor

Investigators: Charles B. Connor, John Stamatakos, Ron Martin, Pete Lafemina, Sammantha Magsino, Brittain E. Hill, and Donald P. Cederquist

1.0 Introduction

The proposed High-Level Waste (HLW) repository at Yucca Mountain (YM), Nevada is located within a geologically active volcanic field. This volcanic field consists of eight basaltic cinder cones formed by volcanic activity within the last one million years, and numerous cinder cones and lava flows formed within the last 5 million years (Faulds et al., 1994; Sawyer et al., 1994; Bradshaw and Smith, 1994; Champion, 1991; Heizler et al., 1994). As is typical for volcanic fields of this kind located throughout western North America, volcanic activity in the YM region is best characterized by the formation of new basaltic volcanoes at a low recurrence rate. Recent estimates of the probability of a new basaltic cinder cone forming within the area of the proposed repository are 1–5 x 10^{-4} for a 10,000 yr period (Crowe and Perry, 1989; Ho et al., 1991; Smith et al., 1991; Margulies et al., 1992; Connor and Hill, 1995). Although probability estimates will likely be refined, current estimates are large enough to be of regulatory concern and must be addressed in performance assessment.

Estimates of the probability of volcanic disruption of the candidate repository are strongly effected by the volume, orientation, shape and frequency of volcanic events. These factors are represented by an area term included in all probability models. If volcanic events are considered to be very spatially limited phenomenon, then the probability of volcanic disruption of the candidate repository is less for a given recurrence rate than if the area affected by an individual volcanic event is large. Consequently, it is important to estimate the area impacted by individual volcanic events in the YM region in as much detail as possible. Current estimates of this area term are based on assumptions about intrusion geometries that may not be conservative (e.g., Barr et al., 1992; Lin et al., 1993; Wilson et al., 1994).

This report presents the preliminary results of two ground magnetic surveys made near Yucca Mountain during May of 1996. One of these surveys was made in Crater Flat and extends from the Little Cones southward to the topographic margin of the basin. This part of Crater Flat is volcanologically and structurally complex (Connor et al., 1996; Ferrill et al (), Stamatakos et al (). A basic goal of geophycial and geological investigations in this area is to futher our understanding of the clustered nature of basaltic volcanism in Crater Flat (Connor and Hill, 1995), the history and recurrence rate of basaltic volcanism in this cluster, and the relationship between volcanoes and prominent structures and stuctural trends in the area. The goals specific of this survey were to:

•Determine the southern extent of lava flows associates with the Little Cones volcanoes

•Map an anomaly south of the Little Cones that was previously identified from aeromagnetic survey as possibly of basaltic origin in sufficinet detail to determine if the anomaly is related to basaltic volcanism, the depth and lateral extent of the magnetic body

•Determine the relationship between these features and basalts that crop out in southernmost Crater Flat near faults that are possibly associated with the Bare Mountain Fault

A second magnetic survey was located in the Amargosa desert south of Lathrop Wells cinder cone in a region where complex aeromagnetic anomalies, possibly produced by buried basaltic volcanoes, had been previously identified (Langenheim et al., 1993; Oliver et al., 1995). There are five anomalies in the Amargosa Desert identified by Langenheim et al. (1993) as being potential volcanoes or related igneous features. These anomalies have been incorporated as volcanic events into some probabilistic volcanic hazard analyses. Of these anomalies, aeromagnetic anomaly A is the most complex and difficult to interpret from the aeromagnetic maps because this anomaly has a comparatively short wavelength relative to flightline spacing. Connor and Hill (1995) assumed that aeromagnetic anomaly A correlates with the drilled and mapped aeromagnetic anomaly B of Langenheim et al. (1993), but noted that the large distances between anomalies in the Amargosa Desert compared with mapped vents in Crater Flat may simply be a function of the low resolution of the aeromagnetic data and that the aeromagnetic data may not capture the complete distribution of volcanic features in the area. Other volcanic hazard analyses have not included anomaly A, possibly because of its uncertain origin (e.g., Crowe et al, 1995; Golder?). Anomaly A is also of great interest because of its proximity to the Lathrop Wells cinder cone and because it is the closest of the Amargosa Desert anomalies to the candidate repository site. Therefore, the goal of the ground magnetic survey anomaly A was to map the anomaly in sufficeint detail to constain the origin of the anomaly and better resolve the distribution of buried magnetized rocks that produce the anomaly.

2.0 Background on the Ground Magnetic Method

Potential field methods are commonly used to develop a three-dimensional view of geologic structures. Identification of these structures is one of the primary goals of geophysical exploration in the YM region (Oliver et al., 1990), and magnetic methods have been among the most successful techniques for the identification of basalts in the YM

region that do not crop out at the surface (Langenheim et al., 1993; Ponce et al., 1992). The principles and utility of magnetic methods for the identification of basaltic volcanic rocks in the YM region have recently been reviewed by Connor and Sanders (1994).

The two surveys were made using a Geometrics model G–858 optically-pumped cesium-vapor magnetometer. This magnetometer provides highly repeatable readings in areas of high magnetic gradient, such as those identified in the Little Cones area, and is capable of collecting data at a much greater sampling rate than other types of magnetometers. Magnetic readings were made with the G-858 at 1 or 2 second intervals. Sensor height was 1 m. The magnetometer was interfaced to a differential global positioning system (GPS) which collected postion information at every second. The differential GPS was further corrected to true map coordinates by tying measurements to benchmarks in Crater Falt and the Amargosa Desert. The ground resolution of the differential GPS is better than 5 m and is typically 1-2 m. Magnetic readings, time, position, and related information was stored in the magnetometer memory and downloaded to a laptop computer at regular intervals. This survey design enabled our team to collect very high resolution data along closely spaced profiles. The Crater Flat survey consists of approximately 35,000 measurments made along 60 km of profile lines within a 32 km^2 area. These data were collected during 4.5 survey days (May 21-May 27, data was not collected on May 26). The Amargosa Desert anomaly A survey consists of approximatley 27,000 measrements made along 40 km of profile lines within a 25 km^2 area and was surveyed during a three day period (May 28-May 30).

The G-858 magnetometer is equipped with a real-time display. Consequently it was possible to modify traverse lines to respond to the presence or absence of short-wavelength magnetic anomalies as the survey progressed. This was particularly important during the survey of buried lava flows associated with the Little Cones.

3.0 Drift Corrections

Total magnetic field measurements were recorded at a base station throughout all data collection. A proton precession magnetometer (Geometrics model G 856) was used for this purpose. Field measurments were drift-corrected using these base station readings. Drift during the sampling period is shown in the following 9 figures

FIGURE 1. Drift measured at 856 base station on May 21

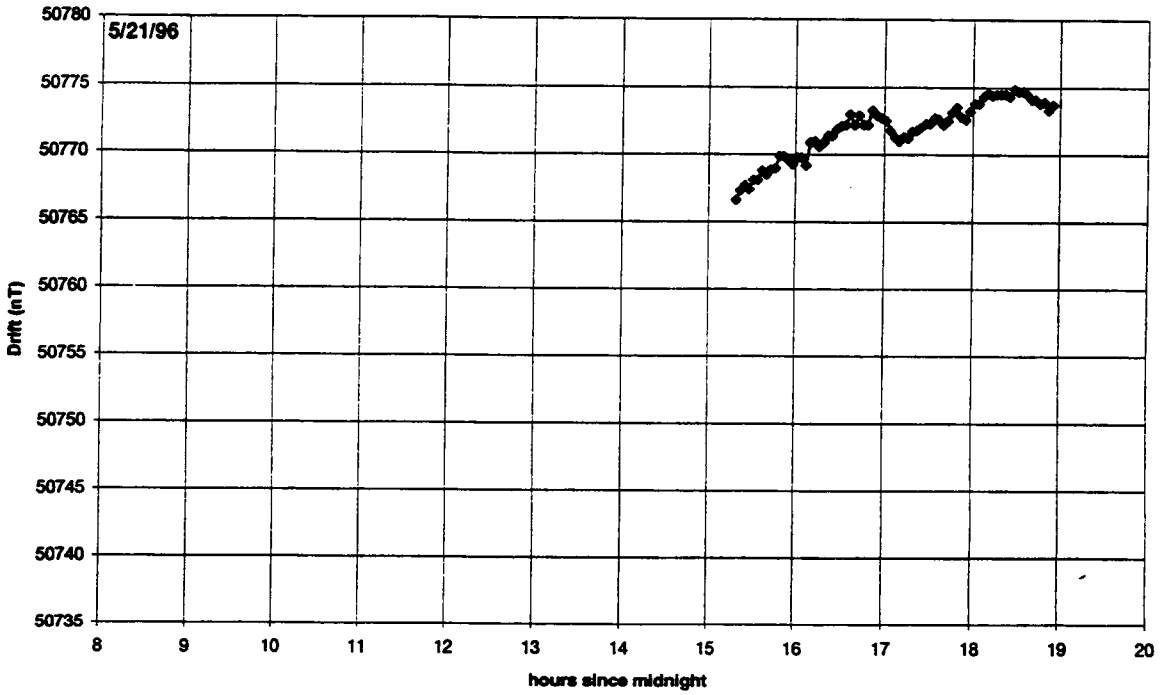

FIGURE 2. Drift measured at 856 base station on May 22

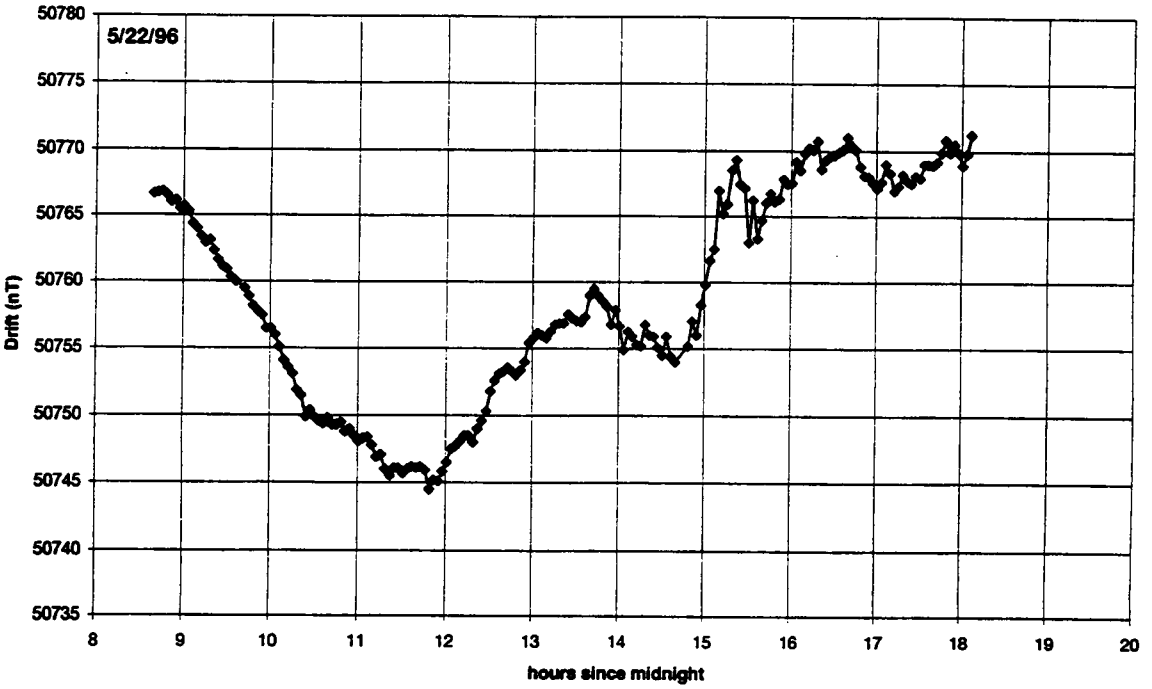

FIGURE 3. Drift measured at 856 base station on May 23

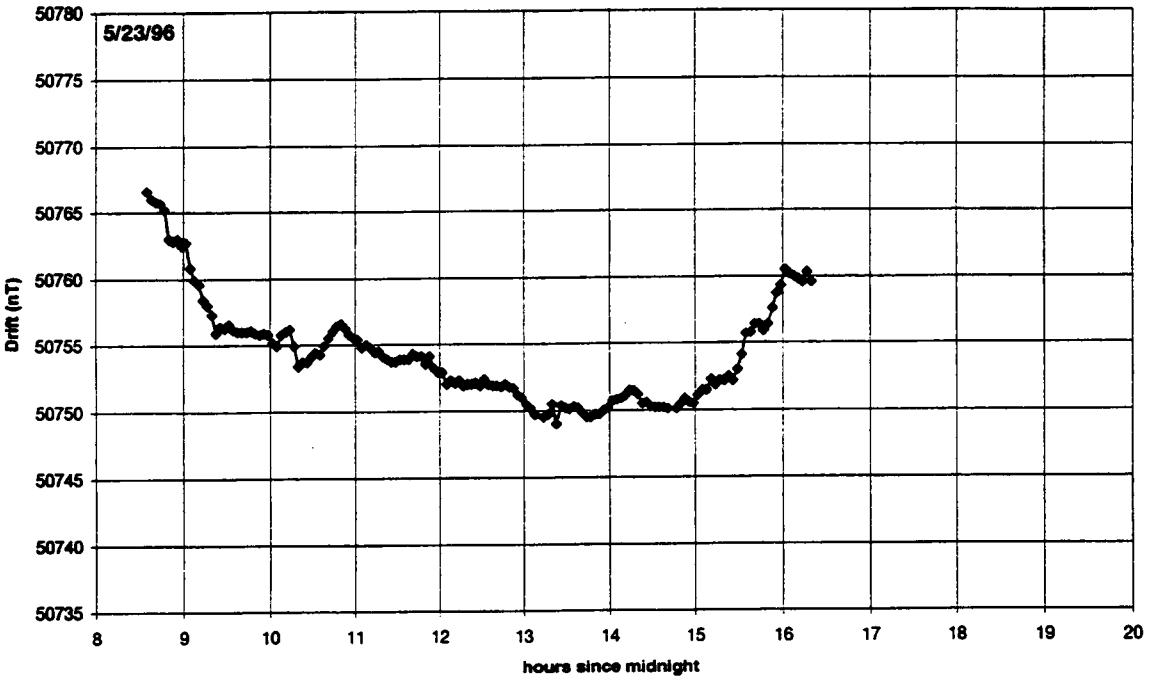

FIGURE 4. Drift measured at 856 base station on May 24

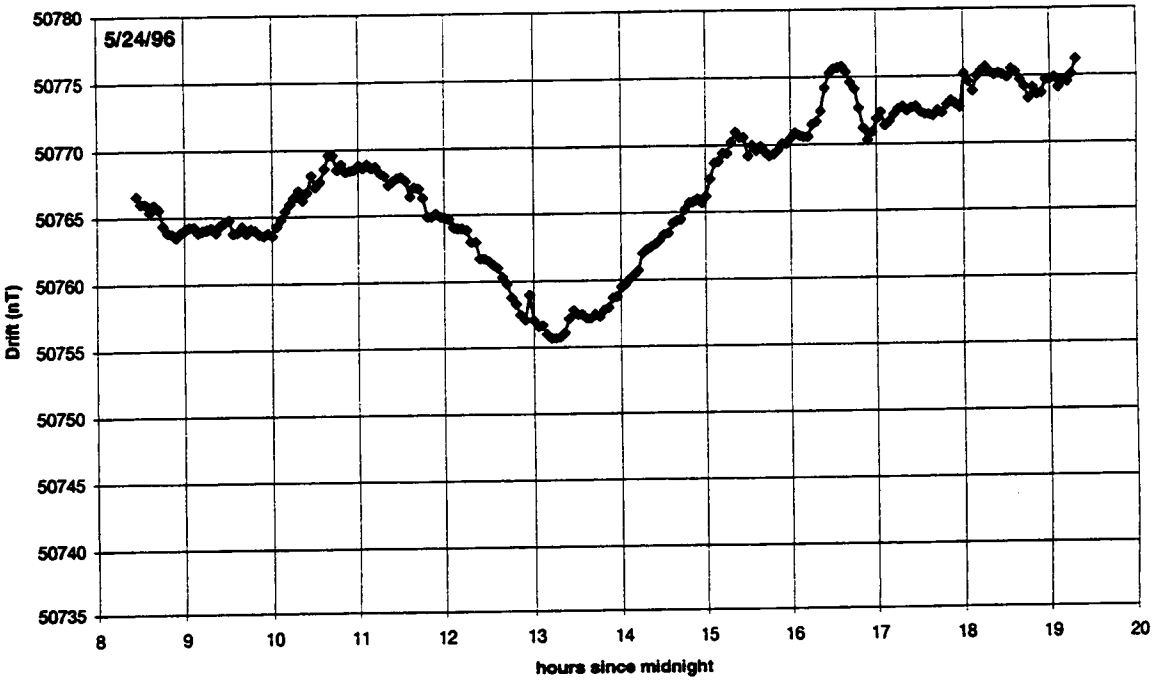

FIGURE 5. Drift measured at 856 base station on May 25

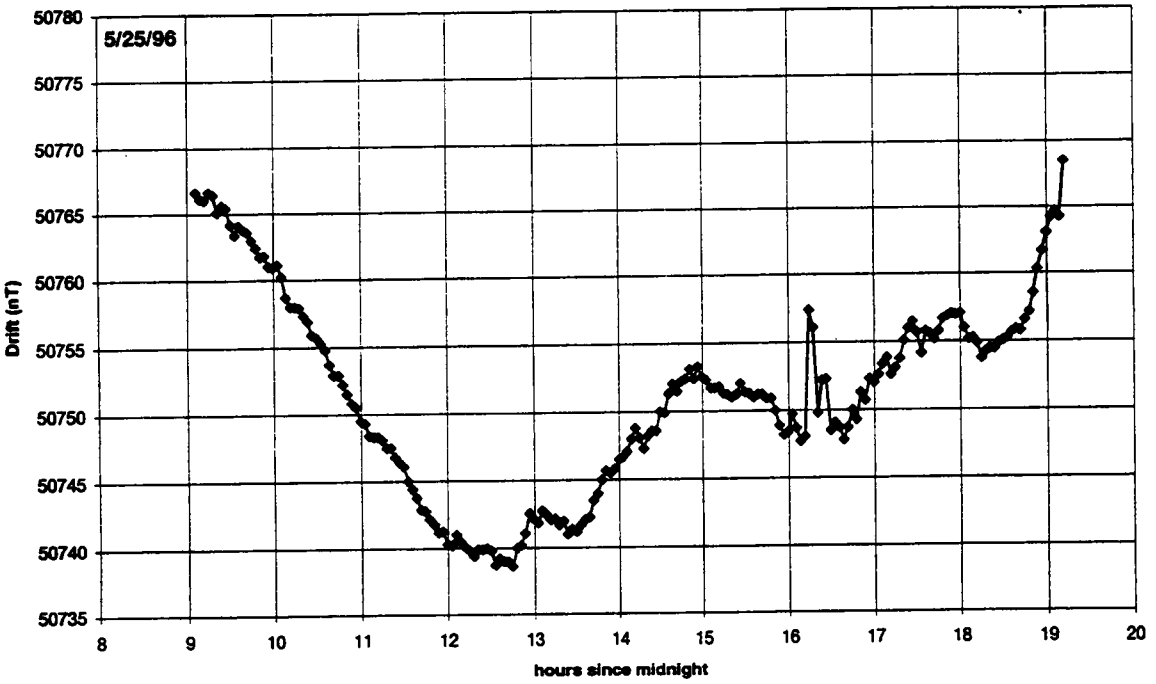

FIGURE 6. Drift measured at 856 base station on May 27

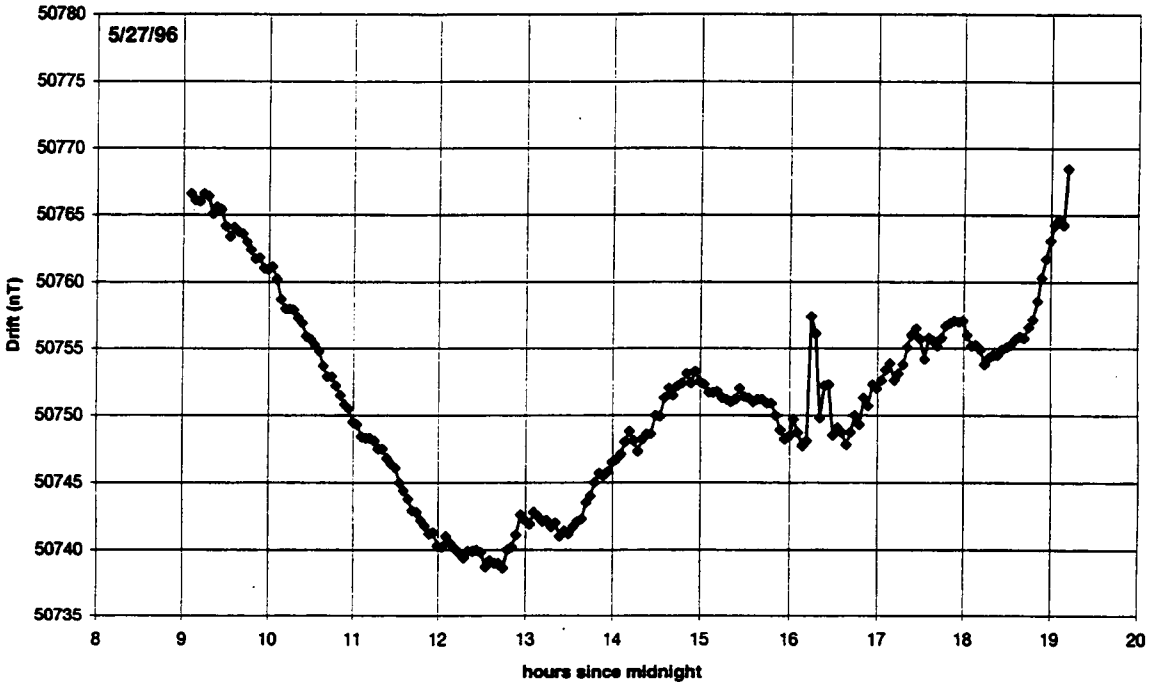

FIGURE 7. Drift measured at 856 base station on May 28

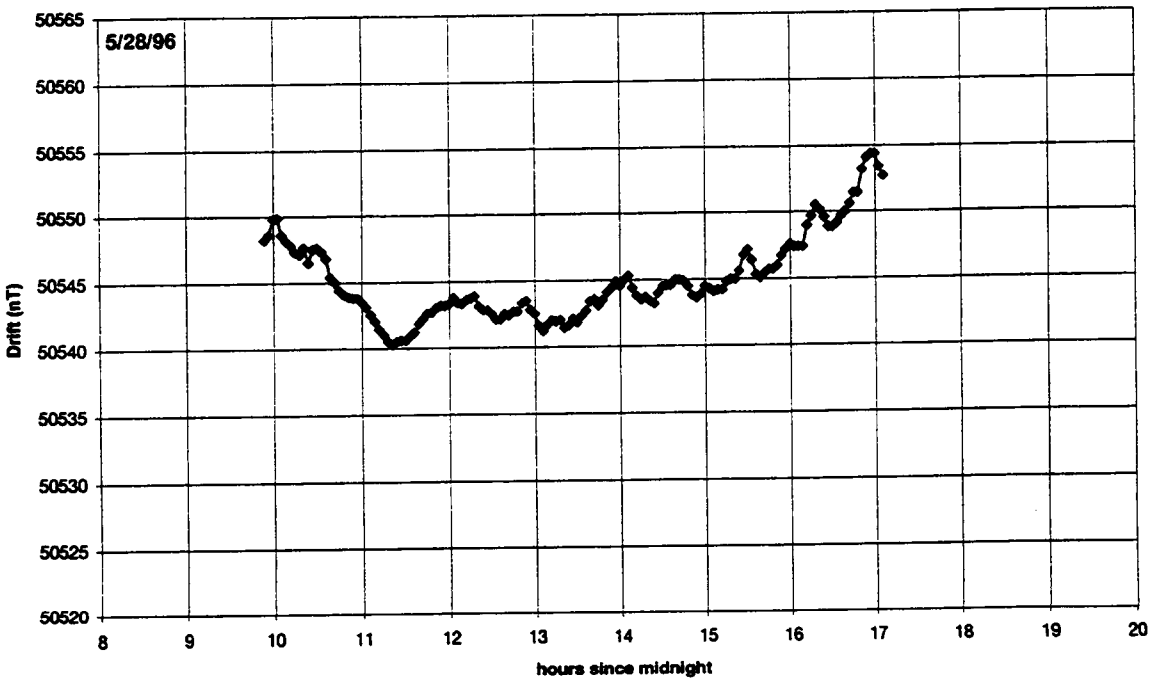

Drift measured at 856 base station on May 29

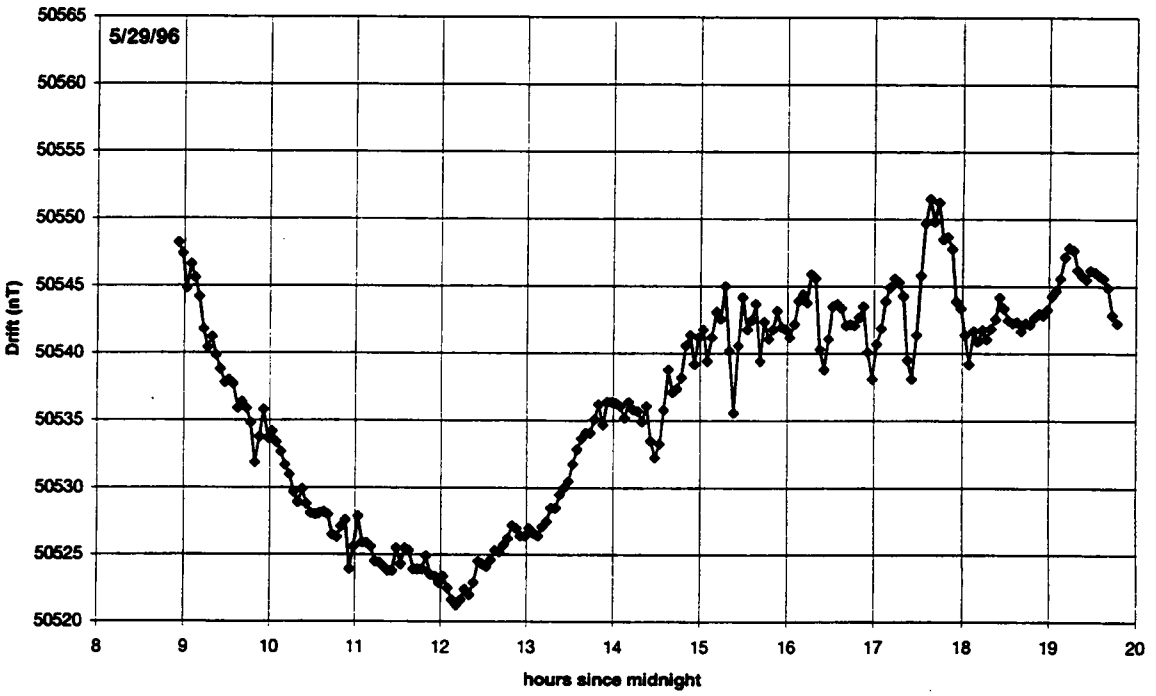

FIGURE 8. Drift measured at 856 base station on May 30

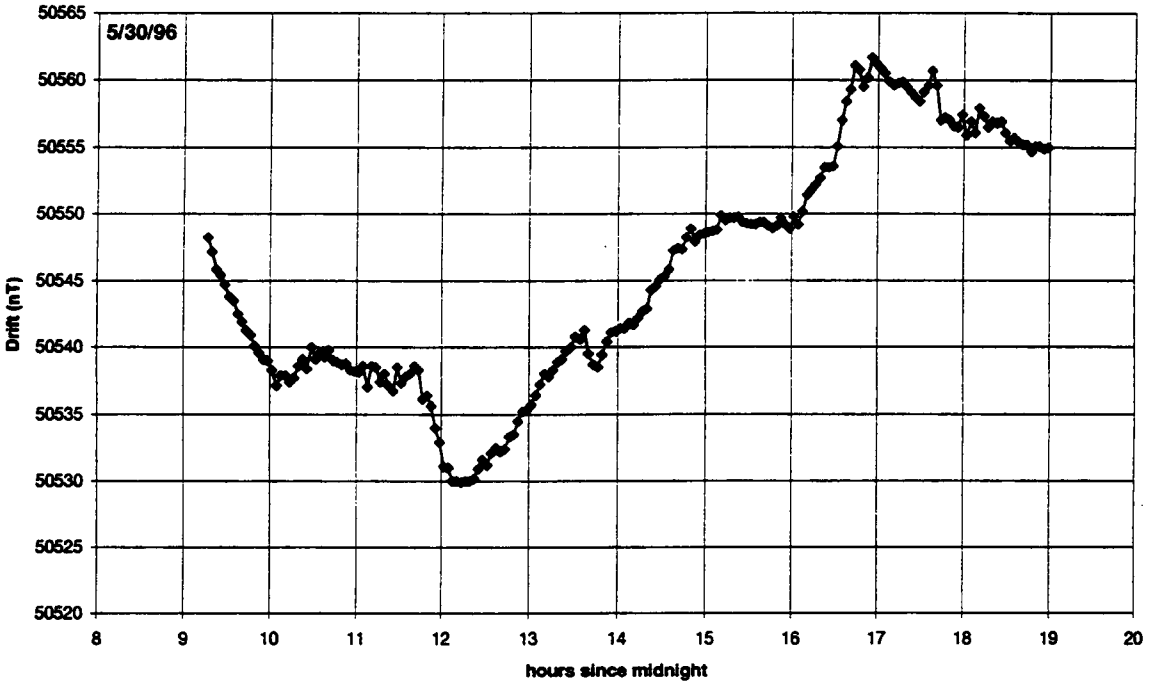

A listing of typical drift data collected by the 856 is:

```
•* 4 142 151001   0 505484
•* 4 142 151301   1 505516
•* 4 142 151601   2 505477
•* 4 142 151901   3 507666
•* 4 142 152201   4 507673
•* 4 142 152501   5 507677
```

•* 4 142 152801 6 507674
•* 4 142 153101 7 507681
•* 4 142 153401 8 507681
•* 4 142 153701 9 507688
•* 4 142 154001 10 507685
•* 4 142 154301 11 507689
•* 4 142 154601 12 507690
•* 4 142 154901 13 507699
•* 4 142 155201 14 507699
•* 4 142 155501 15 507696
•* 4 142 155801 16 507693
•* 4 142 160101 17 507698
•* 4 142 160401 18 507698
•* 4 142 160701 19 507692
•* 4 142 161001 20 507709
•* 4 142 161301 21 507710
•* 4 142 161601 22 507706
•* 4 142 161901 23 507709
•* 4 142 162201 24 507714
•* 4 142 162501 25 507714
•* 4 142 162801 26 507719
•* 4 142 163101 27 507721
•* 4 142 163401 28 507722
•* 4 142 163701 29 507730
•* 4 142 164001 30 507722
•* 4 142 164301 31 507729
•* 4 142 164601 32 507722
•* 4 142 164901 33 507722
•* 4 142 165201 34 507733
•* 4 142 165501 35 507729
•* 4 142 165801 36 507727
•* 4 142 170101 37 507725
•* 4 142 170401 38 507718
•* 4 142 170701 39 507713
•* 4 142 171001 40 507710
•* 4 142 171301 41 507713
•* 4 142 171601 42 507712
•* 4 142 171901 43 507717
•* 4 142 172201 44 507718
•* 4 142 172501 45 507720
•* 4 142 172801 46 507723
•* 4 142 173101 47 507723
•* 4 142 173401 48 507727
•* 4 142 173701 49 507726
•* 4 142 174001 50 507722
•* 4 142 174301 51 507725
•* 4 142 174601 52 507731
•* 4 142 174901 53 507735
•* 4 142 175201 54 507728
•* 4 142 175501 55 507726

```
•* 4 142 175801  56 507732
•* 4 142 180101  57 507738
•* 4 142 180401  58 507738
•* 4 142 180701  59 507743
•* 4 142 181001  60 507746
•* 4 142 181301  61 507744
•* 4 142 181601  62 507745
•* 4 142 181901  63 507745
•* 4 142 182201  64 507745
•* 4 142 182501  65 507743
•* 4 142 182801  66 507749
•* 4 142 183101  67 507747
•* 4 142 183401  68 507747
•* 4 142 183701  69 507745
•* 4 142 184001  70 507741
•* 4 142 184301  71 507741
•* 4 142 184601  72 507738
•* 4 142 184901  73 507739
•* 4 142 185201  74 507733
•* 4 142 185501  75 507737
```

The readings were taken at three minute intervals (local time) and are reported in tenths of nanoteslas. All drift measurements are given in the attached files (on disk) designated by date and .DNL.

Field data were drift corrected using the following program

```
•#include <stdio.h>
•#include <stdlib.h>
•#include <math.h>
•
•void main (int argc,char *argv[]) {
•
•float dtime[500];
•float ddrift[500];
•float x1,x2,y1,y2,m1;
•float drifted, drift_corr, drmag, drtime;
•
•
•int kt, totdrift;
•int ret;
•File *ifp;
•if (fopen(argv[1],"r") == NULL)
•  printf ("file didn't open\n");
•else
•  while (fscanf(ifp,"%lf %lf", &dtime[kt], &ddrift[kt]) != EOF) {
•    kt++;
•  }
```

```
•  fclose(ifp);
•
•totdrift = kt;
•
•kt = 0;
•
•File *ifp2;
•if (fopen(argv[2],"r"); == NULL)
•  printf ("file didn't open\n");
•else
•  while (fscanf(ifp2,"%lf %lf", &drtime, &drmag) != EOF) {
•
•  FOR (kt = 1; kt < totdrift, kt++) {
•
•     IF (dtime[kt]>drtime) {
•       x1 = dtime[kt-1];
•       x2 = dtime[kt];
•       y1 = ddrift[kt-1];
•       y2 = ddrift[kt];
•       break;  /* exit for */
•     } /* end if */
•
•  }/* end kt for */
•
•  m1 = (y2-y1)/(x2-x1);
•  drifted = (drtime-x1)*m1 + y1 - drtime[0];
•  drift_corr = drmag-drifted;
•
•  printf("%lf   %lf    %lf    %lf\n",drift_corr,drifted,drmag,drtime);
•
•} /* end the fscan */
•}
```

This program drift corrects the data to the first measurement made each day. Data from successive days were corrected by minimizing the error across tie lines in the way used in typical aeromagnetic surveys.

The IGRF was then removed from the data set.

The international geomagnetic reference fiedl is a 8 to 10 degree Legendre polynomial that serves as an approximation to the earth's magnetic field. This reference field is ususally removed from magnetic data to remove trends that are not related to local magnetic anomalies.

The IGRF was calculated using a US Geological Survey program at a series of points in the area of the Amargosa Desert survey. The values of the magnetic anomalies at these points indicate that the IGRF is well-approximated across this area as a dipping plane.

The following code is used to approximate the IGRF using selected data points and a linear trend surface.

```
•dim x1(40), x2(40),y(40)
•dim a(3,3), aprime(3,3)
•dim c(3), b(3)
•
•open #1: name "merc.out"
•
•
•do while more #1
•let i = i + 1
•input #1: x1(i), x2(i), y(i)
•loop
•let n = i
•
•
•for i = 1 to n
•
•let sum_x1 = sum_x1 + x1(i)
•let sum_x2 = sum_x2 + x2(i)
•let sum2_x1 = sum2_x1 + x1(i)*x1(i)
•let sum2_x2 = sum2_x2 + x2(i)*x2(i)
•let sum_x1x2 = sum_x1x2 + x1(i)*x2(i)
•
•let sum_y = sum_y + y(i)
•let sum_yx1 = sum_yx1 + y(i)*x1(i)
•let sum_yx2 = sum_yx2 + y(i)*x2(i)
•
•next i
•
•let a(1,1) = n
•let a(1,2) = sum_x1
•let a(1,3) = sum_x2
•let a(2,1) = sum_x1
•let a(2,2) = sum2_x1
•let a(2,3) = sum_x1x2
•let a(3,1) = sum_x2
•let a(3,2) = sum_x1x2
•let a(3,3) = sum2_x2
•
•let c(1) = sum_y
•let c(2) = sum_yx1
•let c(3) = sum_yx2
•
•mat aprime = inv(a)
•mat b = aprime * c
•
•mat print b
•
•for i = 1 to n
```

```
•
•let new_y = b(1) + b(2)*x1(i) + b(3)*x2(i)
•let diff = new_y - y(i)
•!print diff
•next i
•

end
```

The following data were used as input into this program to make the linear correction

• 544596. , 4.05787e+6 , 50870
• 544580. , 4.05699e+6 , 50865
• 544593. , 4.0565e+6 , 50863
• 544597. , 4.056e+6 , 50860
• 544595. , 4.0555e+6 , 50857
• 544602. , 4.05451e+6 , 50851
• 544605. , 4.05411e+6 , 50850
• 544608. , 4.053e+6 , 50844
• 544608. , 4.05214e+6 , 50839
• 544610. , 4.05106e+6 , 50833
• 544610. , 4.05074e+6 , 50831
• 545355. , 4.05763e+6 , 50871
• 545353. , 4.05698e+6 , 50867
• 545336. , 4.05649e+6 , 50864
• 545350. , 4.056e+6 , 50862
• 545351. , 4.0555e+6 , 50859
• 545353. , 4.05483e+6 , 50854
• 545359. , 4.05402e+6 , 50851
• 545358. , 4.053e+6 , 50845
• 545362. , 4.05215e+6 , 50841
• 545352. , 4.05198e+6 , 50840
• 546357. , 4.057e+6 , 50869
• 546360. , 4.05649e+6 , 50867
• 546357. , 4.05599e+6 , 50864
• 546354. , 4.05551e+6 , 50861
• 546357. , 4.05451e+6 , 50856
• 546354. , 4.05402e+6 , 50853
• 546350. , 4.05362e+6 , 50851
• 546353. , 4.05298e+6 , 50848
• 546354. , 4.05227e+6 , 50844
• 543819. , 4.05216e+6 , 50837
• 543848. , 4.05099e+6 , 50831
• 546820. , 4.0555e+6 , 50862
• 546807. , 4.05451e+6 , 50857
• 546814. , 4.05401e+6 , 50854
• 546830. , 4.05362e+6 , 50852

where the values are easting, northing, and IGRF (nT).

Running the code, the equation for the surface is:

IGRF = 27562.4 + 2.32373e-3 (Easting) + 5.43193e-3 (Northing)

The error is less than 1 nT at each of the 30 points were IGRF was determined using the USGS program.

The IGRF correction to the data was done in Arc/Info on a point by point basis using the above equation.

IGRF corrected = drift corrected - IGRF correction

This completes the dirft corrections done.

4.0 Results of the The Crater Flat Survey

The Crater Flat survey was made in the southern portion of Crater Flat, a tectonically active alluvial basin of the west side of the Yucca Mountain block and bounded on its western margin by the Bare Mountain fault. The survey area extends south from the two Little Cones, small pyroclastic cones located in the southern part of Crater Flat. These cones are the southernmost in a 12-km long alignment of five Quaternary cinder cones that trends NNE across the valley and includes, Red Cone, Black Cone, and Northern Cone. This alignment is arcuate: the azimuth at the north end of the alignment, between Black Cone and Northern Cone, is approximately 025°; the azimuth at the southern end of the alignment, between the Little Cones and Red Cone is approximately 040°. NE and SW Little Cones are located near the main axis of deposition in Crater Flat Valley on a broad alluvial surface that slopes gently to the south. Faulds et al. (1994) referred to this alluvium as the Quaternary Little Cones Alluvium and described it as fan skirt and low basin remnants of Late Pleistocene to Holocene age. Faulds et al. (1994) report 14C rock varnish ages on alluvial material of this deposit of 6,645±245 and 11,135±105 yBP. Except for active washes, this alluvial surface is the youngest in Crater Flat.

Stamatakos et al. (1996) have recently reviewed the ages of the Little Cones and their relationship to the development of the Crater Flat Basin. The radiometric ages for the Little Cones and other cinder cones in the alignment are probablematic because many of the age determinations yield dates that fall within periods of normal polarity. However, all of the cinder cones in the alignment carry a distinctive reversed magnetic polarity. Stamatakos et al. (1996) concluded that the age of the Little Cones lies somewhere within the upper reversed interval of the Matuyama epoch, but that further resolution of the discrepencies in the radiometric ages is necessary.

Connor et al. (1996) made a ground magnetic map of the Little Cones using a proton-precession magnetometer. They identified a compound lava flow field surrounding the Little Cones, buried beneath a thin veneer of alluvium. Small portions of this lava flow field were mapped using a G-858 magnetometer and the flow edge and thickness were modeled using thin vertically sided polygons, following the computational procedures developed by Plouff (1974). Connor et al. (1996) noted that those ground magnetic surveys did not constrain the southern extent of lava flows from the Little Cones.

A prominent magnetic anomalies in sothern Crater Flat is not associated with mapped basalts. A comparatively large-amplitude anomaly occurs south of the Little Cones (Kane and Bracken, 1983). Crowe et al. (1986) suggested that this anomaly may be produced by basalt. In contrast to the Little Cones and other Quaternary and Pliocene basalts in the region, this anomaly indicates a normal polarity magnetization, suggesting a different time of emplacement (normal polarity chron) than other mapped basalts in Crater Flat.

Basalt crops out south of this anomaly in southernmost Crater Flat. This basalt is mapped as Miocene in age, primarily through assumed correlation with Miocene basalt that crops out further east at the southern end of Crater Flat.

Sample point distribution for the Crater Flat survey is shown in the color figure on the following page (not numbered). Data collection was concentrated to delineate several magnetic features. These are:

•The southern extent of lava flows associated with the Little Cones

•The character of the large-amplitude normal polarity anomaly south of the Little Cones

•The relationship between these features and the mapped basalts in southernmost Crater Flat.

The survey extends from just north of the Little Cones to the topographic margin of the basin on the south. The survey area is bounded on the west by the main Crater Flat road and by the east flank of Black Marble Mountain. The survey was extended far enough to the east to clearly delineate the extent of lava flows from the Little Cones and to bound the large amplitude normal polarity anomaly. The non-drift-corrected magnetic map of the region is shown in the color figure on the following page (not numbered). The data were countoured using a minimum tension gridding algorithm and a grid spacing of 25m.

The extent of the Little Cones lava flows are clearly visible from the distribtuion of short-wavelength, large-amplitude anomalies. These lava flows extend approximately 1.5 km south of the Little Cones, south of the road that crosses southern Crater Flat. Total area of the lava flows is approimately 2.2 km2. This is approximately the same area covered by mapped lava flows associated with Red and Black Cones, 3.0 and 2.6 km^2 , respectively, and Lathrop Wells, 1.9 km^2. An important difference is that the Little Cones lavas flowed well south of the cones compared with the more equant distribution of the lava flow fields around Red and Black cones, indicating depositon on more tilted paleosurface, actually more simialr to Lathrop Wells.

Crater Flat Grnd Magnetic Survey, 1996

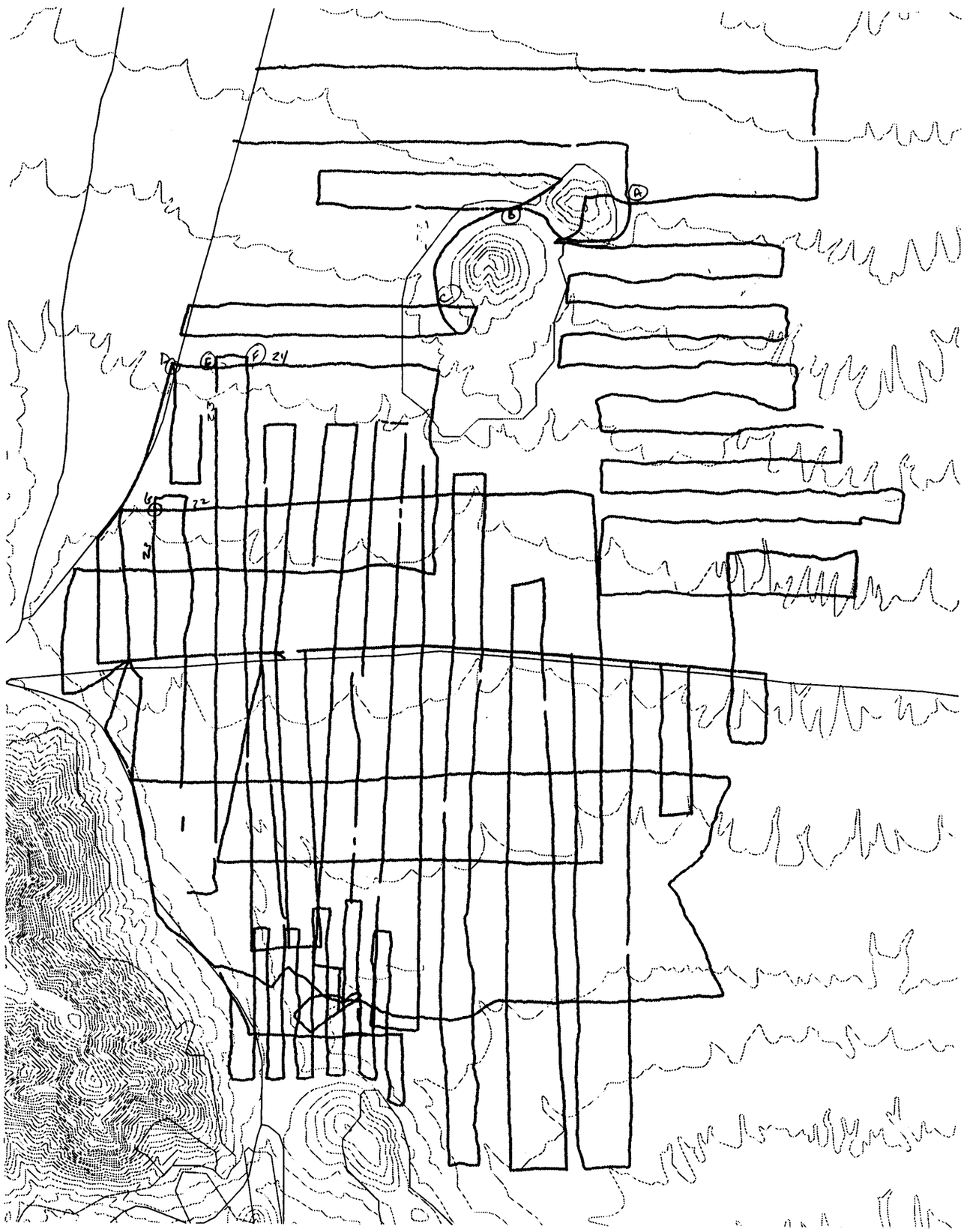

Scale: 15000
Sammantha Magsino / 15 Jul 96 17:56:54 Monday

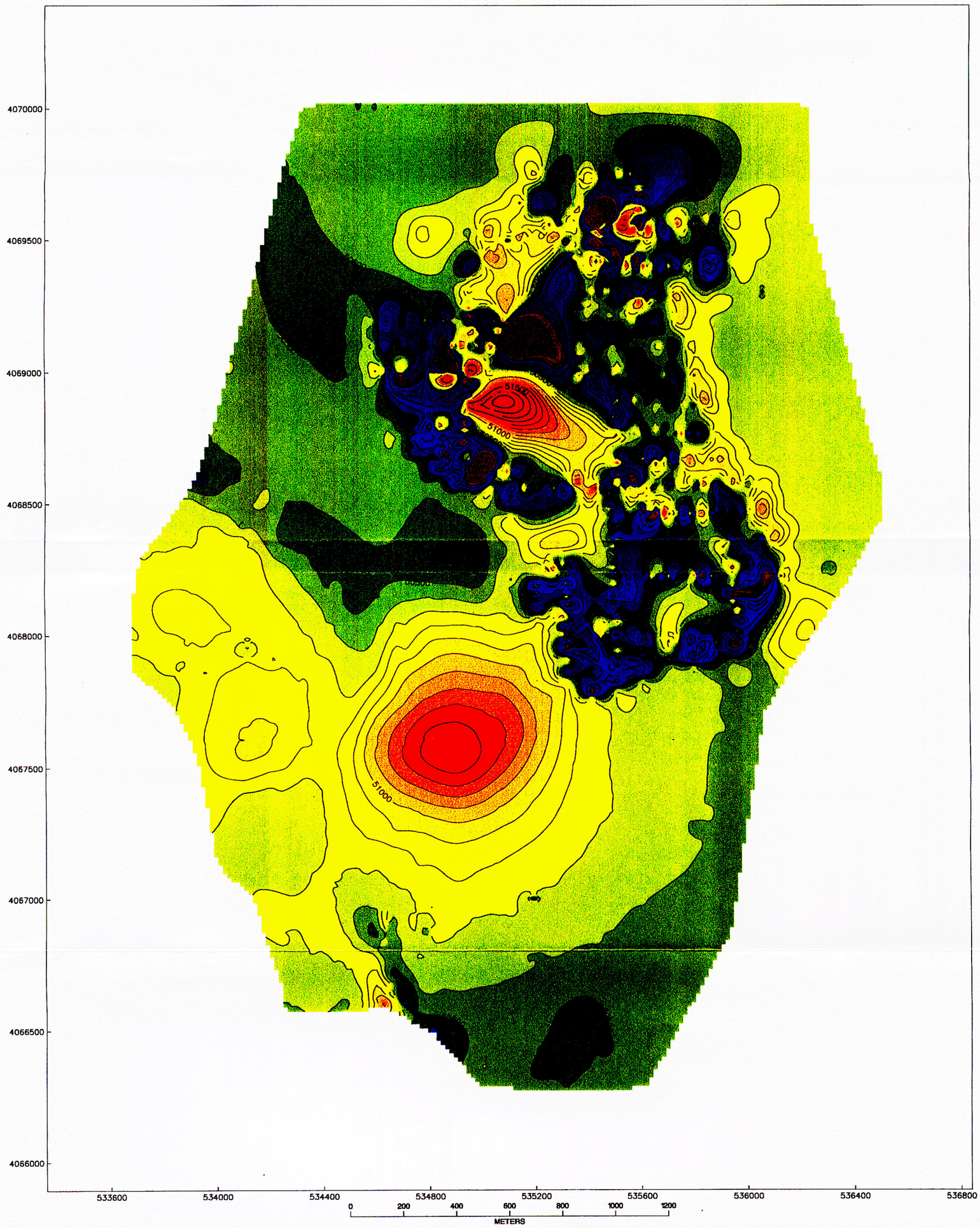
4070000
4069500
4069000
4068500
4068000
4067500
4067000
4066500
4066000
51500
51000
51000
533600
534000
534400
534800
535200
535600
536000
536400
536800
0
200
400
600
800
1000
1200
METERS

It is interesting to note that the aeromagnetic map suggests the presence of this anomaly, but the flight elevation so strongly attenuates the anomaly that it is not easily distinguishable from the longer wavelength normal polarity anomaly to the southwest.The large-amplitude positive anomaly identified on the aeromagnetic maps is located 2 km south of SW Little Cone. Detailed ground magnetic mapping indicates that this anomaly is comprised of a strong positive and comapratively weak negative anomaly located north of the positive, consistent with a normal magnetic polarity and steep inclination. The maximum positive and negative values are separated by 900 m and the peak-to-peak amplitude of the anomaly is 1150 nT. The negative portion of the anomaly is truncated by anomalies associated with the Little Cones lava flows (Figure 9 on page 20).

FIGURE 9. .N-S traverse across the magnetic anomaly

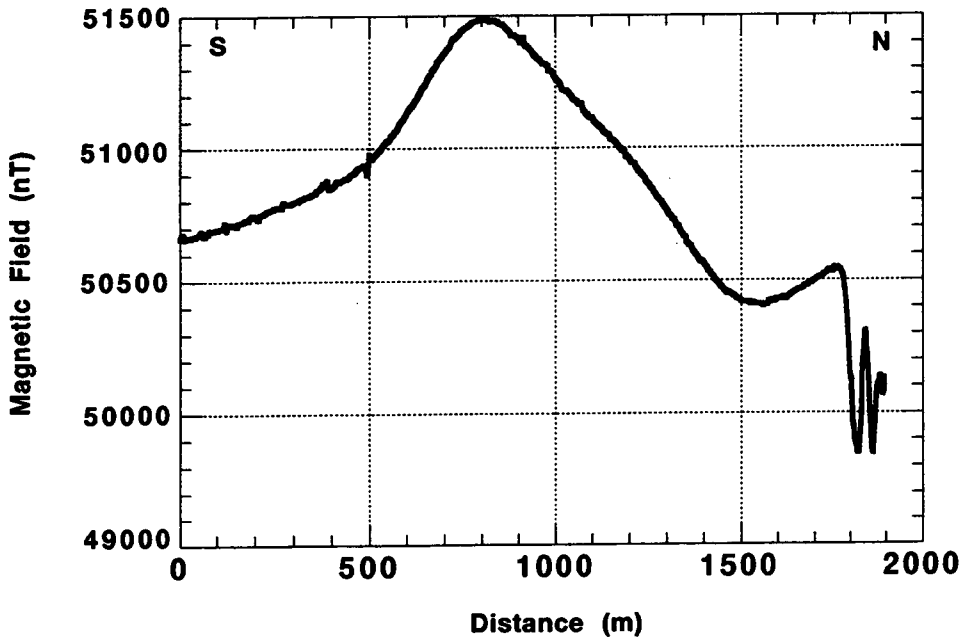

Preliminary models suggest that the normal polarity anomaly is the result of highly magnetized rock buried in alluvium at depths of 150-200 m. In preliminary models we have used remanent magnetizations of 1-2 A/m with declination of 0° and inclination of 60°. These data are most easily modeled using a thin (less than 40 m thick) tabular body that is roughly circular in shape with a diameter of 750-850 m. The fit is improved by thickening this body slightly toward its center. Such a model is consistent with a basaltic origin of the anomaly. The size and shape of the causativie body, although indeterminate, is consistent with a buried lava flow, thickening slightly toward the vent area.

The third magnetic feature on the map is a linear set of dominantly negative anomalies in the southern portion of the map area. These anomalies trend with an azimuth of 150°. The amplitude of the anomaly varies along strike, but is commonly 350 nT measured from peak-to-peak and the wavelength of the anomaly is less than 200 m. An E-W profile across the anomaly is shown in Figure 10 on page 21.

FIGURE 10. E-W profile across a buried dike in southern crater Flat

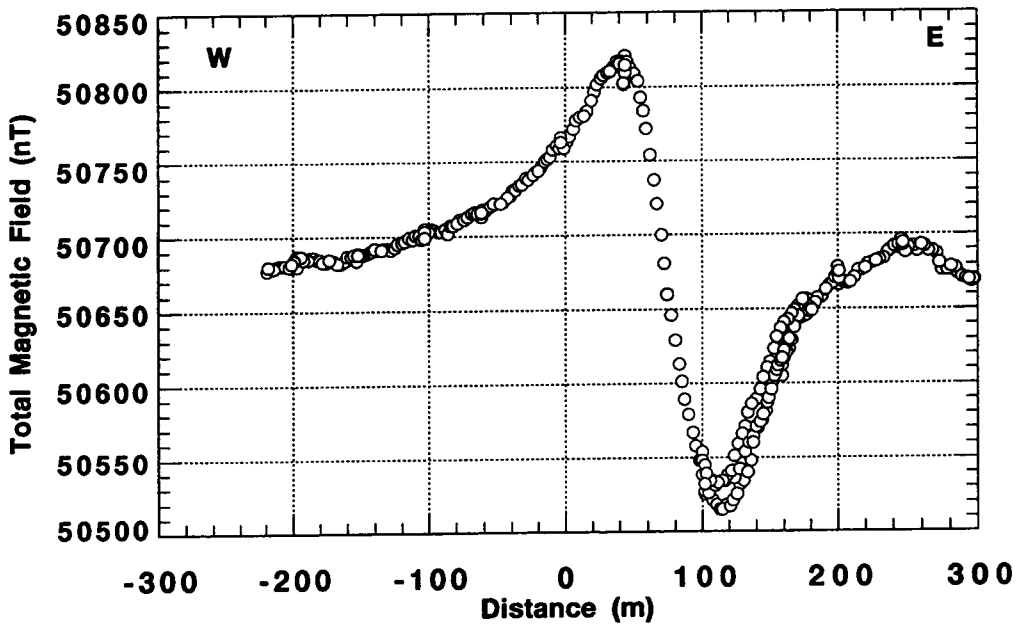

5.0 Direction Determination of the Southern Crater Flat Basalts

Field samples were drilled for collection with a 2.5 cm diameter core drill and analyzed to determine their polarity at the University of Michigan Department of Geological Sciences paleomagnetics laboratory. Samples were trimmed into 2.5 cm long specimens at the lab. Natural Remanent Magnetizations (NRMs) were measured on a spinner-magnetometer to determine their "in field" magnetization. The specimens were then thermally demagnetized to remove any present day field overprint which they may carry. Site M3 yielded an NRM of 143.5°, -83.0° (k = 437.1, a95 = 2.7°) and M4 yielded an NRM of 124.3°, -31.5° (k = 19.2, a95 = 13.0°). As the primary objective was to determine polarity, the thermal demagnetization steps were quite large and were 100, 200,

300, 400, and 475 degrees. The specimens from site M3 acted similarly during demagnetization yielding a mean direction of 146.7°, -65.8° (k = 93.8, a95 = 5.8°). The mean direction for site M4 was 128.3°, -42.5° (k = 25.0, a95 = 10.5°). Site M4 however had a more wide-spread distribution of NRMs than site M3 and the individual specimen directions migrated in different trends during demagnetization. Thus it was determined that a great circle analysis of these trends be performed. The results showed that the intersection of the great circles clustered at 146.6°, -59.3° with a mean angular deviation of 14.1° . This is in good agreement with the direction for site M3 and lies just outside of the a95 error cone of confidence for site M3. Had site M3 been demagnetized further, the directions for both sites may have coincided as the directions for site M3 are following a trend of shallowing inclination. Although the specimens were not heated to their unblocking temperatures, their recent age along with their lack of a significant overprint, the great circle analyses of site M4 specimens, and the general agreement between sites M3 and M4, the directions obtained can be considered good results.

These results are useful because the anomaly shown in Figure 10 on page 21 can be modeled using a dike of declination 120-140° and inclination of -45°.

6.0 Amargosa Desert Anomaly A

Sample locations for the Amargosa Desert survey are shown on the color figure on the following page (attached and not numbered).

High-resolution ground magnetic mapping of anomaly A reveals that this anomaly is actually a composite of four individual magnetic bodies. The polarity of these anomalies indicate that three of the anomalies are associated of reversely magnetized rocks and the fourth anomaly is associated with normally magnetized rocks.

The map pattern of the anomalies and their ampolitudes indicate that these anomalies are most likely associated with basalt buried at shallow depths.The three reversely magnetized bodies are distributed along a 4 km NE trending alignment parallel to the Quaternary Crater Flat alignment.

The normally polarized body is located 3.5 km SSE of Lathrop Wells cinder cone and is colinear with the elongation of this cone.

Amargosa Grnd Magnetic Survey, 1996

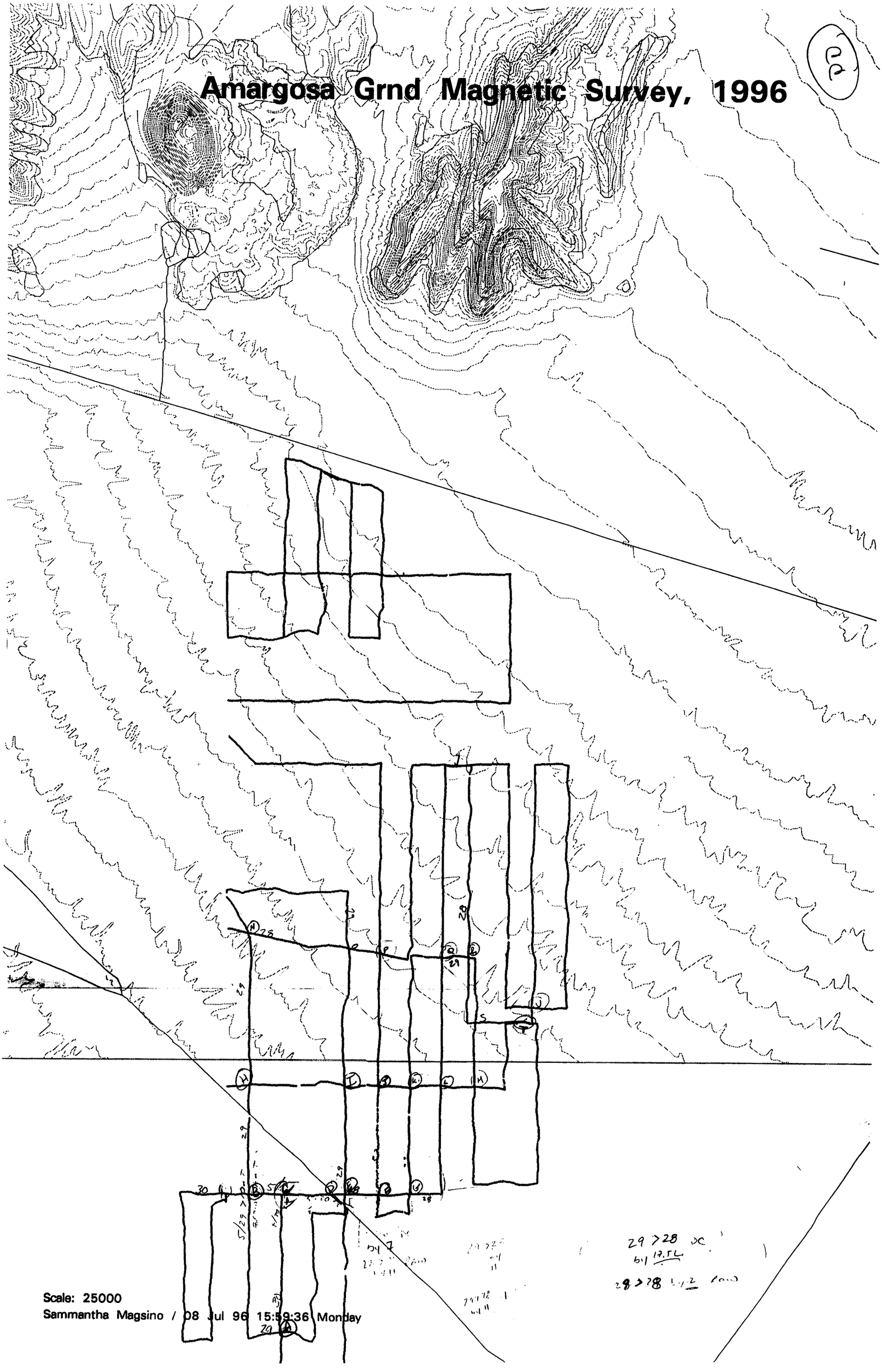

Scale: 25000
Sammantha Magsino / 08 Jul 96 15:59:36 Monday

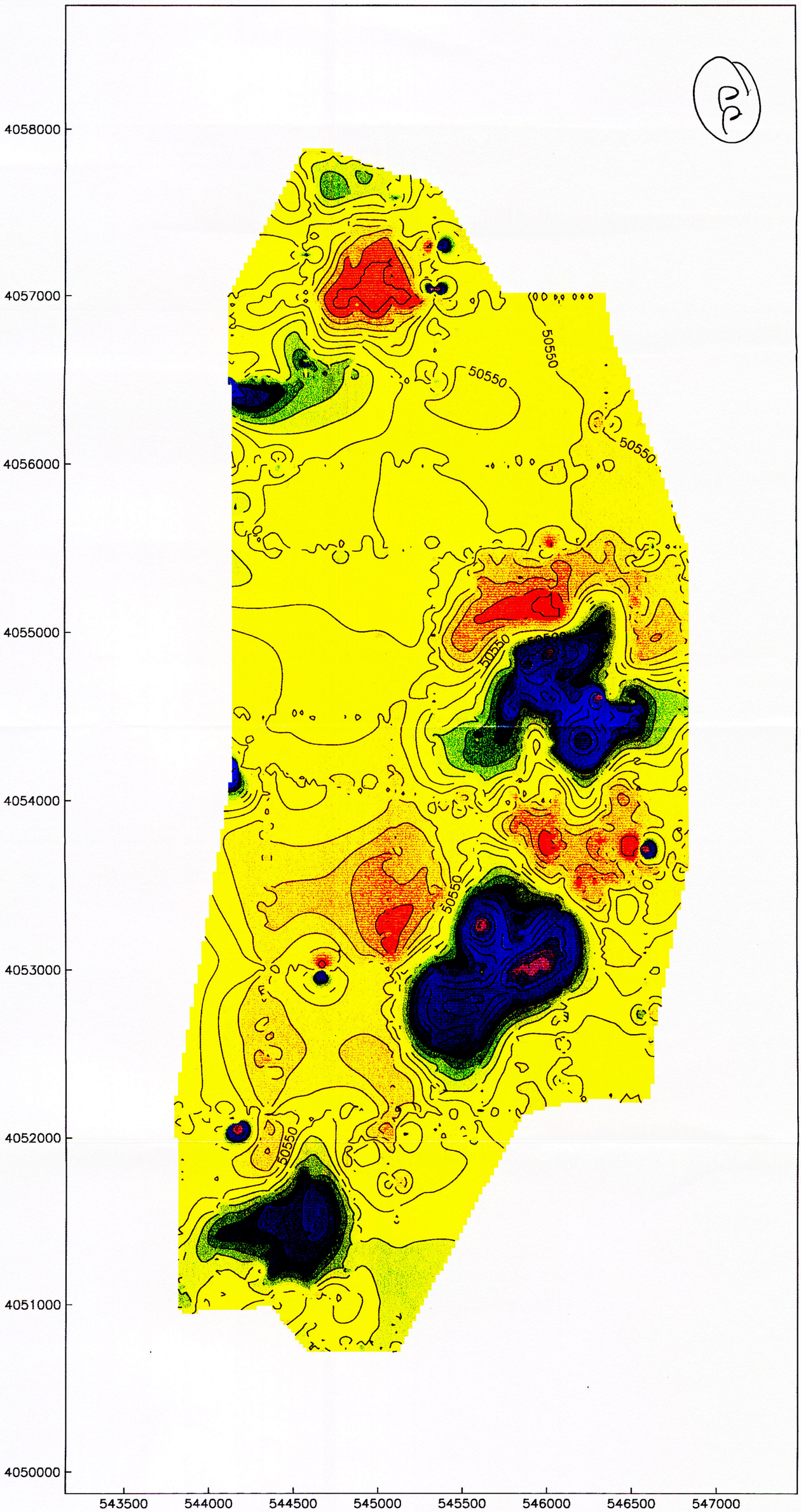
4058000
4057000
4056000
4055000
4054000
4053000
4052000
4051000
4050000
543500
544000
544500
545000
545500
546000
546500
547000
50550
50550
50550
50550
50550
50550

Hilbert Transform in 2D

Chuck Connor

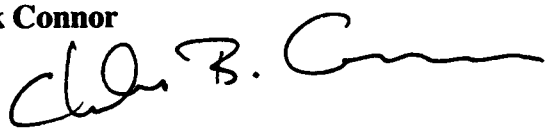

A solution is calculated for the automatic interpretation of 2D magnetic bodies using the techniques developed by Nabighian. This involves processing magnetic profile data using the Hilbert Transform.

1.0 Introduction

Several methods exist for processing magnetic profile data with the goal of inferring subsurface geometry in a relatively automatic manner. These methods include calculation by Werner deconvolution, inverse solution using the Marquardt algorithm, and use of the Hilbert Transofrm. The goal here is to implement a scheme for calculating the location and depth to edges of magnetic bodies using the Hilbert transform.

This technique was introduced by Nabighian (The analytic signal of two-dimensional magnetic bodies with polygonal cross-section: its propoerties and use for automated anomaly interpretation, Geophysics 37: 507-517; mments on the analytic signal of two-dimensional magnetic bodies with polygonal cross-section, Geophysics 39: 85-92).

The basic idea behind this technique is to automatically calculate properiteis, such as lateral extent and depth, of magnetized bodies directly from the observed total field profile. Nabighian does this in 2D for a polygonal shaped body, essentially using the solution first proposed by Talwani.

$$\Delta M(x) = 2kFc\sin d\left[(\theta_1 - \theta_2)\cos\phi + \sin\phi\ln\frac{r_1}{r_2}\right]$$

where $\Delta M(x)$ is the total magnetic field; k is the susceptibility, F is the Earth's magnetic field, c is 1 - $\cos^2 i \sin^2 A$, ϕ is $2I$ - d- 90, i is the inclination of the Earth's field, A is

the declination of the field, θ and r are geometric terms, and d is the dip of the body. $\tan I = \tan i / (\cos A)$.

The above equation is differentiated with repsect to horizontal distance x letting the body extend to infinite depth and

$$T(x) = \frac{\partial(\Delta M)}{\partial(x)} = 2kFc\sin d\left[\frac{(h-y)\cos\phi + x\sin\phi}{(h-y)^2 + x^2}\right]$$

The vertical derivative can be defined by differentiating the solution with respect to y:

$$T_1(x) = \frac{\partial(\Delta M)}{\partial(y)} = 2kFc\sin d\left[\frac{x\cos\phi + (h-y)\sin\phi}{(h-y)^2 + x^2}\right]$$

2.0 Assumptions made in the model

The following program was used to calculate the magnetic anomaly associated with a buried prism. This is the algorithm by Rao and Babu.

```
•OPEN #1: name "magN1", create newold
•ERASE #1
•!
•
•set window 0,1024,-1000,1000
•!print "input the width (a1,a2)"
•!input a1,a2
•LET a1 = 400.0001
•LET a2 = 700.001
•
•!print "input the length (b1,b2)"
•!input b1,b2
•
•LET b1 = -10300.00001
•LET b2 = 10600.50001
•
•!print "input the depth (h1,h2)"
•!input h1,h2
•
•LET h1 = 50
•LET h2 = 10000
•
•!print "Input the angle from north, in degrees"
•!input thet
```

```
•
•LET thet = 0
•LET thet = thet *pi/180
•
•
•!Print "Input the inclination and declination of the Earth's field"
•!print "I,D"
•!input I,D
•LET I = 25
•LET d = 0
•LET I = I*pi/180
•LET D = D*pi/180
•
•LET p = cos(I)*cos(D-thet)
•LET q = cos(I)*sin(D-thet)
•LET r = sin(I)
•
•!print "input the inclination and declination of the vector of magnetization"
•!input Io,Do
•!print "input the intensity of magnetization"
•!input EI
•
•LET Io = 25
•LET Do = 0
•LET EI = 100
•LET Io = Io*pi/180
•LET Do = Do*pi/180
•
•LET L = cos(Io)*cos(Do-thet)
•LET M = cos(Io)*sin(Do-thet)
•LET N = sin(Io)
•
•LET g1 = EI*(M*r + N*q)
•LET g2 = EI*(L*r + N*p)
•LET g3 = EI*(L*q + M*p)
•LET g4 = EI*(N*r - M*q)
•LET g5 = EI*(N*r - L*p)
•
•
•!let y = 35
•FOR k1  = 1 to 1024
•
•     LET x = k1
•     LET y = 500
•
•     LET xp = x*cos(thet) + y *sin(thet)
•     LET yp = -x*sin(thet) + y*cos(thet)
•
•     LET ap1 = a1-xp
•     LET ap2 = a2 -xp
```

```
•       LET bp1 = b1 - yp
•       LET bp2 = b2 - yp
•
•       LET r1 = sqr(ap1^2 + bp1^2 + h1^2)
•       LET r2 = sqr(ap1^2 + bp1^2 + h2^2)
•       LET r3 = sqr(ap2^2 + bp1^2 + h1^2)
•       LET r4 = sqr(ap2^2 + bp1^2 + h2^2)
•       LET r5 = sqr(ap1^2 + bp2^2 + h1^2)
•       LET r6 = sqr(ap1^2 + bp2^2 + h2^2)
•       LET r7 = sqr(ap2^2 + bp2^2 + h1^2)
•       LET r8 = sqr(ap2^2 + bp2^2 + h2^2)
•
•       LET f1 = (r2+ap1)*(r3+ap2)*(r5+ap1)*(r8+ap2)/
((r1+ap1)*(r4+ap2)*(r6+ap1)*(r7+ap2))
•       LET f2 = (r2+bp1)*(r3+bp1)*(r5+bp2)*(r8+bp2)/
((r1+bp1)*(r4+bp1)*(r6+bp2)*(r7+bp2))
•       LET f3 = (r2+h2)*(r3+h1)*(r5+h1)*(r8+h2)/((r1+h1)*(r4+h2)*(r6+h2)*(r7+h1))
•       LET f4 = atn(ap2*h2/(r8*bp2))-atn(ap1*h2/(r6*bp2))-atn(ap2*h2/
(r4*bp1))+atn(ap1*h2/(r2*bp1))-atn(ap2*h1/(r7*bp2))+atn(ap1*h1/
(r5*bp2))+atn(ap2*h1/(r3*bp1))-atn(ap1*h1/(r1*bp1))
•       LET f5 = atn(bp2*h2/(r8*ap2))-atn(bp2*h2/(r6*ap1))-atn(bp1*h2/
(r4*ap2))+atn(bp1*h2/(r2*ap1))-atn(bp2*h1/(r7*ap2))+atn(bp2*h1/
(r5*ap1))+atn(bp1*h1/(r3*ap2))-atn(bp1*h1/(r1*ap1))
•
•       LET T = g1*log(f1) + g2*log(f2) + g3*log(f3) + g4*(f4) + g5*(f5)
•
•  print #1: T
•  plot x,t
•NEXT k1
•
•
•END
```

```
•
•! This program calculates the Hilbert transofrm
•! for a line of data using the 2D solution
•! of Nabighian (1972), The Analytic Signal
•! of two-dimensional magnetic bodies with
•! polygonal cross-section: its propoerties and
•! use in automated anomaly interpretation, Geophysics
•! vol. 37: 507-517.
•
•LIBRARY "realft"
•LIBRARY "four1"
•
•! in this simple example the profile is assumed
```

```
•! to be 1024 units long, nn = 1024
•! the distance between between measurements
•! is 1 unit, delta_dist = 1
•
•set window 0, 1024,0,1
•let delta_dist = 1
•LET nn = 1024
•LET n = nn/2  ! n must be an integer power of 2
•
•! the array mag contains the
•! original magnetic data (total
•! field)
•! the array t contains the horizontal
•! gradient of the magnetic field
•! the array a contains the amplitude squared
•! analytic signal
•
•DIM mag(1024), t(1024), a(1024), v(1024)
•
•!open the file containing the array of
•! total field magnetic values
•open #1: name "magN1"
•do while more #1
•let kt = kt + 1
•input #1: mag(kt)
•loop
•let kt = 0
•
•open #2: name "hilbert.out", create newold
•erase #2
•
•!find the horizontal gradient
•For i = 1 to nn-1
•let t(i) = (mag(i+1) - mag(i))/delta_dist
•next i
•let t(nn) = t(nn-1)
•
•
•!calculate the forward fourier
•! transform for a single real function
•! realft is a Numerical Recipes subroutine
•! that calculates the Fourier Transform for a real
•! series. The routine replaces t with the positive
•! half of the Fourier transform
•LET isign = 1  !forward fft
•CALL realft (t(), n, isign)
•
•FOR i = 3 to nn
•   let t(i) = 2*t(i)
•NEXT i
```

```
•
•
•LET isign = -1
•CALL four1 (t(), n, isign)
•
•let kt = 0
•FOR i = 1 to  nn - 1 step 2
•   let kt = kt + 1
•   let a(kt)  = t(i)*t(i) +  t(i+1)*t(i+1)  !input the real array
•   let v(kt) = t(i+1)
•NEXT i
•
•
•let maxa = -1e30
•let mina = 1e30
•
•For i = 1 to nn-1
•let t(i) = (mag(i+1) - mag(i))/delta_dist
•next i
•let t(nn) = t(nn-1)
•
•
•for i = 1 to nn
•if a(i) > maxa then let maxa = a(i)
•if a(i) < mina then let mina = a(i)
•next i
•!
•for i = 1 to nn
•let a(i) = (a(i) - mina)/(maxa-mina)
•plot 2*i,a(i);
•print #2: 2*i, mag(i), t(i), a(i), v(i)
•
•if a(i) => .49 and a(i) < .51 then
•print 2*i, a(i)
•end if
•
•if a(i) => .79 and a(i) < .81 then
•print 2*i, a(i)
•end if
•
•next i
•
•plot
•
•end
```

July 15, 1996

Probability Abstract for GSA

Chuck Connor

An abstract based on probability work was submitted to the Geological Socieity of America

INTEGRATING STRUCTURAL MODELS INTO PROBABILISTIC VOLCANIC HAZARD ANALYSES: AN EXAMPLE FROM YUCCA MOUNTAIN, NV (a)

CONNOR, C.B., STAMATAKOS, J., FERRILL, D.A., and HILL, B.E., Center for Nuclear Waste Regulatory Analyses, Southwest Research Institute, 6220 Culebra Rd., San Antonio, Tx, 78238, cconnor@swri.edu.

The proposed high-level nuclear waste repository at Yucca Mountain (YM) is located within an active volcanic field characterized by small-volume basaltic eruptions and low recurrence rates. Because the eruption of basalt through a nuclear waste repository could be deleterious, the probability and consequences of volcanic activity must be evaluated for a performance period which may be as long as 10^6 yr. In order to bound probability, we integrate structural models into nonhomogeneous Poisson analyses of the spatio-temporal pattern of volcanism on local and regional scales. Locally, short alignments of cones near YM trend NNE parallel to faults that have high dilation-tendency. These alignments include five Quaternary cones 8-15 km west of YM. New results from high-resolution ground magnetic surveys reveal a parallel alignment of three (Pliocene?) volcanic centers buried in alluvium 20-25 km south of the proposed repository. The effect of fault dilation tendency on probability is estimated quantitatively by mapping the density of high-dilation tendency faults across the region, normalized by overall fault density, and weighing probability by this distribution. Because high dilation-tendency faults bound and penetrate the YM block, the probability of volcanic eruptions increases at YM compared to models that do not include structural control. An excellent regional correlation is identified between Miocene Quaternary basalts and faults with large offsets, illustrated by the amplitude of the horizontal gravity gradient. Incorporating these regional geophysical data in nonhomogeneous Poisson models results in a broad NNW trend in probability distribution across Crater Flat and YM. A structural model in which Crater Flat is a half-graben above the listric Bare Mountain

fault can explain the superposition of local NNE trending vent alignments on an overall NNW trend. Cumulatively, integration of structural models suggests probabilities of volcanic eruptions at the YM repository of 10^{-8}–10^{-7}/ yr.

(a) Work supported by the U.S. Nuclear Regulatory Commission (Contract NRC-02-93 005). This work is an independent product of the Center for Nuclear Waste Regulatory Analyses and does not necessarily reflect the views or regulatory position of NRC.

Key Words: Volcanic hazards, probability, structure, Yucca Mountain

NRC initially approved the above abstract, then suggested the following changes after the abstract was submitted.

INTEGRATING STRUCTURAL MODELS INTO PROBABILISTIC VOLCANIC HAZARD ANALYSES: AN EXAMPLE FROM YUCCA MOUNTAIN, NV (a)

CONNOR, C.B., STAMATAKOS, J., FERRILL, D.A., and HILL, B.E., Center for Nuclear Waste Regulatory Analyses, Southwest Research Institute, 6220 Culebra Rd., San Antonio, Tx, 78238, cconnor@swri.edu.

The proposed high-level nuclear waste repository at Yucca Mountain (YM) is located within a volcanic field characterized by small-volume basaltic eruptions and low recurrence rates. Probability and consequences of future volcanic events at YM are being evaluated because they are key input parameters for assessing the performance of the proposed repoistory. In order to bound probability, we integrate structural models into nonhomogeneous Poisson analyses of the spatio-temporal pattern of volcanism on local and regional scales. Locally, short alignments of cones near YM trend NNE parallel to faults that have high dilation-tendency. These alignments include five Quaternary cones 8-15 km west of YM. New results from high-resolution ground magnetic surveys reveal a parallel alignment of three (Pliocene?) volcanic centers buried in alluvium 20-25 km south of the proposed repository. The effect of fault dilation tendency on probability is estimated quantitatively by mapping the density of high-dilation tendency faults across the region, normalized by overall fault density, and weighing probability by this distribution. Because high dilation-tendency faults bound and penetrate the YM block, the probability of volcanic eruptions increases at YM compared to models that do not include structural control. An excellent regional correlation is identified between Miocene-Quaternary basalts and faults with large offsets, illustrated by the amplitude of the horizontal gravity gradient. Incorporating these regional geophysical data in nonhomogeneous Poisson models results in a broad NNW trend in probability distribution across Crater Flat and YM. A structural model in which Crater Flat is a half-graben above the listric Bare Mountain fault can explain the superposition of local NNE trend-

ing vent alignments on an overall NNW trend. Cumulatively, integration of structural models suggests probabilities of volcanic eruptions at the YM repository of 10^{-8}–10^{-7}/yr.

(a) Work supported by the U.S. Nuclear Regulatory Commission (Contract NRC-02-93 005). This work is an independent product of the Center for Nuclear Waste Regulatory Analyses and does not necessarily reflect the views or regulatory position of NRC.

Volcanic hazards, probability, structure, Yucca Mountain

ADDITIONAL INFORMATION FOR SCIENTIFIC NOTEBOOK #: 115E
(4 of 17)

Document Date:	07/15/1996
Availability:	Southwest Research Institute® Center for Nuclear Waste Regulatory Analyses 6220 Culebra Road San Antonio, Texas 78228
Contact:	Southwest Research Institute® Center for Nuclear Waste Regulatory Analyses 6220 Culebra Road San Antonio, Texas 78228 Attn.: Director of Administration 210.522.5054
Data Sensitivity:	■"Non-Sensitive" □ Sensitive □"Non-Sensitive - Copyright" ☐ Sensitive - Copyright
Date Generated:	07/15/1996
Operating System: (including version number)	Windows
Application Used: (including version number)	NA
Media Type: (CDs, 3 1/2, 5 1/4 disks, etc.)	1 - 3 ½ disk
File Types: (.exe, .bat, .zip, etc.)	dnl
Remarks: (computer runs, etc.)	Media contains: Drift Correction Data.

PROCEDURE FOR SAMPLING RN IN THE FIELD

Chuck Connor

Chuck B. Connor

November 18, 1996

PROCEDURE FOR SAMPLING RN IN THE FIELD

Chuck Connor

Chuck B. Connor

A PROCEDURE FOR MEASURING RADON GAS CONCENTRATION IN SOILS IN THE FIELD IS PROVIDED.

Scientific Notebook No. 115

1.0 Overview

Applies To FY96-97 work BFC 2/5/97

The E-perm electret radon monitoring system is used. The E-perm system consists of three components: 1) an electrostatically charged teflon disk, called an electret, which ionizes in the presence of radiation in the presence of radon decay, (ii) an ion chamber of fixed volume into which the electret is loaded, (3) a reader to measure the change in the voltage on the electret. Details on the operation procedure are in: E-perm System Manual for the Use of Electret Passive Environmental Radon Monitor (E-Perm) system for Measurement of Radon in Air, RadElect, Inc., Fredricksburg, Md, USA.

This is an EPA approved procedure for sampling radon.

In our experiments, an S type ion chamber is used with long term electrets. The following illustration, taken from E-perm System Manual for the Use of Electret Passive Environmental Radon Monitor (E-Perm) system for Measurement of Radon in Air, RadElect, Inc., Fredricksburg, Md, USA, illustrates the S chamber in open and closed positions.

FIGURE 1. S Chamber electret

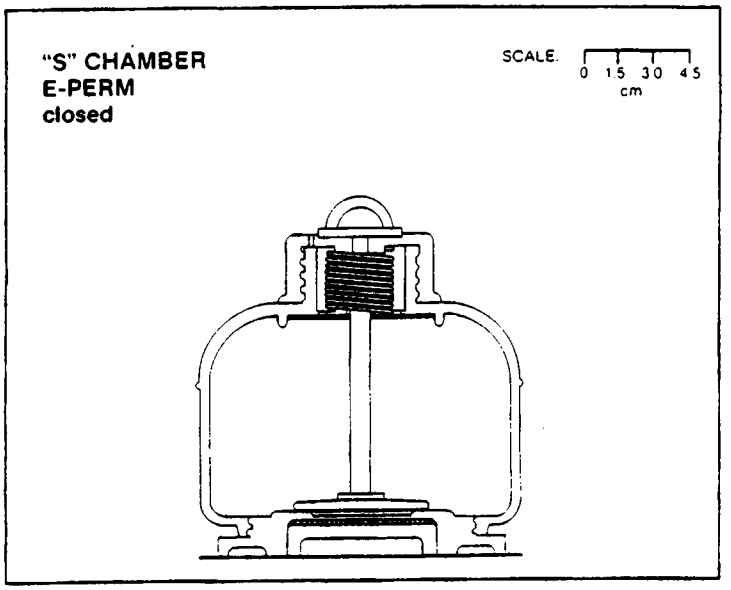

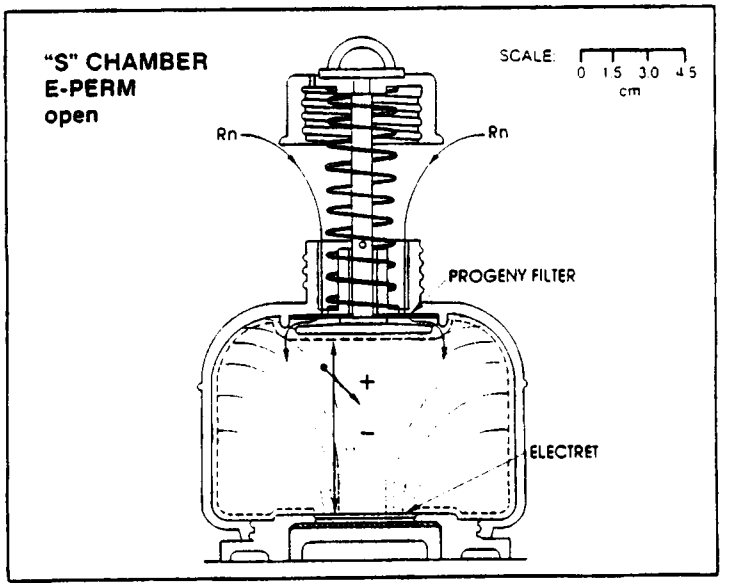

2.0 Setting up the Radon Station

The following steps are taken during set up of the field Rn station

1. After radon site selection (based on geology) a hole is dug 40 cm deep in the soil or volcanic ash.
2. A 50 cm long 4 inch diameter PVC tube is placed vertically in the hole. The hole is backfilled about the tube.
3. The ion chamber with the electret is opened and suspended in the PVC tube by a string. The chamber is suspended approximately 45 cm below the top of the PVC tube (just above the base of the tube).
4. The tube is covered with a plastic bag and sealed with duct tape to minimize atmospheric mixing.
5. The time at which the tube is sealed is noted.

FIGURE 2. Radon Station schematic

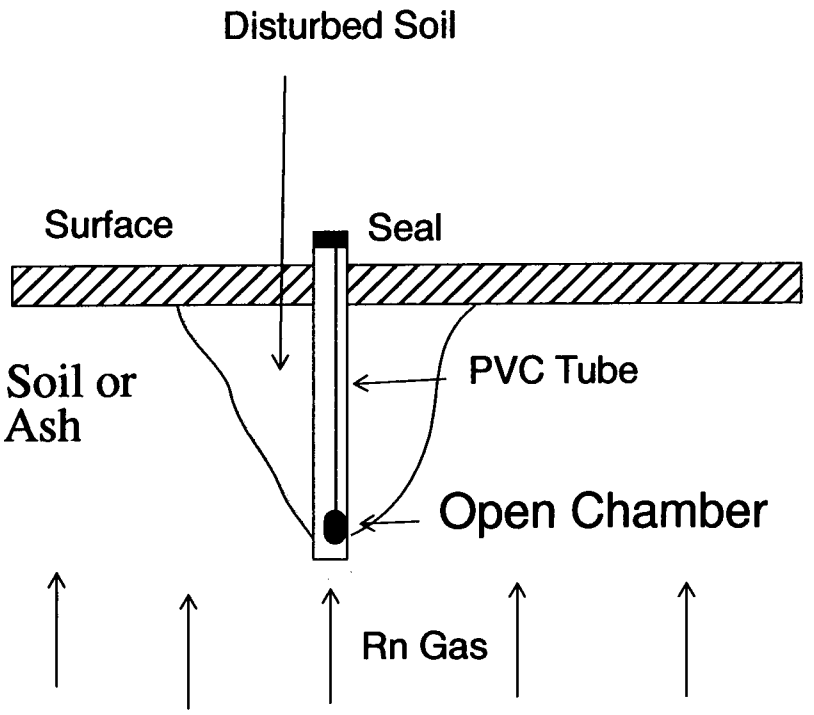

3.0 Collecting Measurements

The following steps are taken to collect Rn measurements

1. Return to the Rn station at least 24 hr and up to 1 week after the station is installed.
2. Break the seal on the PVC tube
3. The ion chamber is extracted from the tube and the electret is checked for moisture. Presence of moisture will zero the voltage.
4. Electret voltage is read using an electret voltage reader.
5. Electret voltage and time are recorded.
6. Chamber is placed back in the tube and the tube is resealed.

4.0 Reducing Measurements

The following steps are taken to convert measured volts into picoCuries per liter (pC/l)

1. The duration of exposure is determined
2. the change in voltage during this time is determined
3. the calibration factor is calculated using the formula

CF = A * B * (I + F)/2

where CF = calibration factor

A = 1.8864 (specific to long term electrets)

B = 0.000638 (specific to long term electrets)

I = initial voltage

F = Final Voltage

4. The radon concentration is calculated

Rn (pC/l) = (I-F)/(CF*T)

where Rn = radon concentration

CF = calibration factor

I = the initial electret voltage

F = the final electret voltage

T = time exposure in days

5. A barometric pressure calculation is made to adjust for the expected number of molecules of gas in the chamber at 3000 m elevation (the elevation of Paricutin). Each measurement is multiplied by a factor of 1.2. This is constant over the survey area within the precision of measurements.

These calculations are done on a spreadsheet.

5.0 Calibration

Elecrets are not calibrated. Once the voltage reading on the electret drops below 200 V, the electret is discarded.

The reader is factory calibrated. To determine if the reader is in calibration, procedures are followed as outlined in: E-perm System Manual for the Use of Electret Passive Environmental Radon Monitor (E-Perm) system for Measurement of Radon in Air, RadElect, Inc., Fredricksburg, Md, USA.

Specifically, the voltages of a set of two factory calibrated electrets are read using the electret reader before and after measuring each set of field measurement electrets. The voltage on the two factory set electrets must be within 2V of factory specifications.

Several steps are taken in the field to insure quality results

First, two radon detectors are deployed in the same PVC tube in some cases. When both chambers in the tube are open, readings should be within several picoCuries per liter for both detectors. In practice one or two such stations are deployed in a given survey.

Second, two radon detectors are deployed in the same PVC tube, with one chamber open and the other closed. The closed chamber should read zero voltage change. If not, the likely cause of the voltage drop is high background gamma radiation.

Third, tubes can be deployed close to one-another. In this case readings between tubes should be relatively close, except in areas of high radon flux, which tend to have high variability as well.

FIGURE 3. Checking Radon

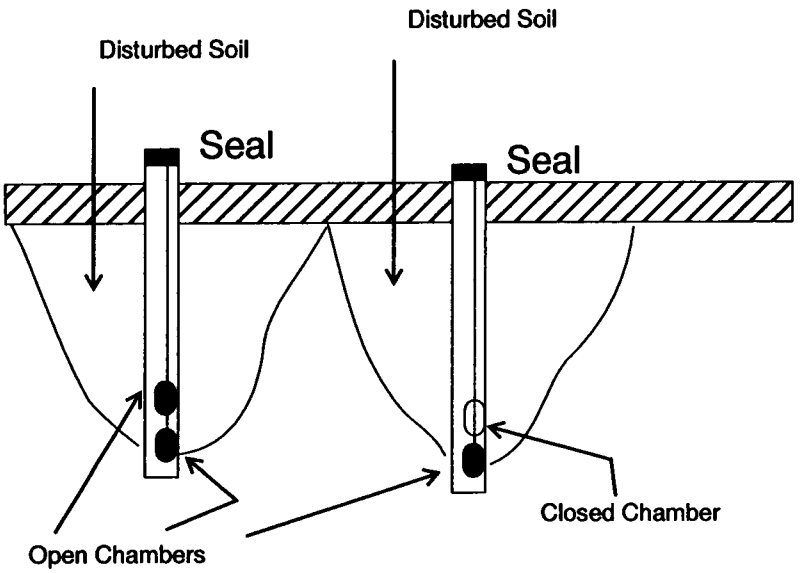

Temperatures at the Cone 1004 Dike

Chuck Connor

Abstract: The 1975 Tolbachik eruption resulted the formation of three basaltic cinder cones. During this eruption, shallow dike injection into a nearby cinder cone, Cone 1004, caused deformation and slumping of the cone. In 1995, temperatures, measured at 2-m-depth, electromagnetic anomalies, and geologic units were mapped on the slump block. These data reveal details about the cooling rates of a shallow dike in the slump block, including (1) measured temperatures up to 475°C and exceeded 200°C along a 160-m-long and 30-m-wide zone that trends oblique to bedding; (2) a low resistivity zone at 80 m depth that may delimit a larger intrusion beneath the shallow dike; and (3) a dry-out zone extending 15-20 m from the axis of the thermal anomaly and a condensation zone beyond this dry-out zone, characterized by steaming ground and high convective heat flux. Analytic models indicate that the surprisingly high temperatures persist because of the low thermal diffusivity of the scoria into which the dike is injected, a direct result of the scoria's high porosity. Two-phase nonisothermal flow models suggest the observed patterns of dry-out and condensation are expected for small volume fractions of water in the scoria (≤10%). Thus, field observations from Tolbachik provide a graphic example of the roles of rock thermophysical properties and water in the unsaturated zone on rates of dike cooling.

1.0 INtroduction

One-dimensional time-transient heat conduction models have been used to show that dike cooling is a rapid process, essentially complete after a few months or years in the case of a large dike (e.g., McBirney, 1984; Delaney, 1987). The Great Tolbachik Fissure Eruption (GTFE), Kamchatka Russia, occurred in 1975 and resulted in the formation of three closely spaced cinder cones and eruption of 0.45 km3 (dense rock equivalent) of basalt. Igneous dikes and dike segments intruded to extremely shallow depths during the eruption, sometimes hundreds of meters from active vents. This remarkable geologic event provides a unique opportunity to measure the surface thermal anomalies produced by dikes twenty years after their injection, and to observe patterns in water vapor convection and the extent of dry-out zones associated with these thermal anomalies.

Observations at the Tolbachik cinder cones elucidate the complexity of dike cooling in the natural environment. At Tolbachik, these complexities include significant variation in the thermo-physical properties of rock, the presence of a deeper, larger intrusion, the development of dry-out zones around the dike which potentially limit alteration despite long cooling times, and other perturbations in water saturation in the rock surrounding the dike intrusion. Observations from Tolbachik are used to evaluate the relative importance of these complicating factors using numerical models that consider the thermo-physical rock properties and two-phase transport of water in the unsaturated zone, in addition to simple heat conduction (Lichtner, 1996; Seth and Lichtner, 1996).

Three of the cinder cones formed during the GTFE creating a N-trending alignment. These three cones and their associated lava flows erupted between July and September, 1975 (Magus'kin et al., 1983; Doubik et al., 1995). The three cinder cones extend an alignment that includes three older (Holocene) cinder cones that are south of the 1975 cones. The northernmost of these Holocene cinder cones is Cone 1004. A period of dike injection during the eruption of the first of the 1975 cones, Cone I, resulted in deformation of Cone 1004. This deformation was manifest in the slow uplift and lateral sliding of a coherent block of Cone 1004 scoria during a period of several days in late July and August, 1975. The ENE-trending valley between the slump block and Cone 1004 is approximately 240 m long and 100 m wide (Figure 1). Pit craters opened at the base of Cone I and along the axis of the valley during deformation. This activity was followed by the formation of a lava vent, 285 m from the base of Cone I, slightly offset from the axis of the valley (Figure 1). This vent is at an elevation 45 m below the current floor of the valley. By 31 July, the lava flows issuing from the vent were more than 1 km long.

2.0 Measured Temperatures of a Cooling Dike

Ground temperatures on the Cone 1004 slump block were mapped in July and August, 1995. This was accomplished by measuring temperatures at depths of 1.75–2.0 m, using 2-m-long probes and ungrounded chromel-alumel thermocouples. Probes were allowed to equilibrate in thermal areas for 1-2 hours. Measurements were made at 310 stations on the slump block, concentrating on one 160-m-long and 50-m-wide thermal zone (Figure 1, color figure on next unnumberd page). Ground temperatures outside of thermal areas were typically 0-23°C. Temperatures within the thermal zone were as high as

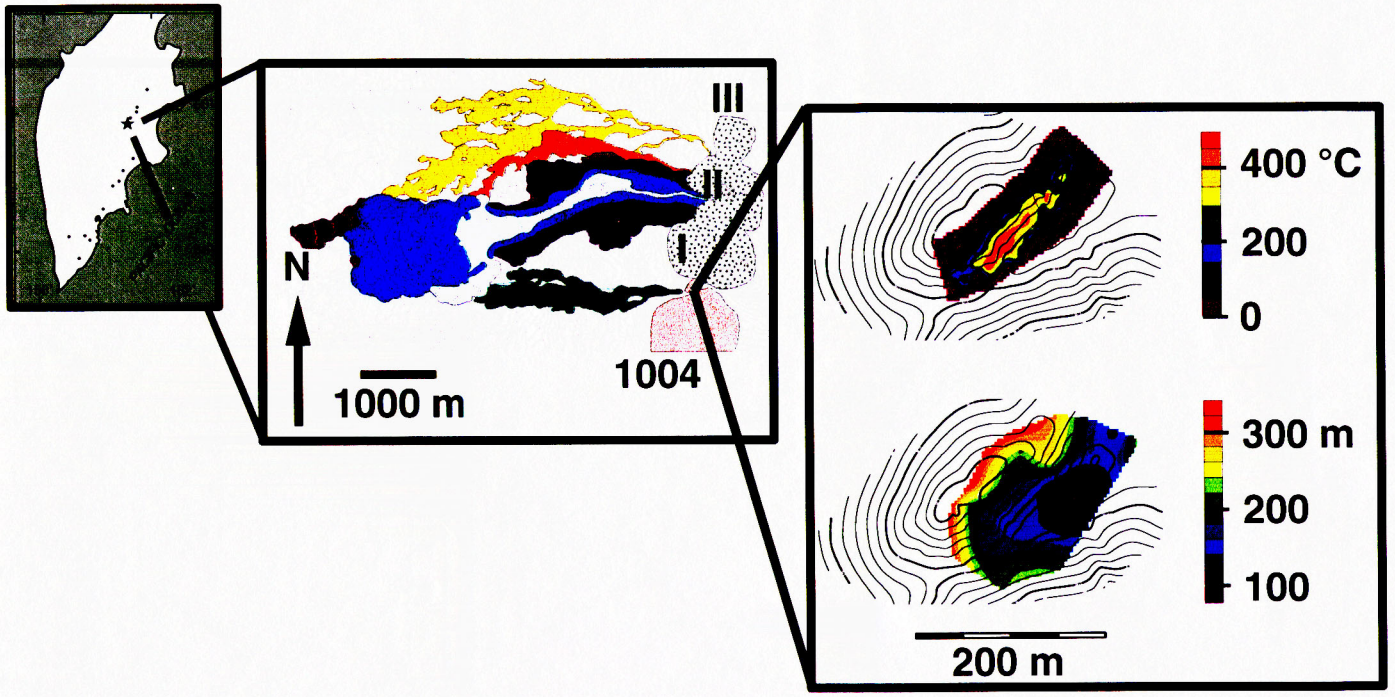
III
II
I
N
1000 m
1004
400 °C
200
0
300 m
200
100
200 m

475°C. The scoria at the surface over the thermal zone is typically 100-120°C and remains dry during rain. Small patches of steaming ground occur 20-30 m upslope from the axis of the thermal anomaly; during rainfall these patches grow is area and emit steam.

Table 1: Temperatures measured at 1.75-2 m depth

UTM East	UTM North	Temperature (°C)
577652.9375	6170793.5	2
577648.375	6170803.5	10
577646.125	6170808.5	151
577643.4375	6170813.5	174
577641.0625	6170818.5	131
577638.5	6170823.5	113
577636.3125	6170828.5	105
577633.6875	6170833.5	52
577631.5	6170838.5	45
577629.0625	6170843.5	39
577626.9375	6170848	38
577624.5	6170853	36
577663.125	6170796	37
577660.4375	6170801	37
577657.75	6170806	32
577655.125	6170810.5	46
577652.5	6170815.5	139
577649.8125	6170820	354
577647.125	6170825	224
577644.4375	6170830	92
577641.875	6170834.5	54

Table 1: Temperatures measured at 1.75-2 m depth

UTM East	UTM North	Temperature (°C)
577639.0625	6170839.5	52
577636.5	6170844	37
577633.75	6170849	37
577631.0625	6170854	52
577671.5	6170802	28
577668.875	6170807	110
577666.1875	6170811.5	328
577663.6875	6170816.5	468
577661.0625	6170821.5	445
577658.375	6170826	352
577655.6875	6170831	275
577653	6170836	146
577650.4375	6170840.5	60
577647.6875	6170845.5	52
577680.375	6170808	0
577677.75	6170812.5	16
577674.9375	6170817.5	219
577672.375	6170822	413
577669.6875	6170827	420
577667	6170832	441
577664.3125	6170837	306
577661.6875	6170841.5	273
577659.0625	6170846.5	136
577656.375	6170851.5	53
577653.8125	6170856	49

Table 1: Temperatures measured at 1.75-2 m depth

UTM East	UTM North	Temperature (°C)
577651.0625	6170861	38
577648.5	6170865.5	32
577688.9375	6170814	0
577686.4375	6170819	50
577683.75	6170823.5	149
577681.0625	6170828.5	386
577678.5	6170833	460
577675.8125	6170838	475
577673.1875	6170843	420
577670.5625	6170847.5	350
577667.875	6170852.5	273
577665.125	6170857	108
577662.4375	6170862	50
577697.75	6170820	16
577695.0625	6170824.5	236
577692.375	6170829.5	348
577689.75	6170834.5	405
577687.125	6170839	447
577684.4375	6170844	412
577681.8125	6170848.5	452
577679.125	6170853.5	382
577676.5	6170858.5	267
577673.8125	6170863	32
577671.125	6170868	75
577706.3125	6170826	

Table 1: Temperatures measured at 1.75-2 m depth

UTM East	UTM North	Temperature (°C)
577703.75	6170830.5	28
577701.0625	6170835.5	73
577698.375	6170840	290
577695.6875	6170845	352
577693.125	6170850	390
577690.375	6170854.5	412
577687.75	6170859.5	384
577685.1875	6170864	323
577682.4375	6170869	217
577679.8125	6170874	113
577677.125	6170878.5	52
577674.4375	6170883.5	42
577671.75	6170888.5	37
577715.125	6170831.5	11
577712.5	6170836.5	14
577709.75	6170841	44
577707.0625	6170846	146
577704.375	6170851	285
577701.75	6170855.5	354
577699.0625	6170860.5	408
577696.375	6170865.5	380
577693.75	6170870	325
577691.0625	6170875	205
577688.4375	6170880	56
577685.6875	6170884.5	42

Table 1: Temperatures measured at 1.75-2 m depth

UTM East	UTM North	Temperature (°C)
577683.0625	6170889.5	33
577680.4375	6170894	40
577723.5625	6170837.5	23
577721	6170842.5	6
577718.4375	6170847.5	19
577715.6875	6170852	77
577713.125	6170857	248
577710.4375	6170861.5	353
577707.6875	6170866.5	409
577705.0625	6170871	404
577702.375	6170876	373
577699.6875	6170881	302
577697.0625	6170885.5	232
577694.375	6170890.5	31
577691.6875	6170895.5	50
577689.0625	6170900	48
577686.4375	6170905	44
577732.375	6170843.5	7
577729.6875	6170848.5	3
577727.0625	6170853	16
577724.375	6170858	40
577721.75	6170863	67
577719.0625	6170867.5	231
577716.5	6170872.5	279
577713.6875	6170877	352

Table 1: Temperatures measured at 1.75-2 m depth

UTM East	UTM North	Temperature (°C)
577711	6170882	382
577708.375	6170887	330
577705.625	6170892	268
577703	6170896.5	43
577700.3125	6170901.5	48
577697.6875	6170906	48
577695.0625	6170911	48
577740.9375	6170849.5	9
577738.4375	6170854.5	7
577735.625	6170859.5	23
577733.0625	6170864	18
577730.4375	6170868.5	52
577727.6875	6170873.5	167
577725.0625	6170878.5	262
577722.4375	6170883	237
577719.8125	6170888	364
577717.125	6170892.5	402
577703.75	6170916.5	48
577749.4375	6170855.5	4
577746.4375	6170860	5
577743.625	6170863.5	11
577740.3125	6170868.5	35
577737.4375	6170872.5	68
577733.875	6170877.5	169
577730.8125	6170882	368

Table 1: Temperatures measured at 1.75-2 m depth

UTM East	UTM North	Temperature (°C)
577727.5625	6170886.5	423
577724.5625	6170891	406
577721.5625	6170895	238
577718.125	6170899.5	51
577714.875	6170904	51
577711.875	6170908	23
577708.625	6170913	4
577755.625	6170864.5	19
577751.875	6170869.5	24
577748.5	6170873	12
577744.5625	6170877	28
577741.25	6170881	190
577737.5625	6170885	271
577734	6170889	295
577730.6875	6170893	398
577727.0625	6170897	384
577723.4375	6170901	188
577716.125	6170909	50
577712.375	6170912.5	2
577762.25	6170873.5	11
577758.0625	6170877.5	13
577753.8125	6170881	14
577750.5	6170884	35
577746.5	6170887.5	59
577742.1875	6170891	124

Table 1: Temperatures measured at 1.75-2 m depth

UTM East	UTM North	Temperature (°C)
577738.25	6170895	314
577734.3125	6170898.5	5
577768.375	6170882	5
577764.5625	6170885.5	7
577760.75	6170889	5
577756.75	6170893	11
577752.6875	6170896.5	20
577748.8125	6170900	25
577745.1875	6170903	109
577741.3125	6170906.5	294
577737.3125	6170910	296
577733.375	6170913.5	197
577729.1875	6170917.5	49
577725.3125	6170921	47
577721.625	6170924	4
577774.625	6170891	4
577770.9375	6170894.5	14
577766.625	6170898	15
577762.8125	6170901.5	28
577759	6170905	50
577755	6170908.5	103
577750.8125	6170912	215
577747	6170915.5	284
577743.25	6170919	253
577739.3125	6170922.5	146

Table 1: Temperatures measured at 1.75-2 m depth

UTM East	UTM North	Temperature (°C)
577735.125	6170926	56
577731.5	6170929.5	42
577727.375	6170933	42
577719.5	6170940.5	2
577781.3125	6170899.5	12
577777.25	6170903.5	7
577773.0625	6170907	12
577769.25	6170910.5	24
577764.9375	6170914	91
577761.5625	6170917	27
577729.5	6170945.5	4
577787.375	6170908.5	6
577783.625	6170912	11
577779.4375	6170915.5	13
577775.5625	6170919	43
577771.75	6170922.5	61
577767.8125	6170926	67
577764	6170929.5	59
577759.9375	6170933	65
577756	6170936.5	63
577752.125	6170940	36
577747.9375	6170943.5	21
577732.125	6170957.5	10
577793.75	6170917	12
577785.8125	6170924.5	14

Table 1: Temperatures measured at 1.75-2 m depth

UTM East	UTM North	Temperature (°C)
577778.25	6170931.5	56
577770.4375	6170939	55
577766.5625	6170942.5	17
577762.75	6170945.5	20
577758.6875	6170949.5	18
577743	6170963.5	25
577643.5	6170790	26
577641.375	6170795.5	89
577639.375	6170801	230
577637.5	6170806	274
577635.375	6170811.5	152
577633.3125	6170816.5	130
577631.3125	6170821.5	129
577629.3125	6170827	45
577627.25	6170832	42
577625.25	6170837	37
577623.1875	6170842.5	69
577621.1875	6170847.5	52
577633.6875	6170787	34
577631.875	6170792.5	33
577630.25	6170798	59
577628.6875	6170803	45
577627.0625	6170808.5	173
577625.375	6170814	151
577623.875	6170819	67

Table 1: Temperatures measured at 1.75-2 m depth

UTM East	UTM North	Temperature (°C)
577622.1875	6170824.5	35
577620.75	6170830	39
577619.0625	6170835	34
577617.5625	6170840.5	34
577615.9375	6170846	43
577624.375	6170783	21
577622.6875	6170789	24
577621.375	6170794	41
577619.5	6170800	34
577617.9375	6170805	57
577616.375	6170811	53
577614.875	6170816	31
577613.125	6170821.5	14
577611.6875	6170826.5	18
577610.1875	6170832	19
577608.5	6170837.5	22
577607	6170843	0
577733.4375	6170942	50
577737.5625	6170938.5	59
577741.5	6170935	62
577745.5625	6170931.5	266
577749.375	6170928	283
577757.4375	6170920.5	8

This thermal anomaly is interpreted to be produced by a shallow cooling igneous dike because of its high temperature, the length and narrow width of the anomaly, its relationship to the lava vent SW of the slump block, and because the anomaly trends oblique to bedding exposed in the slump block. A similar high temperature zone was identified on the slopes of Cone 1004 and is also inferred to be a dike, although this thermal anomaly was not mapped in detail. CC

The following figure (Figure 1 on page 23) shows the mapped geology of the slump block. The thermal anomaly cuts across this observed bedding in the slump block.

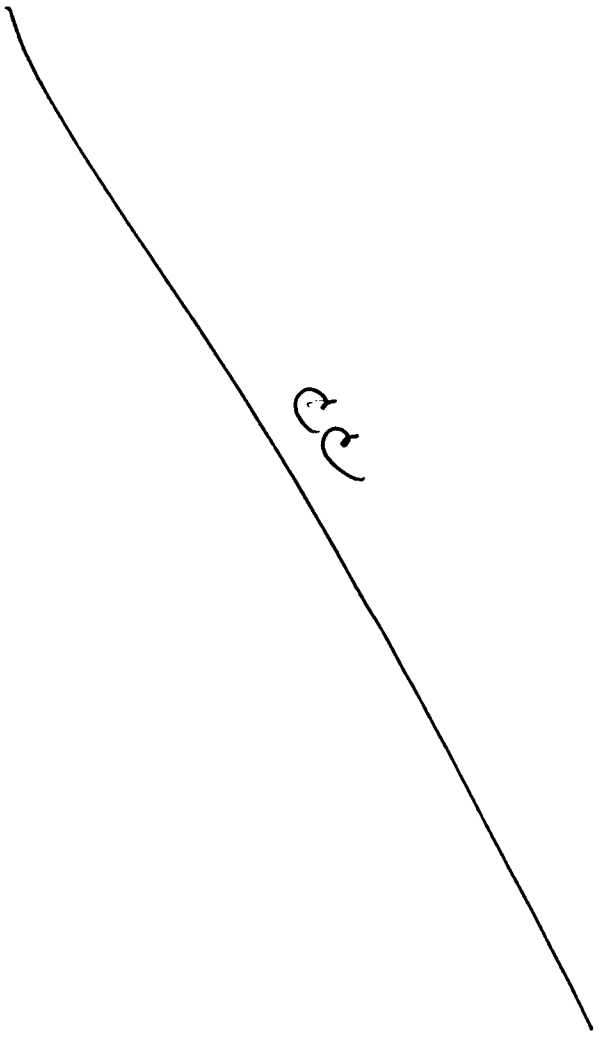

3.0 Elevation Measurements

Table 2: Topographic Measurements on the Cone 1004 Slump Block

UTM East	UTM North	Elevation (m)
577652.9	6170794	99
577650.8	6170799	100
577648.4	6170804	101
577646.1	6170809	103
577643.4	6170814	106
577641.1	6170819	109
577638.5	6170824	112
577636.3	6170829	115
577633.7	6170834	116
577631.5	6170839	121
577629.1	6170844	125
577626.9	6170848	128
577689.5	6170748	126
577684.4	6170758	121
577679.1	6170767	115
577673.8	6170777	109
577668.4	6170787	103
577663.1	6170796	100
577657.8	6170806	101
577655.1	6170811	102
577652.5	6170816	104
577649.8	6170820	107

Table 2: Topographic Measurements on the Cone 1004 Slump Block

UTM East	UTM North	Elevation (m)
577647.1	6170825	110
577644.4	6170830	113
577641.9	6170835	115
577639.1	6170840	117
577636.5	6170844	120
577633.8	6170849	122
577631.1	6170854	124
577628.4	6170859	129
577671.5	6170802	99
577666.2	6170812	100
577663.7	6170817	101
577661.1	6170822	104
577658.4	6170826	107
577655.7	6170831	110
577653	6170836	117
577650.4	6170841	117
577647.7	6170846	120
577706.9	6170760	126
577701.6	6170770	119
577696.3	6170779	113
577690.9	6170789	107
577685.8	6170798	101
577680.4	6170808	96

Table 2: Topographic Measurements on the Cone 1004 Slump Block

UTM East	UTM North	Elevation (m)
577677.8	6170813	98
577674.9	6170818	101
577672.4	6170822	103
577669.7	6170827	106
577667	6170832	109
577664.3	6170837	112
577661.7	6170842	115
577659.1	6170847	118
577656.4	6170852	121
577653.8	6170856	124
577643.2	6170875	129
577637.8	6170885	124
577632.4	6170895	120
577627.1	6170904	116
577621.8	6170914	111
577616.4	6170924	107
577611.1	6170933	102
577605.8	6170943	98
577688.9	6170814	95
577686.4	6170819	95
577683.8	6170824	97
577681.1	6170829	99
577678.5	6170833	101

Table 2: Topographic Measurements on the Cone 1004 Slump Block

UTM East	UTM North	Elevation (m)
577675.8	6170838	104
577673.2	6170843	107
577670.6	6170848	110
577667.9	6170853	113
577665.1	6170857	116
577662.4	6170862	119
577659.8	6170867	121
577657.2	6170872	124
577654.6	6170877	127
577652.6	6170880	129
577651.8	6170882	130
577713.6	6170791	108
577708.4	6170801	102
577703.1	6170810	97
577697.8	6170820	93
577695.1	6170825	94
577692.4	6170830	96
577689.8	6170835	98
577687.1	6170839	101
577684.4	6170844	104
577681.8	6170849	106
577679.1	6170854	109
577676.5	6170859	112

Table 2: Topographic Measurements on the Cone 1004 Slump Block

UTM East	UTM North	Elevation (m)
577673.8	6170863	115
577671.1	6170868	118
577706.3	6170826	92
577703.8	6170831	92
577701.1	6170836	94
577698.4	6170840	96
577695.7	6170845	99
577693.1	6170850	102
577690.4	6170855	105
577687.8	6170860	108
577685.2	6170864	111
577682.4	6170869	114
577679.8	6170874	117
577677.1	6170879	119
577674.4	6170884	123
577671.8	6170889	126
577669.7	6170892	128
577736.1	6170794	112
577731.1	6170803	106
577725.8	6170813	102
577720.4	6170822	96
577715.1	6170832	91
577712.5	6170837	91

Table 2: Topographic Measurements on the Cone 1004 Slump Block

UTM East	UTM North	Elevation (m)
577709.8	6170841	93
577707.1	6170846	95
577704.4	6170851	98
577701.8	6170856	101
577699.1	6170861	104
577696.4	6170866	107
577693.8	6170870	110
577691.1	6170875	113
577688.4	6170880	116
577685.7	6170885	119
577683.1	6170890	122
577680.4	6170894	125
577723.6	6170838	90
577721	6170843	90
577718.4	6170848	92
577715.7	6170852	94
577713.1	6170857	97
577710.4	6170862	100
577707.7	6170867	103
577705.1	6170871	105
577702.4	6170876	108
577699.7	6170881	111
577697.1	6170886	114

Table 2: Topographic Measurements on the Cone 1004 Slump Block

UTM East	UTM North	Elevation (m)
577694.4	6170891	116
577691.7	6170896	120
577689.1	6170900	122
577686.4	6170905	124
577681.1	6170915	121
577675.7	6170924	117
577670.4	6170934	113
577665.1	6170944	109
577659.8	6170953	105
577654.4	6170963	101
577649.1	6170973	97
577777.7	6170762	133
577775	6170767	130
577772.4	6170772	127
577769.7	6170776	125
577767	6170781	122
577764.4	6170786	118
577761.7	6170791	116
577759	6170796	114
577753.7	6170805	107
577751	6170810	105
577748.4	6170815	103
577745.8	6170820	100

Table 2: Topographic Measurements on the Cone 1004 Slump Block

UTM East	UTM North	Elevation (m)
577743.1	6170825	98
577740.4	6170829	96
577737.8	6170834	93
577735.1	6170839	91
577732.4	6170844	89
577729.7	6170849	89
577727.1	6170853	91
577724.4	6170858	94
577721.8	6170863	96
577719.1	6170868	99
577716.5	6170873	102
577713.7	6170877	105
577711	6170882	108
577708.4	6170887	112
577705.6	6170892	115
577703	6170897	118
577700.3	6170902	121
577697.7	6170906	123
577695.1	6170911	125
577792.9	6170773	135
577789.9	6170777	133
577786.8	6170782	129
577783.4	6170787	126

Table 2: Topographic Measurements on the Cone 1004 Slump Block

UTM East	UTM North	Elevation (m)
577780.8	6170791	122
577777.6	6170796	119
577774.7	6170800	116
577771.6	6170805	113
577768.5	6170809	110
577765.4	6170814	108
577762.3	6170819	105
577759.5	6170823	103
577756.3	6170828	100
577753.4	6170832	98
577750.4	6170836	95
577747.3	6170841	93
577744.3	6170846	91
577740.9	6170850	89
577738.4	6170855	88
577735.6	6170860	90
577733.1	6170864	92
577730.4	6170869	95
577727.7	6170874	98
577725.1	6170879	101
577722.4	6170883	104
577719.8	6170888	107
577717.1	6170893	110

Table 2: Topographic Measurements on the Cone 1004 Slump Block

UTM East	UTM North	Elevation (m)
577705.6	6170914	124
577804.7	6170775	133
577801.9	6170779	130
577798.7	6170783	127
577795.7	6170788	124
577792.6	6170792	121
577789.4	6170797	118
577786.4	6170802	115
577783.4	6170806	112
577780.6	6170810	109
577777.3	6170815	106
577774.4	6170819	104
577771.4	6170824	102
577768.4	6170828	100
577765.4	6170833	98
577762.4	6170838	96
577759.1	6170842	94
577755.9	6170847	92
577752.8	6170851	90
577749.4	6170856	88
577746.4	6170860	88
577743.6	6170864	90
577740.3	6170869	92

Table 2: Topographic Measurements on the Cone 1004 Slump Block

UTM East	UTM North	Elevation (m)
577737.4	6170873	95
577733.9	6170878	99
577730.8	6170882	102
577727.6	6170887	105
577724.6	6170891	108
577721.6	6170895	111
577718.1	6170900	115
577807.6	6170788	125
577804.6	6170793	122
577801.8	6170797	120
577798.8	6170802	118
577795.6	6170806	115
577792.5	6170811	112
577789.6	6170815	110
577786.5	6170820	108
577783.4	6170824	105
577780.3	6170829	103
577777.3	6170833	101
577774.3	6170838	100
577771.3	6170842	98
577768.3	6170847	96
577765.1	6170851	94
577762.1	6170856	92

Table 2: Topographic Measurements on the Cone 1004 Slump Block

UTM East	UTM North	Elevation (m)
577759.3	6170860	90
577755.6	6170865	87
577751.9	6170870	88
577748.5	6170873	89
577744.6	6170877	92
577741.3	6170881	95
577737.6	6170885	98
577734	6170889	101
577730.7	6170893	104
577727.1	6170897	107
577723.4	6170901	111
577720	6170905	115
577716.1	6170909	117
577712.4	6170913	120
577708.9	6170917	120
577814.1	6170829	110
577810.3	6170832	108
577806.3	6170836	106
577802.4	6170839	104
577798.4	6170843	102
577794.4	6170846	100
577790.6	6170850	99
577786.4	6170853	97

Table 2: Topographic Measurements on the Cone 1004 Slump Block

UTM East	UTM North	Elevation (m)
577782.3	6170857	95
577778.4	6170860	93
577774.4	6170864	92
577762.3	6170874	86
577758.1	6170878	87
577753.8	6170881	89
577750.5	6170884	92
577746.5	6170888	95
577742.2	6170891	98
577738.3	6170895	101
577734.3	6170899	104
577703.1	6170926	118
577768.4	6170882	86
577764.6	6170886	88
577760.8	6170889	90
577756.8	6170893	90
577752.7	6170897	94
577748.8	6170900	97
577745.2	6170903	100
577741.3	6170907	104
577737.3	6170910	107
577774.6	6170891	86
577770.9	6170895	85

Table 2: Topographic Measurements on the Cone 1004 Slump Block

UTM East	UTM North	Elevation (m)
577766.6	6170898	87
577762.8	6170902	90
577759	6170905	93
577755	6170909	96
577750.8	6170912	99
577747	6170916	102
577743.3	6170919	105
577739.3	6170923	109
577735.1	6170926	112
577731.5	6170930	115
577727.4	6170933	118
577861.1	6170829	103
577845.4	6170843	101
577829.1	6170858	99
577813.1	6170872	95
577797.6	6170886	92
577781.3	6170900	86
577777.3	6170904	84
577773.1	6170907	86
577769.3	6170911	88
577764.9	6170914	91
577761.6	6170917	94
577757.4	6170921	98

Table 2: Topographic Measurements on the Cone 1004 Slump Block

UTM East	UTM North	Elevation (m)
577787.4	6170909	88
577783.6	6170912	88
577779.4	6170916	89
577775.6	6170919	91
577771.8	6170923	94
577767.8	6170926	97
577764	6170930	99
577759.9	6170933	103
577756	6170937	106
577752.1	6170940	108
577747.9	6170944	110
577744.4	6170947	112
577868.3	6170850	101
577852.4	6170865	97
577837.3	6170878	94
577821.4	6170892	92
577805.6	6170907	91
577793.8	6170917	92
577789.9	6170921	92
577785.8	6170925	92
577782.2	6170928	92
577778.3	6170932	94
577774.5	6170935	96

Table 2: Topographic Measurements on the Cone 1004 Slump Block

UTM East	UTM North	Elevation (m)
577770.4	6170939	99
577750.9	6170957	112
577663.5	6170739	125
577659.5	6170749	120
577655.5	6170759	114
577651.5	6170770	108
577647.7	6170780	102
577643.5	6170790	99
577641.4	6170796	100
577639.4	6170801	101
577637.5	6170806	103
577635.4	6170812	106
577633.3	6170817	109
577631.3	6170822	113
577629.3	6170827	116
577627.3	6170832	119
577625.3	6170837	122
577623.2	6170843	124
577621.2	6170848	127
577633.7	6170787	99
577631.9	6170793	101
577630.3	6170798	102
577628.7	6170803	105

Table 2: Topographic Measurements on the Cone 1004 Slump Block

UTM East	UTM North	Elevation (m)
577627.1	6170809	107
577625.4	6170814	110
577623.9	6170819	113
577622.2	6170825	116
577620.8	6170830	119
577619.1	6170835	122
577617.6	6170841	126
577615.9	6170846	128
577640.3	6170730	121
577637	6170741	117
577633.9	6170751	113
577630.6	6170762	109
577627.5	6170773	104
577624.4	6170783	99
577622.7	6170789	100
577621.4	6170794	102
577619.5	6170800	105
577617.9	6170805	108
577616.4	6170811	111
577614.9	6170816	114
577613.1	6170822	117
577611.7	6170827	119
577610.2	6170832	122

Table 2: Topographic Measurements on the Cone 1004 Slump Block

UTM East	UTM North	Elevation (m)
577608.5	6170838	125
577607	6170843	126
577614.7	6170780	99
577609.8	6170797	103
577606.6	6170807	108
577620.9	6170723	118
577617.7	6170734	114
577614.4	6170745	109
577611.4	6170755	103
577608.3	6170766	101
577604.9	6170777	98
577603.1	6170783	99
577601.4	6170788	100
577599.9	6170793	102
577598.4	6170799	104
577596.7	6170804	107
577595.3	6170809	108
577593.6	6170814	110
577591.9	6170820	112
577590.4	6170825	114
577589	6170830	115
577587.2	6170836	116
577585.6	6170766	92

Table 2: Topographic Measurements on the Cone 1004 Slump Block

UTM East	UTM North	Elevation (m)
577586.4	6170784	97
577587.6	6170807	105
577544.6	6170753	81
577551.9	6170772	87
577557.9	6170788	94
577560.6	6170811	102
577572.9	6170820	108
577577.4	6170832	113
577557.6	6170828	103
577539.2	6170824	93
577517.4	6170820	84
577497.9	6170815	77
577542.6	6170897	86
577559.2	6170883	95
577575.3	6170870	105
577591.1	6170856	116
577477.8	6170812	68
577457.9	6170808	61
577697.1	6170936	113
577691.3	6170945	110
577685.8	6170954	106
577679.9	6170963	102
577674.1	6170973	98

Table 2: Topographic Measurements on the Cone 1004 Slump Block

UTM East	UTM North	Elevation (m)
577668.4	6170982	94
577716.3	6170937	119
577728.8	6170949	114

Topographic measurements were made using tape and compass techniques. The data wer elinked to "real-world" UTM coordinates using a hand-held GPS. GPS data were collected at the top of the slump block at 577630N and 6170860E ± 23 m. Elevations are relative, using the saddle in the valley floor as 100 m. Elevations are good to about 1 m.

FIGURE 1. Geology of the slump block

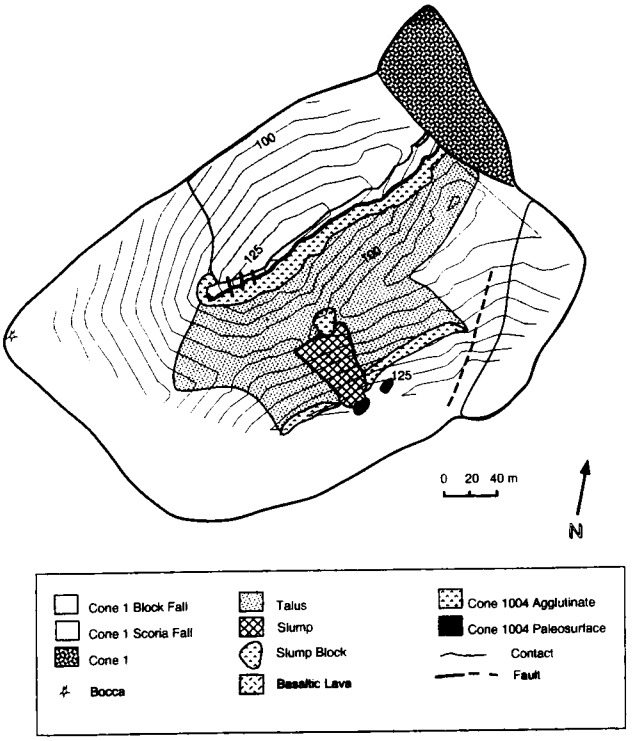

4.0 Electomagnetic data

Electromagnetic (EM) soundings were made to investigate the character of the thermal anomaly at greater depths. Dry or nearly dry scoria has an infinite resistivity (> 10,000) except when heated to temperatures in excess of 600°C. Above 600°C the resistivity of basalt is 1-10 (Rai and Manghnani, 1977; Kauahikaua et al., 1986). Twenty-four EM stations were occupied on the Cone 1004 slump block using a large-loop-source. The results indicate a region of very low resistivity exists at depths of approximately 80-300 m beneath the valley that separates the slump block from Cone 1004 (Figure 1). This EM anomaly is interpreted to indicate the position of a volume of rock heated about 600°C. The depth of this low resistivity anomaly correlates well with the elevation of the lava vent (Figure 1) and this supports the interpretation that the anomaly is produced by a basalt intrusion larger than the map extent of the surface thermal anomaly. The presence of this more voluminous intrusion explains the tremendous deformation asso-

ciated with the formation of the slump block. Thus, the surface thermal anomalies are related to shallow dike that intruded the scoria above this more voluminous intrusion.

Table 3: Electromagnetic Data

UTM East	UTM North	Depth to Conduction Zone (m)
577805.000000	6170927.000000	145
577822.187500	6170921.000000	228
577760.250000	6170944.500000	203
577777.187500	6170938.500000	163
577736.875000	6170946.500000	280
577778.875000	6170906.500000	157
577754.125000	6170886.000000	116
577734.687500	6170864.500000	86
577713.000000	6170846.000000	146
577696.687500	6170825.500000	147
577672.875000	6170818.000000	169
577655.312500	6170810.500000	170
577627.687500	6170797.500000	302
577621.250000	6170833.500000	318
577625.875000	6170850.000000	307
577644.312500	6170872.500000	318
577660.812500	6170908.500000	322
577687.875000	6170928.000000	324
577642.250000	6170851.500000	212
577654.812500	6170864.500000	246

Table 3: Electromagnetic Data

UTM East	UTM North	Depth to Conduction Zone (m)
577679.562500	6170890.000000	219
577697.437500	6170906.000000	222
577728.750000	6170900.000000	257
577675.312500	6170765.000000	218
577704.812500	6170776.500000	235
577736.125000	6170783.500000	215

FIGURE 2. Location of EM stations - from Igor Federchenko, superimposed on topography

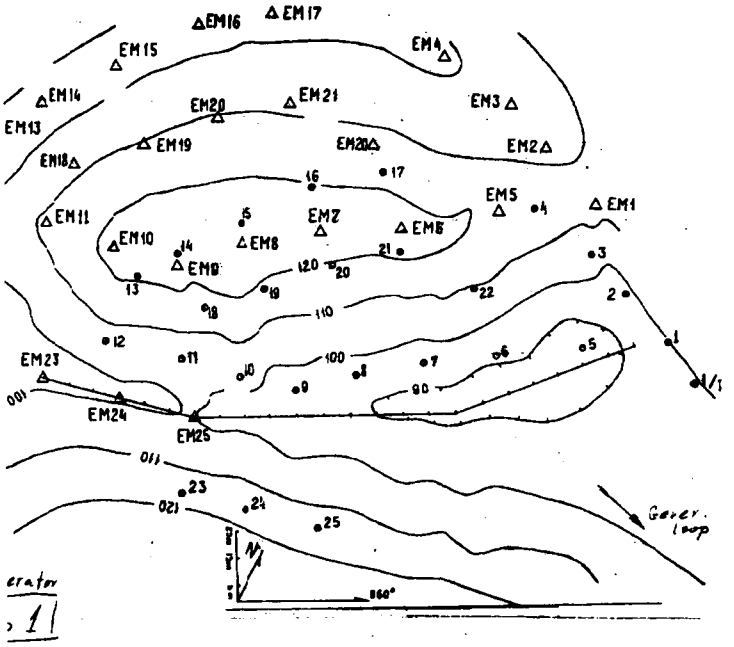

measured by C. Connor

FIGURE 3. Location of Depth to conduction zone, from Igor Federchenko

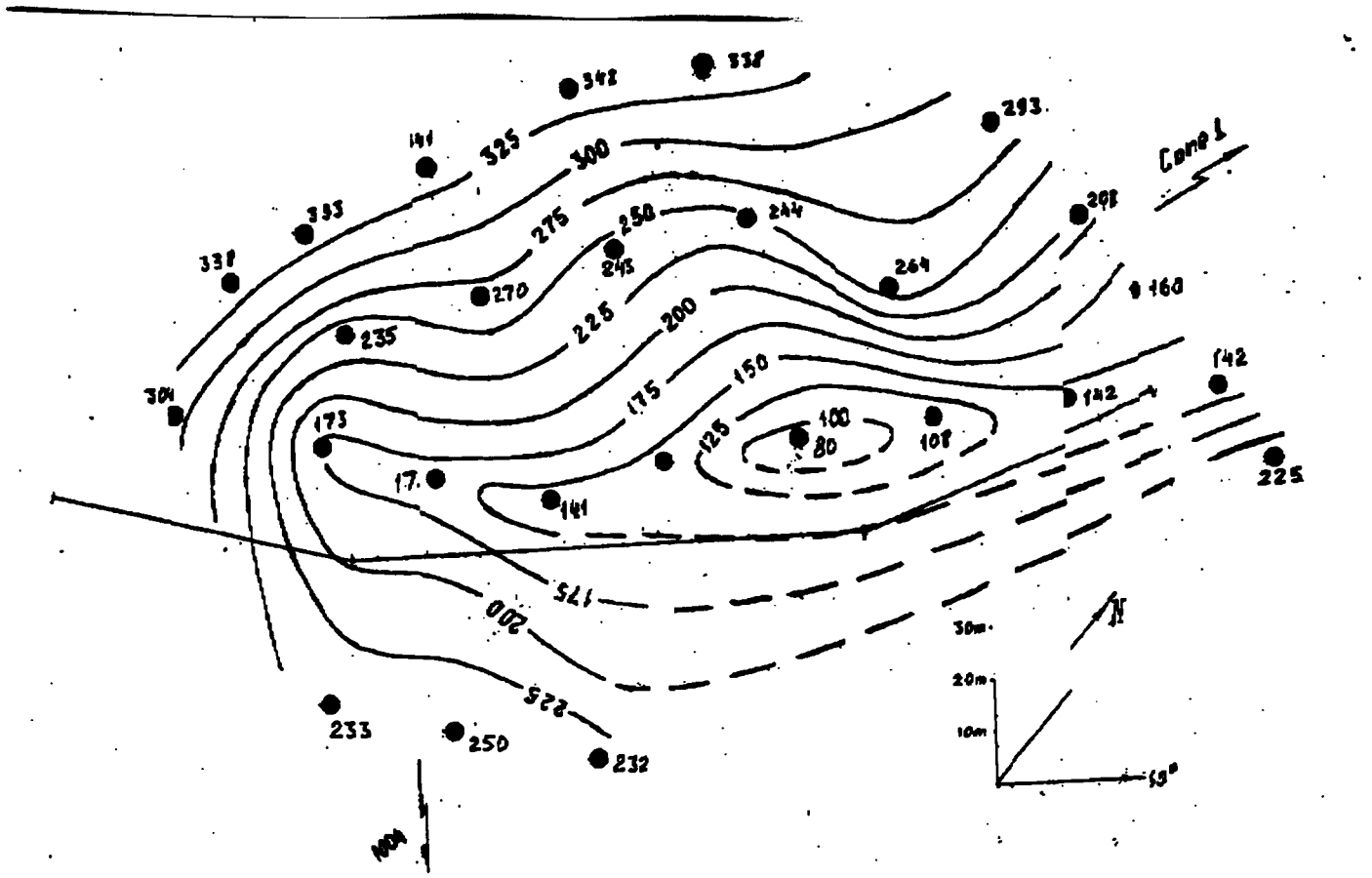

5.0 Models of Dike Cooling

Surface temperature data alone are not sufficient to uniquely model dike geometry. For instance, numerous factors, such as change in dike width or depth, or even change in the porosity of scoria surrounding the dike, could account for the temperature variation observed along the axis of the thermal anomaly. Nonetheless, thermal models can be used to explore the relative importance of several factors that may contribute to the extended period of cooling of the shallow dike in the slump block. These factors include: (i) a difference in bulk thermal conductivities of the dike and the scoria it intrudes; (ii) heat transfer into the dike from a more voluminous intrusion at depth, as detected by the EM survey; and (iii) low heat transfer between the scoria and the atmosphere. Dike cooling was modeled and compared to observations from Tolbachik to explore the sensitivity of cooling rates to these factors.

The effect of differences in thermal conductivities between the dike and scoria on temperature can be investigated using a one-dimensional time-transient conduction model:

geometric mean thermal conductivity, and Km – thermal conductivity estimated using Maxwell's relation.

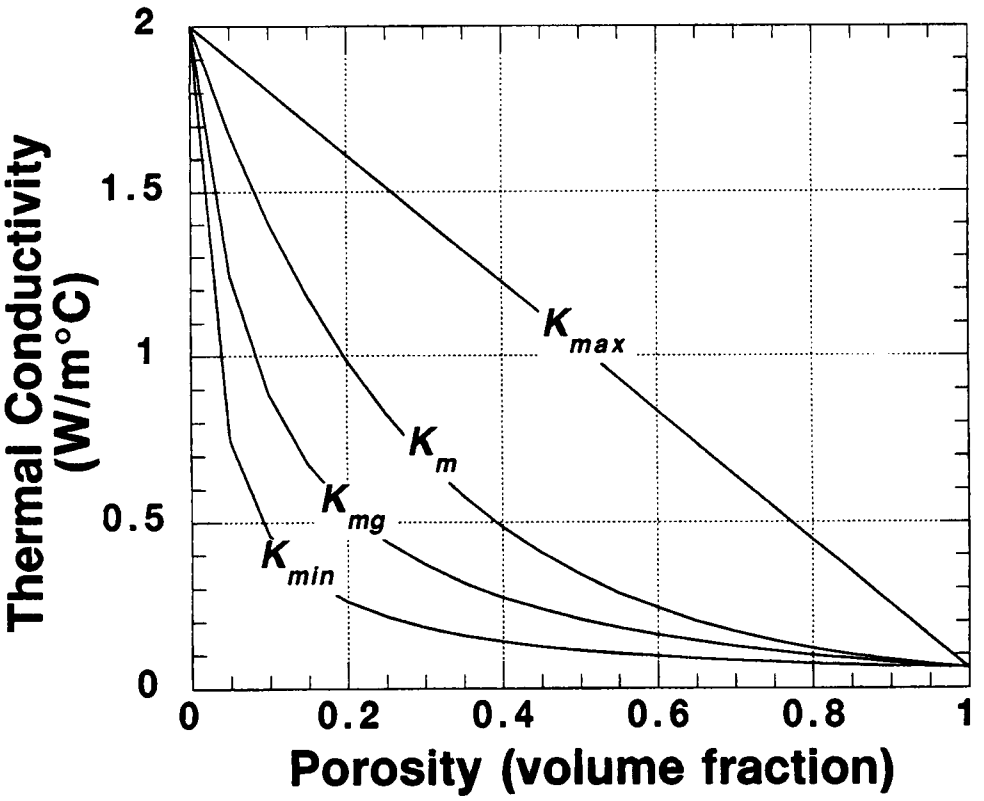

Temperature and saturation also affect bulk thermal conductivity. However, the thermal conductivities of water (= 0.5 W/m°C at 100°C) and steam (= 0.03 W/m°C at 100°C) are much closer to air than to dense basalt. Thus, in partially saturated scoria, porosity largely controls bulk thermal conductivity.

Field measurements were also made to determine the bulk thermal conductivity of the Cone 1004 scoria, using the shallow temperature gradient, measured between 10 cm and 2 m depths, and heat flux, measured by a micro-foil heat flux sensor anchored to an aluminum plate. Bulk conductivity is estimated from these data by application of Fourier's Law.

$$q = -K\frac{\Delta T}{\Delta x}$$

Measured bulk thermal conductivity varies in the vicinity of the thermal anomaly, but is minimum and most consistent in the zone of highest temperature gradient near the axis of the thermal anomaly. For measurements made in the highest temperature zone, thermal conductivity of the scoria is 0.21±0.07 W/m°C. In cooler areas (30-100°C), typi-

cally 15 - 40 m from the axis of the thermal anomaly, apparent bulk thermal conductivity was between 1 and 5 W/m°C. These very high values measured in cooler areas are not true measures of bulk thermal conductivity. Instead, high heat flux values are measured where there is large component of convective heat transfer due to the circulation and condensation of water vapor. Therefore, measurements made using the heat flux sensor also provide a way of mapping the lateral extent of dry-out way from the cooling dike.

Field measurements of bulk thermal conductivity in the highest temperature zone are in good agreement with models (Figure 4) of the decrease in bulk thermal conductivity as a function of porosity. The scoria in the dike zone has a bulk thermal conductivity of approximately 0.2 W/m°C, about one order of magnitude less than that of dense basalt. Field measurements of bulk thermal conductivity also indicate that a dry-out zone extends approximately 15-20 m from the axis of the thermal anomaly.

FIGURE 5. Field measurements of bulk thermal conductivity

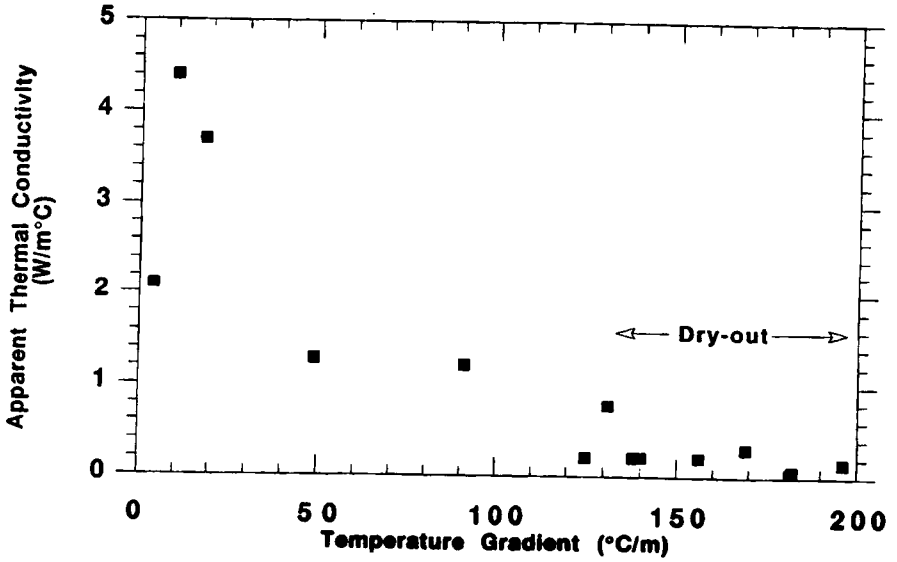

An analytical solution for one-dimensional time-transient heat conduction is achieved using a LaPlace Transform (Carslaw, 1921; Ozisik,1980):

$$T(x,t) = T_r + (T_d - T_r)\left(\frac{K_d}{K_r}\right)\sqrt{\frac{\alpha_r}{\alpha_d}}\left(\frac{1}{\gamma_r}\right)\cdots$$

$$\cdots \sum_{n=0}^{\infty}\left(\frac{\gamma_d}{\gamma_r}\right)^n\left\{erfc\left[\frac{2an\sqrt{\frac{\alpha_r}{\alpha_d}} + (x-a)}{2\sqrt{\alpha_r t}}\right] - erfc\left[\frac{2a(n+1) + (x-a)\sqrt{\frac{\alpha_d}{\alpha_r}}}{2\sqrt{\alpha_d t}}\right]\right\}$$

and

$$\gamma_d = \frac{K_d\sqrt{\alpha_r} - K_r\sqrt{\alpha_d}}{K_r\sqrt{\alpha_d}}$$

$$\gamma_r = \frac{K_d\sqrt{\alpha_r} + K_r\sqrt{\alpha_d}}{K_r\sqrt{\alpha_d}}$$

T(x,t) is the temperature at time t, x meters from the dike wall, Tr and Td are the initial wallrock and dike temperatures, respectively (subscripts d and r refer to dike and wallrock throughout), a is the half-width of the dike, and n is the number of terms in the solution of Laplace's transform. In practice, excellent convergence is achieved after n = 10 iterations, using representative thermo physical properties for the dike and scoria .

Varying scoria porosity from 20 - 50% strongly affects rates of dike cooling by conduction. For example, twenty years after the intrusion of a 5-m-wide dike, maximum temperatures vary between 250-440°C with this range of scoria porosity (Figure 6). In

contrast, welded ignimbrite, assumed to have similar thermo-physical properties to the dike (Table 1), cools to approximately 100°C at the dike contact after 20 years.

FIGURE 6. Cooling history is dependent on the thermo-physical properties of the rock intruded. Here, expected temperatures are shown for a 5-m-wide dike 20 yr after intrusion, calculated using a one-dimensional time transient conduction model varying scoria porosity from 20-50% (Table 1). In contrast, a dike in welded ignimbrite cools much faster.

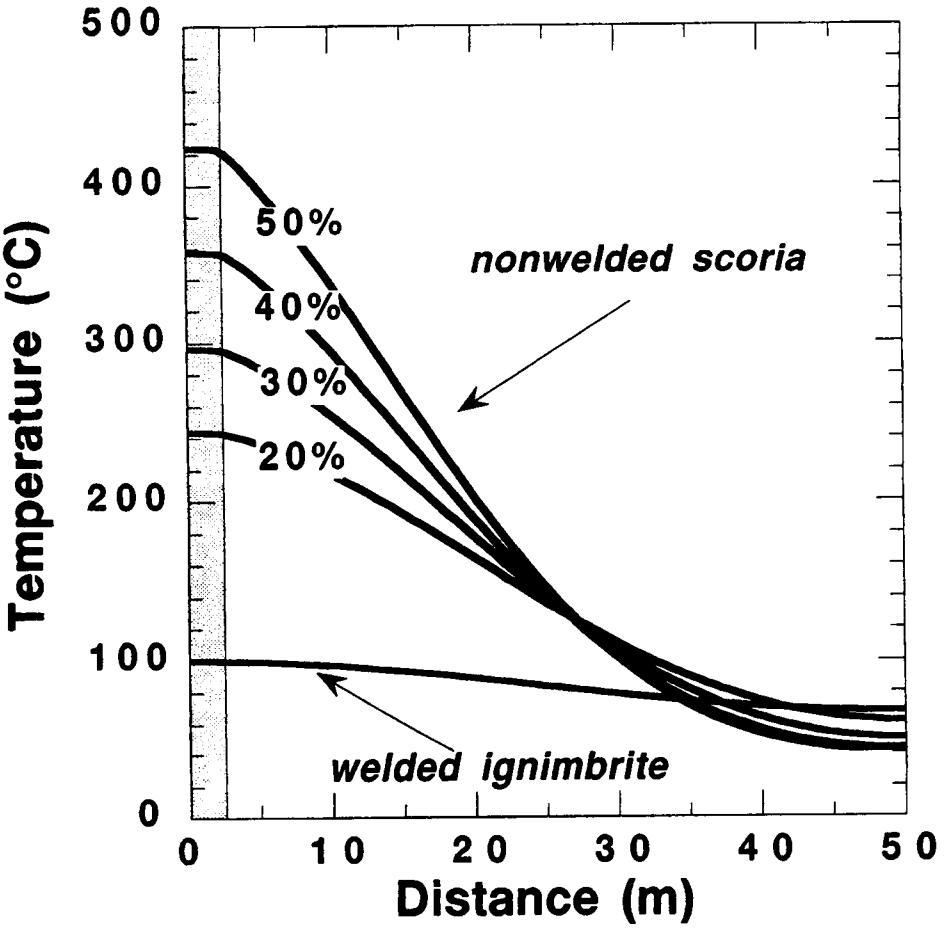

Two-dimensional modeling of heat conduction by finite differences (White, 1984) suggests that the top of the dike must be close to the surface of the Cone 1004 slump block, probably within 10 m, even assuming dike widths of up to 10 m. In addition, the high temperatures (> 400°C) observed at a depth of 2 m (Figure 1) can only be achieved if convective heat transfer between the scoria and the atmosphere is inefficient. Otherwise, cooling by convective heat transfer at the surface would have completely cooled the ground above 2 m depth during the last 20 yr. The finite difference models suggest that conduction of heat along the dike from an intrusion at 80 m, modeled as a von Neumann boundary condition, has a negligible influence on near-surface temperature profiles. Despite the large contrast in thermal conductivity between the dike and scoria,

heat transfer vertically along the dike is a slow process. Proceeding at a rate proportional to , the rate of heat transfer away from the dike near the surface is not greatly affected by heat transfer from the larger intrusion at depth identified by the EM anomaly.

Although water does not strongly affect rates of conduction in the scoria, the presence of even a small amount of water in the unsaturated zone may have an effect on rates of dike cooling when convection is considered. The theoretical basis for models of thermally-driven redistribution of moisture in the unsaturated zone, and the effects of moisture on rates of cooling, are amply discussed in Tsang and Pruess (1987), Buscheck and Nitao (1993), and Lichtner and Walton (1994). MULTIFLO (Lichtner, 1996; Seth and Lichtner, 1996) was used to model the change in water content within the unsaturated zone in response to dike injection, using various initial volume fractions of liquid water. MULTIFLO solves conservation equations for mass and energy in time and space for a nonisothermal two-phase system. Darcy's law combined with binary diffusion in the gas phase is used to compute liquid and gas fluxes in the scoria and dike. Heat flow takes place by conduction through the solid portions of the dike and scoria, or by convection of water and water vapor through the pore spaces in the scoria and fractures in the dike.

Application of the MULTIFLO model suggests that a 5-m-wide dike will be approximately 100°C cooler 20 yr after the dike is emplaced in scoria, if the scoria initially contains an average of 10 percent water and cools by conduction and convection, rather than cooling by pure conduction only (Figure 7). High-temperature gradients near the dike create a dry-out zone within which the volume fraction of water is zero, and heat transfer is by conduction only. In the case of 0.1 initial volume fraction of water, the dry-out zone is 20 m wide after 20 yr of cooling of the 5-m-wide dike, in good agreement with our observations at Tolbachik. Groundwater is vaporizing beyond the dry out zone. Vaporization of groundwater results in flow of liquid water and water vapor away from the dike. This water vapor cools and condenses between 20 and 60 m from the dike. As a result, the volume fraction of water increases within this zone and temperature is near 100°C (Figure 4). Gravity drainage of liquid water and buoyant rise of water vapor in and near the condensation zone likely sets up fluid flow about the cooling dike. Rates of rock alteration are believed to be highest in this zone because of the presence of this two-phase flow at moderate (i.e., 100°C) temperatures. In contrast, rates of rock alteration may be lowest within the dry-out zone closest to the dike, where liquid water is absent. This geometry will persist until the dike cools and the dry-out zone collapses.

FIGURE 7. Water in the unsaturated zone is redistributed during dike cooling. Twenty years after injection of a 5-m-wide dike into scoria with 10% initial saturation, the dry-out zone extends 15-20 m from the dike contact. A condensation zone develops from 20-60 m , within which saturation nearly doubles and temperature is buffered at approximately

100°C. For these conditions, the dike cools slightly faster than indicated by a pure conduction model with 50% porosity (Figure 6).

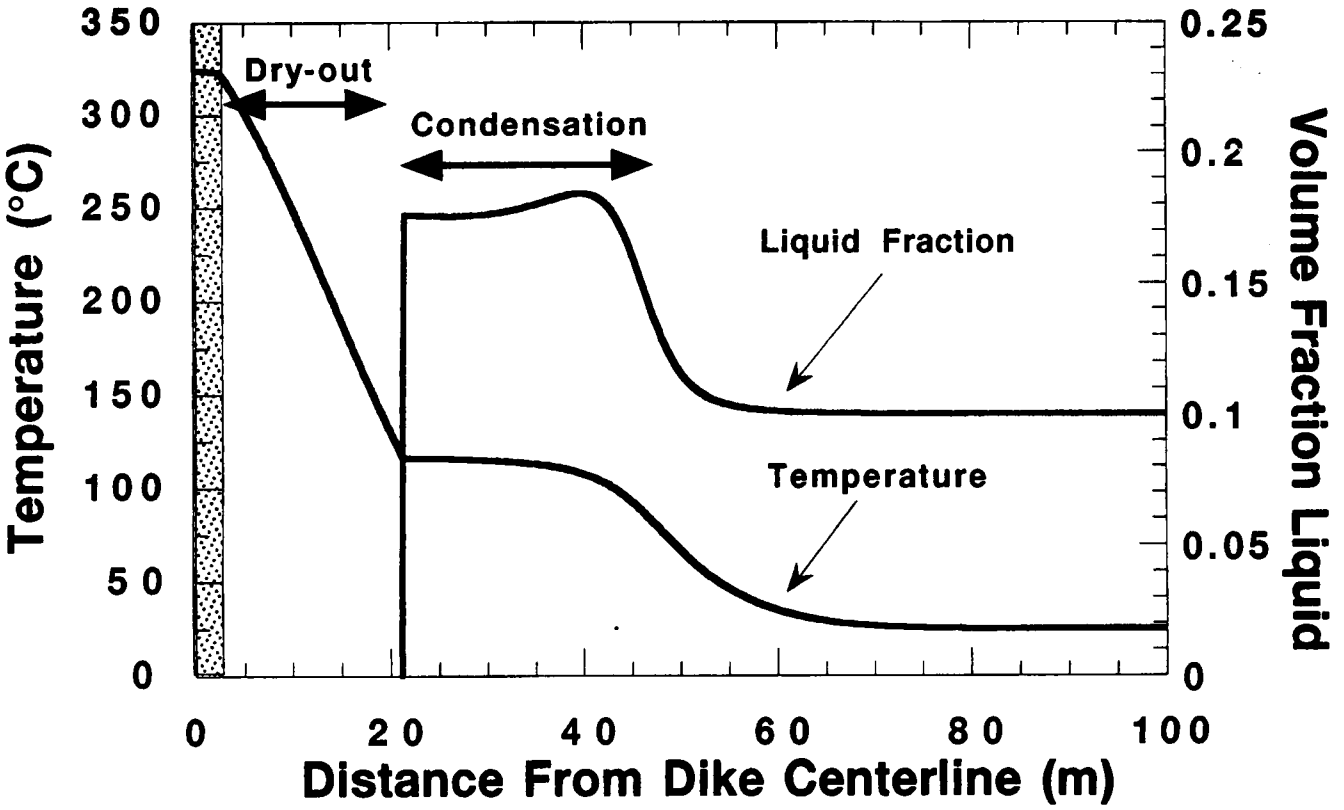

6.0 Conclusions

Field observations on the Cone 1004 slump block provide empirical evidence that dike cooling can require long periods of time and is significantly impacted by the difference between the thermo physical properties of the dike and the scoria it intrudes. At Cone 1004, the scoria limits heat flux from the dike, greatly prolonging cooling. Based on rates of cooling over the last 20 yr, this dike will require at least 100 yr to cool below 100°C. Redistribution of moisture in response to the dike intrusion increased saturation 20-40 m from the dike. Modeling suggests that the dry-out zone observed at the surface persists at depth in the scoria closest to the dike and is bounded by a zone of increased water saturation. Development of this dry-out zone limits rates of rock alteration immediately around the dike, but alteration might be more intense at distances of 20-40 m from the dike, in areas of increased water saturation, moderate temperatures, and in the presence of active fluid (water and vapor) flow.

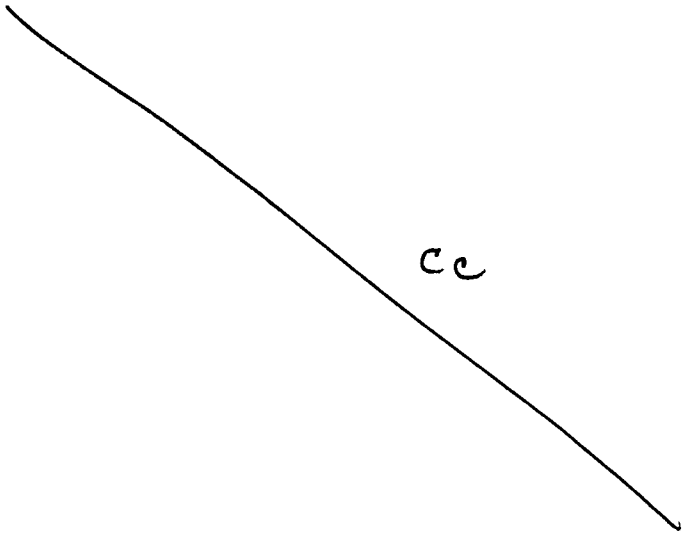

7.0 References

Bailsford, A.D. And Major, K.G., 1964, The thermal conductivity of aggregates of several phases, including porous materials: British Journal of Applied Physics, v. 15, p. 313-319.

Beck, A.E., 1976, An improved method of computing thermal conductivity of fluid-filled sedimentary rocks: The Log Analyst, v. A-11, p. 30-38.

Buscheck, T.A., and Nitao, J.J., 1993, The analysis of repository-heat-driven hydrothermal flow at Yucca Mountain, in Proceedings, Site Characterization and Model Validation, Focus '93: American Nuclear Society, p. 127-144.

Carslaw, H.S., 1921, Introduction to the Mathematical Theory of Conduction of Heat in Solids, Second Edition: MacMillian and Co, London, U.K, 268 pp.

Delaney, P.T., 1987, Heat transfer during emplacement and cooling of mafic dykes, in H.C. Halls and W.F. Fahrig, eds., Mafic Dyke Swarms: Geological Association of Canada Special Paper 34, p. 31-46.

Doubik, Y., Ovsyannikov, A.A., Connor, C.B., Martin, R., and Doubik, P., 1995, Development of the 1975 Tolbachik cinder cone alignment - Nature of areal and lateral basaltic volcanism: Eos, Transactions of the American Geophysical Union, v. 76(46), p. F540.

Fedotov, S., Balesta, S.T., Dvigalo, V.N., Razina, A.A., Flerov, G.B., and Chirkov, A.M., 1990, New Tolbachik volcanoes, in S. Fedotov and Y.P. Masurenko, eds., Active Volcanoes of Kamchatka: Nauka Publishers, Moscow, p. 275-279.

Kauahikaua, A.J., Jackson, D.B., and Zablocki, C.J., 1986, Resistivity structure at a depth of 5 km beneath Kilauea volcano, Hawaii from large-loop-source electromagnetic measurements (0.04 8 Hz): Journal of Geophysical Research, v. 91, p. 8,267-8,283.

Lichtner, P.C., 1996, Continuum formulation of multicomponent-multiphase reactive transport, in P.C. Lichtner, C.I. Steefel, and E.H. Oelkers, eds., Reactive Transport in Porous Media: Reviews in Mineralogy 34, p. 1-81.

Lichtner, P.C., and Walton, J.C., 1994, Near-field liquid-vapor transport in a partially saturated high-level nuclear waste repository: Center for Nuclear Waste Regulatory Analyses, CNWRA94 022.

Magus'kin, M.A., Enman, V.B., and Tselishchev, V.S., 1983, Changes in the height, volume, and shape of the new Tolbachik volcanoes of the Northern Breakthrough, in S.A. Fedotov and Ye.K. Markinin, eds., The Great Tolbachik Fissure Eruption, 1975-1976: Cambridge University Press, Cambridge, Ma, p. 307-315.

McBirney, A.R., 1984, Igneous Petrology: Freeman Cooper, San Francisco, CA, 504 pp.

Ozisik, M.N., 1980, Heat Conduction, John Wiley and Sons: New York, NY, 687 pp.

Rai, M.P., and Manghnami, M.H., 1977, Electrical conductivity of basalts to 1,550 °C, in H. Dick, ed., Magma Genesis, Proceedings of the American Geophysical Union Chapman Conference on Partial Melting in the Earth's Upper Mantle: Oregon Department of Geology and Mineralogy Bulletin, v. 96, p. 219-232.

Seth, M.S., and Lichtner, P.C., 1996, User's manual for MULTIFLO: Part 1, Metra, 1.0, Two phase nonisothermal flow simulator: Center for Nuclear Waste Regulatory Analyses, CNWRA96 005.

Somerton, W.H., 1958, Some thermal characteristics of porous rocks: Journal of Petroleum Technology, v. AIME 2008, p. 61-64.

Tsang, Y.W., and Pruess, K., 1987, A study of thermally induced convection near a high-level nuclear waste repository in partially saturated fractured tuff: Water Resources Research, v. 23, p. 1,958-1,966.

White, F.M., 1984, Heat Transfer, Addison-Wesley Publishing: Reading, Ma, 588 pp.

8.0 Finite Difference Code

The following is th finite difference code used in 2D calculations

```
•! Program Cooling Dike Finite DIff
•! Language: TrueBasic
•!Author: Chuck Connor
•!Date: Jan, 1995
•
•!Purpose
•!This program calculates the transient temperature within a
•! cylinder using explicit finite difference methods the output
•! includes a Heissler approximation for comparison
•
•!Files: the File "test" is created and/or erased by this program
•!Matrices: matrix t(r,k) contains the temperature values
•!        for the cylinder, were r is the radius of the cylinder
•!        and k is one-half the length of the cylinder
•!        matrix temp(r,k) contains temperature values at
•!        intermediate steps
•!Constants: rn = radius of cylinder (m)
•!         kn = half-length of cylinder (m)
•!          delz = step in k -direction (m)
•!          delr = step in r direction (m)
•!          alpha = thermal diffusivity of cylinder (m2/s)
•!           kond = thermal conductivity of cylinder (W/mC)
```

```
•!          h0 = heat transfer coeff. (W/m2C)
•!          delt = time step (s)
•!          t0 = fluid temperature (C)
•!          r0 = radius of cylinder (m)
•!          b1 = constant for Heissler Approx (only if Bi = 4)
•!          c1 = constant for Heissler Approx (only if Bi = 4)
•!
•DIM t(0:50,0:50), temp(0:50,0:50), specific_heat(0:50,0:50), density(0:50,0:50),
cond(0:50,0:50)
•DIM xpos(0:50,0:50),ypos(0:50,0:50)
•LET itot = 50
•LET jtot = 50
•LET delt =5*24*60*60          !one day
•
•OPEN #1: name "test" , create newold
•ERASE #1
•
•! initial test
•
•!MAT specific_heat = 800       !J/kgC
•!MAT density = 2600            !kg/m3
•!MAT cond = 1                  !W/mC
•
•FOR i = 0 to 50
•   FOR j = 0 to 50
•      LET xpos(i,j) = i
•      LET ypos(i,j) = j
•   NEXT j
•NEXT i
•
•FOR i = 0 to 10
•   FOR j = 0 to 25
•      LET t(i,j) = 1000
•      LET specific_heat(i,j) = 950
•      LET density(i,j) = 2800
•      LET cond(i,j) = 1.2
•   NEXT j
•NEXT i
•
•FOR i = 11 to jtot
•   FOR j = 26 to jtot
•      LET t(i,j) = 50
•      LET specific_heat(i,j) = 1000
•      LET density(i,j) = 1200
•      LET cond(i,j) = 0.1
•
•   NEXT j
•NEXT i
•
•FOR i = 0 to 10
```

```
•  FOR j = 26 to jtot
•     LET t(i,j) = 50
•     LET specific_heat(i,j) = 1000
•     LET density(i,j) = 1200
•     LET cond(i,j) = 0.1
•
•  NEXT j
•NEXT i
•
•FOR i = 11 to itot
•  FOR j = 0 to 25
•     LET t(i,j) = 50
•     LET specific_heat(i,j) = 1000
•     LET density(i,j) = 1200
•     LET cond(i,j) = 0.1
•
•  NEXT j
•NEXT i
•
•!convective boundary condition constants
•LET condgas = 1.2
•LET heat_trans = 10
•LET temp_gas = 50
•
•!PRINT "sigr = ";sigr
•!LET error = 1/(2*(2+bir))
•!PRINT "error = "; error
•!IF error < sigr then PRINT "sigma is too big!    !!!"
•
•FOR tim = delt to 1387*delt step delt
•
•  ! 1 interior node
•  FOR i = 1 to itot-1
•     FOR j = 1 to jtot-1
•
•        LET t1 = t(i,j)
•        LET t2 = t(i+1,j)
•        LET t3 = t(i-1,j)
•        LET t4 = t(i,j-1)
•        LET t5 = t(i,j+1)
•
•        LET dx1 = xpos(i,j) - xpos(i-1,j)
•        LET dx2 = xpos(i,j) - xpos(i+1,j)
•        LET dy1 = ypos(i,j) - ypos(i,j+1)
•        LET dy2 = ypos(i,j) - ypos(i,j-1)
•
•        LET thermal_diff = cond(i,j)/(specific_heat(i,j)*density(i,j))
•        LET tt = (t2-t1)/dx2^2 + (t3-t1)/dx1^2 + (t5-t1)/dy1^2 + (t4-t1)/dy2^2
•
•        LET temp(i,j) = delt*thermal_diff*tt + t1
```

```
•
•    NEXT j
•  NEXT i
•
•  ! 2 top of surface (convective)
•
•  LET j = jtot
•  FOR i = 1 to itot-1
•
•     LET t1 = t(i,j)
•     LET t2 = t(i+1,j)
•     LET t3 = t(i-1,j)
•     LET t4 = t(i,j-1)
•     LET dx1 = xpos(i,j) - xpos(i-1,j)
•     LET dx2 = xpos(i,j) - xpos(i+1,j)
•     LET dy2 = ypos(i,j) - ypos(i,j-1)
•
•     LET bi = heat_trans*dy2/condgas
•     LET thermal_diff = cond(i,j)/(specific_heat(i,j)*density(i,j))
•     LET sigm = thermal_diff*delt/dy2^2
•
•     LET tt = t4/dy2^2 + t2/(2*dx2^2) + t3/(2*dx1^2) + bi*temp_gas/dy2^2
•     LET ttt = 1 - 4*sigm - 2*sigm*bi
•
•     LET temp(i,j) = thermal_diff*delt*tt + t1*ttt
•
•
•  NEXT i
•
•  ! 3 no change in t with x far from dike
•
•  LET i = itot
•  FOR j = 1 to jtot-1
•
•     LET t1 = t(i,j)
•     LET t3 = t(i-1,j)
•     LET t4 = t(i,j-1)
•     LET t5 = t(i,j+1)
•
•     LET dx1 = xpos(i,j) - xpos(i-1,j)
•     LET dy1 = ypos(i,j) - ypos(i,j+1)
•     LET dy2 = ypos(i,j) - ypos(i,j-1)
•
•     LET thermal_diff = cond(i,j)/(specific_heat(i,j)*density(i,j))
•     LET tt = 2*(t3-t1)/dx1^2 + (t5-t1)/dy1^2 + (t4-t1)/dy2^2
•
•     LET temp(i,j) = delt*thermal_diff*tt + t1
•
•
•  NEXT j
```

```
•
•
•  ! 4 i=0 side of surface
•  LET i = 0
•  FOR j = 1 to jtot-1
•     LET t1 = t(i,j)
•     LET t2 = t(i+1,j)
•     LET t4 = t(i,j-1)
•     LET t5 = t(i,j+1)
•
•     LET dx2 = xpos(i,j) - xpos(i+1,j)
•     LET dy1 = ypos(i,j) - ypos(i,j+1)
•     LET dy2 = ypos(i,j) - ypos(i,j-1)
•
•     LET thermal_diff = cond(i,j)/(specific_heat(i,j)*density(i,j))
•     LET tt = 2*(t2-t1)/dx2^2 + (t5-t1)/dy1^2 + (t4-t1)/dy2^2
•
•     LET temp(i,j) = delt*thermal_diff*tt + t1
•
•
•  NEXT j
•
•  ! 5 insulated condition at bottom of surface
•
•  LET j = 0
•  FOR i = 1 to itot-1
•
•     LET t1 = t(i,j)
•     LET t2 = t(i+1,j)
•     LET t3 = t(i-1,j)
•     LET t5 = t(i,j+1)
•
•
•     LET dx1 = xpos(i,j) - xpos(i-1,j)
•     LET dx2 = xpos(i,j) - xpos(i+1,j)
•     LET dy1 = ypos(i,j) - ypos(i,j+1)
•
•     LET thermal_diff = cond(i,j)/(specific_heat(i,j)*density(i,j))
•     LET tt = (t2-t1)/dx2^2 + (t3-t1)/dx1^2 + 2*(t5-t1)/dy1^2
•
•     LET temp(i,j) = delt*thermal_diff*tt + t1
•
•
•
•  NEXT i
•
•
•
•  ! 6 x = 0 top of surface with convective boundary
•
```

```
• LET j = jtot
• LET i = 0
• LET t1 = t(i,j)
• LET t2 = t(i+1,j)
• LET t4 = t(i,j-1)
•
• LET dx2 = xpos(i,j) - xpos(i+1,j)
• LET dy2 = ypos(i,j) - ypos(i,j-1)
•
• LET bi = heat_trans*dy2/condgas
• LET thermal_diff = cond(i,j)/(specific_heat(i,j)*density(i,j))
• LET sigm = thermal_diff*delt/dy2^2
•
• LET tt = t4/dy2^2 + 2*t2/(2*dx2^2) + bi*temp_gas/dy2^2
• LET ttt = 1 - 4*sigm - 2*sigm*bi
•
• LET temp(i,j) = thermal_diff*delt*tt + t1*ttt
•
• ! 7 x = itot top of surface with convective boundary
•
• LET j = jtot
• LET i = itot
• LET t1 = t(i,j)
• LET t3 = t(i-1,j)
• LET t4 = t(i,j-1)
•
• LET dx1 = xpos(i,j) - xpos(i-1,j)
• LET dy2 = ypos(i,j) - ypos(i,j-1)
•
• LET bi = heat_trans*dy2/condgas
• LET thermal_diff = cond(i,j)/(specific_heat(i,j)*density(i,j))
• LET sigm = thermal_diff*delt/dy2^2
•
• LET tt = t4/dy2^2 + 2*t3/(2*dx1^2) + bi*temp_gas/dy2^2
• LET ttt = 1 - 4*sigm - 2*sigm*bi
•
• LET temp(i,j) = thermal_diff*delt*tt + t1*ttt
•
•
• ! 8  i = 0, j = 0 (lower right hand corner of surface)
•
• LET i = 0
• LET j = 0
•
• LET t1 = t(i,j)
• LET t2 = t(i+1,j)
• LET t5 = t(i,j+1)
• LET dx2 = xpos(i,j) - xpos(i+1,j)
• LET dy1 = ypos(i,j) - ypos(i,j+1)
•
```

```
•
•  LET thermal_diff = cond(i,j)/(specific_heat(i,j)*density(i,j))
•  LET tt = 2*(t2-t1)/dx2^2 + 2*(t5-t1)/dy1^2
•
•  LET temp(i,j) = delt*thermal_diff*tt + t1
•
•  ! 9 i = itot, j = 0 (lower left-hand corner of surface)
•  LET i = itot
•  LET j = 0
•
•  LET t1 = t(i,j)
•  LET t3 = t(i-1,j)
•  LET t5 = t(i,j+1)
•
•  LET dx1 = xpos(i,j) - xpos(i-1,j)
•
•  LET dy1 = ypos(i,j) - ypos(i,j+1)
•
•  LET thermal_diff = cond(i,j)/(specific_heat(i,j)*density(i,j))
•  LET tt = 2*(t3-t1)/dx1^2 + 2*(t5-t1)/dy1^2
•
•  LET temp(i,j) = delt*thermal_diff*tt + t1
•
•
•
•
•  MAT t = temp
•
•NEXT tim
•
•PRINT #1: 51,51
•PRINT #1: 0,700
•FOR q = 1 to 51
•   PRINT #1: q;
•NEXT q
•PRINT #1
•FOR q = 1 to 51
•   PRINT #1: q;
•NEXT q
•PRINT #1
•FOR k = 0 to 50
•   FOR i = 0 to 50
•
•      WHEN error in
•
•         PRINT #1: t(i,k);
•
•      USE
•         PRINT #1: 0;
•
```

```
•      END WHEN
•
•   NEXT i
•   PRINT #1
•NEXT k
•END
•
```

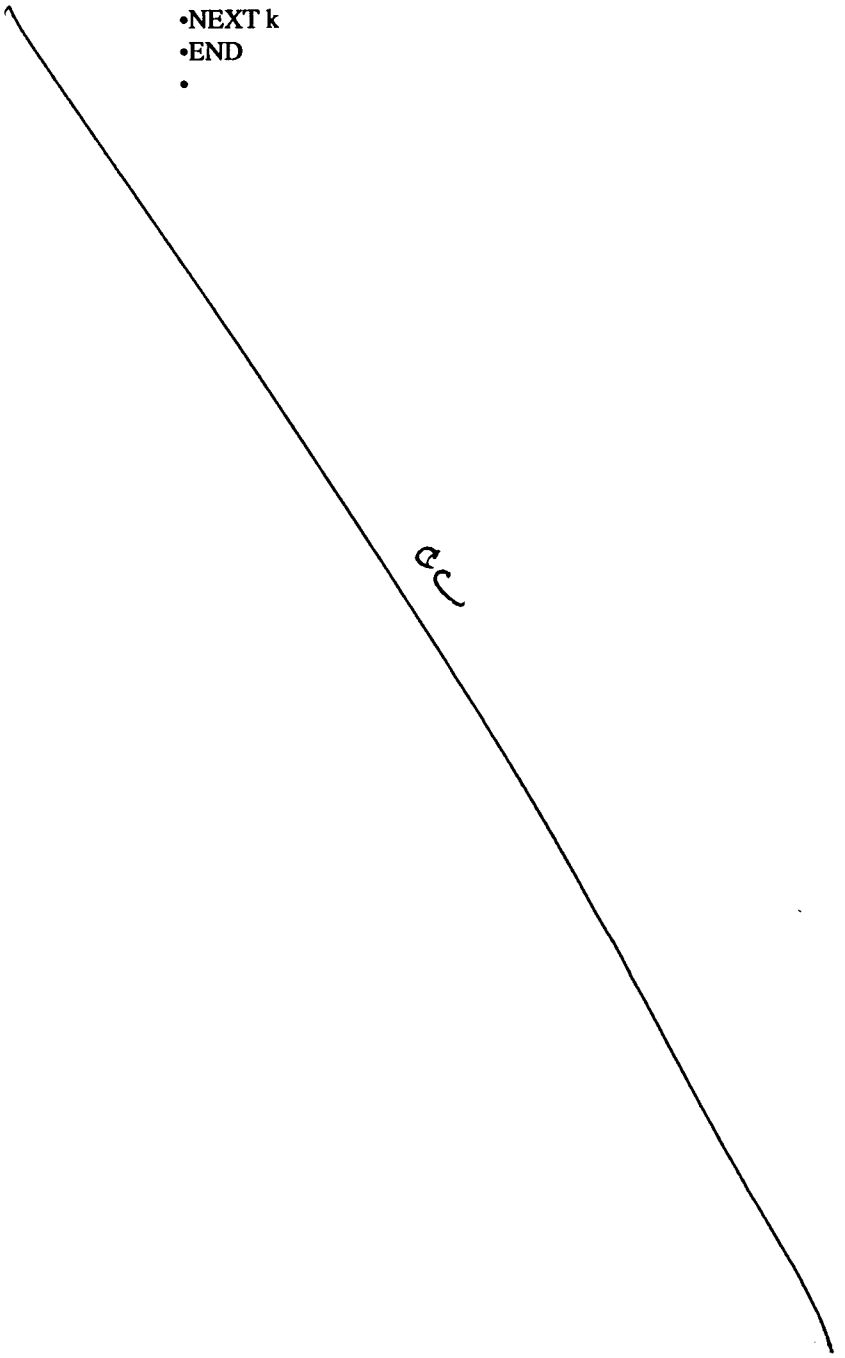

Integrating Structure into Probability Estimates

Chuck Connor

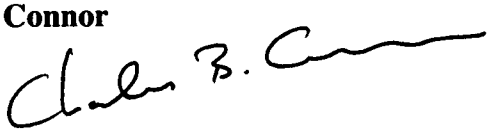

Probabilistic hazard analyses for potential volcanic disruption of a proposed high level radioactive waste repository at Yucca Mountain, Nevada, are developed by convolution of spatio-temporal patterns in basaltic volcanism with structural geology.

1.0 Introduction

Yucca Mountain, Nevada, is the proposed site of the first U.S. high-level radioactive waste repository. If licensed, plans call for permanent disposal of 70,000 metric tons of radioactive waste in a 5-6 km2 facility excavated 300 m beneath the crest of Yucca Mountain (Note). Volcanic eruptions are considered a potential hazard during the 104 yr performance period of the proposed repository site because Yucca Mountain (YM) is located in an area that has experienced recurring small-volume basaltic volcanic activity during the last 8 m.y., since the cessation of large-volume silicic volcanism in the Miocene (Fleck et al., 1996). This volcanic activity resulted in the formation of more than 30 cinder cones and associated lava flows in the YM region, which itself is part of a larger magmatic system in southern Nevada and southeastern California (Yogozinski and Smith, 1995) that consists of at least 60 volcanoes ranging in age from about 8 Ma to approximately 0.1 Ma.

Such low recurrence rate basaltic volcanic activity occurs where magmas are generated by uplift of fertile mantle during crustal extension. Magma ascent through the crust is enhanced by crustal structures produced by extension, leading to correlation between basatic volcanism and structure across a range of scales, from the superposition of individual faults and vents to the occurrence of entire volcanic fields at the margins of extensional basins. The goal of volcanic hazard analysis is to quantify these often complex geological relationships probabilistically.

The following analyses explore the bounds of probability estimates of volcanic disruption using a full range of models based on spatial and temporal patterns of basaltic volcanism. In particular, a method is developed to explore the influence of crustal structure on the distribution of volcanoes near YM.

The relationship between structure and volcanism has been used to suggest both higher and lower probabilities of volcanic disruption of the repository than are predicted using spatio-temporal patterns in vent distribution. Smith et al. (1991) suggested a narrow NE-trending structurally controlled source zone of potential volcanism extending through the repository site, resulting in comparatively high probabilities of volcanic disruption of the site. Alternatively, some structure models exclude the repository from volcanic source zones. For example, Crowe and Perry (1989) proposed the NNW-trending Crater Flat volcanic zone, with its eastern boundary located west of the repository site, resulting in very low probabilities. Thus, wide variation in probability estimates is a direct result of the varying ways in which these source zones have been drawn.

The analyses presented here avoid the source zone concept altogether by casting structural information as a discretized probability density distribution, readily comparable to spatial and spatio-temporal probability distributions. Two data sets are used to represent crustal structure in this analysis: gravity data, that reveal large scale variations in crustal density-distribution, and the distribution of high dilation tendency faults. Lateral variations in gravity are produced by the juxtaposition of relatively dense Paleozoic and Pre-Cambrian sedimentary and metasedimentary rocks and less dense Tertiary and Quaternary felsic tuffs and alluvium. Strong horizontal gravity gradients are largely due to faults, some of which may cross-cut the entire 15 km brittle crust (Note). High-dilation tendency faults are those favorably oriented for dilation in the contemporary stress and, therefore, may serve as pathways for ascent of basaltic magma through the crust.

YM is part of a structural half-graben That includes Crater Flat (Figure 1) and is bounded on the west by the east dipping Bare Mountain fault (note). Plio-Quaternary volcanoes in Crater Flat all lie within or near high gravity-gradient areas associated with the Crater Flat basin. Two episodes of volcanism, the eruption of the Little Cones (Stamatakos et al., 1996) and the eruption of Miocene basalt south of the Little Cones (Figure 1), and a possible third episode suggested by the presence of a shallowly buried body of highly magnetized rock in southern Crater Flat, all occur very close to the steepest gravity gradient in the region produced by the Bare Mountain fault. The repeated occurrence of volcanic activity in this small area of the basin suggests that the Bare Mountain fault , provide a pathway for ascending magmas. Topographically, the 0.1 Ma Lathrop Wells cinder cone (Note) lies outside Crater Flat but, based on the gravity data, is within the larger N-trending basin and at the margin of the prominent basement low in southernmost Crater Flat. Aeromagnetic anomalies (Langenheim et al., 1993) in the Amargosa Valley produced by buried Pliocene (?) basalts also lie within or at the margins of the southern extension of this basin. The easternmost of these buried basalts lies close to N-trending gravity anomaly demarcating the eastern edge of Amargosa Valley alluvial basin in this area. Therefore, the horizontal gravity-gradient is a geophysical data set that is both easily cast as a discrete density distribution and that is sensitive to structures that may have influenced past patterns of volcanism near YM.

Our recent geophysical surveys in the YM region demonstrate the correlation between volcanism and structure on local scales (Note). For example, ground magnetic surveys south of Lathrop Wells have revealed an alignment of three reversely magnetized anomalies, interpreted as buried basaltic cones. This alignment parallels the Quaternary Crater Flat alignment (Figure 1). At Northern Cone, the closest Quaternary volcano to YM,

magnetic surveys indicate that the cone is emplaced along N-S trending faults buried by a thin veneer of alluvium.

2.0 Basic Approach

The basic apporach to integrating structure takes place in the following steps

1. develop a probability surface based on near neighbor or similar spatio-temporal model of volcanism
2. normalize this plot, so that the integral across the region = 1
3. develop a surface over the same area and grid spacing as the spatio-temporal model that represents structure
4. normalize this plot so the integral across the region = 1
5. multiply these maps together and renormalize so the integral across the region = 1; this map is the weighted structural probability model
6. multiply the weighted structural model with a surface of the probability that an volcanic event centered on a grid node will intersect (or disrupt) the reposiotry, calculated at the same grid spacing and over the same area as the weighted structural model
7. sum the probabilities across the resulting map. Now you have the probability of volcanism disrupting the repository if the probability of volcanism in the region = 1.
8. multiply by a regional recurrence rate of volcanism
9. calculate probability using Poisson's model.

2.1 Step 1 and 2- estimation of the spatio-temporal model

This is done using techniques described in Connor and Hill (1995, J. Geophys. Res. 100: 10,107-10,125). I concentrated on using two spatio - temporal models. The first is the Epanechnikov model, which depends on a smoothing parameter, h. The probability of volcanism at a specific spot (like the repo.) will depend on the values chosen for h. In previous work (Connor and Hill, 1995, J. Geophys. Res. 100: 10,107-10,125), it was determined that h = 18-20 km gives a mximum for the probability of disruption of the repository. This is because the repository is about 20 km from numerous volcanoes in Crater Flat and Lathrop Wells. So, using the h=20 for the spatio-temporal model gives an upper bound on probability, based on this spatio-temporal apporach. A map of the probability of volcanism in the region is shown in Figure 1 on page 4,calculated using the Epanechnikov kernel function. Map coordinates are in UTM. The figure (and following simialr maps) are colored in Spy Glass transform.

FIGURE 1. Epanechnikov kernel map with smoothing parameter h = 20 km, normalized so the integral over the map area = 1

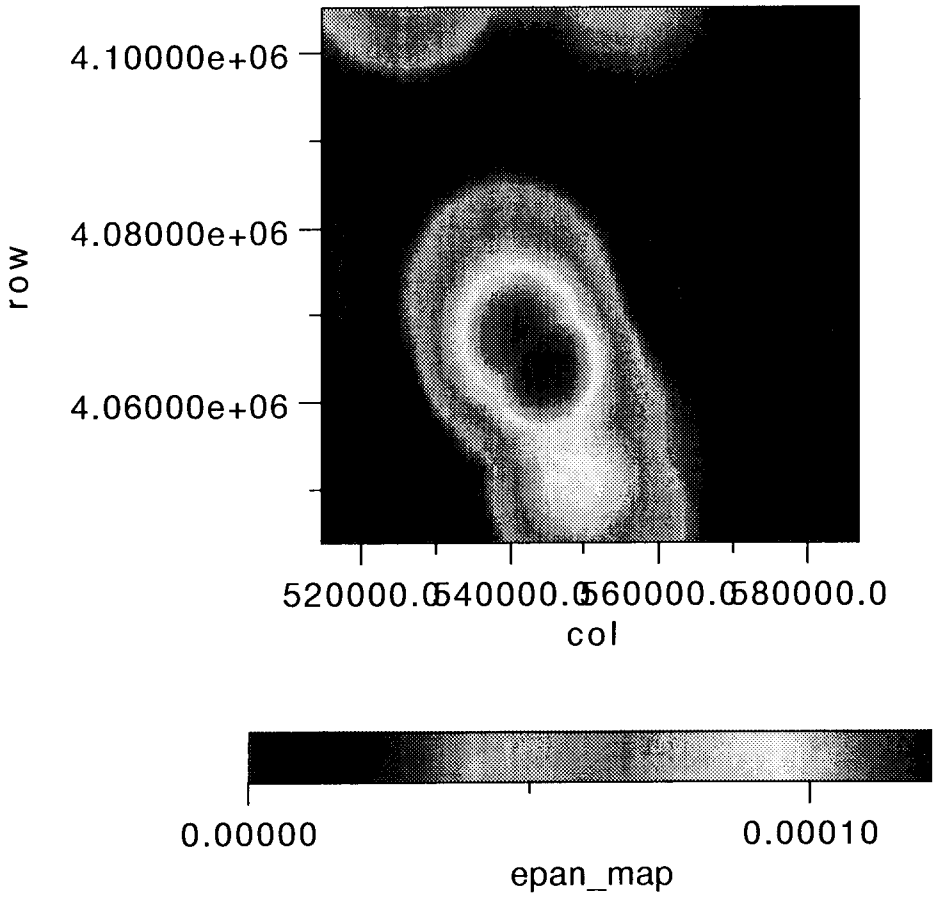

An alternative apporach is a near neighbor model discussed in Connor and Hill (1995, J. Geophys. Res. 100: 10,107-10,125) and Condit and Connor (Geol. Soc. Am. Bull. 208: 1,225-1,241). In this apporach the probability of disrutpion depends on the number of near-neighbors used. Basically, using many near-neighbors smears probability out over a large area, and using a small number of near-neighbors concentrates probability near the youngest volcanoes.

In this case I use m=8 near-neighbors. Integrating an m=8 near-neighbor model across the region gives a regional recurrence rate of 5 volcanoes per million years. Since 8 volcanoes in the region erupted in the last one million years, m = 8 gives a reasonable lower bound to the probability calculations. A map of the near-neighbor probability is shown in Figure 2 on page 5. The map is normalized so the integral across the map area = 1.

FIGURE 2. Near-neighbor map of the region

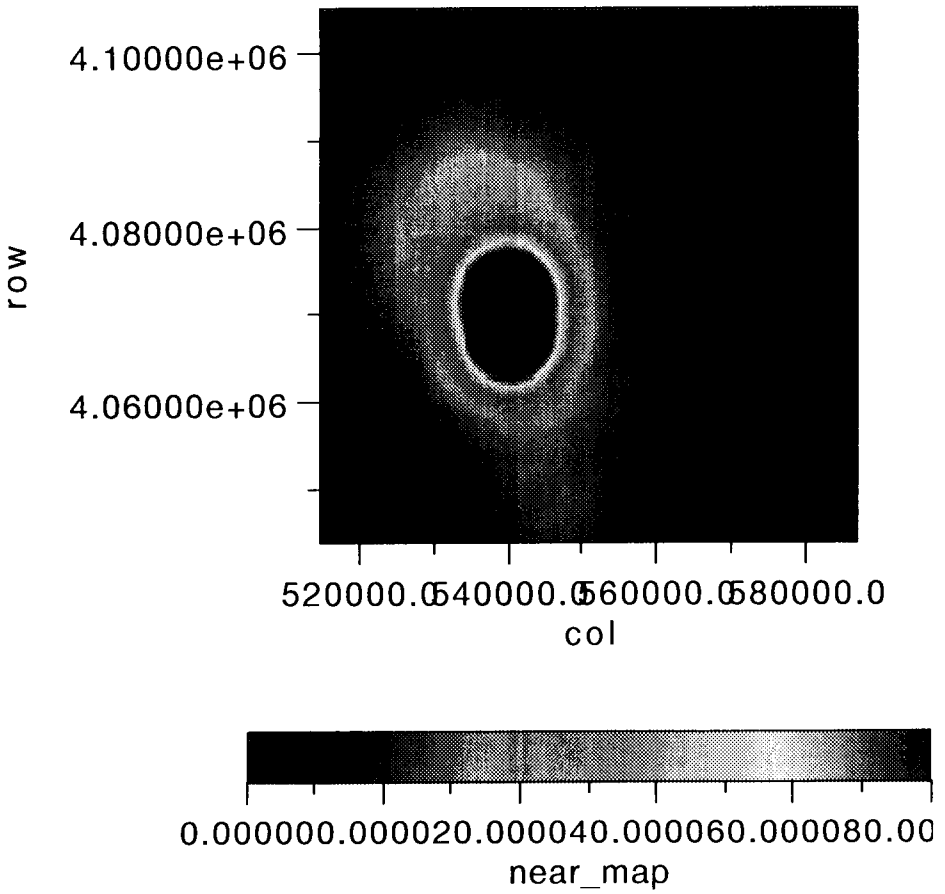

Other map calculations are possible to generate other probability surfaces based on spatio-temporal models. The idea here is that the two maps represent a reasonable range of values, based on nonhomogeneous methods.

In the above, map normalization takes place as follows. The map is calculated at each grid node, the grid nodes are summed, each grid node is devided by the sum. The renormalization is checked by summing the grid nodes again and determining that their sum = 1. The summation is done in Spyglass transform using the command:

print sum(map) where map is the matrix of grid nodes.

2.2 Steps 3 and 4 - structural maps

Gravity data were obtained from the Lawrence Berkely Lab where gravtiy data fro the NTS are archived. The gravity data set we obtained consists of about 8,000 measurments that are given as a complete bouguer correction. These data are shown and contoured on the following unnumbered pages.

Gravity data were interpolated onto a grid using a bicubic spline interpolation algorithm from Earthvision software. The amplitude of the horizontal gravity gradient was calculated from this grid using finite differences. The resulting grid was then normalized.

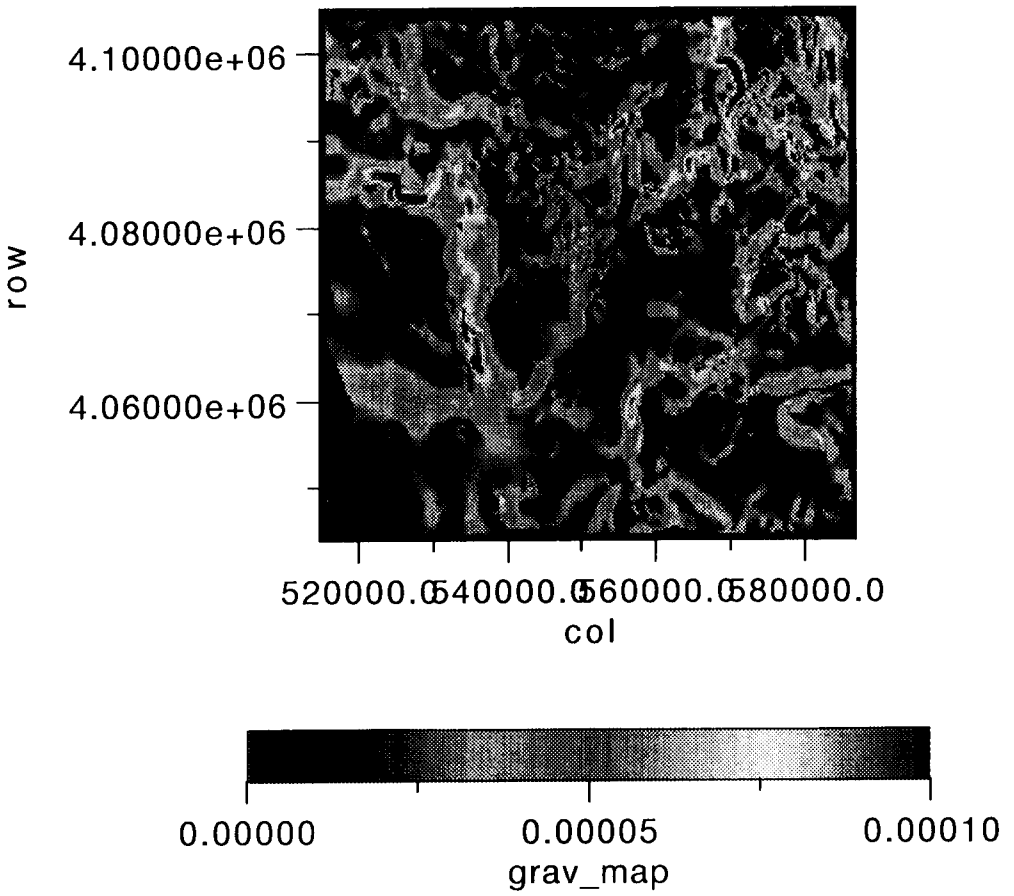

The gravity gradient and near-neighbor maps are then combined using the equation:

$$\lambda_s(x, y) = \frac{1}{k}(\lambda_n(x, y) \cdot s(x, y)^w)$$

where

$$k = \sum_X \sum_Y (\lambda_n(x, y) \cdot s(x, y)^w)$$

The following sequence of commands are from a script in Spyglass transform to calculate probabilities - note that it makes no difference when the normalization takes place

•mix = pow(grav_map,2)
•try1 = mix*near_map
•print sum(try1)
•* Result: 1.08151e-09
•try2=try1/1.08151e-09
•print sum(try2)
•* Result: 1
•print sum(mix)
•* Result: 4.05635e-05
•try1 = mix/4.05635e-05
•try3 = near_map*try1
•print sum(try3)
•* Result: 2.66622e-05
•try3 = try3/2.66622e-05

The following maps show the significance of various weights, w, in the map analysis

to calculate with w = 0.25:

•mix = pow(grav_map,.25)
•try = near_map*mix
•print sum(try)
•* Result: 0.0673039
•try1=try/0.0673039
•

FIGURE 3. m=8 near-neighbors, gravity gradient data, w = 0.25

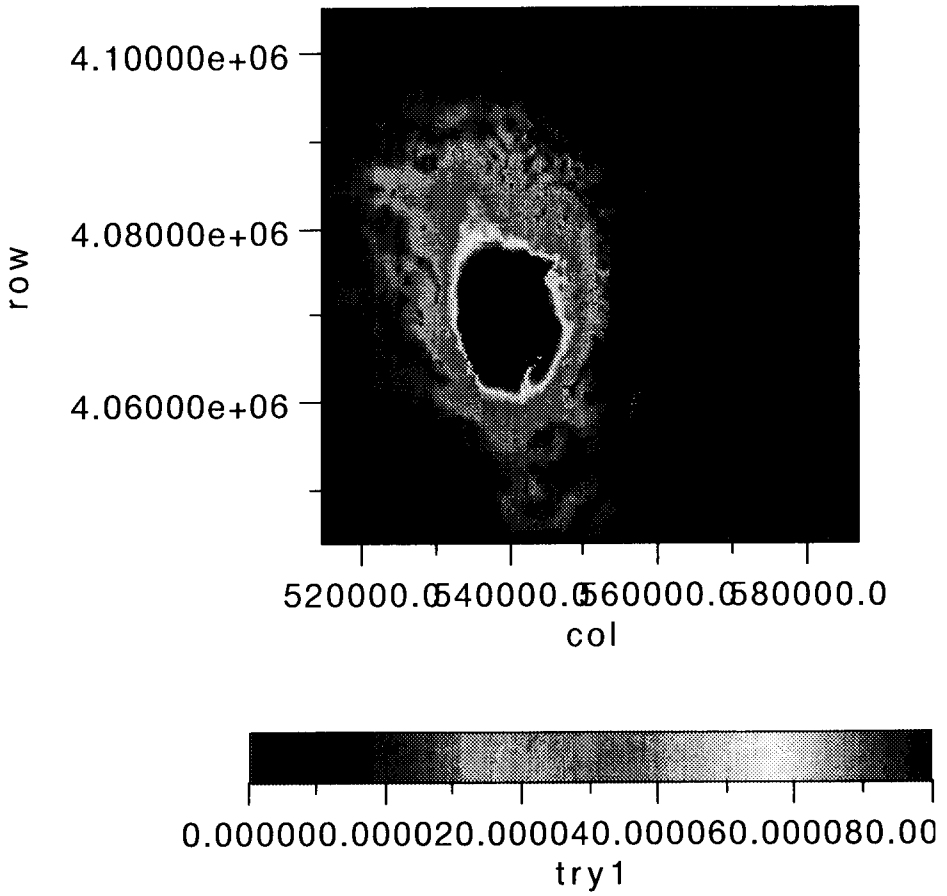

to calculate with w = 0.5:

- mix = pow(grav_map,.5)
- try = near_map*mix
- print sum(try)
- * Result: 0.00478614
- try = try/0.00478614

FIGURE 4. mix of near-neighbor model (m=8), and the grvity gradient map with w = 0.5

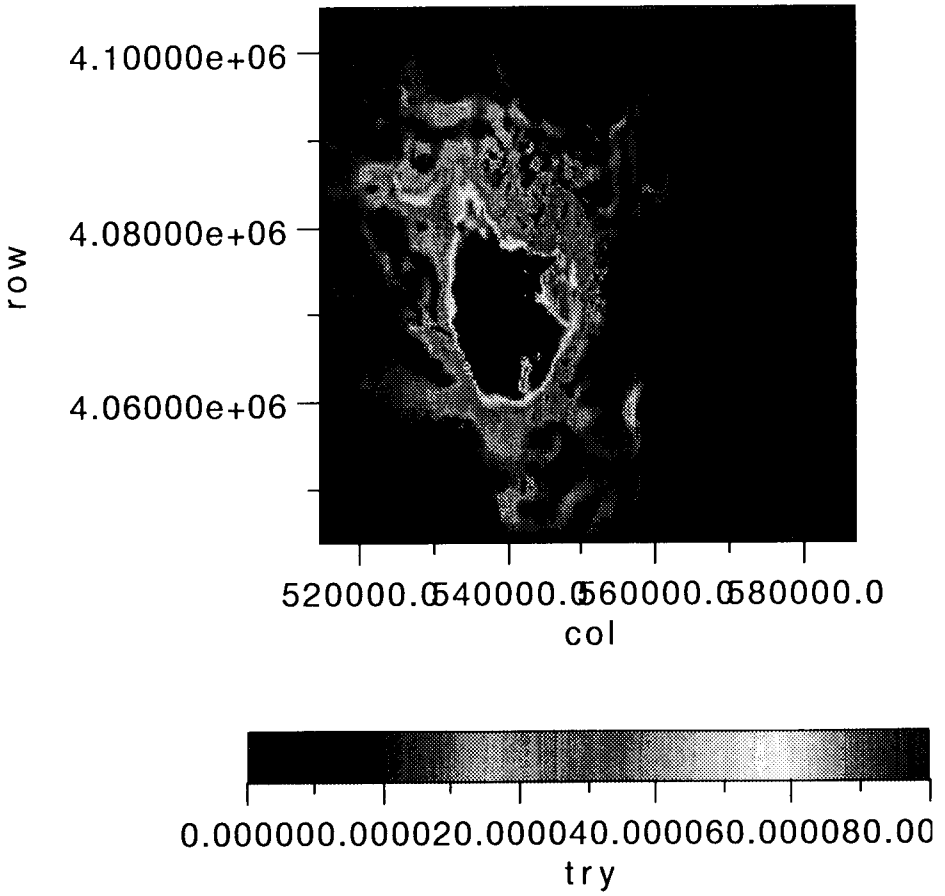

FIGURE 5. mix of gravity and near-neighbor model with w = 1

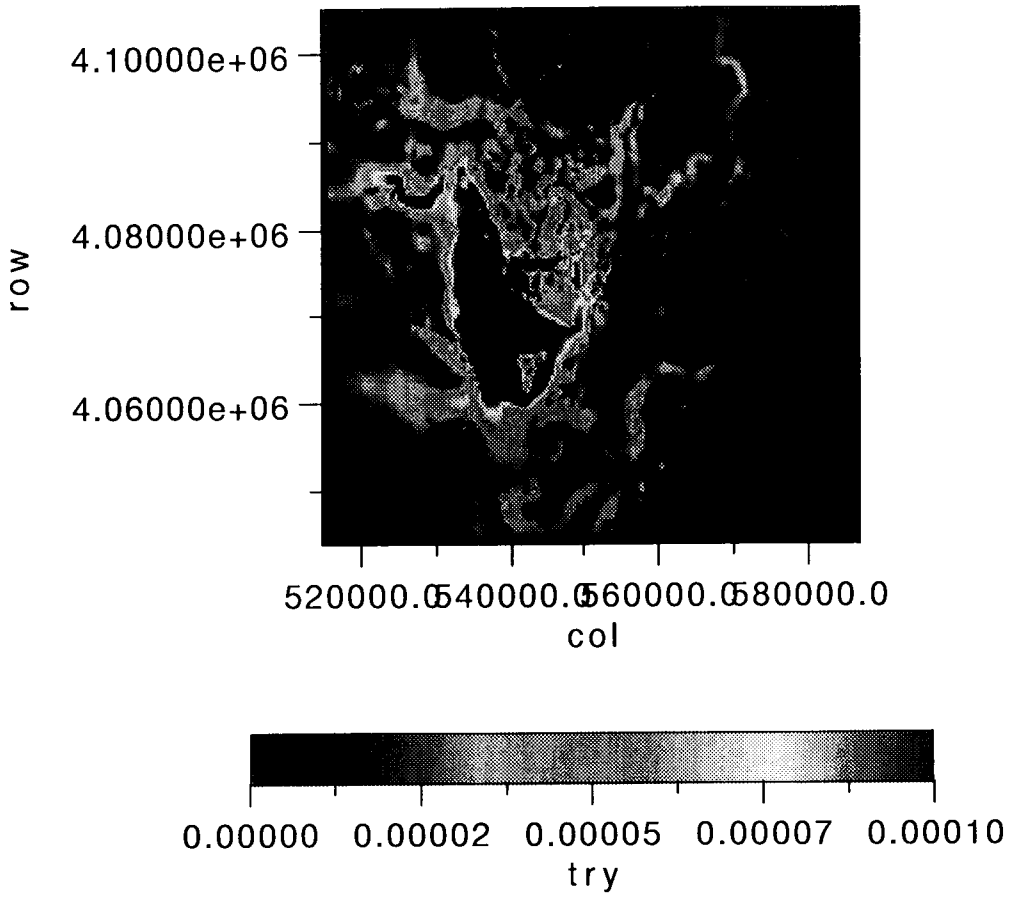

FIGURE 6. mix of gravity gradient and near-neighbor model, w = 2

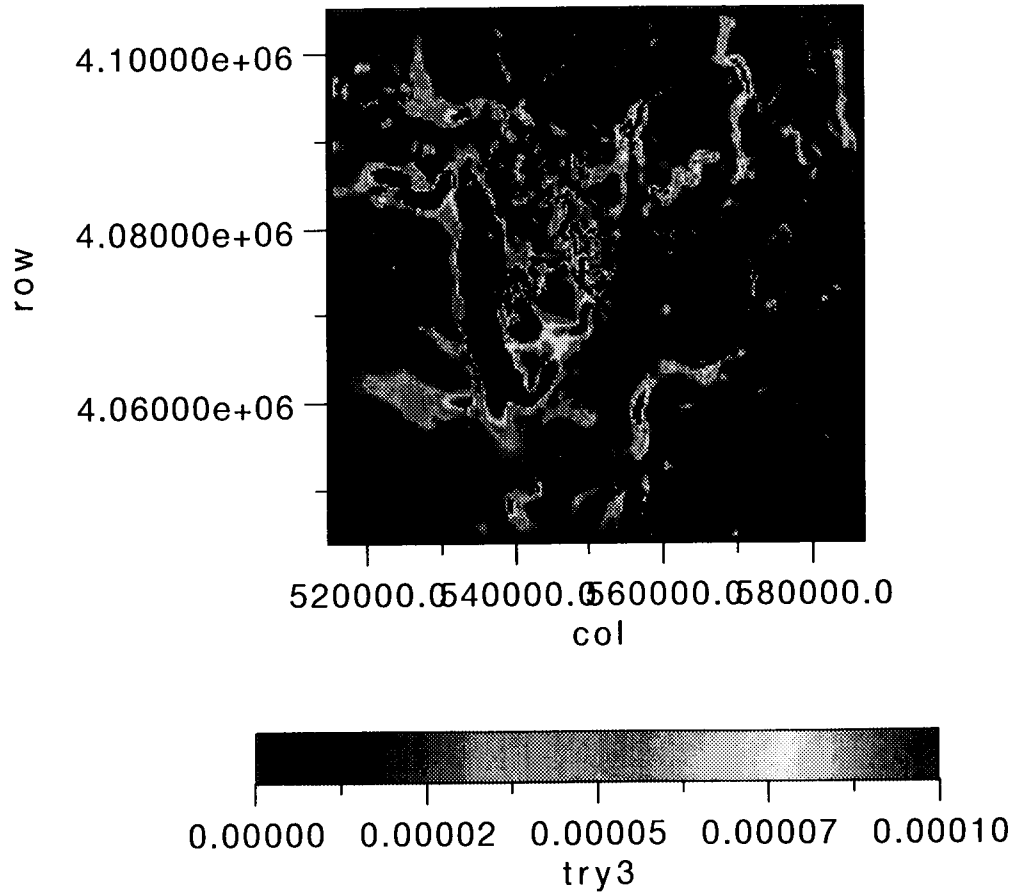

FIGURE 7. near neighbore m=8 model with grvity gradient and w = 3

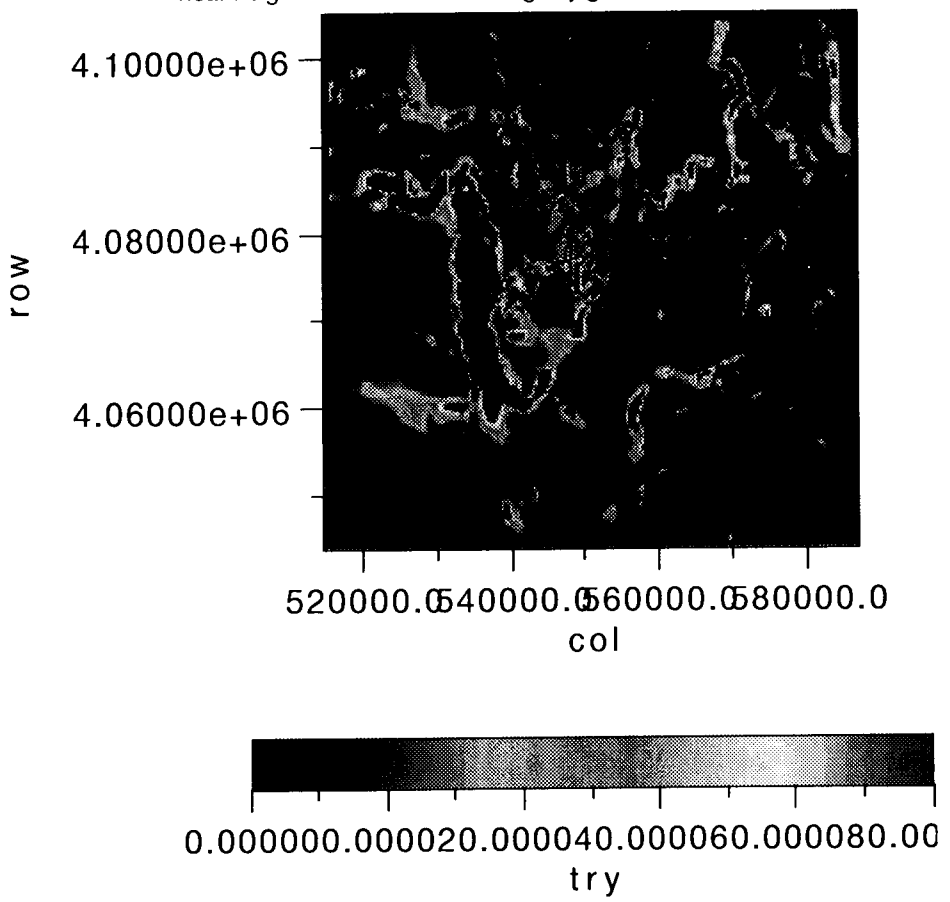

Based on these results it is clear that the function distributes probability between the two end-members between w = 0 and w = 4.5. It looks like values between w = 0.5 and w=2 best capture the current volcano distribution.

Also tried using different weighting functions additively. For example, in a "mixing" process the equation would be

$$\lambda_s = w \cdot \lambda_n + (1 - w) \cdot s$$

FIGURE 8. additive mixing model with w = 0.5, using m = 8 near neighbors and gravity gradient data

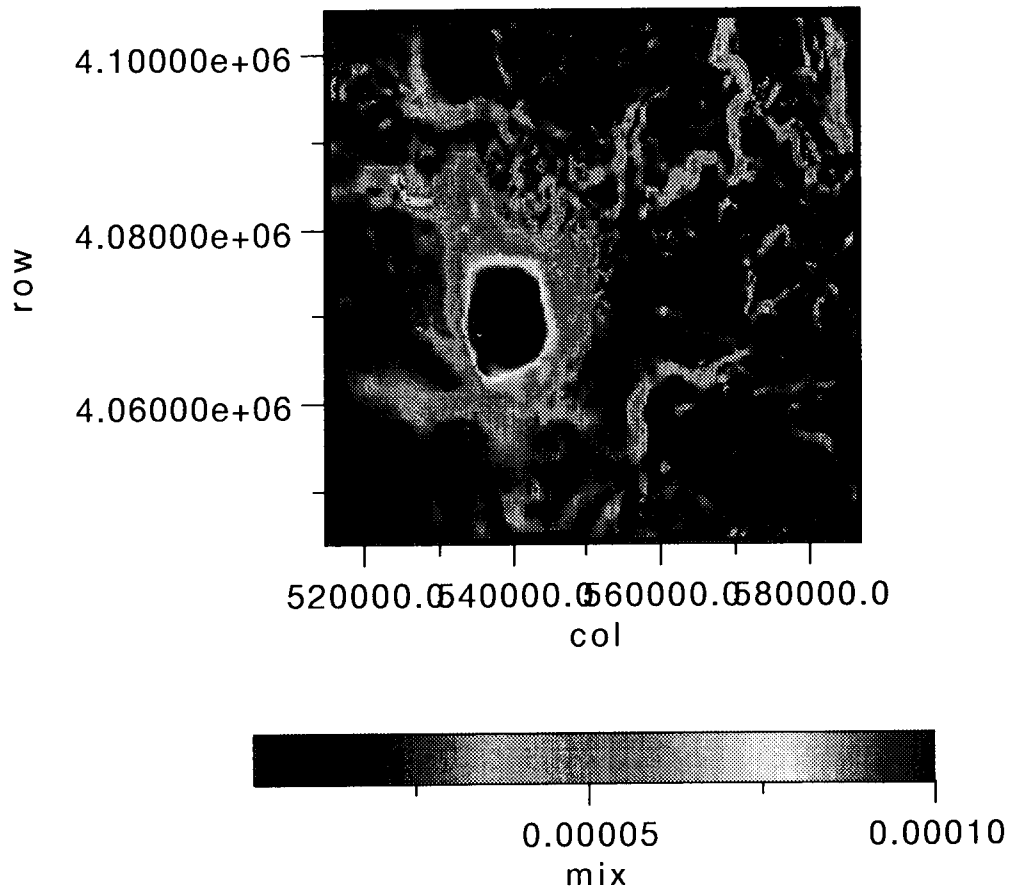

FIGURE 9. Additive mixing model with m=8 near-neighbors, gravity gradient data and w= 0.1

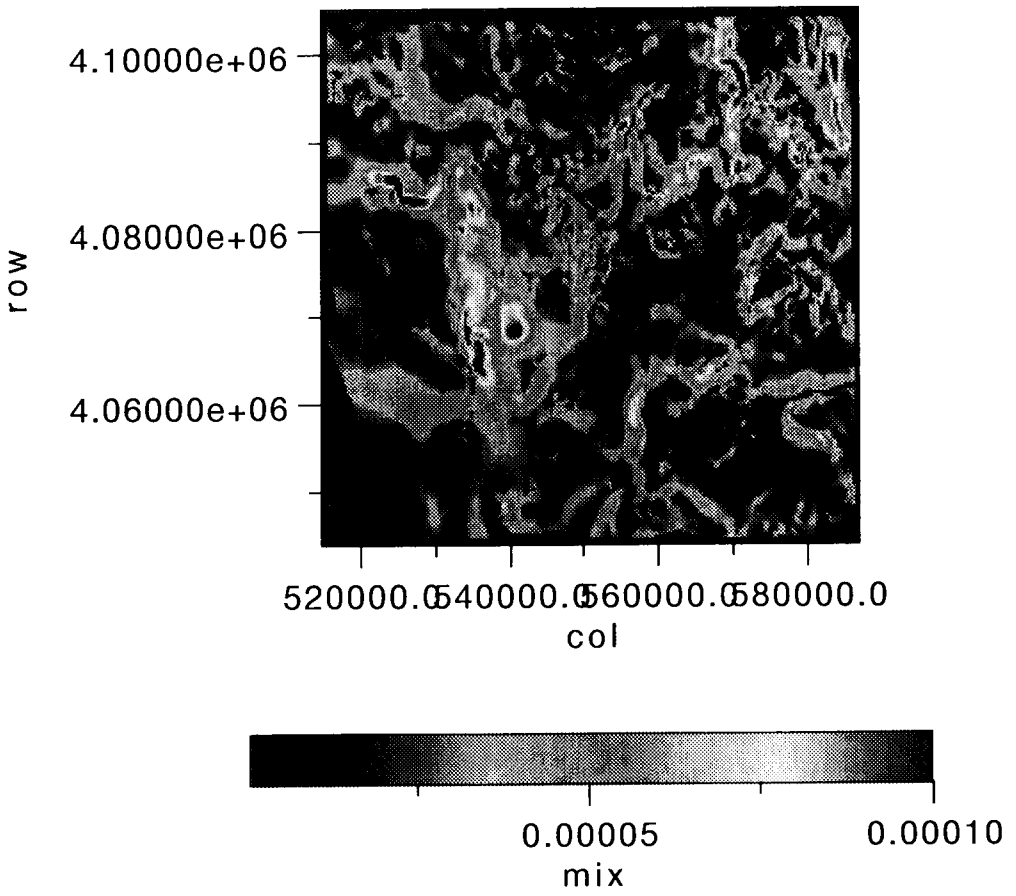

The clear problem with this apporach is that it doesn't look at the intersection of the two probability surfaces. Geologically, you need both a magma source zone and crustal structur to help transport.

Integrating Structure into Probability Estimates Part III

Chuck Connor

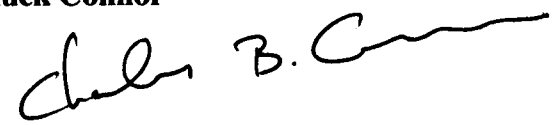

Volcanoes in the YMR appear to lie in areas with high ghorizontal gravity gradients. A test is done to compare gravity gradients where volcanoes are located to the magnitude of gravity gradient overall.

1.0 Introduction

Qualtitatively, there appears to be a good correlation between the gravity gradient data in the YMR and the distribution of volcanoes. (see color figure on the following unumbered page).

This correlation is expectd if magmas tend to ascend along major fault zones, breaking out of these major fault zones in the upper crust. Because gravity change correlates with abrupt lateral density variations produced by faults, the gravity data is a marker of the distribution of major crustal features.

Is there a significant statistical relationship between Quaternary volcano distribution and high-gravity gradients in the YMR?

2.0 Method

The following computer program was used to generate the distributions

```
•!....+....1....+....2....+....3....+....4....+....5....
•! 514751.      4.10503e+6    0
•! 515085.      4.10503e+6    0
•! 515418.      4.10503e+6    0
•! 515751.      4.10503e+6    0
•
```

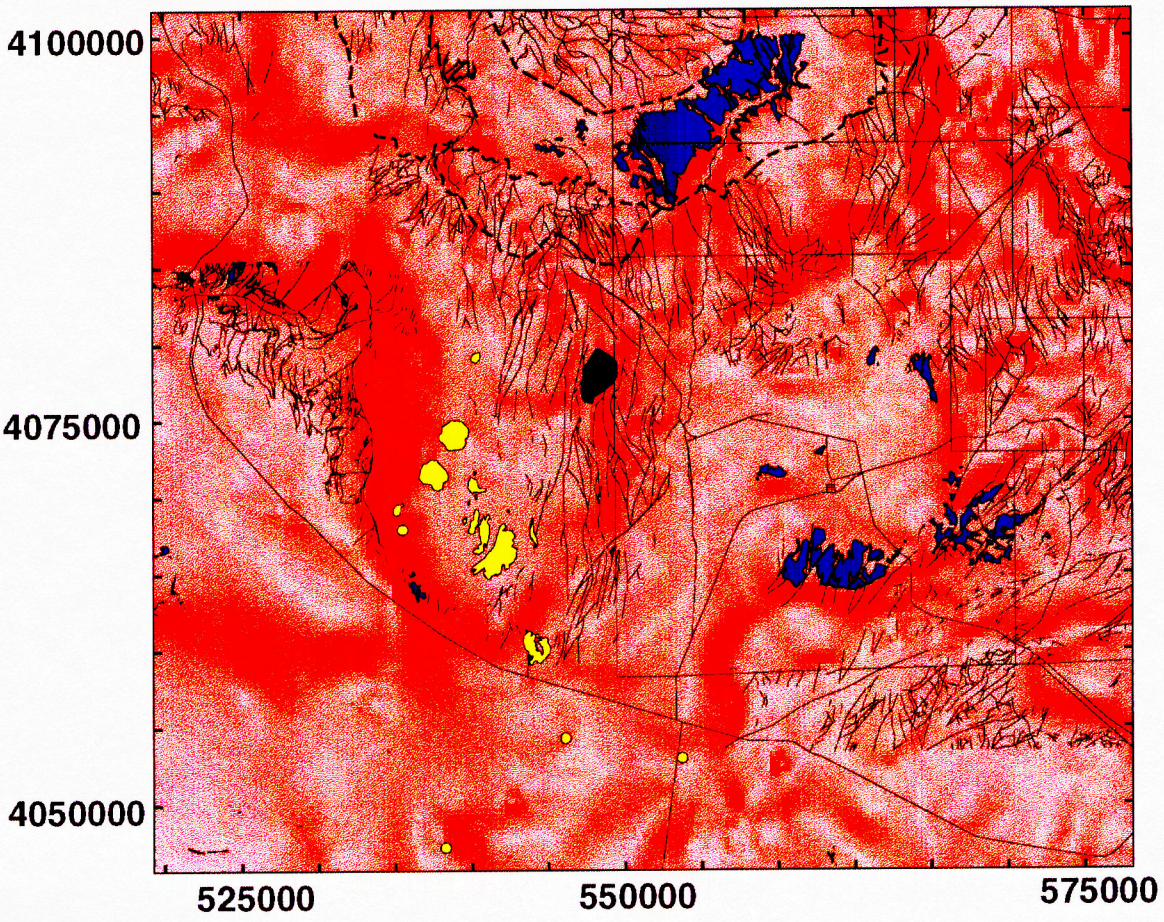
4100000
4075000
4050000
525000
550000
575000

```
•
•let ncx = 540330
•let ncy = 4079130
•let bcx = 538840
•let bcy = 4073990
•let rcx = 537450
•let rcy = 4071470
•let lcnex = 535500
•let lcney = 4069490
•let lcswx = 535131
•let lcswy = 4069220
•let lwx = 543780
•let lwy = 4060380
•let cfax = 540232
•let cfay = 4071610
•let cfbx = 540330
•let cfby = 4070050
•let cfcx = 540365
•let cfcy = 4068790
•let cfdx = 540696
•let cfdy = 4067830
•let cfex = 540300
•let cfey = 4068390
•let cffx = 540660
•let cffy = 4067470
•let avbx = 553720
•let avby = 4052990
•let avax = 546130
•let avay = 4054260
•let avex = 538300
•let avey = 4047200
•let avcx = 547050
•let avcy = 4042950
•let avdx = 549430
•let avdy = 4040080
•
•open #4: name "grav_grad kal", create newold
•erase #4
•open #3: name "gravity_histo", create newold
•erase # 3
•
•dim mtx(184,215)
•!PRINT "INPUT FILE NAME"
•!INPUT RECURR$
•open #1: name "grav_grd.xyz"
•for y =1 to 184 step 1
•for x = 1 to 215 step 1
•
•!for y =1 to 184 step 1
•input #1: lin$
```

```
•
•let mtx(y,x) = val(lin$[33:44])
•if mtx(y,x) > maxmtx then let maxmtx = mtx(y,x)
•let xloc = val(lin$[1:10])
•let yloc = val(lin$[15:30])
•
•if abs(xloc-ncx) < 500 and abs(yloc-ncy) < 500 then print #3: "nc: ";mtx(y,x)
•if abs(xloc-bcx) < 500 and abs(yloc-bcy) < 500 then print #3:"bc: ";mtx(y,x)
•if abs(xloc-rcx) < 500 and abs(yloc-rcy) < 500 then print #3:"rc: ";mtx(y,x)
•if abs(xloc-lcnex) < 500 and abs(yloc-lcney) < 500 then print #3:"lcne: ";mtx(y,x)
•if abs(xloc-lcswx) < 500 and abs(yloc-lcswy) < 500 then print #3:"lcsw: ";mtx(y,x)
•if abs(xloc-lwx) < 500 and abs(yloc-lwy) < 500 then print #3:"lw: ";mtx(y,x)
•if abs(xloc-cfax) < 500 and abs(yloc-cfay) < 500 then print #3:"cfa: ";mtx(y,x)
•if abs(xloc-cfbx) < 500 and abs(yloc-cfby) < 500 then print #3:"cfb: ";mtx(y,x)
•if abs(xloc-cfcx) < 500 and abs(yloc-cfcy) < 500 then print #3:"cfc: ";mtx(y,x)
•if abs(xloc-cfdx) < 500 and abs(yloc-cfdy) < 500 then print #3:"cfd: ";mtx(y,x)
•if abs(xloc-cfex) < 500 and abs(yloc-cfey) < 500 then print #3: "cfe: ";mtx(y,x)
•if abs(xloc-avax) < 500 and abs(yloc-avay) < 500 then print #3:"ava: ";mtx(y,x)
•if abs(xloc-avbx) < 500 and abs(yloc-avby) < 500 then print #3:"avb: ";mtx(y,x)
•if abs(xloc-avcx) < 500 and abs(yloc-avcy) < 500 then print #3:"avc: ";mtx(y,x)
•if abs(xloc-avdx) < 500 and abs(yloc-avdy) < 500 then print #3:"avd: ";mtx(y,x)
•if abs(xloc-avex) < 500 and abs(yloc-avey) < 500 then print #3:"ave: ";mtx(y,x)
•
•if counter = 5 then
•let counter = 0
•if mtx(y,x) > 0 then print #4: mtx(y,x)
•end if
•let counter = counter + 1
•next x
•next y
•
•print maxmtx
•
•
•!OPEN #2: name "hi_FAULTS.TRAN", create newold
•!ERASE #2
•
•!PRINT #2: 184,215
•!PRINT #2: 0,0
•!FOR j = 1 to 184
•!   PRINT #2: 4105030-(j-1)*333;
•!NEXT j
•!FOR i = 1 to 215 step 1
•!   PRINT#2: (i-1)*333 + 515085;
•!NEXT i
•!PRINT
•!
•!
•!PRINT
•!MAT PRINT #2: mtx
```

•!
•
•
•end
•

3.0 Results

The results of the analysis are plotted in Figure 1 and relevant statistics are shown in Table 1.

FIGURE 1. Cumulative probability distribution of all gravity gradients (solide circles) and gravity gradients near Quaternary volcanoes (open circles)

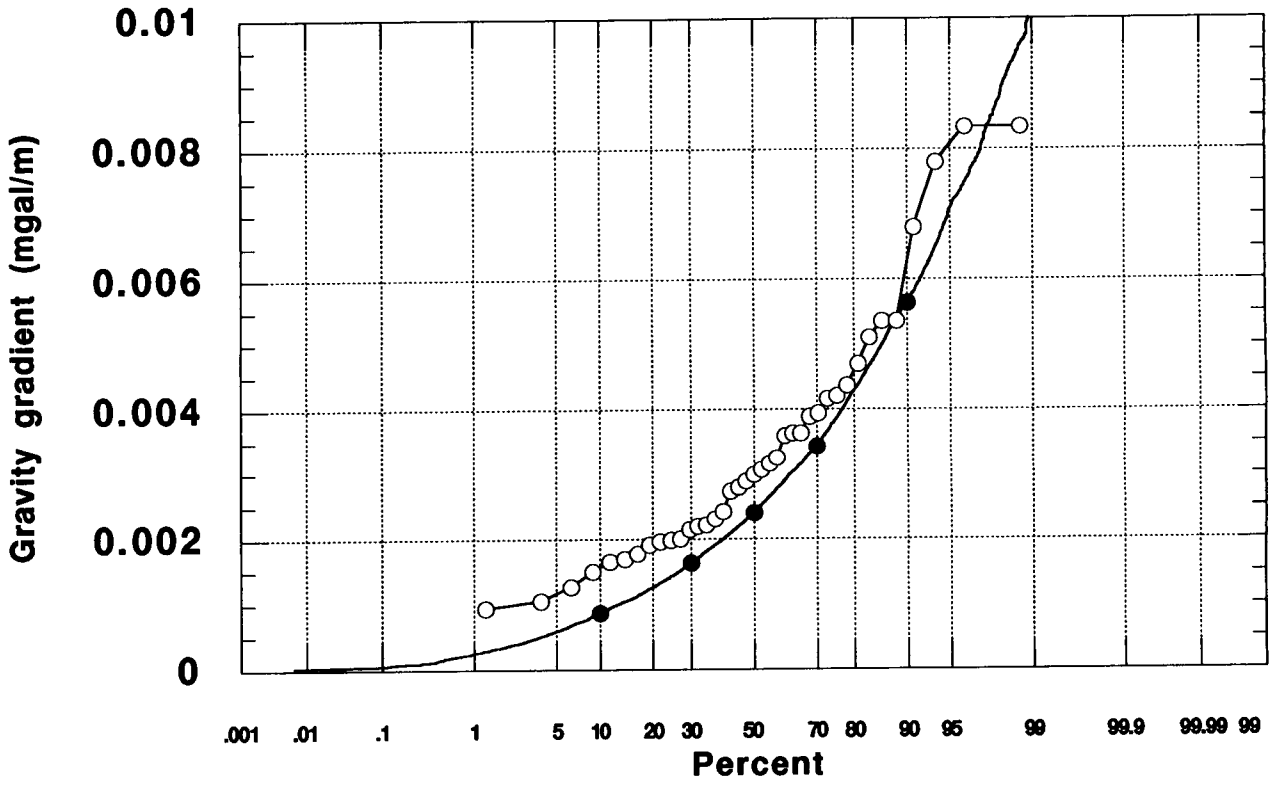

TABLE 1. Distribution of gravity-gradients in the YMR and their relationships to volcano locations

	All Data	Plio - Quaternary Volcanoes	Quaternary Volcanoes
Minimum	3.33e-05	0.000419	0.0009357
Maximum	0.0237373	0.008697	0.008339
Points	7435	126	39
Mean	0.002916	0.002979	0.003413
Median	0.002400	0.002161	0.00298
RMS	0.003586	0.003510	0.003901
Std	0.002088	0.001863	0.001915
Variance	4.36e-06	3.47e-06	3.668e-06

These distributions can be compared using a Student T-test. The null hypothesis is that the mean of all gravity gradient data is equal to the mean of all gravity gradients sampled near Quaternary volcanoes. The alternate hypothesis is that the gravity gradient measured near Quaternary volcanoes is greater than the mean of all gravity gradient data.

The t-test is calculated using :

$$t = \frac{x_1 - x_2}{s_p \sqrt{\frac{1}{n_1} + \frac{1}{n_2}}}$$

where,

$$s_p = \sqrt{\frac{(n_1 - 1)s_1 + (n_2(-1))s_2}{n_1 + n_2 - 2}}$$

In this case t = 1.48

This value is looked-up in a standard t- table. The one used here is from Taylor (1990, Statistical Techniques in Data Analysis, Lewis Publishers, Boca Raton, FL).

The null hypothesis is rejected with 90% confidence (one-tailed test). The null hypothesis would not be rejected with 95% confidence.

Testing against the distribution of Pliocene and Quaternary volcanoes, the null hypothesis is not rejected at the 90% confidence level.

4.0 Discussion

The statistical test confirms the observation that there is some corrleation between gravity gradient and Quaternary volcano distribution. This indicates that gravity gradients might be useful in considering future potential volcano distributions.

The correlation is not greater because there are several high gravity gradient areas on the map that have no associated volcanism. Thus it is likely that an intersection of magma source regions and crustal structure is required to produce a high probability zone.

Pliocene volcanoes correlate poorly with steep gravity gradients. This is primarily because the Pliocene volcanoes in Crater Flat are in a particularly low gravity gradient area. However, they are also located in an area the has the highest recurrence rate of volcanism. Hence - structure is overwhelmed by the comapratively high magma supply?

Spyglass conversion

Chuck Connor

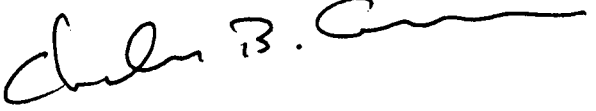

A continuing problem is getting data out of Spyglass Transform into a simple file format that can be read by other programs. The following TrueBasic program acheives this. The program was tested on several files.

1.0 Program

```
•DIM y_val$(700), x_val$(700), z_val$(40000)
•!this program takes a text file generated
•! by Spyglass tranform and turns it
•! into an x,y,z file
•! easy to use in Basic, etc.
•
•
•OPEN #1: name "epan_map.txt"
•OPEN #2: name "epan_map.xyz" , create newold
•ERASE #2
•
•LINE INPUT #1: dum$
•LET tracker = 0
•
•FOR i = 1 to len(dum$)
•   LET t$ = dum$[i:i]
•
•   IF t$ <> "" and i <> len(dum$) then
•      LET tracker = tracker +1
•   ELSE
•      LET strg_num$ = dum$[i-tracker:i-1]
•      LET tracker = 0
•      LET kount = kount + 1
•      LET y_val$(kount) = (strg_num$)
•   END IF
•NEXT i
```

```
•
•LET y_kount = kount
•
•DO while more #1
•  LINE INPUT #1: dum$
•  LET tracker = 0
•  LET kount = 0
•  FOR i = 1 to len(dum$)
•     LET t$ = dum$[i:i]
•     IF t$ <> " " and i <> len(dum$) then
•       LET tracker = tracker +1
•     ELSEIF tracker > 2 then
•       LET strg_num$ = dum$[i-tracker:i-1]
•       LET tracker = 0
•       LET kount = kount + 1
•
•       IF kount = 1 then
•         LET x_value$ = (strg_num$)
•       ELSE
•         LET zkount = zkount + 1
•         LET z_val$(zkount) = (strg_num$)
•         PRINT #2: x_value$, y_val$(zkount), z_val$(zkount)
•       END IF
•
•     END IF
•
•  NEXT i
•  LET zkount = 0
•LOOP
•END
•
```

6 of 17

SCIENTIFIC NOTEBOOK

Project 20-5708-461

#115

BY

Charles Connor

SCIENTIFIC NOTEBOOK

Project 20-5708-461

#115

BY

Charles Connor

Southwest Research Institute
Center for Nuclear Waste Regulatory Analyses
San Antonio, Texas

Structure and Volcanism Continued

Chuck Connor

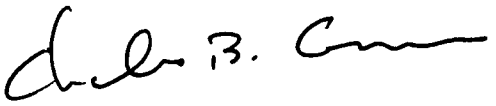

results of looking at the ratio of high dilation tendency faults to all faults on volcanism probability

#20-5708-461

1.0 Overview

Several formulations are possible of how structure should be folded into probability calculations. The following looks at fault density and the ratio of high dilation tendency faults in probability calculations.

One approach is to use Nt/Nf: where Nt = density of faults with dilation tendency greater than 0.8, and Nf is the density of all faults in the region. This ratio is normalized by the sum(Nt/Nf) in all probability calculations.

The calculations were made in SpyGlass transform.

2.0 Input Data

The following data/models were used as Input:

FIGURE 1. Density of high-dilation tendency faults (m length/5km2*pi)

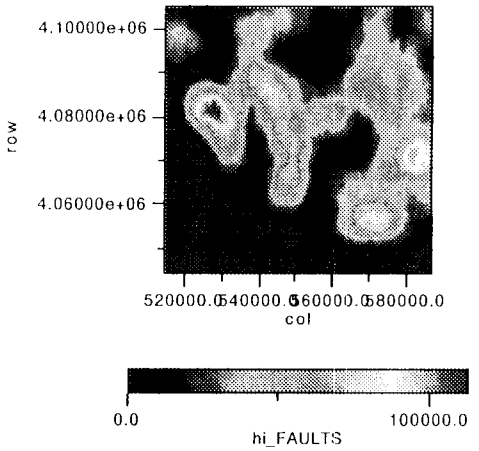

FIGURE 2. density of low dilation tendency faults (m/5km2*pi)

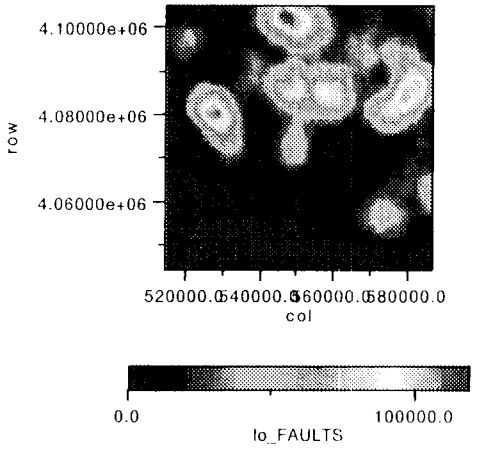

FIGURE 3. "Dike map", probability that given event, dike will intersect repository

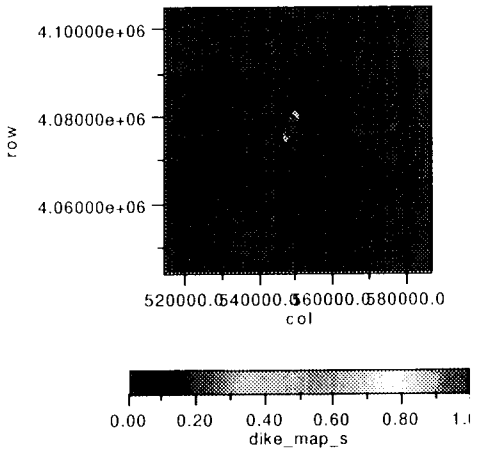

FIGURE 4. Epanchnikov solution (h= 20 km)

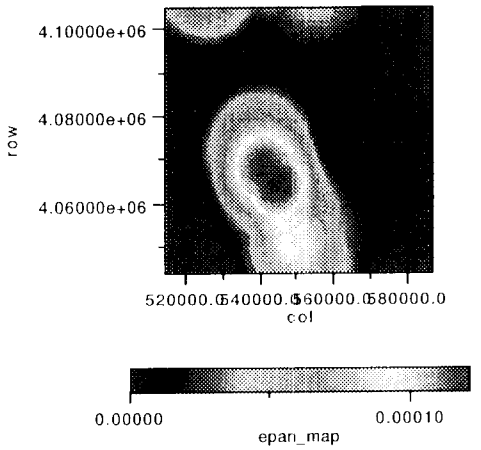

FIGURE 5. Near neighbor map (m= 8)

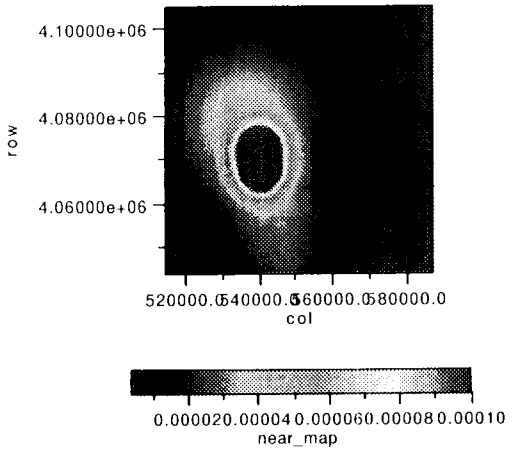

3.0 Results

3.1 Epanechnikov results

Blending the ratio of Nt/Nf with the epanechnikov map h = 20 for different weights w.

Define the normalized matrix:

rat = hi_FAULTS/(hi_FAULTS+lo_FAULTS)

rat_zap = zapnan(rat,0.0)

print sum(rat_zap)

* Result: 18382.4

norm_rat_faults = rat_zap/18382.4

print sum(norm_rat_faults)

* Result: 1

w = 0:

try = epan_map*dike_map_s

print sum(try)

* Result: 0.00732703

w = 0.5:

norm_rat_faults5 = pow(norm_rat_faults,0.5)

try = norm_rat_faults5*epan_map

print sum(try)

* Result: 0.00480539

try1 =try/ 0.00480539

try2 = try1*dike_map_s

print sum(try2)

* Result: 0.00900145

w= 1:

try = norm_rat_faults*epan_map

print sum(try)

* Result: 2.92597e-05

try = try/2.92597e-05 * dike_map_s

print sum(try)

* Result: 0.00873244

w= 1.5:

norm_rat_faults15 = pow(norm_rat_faults,1.5)

try = norm_rat_faults15*epan_map

print sum(try)

* Result: 1.81836e-07

try1 = try/1.81836e-07

try2 = try1*dike_map_s

print sum(try2)

* Result: 0.00830494

w = 2.5

norm_rat_faults25 = pow(norm_rat_faults,2.5)

try = norm_rat_faults25*epan_map

print sum(try)

* Result: 7.3573e-12

try1 = try/7.3573e-12

try2 = try1*dike_map_s

print sum(try2)

* Result: 0.00718207

w = 2

norm_rat_faults2 = norm_rat_faults*norm_rat_faults

try = norm_rat_faults2*epan_map

print sum(try)

* Result: 1.14873e-09

try = try/1.14873e-09 * dike_map_s

print sum(try)

* Result: 0.00777417

w = 3:

norm_rat_faults3 = pow(norm_rat_faults,3)

try = norm_rat_faults3*epan_map

print sum(try)

* Result: 4.76812e-14

try1 = try/4.76812e-14

try2 = try1*dike_map_s

print sum(try2)

* Result: 0.00656078

w = 3.5:

norm_rat_faults35 = pow(norm_rat_faults,3.5)

try = norm_rat_faults35*epan_map

print sum(try)

* Result: 3.1223e-16

try1 = try/ 3.1223e-16

try2 = try1*dike_map_s

print sum(try2)

* Result: 0.0059347

w = 4.0:

norm_rat_faults4 = pow(norm_rat_faults,4)

try = norm_rat_faults4*epan_map

print sum(try)

* Result: 2.06346e-18

try1 = try/2.06346e-18

try2 = try1*dike_map_s

print sum(try2)

* Result: 0.00532207

w = 4.5:

norm_rat_faults45 = pow(norm_rat_faults,4.5)

try = norm_rat_faults45*epan_map

print sum(try)

* Result: 1.37495e-20

try1 = try/1.37495e-20

try2 = try1*dike_map_s

print sum(try2)

* Result: 0.00473614

3.2 Near - neighbor results

Results Using the Near-neighbor method, m = 8 near-neighbors

w = 0:

try1 = dike_map_s*near_map

print sum(try1)

* Result: 0.00495951

w = 0.5

norm_rat_faults5 = pow(norm_rat_faults,0.5)

try = norm_rat_faults5*near_map

print sum(try)

* Result: 0.00511705

try1 = try/0.00511705

try2 = dike_map_s*try1

print sum(try2)

* Result: 0.00572475

w = 1:

try = near_map*norm_rat_faults

print sum(try)

* Result: 3.0707e-05

try1 = try/3.0707e-05

try2 = dike_map_s*try1

print sum(try2)

* Result: 0.00563813

w = 1.5:

norm_rat_faults5 = pow(norm_rat_faults,1.5)

try = norm_rat_faults5*near_map

print sum(try)

* Result: 1.87783e-07

try1 = try/1.87783e-07

try2 = dike_map_s*try1

print sum(try2)

* Result: 0.00545216

w = 2:

norm_rat_faults2 = norm_rat_faults*norm_rat_faults

try = norm_rat_faults2*near_map

print sum(try)

* Result: 1.1658e-09

try1 = try/1.1658e-09

try2 = dike_map_s*try1

print sum(try2)

* Result: 0.00519642

w = 2.5:

norm_rat_faults25 = pow(norm_rat_faults,2.5)

try = norm_rat_faults25*near_map

print sum(try)

* Result: 7.32888e-12

try1 = try/7.32888e-12

try2 = dike_map_s*try1

print sum(try2)

* Result: 0.00489376

w = 3

norm_rat_faults3 = pow(norm_rat_faults,3)

try = norm_rat_faults3*near_map

print sum(try)

* Result: 4.6571e-14

try1 = try/4.6571e-14

try2 = dike_map_s*try1

print sum(try2)

* Result: 0.00456207

w = 3.5:

norm_rat_faults35 = pow(norm_rat_faults,3.5)

try = norm_rat_faults35*near_map

print sum(try)

* Result: 2.98726e-16

try1 = try/2.98726e-16

try2 = dike_map_s*try1

print sum(try2)

* Result: 0.00421545

w = 4:

norm_rat_faults4 = pow(norm_rat_faults,4)

try = norm_rat_faults4*near_map

print sum(try)

* Result: 1.93221e-18

try1 = try/1.93221e-18

try2 = try1*dike_map_s

print sum(try2)

* Result: 0.00386493

w = 4.5

norm_rat_faults45 = pow(norm_rat_faults,4.5)

try = norm_rat_faults45*near_map

print sum(try)

* Result: 1.25916e-20

try1 = try/1.25916e-20

try2 = dike_map_s*try1

print sum(try2)

* Result: 0.0035191

TABLE 1. Summary of the results: probability of disruption if volcanism occurs in the region

W	Epan	NN
0	.007	.0050
0.5	.009	.0057
1.0	.009	.0056
1.5	.0083	.0055
2.0	.0078	.0051
2.5	.0072	.0049
3.0	.0066	.0046
3.5	.0059	.0042
4.0	.0053	.0039
4.5	.0047	.0035

4.0 Using normalized nT only

Can also calculate probability simply based on the distribution of high-dilation tendency faults (suggested by R. Mantufel). Here the input structure data file is hi_faults (Figure 1, "Density of high-dilation tendency faults (m length/km2)," on page 2). Again, results ar weighted by w; only near - neighbor method is used for input probability (Figure 5, "Near neighbor map (m= 8)," on page 4).

w = 0.5

norm_hi_faults5 = pow(norm_hi_faults,0.5)

try = norm_hi_faults5*near_map

print sum(try)

* Result: 0.00424478

try1 = try/0.00424478

try2 = dike_map_s*try1

print sum(try2)

* Result: 0.00920795

w = 1:

try = norm_hi_faults*near_map

print sum(try)

* Result: 2.46152e-05

try1 = try/2.46152e-05

try2 = try1*dike_map_s

print sum(try2)

* Result: 0.0125253

w = 1.5:

norm_hi_faults15 = pow(norm_hi_faults,1.5)

try = norm_hi_faults15*near_map

print sum(try)

* Result: 1.59522e-07

try1 = try/1.59522e-07

try2 = dike_map_s*try1

print sum(try2)

* Result: 0.0152592

w = 2:

norm_hi_faults2 = norm_hi_faults*norm_hi_faults

try = norm_hi_faults2*near_map

print sum(try)

* Result: 1.11323e-09

try1 = try/1.11323e-09

try2 = try1*dike_map_s

print sum(try)

* Result: 1.11323e-09

print sum(try2)

* Result: 0.0172781

w = 2.5:

norm_hi_faults25 = pow(norm_hi_faults,2.5)

try = norm_hi_faults25*near_map

print sum(try)

* Result: 8.18137e-12

try1 = try/8.18137e-12

try2 = dike_map_s*try1

print sum(try2)

* Result: 0.0185928

w = 3:

norm_hi_faults3 = pow(norm_hi_faults,3)

try = norm_hi_faults3*near_map

print sum(try)

* Result: 6.24681e-14

try1 = try/6.24681e-14

try2 = dike_map_s*try1

print sum(try2)

* Result: 0.0192731

w = 3.5:

norm_hi_faults35=pow(norm_hi_faults,3.5)

try = norm_hi_faults35*near_map

print sum(try)

* Result: 4.91388e-16

try1 = try/4.91388e-16

try2 = try1*dike_map_s

print sum(try2)

* Result: 0.0194071

w = 4.0:

norm_hi_faults4=pow(norm_hi_faults,4)

try = norm_hi_faults4*near_map

print sum(try)

* Result: 3.96083e-18

try1 = try/3.96083e-18

try2 = try1*dike_map_s

print sum(try2)

* Result: 0.0190855

w = 4.5:

norm_hi_faults45=pow(norm_hi_faults,4.5)

try = norm_hi_faults45*near_map

print sum(try)

* Result: 3.25971e-20

try1 = try/3.25971e-20

try2 = try1*dike_map_s

print sum(try2)

* Result: 0.0183963

TABLE 2. Summary of the results using only high dilation tendency faults, probability assuming a volcano will occur in the region

w	NN
0	0.005
0.5	0.009
1.0	0.013
1.5	0.0152
2.0	0.0172
2.5	0.0186
3.0	0.0192
3.5	0.0194
4.0	0.0191
4.5	0.0184

Structure and Volcanism Continued

Chuck Connor

Testing against the location of exisitng cinder cones.

Acct # 20-5708-461

1.0 Overview

The results of the probability calculations are tested against the locations of exisiting cinder cones.

2.0 Code

The following truebasic code was used to calculate probabilites at the locations of cinder cones

written by C. Connor

```
•!input data sets look like
•!....+....1....+....2....+....3....+....4....+....5....
•!4062739.00    579687.00    4.614e-06
•!4062739.00    580020.00    4.557e-06
•!4062739.00    580353.00    4.502e-06
•!4062739.00    580686.00    4.447e-06
•!4105030.00    516750.00     0.000e+00
•!4105030.00    517083.00     0.000e+00
•!4105030.00    517416.00     0.000e+00
•!4105030.00    517749.00     0.000e+00
•!4105030.00    518082.00     0.000e+00
```

```
•
•!These are the geographic coordinates of the cones
•LET ncx = 540330
•LET ncy = 4079130
•LET bcx = 538840
•LET bcy = 4073990
•LET rcx = 537450
•LET rcy = 4071470
•LET lcnex = 535500
•LET lcney = 4069490
•LET lcswx = 535131
•LET lcswy = 4069220
•LET lwx = 543780
•LET lwy = 4060380
•LET cfax = 540232
•LET cfay = 4071610
•LET cfbx = 540330
•LET cfby = 4070050
•LET cfcx = 540365
•LET cfcy = 4068790
•LET cfdx = 540696
•LET cfdy = 4067830
•LET cfex = 540300
•LET cfey = 4068390
•LET cffx = 540660
•LET cffy = 4067470
•LET avbx = 553720
•LET avby = 4052990
•LET avax = 546130
•LET avay = 4054260
•LET avex = 538300
•LET avey = 4047200
•LET avcx = 547050
•LET avcy = 4042950
•LET avdx = 549430
•LET avdy = 4040080
•!OPEN #1: name "grav_grd.xyz"
•!OPEN #2: name "near_map.xyz"
•OPEN #4: name "thres.out", create newold
•ERASE #4
•OPEN #3: name "thres.cones", create newold
•ERASE #3
•
•for weight = 0 to 4.5 step 0.5
•OPEN #1: name "grav_grd.xyz"
•OPEN #2: name "epan_map.xyz"
•
•print #3: "weight = ";weight
•FOR y =1 to 184 step 1
•  PRINT ".";
```

```
•  FOR x = 1 to 215 step 1
•
•
•     INPUT #1: lin$
•
•     LET grav = val(lin$[33:41])
•     LET xloc = val(lin$[1:10])
•     LET yloc = val(lin$[15:25])
•
•     INPUT #2: lin$
•     LET near = val(lin$[33:41])
•     LET xloc2 = val(lin$[1:10])
•     LET yloc2 = val(lin$[15:25])
•
•     IF xloc2 <> xloc then PRINT "scream location error"
•     IF yloc2 <> yloc then PRINT "scream location error"
•
•     LET hazard = near*grav^weight
•     LET sum_hazard = sum_hazard + hazard
•
•     !the numbers printed to file #3 have to be divided by the sum_hazard to
•     !normalize them. Also, divide by (.333*.333) for the hazard to be expressed in
•     ! square km.
•     IF abs(yloc-ncx) < 500 and abs(xloc-ncy) < 500 then PRINT #3: "nc: ";hazard
•     IF abs(yloc-bcx) < 500 and abs(xloc-bcy) < 500 then PRINT #3:"bc: ";hazard
•     IF abs(yloc-rcx) < 500 and abs(xloc-rcy) < 500 then PRINT #3:"rc: ";hazard
•     IF abs(yloc-lcnex) < 500 and abs(xloc-lcney) < 500 then PRINT #3:"lcne: ";haz-
ard
•     IF abs(yloc-lcswx) < 500 and abs(xloc-lcswy) < 500 then PRINT #3:"lcsw: ";haz-
ard
•     IF abs(yloc-lwx) < 500 and abs(xloc-lwy) < 500 then PRINT #3:"lw: ";hazard
•     IF abs(yloc-cfax) < 500 and abs(xloc-cfay) < 500 then PRINT #3:"cfa: ";hazard
•     IF abs(yloc-cfbx) < 500 and abs(xloc-cfby) < 500 then PRINT #3:"cfb: ";hazard
•     IF abs(yloc-cfcx) < 500 and abs(xloc-cfcy) < 500 then PRINT #3:"cfc: ";hazard
•     IF abs(yloc-cfdx) < 500 and abs(xloc-cfdy) < 500 then PRINT #3:"cfd: ";hazard
•     IF abs(yloc-cfex) < 500 and abs(xloc-cfey) < 500 then PRINT #3: "cfe: ";hazard
•     IF abs(yloc-avax) < 500 and abs(xloc-avay) < 500 then PRINT #3:"ava: ";hazard
•     IF abs(yloc-avbx) < 500 and abs(xloc-avby) < 500 then PRINT #3:"avb: ";hazard
•     IF abs(yloc-avcx) < 500 and abs(xloc-avcy) < 500 then PRINT #3:"avc: ";hazard
•     IF abs(yloc-avdx) < 500 and abs(xloc-avdy) < 500 then PRINT #3:"avd: ";hazard
•     IF abs(yloc-avex) < 500 and abs(xloc-avey) < 500 then PRINT #3:"ave: ";hazard
•
•     IF counter = 5 then
•       LET counter = 0
•       IF hazard > 0 then PRINT #4: hazard
•     END IF
•     LET counter = counter + 1
•  NEXT x
•NEXT y
•
```

```
•PRINT #3: "sum hazard = "; sum_hazard
•print #3: "**************************************************"
•let sum_hazard = 0
•
•close #1
•close #2
•next weight
•
•END
•
```

3.0 Results

```
•weight = 0
•nc: 7.224e-5
•nc: 7.212e-5
•nc: 7.195e-5
•nc: 7.355e-5
•nc: 7.343e-5
•nc: 7.325e-5
•nc: 7.48e-5
•nc: 7.468e-5
•nc: 7.45e-5
•bc: 9.862e-5
•bc: 9.928e-5
•bc: 9.985e-5
•bc: 1.003e-4
•bc: 1.009e-4
•bc: 1.015e-4
•bc: 1.018e-4
•bc: 1.025e-4
•bc: 1.031e-4
•cfa: 1.107e-4
•cfa: 1.109e-4
•cfa: .000111
•rc: 1.058e-4
•rc: 1.068e-4
•rc: 1.078e-4
•cfa: 1.117e-4
•cfa: 1.119e-4
•cfa: 1.121e-4
•rc: 1.067e-4
•rc: 1.078e-4
•rc: 1.087e-4
•cfa: 1.127e-4
```

•cfa: 1.129e-4
•cfa: .000113
•rc: 1.076e-4
•rc: 1.086e-4
•rc: 1.095e-4
•cfb: 1.149e-4
•cfb: 1.151e-4
•cfb: 1.152e-4
•cfb: 1.155e-4
•cfb: 1.157e-4
•cfb: 1.158e-4
•lcne: .000102
•lcne: 1.036e-4
•lcne: .000105
•cfb: .000116
•cfb: 1.162e-4
•cfb: 1.163e-4
•lcsw: 1.007e-4
•lcne: 1.024e-4
•lcsw: 1.024e-4
•lcne: 1.039e-4
•lcsw: 1.039e-4
•lcne: 1.054e-4
•lcsw: .000101
•lcne: 1.027e-4
•lcsw: 1.027e-4
•lcne: 1.042e-4
•lcsw: 1.042e-4
•lcne: 1.057e-4
•cfc: 1.167e-4
•cfc: 1.169e-4
•cfc: .000117
•lcsw: 1.012e-4
•lcsw: 1.029e-4
•lcsw: 1.045e-4
•cfc: 1.169e-4
•cfe: 1.169e-4
•cfc: 1.171e-4
•cfe: 1.171e-4
•cfc: 1.172e-4
•cfe: 1.172e-4
•cfc: .000117
•cfe: .000117
•cfc: 1.172e-4
•cfe: 1.172e-4
•cfc: 1.173e-4
•cfe: 1.173e-4
•cfe: .000117
•cfd: 1.172e-4
•cfe: 1.172e-4

•cfd: 1.173e-4
•cfe: 1.173e-4
•cfd: 1.173e-4
•cfd: 1.171e-4
•cfd: 1.173e-4
•cfd: 1.173e-4
•cfd: .000117
•cfd: 1.171e-4
•cfd: 1.171e-4
•lw: .000114
•lw: 1.142e-4
•lw: 1.143e-4
•lw: 1.127e-4
•lw: 1.129e-4
•lw: .000113
•lw: 1.112e-4
•lw: 1.114e-4
•lw: 1.115e-4
•ava: 9.558e-5
•ava: 9.591e-5
•ava: 9.613e-5
•ava: 9.511e-5
•ava: 9.544e-5
•ava: 9.566e-5
•ava: 9.452e-5
•ava: 9.485e-5
•ava: 9.507e-5
•avb: 8.69e-5
•avb: 8.565e-5
•avb: 8.432e-5
•avb: 8.747e-5
•avb: 8.622e-5
•avb: 8.489e-5
•avb: 8.795e-5
•avb: 8.67e-5
•avb: 8.537e-5
•ave: 4.253e-5
•ave: 4.546e-5
•ave: 4.829e-5
•ave: 4.147e-5
•ave: 4.44e-5
•ave: 4.723e-5
•ave: 4.032e-5
•ave: 4.324e-5
•ave: 4.608e-5
•sum hazard = .999998
•**********
•weight = .5
•nc: 3.38065e-6
•nc: 3.15355e-6

•nc: 2.93147e-6
•nc: 3.8689e-6
•nc: 3.44261e-6
•nc: 3.0184e-6
•nc: 3.53306e-6
•nc: 3.58853e-6
•nc: 3.31922e-6
•bc: 6.98046e-6
•bc: 6.566e-6
•bc: 5.35758e-6
•bc: 7.25634e-6
•bc: 6.91368e-6
•bc: 7.25068e-6
•bc: 6.4247e-6
•bc: 6.65066e-6
•bc: 6.21942e-6
•cfa: 4.58437e-6
•cfa: 5.1014e-6
•cfa: 5.51548e-6
•rc: 6.7943e-6
•rc: 6.00079e-6
•rc: 5.88572e-6
•cfa: 4.68341e-6
•cfa: 5.55344e-6
•cfa: 5.90311e-6
•rc: 6.21339e-6
•rc: 5.34018e-6
•rc: 4.67915e-6
•cfa: 4.70514e-6
•cfa: 5.40978e-6
•cfa: 5.80164e-6
•rc: 5.75232e-6
•rc: 4.80915e-6
•rc: 3.89149e-6
•cfb: 3.7532e-6
•cfb: 4.01037e-6
•cfb: 4.33036e-6
•cfb: 3.234e-6
•cfb: 3.60197e-6
•cfb: 4.08923e-6
•lcne: 9.00955e-6
•lcne: 9.46113e-6
•lcne: 7.68655e-6
•cfb: 3.12878e-6
•cfb: 3.74734e-6
•cfb: 4.23179e-6
•lcsw: 8.50364e-6
•lcne: 9.54959e-6
•lcsw: 9.54959e-6
•lcne: 8.45685e-6

•lcsw: 8.45685e-6
•lcne: 6.5704e-6
•lcsw: 9.53849e-6
•lcne: 9.083e-6
•lcsw: 9.083e-6
•lcne: 9.19679e-6
•lcsw: 9.19679e-6
•lcne: 8.4527e-6
•cfc: 4.97175e-6
•cfc: 4.98575e-6
•cfc: 5.03236e-6
•lcsw: 9.87361e-6
•lcsw: 8.9114e-6
•lcsw: 9.04755e-6
•cfc: 5.40528e-6
•cfe: 5.40528e-6
•cfc: 5.34956e-6
•cfe: 5.34956e-6
•cfc: 5.28051e-6
•cfe: 5.28051e-6
•cfc: 5.50398e-6
•cfe: 5.50398e-6
•cfc: 5.44822e-6
•cfe: 5.44822e-6
•cfc: 5.39835e-6
•cfe: 5.39835e-6
•cfe: 5.29094e-6
•cfd: 5.28441e-6
•cfe: 5.28441e-6
•cfd: 5.3071e-6
•cfe: 5.3071e-6
•cfd: 5.34456e-6
•cfd: 4.946e-6
•cfd: 5.07382e-6
•cfd: 5.13045e-6
•cfd: 4.61372e-6
•cfd: 4.79252e-6
•cfd: 4.85789e-6
•lw: 7.6414e-6
•lw: 7.36656e-6
•lw: 6.85038e-6
•lw: 7.1251e-6
•lw: 6.80685e-6
•lw: 6.25289e-6
•lw: 6.61336e-6
•lw: 6.34785e-6
•lw: 5.89054e-6
•ava: 4.67854e-6
•ava: 5.21189e-6
•ava: 5.15619e-6

•ava: 5.26982e-6
•ava: 5.53058e-6
•ava: 5.0817e-6
•ava: 5.7401e-6
•ava: 5.38644e-6
•ava: 4.76205e-6
•avb: 4.75892e-6
•avb: 4.83828e-6
•avb: 4.23283e-6
•avb: 3.91862e-6
•avb: 3.63967e-6
•avb: 3.15923e-6
•avb: 2.48262e-6
•avb: 2.77304e-6
•avb: 1.92982e-6
•ave: 2.51431e-6
•ave: 2.52579e-6
•ave: 3.39201e-6
•ave: 2.06019e-6
•ave: 2.03224e-6
•ave: 2.93777e-6
•ave: 1.48802e-6
•ave: 2.03504e-6
•ave: 2.76365e-6
•sum hazard = 4.95168e-2
•**********
•weight = 1
•nc: 1.58206e-7
•nc: 1.37893e-7
•nc: 1.19437e-7
•nc: 2.03513e-7
•nc: 1.61399e-7
•nc: 1.24379e-7
•nc: 1.66879e-7
•nc: 1.72436e-7
•nc: 1.47882e-7
•bc: 4.94086e-7
•bc: 4.34251e-7
•bc: 2.87468e-7
•bc: 5.2497e-7
•bc: 4.73726e-7
•bc: 5.17954e-7
•bc: 4.05469e-7
•bc: 4.31525e-7
•bc: 3.75181e-7
•cfa: 1.8985e-7
•cfa: 2.34664e-7
•cfa: 2.74059e-7
•rc: 4.36319e-7
•rc: 3.37168e-7

•rc: 3.21352e-7
•cfa: 1.96369e-7
•cfa: 2.7561e-7
•cfa: 3.10853e-7
•rc: 3.6182e-7
•rc: 2.64541e-7
•rc: 2.01421e-7
•cfa: 1.96436e-7
•cfa: 2.59218e-7
•cfa: 2.97868e-7
•rc: 3.07521e-7
•rc: 2.12965e-7
•rc: 1.38298e-7
•cfb: 1.22598e-7
•cfb: 1.39731e-7
•cfb: 1.62778e-7
•cfb: 9.0552e-8
•cfb: 1.12136e-7
•cfb: 1.44403e-7
•lcne: 7.95804e-7
•lcne: 8.64024e-7
•lcne: 5.62695e-7
•cfb: 8.439e-8
•cfb: 1.20848e-7
•cfb: 1.53981e-7
•lcsw: 7.18092e-7
•lcne: 8.90573e-7
•lcsw: 8.90573e-7
•lcne: 6.88338e-7
•lcsw: 6.88338e-7
•lcne: 4.09584e-7
•lcsw: 9.00819e-7
•lcne: 8.03319e-7
•lcsw: 8.03319e-7
•lcne: 8.11718e-7
•lcsw: 8.11718e-7
•lcne: 6.75951e-7
•cfc: 2.11811e-7
•cfc: 2.12641e-7
•cfc: 2.1645e-7
•lcsw: 9.63323e-7
•lcsw: 7.7175e-7
•lcsw: 7.83332e-7
•cfc: 2.49932e-7
•cfe: 2.49932e-7
•cfc: 2.44388e-7
•cfe: 2.44388e-7
•cfc: 2.37916e-7
•cfe: 2.37916e-7
•cfc: 2.58921e-7

•cfe: 2.58921e-7
•cfc: 2.53269e-7
•cfe: 2.53269e-7
•cfc: 2.48441e-7
•cfe: 2.48441e-7
•cfe: 2.39265e-7
•cfd: 2.38268e-7
•cfe: 2.38268e-7
•cfd: 2.40113e-7
•cfe: 2.40113e-7
•cfd: 2.43515e-7
•cfd: 2.08906e-7
•cfd: 2.19468e-7
•cfd: 2.24395e-7
•cfd: 1.81935e-7
•cfd: 1.96142e-7
•cfd: 2.01529e-7
•lw: 5.12202e-7
•lw: 4.75186e-7
•lw: 4.10566e-7
•lw: 4.50462e-7
•lw: 4.10392e-7
•lw: 3.46006e-7
•lw: 3.93314e-7
•lw: 3.61716e-7
•lw: 3.11196e-7
•ava: 2.2901e-7
•ava: 2.83222e-7
•ava: 2.76566e-7
•ava: 2.91988e-7
•ava: 3.20488e-7
•ava: 2.69953e-7
•ava: 3.4859e-7
•ava: 3.05891e-7
•ava: 2.38531e-7
•avb: 2.60613e-7
•avb: 2.73309e-7
•avb: 2.12486e-7
•avb: 1.75552e-7
•avb: 1.53644e-7
•avb: 1.17573e-7
•avb: 7.00786e-8
•avb: 8.86941e-8
•avb: 4.36241e-8
•ave: 1.48642e-7
•ave: 1.40335e-7
•ave: 2.38263e-7
•ave: 1.02348e-7
•ave: 9.3018e-8
•ave: 1.82733e-7

•ave: 5.49158e-8
•ave: 9.57766e-8
•ave: 1.6575e-7
•sum hazard = 2.8547e-3
•**********
•weight = 1.5
•nc: 7.40362e-9
•nc: 6.02959e-9
•nc: 4.86623e-9
•nc: 1.07052e-8
•nc: 7.56685e-9
•nc: 5.12524e-9
•nc: 7.88226e-9
•nc: 8.28591e-9
•nc: 6.58866e-9
•bc: 3.49721e-8
•bc: 2.87197e-8
•bc: 1.54245e-8
•bc: 3.79797e-8
•bc: 3.24597e-8
•bc: 3.70002e-8
•bc: 2.55896e-8
•bc: 2.79993e-8
•bc: 2.26325e-8
•cfa: 7.86219e-9
•cfa: 1.07946e-8
•cfa: 1.36177e-8
•rc: 2.80197e-8
•rc: 1.89445e-8
•rc: 1.75453e-8
•cfa: 8.23344e-9
•cfa: 1.36781e-8
•cfa: 1.63693e-8
•rc: 2.10696e-8
•rc: 1.31048e-8
•rc: 8.67047e-9
•cfa: 8.20106e-9
•cfa: 1.24209e-8
•cfa: 1.52931e-8
•rc: 1.64401e-8
•rc: 9.43075e-9
•rc: 4.91495e-9
•cfb: 4.00467e-9
•cfb: 4.86859e-9
•cfb: 6.11879e-9
•cfb: 2.53546e-9
•cfb: 3.49103e-9
•cfb: 5.09927e-9
•lcne: 7.02925e-8
•lcne: 7.89058e-8

•lcne: 4.11922e-8
•cfb: 2.27618e-9
•cfb: 3.89723e-9
•cfb: 5.60288e-9
•lcsw: 6.06394e-8
•lcne: 8.30528e-8
•lcsw: 8.30528e-8
•lcne: 5.60266e-8
•lcsw: 5.60266e-8
•lcne: 2.55326e-8
•lcsw: 8.50738e-8
•lcne: 7.10472e-8
•lcsw: 7.10472e-8
•lcne: 7.1643e-8
•lcsw: 7.1643e-8
•lcne: 5.4055e-8
•cfc: 9.02372e-9
•cfc: 9.06909e-9
•cfc: 9.30987e-9
•lcsw: 9.39869e-8
•lcsw: 6.68355e-8
•lcsw: 6.78204e-8
•cfc: 1.15565e-8
•cfe: 1.15565e-8
•cfc: 1.11645e-8
•cfe: 1.11645e-8
•cfc: 1.07194e-8
•cfe: 1.07194e-8
•cfc: 1.21803e-8
•cfe: 1.21803e-8
•cfc: 1.17736e-8
•cfe: 1.17736e-8
•cfc: 1.14337e-8
•cfe: 1.14337e-8
•cfe: 1.082e-8
•cfd: 1.07432e-8
•cfe: 1.07432e-8
•cfd: 1.08636e-8
•cfe: 1.08636e-8
•cfd: 1.10953e-8
•cfd: 8.82367e-9
•cfd: 9.49311e-9
•cfd: 9.81455e-9
•cfd: 7.17433e-9
•cfd: 8.02748e-9
•cfd: 8.36042e-9
•lw: 3.43328e-8
•lw: 3.06523e-8
•lw: 2.46065e-8
•lw: 2.8479e-8

•lw: 2.47429e-8
•lw: 1.91464e-8
•lw: 2.33915e-8
•lw: 2.06115e-8
•lw: 1.64405e-8
•ava: 1.12098e-8
•ava: 1.53907e-8
•ava: 1.48344e-8
•ava: 1.61783e-8
•ava: 1.85717e-8
•ava: 1.43406e-8
•ava: 2.11695e-8
•ava: 1.73713e-8
•ava: 1.1948e-8
•avb: 1.4272e-8
•avb: 1.54389e-8
•avb: 1.06667e-8
•avb: 7.86466e-9
•avb: 6.48589e-9
•avb: 4.37554e-9
•avb: 1.97815e-9
•avb: 2.83683e-9
•avb: 9.86136e-10
•ave: 8.78752e-9
•ave: 7.79712e-9
•ave: 1.67362e-8
•ave: 5.08454e-9
•ave: 4.25754e-9
•ave: 1.13662e-8
•ave: 2.02668e-9
•ave: 4.50761e-9
•ave: 9.94084e-9
•sum hazard = 1.80456e-4
•**********
•weight = 2
•nc: 3.4647e-10
•nc: 2.63652e-10
•nc: 1.98265e-10
•nc: 5.6312e-10
•nc: 3.54755e-10
•nc: 2.11195e-10
•nc: 3.72307e-10
•nc: 3.98155e-10
•nc: 2.93547e-10
•bc: 2.47537e-9
•bc: 1.89941e-9
•bc: 8.27621e-10
•bc: 2.74769e-9
•bc: 2.22414e-9
•bc: 2.64312e-9

•bc: 1.61498e-9
•bc: 1.81672e-9
•bc: 1.36528e-9
•cfa: 3.25594e-10
•cfa: 4.9655e-10
•cfa: 6.76652e-10
•rc: 1.79938e-9
•rc: 1.06444e-9
•rc: 9.5795e-10
•cfa: 3.45216e-10
•cfa: 6.78827e-10
•cfa: 8.61996e-10
•rc: 1.22693e-9
•rc: 6.49184e-10
•rc: 3.73233e-10
•cfa: 3.42388e-10
•cfa: 5.95165e-10
•cfa: 7.8518e-10
•rc: 8.78894e-10
•rc: 4.17624e-10
•rc: 1.74671e-10
•cfb: 1.30812e-10
•cfb: 1.69634e-10
•cfb: 2.30005e-10
•cfb: 7.09928e-11
•cfb: 1.08683e-10
•cfb: 1.8007e-10
•lcne: 6.20886e-9
•lcne: 7.20596e-9
•lcne: 3.01548e-9
•cfb: 6.13937e-11
•cfb: 1.25682e-10
•cfb: 2.03871e-10
•lcsw: 5.12071e-9
•lcne: 7.74531e-9
•lcsw: 7.74531e-9
•lcne: 4.56024e-9
•lcsw: 4.56024e-9
•lcne: 1.59164e-9
•lcsw: 8.0344e-9
•lcne: 6.28356e-9
•lcsw: 6.28356e-9
•lcne: 6.32328e-9
•lcsw: 6.32328e-9
•lcne: 4.32271e-9
•cfc: 3.84436e-10
•cfc: 3.86794e-10
•cfc: 4.00433e-10
•lcsw: 9.16987e-9
•lcsw: 5.78812e-9

•lcsw: 5.87186e-9
•cfc: 5.34355e-10
•cfe: 5.34355e-10
•cfc: 5.10037e-10
•cfe: 5.10037e-10
•cfc: 4.82969e-10
•cfe: 4.82969e-10
•cfc: 5.72992e-10
•cfe: 5.72992e-10
•cfc: 5.47315e-10
•cfe: 5.47315e-10
•cfc: 5.26199e-10
•cfe: 5.26199e-10
•cfe: 4.89297e-10
•cfd: 4.84398e-10
•cfe: 4.84398e-10
•cfd: 4.91512e-10
•cfe: 4.91512e-10
•cfd: 5.05537e-10
•cfd: 3.72689e-10
•cfd: 4.10625e-10
•cfd: 4.29267e-10
•cfd: 2.82909e-10
•cfd: 3.28539e-10
•cfd: 3.46832e-10
•lw: 2.30132e-9
•lw: 1.97725e-9
•lw: 1.47475e-9
•lw: 1.8005e-9
•lw: 1.49177e-9
•lw: 1.05947e-9
•lw: 1.39115e-9
•lw: 1.17449e-9
•lw: 8.68549e-10
•ava: 5.48707e-10
•ava: 8.36355e-10
•ava: 7.9568e-10
•ava: 8.96402e-10
•ava: 1.0762e-9
•ava: 7.61806e-10
•ava: 1.2856e-9
•ava: 9.86499e-10
•ava: 5.98473e-10
•avb: 7.81579e-10
•avb: 8.72129e-10
•avb: 5.35466e-10
•avb: 3.52333e-10
•avb: 2.73794e-10
•avb: 1.62838e-10
•avb: 5.58386e-11

•avb: 9.07341e-11
•avb: 2.22919e-11
•ave: 5.19505e-10
•ave: 4.33214e-10
•ave: 1.17559e-9
•ave: 2.52595e-10
•ave: 1.94873e-10
•ave: 7.06993e-10
•ave: 7.47954e-11
•ave: 2.12145e-10
•ave: 5.96202e-10
•sum hazard = 1.23459e-5
•**********
•weight = 2.5
•nc: 1.62139e-11
•nc: 1.15286e-11
•nc: 8.07795e-12
•nc: 2.96214e-11
•nc: 1.66319e-11
•nc: 8.70266e-12
•nc: 1.75853e-11
•nc: 1.91322e-11
•nc: 1.30785e-11
•bc: 1.7521e-10
•bc: 1.2562e-10
•bc: 4.44071e-11
•bc: 1.98786e-10
•bc: 1.52398e-10
•bc: 1.88812e-10
•bc: 1.01923e-10
•bc: 1.17877e-10
•bc: 8.23595e-11
•cfa: 1.34837e-11
•cfa: 2.28413e-11
•cfa: 3.36222e-11
•rc: 1.15553e-10
•rc: 5.98078e-11
•rc: 5.23027e-11
•cfa: 1.44744e-11
•cfa: 3.36892e-11
•cfa: 4.53921e-11
•rc: 7.1447e-11
•rc: 3.21592e-11
•rc: 1.60664e-11
•cfa: 1.42944e-11
•cfa: 2.85183e-11
•cfa: 4.03127e-11
•rc: 4.69859e-11
•rc: 1.84937e-11
•rc: 6.20758e-12

•cfb: 4.27298e-12
•cfb: 5.91047e-12
•cfb: 8.64585e-12
•cfb: 1.9878e-12
•cfb: 3.38351e-12
•cfb: 6.35879e-12
•lcne: 5.48422e-10
•lcne: 6.58074e-10
•lcne: 2.20749e-10
•cfb: 1.65592e-12
•cfb: 4.05312e-12
•cfb: 7.41822e-12
•lcsw: 4.3242e-10
•lcne: 7.2231e-10
•lcsw: 7.2231e-10
•lcne: 3.71176e-10
•lcsw: 3.71176e-10
•lcne: 9.92196e-11
•lcsw: 7.58773e-10
•lcne: 5.55731e-10
•lcsw: 5.55731e-10
•lcne: 5.58099e-10
•lcsw: 5.58099e-10
•lcne: 3.45682e-10
•cfc: 1.63781e-11
•cfc: 1.64967e-11
•cfc: 1.72233e-11
•lcsw: 8.94662e-10
•lcsw: 5.01266e-10
•lcsw: 5.08382e-10
•cfc: 2.47078e-11
•cfe: 2.47078e-11
•cfc: 2.33004e-11
•cfe: 2.33004e-11
•cfc: 2.17604e-11
•cfe: 2.17604e-11
•cfc: 2.6955e-11
•cfe: 2.6955e-11
•cfc: 2.54428e-11
•cfe: 2.54428e-11
•cfc: 2.42166e-11
•cfe: 2.42166e-11
•cfe: 2.21268e-11
•cfd: 2.18409e-11
•cfe: 2.18409e-11
•cfd: 2.22378e-11
•cfe: 2.22378e-11
•cfd: 2.30338e-11
•cfd: 1.57414e-11
•cfd: 1.77616e-11

•cfd: 1.87752e-11
•cfd: 1.11561e-11
•cfd: 1.3446e-11
•cfd: 1.43883e-11
•lw: 1.54257e-10
•lw: 1.27544e-10
•lw: 8.83867e-11
•lw: 1.13831e-10
•lw: 8.99404e-11
•lw: 5.86262e-11
•lw: 8.27356e-11
•lw: 6.69254e-11
•lw: 4.58854e-11
•ava: 2.68586e-11
•ava: 4.54488e-11
•ava: 4.26784e-11
•ava: 4.96675e-11
•ava: 6.23637e-11
•ava: 4.0469e-11
•ava: 7.8073e-11
•ava: 5.60224e-11
•ava: 2.99775e-11
•avb: 4.28017e-11
•avb: 4.92657e-11
•avb: 2.68802e-11
•avb: 1.57844e-11
•avb: 1.15579e-11
•avb: 6.06012e-12
•avb: 1.57619e-12
•avb: 2.90207e-12
•avb: 5.03915e-13
•ave: 3.07124e-11
•ave: 2.40697e-11
•ave: 8.25762e-11
•ave: 1.25486e-11
•ave: 8.91955e-12
•ave: 4.39759e-11
•ave: 2.76034e-12
•ave: 9.98435e-12
•ave: 3.57572e-11
•sum hazard = 9.04366e-7
•**********
•weight = 3
•nc: 7.5877e-13
•nc: 5.04103e-13
•nc: 3.29121e-13
•nc: 1.55815e-12
•nc: 7.79752e-13
•nc: 3.58609e-13
•nc: 8.30616e-13

•nc: 9.1934e-13
•nc: 5.8269e-13
•bc: 1.24016e-11
•bc: 8.30803e-12
•bc: 2.38272e-12
•bc: 1.43814e-11
•bc: 1.04423e-11
•bc: 1.34879e-11
•bc: 6.43248e-12
•bc: 7.64839e-12
•bc: 4.96827e-12
•cfa: 5.58393e-13
•cfa: 1.0507e-12
•cfa: 1.67065e-12
•rc: 7.42064e-12
•rc: 3.36043e-12
•rc: 2.85565e-12
•cfa: 6.0689e-13
•cfa: 1.67195e-12
•cfa: 2.39032e-12
•rc: 4.16052e-12
•rc: 1.5931e-12
•rc: 6.91601e-13
•cfa: 5.96782e-13
•cfa: 1.3665e-12
•cfa: 2.06973e-12
•rc: 2.51188e-12
•rc: 8.1896e-13
•rc: 2.20609e-13
•cfb: 1.39577e-13
•cfb: 2.05936e-13
•cfb: 3.24997e-13
•cfb: 5.56583e-14
•cfb: 1.05335e-13
•cfb: 2.24547e-13
•lcne: 4.84415e-11
•lcne: 6.00977e-11
•lcne: 1.616e-11
•cfb: 4.46639e-14
•cfb: 1.30709e-13
•cfb: 2.69925e-13
•lcsw: 3.65158e-11
•lcne: 6.7361e-11
•lcsw: 6.7361e-11
•lcne: 3.02116e-11
•lcsw: 3.02116e-11
•lcne: 6.18513e-12
•lcsw: 7.16589e-11
•lcne: 4.915e-11
•lcsw: 4.915e-11

•lcne: 4.92584e-11
•lcsw: 4.92584e-11
•lcne: 2.76437e-11
•cfc: 6.97751e-13
•cfc: 7.03579e-13
•cfc: 7.408e-13
•lcsw: 8.7288e-11
•lcsw: 4.34109e-11
•lcsw: 4.40154e-11
•cfc: 1.14245e-12
•cfe: 1.14245e-12
•cfc: 1.06445e-12
•cfe: 1.06445e-12
•cfc: 9.80428e-13
•cfe: 9.80428e-13
•cfc: 1.26803e-12
•cfe: 1.26803e-12
•cfc: 1.18275e-12
•cfe: 1.18275e-12
•cfc: 1.11449e-12
•cfe: 1.11449e-12
•cfe: 1.00061e-12
•cfd: 9.84781e-13
•cfe: 9.84781e-13
•cfd: 1.00612e-12
•cfe: 1.00612e-12
•cfd: 1.04949e-12
•cfd: 6.64877e-13
•cfd: 7.6828e-13
•cfd: 8.21189e-13
•cfd: 4.39923e-13
•cfd: 5.50302e-13
•cfd: 5.96897e-13
•lw: 1.03398e-11
•lw: 8.22734e-12
•lw: 5.29731e-12
•lw: 7.19658e-12
•lw: 5.4226e-12
•lw: 3.2441e-12
•lw: 4.92051e-12
•lw: 3.81357e-12
•lw: 2.42412e-12
•ava: 1.3147e-12
•ava: 2.46976e-12
•ava: 2.28917e-12
•ava: 2.75195e-12
•ava: 3.61387e-12
•ava: 2.14982e-12
•ava: 4.74129e-12
•ava: 3.18146e-12

•ava: 1.50157e-12
•avb: 2.34395e-12
•avb: 2.78297e-12
•avb: 1.34937e-12
•avb: 7.07133e-13
•avb: 4.879e-13
•avb: 2.25531e-13
•avb: 4.44922e-14
•avb: 9.28209e-14
•avb: 1.13912e-14
•ave: 1.81567e-12
•ave: 1.33733e-12
•ave: 5.80036e-12
•ave: 6.23404e-13
•ave: 4.08258e-13
•ave: 2.73536e-12
•ave: 1.01871e-13
•ave: 4.69902e-13
•ave: 2.14454e-12
•sum hazard = 7.02928e-8
•**********
•weight = 3.5
•nc: 3.55085e-14
•nc: 2.20426e-14
•nc: 1.34094e-14
•nc: 8.19624e-14
•nc: 3.6557e-14
•nc: 1.47771e-14
•nc: 3.92329e-14
•nc: 4.41762e-14
•nc: 2.59608e-14
•bc: 8.77803e-13
•bc: 5.49462e-13
•bc: 1.27848e-13
•bc: 1.04044e-12
•bc: 7.1551e-13
•bc: 9.63508e-13
•bc: 4.05961e-13
•bc: 4.96262e-13
•bc: 2.99706e-13
•cfa: 2.31245e-14
•cfa: 4.83322e-14
•cfa: 8.30131e-14
•rc: 4.76542e-13
•rc: 1.88813e-13
•rc: 1.55914e-13
•cfa: 2.5446e-14
•cfa: 8.29766e-14
•cfa: 1.25872e-13
•rc: 2.42277e-13

•rc: 7.89187e-14
•rc: 2.9771e-14
•cfa: 2.49152e-14
•cfa: 6.5478e-14
•cfa: 1.06264e-13
•rc: 1.34286e-13
•rc: 3.62661e-14
•rc: 7.84018e-15
•cfb: 4.55927e-15
•cfb: 7.17531e-15
•cfb: 1.22166e-14
•cfb: 1.55843e-15
•cfb: 3.27929e-15
•cfb: 7.92941e-15
•lcne: 4.27879e-12
•lcne: 5.48834e-12
•lcne: 1.18299e-12
•cfb: 1.20468e-15
•cfb: 4.21524e-15
•cfb: 9.82172e-15
•lcsw: 3.08359e-12
•lcne: 6.28193e-12
•lcsw: 6.28193e-12
•lcne: 2.45904e-12
•lcsw: 2.45904e-12
•lcne: 3.85567e-13
•lcsw: 6.7675e-12
•lcne: 4.34693e-12
•lcsw: 4.34693e-12
•lcne: 4.34759e-12
•lcsw: 4.34759e-12
•lcne: 2.21063e-12
•cfc: 2.97262e-14
•cfc: 3.00074e-14
•cfc: 3.1863e-14
•lcsw: 8.51628e-12
•lcsw: 3.7595e-12
•lcsw: 3.81083e-12
•cfc: 5.28252e-14
•cfe: 5.28252e-14
•cfc: 4.86279e-14
•cfe: 4.86279e-14
•cfc: 4.41737e-14
•cfe: 4.41737e-14
•cfc: 5.96514e-14
•cfe: 5.96514e-14
•cfc: 5.49818e-14
•cfe: 5.49818e-14
•cfc: 5.12907e-14
•cfe: 5.12907e-14

•cfe: 4.52494e-14
•cfd: 4.44026e-14
•cfe: 4.44026e-14
•cfd: 4.55209e-14
•cfe: 4.55209e-14
•cfd: 4.78183e-14
•cfd: 2.80827e-14
•cfd: 3.3232e-14
•cfd: 3.5917e-14
•cfd: 1.73477e-14
•cfd: 2.25221e-14
•cfd: 2.47622e-14
•lw: 6.93078e-13
•lw: 5.30711e-13
•lw: 3.17485e-13
•lw: 4.54981e-13
•lw: 3.26933e-13
•lw: 1.79513e-13
•lw: 2.92636e-13
•lw: 2.17307e-13
•lw: 1.28066e-13
•ava: 6.43533e-14
•ava: 1.3421e-13
•ava: 1.22786e-13
•ava: 1.52479e-13
•ava: 2.09417e-13
•ava: 1.14204e-13
•ava: 2.87933e-13
•ava: 1.80672e-13
•ava: 7.52135e-14
•avb: 1.28362e-13
•avb: 1.57207e-13
•avb: 6.7738e-14
•avb: 3.16793e-14
•avb: 2.05961e-14
•avb: 8.39326e-15
•avb: 1.25591e-15
•avb: 2.96882e-15
•avb: 2.57501e-16
•ave: 1.0734e-13
•ave: 7.43032e-14
•ave: 4.07431e-13
•ave: 3.09701e-14
•ave: 1.86865e-14
•ave: 1.70143e-13
•ave: 3.75959e-15
•ave: 2.21153e-14
•ave: 1.28619e-13
•sum hazard = 5.75378e-9
•**********

•weight = 4
•nc: 1.66171e-15
•nc: 9.63845e-16
•nc: 5.4634e-16
•nc: 4.31141e-15
•nc: 1.7139e-15
•nc: 6.08917e-16
•nc: 1.8531e-15
•nc: 2.12276e-15
•nc: 1.15664e-15
•bc: 6.21321e-14
•bc: 3.63393e-14
•bc: 6.85985e-15
•bc: 7.52724e-14
•bc: 4.90268e-14
•bc: 6.88285e-14
•bc: 2.56206e-14
•bc: 3.21997e-14
•bc: 1.80795e-14
•cfa: 9.57644e-16
•cfa: 2.22328e-15
•cfa: 4.12484e-15
•rc: 3.06027e-14
•rc: 1.06089e-14
•rc: 8.51269e-15
•cfa: 1.06691e-15
•cfa: 4.11801e-15
•cfa: 6.62834e-15
•rc: 1.41083e-14
•rc: 3.90946e-15
•rc: 1.28154e-15
•cfa: 1.04019e-15
•cfa: 3.13748e-15
•cfa: 5.45582e-15
•rc: 7.17895e-15
•rc: 1.60598e-15
•rc: 2.7863e-16
•cfb: 1.48928e-16
•cfb: 2.50006e-16
•cfb: 4.5922e-16
•cfb: 4.36361e-17
•cfb: 1.02091e-16
•cfb: 2.80011e-16
•lcne: 3.77941e-13
•lcne: 5.01215e-13
•lcne: 8.66013e-14
•cfb: 3.2493e-17
•cfb: 1.35938e-16
•cfb: 3.57381e-16
•lcsw: 2.60394e-13

•lcne: 5.85838e-13
•lcsw: 5.85838e-13
•lcne: 2.00152e-13
•lcsw: 2.00152e-13
•lcne: 2.40354e-14
•lcsw: 6.39125e-13
•lcne: 3.84452e-13
•lcsw: 3.84452e-13
•lcne: 3.83723e-13
•lcsw: 3.83723e-13
•lcne: 1.76782e-13
•cfc: 1.26642e-15
•cfc: 1.27981e-15
•cfc: 1.37048e-15
•lcsw: 8.30894e-13
•lcsw: 3.25582e-13
•lcsw: 3.2994e-13
•cfc: 2.44256e-15
•cfe: 2.44256e-15
•cfc: 2.2215e-15
•cfe: 2.2215e-15
•cfc: 1.99027e-15
•cfe: 1.99027e-15
•cfc: 2.80615e-15
•cfe: 2.80615e-15
•cfc: 2.55592e-15
•cfe: 2.55592e-15
•cfc: 2.36049e-15
•cfe: 2.36049e-15
•cfe: 2.04625e-15
•cfd: 2.00206e-15
•cfe: 2.00206e-15
•cfd: 2.05954e-15
•cfe: 2.05954e-15
•cfd: 2.17875e-15
•cfd: 1.18614e-15
•cfd: 1.43745e-15
•cfd: 1.57093e-15
•cfd: 6.84081e-16
•cfd: 9.21756e-16
•cfd: 1.02726e-15
•lw: 4.64569e-14
•lw: 3.42339e-14
•lw: 1.90279e-14
•lw: 2.87647e-14
•lw: 1.97111e-14
•lw: 9.93343e-15
•lw: 1.74038e-14
•lw: 1.23827e-14
•lw: 6.76572e-15

•ava: 3.15003e-15
•ava: 7.29319e-15
•ava: 6.58595e-15
•ava: 8.4485e-15
•ava: 1.21354e-14
•ava: 6.06678e-15
•ava: 1.74859e-14
•ava: 1.02602e-14
•ava: 3.76744e-15
•avb: 7.02952e-15
•avb: 8.88044e-15
•avb: 3.40042e-15
•avb: 1.41922e-15
•avb: 8.69438e-16
•avb: 3.1236e-16
•avb: 3.54514e-17
•avb: 9.49558e-17
•avb: 5.82088e-18
•ave: 6.34577e-15
•ave: 4.12834e-15
•ave: 2.8619e-14
•ave: 1.53856e-15
•ave: 8.55301e-16
•ave: 1.05831e-14
•ave: 1.38749e-16
•ave: 1.04083e-15
•ave: 7.7139e-15
•sum hazard = 4.92941e-10
•**********
•weight = 4.5
•nc: 7.77636e-17
•nc: 4.21455e-17
•nc: 2.22596e-17
•nc: 2.2679e-16
•nc: 8.03523e-17
•nc: 2.50915e-17
•nc: 8.75285e-17
•nc: 1.02003e-16
•nc: 5.15322e-17
•bc: 4.39779e-15
•bc: 2.40335e-15
•bc: 3.68074e-16
•bc: 5.44569e-15
•bc: 3.35932e-15
•bc: 4.91678e-15
•bc: 1.61694e-15
•bc: 2.08926e-15
•bc: 1.09063e-15
•cfa: 3.96585e-17
•cfa: 1.02271e-16

•cfa: 2.04959e-16
•rc: 1.96526e-15
•rc: 5.96083e-16
•rc: 4.6478e-16
•cfa: 4.4734e-17
•cfa: 2.04371e-16
•cfa: 3.49044e-16
•rc: 8.2156e-16
•rc: 1.93666e-16
•rc: 5.51657e-17
•cfa: 4.34272e-17
•cfa: 1.50338e-16
•cfa: 2.80113e-16
•rc: 3.83789e-16
•rc: 7.11179e-17
•rc: 9.90214e-18
•cfb: 4.86474e-18
•cfb: 8.71083e-18
•cfb: 1.7262e-17
•cfb: 1.22181e-18
•cfb: 3.17829e-18
•cfb: 9.88798e-18
•lcne: 3.33831e-14
•lcne: 4.57727e-14
•lcne: 6.33966e-15
•cfb: 8.76408e-19
•cfb: 4.38385e-18
•cfb: 1.3004e-17
•lcsw: 2.1989e-14
•lcne: 5.46339e-14
•lcsw: 5.46339e-14
•lcne: 1.62912e-14
•lcsw: 1.62912e-14
•lcne: 1.49832e-15
•lcsw: 6.03593e-14
•lcne: 3.40017e-14
•lcsw: 3.40017e-14
•lcne: 3.38677e-14
•lcsw: 3.38677e-14
•lcne: 1.4137e-14
•cfc: 5.3953e-17
•cfc: 5.45835e-17
•cfc: 5.89466e-17
•lcsw: 8.10665e-14
•lcsw: 2.81962e-14
•lcsw: 2.8566e-14
•cfc: 1.1294e-16
•cfe: 1.1294e-16
•cfc: 1.01486e-16
•cfe: 1.01486e-16

•cfc: 8.96726e-17
•cfe: 8.96726e-17
•cfc: 1.32009e-16
•cfe: 1.32009e-16
•cfc: 1.18816e-16
•cfe: 1.18816e-16
•cfc: 1.08634e-16
•cfe: 1.08634e-16
•cfe: 9.25349e-17
•cfd: 9.02705e-17
•cfe: 9.02705e-17
•cfd: 9.31812e-17
•cfe: 9.31812e-17
•cfd: 9.92707e-17
•cfd: 5.00995e-17
•cfd: 6.2177e-17
•cfd: 6.87093e-17
•cfd: 2.69757e-17
•cfd: 3.77245e-17
•cfd: 4.26158e-17
•lw: 3.114e-15
•lw: 2.20829e-15
•lw: 1.14041e-15
•lw: 1.81856e-15
•lw: 1.1884e-15
•lw: 5.4967e-16
•lw: 1.03505e-15
•lw: 7.05595e-16
•lw: 3.57433e-16
•ava: 1.54191e-16
•ava: 3.96323e-16
•ava: 3.53255e-16
•ava: 4.68111e-16
•ava: 7.03224e-16
•ava: 3.22283e-16
•ava: 1.0619e-15
•ava: 5.82668e-16
•ava: 1.88711e-16
•avb: 3.84958e-16
•avb: 5.01647e-16
•avb: 1.707e-16
•avb: 6.35803e-17
•avb: 3.67022e-17
•avb: 1.16247e-17
•avb: 1.00071e-18
•avb: 3.0371e-18
•avb: 1.31583e-19
•ave: 3.75152e-16
•ave: 2.29374e-16
•ave: 2.01027e-15

•ave: 7.64341e-17
•ave: 3.91481e-17
•ave: 6.58282e-16
•ave: 5.12056e-18
•ave: 4.89855e-17
•ave: 4.62641e-16
•sum hazard = 4.39803e-11
•**********
•

The probabilities have to be normalized by thr sum_hazard in order to be compared.

This is done in the following graph:

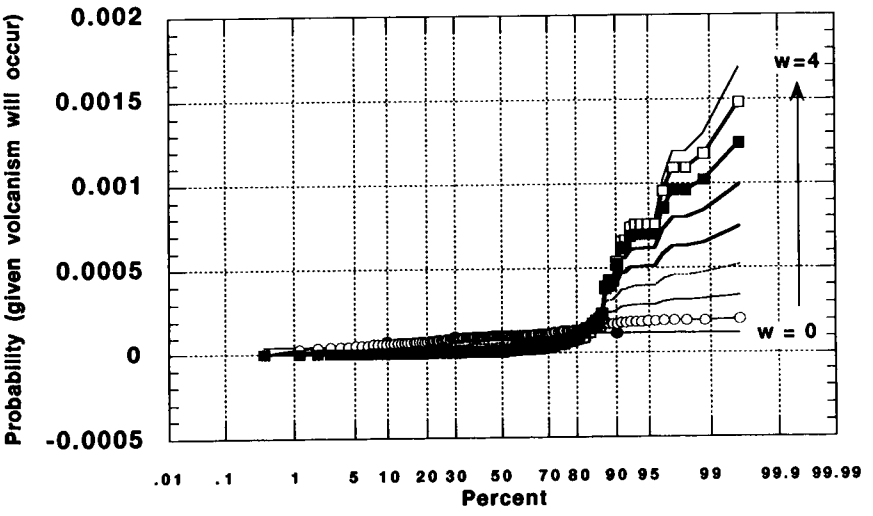

FIGURE 1. With just Quaternary cones

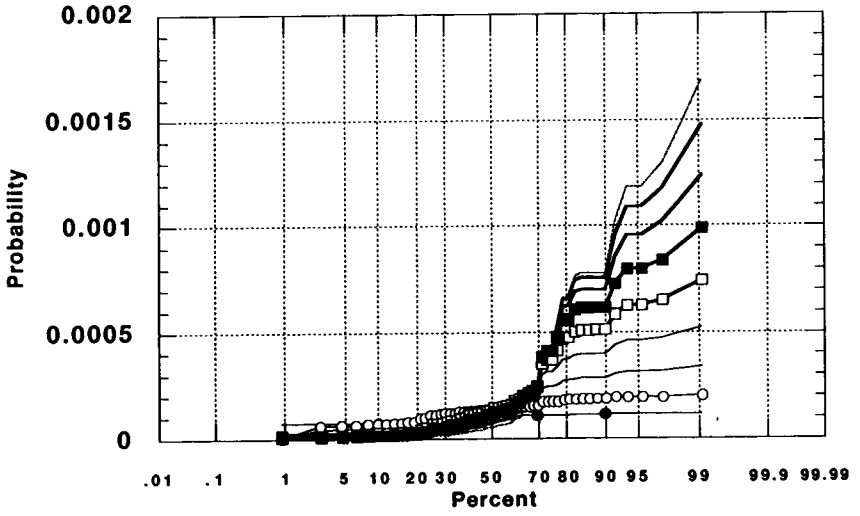

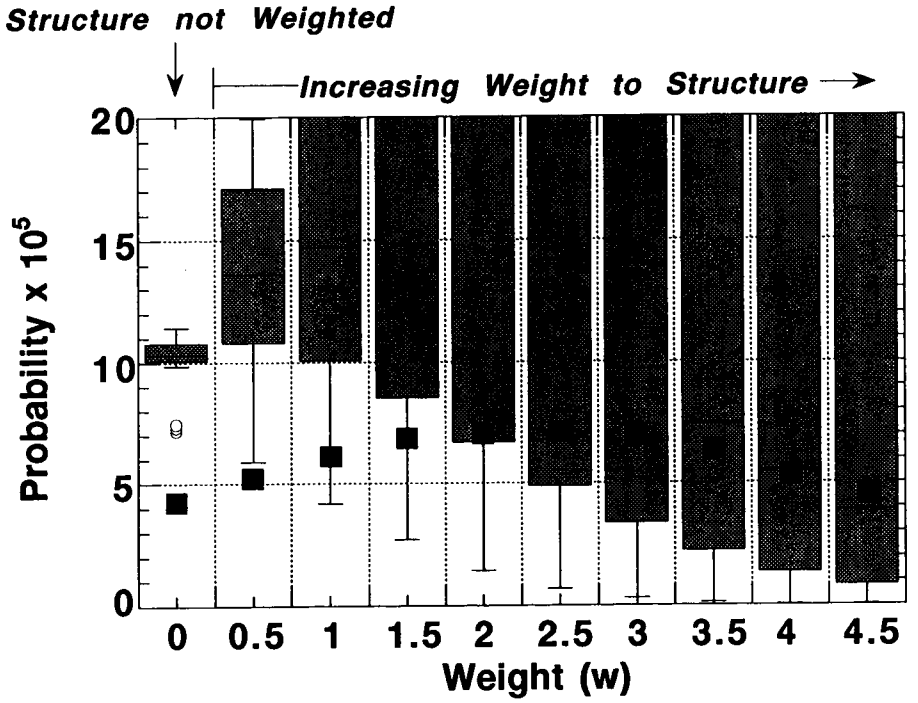

The box plot shows the distribution of probability where Quatrnary volcanoes are located. The median is greatest at weights of 1-2, then decreases at higher weights. This means that models with w = 1 to 2 give highest probabilities where volcanism actually has occurred. Black squares show probability at center of reposiotry for 333m x 333 m area.

Ash Dispersion in Volcano code

Chuck Connor

Chuck Connor

Develop GUI for the ash dispersion part of the volcano code

Acct. ~~20-5708~~ 20-5708-462

1.0 Introduction

The volcano code will include a module for modeling ash dispersion from erupting volcanoes. Calculations made in this module will be take nfrom Suzuki, 1983, as descibed in Jarzemba (1996). Initially, the code will be used to deterministically model ash dispersion from a fixed point.

Assess to the ash module will be from a menu bar for volcanic phenomena:

Ash	Lava	Pyroclastic flow	Lahar	Volcanic debris avalanche

The user will select Ash to access the volcanic ash dispersion module. This will bring up a menu of options for the user.

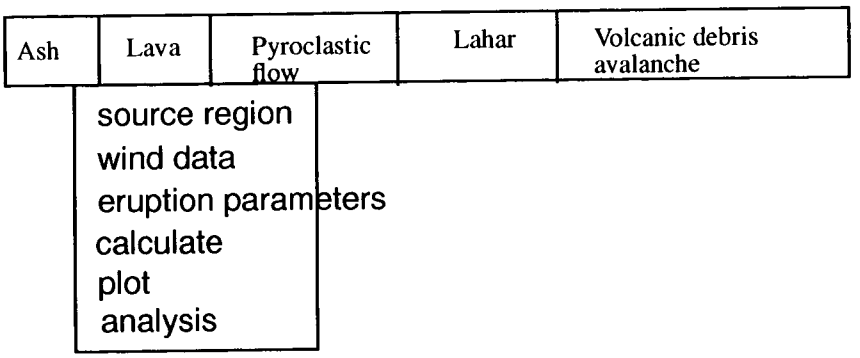

The user selcts one of these options. The first time through, the source region, wind data, and eruption parameters must be input before th calculation is done. The calculation is essesntially a call to Mark Jarzemba's code (now in fortran). The calcualtion must be done before plot and analysis are done (the first time through).

2.0 Source Region

The source region allows the user to select the vent location (source region) of the eruption on the DEM.

The source region subroutine returns the map coordinate (x,y) of the source region. This is in UTM coordinates (the DEM is also in UTM coordinates)

To select the source region, the user moves the mouse cursor across the DEM and selects the source region by clicking the left mouse button. A red dot will be drawn on the source region (centered on the mouse click) and the x,y location of the source region will be returned from the subroutine.

FIGURE 1.

With mouse, user selects vent location (red dot) on DEM and the subroutine returne the

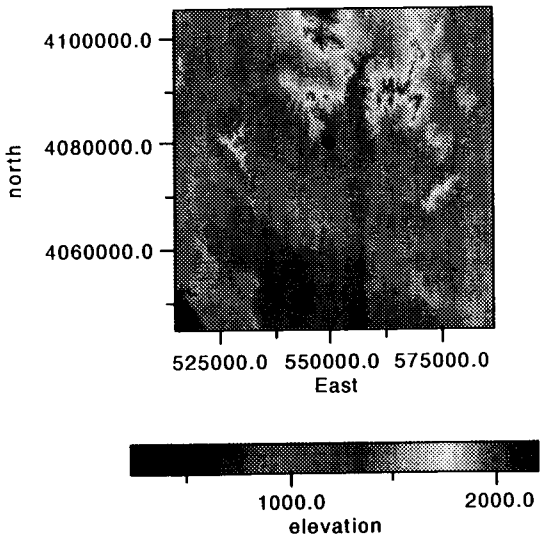

x,y coordinate, in this case approximately 550000.0,4080000

3.0 Select Wind Data

The ash dispersion code depends on wind speed and direction. In the future, this data will be selected from a wind rose diagram of th region, either by the user or using a probabilistic model to sample these data. In the future, the code will enable the user to choose a range of wind speed and direction data to samle variation in wind speed and direction during the course of the eruption. The following will be implemented initially.

When the user selects the wind speed and direction option the following graph will appear. This graph plots wind direction from 0 to 360 degrees and wind speed increseing radially from zero at the center of the plot to 20 m/s at the edge of the plot. The user will use a mounse to select the wind speed and direction on this plot. this wind speed and direction will be returned from the subroutine.

FIGURE 2. Figure for selecting wind speed and direction. In this case, the user has chosen a

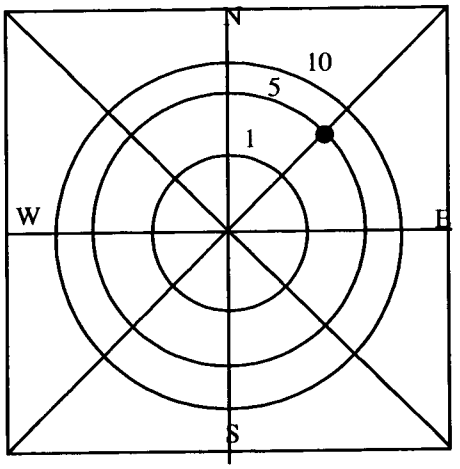

direction of 045 degrees and a wind speed of 5 meters per second.

4.0 Select Eruption Parameters

When the user chooses eruption parameters, a box window will appear and the user will type parameters. These parameters will include:

average particle diameter

standard deviation of particle diameter

particle density

particle shape

eddy diffusivity (beta)

vent radius

column height

eruption duration

This list might not be complete - talk to Britt Hill and Mark Jarzemba

5.0 Calculation

When the user chooses calculation, eruption parameters, wind data, and source area must already be specified. An error message should be given if these are not specified.

The first thing that will appear after calcuation is selected is a window for entering grid parameters. This will specify where calculations will be mad. The user will enter the grid dimensions in UTM coordinates. Defaults should be

the xmax and xmin of the DEM, the ymax and ymin of the DEM, and grid spacing to give 50 grid nodes between xmax and xmin and 50 grid nodes between ymax and ymin.

once the grid dimensions are set, the user should press a "calculate" button.

At this point, Jarzemba's code is called to calcualate expected mass of ash at a given grid node location (grams/square meter) resulting from the eruption. I believe Mark has modified his code to also track expected ash particle size at each grid location and ash thickness at each grid node location. Talk to Britt about the density to use to convert from mass to thickness. These data are returned from the "calculate" subroutine.

Some message should indicate that the calculations are finished.

6.0 Plot

The user has to have calculated before the plot option is selected, otherwise an error message should appear.

Plot will color shade the calculated grid and plot this on the DEM. The user should be able to specify whether ash mass or thickness will be plotted. A rainbow color bar should be selected automatically, with blue as the least mass per unit area, and red being the most mass per unit area. The minimum value for plotting should be 0.1 gm / square meter or 1 mm ash thickness. The color bar should be linear and not be complicated (10 colors). No interpolation should occur between grid nodes.

FIGURE 3. Plot for an example eruption (wind to south)

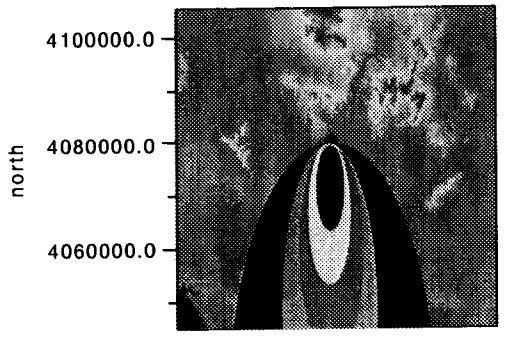

Nothing is returned by this subroutine

7.0 Analysis

In the analysis section, the user should be able to select a point on the plot and data will be reported about the ash at that point.

For example:, if the user selectes the following point, (black dot)a window should appear that gives the mass of ash, thickness of ash, average rate of accumulation of ash,

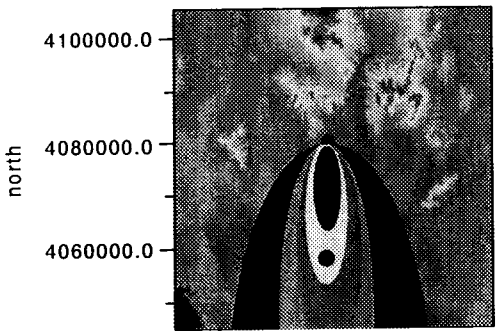

density of ash, mean grainsize and standard deviation of grainsize of ash at this location.

Note that this section will be developed further to include other types of analysis - such as area enclosed by a given isopach, etc.

Review of Bursik et al. ash dispersion model

Chuck Connor

Charles B. Connor

The purpose is to review the ash dispersion model proposed in Bursik et al., 1992.

Acct 20-5708-461

1.0 Introduction

Bursik, M.I., S.N. Carey, and R.S.J. Sparks, 1992, A gravity current model for the May 18, 1980 Mount St. Helens plume, Geophysical Research Letters, v. 19, 1663-1666, propse a simple model for ash dispersion during a volcanic eruption that appears to differ significantly from the suzuki model. The suzuki model is currently used to assess the distribution of ash during a volcanic eruption in the Yucca Mountain area and transport of rad waste away from the site during an eruption. The purpose here is to verify the derivation of the equations used in Bursik et al.

The main differences between suzuki's work and Bursik's work is the physical basis of the model. Suzuki assumes a turbulent dispersal governed by advection and diffusion. Bursik et al., rely on a gravity current scheme, in which lateral spreading of the plume in the crosswind direction is governed by gravity "slumping" as the plume is advected along the wind direction.

Volcanic plumes spread around a level of neutral bouyancy and form umbrellas. As the radial flow of the ash outward from the center of the column approaches the windseep, the column is convected downwind. Upwind, the flow reaches stagnation while downeind the velocity of the colum converges toward the wind velocity.

2.0 Model

Bursik et al model the gravity spreading of the plume assuming that the volumetric flux of ash in the plume remains constant with distance from the vent.

$$Q = Q_o = whu$$

where Q is the volumetric flux of ash

Qo is the initial volumetric flux of ash

w is the width of the plume

h is the thickness of the plume

and u is the wind velocity of the plume

The change in width of the plume, governed by gravitational spreading, with distance from the volcano is expressed as

$$\frac{dw}{dt} = u\frac{dw}{dx} \approx \sqrt{g'h}$$

where $g' = \frac{\rho - \rho_0}{\rho_0} g$. But h must be a function of x as well, so this is a little confusing.

At this point Bursik presents an equation for plume width as a function of x, based on the above equation.

$$dw = \frac{\sqrt{g'h}}{u} dx$$

and the quantity $\sqrt{g'h} = \lambda Nh$ where lambda = a parameter of order 1 that depends on the flow geometry (dimensionless), N is the Brunt-Vaisala frequency of the atmosphere = 0.035 s^{-1}, and h is the plume width. But $h = Q/(wu)$ so...

$$dw = \frac{\lambda N h dx}{u}$$

$$dw = \frac{\lambda N dx}{u}\frac{Q}{wu}$$

$$\frac{1}{2}w^2 = \frac{\lambda N x Q}{u^2}$$

$$w = \frac{\sqrt{2\lambda N x Q}}{u}$$

The total mass of particles of a given size fraction transported past a given point in the plume is given by

$$M = M_o \exp\left(-\int_{x_o}^{x} \frac{v(H_b)}{h(x)\,u(x)} dx \right)$$

where Mo is the total mass of that size fraction erupted and v(Hb) is the settling velocity of the particle size fraction at the base of the plume. Note that above, h(x) is now a function of x, whereas before it was a constant.

if v and u are held constant as a function of x then:

$$\int_{x_o}^{x} \frac{v(H_b)}{h(x)\,u(x)} dx = \int \frac{v}{u}\left[\frac{2\lambda N x}{Q}\right]^{\frac{1}{2}} dx$$

$$\int \frac{v}{u}\left[\frac{2\lambda N x}{Q}\right]^{\frac{1}{2}} dx = \frac{2v}{3u}\sqrt{\frac{2\lambda N}{Q}}\,(x^{3/2} - x_o^{3/2})$$

define

$$\Xi = \frac{2v}{3u}\sqrt{\frac{2\lambda N}{Q}}$$

then

$$M = M_o \exp\left[-\Xi\,(x^{3/2} - x_o^{3/2})\right]$$

Bursik defines the ash fall at the bottom of the ash cloud (point x,y,Hb) as

$$S(x, y, Hb) = -\frac{dM}{dx}\frac{1}{be\sqrt{\pi}}\exp\left(-\frac{y^2}{be^2}\right)$$

based on the idea that the orifginal plume has a gaussian function (!)

$$-\frac{dM}{dx} = -M_o \exp\left[-\Xi\left(x^{3/2} - x_o^{3/2}\right)\right] \times \frac{-3}{2}\Xi x^{1/2}$$

and

$$\frac{3}{2}M_o\Xi\sqrt{x} = \frac{v}{u}M_o\frac{wu}{Q} = \frac{wvM_o}{Q}$$

so

$$S(x, y, Hb) = \frac{w}{be}\frac{vM_o}{Q\sqrt{\pi}}\exp\left[-\Xi\left(x^{3/2} - x_o^{3/2}\right) - \frac{y^2}{be^2}\right]$$

apparently, Burisk substitutes 8 for w/be, so the equation becomes

$$S(x, y, Hb) = 8\frac{vM_o}{Q\sqrt{\pi}}\exp\left[-\Xi\left(x^{3/2} - x_o^{3/2}\right) - \frac{y^2}{be^2}\right]$$

FIGURE 1. relationship between be and w somehow becomes 8

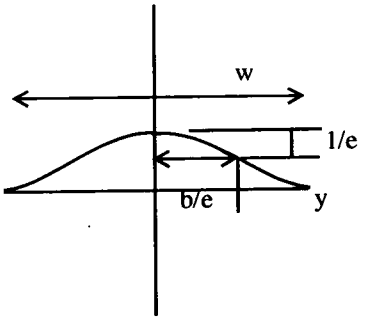

This must be related somehow to the assumed width of the plume and the change in flux away from the plume centerline. It is possible that be = 1/8 w somehow comes out of the guassian relationship but this is really unclear to me! It is interesting to note that the ration of w/be is constant with x, so since w changes with distance from the source be must also be changing. Keeping be = 1/8 w then

$be = \frac{1}{8}\frac{\sqrt{2\lambda NQx}}{u}$ which needs to be substituted in to the above equation

$$S(x, y, Hb) = 8\frac{vM_o}{Q\sqrt{\pi}}\exp\left[-\Xi(x^{3/2} - x_o^{3/2}) - \frac{64u^2y^2}{2\lambda NQx}\right]$$

•This is a simple True Basic code to determine the concentration of ash at the base of the volcanic plume, along the axis of dispersion for a single particle size

```
•
•open #1: name "ash.out", create newold
•erase #1
•
•LET mo = .001*1e9*800
•
•LET u = 9
•LET v = 1
•
•let height = 5000
•LET tau = height/v
•let q = (2.5/.287)^5.3
•LET lambda = .83
•LET N = 0.035
•LET xo = 500
•LET x = xo
•
•LET chi = (2*v)/(3*u) * (2*lambda*N/Q)^0.5
•
•LET so = 8*mo*v/(1.77*Q)
•
•FOR x = xo to 20000 step 500
•
•let ss = so*exp(-chi*(x^(1.5)-xo^(1.5)))
•print #1: x,ss
•NEXT x
•END
•
```

FIGURE 2. Graph of the ash concentration at the base of the plume

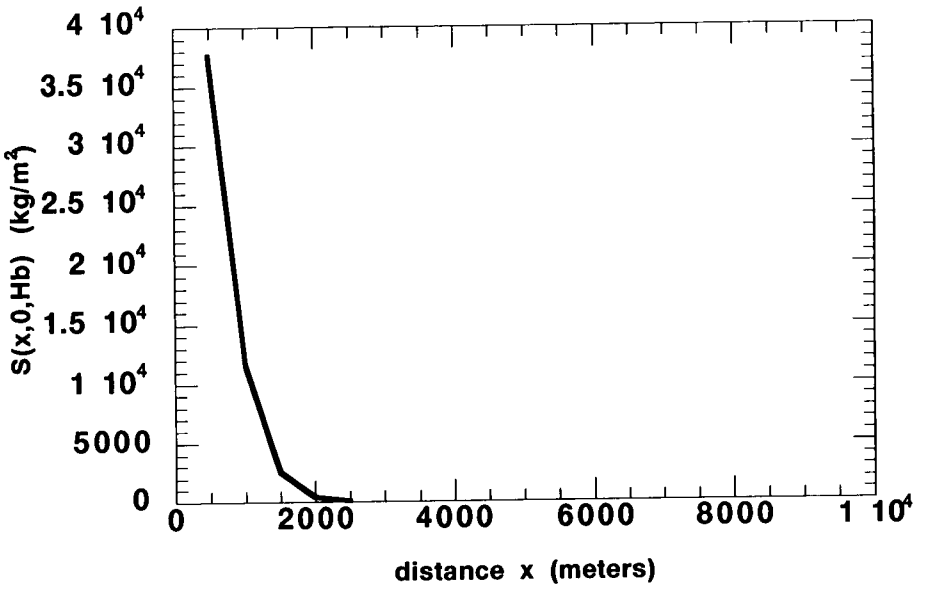

Bursik then uses a convolution with the Green's function to determine the the value of S at the ground level.

3.0 Conclusion

The math in the Bursik paper checks out - at least until convolution with Green's function, at which point several assumptions are made. The problem lies in the initial assumptions about column shape and where ash becomes available for the 2D solution.

Review of Suzuki

Chuck Connor

Chuck B. Connor

The goal is to evaluate the mechanisms by which the suzuki model puts volcanic ash into the atmosphere.

Acct# 20-5708-461

1.0 Introduction

All volcanic ash dispersion models use some assumptions about how ash is distributed in the column and escapes from the ash column into the atmosphere, where it is dispersed. In the case of the suzuki model (Suzuki, T., 1983, A theoretical model for the dispersion of tephra, in Arc Volcanism: Physics and Tectonics, edited by D. Shimozuru and I. Yokoyama, Terra Scientific Publishing Co., Tokyo, pages 95-113), ash has sources at levels, discretized at z+dz. On the other hand, Bursik's models (Bursik, Mi, SN Carey, and RSJ Sparks, 1992, A gravity current model for the May, 18, 1980 Mount St. Helens plume, Geophysical Research Letters 19: 1663-1666, asume all ash is released at a level of neutral bouyancy. A Gaussian plume model would assume that ash is released as a point source. These different assumptions play an important role in how the ash is eventually distributed on the ground surface.

2.0 Suzuki's assumptions

Suzuki makes several simplifying assumptions about the velocity of particles in the column to caluclate the diffusion of particles out of the column. The velocity of particles is taken to be maximum at the vent and to decrease with height to reach zero at the top of the column - makes sense.

2.1 vertical velocity

Suzuki sets the vertical velocity of ash particles in the conduit as:

$$W(z) = W_o\left(1 - \frac{z}{H}\right)^{\lambda}$$

where W(z) is the velocity of the particle at height z

Wo is the initial particle velocity (at the vent)

H is the maximum column height

lambda is a constant that Suzuki sets equal to 1

No explanation is given for the origin of this equation.

FIGURE 1. Change in velocity with height in the eruption column based on Suzuki's model

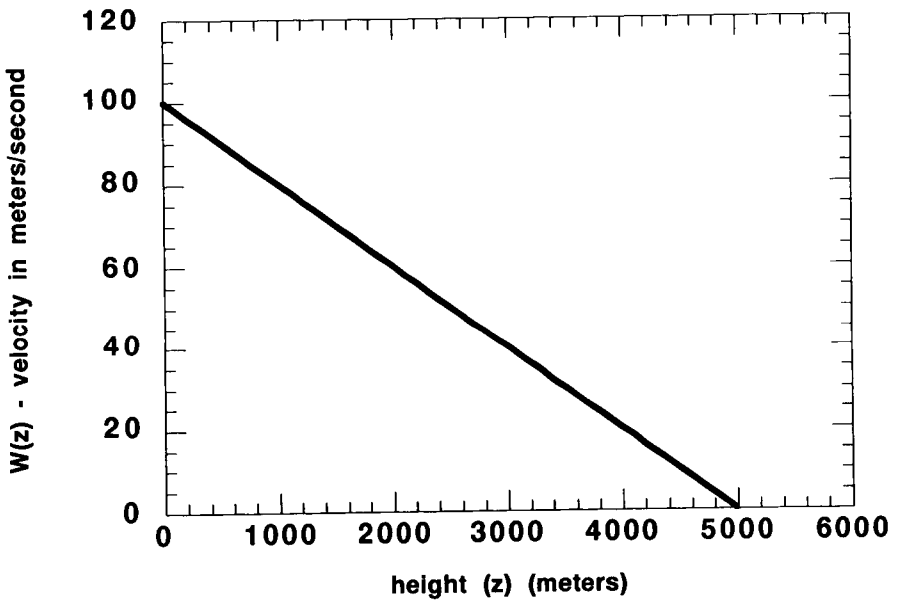

2.2 diffusion parameter, beta

Suzuki uses a diffusion term, beta, to model diffusion in the eruption column as a function of height. Specifically, the diffusion parameter, Y, is

$$Y = \frac{\beta [W(z) - V_o]}{V_o}$$, where beta is a constant.

then the probability density function for dfiffusion becomes

$$P(z) = \frac{\beta W_o Y \exp(-Y)}{V_o H \{1 - (1 + Y_o) \exp(-Y_o)\}}$$

and $$Y_0 = \frac{\beta [W_o - V_0]}{V_o}$$

The amount of particles available at a given level is given by

$$qd, z) = dqP(z)\,dz$$

where dz is the thckness of the height interval and

$$dq = \frac{Q \log\left(\frac{d_{j+1}}{d_j}\right)}{\sigma_d \sqrt{2\pi}} \exp\left\{-\frac{\left(\log\left(\frac{d_j}{d_m}\right)\right)^2}{2\sigma_d^{\,2}}\right\}$$

where

Q = total quanity of erupted material

dm - median particle diameter of Q

sigmad = standard deviation of the particle size distribution

dj - dj+1 - range of particle diameters included in dq - these are assumed to have the same settling velocities, etc.

Note that there are some problems with this formulation. When the settling velocity exceeds the velocity w(z), then the function P(z) as shown above will be less than zero, which is not legimtimate for a probability density function. Physically, particles of a given grain size will not be advected in the column above the point where w(z) < vo. So P(z) should be written:

$$P(z) = \frac{\beta W_o Y \exp(-Y)}{V_o H \{1 - (1 + Y_o)\exp(-Y_o)\}} \ldots w(z) < V_o$$

$$P(z) = 0, otherwise$$

The following code takes into account this check for velocity. If this check is not made, then mass will not be conserved in the model.

```
•dim q(0:1000)
•let dz = 10  ! m - height interval for steps
•
•!eruption information
•let h = 5000  ! m - column height
•let wo = 100  !m/s - initial particle velocity
•let qtotal = 1e12 ! total eruption mass in kilograms
•let beta = 0.1
•
•!particle information
•let dm = 0.105     ! median particle diameter in cm
•let sigmad = .0005 ! standard deviation of particle diameter
•let dj = .1
•let dj1 = .11
•let vo = .01 ! settling velocity in meters/second
•
•!find proportion of particle size
•let dq = qtotal*log10(dj1/dj)/(sigmad*(2*pi)^0.5) * exp(-(log10(dj/dm))^2/(2*sig-
mad^2))
•let dq = qtotal      !given particle size only
•
•for z = 0 to (h-dz) step dz
•let kounter = kounter + 1
•
•let w = wo*(1-(z/H))
•let y = beta*(w-vo)/vo
•let yo = beta*(wo-vo)/vo
•
•let p = beta*wo*y*exp(-y)/(vo*h*(1-(1+yo)*exp(-yo)))
•
•if p < 0 then let p = 0   !settling velocity exceeds the upward velocity
```

```
•                    !particles do not diffuse out above this point
•
•let old_sump = sump
•let sump = p*dz + sump
•
•if sump > 1.0 then      !this if statement fixes the case where
•                    !you have diffused out all the particles
•let sump= 1             ! conserves the mass
•let p = (1-old_sump)/dz
•end if
•
•if z = (h-dz) then          !if its not coming out before - its leaving now
•let sump= 1                 ! conserves the mass
•let p = (1-old_sump)/dz     ! Note that this means the column height is too low
•end if
•
•
•let q(kounter) = dq*p*dz
•let sum = q(kounter) + sum
•print z,q(kounter),sump
•
•next z
•
•print "qtotal = ";qtotal
•print "sum = ";sum
•
•end
```

FIGURE 2. dependence of column diffusion on settling velocity

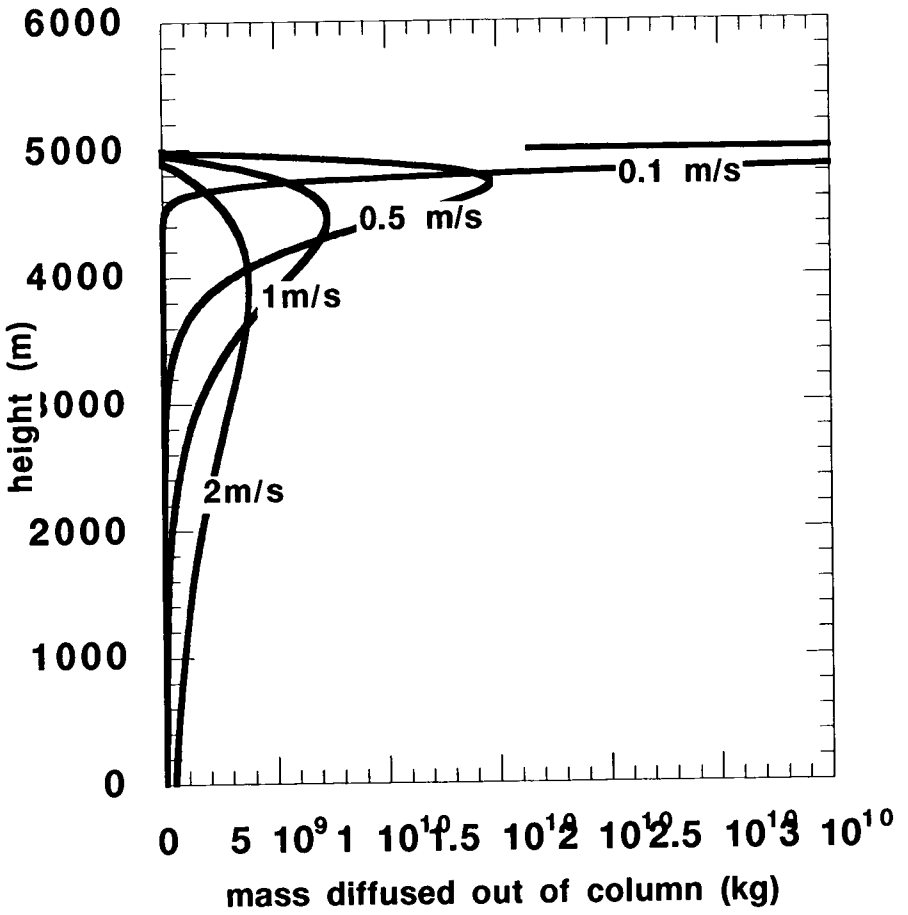

3.0 Conclusions

The Suzuki model makes very simplifying assumptions about the transport of ash into the atmosphere within the eruption column.

It is assumed that the particles have a linear decrease in velocity with height above the vent. This does not account for the convecting part of the column, within which particle velocities can not be linearly decreasing with elevation.

The dispersion of particles out of the column is assumed to follow a lognormal probability distribution, but no justification is given for the use of this assumption.

One has to be careful in the Suzuki model to conserve mass, as the equations presented in the paper don't necessarily do this for some column heights, inital particle velocities, and particle distributions

January 20, 1997
Acct #20-5708-461

Magnetics of the Yucca Mountain region

Chuck Connor

Chuck Connor

Document revision of the Eos article

1.0 Introduction

Critical facilities, such as nuclear power plants and high-level radioactive waste repositories, should be constructed at sites with very low geologic risk. Geologic risks to critical facilities involve events, such as earthquakes or volcanic eruptions, that have low probabilities of occurrence, on the order of 10-5–10-8 /yr, but have potentially large consequences for local and global communities. Estimating the probabilities of such events requires a comprehensive understanding of site geology and the geologic processes that operate in the site region on time scales of 104 to 107 yr. In light of these requirements, geologists and geophysicists must continually improve techniques applied to site characterization. Here we use recent surveys to illustrate the strengths of new high-resolution ground magnetic mapping techniques when applied to a complex site characterization problem: the probability of future volcanic eruptions at Yucca Mountain. These surveys provide one example of how improving geophysical instrumentation will improve site characterization and hazard assessment.

The Risk

Yucca Mountain is the proposed site of the first U.S. high-level radioactive waste repository. Plans call for permanent disposal of 70,000 metric tons of waste at the facility if the proposed repository can be shown to meet several criteria that ensure the protection of public health and safety. One of these criteria is that the probability of volcanic disruption of the repository is low. Given the duration of waste radioactivity and toxicity (on the order of 104 – 105 yr) and the dispersive nature of volcanic eruptions, most recent criteria [Code of Federal Regulations, 1994] require that the consequences of

volcanic eruptions be considered in evaluation of repository suitability if the probability of eruptions through the repository is greater than 10-8 /yr.

Volcanic eruptions are considered a potential hazard at the proposed site of the repository because Yucca Mountain is located within an active basaltic volcanic field. Small basaltic eruptions have occurred in the Yucca Mountain region during the last 8 million years at a low rate, on the order of 3 to 7 eruptions per million years. During the last one million years, most of these eruptions have occurred 10 to 25 km from Yucca Mountain. The most recent eruptions formed Lathrop Wells volcano approximately 100,000 years ago [Turrin et al., 1991], 20 km from the site of the repository (Figure 1). Yet, because sedimentation in the basins adjoining Yucca Mountain is also very recent, additional volcanism is hidden by young alluvial deposits.

FIGURE 1. Location of ground magnetic surveys near Yucca Mountain. Plio-Quaternary volcanoes are shown in yellow (locations of aeromagnetic anomalies are shown as filled green circles). The area of the proposed repository is shown in blue. Faults [Frizzell and

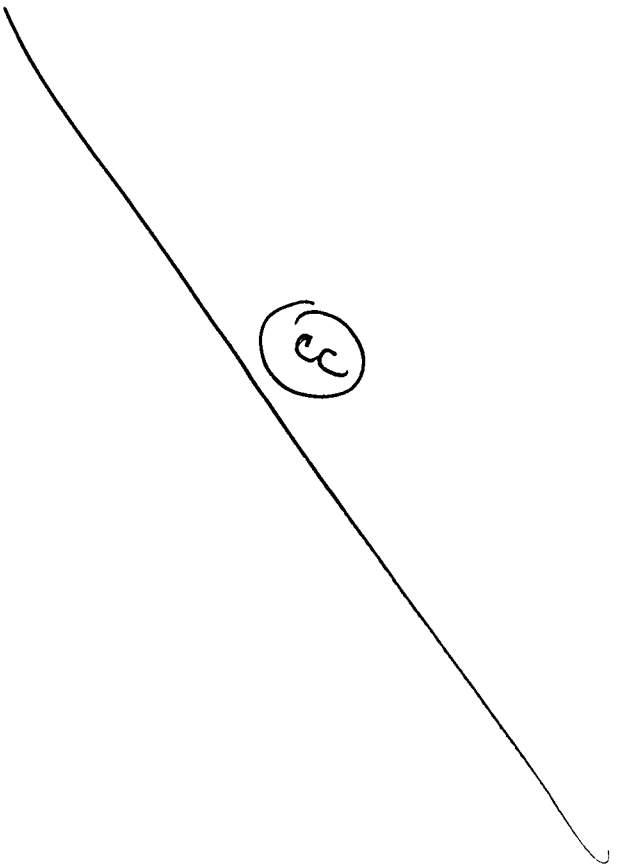

Schulters, 1990] are indicated by red lines and roads by black lines. Coordinates on this and following maps are Universal Transverse Mercator (Clarke 1866 projection).

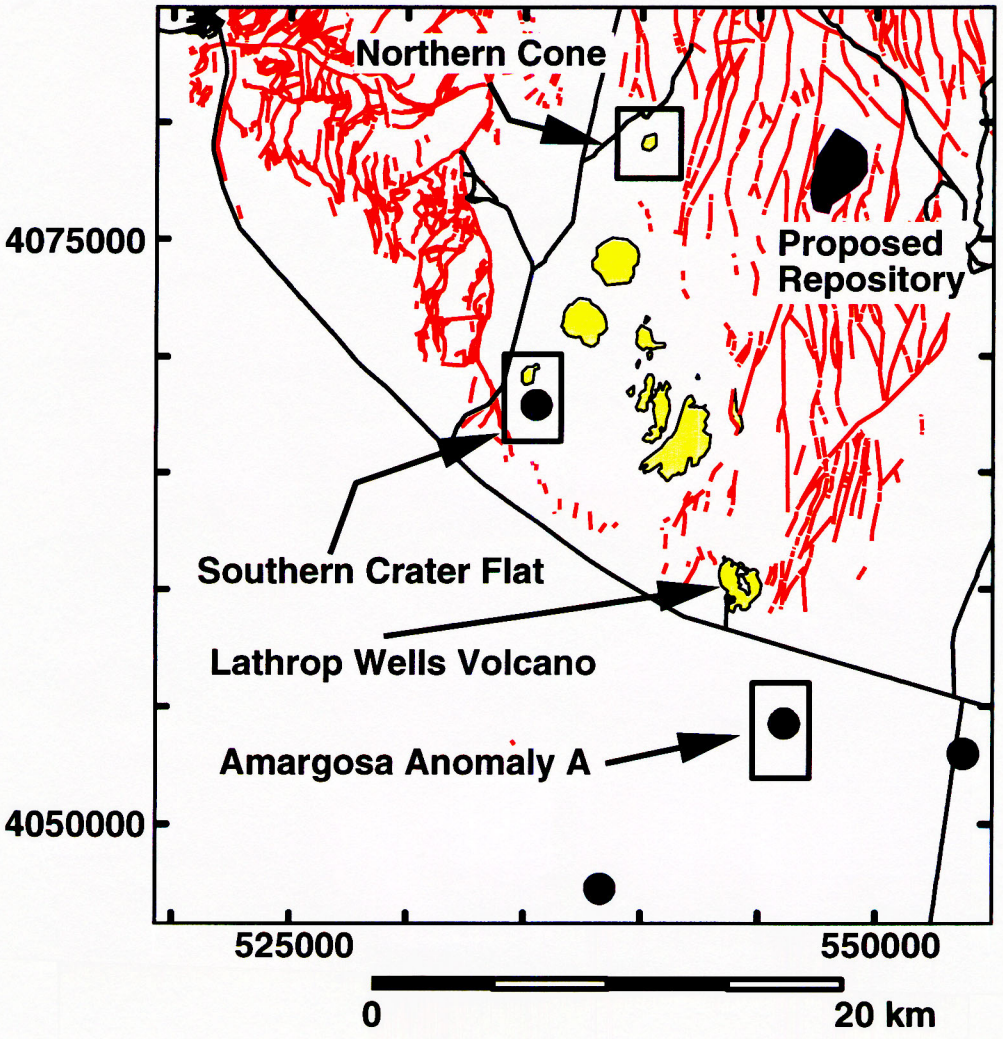

In light of this history of volcanic activity, ground magnetic surveys were conducted near Yucca Mountain to provide a better understanding of Miocene to Quaternary patterns in volcanic activity, to identify additional buried volcanic centers, and to delimit possible relationships between basaltic volcanism and faults, such as those that bound and penetrate the Yucca Mountain block [Connor and Hill, 1995; Fleck et al., 1996; Stamatakos et al., 1996]. The surveys were conducted on behalf of the U.S. Nuclear Regulatory Commission.

The Magnetic Surveys

Magnetic readings were obtained using a cesium-vapor magnetometer interfaced to a differential global positioning system (GPS). High remanent magnetizations of basalt (10-20 Am-1) preclude the use of proton-precession magnetometers in some parts of the survey areas. Real-time differential corrections were made on position data and sent, via RS232 cable, as a string in National Marine Electronics Association (NMEA) protocol to the magnetometer, where the data were stored together with magnetic measurements. Ground resolution of this particular differential GPS is better than 5 m and is typically 1-2 m. These data were downloaded into a geographic information system (GIS) for post-processing. The base station for these surveys included a proton-precession magnetometer, which continuously recorded diurnal variations in the magnetic field, and the GPS base station, consisting of a GPS receiver and telemetry. Although the error associated with the cesium-vapor magnetometer is on the order of 0.1 nT, total error in the survey is typically 1 nT due to errors in position, and reaches 10 nT in areas of high magnetic gradients associated with basalt cover.

The following 20 unnumbered pages describe the drift correction procedure for the magnetic data.

This instrumentation allows investigators to traverse the area, quickly locating anomalies while continuously recording magnetic field and position data. Because the instrumentation provides real-time feedback, the survey team can make rapid and informed decisions to increase survey density where anomaly wavelengths are short enough to warrant it, and leave less interesting areas more sparsely sampled. The three surveys each consist of more than 25,000 magnetic measurements distributed along approximately 60 km of traverse lines. Line spacing varied between 25-500 m, depending on wavelength and complexity of observed anomalies. Our surveys were completed in about two weeks and represent the first detailed ground magnetic maps made of the region for site characterization, which has previously relied on aeromagnetic surveys supplemented by ground magnetic profiles [Kane and Bracken, 1983; Langenheim et al., 1993; Langenheim, 1995].

Southern Crater Flat Southern Crater Flat is a structural half-graben where small-volume basaltic volcanism has repeatedly occurred since cessation of large volume silicic volcanism during the mid-Miocene. Deposition of young alluvial sediments has partially or completely buried volcanoes in the southern part of the basin, obscuring the volcanic history of southern Crater Flat. Magnetic surveys near the Little Cones (two Quaternary cinder cones in the southern part of the basin) were used to map buried volcanoes.

The extent of Quaternary lava flows from the Little Cones is delimited on the ground magnetic map by the distribution of short-wavelength, large-amplitude anomalies (Figure 2). Lava flows from the Little Cones only crop out up to 400 m south of the cones. Ground magnetic surveys indicate the Little Cones lavas are about one order of magnitude more voluminous than indicated by outcrops, extending approximately 1.5 km

south of the Little Cones. The flows are buried 15-30 m beneath a nearly featureless alluvial plain. So, rather than being incongruously small volcanic features compared to nearby cones, the Little Cones and their lava flows exemplify the final stages of inundation and burial of two young cinder cones in an actively subsiding basin [Stamatakos et al., 1996].

FIGURE 2. Ground magnetic map of southern Crater Flat. High amplitude, short-wavelength, predominantly negative anomalies are produced by the reversely magnetized Little Cones lava flows. A long wavelength positive anomaly is produced by a normally magnetized body about 0.5 km2 in area, 20-40 m thick, and buried at 150-200 m. The small NNW-trending magnetic anomaly in the southernmost part of the survey area is related to Miocene basalt outcrops just south of the map. This survey was completed in five days and consists of about 33,000 measurements. Contour interval is 100 nT. These

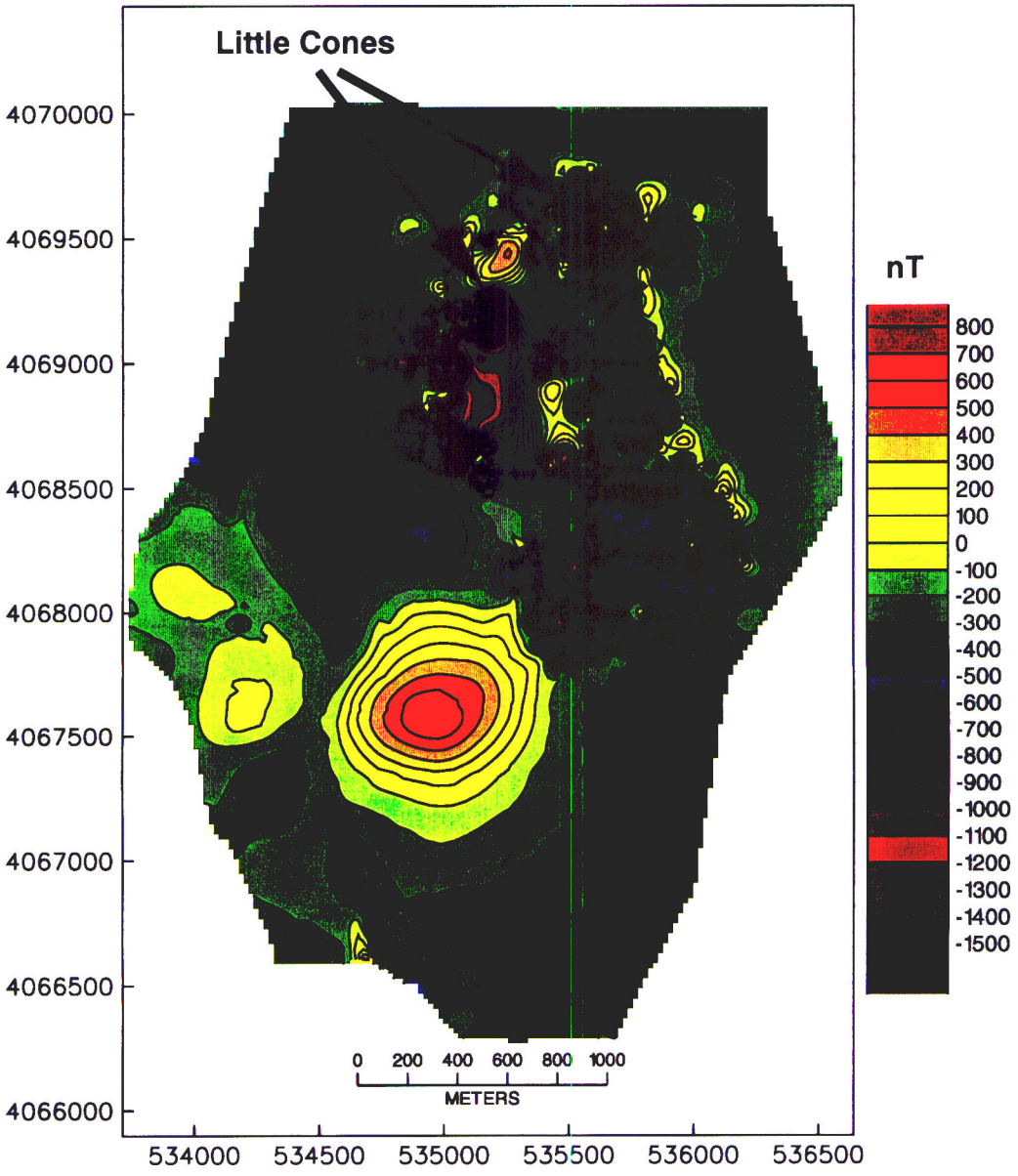

data and those shown on the following maps (Figures 3 and 4) are drift corrected and the International Geomagnetic Reference Field (IGRF) removed.

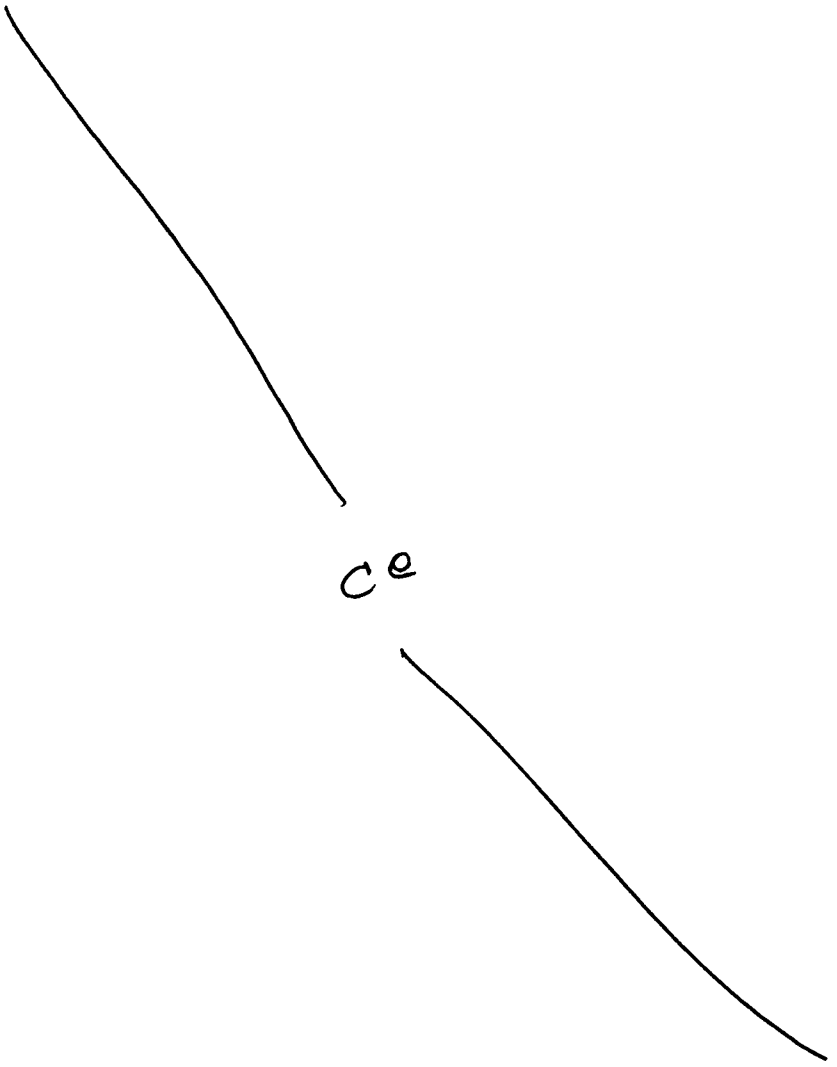

The magnetic map defines the position of an older, completely buried volcano 2 km south of the Little Cones (Figure 2). This large amplitude positive anomaly was first observed on aeromagnetic maps [Kane and Bracken, 1983; Langenheim, 1995]. The anomaly is beautifully symmetric, with maximum positive and negative peaks separated by 750 m and a peak-to-peak amplitude of 1100 nT. The smaller, negative portion of the anomaly is truncated by anomalies associated with the Little Cones lava flows.

A third prominent magnetic feature was discovered near outcrops of Miocene basalt. This feature is a linear magnetic anomaly extending from the southern end of the survey

area to the NNW for approximately 500 m (Figure 2). The causative body is likely a shallow dike associated with the Miocene basalts. Our survey method allowed us to identify the feature in the field and led us to immediately modify our survey to better define the shorter wavelengths and smaller amplitudes observed in this part of the survey area. Thus, the magnetic map reveals a sequence of volcanic activity in southern Crater Flat accompanying basin subsidence. Probability models for volcanic hazards in the area need to account for this pattern of clustering.

Amargosa 'Anomaly A' Five anomalies were identified in Amargosa Valley by Langenheim, et al. (1993) as potentially buried volcanoes or related igneous features. The five anomalies have been incorporated as volcanic events in some probabilistic volcanic hazard analyses for potential future volcanic eruptions at Yucca Mountain [e.g., Connor and Hill, 1995], but not in others [e.g., Geomatrix, 1996], possibly because of their uncertain origin. Of these anomalies, Amargosa Anomaly A (Figure 1) is the most complex and difficult to interpret from aeromagnetic maps because of its comparatively short wavelength relative to flightline spacing. Yet, anomaly A is of great interest because of its proximity to the Lathrop Wells cinder cone, the youngest volcano in the Yucca Mountain region, and because it is the closest of the Amargosa Valley anomalies to the candidate repository site (Figure 1). With these factors in mind, we completed a ground magnetic survey of anomaly A to constrain its origin and to better resolve its distribution in the subsurface.

The ground magnetic map of data collected over Amargosa Anomaly A delineates three separate anomalies associated with shallowly buried, reversely magnetized rock (Figure 3). These anomalies are distributed over 4.5 km on a NE trend, each having an amplitude of 70-150 nT. Although these features can be partially resolved with aeromagnetic data [Langenheim et al., 1993], trenchant details emerge from the ground magnetic survey that are important to probabilistic volcanic hazard analyses and tectonic studies of the region. Such details include the character of the southernmost anomaly, which has a smaller amplitude than those to the north but is nonetheless distinctive, and the NE-trending structure within the negative portion of the central anomaly, which mimics the overall trend of the alignment (Figure 4). The ground magnetic data also enhance the small positive anomalies north of each of the three larger amplitude negative anomalies, reinforcing the interpretation that anomaly A is produced by coherent basalt edifices with strongly reversed remanent magnetizations.

FIGURE 3.

Figure 3. Ground magnetic map of Amargosa Anomaly A showing three aligned anomalies. The high-resolution magnetic survey elucidates structure in the magnetic anomalies, such as their reversed magnetization with steep inclinations and the elongate character of individual anomalies. Such detail in the magnetic map supports the

interpretation that these anomalies are produced by a buried alignment of three volcanoes. Contour interval is 10 nT.

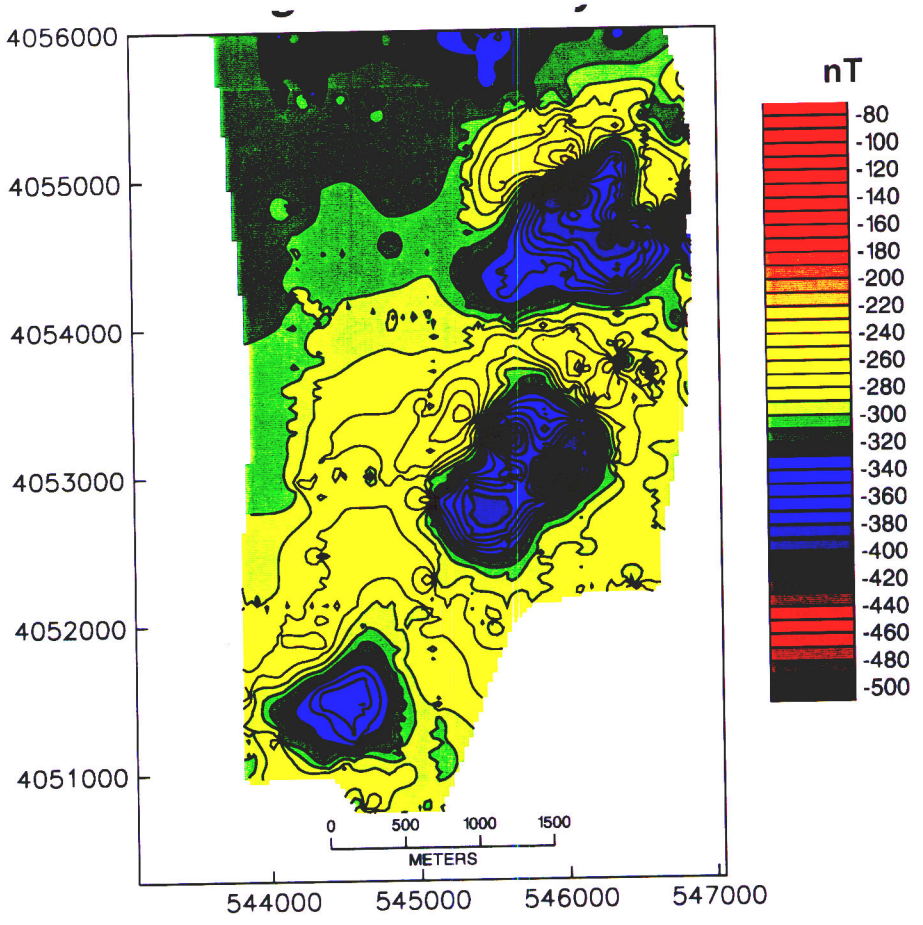

A key result of this survey is identification of the NE trend of the anomalies, quite similar to the alignment of five Quaternary cinder cones in Crater Flat (Figure 1), and to the Sleeping Butte cinder cones, a Quaternary vent alignment 40 km to the northeast. Although the age of the Amargosa Valley alignment is at present uncertain, it suggests that development of NE-trending cone alignments is a pattern of volcanism that has persisted through time in the Yucca Mountain region and supports the idea that future volcanism may exhibit a similar pattern [Smith et al., 1990].

FIGURE 4.

Figure 4. Processing the ground magnetic data within a GIS facilitates comparison of anomalies with other mapped features, such as faults and topography. Here, the ground magnetic map of Northern Cone is superimposed on digitized topographic contours. Mapped faults of Frizzell and Schulters [1990] are shown in red (also see Figure 1), and dirt roads are shown as black lines. Northern Cone is located in the central portion of the map, as indicated by high-amplitude, short wavelength anomalies. The color scale is truncated where magnetic gradients are very high (such as on the cone). Contour interval of topography is 20 ft and changes to 40 ft across a map boundary in the northern part of the figure.

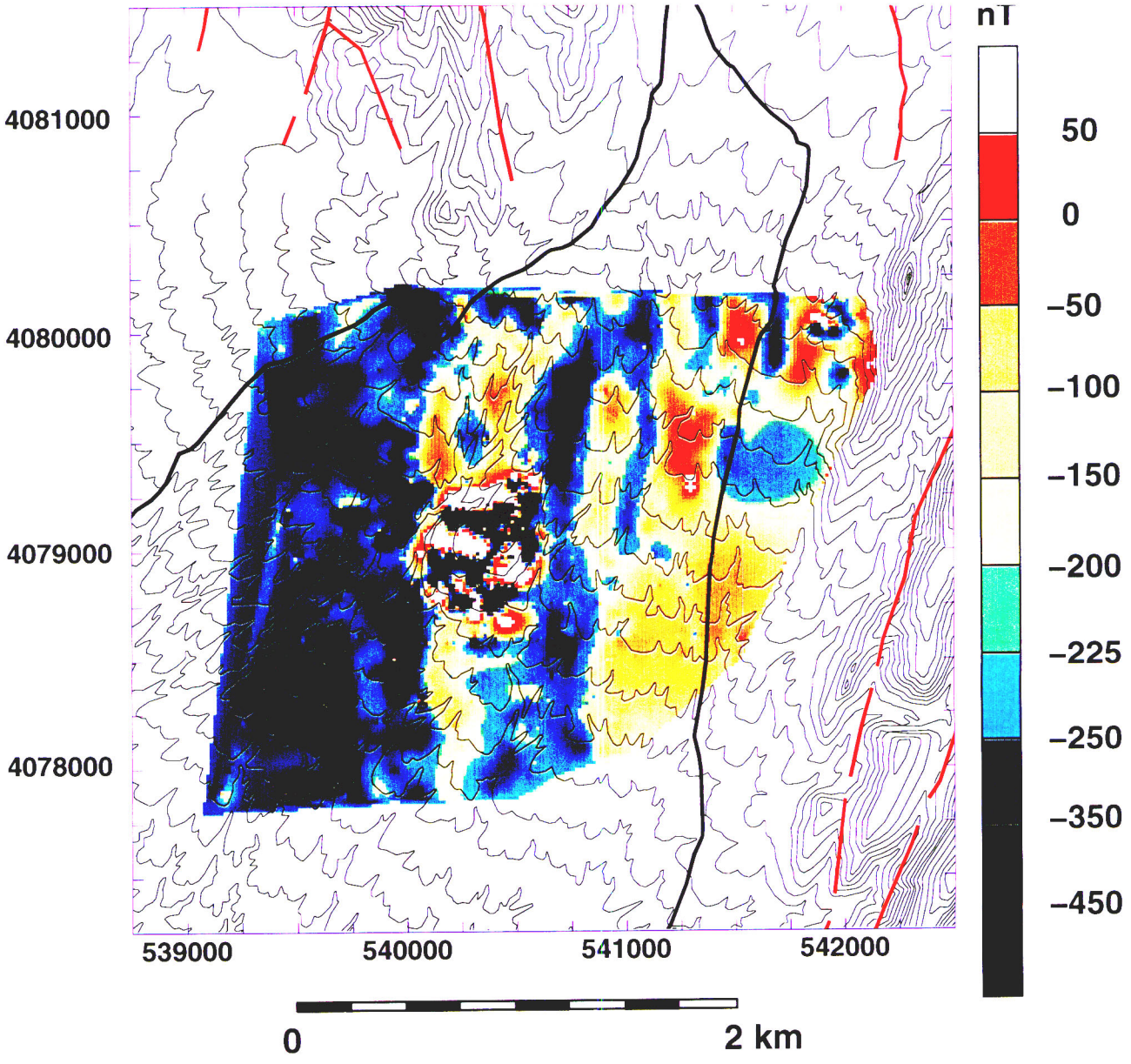

Northern Cone Northern Cone is located in Crater Flat, approximately 8 km from the repository site, and is the closest Quaternary volcano to Yucca Mountain. Its proximity

to the site of the proposed repository makes the structural setting of Northern Cone of particular interest to volcanic hazard assessment. We surveyed primarily along E-W trending lines separated by 100 m over rugged alluvial topography.

Northern Cone consists of approximately 0.4 km2 of highly magnetized (10–20 Am-1) lava flows, near-vent agglutinate, and scoria aprons resting on a thin alluvial fan. Large-amplitude, short-wavelength anomalies were observed over the cone. No evidence of NE-trending structures were discovered that could directly relate Northern Cone to the rest of the Quaternary Crater Flat cinder cone alignment. Instead, prominent linear anomalies surrounding Northern Cone trend nearly N-S and have amplitudes of up to 400 nT (Figure 4). These anomalies likely result from offsets in underlying tuff across faults extending beneath the alluvium.

The relationship between faults and Northern Cone is clarified when the ground magnetic map is compared with topographic and fault maps [Frizzell and Schulters, 1990; Faulds et al., 1994]. The N-trending anomalies at Northern Cone roughly coincide with mapped faults immediately north of the survey area that have topographic expression resulting from large vertical displacements. These mapped faults and faults inferred from the magnetic map are all oriented N to NNE, trends favorable for dilation and dike injection in the current stress state of the crust. Thus, the Northern Cone magnetic survey provides further support for the idea that volcanism on the eastern margin of Crater Flat was localized along faults.

Conclusions

These three surveys are examples of how improved magnetic mapping instrumentation can be used for site characterization. Primarily, the interface between magnetometer and differential GPS results in the real-time feedback of copious geographically-referenced magnetic data to the survey team. Real-time feedback allows for flexibility in survey design and goals as the survey progresses. At Yucca Mountain, this improved instrumentation helped characterize past episodes in volcanism and the relationships between volcanoes and tectonism in the region. Recognition of these relationships is crucial to evaluation of the probable distribution of future volcanic eruptions in the Yucca Mountain region and the phenomenological link between crustal structures and the distribution of volcanoes.

References

Code of Federal Regulations, Title 10 Part 60.122, Code of Federal Regulations, Title 10, Parts 51 to 199, Washington, D.C., Office of Federal Register, National Archives and Records Administration, 612 pp., 1994.

Connor, C.B. and B.E. Hill, Three nonhomogeneous Poisson models for the probability of basaltic volcanism: Application to the Yucca Mountain region, Nevada, J. Geophys. Res., 100, 10,107-10,127, 1995.

Faulds, J.E., J.W. Bell, D.L. Feuerbach, and A.R. Ramelli, Geologic map of the Crater Flat area, Nevada, Nev. Bur. Mines Geol. Map, 101, 1994.

Fleck, R.J. B.D. Turrin, D.A. Sawyer, R.G. Warren, D.E. Champion, M.R. Hudson, and S.A. Minor, Age and character of basaltic rocks of the Yucca Mountain region, southern Nevada, J. Geophys. Res., 101, 8,205-8,227, 1996.

Frizzell, V.A., Jr., and J. Schulters, Geologic map of the Nevada Test Site, southern Nevada, U.S. Geol. Surv. Misc. Invest. Map, I-2046, 1990.

Geomatrix, Probabilistic Volcanic Hazard Analysis for Yucca Mountain, Nevada, Geomatrix Consultants, San Francisco, Rep. BA0000000-1717-2200-00082, 1996.

Kane, M.F. and R.E. Bracken, Aeromagnetic map of Yucca Mountain and surrounding regions, southwest Nevada, U.S. Geol. Surv. Open File Rep., 83-616, 1983.

Langenheim, V.E., K.S. Kirchoff-Stein, and H.W. Oliver, Geophysical investigations of buried volcanic centers near Yucca Mountain, southwest Nevada, in Fourth International Conference on High-Level Radioactive Waste Management, pp. 1840-1846, Am. Nucl. Soc., Las Vegas, Nev., 1993.

Langenheim, V.E., Magnetic and gravity studies of buried volcanic centers in the Amargosa Desert and Crater Flat, southwest Nevada, U.S. Geol. Surv. Open File Rep. 95-564, 1995.

Smith, E.I., T.R. Naumann, D.L. Feuerbach, and J.E. Faulds, The area of most recent volcanism near Yucca Mountain, Nevada: Implications for volcanic risk assessment, in

First International Conference on High-Level Radioactive Waste Management, pp. 81-99, Am. Nucl. Soc., Las Vegas, Nev., 1990.

Stamatakos, J., C. Connor, and R. Martin, Quaternary basin evolution and basaltic volcanism of Crater Flat, Nevada, from detailed ground magnetic surveys of the Little Cones, J. Geol., in press., 1996.

Turrin, B.D., D. Champion, and R.J. Fleck, 40Ar/39Ar age of the Lathrop Wells volcanic center at Yucca Mountain, Nevada, Science, 253, 654-657, 1991.

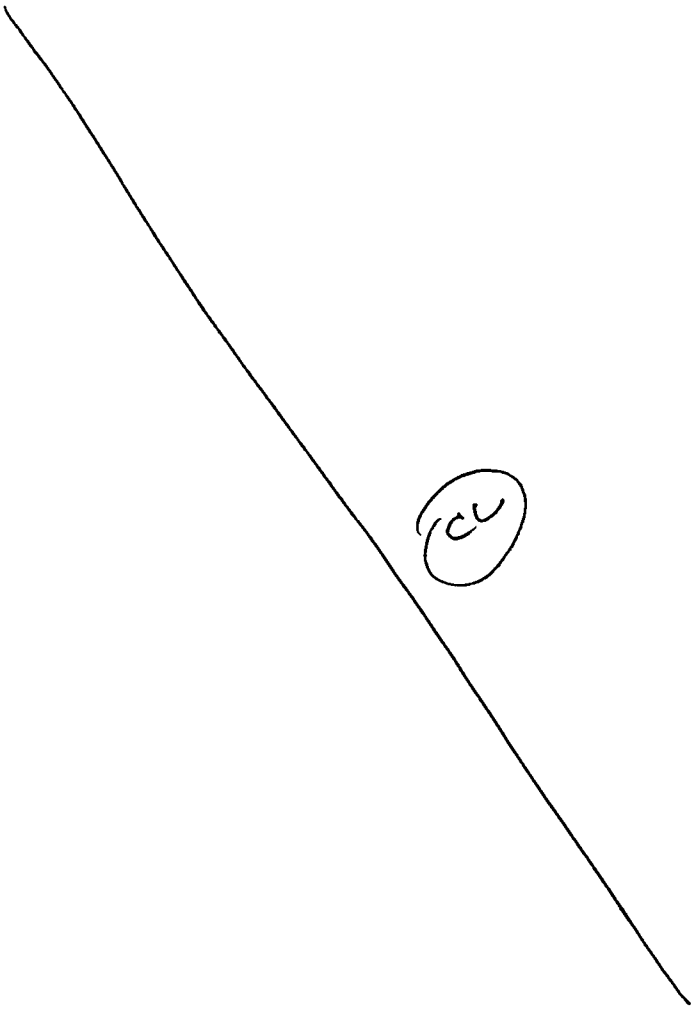

UE

10620

DRIFT CORRECTION PROCEDURES FOR GROUND MAGNETIC DATA COLLECTED AT CRATER FLAT AND THE AMARGOSA VALLEY, NV

Output from the GPS and 858 included multiple latitude, longitude, and timestamps for each recorded magnetic value. These data had to be reconciled in order to drift correct data. Output looked like this:

```
21 $GPGGA,022702,3638.1821,N,11630.3667,W,1,6,02,746,M,-25,M*65 19:27:29.80
05/28/96
21 $GPGGA,022701,3638.1821,N,11630.3667,W,1,6,02,746,M,-25,M*66 19:27:28.60
05/28/96
0  50553.573     0.000 19:27:28.30 05/28/96  0
21 $GPGGA,022700,3638.1818,N,11630.3666,W,1,6,02,746,M,-25,M*6C 19:27:28.00
05/28/96
21 $GPGGA,022659,3638.1813,N,11630.3666,W,1,6,02,746,M,-25,M*6A 19:27:26.70
05/28/96
0  50554.499     0.000 19:27:26.30 05/28/96  0
```

where lines beginning with "21" represent GPS data and lines beginning with "0" represent magnetometer data. Latitude and longitude were each recorded at approximately 1.4 second intervals, while magnetic data were recorded approximately every 2 seconds with their own timestamps.

Each "traverse" of data consisted of several thousand data points. Large traverse files were first split into smaller files (3000 lines each) using TRUEBASIC program SPLITTER.TRU. Integrity of files was checked by looking at start and stop times of each file segment. File segments were run through a TRUEBASIC program, STNREAD.TRU, which matched GPS and magnetic values as closely as possible, converted recorded time to decimal seconds, and placed all data in tabular format (.STN files must begin with a "21" string for program to work).

File segments were then opened in EXCEL, where they were formatted to the correct number of decimal places and sorted in ascending order with respect to time (raw data was in reverse order with respect to time). The recorded time for each reading was converted to seconds since midnight for the day of data collection. File segments were converted to UNIX format and concatenated.

Data collected continuously (at 3 minute intervals) at the base station were formatted in EXCEL. Recorded time of each reading was converted to seconds since midnight. Base station and traverse data were then input into the C+ code DRIFT to correct for diurnal variation in the magnetic field. The DRIFT program determines the slopes of lines connecting successive base station readings with respect to time. For any time *t* as recorded while surveying, the change in magnetic field caused by diurnal variation is calculated and subtracted from the observed magnetic value collected at that time. Sample drift curves are included.

LFT.DOC

STANDARD TRU

CC
2/20

```
!....+....1....+....2....+....3....+....4....+....5....+....6....+....7....+....8....+....+....+....+....+
!6        0.00        0.00 19:27:30.40 05/28/96      3759          0          1  5         0
!0   50553.666      0.000 19:27:30.30 05/28/96   0
!21 $GPGGA,022702,3638.1821,N,11630.3667,W,1,6,02,746,M,-25,M*65 19:27:29.80 05/28/96
!21 $GPGGA,022701,3638.1821,N,11630.3667,W,1,6,02,746,M,-25,M*66 19:27:28.60 05/28/96
!0   50553.573      0.000 19:27:28.30 05/28/96   0
!21 $GPGGA,022700,3638.1818,N,11630.3666,W,1,6,02,746,M,-25,M*6C 19:27:28.00 05/28/96
!21 $GPGGA,022659,3638.1813,N,11630.3666,W,1,6,02,746,M,-25,M*6A 19:27:26.70 05/28/96
!0   50554.499      0.000 19:27:26.30 05/28/96   0
!21 $GPGGA,022658,3638.1808,N,11630.3667,W,1,6,02,746,M,-25,M*60 19:27:26.10 05/28/96
!21 $GPGGA,022657,3638.1802,N,11630.3668,W,1,6,02,746,M,-25,M*6A 19:27:24.60 05/28/96
!0   50548.257      0.000 19:27:24.30 05/28/96   0
!21 $GPGGA,022656,3638.1797,N,11630.3665,W,1,6,02,746,M,-25,M*65 19:27:24.00 05/28/96
!21 $GPGGA,022655,3638.1793,N,11630.3660,W,1,6,02,746,M,-25,M*67 19:27:22.70 05/28/96
!0   50537.110      0.000 19:27:22.30 05/28/96   0

open #1: name "bare1b.stn"
open #2: name "bare1b.out", create newold
erase #2
do while more #1
line input #1: lin$
if lin$[1:2] = "21" then
   let lin1$ = lin$[11:16]
   let lin2$ = lin$[18:26]  !lat
   let lin3$ = lin$[30:39]  !long
   let lin4$ = lin$[65:75]  ! time
   let lin5$ = lin$[77:85]  ! date
   let lin6$ = lin$[60:64]
!print lin3$,lin2$
else if lin$[1:1] = "0" then
   let mag1$ = (lin$[5:15])
   let lin5$ = lin$[38:45]
 ! let hour$ = (lin4$[1:2]) !* 3600
 ! print hour$, "here"
 ! get key dum
   let hour = val(lin4$[1:2]) * 3600
   let min = val(lin4$[4:5]) *60
   let sec = val(lin4$[7:12])
   let timer = hour + min + sec
   let times$ = str$(timer)
   let times$ = times$[1:5]
print #2:  times$;" "; mag1$;" "; lin2$;" "; lin3$;" "; lin4$;" ";lin5$;" "; lin1$;" ";lin6$
end if
loop

end
```

cc
3/20

```
open #1: name "north1.stn"
open #2: name "north1a.stn" , create newold
erase #2
open #3: name "north1b.stn" , create newold
erase #3
!open #4: name "amar7c.stn" , create newold
!erase #4
!open #5: name "amar5d.stn" , create newold
!erase #5
!open #6: name "amar2e.stn" , create newold
!erase #6
!open #7: name "amar2f.stn" , create newold
!erase #7
!open #8: name "amar1g.stn" , create newold
!erase #8
!open #9: name "amar1h.stn" , create newold
!erase #9

do while more #1

line input #1: lin$
let kt = kt + 1


if kt < 3000 then
print #2: lin$
end if

if kt => 3000 and kt < 6000 then
print #3: lin$
end if

if kt => 6000 and kt < 9000 then
print #4: lin$
end if

if kt => 9000 and kt < 12000 then
print #5: lin$
end if

if kt => 12000 and kt < 15000 then
print #6: lin$
end if

if kt => 15000 and kt < 18000 then
print #7: lin$
end if

if kt => 18000 and kt < 21000 then
print #8: lin$
end if

if kt => 21000 then
print #9: lin$
```

cc

4/20

```
end if
loop

print kt
end
```

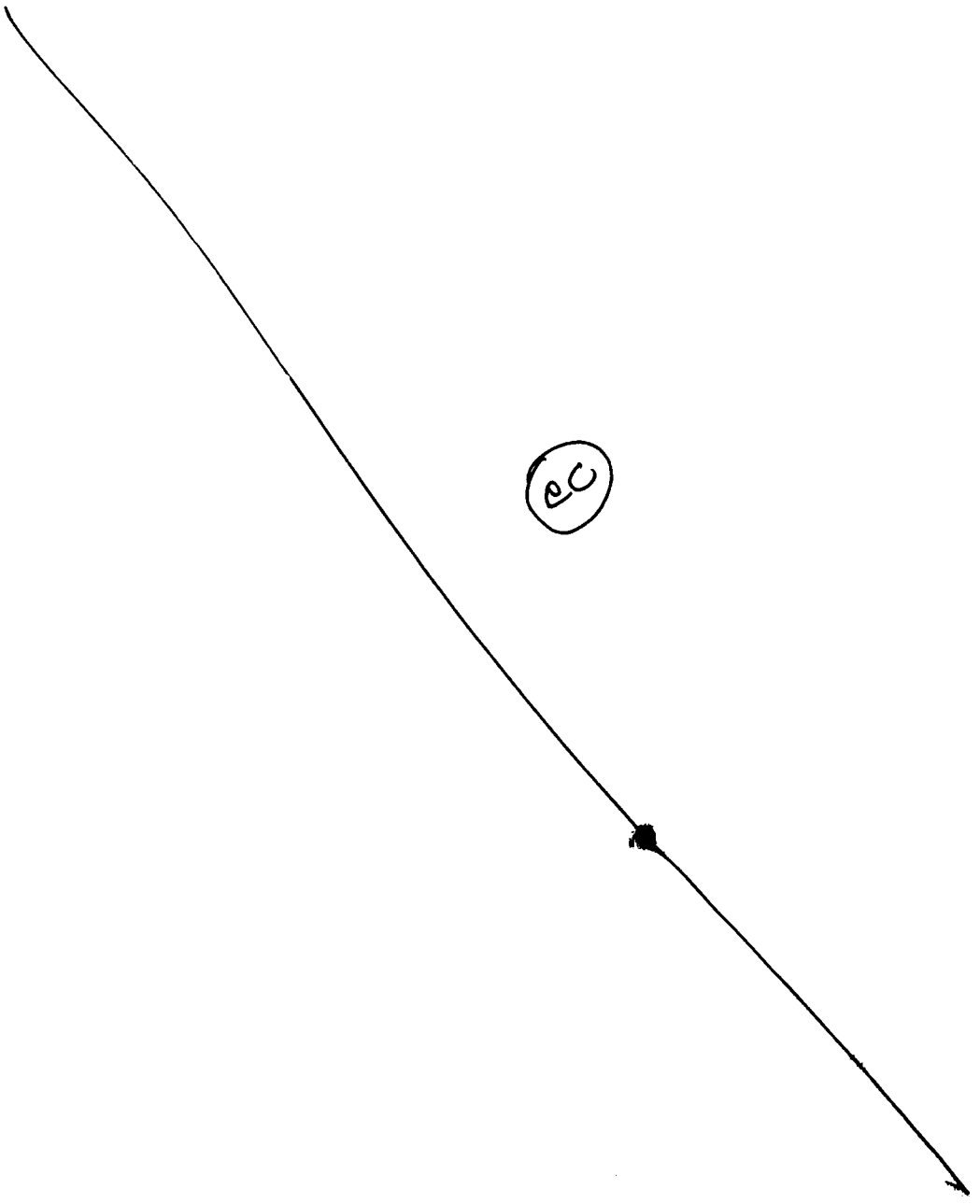

dc
5/20

```
#include <stdio.h>
#include <stdlib.h>
#include <math.h>
/* program to calculate drift corrections */
/* format is for input from the command
   line with the first file the file
   containing the diurnal variation measured at the
   base station and the second file containing the time and magnetic values
   to be corrected */

void main (argc, argv)
    int argc;
    char *argv[];
{

double dtime[500];
double ddrift[500];
double x1,x2,y1,y2,m1;
double drifted, drift_corr, drmag, drtime;
char dum1[10],dum2[10],dum3[10],dum4[10],dum5[10],dum6[10];
int kt, totdrift;
int ret;
FILE *ifp;
FILE *ifp2;

ifp = fopen(argv[1],"r");
if (ifp == NULL) {
   fprintf (stderr,"%s didn't open\n",argv[1]);
   exit(1);
}
while (fscanf(ifp,"%lf %lf %s %s %s", &dtime[kt], &ddrift[kt], dum1, dum2, dum3)
 != EOF) {
   /*printf (" %f %f\n", dtime[kt], ddrift[kt]);*/
   kt++;
}
fclose(ifp);

totdrift = kt;

kt = 0;

if ((ifp2 = fopen(argv[2],"r")) == NULL) {
   fprintf (stderr,"%s didn't open\n",argv[2]);
   exit(1);
}
while (fscanf(ifp2,"%lf %lf %s %s %s %s %s %s", &drtime, &drmag, dum1, dum2, dum
3, dum4, dum5, dum6) !=EOF) {
   for (kt = 1; kt < totdrift; kt++) {

       if (dtime[kt]>drtime) {
          x1 = dtime[kt-1];
          x2 = dtime[kt];
          y1 = ddrift[kt-1];
          y2 = ddrift[kt];
          break;  /* exit for */
       }  /* end if */

   } /* end kt for */

  m1 = (y2-y1)/(x2-x1);
```

cc
4/20

```
  drifted = (drtime-x1)*m1;
  drifted = drifted + ddrift[kt-1] - ddrift[0];
  drift_corr = drmag-drifted;

  printf("%10.2f%10.2f%10.2f%10.0f\t%s\t%s\t%s\t%s\t%s\t%s\n",
        drift_corr,drifted,drmag,drtime,dum1,dum2,dum3,dum4,dum5,dum6);


} /* end the fscan */
fclose(ifp2);
exit(0);
}
```

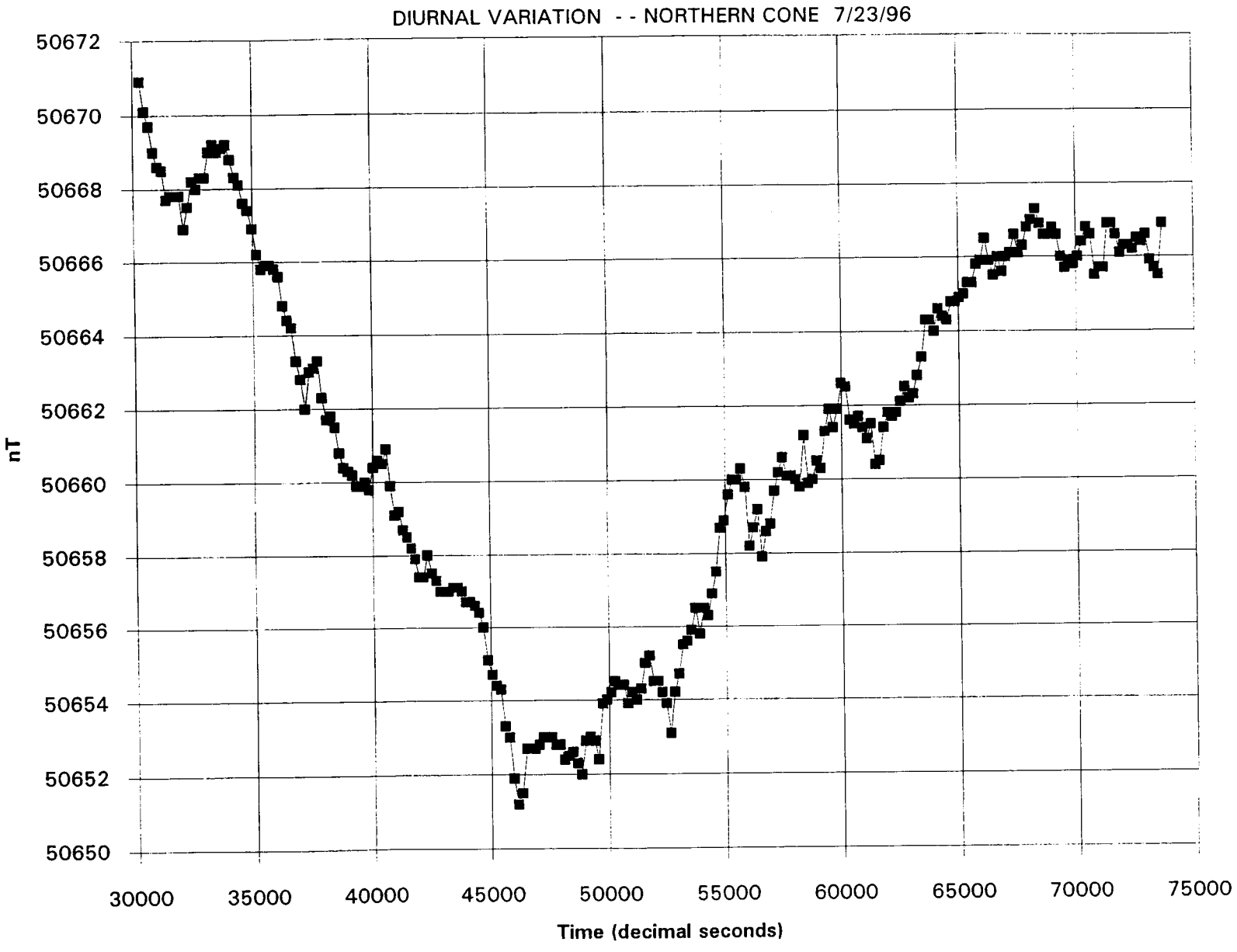
DIURNAL VARIATION - - NORTHERN CONE 7/23/96
50672
50670
50668
50666
50664
50662
50660
50658
50656
50654
50652
50650
nT
30000
35000
40000
45000
50000
55000
60000
65000
70000
75000
Time (decimal seconds)

7/20

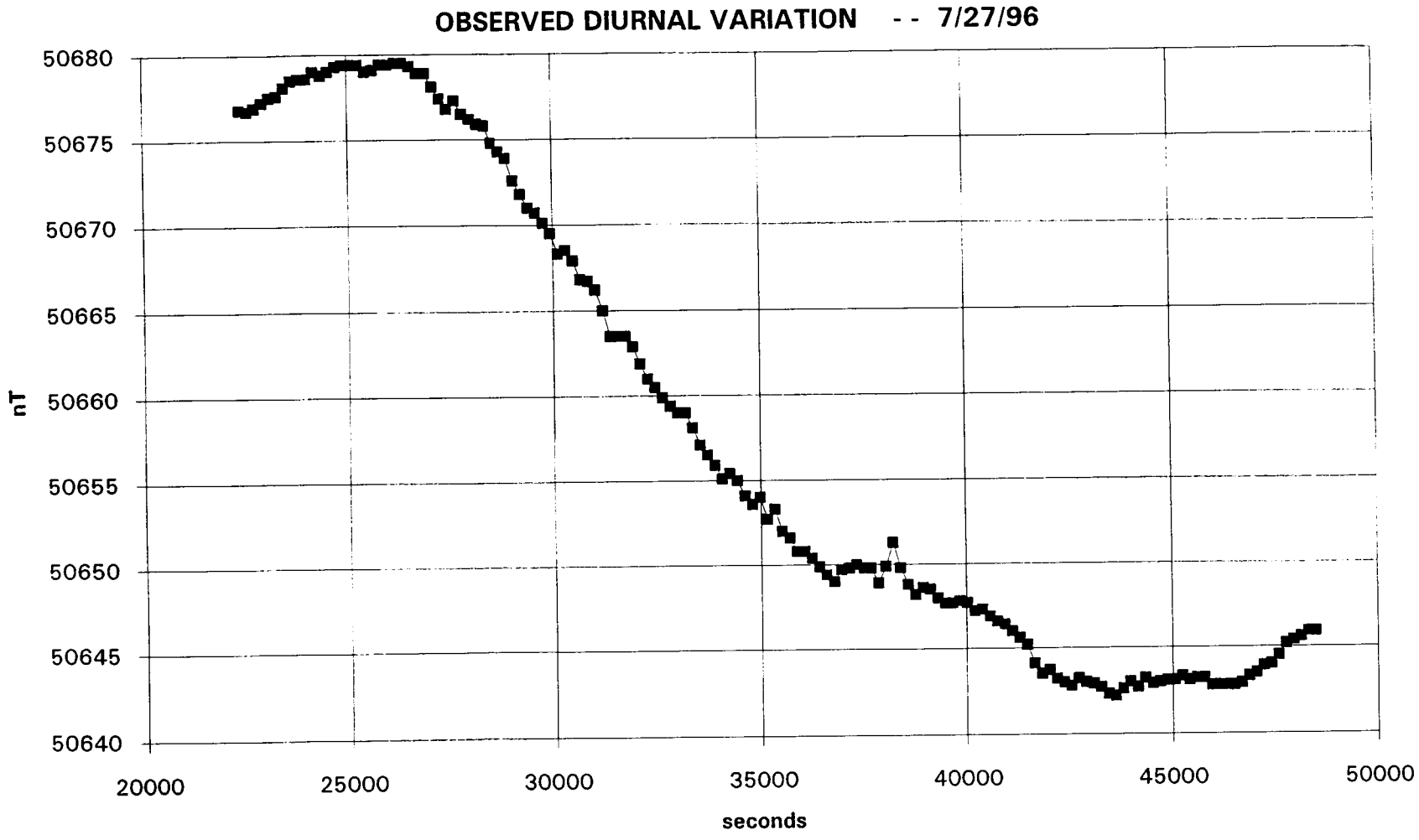
OBSERVED DIURNAL VARIATION -- 7/27/96
50680
50675
50670
50665
50660
50655
50650
50645
50640
nT
20000
25000
30000
35000
40000
45000
50000
seconds

CC
8/20

cc
9/20

Each data file was split into two tables using EXTRACT_XY.NAWK and EXTRACT_ATTRIBUTES.NAWK. EXTRACT_XY.NAWK retrieved latitudes and longitudes from the files, and converted data from degrees and minutes, to decimal degrees. EXTRACT_ATTRIBUTES.NAWK retrieved all other data in the file. The tables were linked in Arc/info using an identifier assigned to each line of data in the nawk scripts. Latitude and longitude were converted to UTM (zone 11) coordinates within Arc. Spurious data points (where GPS lock was lost) were obvious when looking within the arc coverage and were deleted.

In order to correct for diurnal variation from day-to-day, baseline data collected over the same traverse in the morning and evening of each day and on successive days were compared. Sample baseline data graphs are included. Horizontal displacement on the graphs represents a change in the magnetic field caused by diurnal variation. Baseline data were collected in a matter of minutes. The average difference in baseline data from between days was calculated (within EXCEL), and this constant added or subtracted from the drift corrected data directly within the arc coverage.

If no baseline data were collected, data were corrected for daily bias by minimizing error across tie lines. Constants were added or subtracted directly within the arc coverage.

The International Geomagnetic Reference Field (IGRF) was removed from data sets to remove trends not associated with ground magnetic anomalies. The IGRF was calculated for coordinates of several points across the survey area using the US Geological Survey potential field geophysical software. The IGRF values for the points were plotted on graphs with respect to distance to determine if the calculated field maintained linear trends through the surface area. When a linear trend was established, a code was used to calculate the linear trend surface fitting the calculated IGRF values (see scientific notebook July 15, 1996). The result of the code is an equation of the form:

IGRF = a + b*easting +c*northing

where a, b, and c are constants determined by the program. The IGRF was calculated for each data point within Arc/Info using this equation (UTM coordinates need to be added to the coverage attribute table in order to calculate).

The data can now be IGRF corrected by applying the following equation within Arc/Info:

IGRF corrected = drift corrected data - calculated IGRF,

resulting in completely corrected magnetic data.

cc
10/20

```
        yy = substr($0,42,2) + 0.0
        mins = substr($0,44,7) + 0.0
        yy = yy + mins/60.0
        printf ("%d, %.8f, %.8f \n", pntknt, xx, yy)
      }
      END {
            printf ("END \n")
            printf ("END \n")
            printf ("Total points processed: %d \n", recknt)
          } ' $1

exit
```

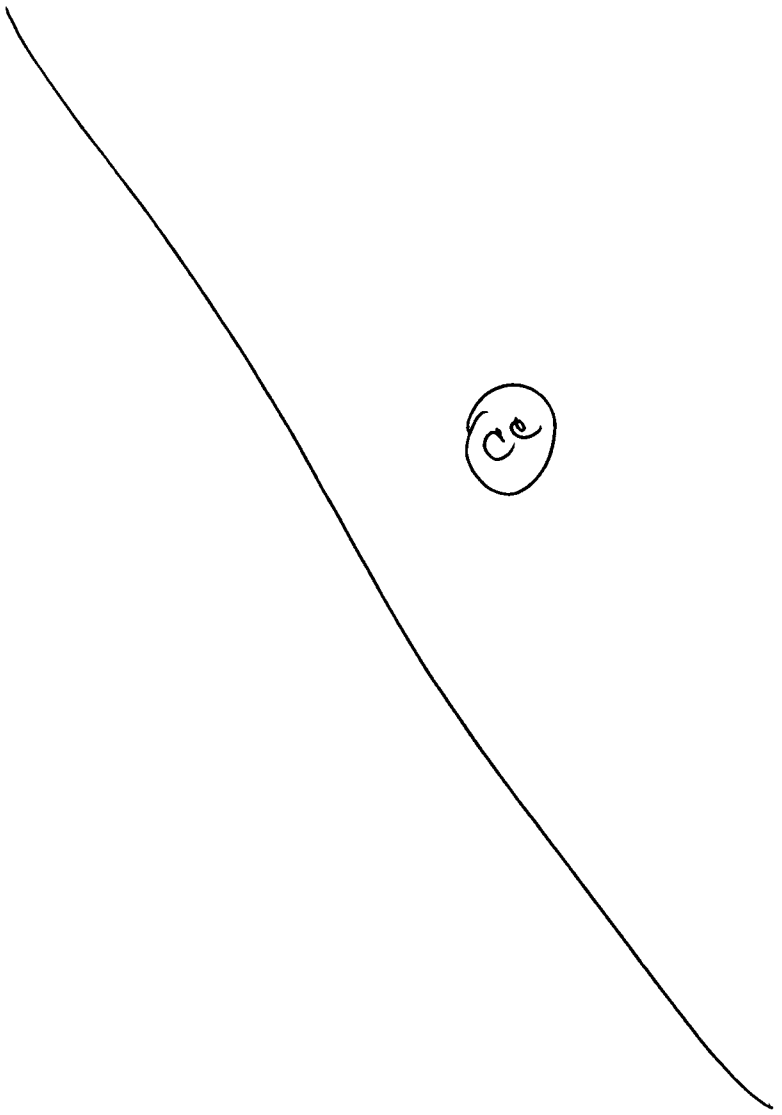

dc

11/20

```
#!/bin/sh
# ------------------------------------------------------------------------
#
#   abstract: shell script will extract X Y pairs and build generate
#             input files for ArcInfo.
#
#   revised:  20-Jun-96  new create by:
#
#                Sammantha Magsino / #20
#                6220 Culebra Rd.
#                San Antonio TX 78238 usa
#                210-522-5308 (phone)
#                210-522-5155 (fax)
#                E-mail: smagsino@swri.edu
#
# ------------------------------------------------------------------------
#

if ( test $# -ne '1' ) then
    echo Usage: $0 "<infile>"
    exit
fi

if ( test ! -f $1 ) then
    echo File: $1 not found.
    exit
fi

# input looks like
#....+....1....+....2....+....3....+....4....+....5....+....6....+....7....+....
8....+....9....+
#  50090.43   3.05  50093.48   56891  3645.5355  11636.1281  15:48:11.80  5/21/9
6  224739  M*68
#  50090.62   3.06  50093.68   56892  3645.5354  11636.1280  15:48:12.90  5/21/9
6  224740  M*66
#  50098.65   3.06  50101.71   56893  3645.5354  11636.1280  15:48:13.90  5/21/9
6  224741  M*67
#  50138.45   3.07  50141.52   56894  3645.5352  11636.1280  15:48:14.80  5/21/9
6  224742  M*62
#  50172.75   3.08  50175.83   56896  3645.5346  11636.1279  15:48:16.00  5/21/9
6  224743  M*60
#  50186.02   3.08  50189.10   56897  3645.5340  11636.1278  15:48:17.10  5/21/9
6  224744  M*60
#  50159.22   3.09  50162.31   56899  3645.5327  11636.1278  15:48:19.00  5/21/9
6  224746  M*63
#  50120.46   3.10  50123.55   56900  3645.5321  11636.1277  15:48:20.10  5/21/9
6  224747  M*6B


nawk ' BEGIN {
               pntknt = 100
               recknt = 0
             }
      {
       pntknt += 10
       recknt++
       xx = substr($0,52,3) + 0.0
       mins = substr($0,55,7) + 0.0
       xx = xx + mins/60.0
       xx = -1.0 * xx
```

cc
12/20

```
#!/bin/sh
# ------------------------------------------------------------------------
#
#   abstract: shell script will extract attribute tables for feeding
#             to ArcInfo.
#
#   revised:  20-Jun-96  new create by:
#
#                Sammantha Magsino / #20
#                6220 Culebra Rd.
#                San Antonio TX 78238 usa
#                210-522-5308 (phone)
#                210-522-5155 (fax)
#                E-mail: smagsino@swri.edu
#
# ------------------------------------------------------------------------
#

if ( test $# -ne '1' ) then
    echo Usage: $0 "<infile>"
    exit
fi

if ( test ! -f $1 ) then
    echo File: $1 not found.
    exit
fi

# input looks like
#....+....1....+....2....+....3....+....4....+....5....+....6....+....7....+....
8....+....9....+
#  50090.43   3.05  50093.48   56891  3645.5355  11636.1281  15:48:11.80  5/21/9
6  224739  M*68
#  50090.62   3.06  50093.68   56892  3645.5354  11636.1280  15:48:12.90  5/21/9
6  224740  M*66
#  50098.65   3.06  50101.71   56893  3645.5354  11636.1280  15:48:13.90  5/21/9
6  224741  M*67
#  50138.45   3.07  50141.52   56894  3645.5352  11636.1280  15:48:14.80  5/21/9
6  224742  M*62
#  50172.75   3.08  50175.83   56896  3645.5346  11636.1279  15:48:16.00  5/21/9
6  224743  M*60
#  50186.02   3.08  50189.10   56897  3645.5340  11636.1278  15:48:17.10  5/21/9
6  224744  M*60
#  50159.22   3.09  50162.31   56899  3645.5327  11636.1278  15:48:19.00  5/21/9
6  224746  M*63
#  50120.46   3.10  50123.55   56900  3645.5321  11636.1277  15:48:20.10  5/21/9
6  224747  M*6B


nawk ' BEGIN {
               pntknt = 100
               recknt = 0
             }
       {
        pntknt += 10
        recknt++
        zmagdc = $1 + 0.0
        zdrift = $2 + 0.0
        zraw = $3 + 0.0
        dsec = $4 + 0.0
```

```
        ttime = $7
        tdate = $8
        t1unk = $9
        t2unk = $10
        printf ("%6d,%8.2f,%6.2f,%8.2f,%8d,%11s,%8s,%6s,%4s\n", pntknt, zmagdc,
zdrift, zraw, dsec, ttime, tdate, t1unk, t2unk)
      }
      END {
          } ' $1

exit
```

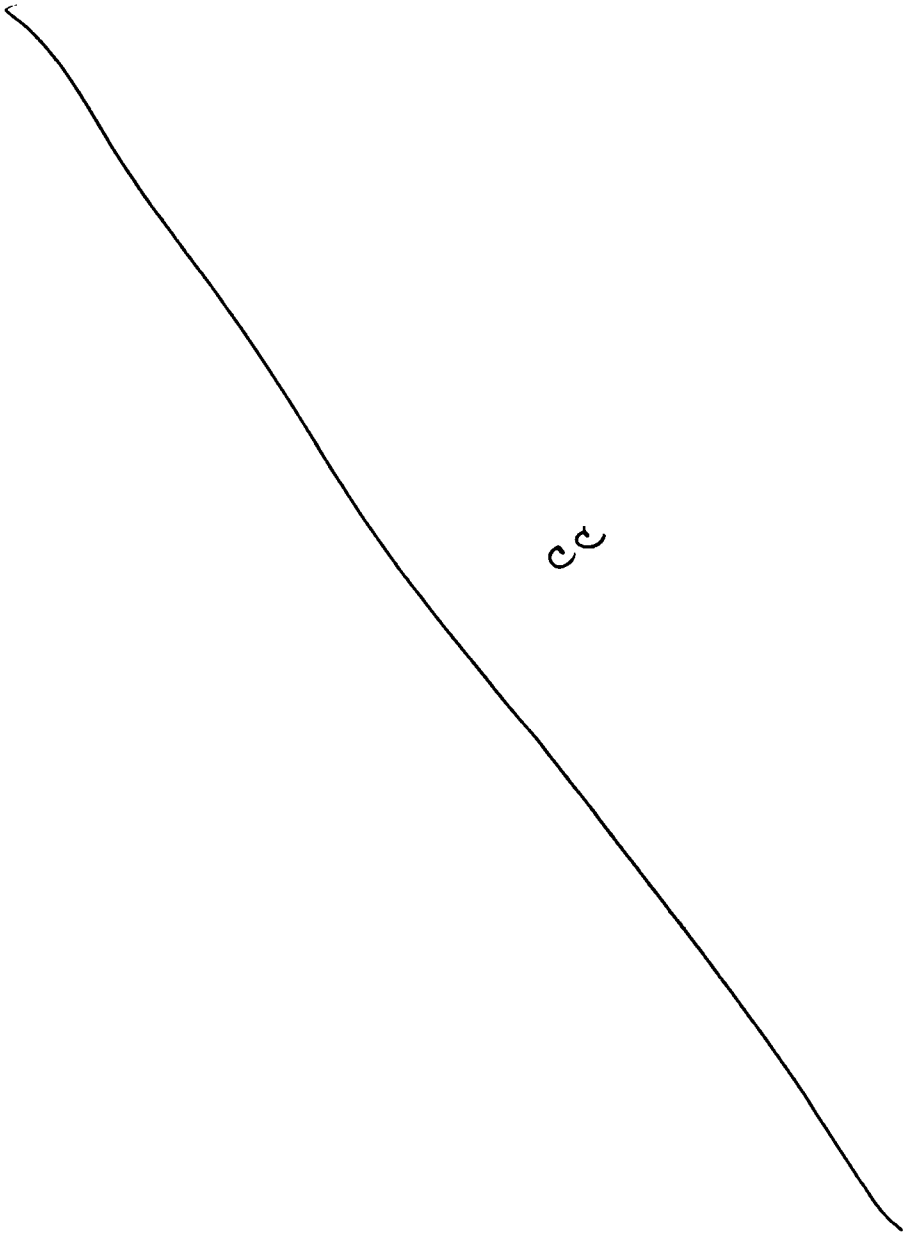

COMPARISON OF BASELINE DATA - - NORTHERN CONE SURVEY 7/96

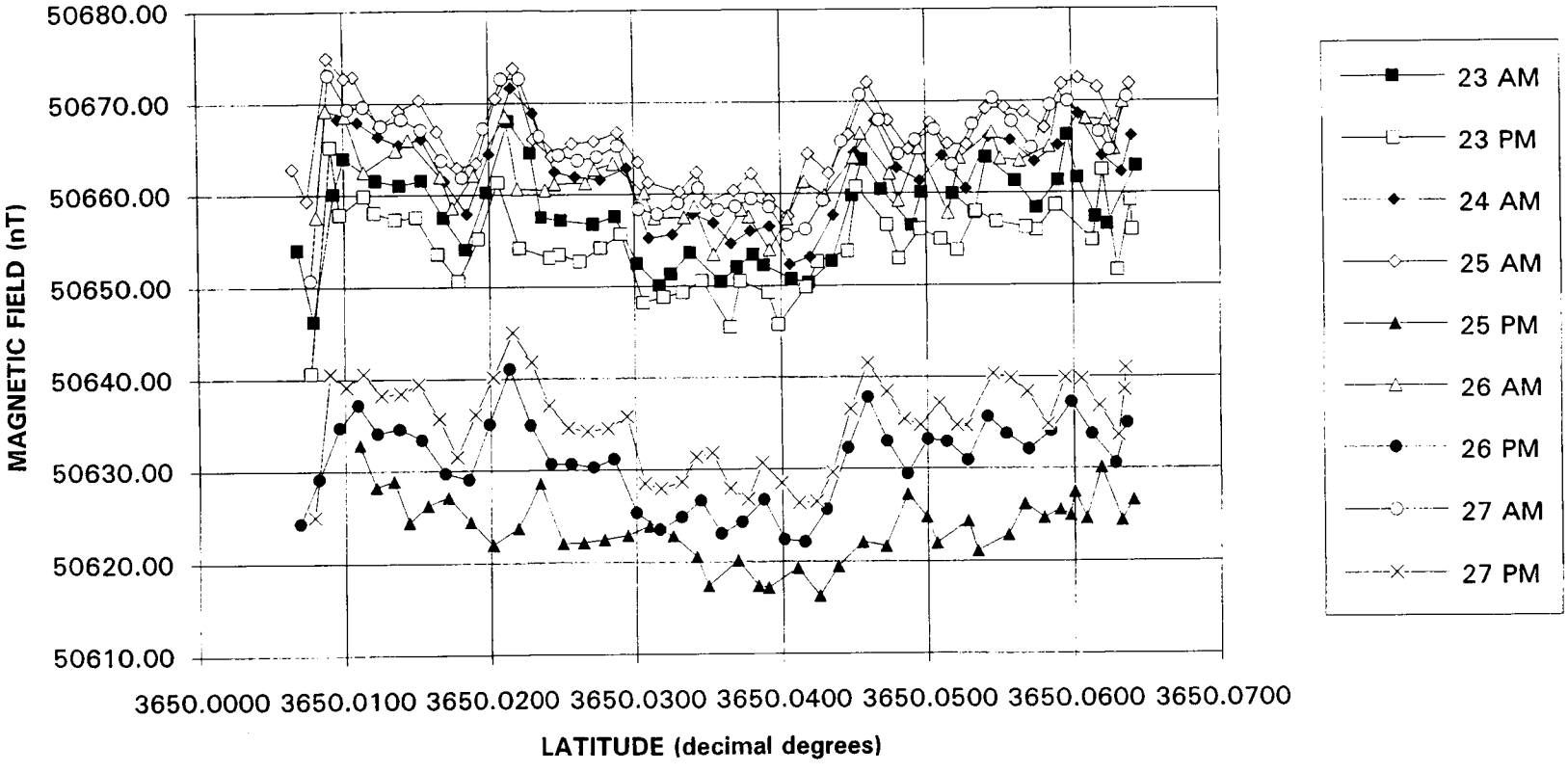

14/20

COMPARISON OF BASELINE DATA - - NORTHERN CONE SURVEY 7/96

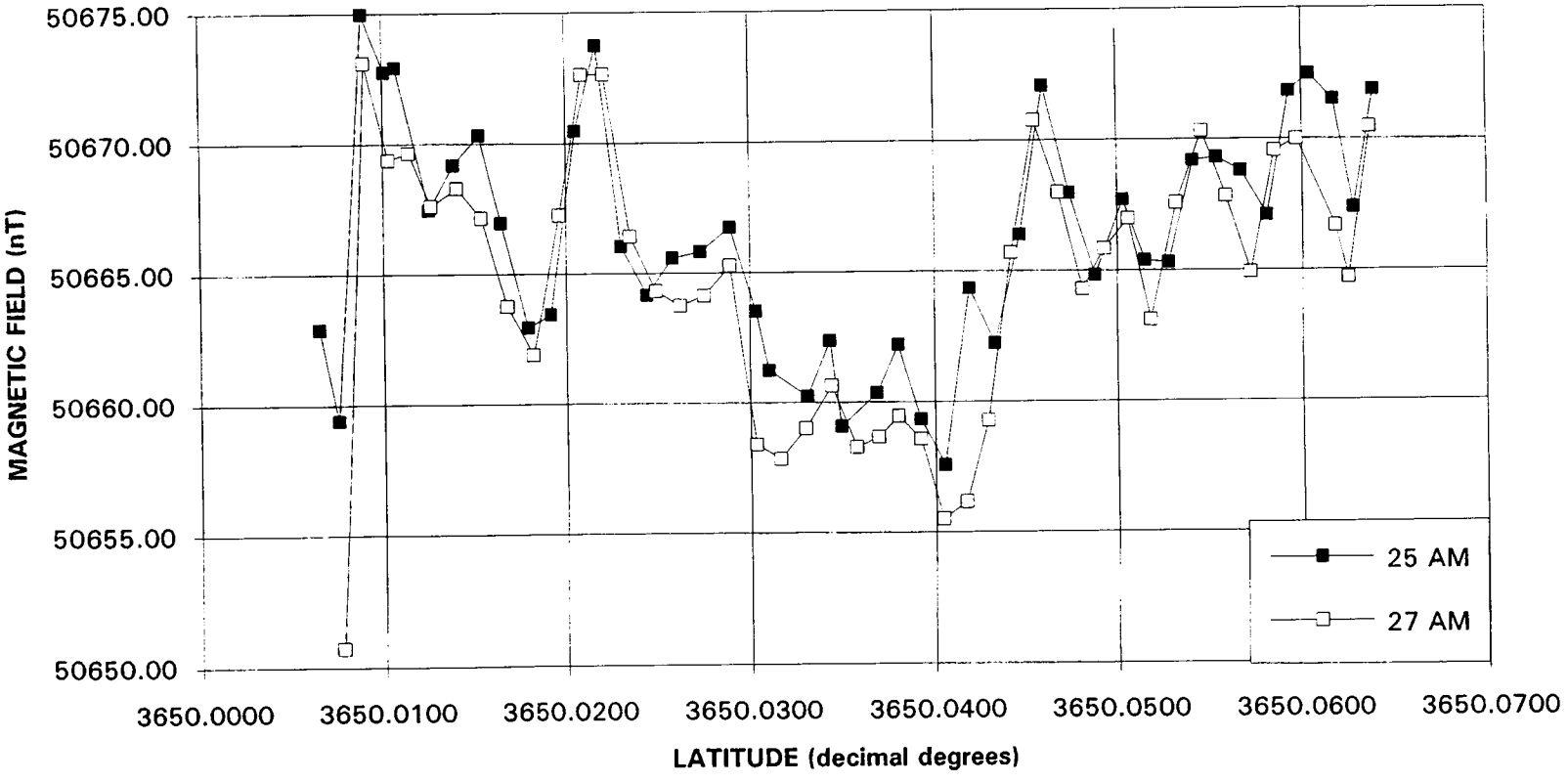

CE
15/20

CL

16/20

GRIDDING OF DATA IN EARTHVISION

Arc/Info coverages were converted into space delimited data files containing x, y, and final corrected magnetic data by creating Arctin files from the coverages, and then ungenerating them to produce a *.pnt file. Values in this file are in scientific notation, but in a format EarthVision cannot read ("E's" must be substituted for "D's" in some entries).

The gridding algorithm used by EarthVision is not well suited to data sets with non-uniform densities. The data sets have very high data density (readings at approximately every 1.5 m) in one direction, and comparatively low density in the other (50 - 200 m spacing). Experimentation with different grid spacing and filtering of initial data is necessary to avoid the loss of a large percentage (50 to 75%) of the data.

EarthVision's minimum tension algorithm does a two-part grid calculation. Initial grid estimate of z-values for nodes are calculated by averaging using an inverse-distance weighting function (see earthVision User Guide, v.1, p.2dg11-12). Single or multiple input data within half a grid cell spacing are used in the determination (the number of input data must be manually set. A default of 4 is set if multiple data are used). Grid nodes are reiteratively evaluated using a biharmonic cubic spline function. **NOTE: Only up to the first 11 (or whatever amount specified when gridding) data points within 1/2 a grid cell spacing are used within the gridding algorithm. Once the data are gridded, the contouring algorithm does <u>not</u> use the original input data, only the gridded data points.**

Experimentation with grid sizes and different filtering methods result in very different maps. Map 1 shows the result when a 16x16 grid was used for contouring the original data. Gridding this data on a 16x16 grid (arrived at by squaring off the default grid cell) resulted in the loss of 10,688 out of 25,568 data points. In order to try and preserve some of the data while gridding, rectangular (15x50) rather than square grid cells were used resulting in a map with linear bias not that could not be supported by data distribution (map 2). 10,249 data points were lost with this grid spacing.

To determine how changing the density of data would affect gridding, these same data was run through a filter to throw out all but every 4th point in the data set. Gridding with a 16x16 spacing resulted in the loss of only 44 points out of 6,392. Map 3 is the resultant map. Filtering the data this way acted as a rough band-pass filter, removing some of the shorter wavelength anomalies and "cleaning up" noise associated with localized features. Map 4 shows (literally) the difference between Map 1 and Map 3. Most of the difference was in area of high gradient on the original map. The filtered map actually uses fewer data points than the original, but there is the advantage of knowing which data were actually used in the gridding.

cc

17/20

USNS 14880

10688 lost

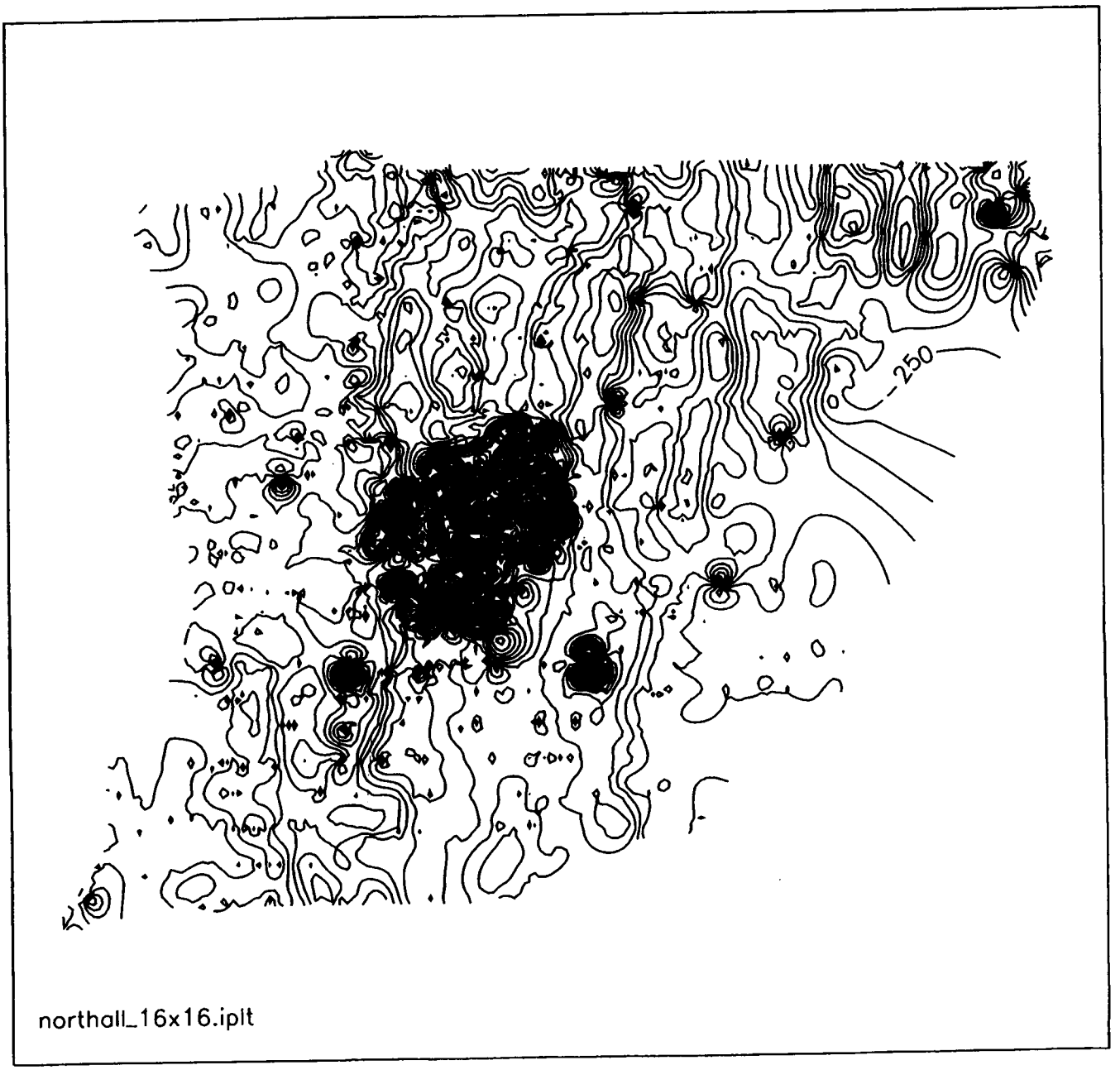

MAP. 1

cc

18/20

25-5-68 in

10249 thrown out

15319 used

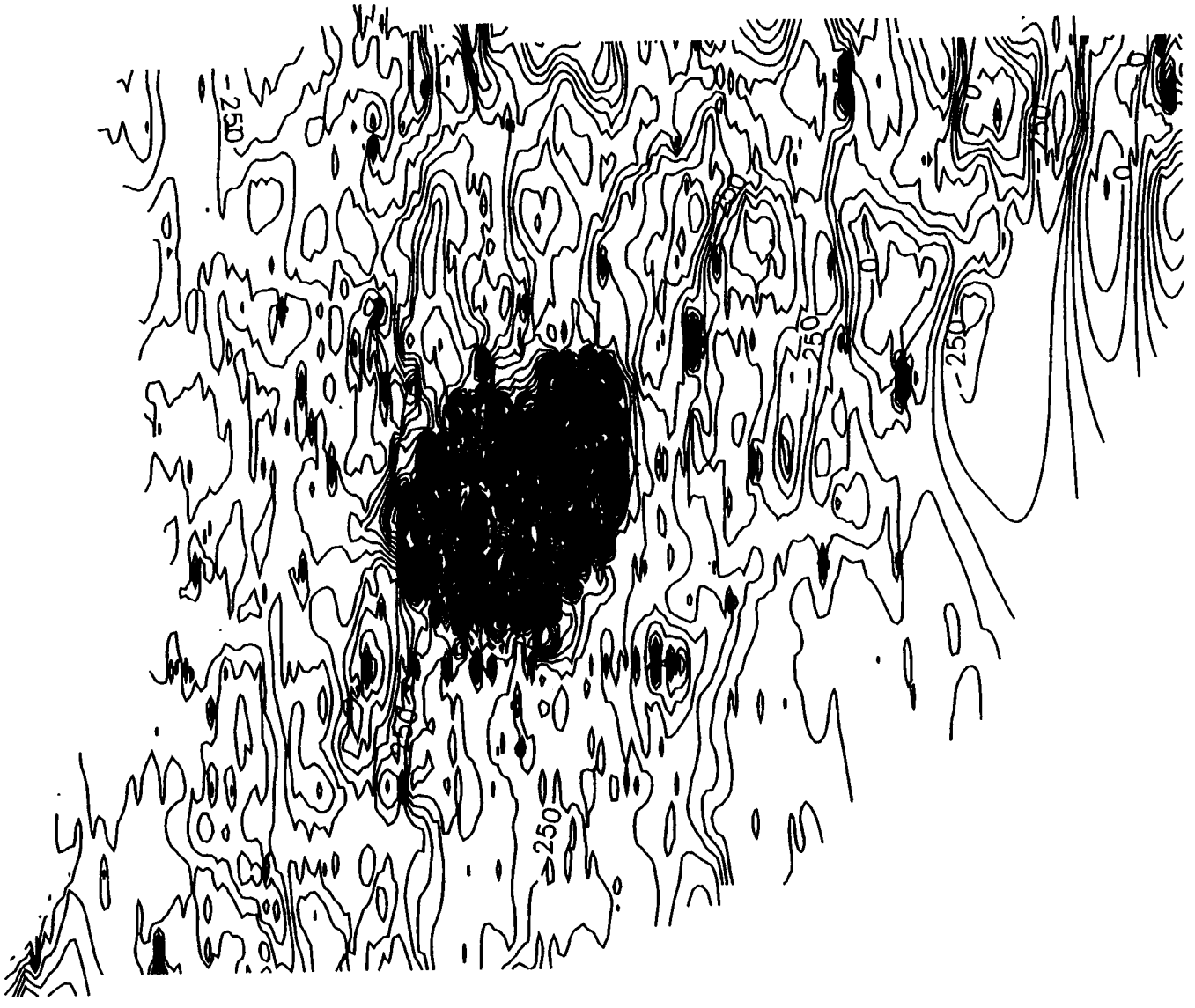

all points 15X50

Map 2

6348 # used
4/4 brown

cc
19/20

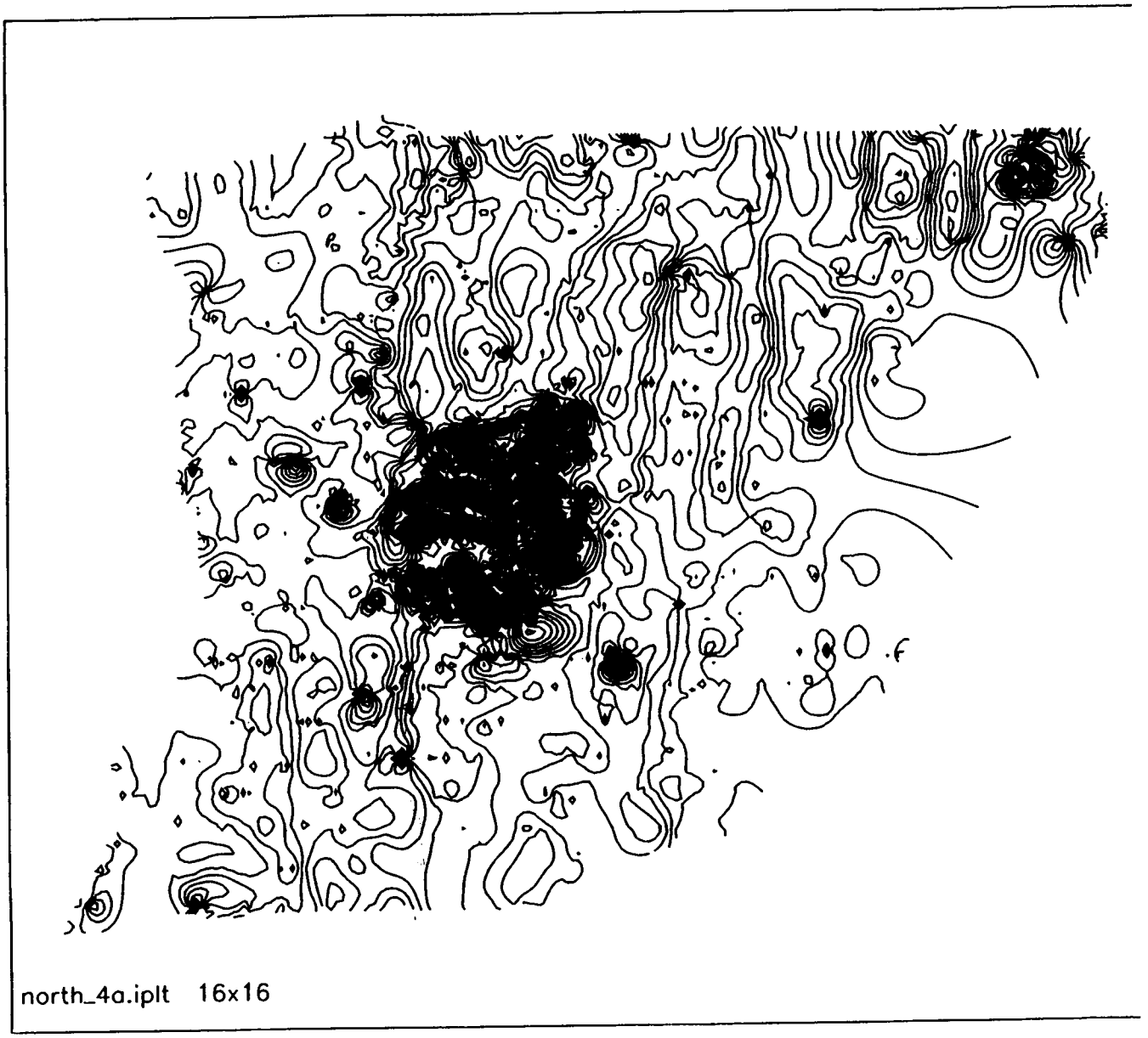

MAP 3.

cc

20/20

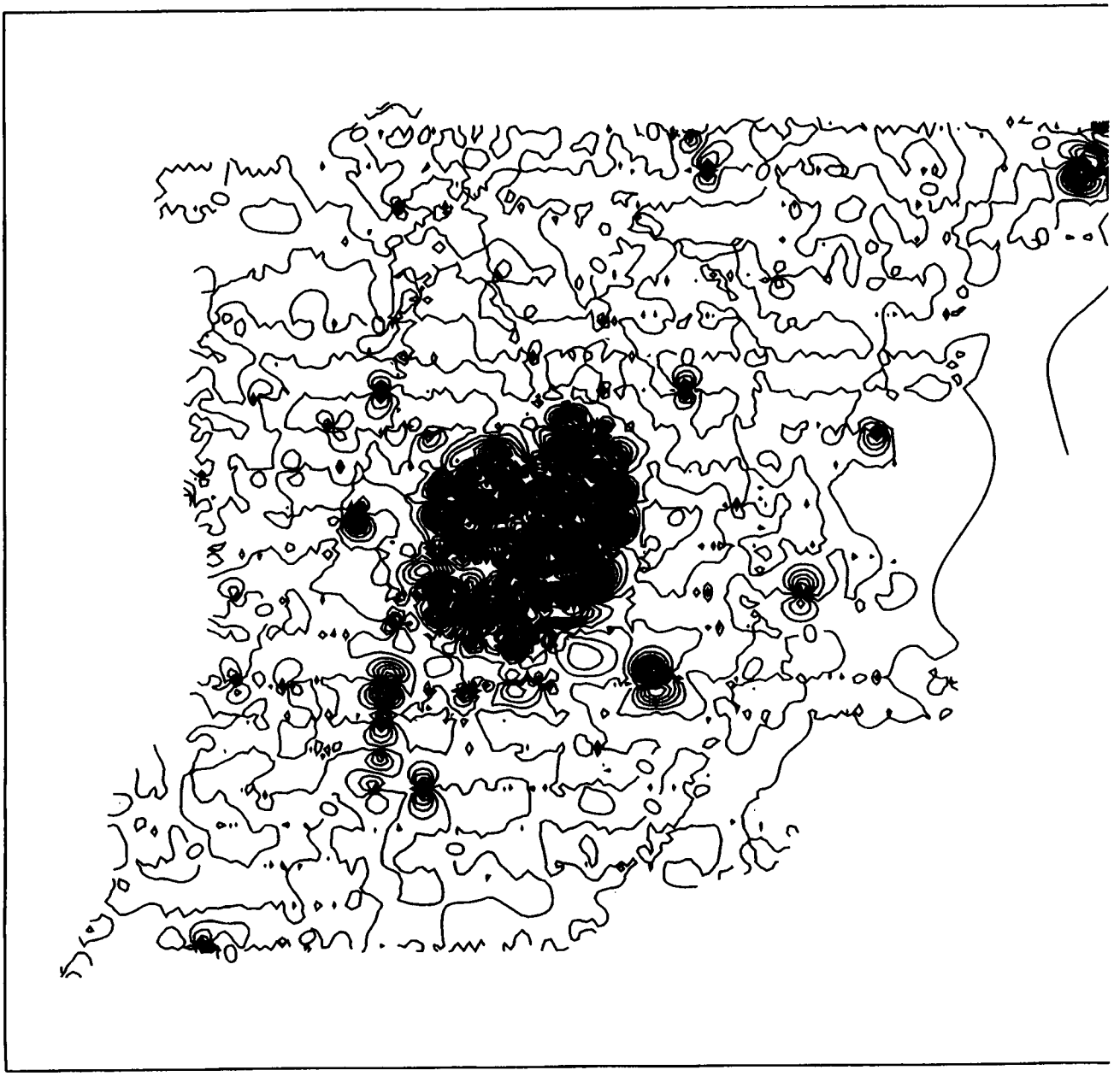

North_diff.ps = North-all-16x16.2grd - North4a.2grd

Mayd